Reinforcement Corrosion: Numerical Simulation and Service Life Prediction

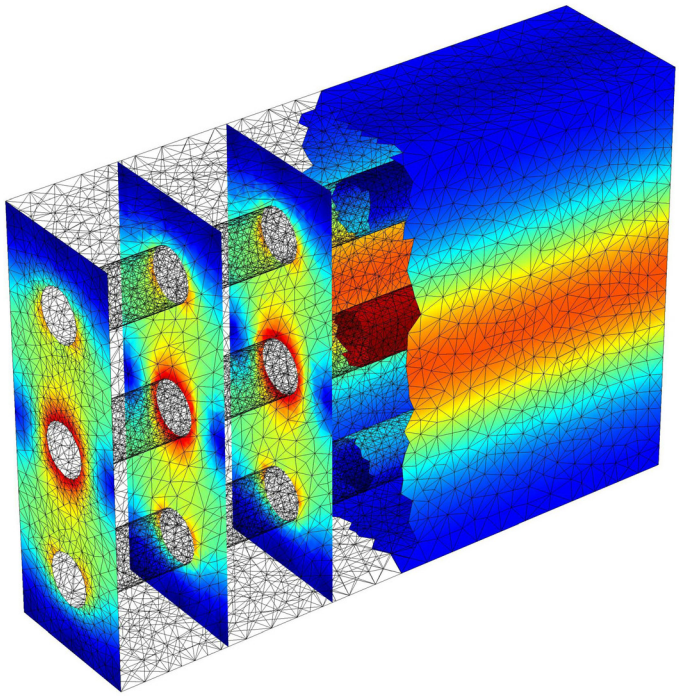

Alexander Michel

PhD Thesis

Department of Civil Engineering

2012

DTU Civil Engineering Report R-266 (UK)
2012

DTU Civil Engineering
Department of Civil Engineering

Reinforcement Corrosion: Numerical Simulation and Service Life Prediction

Alexander Michel

Ph.D. Thesis

Department of Civil Engineering
Technical University of Denmark

2012

Figure front page:
Numerical simulation of potential (surface plot) and corrosion current density (slice plot) distribution in a reinforced mortar specimen.

Reinforcement Corrosion: Numerical Simulation and Service Life Prediction

Printed by Rosendahls-Schultz Grafisk
Department of Civil Engineering
Technical University of Denmark
ISBN: 9788778773494
ISSN: 1601-2917
Report: Byg R-266

Preface

This thesis is submitted as a partial fulfilment of the requirements for the Danish Ph.D. degree. The thesis is based on experimental and numerical investigations carried out as part of the Ph.D. project "Nanotechnology for Civil Engineering Structures: Resistance to Reinforcement Corrosion in Concrete Structures", undertaken at the Department of Civil Engineering at the Technical University of Denmark (DTU Byg), Kgs. Lyngby, Denmark between November 2008 and May 2012.

The project included an external research stay at the University of Newcastle, Australia and two leave of absences; five months at the Norwegian University of Science and Technology (NTNU) in connection with the COIN project (COncrete INnovation centre, www.coinweb.no) and two months at the Danish Expert Centre for Infrastructure.

The principal supervisor of the Ph.D. project was Associate Professor Mette Geiker from DTU Byg with co-supervisors Henrik Stang and John Olesen, also from DTU Byg as well as Steen Lykke from Femern A/S and Leif Vincentsen from Sund & Bælt Holding A/S.

Financial support was provided by Femern Bælt A/S, Sund & Bælt Holding A/S and The Danish Agency for Science, Technology and Innovation

Kgs. Lyngby the 14th of August 2012

Alexander Michel

Acknowledgments

I would like to express my deepest appreciation to my supervisors, Mette Geiker, Henrik Stang, and John Olesen at the Technical University of Denmark as well as Steen Lykke at Femern A/S and Leif Vincentsen at Sund & Bælt Holding A/S. Further, I would like to thank Ulf Jönsson from Femern A/S for his valuable input to the thesis. I enjoyed our numerous discussions during which I gained immeasurable knowledge and experience from them and with them.

I would also like to thank Rob Melchers and his group for the wonderful time at the University of Newcastle, Australia.

Furthermore, I would like to acknowledge the financial support of Femern Bælt A/S, Sund & Belt Holding A/S and The Danish Agency for Science, Technology and Innovation for funding this Ph.D. project. Financial contributions supporting experimental investigations, travelling, and conference attendances from Otto Mønsteds Fond, COWIfonden, Otticon Fonden, Taumoses Legat, and Larsen and Nielsen Fonden were also much appreciated

Further, I would like to thank my colleagues and fellow Ph.D. students at the Technical University of Denmark for the fantastic time at and outside the university over the past years; special thanks to Anders, Anna, Brad, Christian, Ieva, Jacob, Jan, Jonas, Lárus, and Rasmus.

Finally, I would like to thank my family and friends close to me for the constant support and encouragement during the past years.

Abstract

Modelling of deterioration processes in concrete structures plays an increasing role in the design of reinforced concrete structures. Large sums are spent every year to ensure the durability of concrete structures, especially towards reinforcement corrosion. Improved durability provides increased structural reliability, economical improvements in form of less need for maintenance and repair as well as increased sustainability due to an increased energy and resource efficiency. Several service life prediction models dealing with reinforcement corrosion in concrete structures can be found in the literature. However, the applicability of these models to determine the service life of concrete structures in aggressive environments needs to be investigated as the majority of the models a) assume an initial pristine state of the reinforced concrete structure neglecting the presence of cracks and other defects and b) define the end of service life once reinforcement corrosion is initiated neglecting corrosion processes during the propagation stage.

The goal of this work was to develop a framework for the service life prediction of reinforced concrete covering initiation and propagation of chloride-induced reinforcement corrosion. The framework includes coupled models describing transport of various substances and corrosion of reinforcement in cracked and uncracked concrete. The framework further allows for subsequent prediction of corrosion-induced mechanical damages.

To describe the transport of various substances in concrete, a heat and mass transport model was applied, which is based on thermodynamic principles. To incorporate the influence of temperature and chloride on the moisture sorption, extensions were made using experimental results. The impact of chlorides on the moisture sorption was accounted for using experimental data available in the literature. To quantify the impact of temperature on the moisture sorption, experimental investigations were undertaken by means of time domain reflectometry (TDR), in which concrete specimens were subjected to varying temperatures. Using TDR measurements in combination with multi layer adsorption theory, it was shown that it is possible to quantify the impact of temperature on the moisture sorption of cementitious materials to a large extent. To incorporate the impact load-induced cracks have on the ingress, a simplified crack geometry was used, which may be divided into two parts; 1) a coalesced crack length that behaves as a free surface for moisture ingress, and 2) an isolated micro-cracking length that resists ingress similarly to the bulk material. The ability of the applied transport model to simulate the moisture ingress in cracked and uncracked concrete specimens was demonstrated comparing experimental ingress results and numerical simulations.

The corrosion model, which is coupled to the transport model, was used to describe electrochemical processes at the reinforcement surface. The corrosion model was

based on generally accepted physical laws describing thermodynamics and kinetics of electrochemical processes. The applicability of the model to capture various reinforcement corrosion phenomena, such as activation, resistance, and concentration polarisation as well as the impact of temperature and relative humidity was demonstrated comparing experimental data and numerical simulations. In addition, experimental investigations were carried out to study the impact of load-induced cracks on the risk of reinforcement corrosion. Instrumented rebars, developed in a previous study, were used to assess the potential for initiation of corrosion along the reinforcement surface. Good correlations were found between the extent of separation between concrete and reinforcement and the risk of corrosion along the reinforcement surface, which supports earlier observations on the detrimental impact of the concrete-reinforcement interfacial condition.

To describe corrosion-induced mechanical damages, a thermal analogy was used modelling the expansive nature of solid corrosion products. Input for the mechanical model was the corrosion rate predicted by the corrosion model. The mechanical model further accounted for the penetration of solid corrosion products into the available pore space of the surrounding cementitious materials. Based on x-ray attenuation measurements, a concept describing the penetration of solid corrosion products was developed. The capability of the mechanical model to simulate corrosion-induced concrete cracking was shown comparing numerical simulations with experimental data obtained from accelerated corrosion tests.

During this Ph.D. study, the framework for the service life prediction of reinforced concrete was established and the individual models tested comparing laboratory data and numerical simulations. However, for a validation of the framework combining all models additional (in-situ) investigations are required.

Resumé (in Danish)

Store summer bruges hvert år for at sikre holdbarheden af betonkonstruktioner, især mod armeringskorrosion. Forbedret holdbarhed giver øget konstruktiv pålidelighed, økonomiske forbedringer i form af mindre behov for vedligeholdelse og reparation samt øget bæredygtighed på grund af en øget energi-og ressourceeffektivitet. Modellering af nedbrydningsprocesser spiller en stadig større rolle ved projektering af armerede betonkonstruktioner, og der findes i litteraturen flere modeller til forudsigelse af udviklingen af armeringskorrosion i betonkonstruktioner. Anvendeligheden af flere af disse såkaldte levetidsmodeller er dog begrænset af, at de dels er basert på antagelsen af, at betonen er fri fra revner og andre defekter, dels definerer begyndende korrosion som slutningen af levetiden og derved ikke tager højde for, at et vist korrosionomfang ikke nødvendigvis har indflydelse på den konstruktive opførsel.

Formålet med det her rapporterede arbejde var at udvikle en skabelon for levetidmodellering af armeret beton udsat for chlorid-initieret armeringskorrosion og omfattende både initierings og propagerings fasen. Skabelonen omfatter koblede modeller, der beskriver transport af stoffer og korrosion af armering i revnet og urevnet beton. Skabelonen giver desuden mulighed for efterfølgende beregning af udviklingen af korrosion-inducerede mekaniske skader.

Transport af stoffer i beton beregnes vha. en varme- og massetransport model, som er baseret på termodynamiske principper. Indflydelsen af temperaturen og chlorid på fugtsorption modelleres på basis af eksperimentelle resultater. Indflydelsen af chlorid er beskrevet vha. Litteratdata, mens effekten af temperaturen på fugtsorption blev bestemt vha. ”Time Domain Reflectometry” (TDR). TDR-målinger i kombination med fler-lag-adsorptionsteori gav således i vid udstrækning mulighed for at kvantificere virkningen af temperaturen på fugtsorption af cementbaserede materialer. Indflydelsen af bøjningsrevner på indtrængning af stoffer er beskrevet vha. en forenklet revnegeometri, som kan opdeles i to dele: 1) en revnedel, der fremtræder som en fri overflade, og 2) en isoleret del, der modstår indtrængen i lighed med bulkmaterialet. Evnen af transportmodellen til at simulere fugtindtrængning i revnet og urevnet beton er eftervist ved sammenligning af eksperimentelle data og numeriske simulationer.

Korrosionensmodellen, som er koblet til transportmodellen, anvendes til at beskrive de elektrokemiske processer på armeringens overflade. Modellen er baseret på almindeligt anerkendte fysiske love, der beskriver termodynamikken og kinetikken af de elektrokemiske processer. Anvendeligheden af korrosionmodellen til at beskrive forskellige korrosionsfænomener som aktiverings-, modstands- og koncentrationspolarisering samt indflydelsen af temperatur og relativ fugtighed er vist sammenligning af eksperimentelle data og numeriske simulationer. Eksperimentelle undersøgelser blev udført for at undersøge virkningen af bøjningsrevner på risikoen for armeringskorrosion. Armeringsstænger instrumenterede med isolerede korrosionssensorer (udviklet i

et tidligere ph.d. projekt) blev anvendt til at måle det elektrokemiske potentiale langs armeringens overfladen. Der blev fundet god sammenhæng mellem graden af adskillelse mellem beton og armering og risikoen for korrosion langs armeringens overflade. Dette understøtter tidligere observationer af den skadelige virkning af defekter ved armerings overflade.

Korrosioninducerede mekaniske skader modelleres vha. en termisk analogi, som beskriver den ekspansive karakter af faste korrosionsprodukter. Den mekaniske model tager hensyn til, at ikke al korrosion medfører ekspansion, idet en del af de faste korrosionsprodukter trænger ind i det tilgængelige porerum i den omkringliggende beton. Indtrængning af faste korrosionsprodukter i betonen er modelleret på basis af røntgenmålinger. Den mekaniske models evne til at simulere korrosion-induceret revnedannelse i beton er eftervist ved sammenligning af numeriske simuleringer og eksperimentelle data fra accelererede korrosionstest.

Under ph.d. studiet er der udviklet en skabelon med tilhørende transport, korrosions- og mekaniske modeller til levetidsforudsigelse af armeret beton i chloridholdigt miljø. De enkelte modeller er eftervist ved sammenligning af laboratoriedata og numeriske simuleringer, mens en samlet eftervisning af alle modeller forudsætter indsamling af yderligere (in-situ) data.

Table of Contents

Part I

Introduction and Summary

Chapter 1

Introduction

1.1 Background

Concrete is nowadays the most used manmade building material in the world with an annual production of approximately 10 billion tons. Low price, excellent material properties, and reasonable energy consumption for production are main reasons for the success of concrete compared to other building materials, such as steel or wood. Moreover, the raw materials required for concrete production can be found in almost any place of the world. Easy transport of the compounds by means of common infrastructure allows for mixing and casting of the final material on-site as well as in prefabrication sites. Further advantage of concrete is given by its initial state, i.e. before setting and hardening. Initially, concrete is quasi-liquid allowing moulding it in almost any shape to fulfil architectural and aesthetic requirements.

For structural purposes, concrete is often reinforced with steel, which helps to overcome shortcomings of both materials. Concrete has a high compressive strength, but a low tensile strength and is therefore reinforced for structural purposes, while the steel is protected by the concrete from potentially harming environmental exposure. Some examples of structural applications of reinforced concrete are illustrated in Figure 1.1. Under certain circumstances, however this “symbiosis” can be destroyed resulting in a deterioration of the structure. Corrosion of steel embedded in concrete is one of the major deterioration mechanisms causing considerable losses to society due to maintenance and repair needs. In the European Union more than € 250 billion are spent annually for maintenance and repair of concrete structures due to deterioration [*Li 2004*], in which corrosion of reinforcing steel is estimated to be related to the major part of the degradation problems [*Rendell et al. 2002*]. Corrosion-induced damages,

such as concrete cracking, spalling, delamination, and cross sectional reduction of the reinforcement, may cause aesthetic damages, decrease the load bearing capacity of a structure, and in the worst-case lead to fatal structural consequences, such as failure.

Typically, the high alkalinity (pH ≈13), as a result of the cement hydration, and oxygen availability lead to the formation of a thin iron oxide layer (passive film) at the steel surface [*Arup 1983*, *Küter 2009*] protecting the reinforcement. Under these conditions, the resulting corrosion rates (~0.1 μm/year) are negligible from an engineering point of view. In addition, the concrete cover itself hinders the ingress of aggressive substances, such as carbon dioxide, chloride ions, moisture, and oxygen, providing additional protection for the reinforcement. Well designed and executed reinforced concrete structures (especially concretes with low water-to-cement ratios (w/c) or supplementary cementitious materials (SCMs)), i.e. with a dense, sufficient, and pristine concrete cover, are able to withstand corrosion for several decades as the transport kinetics through an intact and dense concrete cover are considerably limited.

Figure 1.1 *Different structural and architectural applications of reinforced concrete structures. Top left and top right: Sydney Opera House, Sydney; bottom left: Rolex Learning Centre at École Polytechnique Fédérale de Lausanne (EPFL), Lausanne; bottom right: City Centre San Francisco, San Francisco (Author's photos).*

In practice however, cracks can be found in nearly all reinforced concrete structures originating e.g. from poor execution, wrong mix designs, hygral or thermal shrinkage and/or mechanical loading. While some of these cracks can be avoided by a careful mix design and execution of the reinforced concrete structure, load-induced cracking is inevitable.

1.2 Service life

For centuries, the design of concrete structures was governed by the capability to withstand static and dynamic loads. Within the past century, the development of experiments and stringent theories led to an increased understanding of the stress and strain state in materials when subjected to loads and forces. Today, increasing computational power and modern design tools indeed enable civil engineers to design complex concrete structures and determine deformations and stresses within acceptable limits. This increased understanding of the mechanical response of concrete structures along with the development of new high performance materials allows for a reduced consumption of materials when designing and building modern concrete structures.

However, due to rising awareness of the need for sustainable design and ever increasing service life requirements for modern concrete structures (up to 100 or even 200 years of expected service life), the design and dimensions (e.g. water-to-cement ratio or concrete cover thickness) of reinforced concrete structures in aggressive environments is at present mainly governed by durability issues. As a result, the development of models to design and determine the (residual) service life of reinforced concrete structures has gained momentum within the past decades in the civil engineering community, in particular with respect to reinforcement corrosion.

The service life of a reinforced concrete structure may be defined as the length of time during which a desired level of functionality is maintained. Typically, the end of service life is defined by a limit state, which is given by the owner of the structure. Frequently used limit states are for instance the initiation of reinforcement corrosion, appearance of rust stains, corrosion-induced damages or failure of the structure. Once the defined limit state is reached, repair strategies or deconstruction may be initiated by the owner. Detailed information on repair strategies for concrete structures suffering from reinforcement corrosion can be found in e.g. [*DS/EN 1504*].

Durable design of reinforced concrete structures is most often realised using standards and codes (e.g. [*Eurocode2 2004*]) or simply experience, which are often based on simplified assumptions and do not account for important phenomena affecting the service life. Less frequently, service life models and recommendations, such as DuraCrete [*DuraCrete 2000*], *fib* [*fib Bulletin 34 2006*], Life-365 [*Ehlen et al. 2009, Life-365 Consortium II 2010*], 4sight [*Synder 2001*], Hetek [*Nilsson et al. 1996, Frederiksen & Poulsen 1997*], DuCOM [*Maekawa et al. 1999*], and Stadium® [*Samson et al.*

2007], are used by civil engineers to estimate the service life and design durable structures.

1.3 Service life prediction

In general, the basic concept developed by [*Tuutti 1982*], which is illustrated in Figure 1.2 ('typical service life model'), is employed in all of the previously mentioned service life models and recommendations to determine the (residual) service life of reinforced concrete structures exposed to aggressive environments. According to [*Tuutti 1982*] the service life of a structure is comprised of two distinct phases; 1) the initiation phase during which aggressive substances penetrate the concrete cover, eventually causing initiation of reinforcement corrosion and 2) the propagation phase, when reinforcement corrosion-induced damages cause an increased rate of deterioration.

Reinforcement corrosion (depassivation) is typically initiated as a result of either concrete carbonation or chloride ingress. Carbonation due to the penetration of carbon dioxide through the protecting concrete cover leads to a neutralisation of the cement paste with a corresponding reduction of the pH (to approximately 9) initiating reinforcement corrosion. Also, penetration of chloride ions through the concrete cover and the accumulation beyond a certain critical concentration near the reinforcement surface can lead to the destruction of the passive film. Reinforcement corrosion may subsequently be initiated provided that enough moisture and oxygen is present in the vicinity of the reinforcement. In contrast to carbonation-induced corrosion, chloride-induced corrosion results typically in the formation of macro-cells (localised corrosion). These macro-cells are usually characterised forming distinct anodic and cathodic regions along the reinforcement, with considerably higher corrosion rates compared to carbonation-induced corrosion.

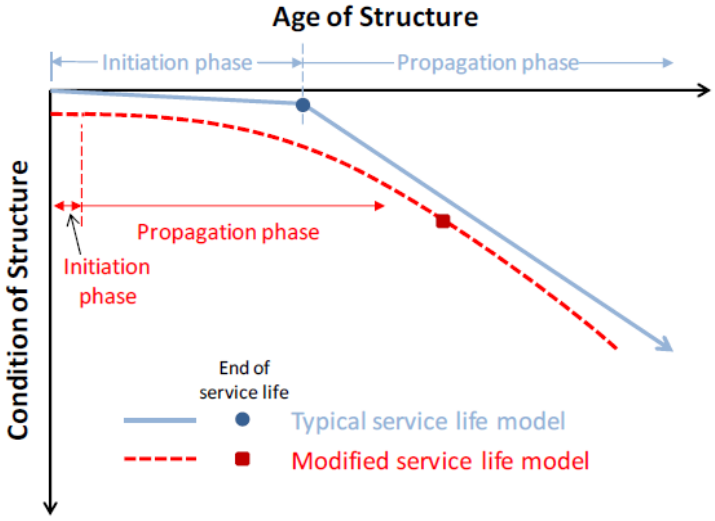

Figure 1.2 *Service life model proposed by [Tuutti 1982] and modified service life model taking initial structural defects into account, from [Pease et al. 2012].*

Once corrosion is initiated, the rate of structural deterioration is often considerably increased compared to the initiation phase. The expansive nature of most of the solid corrosion products may result in the formation of cracks in the concrete cover, concrete spalling or delamination. Strength and serviceability of reinforced concrete structures may be further affected by the cross sectional reduction of the reinforcement leading in the worst case to failure. Therefore, extensive research has been carried out within the past decades studying and developing models and tools to describe mechanical degradation mechanisms of corroding reinforced concrete structures, see e.g. [*Bazant 1979, Andrade et al. 1993, Alonso et al. 1998, Liu et al. 1998, Noghabai 1999, Ouglova et al. 2006, Caré et al. 2008, Chernin et al. 2009, Val et al. 2009*]. More recently, the research community also placed focus on studying the corrosion processes in reinforced concrete structures once corrosion is initiated and developed models to describe the propagation phase, see e.g. [*Jäggi 2001, Kranc et al. 2001, Maruya et al. 2003, Ouglova et al. 2005, Isgor et al. 2006, Osterminski et al. 2006, Warkus et al. 2006, Warkus et al. 2008*].

Although the aforementioned service life models and recommendations are generally accepted and used in civil engineering for the design of durable reinforced concrete structures, several key issues remain that must be included in service life modelling for a more accurate qualification and quantification of the service life of concrete structures.

As mentioned earlier, the end of service life is defined by a limit state at which either repair/maintenance or deconstruction of the structure is required. Current service life models (see e.g. DuraCrete, *fib*, Life-365, 4sight, and Hetek) describe the (residual) service life of reinforced concrete structures analysing the ingress of aggressive substances into the concrete. Once a defined limit state is reached, e.g. a critical chloride threshold in case of chloride-induced corrosion, the initiation phase of reinforcement corrosion and often the service life of a reinforced concrete structure is ended. In some cases, non-commercial service life models consider the propagation phase (e.g. Life-365, *fib*), although only as a fixed length of time [*Life-365 Consortium II 2010*] or based on expert opinions *[fib Bulletin 34 2006*]. In the Life-365 service life model, the propagation period is fixed to 6 years for regular reinforcement, 20 years if epoxy-coated steel is used or can be changed according to local expertise. To determine the propagation period in the *fib* model code, expert opinions were used to estimate the time to concrete cracking or spalling (defined as ultimate limit states) for carbonation-induced reinforcement corrosion. Although mentioned in the *fib* model code, various phenomena and processes affecting the corrosion rate and consequently the formation of solid expansive corrosion products (e.g. activation and concentration polarisation, moisture content, and arrangement of reinforcement) are not taken into account.

Furthermore, the impacts of cracks on the ingress of aggressive substances as well as the corrosion process itself need to be considered, especially load-induced and shrinkage cracks, which are inevitable in reinforced concrete structures (apart from pre- and

post-tensioned concrete structures) and already included in the design of reinforced concrete structures, see e.g. [*Eurocode2 2004*]. Current assumptions made in most service life models (see e.g. DuraCrete, *fib*, Life-365, 4sight, and Hetek) of initial pristine state of the reinforced concrete structure, may lead to a considerable overestimation of the time-to corrosion initiation.

Hence, for a more accurate qualification and quantification of the service life of concrete structures, the impact of cracks on the ingress behaviour of aggressive substances and corrosion processes as well as the propagation phase of reinforcement corrosion must be considered in such models to represent realistic scenarios for reinforced concrete structures.

The concept of a modified service life model is also illustrated in Figure 1.2 (as indicated by the broken red line), along with the typical service life approach suggested by Tuutti [*Tuutti 1982*]. The modified service life model takes into account more realistic initial conditions of concrete structures, as indicated by the imperfect structural condition at the beginning of the structure's lifetime. This means that the end of service life can no longer be defined as the time of corrosion initiation; in fact, the propagation of reinforcement corrosion must be included to obtain a reasonable service life. Consequently, limit states may be defined, which correspond to different damage levels that are acceptable for different types of structures. Such limit states may be for example a) unacceptable aesthetics due to rust staining, b) formation of cracks or concrete spalling, and c) the structural safety of the structure is comprised.

1.4 Objectives

Considering the aforementioned considerations, the objectives of this Ph.D. project were:

- Development of a theoretical framework that combines reinforcement corrosion processes, transport processes, and mechanical performance, including:
    - Quantification and modelling of parameters influencing the initiation and propagation of the reinforcement corrosion process, taking into account material properties and boundary conditions.
    - Quantification and modelling the impact cracks have on the ingress of various substances and the reinforcement corrosion process.
    - Quantification and modelling of corrosion-induced damages during the propagation phase of reinforcement corrosion.
- Establish, test and demonstrate the applicability of the theoretical framework for the modelling of reinforcement corrosion in concrete.

1.5 Scope

1.5.1 Research approach

Taking into account the modified service life model presented in Figure 1.2 and bearing in mind the aforementioned considerations, models necessary for a service life prediction of reinforced concrete structures subjected to aggressive environments may be identified. The fundamental concept of the proposed framework is given in Figure 1.3 illustrating models to assess the reinforcement corrosion state and rate and subsequently determine the service life.

To allow for the service life prediction of reinforced concrete structures, three models are included in the framework, i.e. a material and transport model, a corrosion model, and a mechanical model. While the corrosion model describes the electrochemical processes taking place at the reinforcement surface, the material and transport model simulates the ingress of various substances and heat. The corrosion and transport model are fully coupled, which allows for the simulation of initiation and propagation of reinforcement corrosion. Load-induced as well as corrosion-induced damages are described by the mechanical model. Information from the mechanical model maybe further coupled to the transport model to account for the impact of concrete damages (e.g. cracks, slip and separation between reinforcement and concrete) on the ingress of various substances.

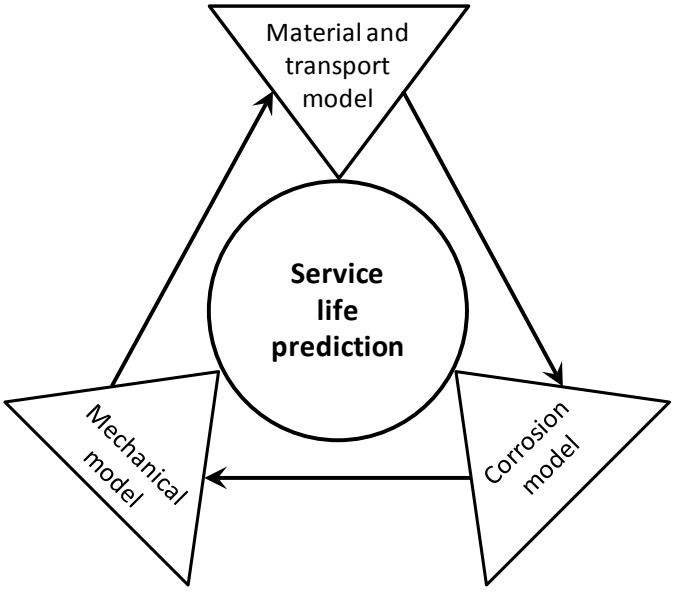

Figure 1.3 *Proposed framework and models to predict the service life of a reinforced concrete structure subjected to corrosion, from [Michel et al. 2010].*

To describe the interaction between the environmental exposure and the 'inner climate' of concrete structures, material and transport models are needed. The description of the transport and state of heat and mass is a key issue for the service life prediction of reinforced concrete structures. The thermodynamics and kinetics of the reinforcement corrosion process are highly coupled to the presence of different substances, such as moisture, oxygen, chloride ions, and carbon dioxide. Models describing the transport and state of these substances, potentially leading to reinforcement corrosion, must take into account the most common transport mechanisms in porous media, as for example diffusion, convection or migration. Furthermore, potential interactions between the various substances under consideration must be accounted for in such models.

For an accurate description of the service life, corrosion models are indispensable describing the electrochemical processes at the steel surface and in the surrounding concrete. Both, thermodynamics, i.e. the likelihood of certain electrochemical reactions and their tendencies to occur in a certain environment, and kinetics of the corrosion process, i.e. information on the corrosion rate, must be treated within such a framework. Thus, the corrosion model must be coupled to the material and transport model, as the thermodynamics and kinetics of the corrosion process are highly dependent on the presence of certain substances. For example, the tendency of corrosion initiation in case of chloride-induced corrosion is attributed to the local breakdown of the protecting passive layer, which is mostly related to the presence of chloride ions. Concerning corrosion kinetics, it is well known, that moisture, oxygen, and temperature have considerable effects on the corrosion rate. The moisture content is one of the main parameters controlling for example the concrete resistivity, which is inversely proportional to the corrosion rate.

As mentioned previously, (load-induced) cracks are inevitable in reinforced concrete structures (apart from pre- and post-tensioned concrete structures). The formation of cracks due to applied loads is accompanied with a debonding and separation between the steel and concrete, which has considerable effects on the ingress of aggressive substances and subsequent initiation of corrosion [*Pease 2010*]. Thus, mechanical models must be used that are capable of describing structural degradations of the concrete and concrete/steel interface due to various damage phenomena associated with load-induced cracking. Moreover, additional corrosion-induced damages such as concrete cracking, spalling or delamination as well as cross sectional reduction of the reinforcement and the corresponding reduction in load bearing capacity must be part of the modelling process.

More detailed state-of-the-art reviews of the various processes and phenomena associated with the models presented in Figure 1.3 are given in the corresponding chapters of this Ph.D. thesis.

1.5.2 Limitations and assumptions

To limit the scope of the work the following limitations and assumptions are made:

Heat and mass transport in porous media

- The transport of heat and mass in the cementitious material is described by macroscopic transport functions.
- Changes in the microstructure due to the interaction of chloride ions with the solid phases of cementitious materials are indirectly accounted for by experimental observations on the moisture sorption behaviour.
- The impact of sorption hysteresis on the moisture state is not included in the present model.
- Potential self-healing of cementitious materials is not accounted for when modelling the impact cracks have on the ingress of aggressive substances.

Corrosion of steel in concrete

- Electrochemical half-cell reactions are preselected.
- Critical chloride thresholds are constant over time.
- Potential self-healing of cementitious materials, penetration of solid corrosion products into cracks, and closure of cracks due to stress relaxation are neglected.

Corrosion-induced concrete damage

- Formation of solid corrosion products is assumed.
- Solid corrosion products are assumed to form uniformly around and in the vicinity of the reinforcement.

1.6 Organization of thesis

This Ph.D. thesis is comprised of two parts:

- In Part I, the main thesis, previous research, descriptions and results of experimental and modelling work are presented. Finally, Part I of the thesis is concluded with a discussion of the results and findings and conclusions are drawn from that. An overview of the work conducted throughout the Ph.D. study including related publications is schematically presented in Figure 1.4. Experimental work and techniques conducted in collaboration with others are briefly presented in Table 1.1
- Part II is a collection of papers prepared during the Ph.D. project.

Chapter 2 of the thesis provides an overview of the most important transport phenomena in porous media and their coupling. Initially, the fundamentals of coupled heat and mass transfer are presented. Subsequently, the influence of temperature and chloride ions on the moisture sorption in cementitious materials and consequences for the transport processes are dealt with. Results of time domain reflectometry (TDR) measurements in combination with multilayer adsorption theory are used to model the impact of temperature on the amount of adsorbed water of different cementitious materials. Further, experimental results of x-ray attenuation measurements are used to model and quantify the impact of cracks on the ingress of moisture. Finally, an example of the capability of the employed material and transport model is provided.

Chapter 3 deals with the numerical simulation of corrosion processes in reinforced concrete structures. Basic principles of reinforcement corrosion processes in concrete are presented initially. Experimental results and data from the literature are used in the following to quantify and model the impact of temperature, oxygen, and chloride on the initiation and propagation of reinforcement corrosion. Subsequently, experimental results on the impact of cracks on the initiation of reinforcement corrosion in plain and steel fibre reinforced concrete are presented. Finally, a numerical example to demonstrate the use of the proposed model to predict the service life is presented, in which a simple beam geometry with and without a crack is studied.

Chapter 4 addresses the modelling of corrosion-induced concrete damages. The basic concept of a finite element based modelling approach for the simulation of corrosion-induced concrete cracking is presented. Experimental results of x-ray attenuation and digital image correlation are presented, which allow for the improvement of the performance of corrosion-induced cracking models. These experimental results are subsequently used to further develop a finite element based cracking model, which includes the penetration of solid corrosion products into cementitious materials.

Chapters 5 and 6 summarise and discus selected experimental and modelling work presented in the preceding chapters and from the appended papers in Part II. These results and findings are put into perspective of service life prediction for reinforced concrete structures subjected to chloride-induced corrosion as a conclusion of the thesis. Finally, recommendations for future work are given.

Table 1.1 *Overview of experimental work and techniques conducted in collaboration with others throughout the Ph.D. project.*

Chapter	Paper	Experimental technique	Information on	In collaboration with
II	I	Time domain reflectometry	Impact of temperature on moisture sorption	*Henryk Sobczuk*: Lublin University of Technology, Poland
	II	X-ray attenuation	Impact of cracks on ingress of moisture	*Brad Pease (Ph.D. project)*: Technical University of Denmark (DTU), Denmark
III	III	Potentiodynamic linear polarization, galvanostatic pulse	Influence of temperature and moisture on kinetics of reinforcement corrosion	*Peter Vagn Nygaard*: Swiss Federal Laboratories for Materials Science and Technology (EMPA), Switzerland
	VI VII	Photogrammetry, digital image correlation	Description of concrete-steel interfacial damage	*Anders Solgaard (Ph.D. project)* and *Brad Pease*: Technical University of Denmark (DTU), Denmark
	VIII	Corrosion potential measurements	Relation between damage at the concrete-steel interface and initiation of reinforcement corrosion	*Anders Solgaard (Ph.D. project)* and *Brad Pease*: Technical University of Denmark (DTU), Denmark
IV	X	X-ray attenuation	Penetration of corrosion products	*Brad Pease*: Technical University of Denmark (DTU), Denmark
	XII	Photogrammetry, digital image correlation	Elastic modulus of reinforcement corrosion products	*Brad Pease* and *Anna Thybo (Ph.D. project)*: Technical University of Denmark (DTU), Denmark

Chapter 2	Chapter 3	Chapter 4
Transport of mass and heat in porous media	Corrosion of steel in concrete	Corrosion-induced concrete damage
Paper I - Paper II	Paper III - Paper VIII	Paper IX - Paper XIII

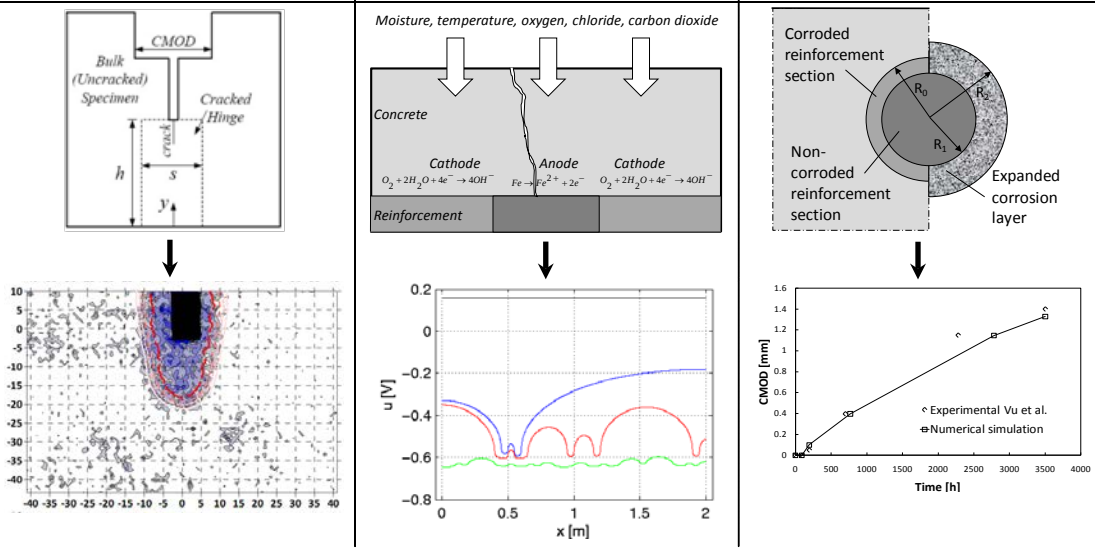

Figure 1.4 *Main topics of each chapter of the Ph.D. thesis and corresponding publications.*

Chapter 2

Transport of mass and heat in porous media

2.1 Introduction

This chapter provides an overview of the most important transport phenomena in porous media and their coupling. The chapter is comprised of several sections. In Sections 2.2 and 2.3, the fundamentals of coupled heat and mass transfer are presented. However, the intention of the sections is not to give a complete review of the various transport phenomena and there derivations from thermodynamic principles as this information can be found elsewhere, see e.g. [*Philip et al. 1957, De Vries 1958, Lykow 1958, Krischer 1978, Dullien 1979, Bear et al. 1991*]. The intention is to introduce common terms and concepts related to the work carried out during this Ph.D. study.

The influence of temperature and chloride ions on the moisture sorption of cementitious materials and consequences for the transport processes are illustrated in Section 2.4. Full details on the potential use of time domain reflectometry (TDR) measurements to quantify and model the impact of temperature on the moisture sorption of cementitious materials can be found in Paper I. A comparison of experimental and numerical results on the impact cracks have on the ingress of moisture is given in Section 2.5. A more thorough description of the experimental data obtained by x-ray attenuation measurements and the employed isothermal moisture transport model are provided in Paper II. Section 2.6 illustrates modelling results of the employed material and transport model and compares these to experimental data obtained from an in-situ exposure site. Finally, the chapter is summarised and conclusions are drawn from the findings in Section 2.7.

2.2 Coupled heat and moisture transport

Porous media, which include nearly all (non-metallic) building materials, tend to interact with the environment and fixate moisture in liquid and vapour state. If an equilibrium state is reached, the resulting moisture content is commonly referred to as equilibrium moisture content, sorption moisture content or hygroscopic moisture content. Is the equilibrium disturbed, e.g. due to varying exposure conditions, a mass transfer (or energy transfer in case of heat transport) will take place. Thereby, different transport mechanisms may contribute to the overall mass transport depending on the individual driving potentials. Both processes, i.e. moisture transport and storage, take place in the available pore space of the material. Hence, for a complete description of these processes, the pore space must be described in a mathematically exact way. However, considering the complexity of the concrete pore structure, it becomes clear how difficult it is to find a simple mathematical model to characterise the pore space and its influence on moisture transport and storage processes. Because size, character, and form of the pore space directly affect the fixation and transport of heat and mass in porous media.

The phenomena typically considered for the heat and mass transfer in porous media are transport of moisture, comprised of a liquid and vapour phase, transport of air and transport of heat. Other processes may also take place; however, there overall contribution to the heat and mass transport may be neglected [*Janssen et al. 2007*]. Assuming that contributions due to [*Janssen et al. 2007*]:

- air transfer, gravity, radiation, liquid transport due to temperature gradients, and effects of the gaseous phase on the moisture and heat storage are negligible as well as that temperatures remain below the boiling temperature of water

the transport equations to describe the coupled heat and moisture flow in porous media may be given as follows, see e.g. [*Philip et al. 1957, De Vries 1958, Lykow 1958, Dullien 1979, Bear et al. 1991*]:

$$\begin{aligned} \rho C \frac{\partial T}{\partial t} &= \nabla\left(k_{T,T}\nabla T + k_{T,pC}\nabla pC\right) \\ \frac{\partial \theta_l}{\partial p_c}\frac{\partial p_c}{\partial pC} = C_{pC}\frac{\partial pC}{\partial t} &= \nabla\left(k_{pC,pC}\nabla pC + k_{pC,T}\nabla T\right) \end{aligned} \tag{2.1}$$

where ρ is the mass density of concrete, C the specific heat capacity of concrete, T the temperature, t the time, pC the logarithm of the capillary pressure, θ_l the moisture content, p_c the capillary pressure, C_{pC} the moisture capacity and k transport coefficients for the heat, T, and moisture transfer, pC, respectively.

While the transport equations can be derived from thermodynamic principles and are therefore commonly accepted within the research community, different approaches to determine and describe the transport coefficients can be found. As mentioned earlier, multiple transport processes, e.g. vapour diffusion, diffusion, and capillary suction,

may contribute to the overall moisture transport at the same time. Therefore, experimental determination of the individual transport coefficients for the various phenomena in porous media, such as concrete, may be very difficult if not impossible. Based on the chosen driving potential for the moisture transport, different approaches to describe the moisture transport were developed within the past decades. A detailed overview of the various approaches to describe the transport coefficients can be found e.g. in [*Scheffler 2009*] and the literature cited therein. In general, the different approaches to describe the mass transport can be divided into diffusivity, see e.g. [*Krus 1995, Pel 1995, Carmeliet et al. 2002, Villmann et al. 2006*] and conductivity approaches, see e.g. [*Dullien 1979, Rode 1990, Xu et al. 1997, Scheffler 2009*].

Within the present thesis, the model developed in [*Scheffler 2009, Scheffler et al. 2010*] was used to describe the moisture dependent vapour and liquid moisture transport in porous media as the model is founded on a physical basis maintaining a high flexibility and adjustability. Furthermore, the applicability of the model to accurately model the moisture transport in various types of porous media was presented e.g. in [*Scheffler et al. 2010*].

The model is based on a conductivity approach to describe the coupled vapour and liquid moisture flow in porous media. To take into account the reduced vapour permeability in the presence of moisture, a scaling function is applied [*Scheffler 2009, Scheffler et al. 2010*], which is derived from a mechanistic modelling approach considering the microstructure of the porous media. A similar function is employed in the model to describe the moisture dependency of the liquid moisture transport. A more thorough description of the transport coefficients taking into account the coupled vapour and liquid moisture flow in porous media is given in Paper II and Section 2.6. The paper also includes information on the employed moisture storage function.

2.3 Multi-ion transport and chloride binding

The transport of ions in porous media is mainly governed by three different transport phenomena, i.e. diffusion, migration and convection. Nernst-Planck equation allows for the description of multi-ion transport in porous media taking into account these transport phenomena and may be given as follows:

$$\frac{\partial c_i}{\partial t} = \nabla\left(D_i \nabla c_i + z_i u_{m,i} F c_i \nabla V - c_i v\right) \tag{2.2}$$

where the left hand term of the equation describes the change of concentration of ions considered over time, i.e. the total flux of ions. While the first term on the right hand side accounts for the diffusion of the considered ions, the second and third term describe the movement of ions due to migration, i.e. under the influence of electrostatic potentials, and convection, respectively. In the equation, c_i is the ionic concentration, D_i the ionic diffusion coefficient, z_i the charge number of the ionic species, $u_{m,i}$ the

ionic mobility, *F* Faraday's constant, *V* the electrostatic potential and *v* the velocity of the solvent.

To account for the impact of moisture on the diffusion of ions the relation proposed in [*Buchwald 2000*] may be used:

$$D_i(S_l) = D_i^0 S_l^{\xi} \tag{2.3}$$

where D_i^0 is the free diffusion coefficient in bulk water, S_l the degree of saturation and ξ a model parameter.

Ions are known to be physically adsorbed and/or chemically bound in concrete, commonly referred to as binding. The bound ions will not participate further in the ingress. With respect to reinforcement corrosion, especially the binding processes of chloride ions are of interest as only free chloride ions may initiate reinforcement corrosion. While physical adsorption takes place at pore walls [*Nilsson et al. 1996, Xi et al. 1999*], mainly Friedel's salt is formed with solid cement hydration products during chemical binding [*Nilsson et al. 1996, Birnin-Yauri et al. 1998, Xi et al. 1999*]. Among others, the chloride binding may be described by means of binding isotherms [*Luping et al. 1993, Justnes 1998, Zibaru 2001, Yuan et al. 2009*] through an apparent diffusion coefficient for chloride ions [*Saetta et al. 1993, fib Bulletin 34 2006, Caré 2008, Bastidas-Arteaga et al. 2011*].

Assuming that the chloride binding can be described by a Langmuir binding isotherm, see e.g. [*Tang et al. 1993*], the apparent chloride diffusion coefficient may be given as follows [*Glass et al. 2000*]:

$$D_{cl,bind}(S_l) = D_{cl}^0(S_l)\frac{1}{1 + \alpha_{bind}/(\theta_l(1 + \beta_{bind}c_{cl})^2)} \tag{2.4}$$

where α_{bind} and β_{bind} are model parameters describing the chloride binding capacity of the cementitious material.

2.4 Influence of temperature and chloride

Chloride ions and temperature are known to affect the moisture storage and transport properties of cementitious materials, see e.g. [*Pihlajavaara 1965, Hundt et al. 1978, Bonnet 1997, Radjy 2003, Ishida 2007, Koniorczyk et al. 2009*]; however, experimental data and models based on stringent theories describing the effects on the moisture storage and transport are scarce in literature.

2.4.1 Influence of temperature

As presented in Section 2.2, transport of moisture due to temperature gradients, also referred to as thermo diffusion, is commonly neglected, as the contribution to the total moisture transport is insignificant [*Janssen et al. 2007*]. The effect of temperature on the moisture state however should not be neglected.

In the hygroscopic range, the state of moisture is either adsorbed (bound) or capillary condensed (free). Although recognised, the influence of temperature on the moisture sorption of cementitious materials is poorly investigated. Gravimetrical sorption measurements of cementitious materials are very time consuming and only a limited amount of experimental studies can be found in the literature on the impact of temperature, see e.g. [*Pihlajavaara 1965, Hundt et al. 1978, Radjy et al. 2003, Ishida et al. 2007, Poyet 2009*]. Hundt et al. [*Hundt et al. 1978*] investigated the impact of temperature on the moisture sorption for 3.6 year old concrete specimens with a water-to-cement ratio (w/c) of 0.565 and 0.575 at four different temperatures (20, 45, 57.5 and 70°C). Furthermore, results were presented in [*Hundt et al. 1978*] for mortar specimens with a w/c of 0.5 and cement pastes with w/c of 0.4, 0.45, 0.5 and 0.55. Selected results from [*Hundt et al. 1978*] are reproduced and presented in Figure 2.1.

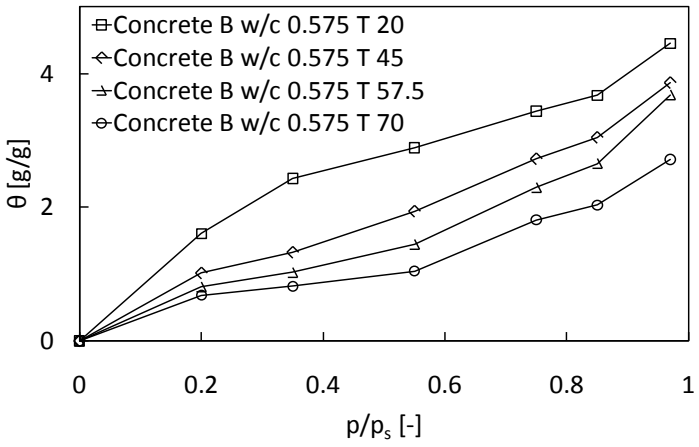

(a)

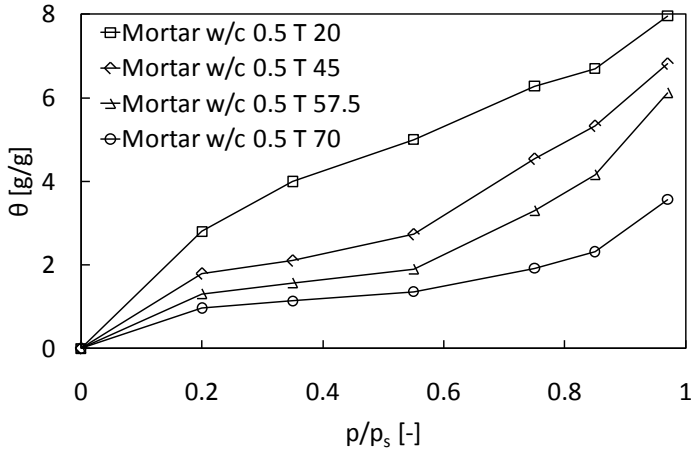

(b)

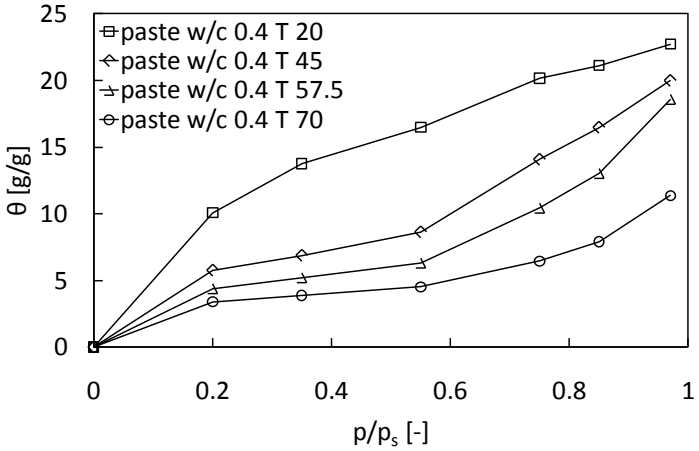

(c)

Figure 2.1 *Sorption isotherms for concrete (a), mortar (b), and cement paste (c) at various temperatures (experimental data reproduced from [Hundt et al. 1978]).*

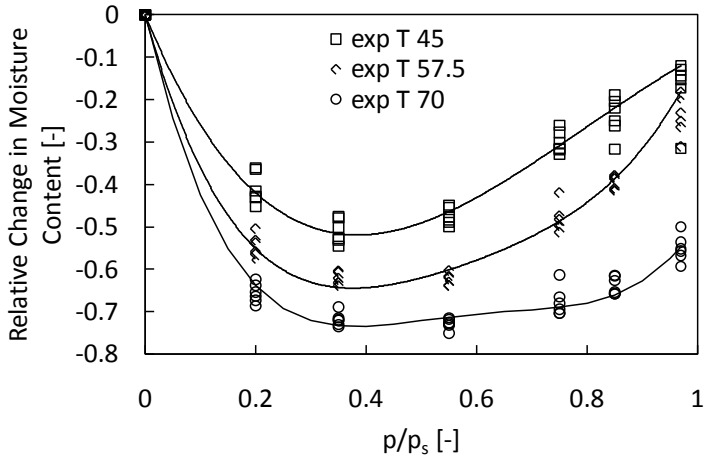

Figure 2.2 *Relative change in moisture content for all materials presented in [Hundt et al. 1978] with respect to the chosen reference temperature of 20*°C *(note: experimental data is illustrated by markers, solid lines are only for visual support).*

For all materials tested in [*Pihlajavaara 1965, Hundt et al. 1978, Poyet 2009*] the same impact of the temperature on the moisture sorption can be seen; as temperature is increasing, the moisture content at equilibrium is decreasing. This effect appears to be independent for all tested materials. Figure 2.2 illustrates the relative change in moisture content (compared to the reference temperature of 20°C) for all investigated materials in [*Hundt et al. 1978*], i.e. concrete, mortar, and cement paste with varying w/c. The results show that within the investigated range of temperatures, the relative change in moisture content for all materials is very similar, which indicates that a common physical phenomenon is related to the process.

Paper I presents experimental investigations on sealed concrete specimens with defined moisture contents, which were subjected to various temperatures and monitored by means of time domain reflectometry (TDR). TDR was originally developed to detect defects in cables and electrical wires [*Moffitt 1964*]. More recently, the TDR technique was applied to other porous media, such as soil or masonry, to determine and monitor moisture contents [*Topp et al. 1980, Dobsen et al. 1985, Phillipson et al. 2008*]. To determine the impact of temperature on the moisture sorption, results of TDR measurements were combined with multi-layer adsorption theory and material specific parameters. The required material parameters, i.e. specific surface area and number of adsorbed water layers, were obtained from gravimetrical sorption measurements at reference temperature provided in [*Hundt et al. 1978*]. While the specific surface was determined by means of the excess surface work [*Adolphs et al. 1996*], the average number of adsorbed water layers was determined from the so-called "t-curve" at a reference temperature [*Hagymassy et al. 1969*].

Results of the modelled impact of temperature based on the TDR measurements and experimentally obtained water vapour sorption isotherms for different temperatures are presented in Figure 2.3 (a), (b), and (c) for concrete, mortar, and cement paste.

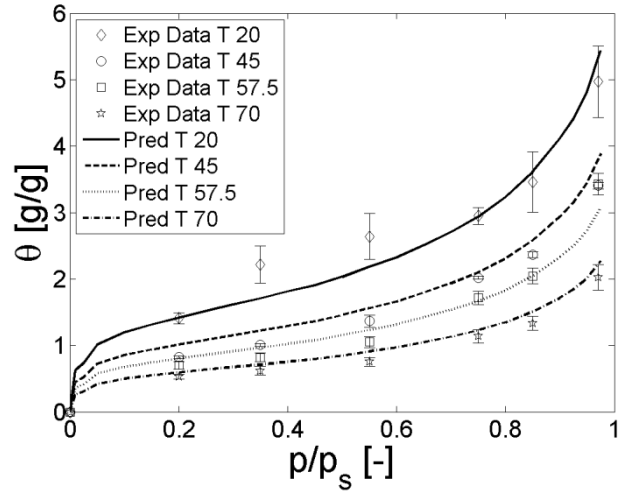

(a)

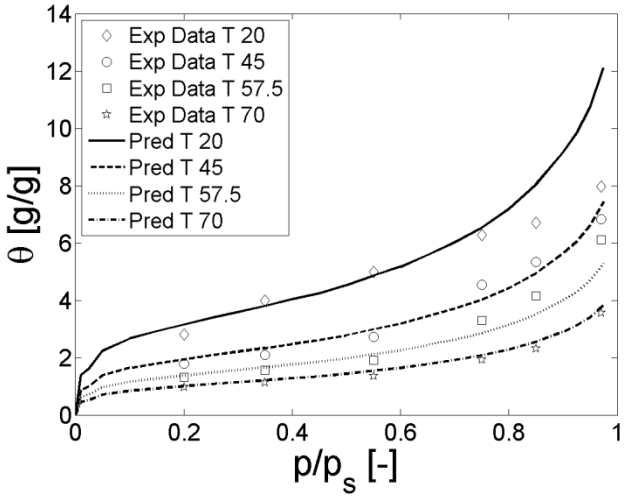

(b)

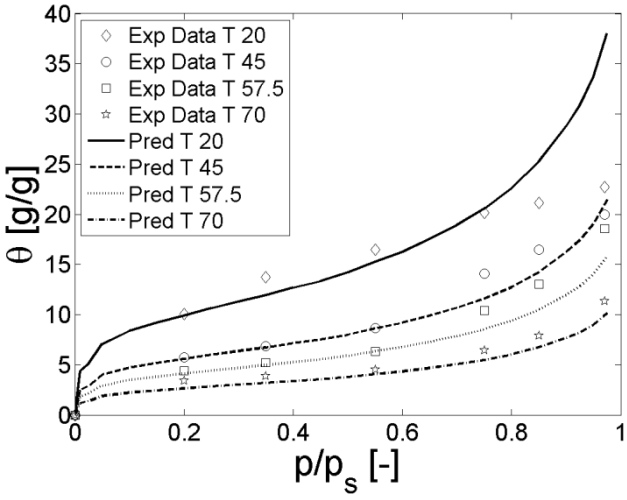

(c)

Figure 2.3 *Comparison between modelled (lines) and experimental (markers) sorption isotherms at various temperatures for (a) concrete w/c 0.565, (b) mortar w/c 0.5, and (c) cement paste w/c 0.4 (experimental data reproduced from [Hundt et al. 1978]).*

Although the experimental data presented in the literature [*Hundt et al. 1978*] could be predicted very well by the analysis of the TDR measurements, no stringent general theory could be developed to describe the impact of temperature on moisture sorption in Paper I. Therefore, to account for the impact of temperature on the moisture storage in the heat and mass transport model, experimental data provided in [*Pihlajavaara 1965, Hundt et al. 1978, Poyet 2009*] is employed. As shown earlier (see Figure 2.2), the relative change in moisture content appears to be similar for the various cementitious materials and mix designs. This fact is used in the present model to account for the impact of temperature on the moisture sorption of cementitious materials extending the state equation for the moisture transport (moisture storage function). As in the present model the moisture transport due to a liquid and vapour phase is assumed, the extended state equation including the impact of temperature may be given as follows:

$$pC = p_v - p_l - \Delta p_T = pC(\theta_l, T) \tag{2.5}$$

where p_v is the pressure of the water vapour phase, p_l the pressure of the liquid water phase, Δp_T is the change in pressure due to temperature variations (see Figure 2.2) and $pC(\theta_l,T)$ is the capillary pressure curve as a function of the moisture content, θ_l, and temperature, T.

2.4.2 Influence of chloride

In an ion containing solution the vapour pressure above the solution is lower than in the pure solution. In the presence of chloride ions the phenomenon may be described by Raoult's law (neglecting possible changes in the microstructure) as follows:

$$\Delta p_{v,cl} = \chi_{cl} p_v \tag{2.6}$$

where χ_{cl} is the molar fraction of chloride ions in the solution and $\Delta p_{v,cl}$ is the change in vapour pressure due the presence of chloride ions.

Experimental studies on the impact of ions on the moisture sorption of cementitious materials are rare in the literature, see e.g. [*Bonnet 1997, Koniorczyk et al. 2009*]. Bonnet [*Bonnet 1997*] determined water vapour sorption isotherms for mortar specimens with varying concentrations of sodium chloride. Experimental results of the study are given in Figure 2.4. With increasing sodium chloride concentrations, higher water contents are observed at lower relative humidities. A comparison between the experimental results and Eq. (2.6) is illustrated in Figure 2.4. A good agreement between the experimental data and Eq. (2.6) can be seen for ion concentrations up to approximately 4.5 mol/L. For higher ion concentrations a deviation from Eq. (2.6) can be observed, which might be attributed to changes in the microstructure, which are not taken into account. However, such high concentrations are rather unlikely under natural conditions.

Similar to the impact of temperature on the moisture sorption, the influence of chloride ions is described extending the state equation in the model. Accordingly, to ac-

count for the impact of chloride ions on the moisture sorption the state equation (see Eq. (2.5)) may be written as follows:

$$pC = \left(p_v - \Delta p_{v,cl}\right) - p_l - \Delta p_T = pC(\theta_l, c_{cl}, T) \tag{2.7}$$

where $pC(\theta_l,c_{cl},T)$ is the capillary pressure curve as a function of the moisture content, θ_l, temperature, T, and chloride concentration, c_{cl},.

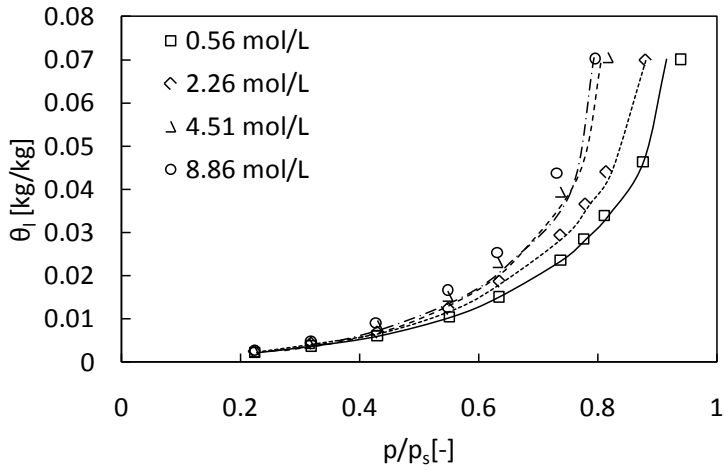

Figure 2.4 *Comparison between experimental and modelled (Eq. 2.6) water vapour sorption isotherms of mortar specimens with varying sodium chloride concentrations (experimental data reproduced from [Baroghel-Bouny 2011]).*

2.5 Impact of cracks

Current service life models determine the (residual) service life of reinforced concrete structures modelling the transport mechanisms of potentially aggressive substances into concrete. In most cases, these service life models assume that the structure is a homogeneous, defect-free, system, see e.g. *fib* [*fib Bulletin 34 2006*] or Life-365 [*Ehlen et al. 2009, Life-365 Consortium II 2010*]. In real structures, however, cracks are inevitable, especially in the concrete cover that is protecting the reinforcement from the penetration of aggressive substances. These cracks may have a major impact on the durability of reinforced concrete structures, as they may provide easy access to aggressive substances, especially moisture and chloride ions [*Pease 2010*].

Within the past decades, several studies have been devoted to investigate the influence of cracking on the ingress of corrosion initiating substances. In general, laboratory and field experiments concluded that the presence of cracks facilitate rapid ingress regardless of the controlling ingress mechanism(s) [*Jacobsen et al. 1996, Aldea et al. 1999, Edvardsen 1999, Rodriguez et al. 2003, Lindquist et al. 2006, Pease et al. 2009*], and cause considerable reductions in the time to corrosion initiation [*Schießl 1976, Schießl et al. 1997, Otieno et al. 2010, Pease et al. 2011*]. Active reinforcement corrosion was observed after only weeks (in some cases even days) under experi-

mental conditions [*Schießl et al. 1997, Otieno et al. 2010, Pease et al. 2011*] and within one year under field conditions [*Schießl 1976*].

A numerical model for the ingress of moisture in cracked steel fibre reinforced concrete is introduced in Paper II. Modelling results were compared to experimental results from steel fibre reinforced concrete wedge splitting test (WST) specimens conditioned to 50% relative humidity, cracked to varying crack geometries, and exposed to liquid water. The experimental data was obtained by [*Pease 2010*], who investigated the influence of concrete cracking on the ingress of moisture by means of x-ray attenuation measurements. From his work, Pease [*Pease 2010*] concluded that the total crack length may be divided into two parts; 1) a coalesced crack length that behaves as a free surface for moisture ingress, and 2) an isolated micro-cracking length that resists ingress similarly to the bulk material. The assumptions for modelling the ingress of the moisture in cracked concrete are illustrated in Figure 2.5. Details on specimen geometry, material properties, and measurement and analyses techniques can be found in Paper II.

Experimental and model results on the ingress of moisture are given in Figure 2.6 and Figure 2.7 for WST specimens with different extents of damage and at different times after exposure to liquid water. More results, i.e. for additional extents of damage, can be found in Paper II. The employed transport model and assumptions appear to accurately estimate the impact of cracking on the extent, both vertically and horizontally, of moisture ingress using simplified crack geometries. However, local variations in the moisture content (characteristic for the experimental data) are not represented by the model results. This contradiction is due to the assumption of homogeneous material properties in the model, while the cement content (or inversely, aggregate content) varies naturally with location in the experimental specimens.

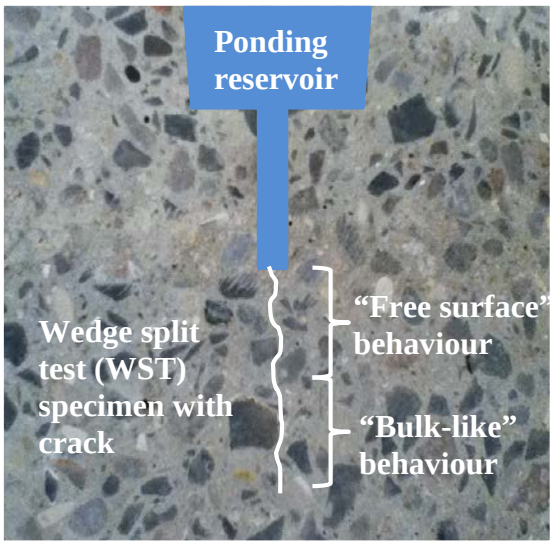

Figure 2.5 *WST specimen with assumptions on the crack behaviour for modelling the ingress of moisture in cracked concrete.*

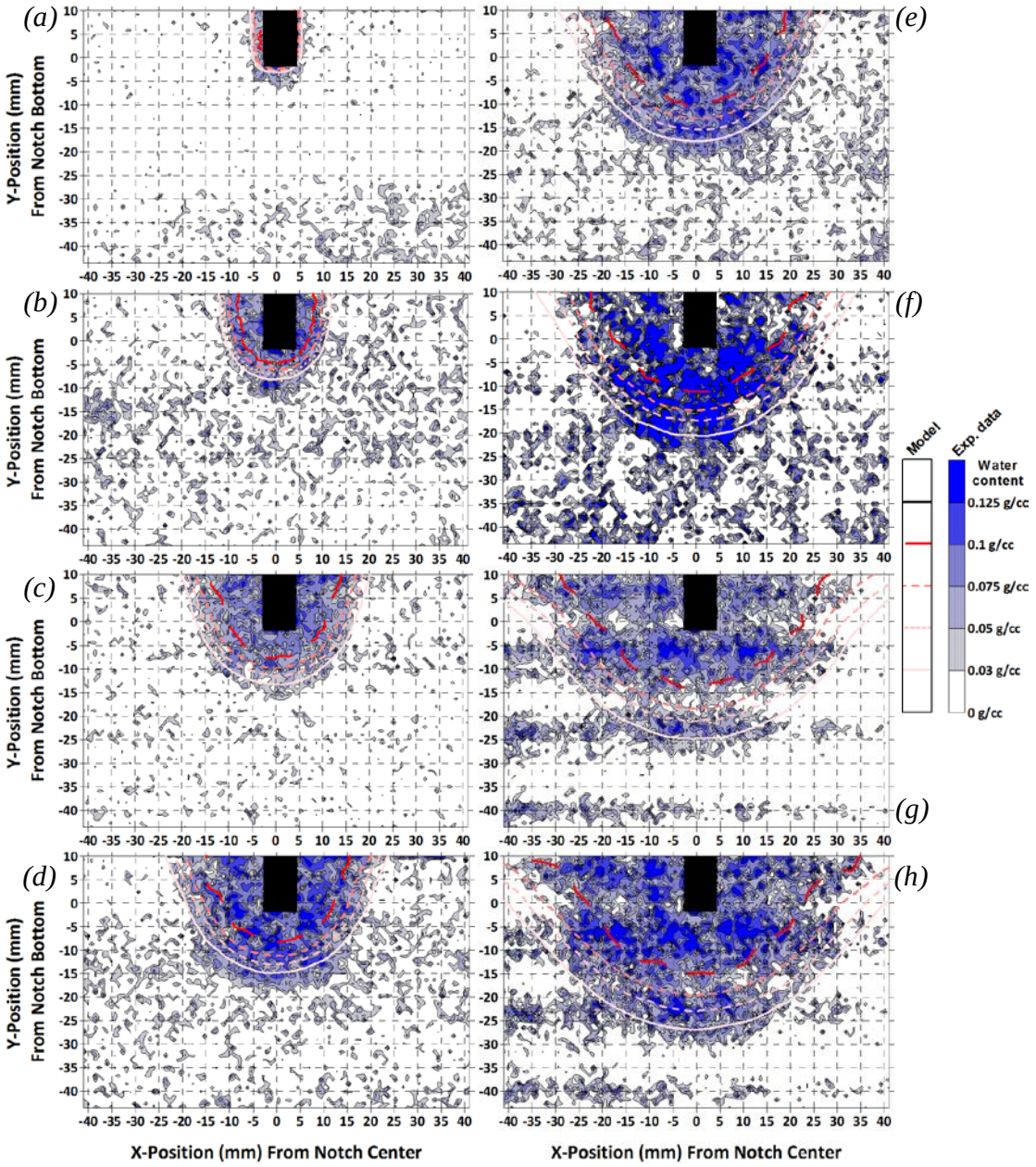

Figure 2.6 *Experimental and modelled ingress results for 70% peak load WST specimen after (a) 3, (b) 30 minutes, (c) 1.5, (d) 2, (e) 3, (f) 4, (g) 6, and (h) 7 hours of exposure to liquid water, from [Pease et al. 2012].*

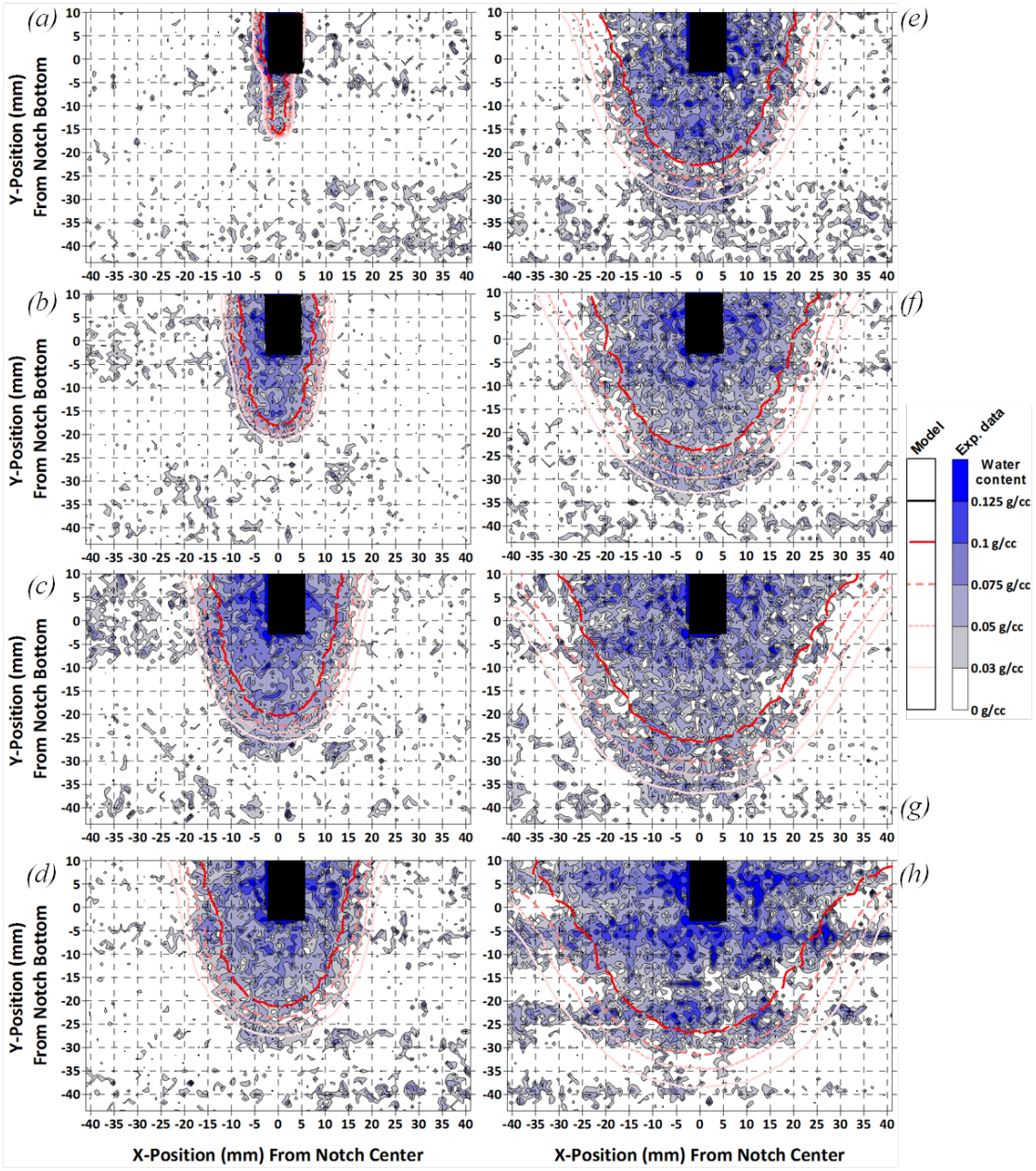

Figure 2.7 *Experimental and modelled ingress results for 0.10 mm CMOD WST specimen after (a) 3, (b) 30 minutes, (c) 1.5, (d) 2, (e) 3, (f) 4, (g) 6, and (h) 7 hours of exposure to liquid water, from [Pease et al. 2012].*

2.6 Case study

To demonstrate the applicability of the heat and mass transport model presented in this chapter and Paper II, numerical simulations on the ingress of chloride were compared to experimental data presented in [*De Weerdt et al. 2012*]. The model also includes the influence of temperature and chloride on the moisture storage and transport as presented in Section 2.4.

De Weerdt [*De Weerdt et al. 2012*] investigated the ingress of chloride in a concrete wall element ($1.35\times1.55\times0.25m^3$) placed in the tidal zone of the Trondheim Fjord. The wall element was cast in November 2001 and reinforced (Ø12) on both sides with a cover depth of 20 and 50mm. The concrete composition of the wall element is given in Table 2.1. More detailed information on the cement and concrete composition can be found in [*Justnes 2002*].

From three days after casting, the wall element was subjected to alternating wetting and drying cycles in the tidal zone. After approximately two and ten years of exposure, cores were drilled and chloride profiles determined. The cores did not contain steel reinforcement. After extraction, the cores were profile ground and the resulting concrete dust was analyzed for the total chloride content. Additional information on the extraction of the cores, drilled after approximately ten years can, be found in [*Østnor 2011*]. For the chloride analysis, 5g of the concrete powder from each section was dissolved in 50ml 80°C (1:10) nitric acid (HNO_3), and filtrated after one hour. The solution was then analysed using the mercury (II) thiocyanate method [*Basett et al 1978*] to determine the chloride content. Finally, the chloride concentration in the solution was normalised to the dry concrete mass (weight after drying at 105°C). Further information on the chloride analysis is provided in [*De Weerdt et al. 2012*]. The experimentally determined chloride profiles after approximately two and ten years of exposure are given in Figure 2.8.

Table 2.1 *Concrete composition of wall element [Justnes 2002].*

	Value	Unit
CEM I 42.5 R	366	kg/m^3
Limestone filler	44	kg/m^3
0-2 mm Bjørkmyr sand	210	kg/m^3
0-8 mm Årdal sand	843	kg/m^3
8-11 mm Årdal aggregate	344	kg/m^3
11-16 mm Årdal aggregate	344	kg/m^3
Water	171	kg/m^3
Air entrainer	0.17	kg/m^3
Super plasticizer	2.20	kg/m^3
Blain fineness	362	m^2/kg

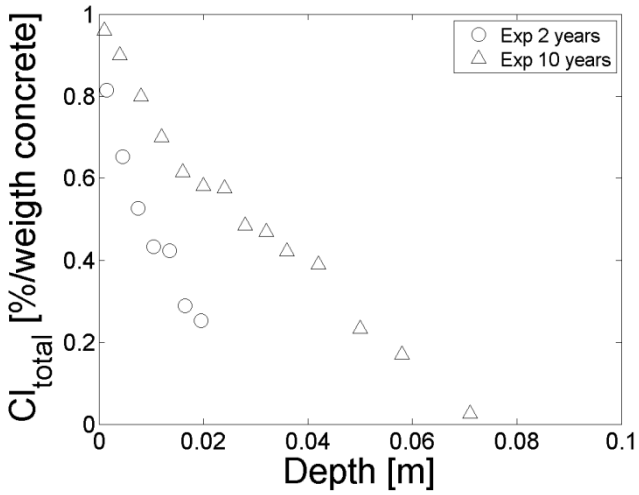

Figure 2.8 *Chloride profiles after approximately two and ten years of exposure in the tidal zone of the Trondheim Fjord.*

To simulate the chloride ingress in the wall element Equations (2.1) - (2.4) were used. The coupled heat and moisture transport was described by Equation (2.1) in which the transport coefficients are given as follows:

$$
\begin{aligned}
k_{T,T} &= \lambda \\
k_{T,pC} &= -l_{lv}\frac{D_v(\Theta_l)}{R_v T}\frac{p_{v,sat}\varphi}{\rho_l R_v T}\frac{\partial p_c}{\partial pC} \\
k_{pC,pC} &= -K_l(\Theta_l)\frac{\partial p_c}{\partial pC} - \frac{D_v(\Theta_l)}{R_v T}\frac{p_{v,sat}\varphi}{\rho_l R_v T}\frac{\partial p_c}{\partial pC} \\
k_{pC,T} &= \frac{D_v(\Theta_l)}{R_v T}\frac{p_{v,sat}\varphi}{\rho_l R_v T}\frac{\partial p_{v,sat}}{\partial T}
\end{aligned}
\tag{2.8}
$$

where λ is the thermal conductivity, l_{lv} the specific latent heat of evaporation, $D_v(\theta_l)$ the moisture dependent vapour diffusion coefficient, R_v the gas constant of water vapour, $p_{v,sat}$ the saturation vapour pressure, ρ_l the mass density of water, φ the relative humidity and $K_l(\theta_l)$ the liquid conductivity coefficient. Detailed information on the determination of the moisture dependent vapour diffusion coefficient, $D_v(\theta_l)$, and the liquid conductivity coefficient, $K_l(\theta_l)$, are given in Paper II.

To incorporate the influence of temperature and chloride on the moisture sorption and transport, Equation (2.7) was used in which the logarithm of the capillary pressure, *pC*, is a function of the chloride content and the temperature. Consequently, the moisture content, θ_l, liquid conductivity coefficient, $K_l(\theta_l)$, and moisture dependent vapour diffusion coefficient , $D_v(\theta_l)$, are also dependent on the capillary pressure, *pC*, chloride content, c_{Cl}, and temperature, *T*.

Multi-ion transport was modelled using Equation (2.2), including seven ionic species, i.e. chloride, magnesium, hydroxyl, calcium, sodium, potassium, and sulphate ions. To account for the moisture dependency of the ionic diffusion coefficients, Equation

(2.3) was used and chloride binding was described by Equation (2.4). Potential ionic transport due to convection was included determining the velocity of the solvent from Equation (2.1).

Moisture storage and transport properties of the wall element, used in the numerical simulation to model the chloride ingress, for selected temperatures and chloride concentrations are presented in Figure 2.9. The plots highlight the impact of varying capillary pressure, chloride content, and temperature on the moisture content, moisture capacity and conductivity as described in Sections 2.4.1 and 2.4.2, respectively. With increasing temperature, the moisture content at equilibrium is decreasing as shown in Figure 2.9 (a) and (b). As the relative conductivity is dependent on the shape of the sorption isotherm (see Paper II), the conductivity is also affected by temperature variations as illustrated in Figure 2.9 (d). Figure 2.9 also indicates the impact of chlorides on the moisture storage and transport behaviour. As presented earlier, the vapour pressure above an ion containing solution is lower than in a pure solution, which affects the moisture storage behaviour as presented Figure 2.9 (a) and (b) and, similar to varying temperatures, alters the moisture transport properties, as illustrated in Figure 2.9 (d).

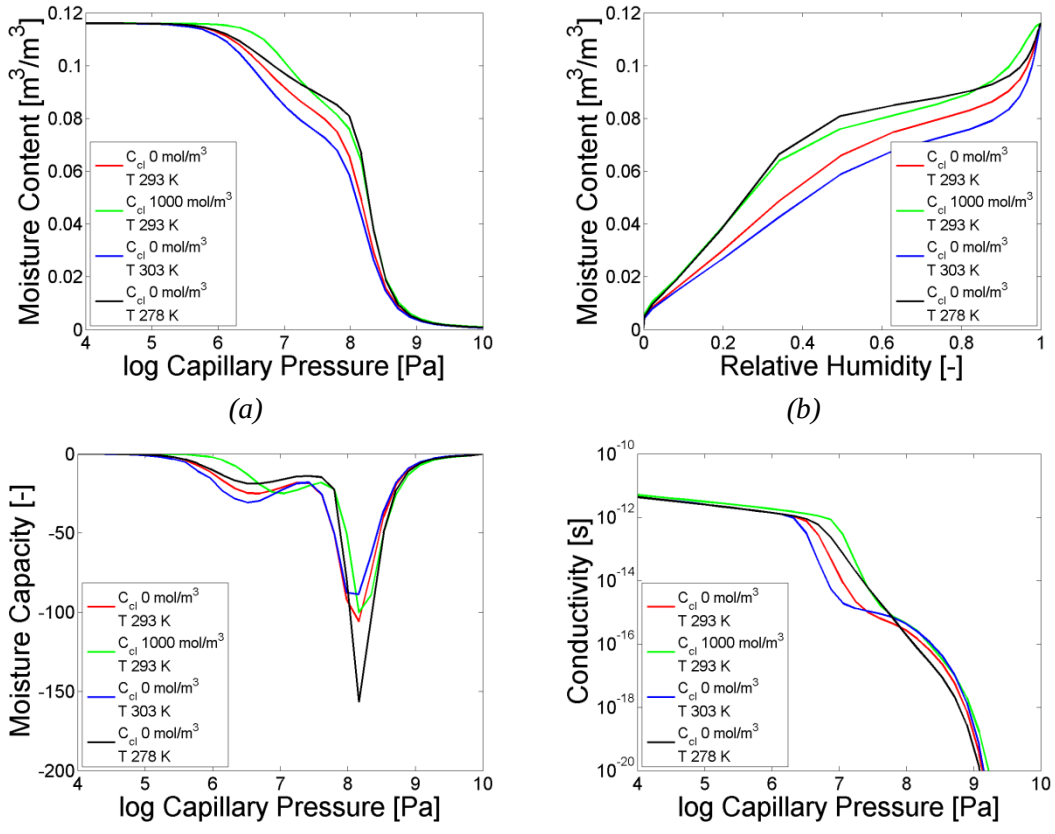

Figure 2.9 *(a) and (b) moisture storage, (c) moisture capacity, and (d) moisture conductivity of the concrete wall element as a function of capillary pressure and for selected temperatures and chloride concentrations in the solution.*

Experimental and numerical results of the chloride ingress in the concrete wall element are compared in Figure 2.10 (a) and the model parameters for the numerical simulation are given in Table 2.2. It can be seen from the presented results that the heat and mass transport model can simulate the chloride ingress over time, i.e. chloride content and penetration depth. In addition, the chloride ingress was modelled using the chloride ingress model given in [*fib Bulletin 34 2006*] (assuming a w/c of 0.4) and compared to the experimental data (see Figure 2.10 (b)). While the chloride content and penetration depth after approximately two years is captured well with the *fib* model, chloride ingress is considerably underestimated after approximately ten years of exposure using an suggested ageing factor of 0.3 [*fib Bulletin 34 2006*]. A better agreement with the experimental data was obtained using an ageing factor of zero; however, penetration depth is then considerably overestimated (see Figure 2.10 (b)).

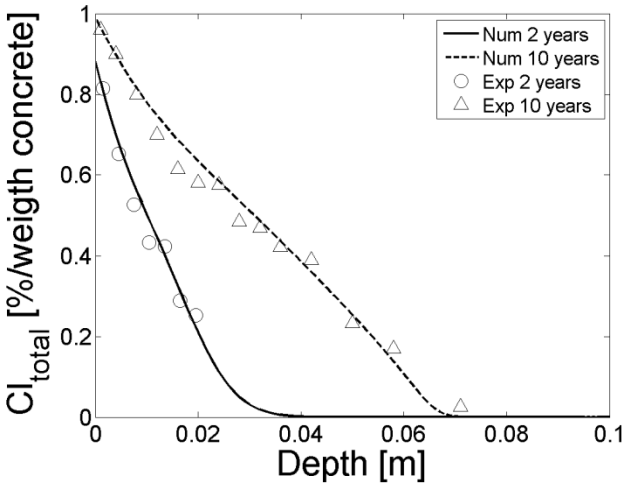

(a)

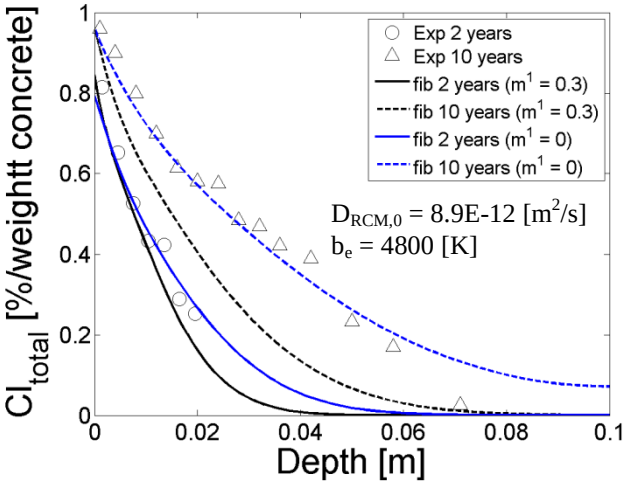

(b)

Figure 2.10 *(a) experimental and numerical chloride profiles using the employed heat and mass transfer model and (b) experimental and numerical chloride profiles using the fib chloride ingress model (with and without ageing factor).*

Table 2.2 *Model parameters to simulate the chloride ingress in a concrete wall element subjected to the tidal zone of the Trondheim Fjord.*

	Model Parameter	Symbol	Value	Unit
Moisture transport parameters	Saturated conductivity	$K_{l,sat}$	5E-11	[s]
	Vapour diffusion resistance number	μ	50	-
	Non-physical model parameter	n_{sp}	3	-
Moisture storage parameters	Non-physical model parameter	l_1	0.6	-
	Non-physical model parameter	l_2	0.4	-
	Non-physical model parameter	n_1	3	-
	Non-physical model parameter	n_2	1.5	-
	Non-physical model parameter	a_1	7E-09	-
	Non-physical model parameter	a_2	4E-04	-
	Maximum water content	w_{max}	0.116	[m^3/m^3]
Initial conditions	Initial relative humidity	φ_{init}	0.92	-
	Initial absolute temperature	T_{init}	293.15	[K]
Chloride binding parameters	Non-physical model parameter	α_{bind}	4	-
	Non-physical model parameter	β_{bind}	3.3	-
	Non-physical model parameter	ξ	1.7	-
Heat transport parameters	Specific latent heat of evaporation	l_{lv}	2257	[J/m^3]
	Thermal conductivity concrete	λ_{conc}	1.4	[W/m K]
	Density concrete	ρ_{conc}	2400	[kg/m^3]
	Specific heat capacity concrete	C_{conc}	880	[J/kg K]
Multi-ion transport parameters	Ionic - diffusion coefficient chloride	D^0_{Cl}	2.03E-09	[m^2/s]
	Ionic - diffusion coefficient sodium	D^0_{Na}	1.33E-09	[m^2/s]
	Ionic - diffusion coefficient hydroxyl	D^0_{OH}	5.33E-09	[m^2/s]
	Ionic - diffusion coefficient potassium	D^0_{K}	1.96E-09	[m^2/s]
	Ionic - diffusion coefficient sulphate	D^0_{SO4}	1.04E-09	[m^2/s]
	Ionic - diffusion coefficient calcium	D^0_{Ca}	0.79E-09	[m^2/s]
	Ionic - diffusion coefficient magnesium	D^0_{Mg}	0.71E-09	[m^2/s]

2.7 Summary and conclusions

Chapter 2 dealt with the heat and mass transport in porous media, which is a key issue for the service life prediction of reinforced concrete associated with chloride-induced corrosion. A numerical model to describe the state and transport of various substances was presented taking into account the impact of cracks on the mass transport. The influence of temperature and chloride ions on the moisture state and transport was presented in Section 2.4. Experimental and numerical results dealing with the impact of temperature on the moisture state were presented in Section 2.4.1 and Paper I. Furthermore, it was shown that the presented heat and mass transport model can accurately capture the effect of cracks on the moisture ingress comparing model results to experimental results presented in Section 2.5 and Paper II. Finally, the applicability of the model was shown in Section 2.6 simulating the chloride ingress in a concrete wall element subjected to tidal zone of the Trondheim Fjord.

From the work presented in this chapter the following conclusion can be drawn:

- The impact of chloride ions on the moisture sorption can be described by Raoult's law as indicated by a comparison with experimental data found in the literature. However, for higher chloride ion concentrations (above approximately 4.5 mol/L) the experimental data is differing from Raoult's law. This deviation may be explained by changes in the microstructure of the material, which is not captured by Raoult's law. For a more accurate description of the impact of chloride ions on the moisture sorption in cementitious materials, material models dealing with the chemical interactions between the hydrated cement phases and chloride ions may be used. Although such models may not be feasible for practical engineers, more sophisticated models may contribute to an improved understanding of chloride binding processes and subsequent alterations of the microstructure of cementitious materials.
- To determine the impact of temperature on the moisture state, results of time domain reflectometry (TDR) measurements in combination with multi-layer adsorption theory were used. Comparisons of numerical predictions with experimental results presented in the literature on the impact of temperature on the moisture state revealed very good correlations for a range of cementitious materials, i.e. cement paste, mortar, and concrete with varying water-to-cement ratios. However, further studies are required to reinforce the hypothesis that TDR measurements can be used to describe the impact of temperature on the sorption behaviour of cementitious materials.
- The effect of cracks on the moisture ingress could be modelled with a simplified crack geometry assuming that the total crack length can be divided into two parts: 1) a coalesced crack length, which behaves as a free surface for moisture ingress and 2) an isolated micro-cracking portion of constant length, which resists ingress similarly to the bulk material. Although, the assumptions

resulted in a very good agreement with the experimental observations, further investigations are need. The determined length of the isolated portion of the crack obeying “bulk-like” behaviour may be different for other materials or mix designs. In particular, strain-hardening materials may exhibit considerable different ingress behaviour. However, the length of the coalesced crack may be estimated by means of fracture mechanical tools, such as the crack hinge model or non-linear finite element analysis. Further, potential self-healing of cementitious materials and/or closure of cracks due to stress relaxation is not considered in the present model. These effects may hinder the ingress of aggressive substances and subsequently affect the reinforcement corrosion process.

- To demonstrate the applicability of the employed heat and mass transport model, including the effects of temperature and chloride on the moisture storage and transport, the chloride ingress in a concrete wall element was modelled. Although, simulations of chloride content and penetration depth after approximately two and ten years of exposure are in good agreement with the experimental data, further work is needed to improve the presented heat and mass transport model. In particular, changes in the hydrated cement phases due to chloride binding need to be further investigated to describe potential modifications in the microstructure of cementitious materials affecting among others moisture storage and transport.

Chapter 3

Corrosion of steel in concrete

3.1 Introduction

This chapter provides a brief overview of the fundamental corrosion processes of steel in reinforced concrete and how these can be used to model corrosion of steel in concrete. The chapter is comprised of several sections. In Section 3.2, the fundamental corrosion processes in reinforced concrete are presented in terms of basic thermodynamic and kinetic principles. The intention of the section is to give a brief review of the thermodynamics and kinetics of the corrosion process and introduce common terms and concepts related to the work carried out during this Ph.D. study. For more detailed information on the thermodynamics and kinetics of corrosion of steel in concrete references are made to e.g. [*Schießl 1988, Jäggi 2001, Bardal 2004, Böhni 2005, Küter 2009, Nygaard 2009, Pease 2010*].

The numerical model developed to describe the corrosion process of steel in concrete is presented in Section 3.3. A more detailed description of the corrosion model and the coupling with the heat and mass transfer in cementitious materials is given in Paper III and Paper IV. Section 3.3 also includes a study on the influence of individual parameters on the kinetics of the corrosion process. The parametric study covers the influence of the anode-to-cathode area ratio, temperature, moisture, and oxygen. Results of numerical simulations are compared to experimental data either found in literature or obtained in connection with the Ph.D. studies (Paper V presents results of experimental investigations on the short-term influence of temperature on reinforcement corrosion). The influence of cracks on the risk of corrosion initiation in plain reinforced concrete and steel fibre reinforced concrete is dealt with in Section 3.4 and Paper VI, Paper VII, and Paper VIII. Section 3.5 demonstrates the potential use of the

developed electrochemical corrosion model for the service life prediction of reinforced concrete in corrosive environments by means of a numerical example. The electrochemical model is fully coupled to the heat and mass transfer model presented in Chapter 2, accounting for the impact of temperature, moisture, oxygen and chloride on the initiation and propagation of reinforcement corrosion. The findings of this chapter are summarised and conclusions drawn in Section 3.6.

3.2 Fundamentals of reinforcement corrosion

Corrosion of steel in concrete can be described by the same electrochemical processes as the corrosion of a metal in an electrolyte [*Schießl 1988*]. Figure 3.1 gives an overview of the electrochemical and physical processes describing the corrosion of steel in concrete, which was proposed by [*Küter 2009*]. Two electrochemical half-cell reactions must take place at the metal surface, the anodic (oxidation) and the cathodic (reduction) half-cell reaction, for corrosion to occur. The anodic half-cell reaction is thereby always characterised by liberating electrons, which are consumed in the cathodic half-cell reaction. To avoid local accumulation of electrical charges, the liberated electrons are conducted through the metal to the cathode establishing an electronic connection between the anode and cathode. The electrical circuit is then closed by an ionic exchange current through the electrolyte. Typically, the oxidation of iron is assumed as anodic half-cell reaction, which can be given as follows:

$$Fe \rightarrow Fe^{2+} + 2e^{-} \tag{3.1}$$

At the cathode the reduction of oxygen is commonly assumed, which can be given as follows:

$$\frac{1}{2}O_2 + H_2O + 2e^{-} \rightarrow 2OH^{-} \tag{3.2}$$

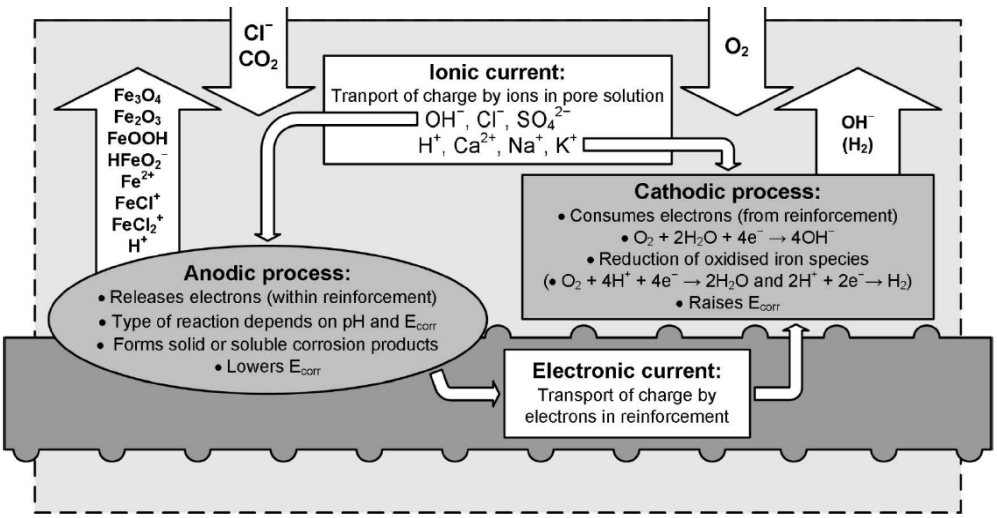

Figure 3.1 *Overview of electrochemical and physical processes describing corrosion of steel in concrete, from [Küter 2009].*

However, depending on the potential and pH at the steel surface, other cathodic reactions, such as the reduction of hydrogen or water, may take place. A detailed overview of thermodynamically feasible anodic and cathodic reactions associated with reinforcement corrosion can be found in e.g. [*Küter 2009*]. For a thorough description of the corrosion process, thermodynamics and kinetics must be considered.

3.2.1 Thermodynamics of reinforcement corrosion

Among others, thermodynamics provide the possibility to investigate and assess the likelihood of reactions (in the case of corrosion: anodic and cathodic half-cell reactions) to occur under certain conditions. The corrosion process, which can be understood as a transformation of one thermodynamical state to another, can be related to the change of free enthalpy (also referred to as Gibbs free energy), which may be written as follows:

$$\Delta G = -zFE_0 \tag{3.3}$$

where ΔG is the free enthalpy (or Gibbs free energy), z the valence, F Faraday's number and E_0 the equilibrium potential of the reaction.

In general, three cases may be described by ΔG (assuming constant temperature and pressure) [*Bardal 2004*]:

- A negative value indicates that the reaction is spontaneous and the system can carry out work.
- A value of zero for the free enthalpy indicates that the system is in equilibrium and the reaction is thermodynamically not favoured to take place in either direction.
- A positive value indicates that energy must be supplied for the reaction to take place.

To describe the equilibrium potentials, E_0, of half-cell reactions for the corrosion process, Nernst equation can be used, which may be written as follows [*Perez 2004*]:

$$E_0 = E_0^0 - \frac{RT}{zF} ln\left(\frac{\alpha_{Red/Ox}}{\alpha_{Ox/Red}}\right) \tag{3.4}$$

where, E_0^0 is the standard equilibrium potential, R the gas constant, T the absolute temperature and $\alpha_{Red/Ox}$ the chemical activity of the reductant and oxidant, respectively.

Nernst equation may be further used to construct pH - potential diagrams, or more frequently called Pourbaix diagrams, providing a graphical overview of thermodynamically favoured reactions (i.e., reactions with a negative free enthalpy) as a function of the pH and the half-cell potential. The Pourbaix diagram for iron in water (commonly used to investigate corrosion reactions of steel in concrete [*Küter 2009*])

is illustrated in Figure 3.2. Three distinct regions describing the possible thermodynamic states of iron (steel) can be indentified from the figure:

- The immune region, in which iron is stable and corrosion is thermodynamically not possible [*Perez 2004*].
- The passive region, in which the formation of Fe_2O_3 and Fe_3O_4 is thermodynamically favoured. Fe_2O_3 and Fe_3O_4, which have the ability to form a passive film on the surface, are known to have a low ionic conductivity and low porosity, which greatly limits the corrosion process [*Bardal 2004*].
- The active region, in which soluble corrosion products, e.g. Fe^{2+} and Fe^{3+}, are formed as a result of the anodic half-cell reaction. The soluble reaction products may continue to react with other ions present in the electrolyte forming solid corrosion products. More detailed information on the potential formation of further corrosion products can be found e.g. [*Küter 2009*] and the literature cited within.

However, the application of "pure" Pourbaix diagrams may be limited, as only reactions of pure metals with pure water are described and the formation of species from these. A typical example for a limited application of "pure" Pourbaix diagrams with respect to reinforced concrete is reinforcement corrosion initiation due to chloride ions, which is associated with a local breakdown of the passive film, see e.g. [*Moreno et al. 2004, Vidal et al. 2007*]. Further, the pH refers to the conditions in the vicinity of the steel surface, which may be greatly altered once corrosion is initiated and the cathodic reactions are ongoing. In particular, the reduction of hydrogen or water may alter the local pH considerably as a result of the formation of H^+ or OH^- during these reactions [*Bardal 2004*]. A possibility to overcome the shortcoming of pure systems in traditional Pourbaix diagrams was presented in [*Küter 2009*], who superimposed "pure" Pourbaix diagrams for various systems, e.g. iron in water and chloride in water

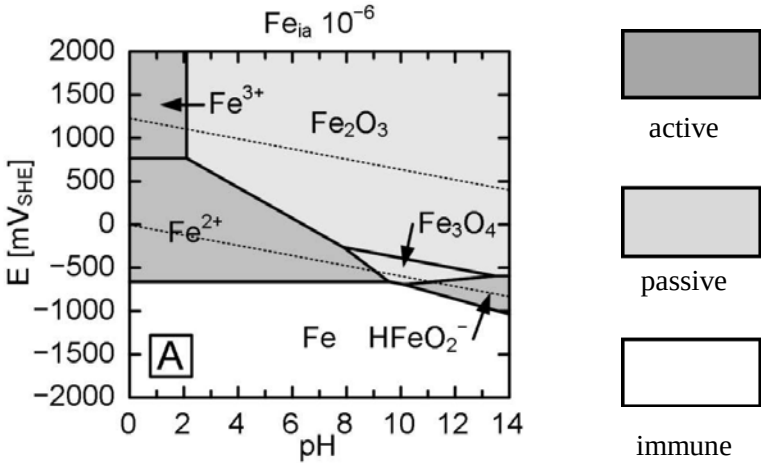

Figure 3.2 *Pourbaix diagram for Fe-H_2O system at 25°C and an Fe ion activity of 10^{-6} mol/L, from [Küter 2009].*

to describe thermodynamically favoured reaction products due to chloride-induced corrosion. A detailed study on the use of (superimposed) Pourbaix diagrams to understand corrosion reactions under various conditions and the potential use to derive corrosion countermeasures from such diagrams can be found in [*Küter 2009*].

Pourbaix diagrams may also be used to relate half-cell potential (frequently referred to as free corrosion potential or open circuit corrosion potential) measurements to the thermodynamic state of steel in concrete. Half-cell potential measurements are a common in-situ measurement technique where the half-cell potential of the steel is measured against a reference electrode [*RILEM TC 154-EMC 2003*]. For example, in a carbonated concrete the pH is approximately eight. While a half-cell potential of 200 mV_{SHE} would indicate a passive state of the steel (see Figure 3.2), a half-cell potential of -400 mV_{SHE} would indicate active reinforcement corrosion (see Figure 3.2). Reference electrodes for half-cell potential measurements may be embedded in the concrete or placed temporarily at the concrete surface. Frequently used reference electrodes and their potential against the standard potential of hydrogen are given in Table 3.1.

Table 3.1 *Commonly used reference electrodes for half-cell potential measurements and their potential against the standard potential of hydrogen.*

Reference Electrode	E_H [mV]
Standard hydrogen electrode (SHE)	0
Copper/copper sulphate (CSE)	+318
Standard calomel electrode (SCE)	+245
Silver/silver chloride electrode (0.1M) (SSCE)	+288

3.2.2 Kinetics of reinforcement corrosion

Although thermodynamics provide means to assess the possibility of corrosion reactions to occur under various conditions, no information on the rate of these reactions is obtained. Therefore, the kinetics of the electrochemical reactions must be considered to fully assess the corrosion mechanism.

Once corrosion is initiated, the potentials of the half-cell reactions on the steel surface are shifted from their equilibrium potentials, E_0, and a (corrosion) current will start to flow. The shift from the equilibrium potential is known as polarisation and the kinetics of the electrochemical half-cell reactions are governed by the degree of polarisation. A measure for the polarisation is the overpotential, η, which is the difference between the half-cell potential, $E_{c/a}$, and the equilibrium potential, $E_{0a/0c}$. Information on the polarisation of electrodes (anode and cathode) can be summarised in so-called Evan's diagrams relating the half-cell potential to the corrosion current.

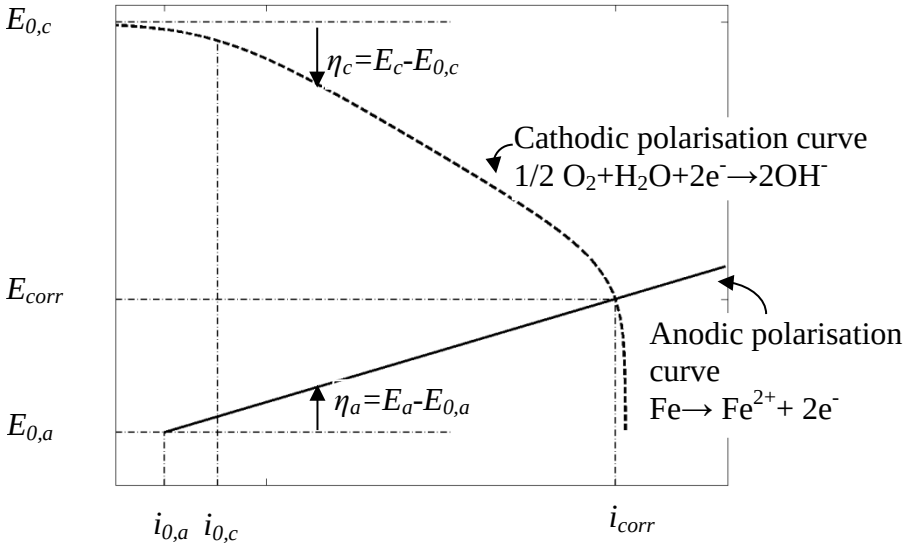

Figure 3.3 *Evan's diagram illustrating the anodic and cathodic polarisation on the steel surface, after [Martín-Pérez 1999]*.

The Evan's diagram for the anodic and cathodic half-cell reactions assuming the formation of Fe^{2+} at the anode and OH^- at the cathode is given in Figure 3.3. The corrosion potential (also referred to as mixed potential), E_{corr}, and the corrosion current density, i_{corr}, can be determined from the intersection of the anodic and the cathodic polarisation curve.

Depending on the mechanism, four types of polarisation acting individually or in combination may be distinguished; namely, activation, concentration, resistance, and crystallisation polarisation [*Shreir 1994*]. In the present work, crystallisation polarisation is neglected and only the effects of activation, concentration, and resistance polarisation are taken into account, sees e.g. [*Koryta et al. 1970, Fontana et al. 1978, Bardal 1994*].

- Activation polarisation arises when the half-cell reaction itself is hindered, i.e. the mass or charge transfer through the electrical double layer is hindered.
- Concentration polarisation, also referred to as diffusion polarisation, arises when the transport of reactants or reaction products between the electrode and electrolyte is hindered resulting in a depletion or accumulation of these species.
- Resistance polarisation arises when the electrolyte, passive film or other materials provide a significant ohmic resistance.
- Crystallisation polarisation arises when the dissolution of metal atoms from the crystal structure or vice versa is hindered.

For activation polarisation, the relation between the corrosion current and the half-cell potential may be described by the Butler-Volmer equation as follows (assuming that

the electrochemical reactions take place at separate electrodes and the polarisation is high) [*Stern et al. 1957*]:

$$i = i_0 exp(\Psi) \ \ with \ \ \Psi = ln(10)\frac{E - E_0}{b} \tag{3.5}$$

where i is the corrosion current density, i_0, the exchange current density, and b the Tafel constant, which is defined as follows:

$$b = ln(10)\frac{RT}{\alpha zF} \tag{3.6}$$

where α is the symmetry factor.

To include the effects of concentration polarisation on the relation between the half-cell potential and the corrosion current density, Equation 3.5 can be extended and written as follows [*Böhni 2005*]:

$$i = i_0 exp\left(\frac{1 - \Psi}{1 + \mathrm{i_0/i_{lim}}\Psi}\right) \tag{3.7}$$

where i_{lim} is the limiting corrosion current density, which can be defined as follows [*Bardal 2004*]:

$$i_{lim} = \frac{zFD_{O2}}{\delta}c_{O2} \tag{3.8}$$

where D_{O2} is the oxygen diffusion coefficient, c_{O2} the oxygen concentration at the electrode surface and δ the diffusion layer thickness.

A number of factors influence the shape of the polarisation curve, which in turn governs the kinetics of the corrosion process. Among others, the surface state of the electrode, temperature, electrolyte flow rate, moisture content, and geometry are decisive for the overpotential at the anode and cathode [*Bardal 2004*]. For example, the temperature, moisture content, and geometry are important parameters for diffusion-controlled corrosion. A dense concrete cover and high moisture content considerably hinders the oxygen transport from the concrete surface to the electrode. This may lead to a depletion of oxygen at the cathode ceasing the cathodic half-cell reaction (assuming reduction of oxygen as governing half-cell reaction) and subsequently the corrosion process itself. Furthermore, several electrochemical parameters, such as the exchange current density, i_0, or the equilibrium potential, E_0, are influenced by temperature (see e.g. Equations (3.4) and (3.6)).

The influence of various parameters, such as geometrical arrangement of the anode and cathode, moisture content, temperature, and oxygen on the kinetics of the corrosion process is dealt with in the next section. Results of numerical simulations are compared to experimental data, either provided in the literature or carried out in connection with the Ph.D. studies.

3.3 Modelling reinforcement corrosion

Corrosion models are indispensable for the determination of the service life of concrete structures describing the electrochemical processes at the steel surface and in the surrounding concrete. Both, thermodynamics, i.e. the likelihood of electrochemical reactions to occur in a certain environment, and kinetics of the corrosion process, i.e. information on the corrosion rate, must be treated within such a framework. Since the thermodynamics and kinetics of the corrosion process are highly dependent on the presence of certain substances (see previous sections), corrosion models must be coupled to material and transport models. For example, the tendency of corrosion initiation in case of chloride-induced corrosion is attributed to the local breakdown of the protecting passive layer, which is related to the presence of chloride ions. Concerning corrosion kinetics, it is well known, that moisture, oxygen, and temperature have considerable effects on the corrosion rate. The moisture content is one of the main parameters controlling for example the concrete resistivity, which is inversely proportional to the corrosion rate.

Various models have been developed within the past decades, describing the initiation, see e.g. [*Hansen et al. 1996, Marsavina et al. 2009, Marques et al. 2010, Bastidas-Arteaga et al. 2011*], and propagation, see e.g. [*Bazant 1979, Isgor et al. 2006, Warkus et al. 2006*], of reinforcement corrosion to facilitate the service life prediction of reinforced concrete structures. However, most of the available models focus on specific aspects affecting reinforcement corrosion, such as the influence of concrete resistivity, see e.g. [*Osterminski et al. 2006, Huet et al. 2007, Warkus et al. 2008*], neglect the impact of important structural details, such as cracks and defects, see e.g. [*Jäggi 2001, Hasegawa et al. 2004, Ghods et al. 2007*], and treat either the initiation or propagation phase of reinforcement corrosion in concrete structures explicitly, see e.g. [*Kranc et al. 2001, Maruya et al. 2003, Ouglova et al. 2005*].

The theoretical framework of the proposed corrosion model and coupling with material and transport models is presented in Paper III and Paper IV. In principle, two physical laws can be used to describe the electrochemical processes in the concrete pore solution acting as electrolyte [*Warkus et al. 2006*]. The first one is Laplace's equation, which describes the potential distribution in the electrolyte assuming electrical charge conservation and isotropic conductivity:

$$\nabla^2 E = 0 \tag{3.9}$$

The second is Ohm´s law, which can be used to determine the rate of dissolution of iron at any point on the steel surface in concrete if the potential distribution around that point and the resistivity of the electrolyte is known [*Isgor et al. 2006*]:

$$i_{corr} = -\frac{1}{\rho_{conc}} \frac{\partial E}{\partial n} \tag{3.10}$$

where ρ_{conc} is the concrete resistivity and *n* the direction normal to the rebar surface.

3.3.1 Modelling initiation and propagation of reinforcement corrosion

To link corrosion initiation, i.e. the formation of anodic regions at the reinforcement surface, and propagation of reinforcement corrosion a conditional statement is defined along the reinforcement surface. Since the present work is dealing with chloride-induced corrosion, the conditional statement comprises the definition of a critical chloride threshold for elements along the reinforcement surface, which might be defined as follows:

$$BC_{Steel} = \begin{cases} i_a \\ i_c \end{cases} for \begin{matrix} c_{cl} \geq c_{crit} \\ c_{cl} < c_{crit} \end{matrix} \tag{3.11}$$

where BC_{Steel} is the boundary condition along the steel surface, i_a the anodic polarisation curve (see also Eq. 3.5), i_c the cathodic polarisation curve (see also Eq. 3.7), c_{cl} the chloride concentration along the reinforcement, and c_{crit} the critical chloride threshold defined along the reinforcement elements. A similar conditional statement for elements along the steel surface may be derived in case of carbonation-induced corrosion.

Within the literature, varying critical chloride threshold values can be found, ranging from 0 to approximately 2% of weight cement [*Angst et al. 2009*]. Among others, the critical chloride threshold is influenced by defects present along the reinforcement [*Buenfeld et al. 2004, Nygaard et al. 2005*], material properties and exposure conditions [*fib 1992*] as well as the electrochemical potential [*Angst et al. 2009*]. A qualitative representation of the critical chloride threshold as a function of material properties and exposure conditions is given in Figure 3.4 as proposed in [*fib 1992*]. Experimental results of the impact of interfacial voids on the critical chloride threshold were investigated in [*Buenfeld et al. 2004*] and are illustrated in Figure 3.5. From the results presented in Figure 3.4 and Figure 3.5, it becomes clear that a single critical chloride threshold defining the initiation of corrosion in a concrete structure is very unlikely. Therefore, the critical chloride threshold is varied randomly, ranging from 0 to 2% of weight cement, along the reinforcement surface in the present model to account for the influence of various parameters and represent a realistic structure with defects, voids, etc. present at the concrete steel interface.

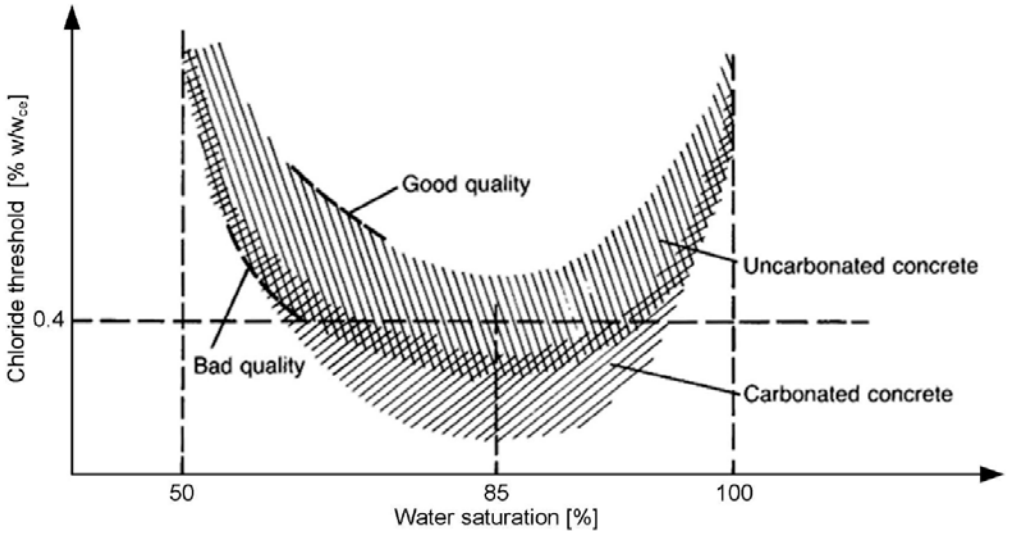

Figure 3.4 *Critical chloride threshold as a function of material properties and exposure conditions, after [fib 1992].*

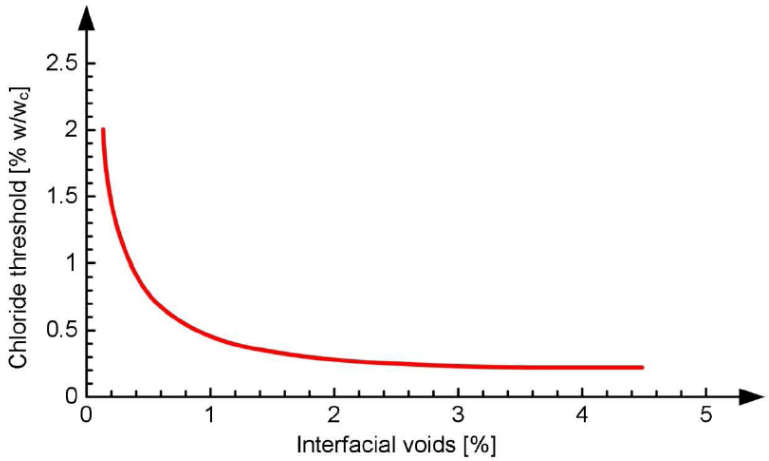

Figure 3.5 *Critical chloride threshold as a function of interfacial voids, after [Buenfeld et al. 2004].*

3.3.2 Influencing parameters

Corrosion processes in reinforced concrete structures are highly complex and affected by interactions of the steel and concrete with ambient conditions. The electrochemical half-cell reactions of the active (anode) and the passive rebar surface (cathode) as well as the heat and mass transfer of various species are controlling the corrosion progress within the concrete structure. Which of these parameters mainly control the corrosion rate is determined by numerous factors such as temperature, moisture content, admixture of concrete, geometric arrangement of reinforcement and many more.

To investigate the influence of various parameters on the kinetics of the corrosion process a parametric study with a simplified model geometry was conducted. Within the parametric study, the effects of anode-to-cathode area ratio, oxygen, temperature, and moisture content on the corrosion current density were investigated. Wherever possible, results of the numerical model were compared to experimental results, either provided in the literature or carried out in connection with the Ph.D. studies. A simple beam geometry was chosen for the parametric study with predefined anodic and cathodic areas along the reinforcement. As half-cell reactions, the oxidation of iron (anode) and the reduction of oxygen (cathode) were considered, which are most common under natural environments. Electrochemical parameters, such as the equilibrium potential, exchange current density or limiting current density, were determined from the thermodynamic and kinetic principles presented in Section 3.2. Material properties, such as resistivity, were taken from the corresponding literature when compared to experimental results. The geometry of the beam and the mesh are shown in Figure 3.6.

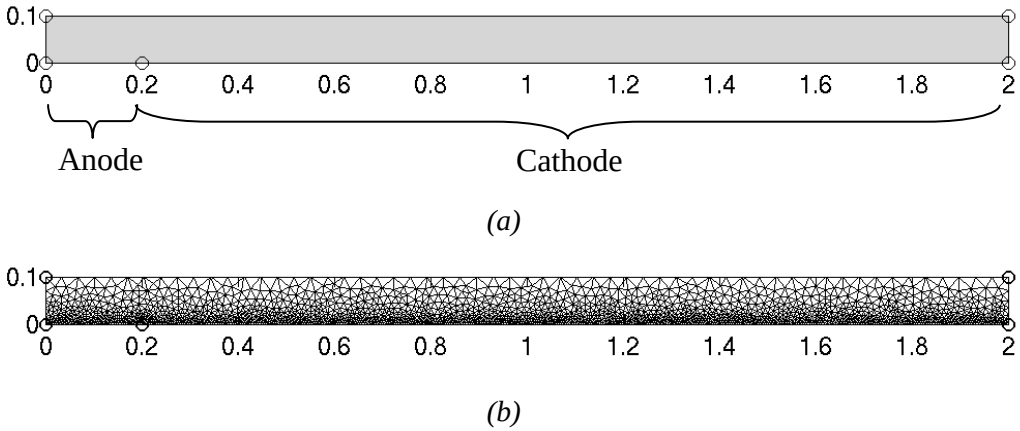

Figure 3.6 *Simplified model to study the influence of various parameters on the reinforcement corrosion process. (a) geometry with predefined anodic and cathodic areas and (b) mesh (all dimensions in m).*

3.3.2.1 Anode-to-cathode area ratio

Defects in reinforcement coatings, e.g. paint or epoxy, or in the concrete cover can result in the formation of small anodic sites compared to the cathodic area, which may considerably increase the corrosion rate at the location of the defect. The impact of the anode-to-cathode area ratio on the corrosion current density is illustrated in Figure 3.7 and the model parameters are presented in Table 3.2. To avoid the influence of resistance and concentration polarisation on the kinetics of the corrosion process, the concrete resistivity was defined close to zero and the limiting current density was set to "virtual" infinity.

Results of the numerical simulation are presented for the anodic corrosion current density and the (total) corrosion current. The corrosion current is thereby determined as the area under the anodic corrosion current density curve. Initially, a steep decrease in the corrosion current density can be observed, while the corrosion current is increasing. For an anode-to cathode ratio of approximately 1.75 the maximum corrosion current can be found. The location of the maximum corrosion current may be interpreted as a thermodynamic state of the system at which an "equilibrium anode-to-cathode area ratio" is formed along the reinforcement minimising the total energy [*Stern et al. 1957*]. The location of the maximum corrosion current depends thereby on the anodic and cathodic Tafel constants. For equal anodic and cathodic Tafel constants, i.e. $b_a = b_c$, the maximum corrosion current is located at an anode-to-cathode area ratio of one, while the location is shifted towards zero or infinity for any other combination of Tafel constants.

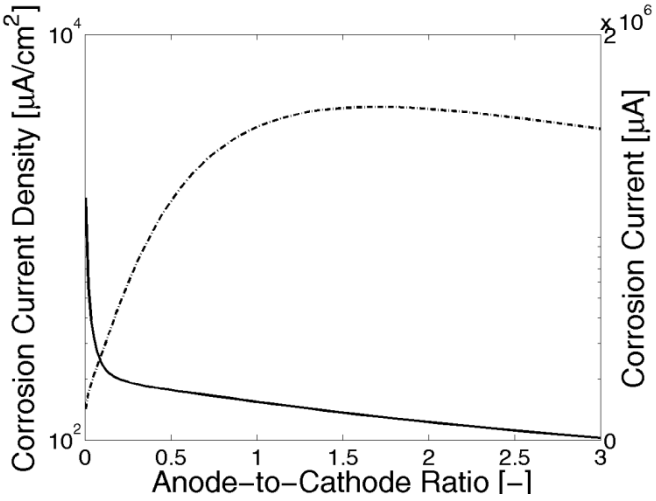

Figure 3.7 *Influence of anode-to-cathode area ratio on the corrosion current density (solid line) and corrosion current (broken line) for simplified model geometry (see Table 3.2 for model parameters and assumptions).*

Table 3.2 *Model parameters for numerical simulations to investigate the impact of anode-to-cathode area ratio on the corrosion current density (T 20°C).*

Model Parameter	Symbol	Value	Unit
Concrete resistivity	ρ_{conc}	1E-06	Ωm
Anodic exchange current density	i_{0a}	1.88E-04	A/m^2
Anodic equilibrium potential	E_{0a}	-0.78	V_{SCE}
Anodic Tafel constant	b_a	0.06	V/dec
Cathodic exchange current density	i_{0c}	6.25E-06	A/m^2
Cathodic equilibrium potential	E_{0c}	0.16	V_{SCE}
Cathodic Tafel constant	b_c	0.16	V/dec
Limiting current density	i_{lim}	1E06	A/m^2

3.3.2.2 Temperature

Concrete structures are constantly subjected to temperature gradients as a result of daily or seasonal temperature variations. Experimental investigations on the influence of temperature on the kinetics of the corrosion process are presented in Paper V. Concrete specimens with partly embedded reinforcement (passively and actively corroding) were conditioned at different relative humidities and subsequently subjected to varying temperatures to investigate the short-term impact of temperature on the corrosion process. Potentiodynamic linear polarisation resistance and galvanostatic pulse measurements were used to measure and determine the free corrosion potential, polarisation and ohmic resistance. From that, the corrosion rate of each reinforcement bar in the specimens was calculated. More details on the materials, geometry and conditioning of specimens, and measurement techniques are presented in Paper V.

Results of the experimental study are compared to numerical results in Figure 3.8 and the model parameters for the numerical simulation are given in Table 3.3. The concrete resistivity was taken from the experimental data provided in Paper V and the impact of temperature on the equilibrium potentials and Tafel constants for the anodic and cathodic half-cell reaction was determined from Equation (3.4) and (3.6). Only small variations in the Tafel constants and equilibrium potentials were found due to the temperature variations, which is in agreement with the experimental observations presented in Paper V. However, the effect of temperature on the exchange current density is considerable [*Hurlen 1960*]. To account for the impact of temperature on the exchange current density the following equation may be used [*Tanaka et al. 1964*]:

$$i_{0,T} = i_{0,Ref} exp\left(\left(\frac{\alpha z F E_0}{R}\right)\left(\frac{1}{T} - \frac{1}{T_{Ref}}\right)\right) \tag{3.12}$$

where $i_{0,T}$ is the exchange current density at temperature, T and $i_{0,Ref}$ the exchange current density at the reference temperature, T_{Ref}.

Table 3.3 *Model parameters for numerical simulations to investigate the impact of temperature on the corrosion current density.*

Model Parameter	Symbol	Value	Unit
Concrete resistivity	ρ_{conc}	Paper V	Ωm
Anodic exchange current density	i_{0a}	Equation (3.12)	A/m^2
Anodic equilibrium potential	E_{0a}	Equation (3.4)	V_{SCE}
Anodic Tafel constant	b_a	Equation (3.6)	V/dec
Cathodic exchange current density	i_{0c}	Equation (3.12)	A/m^2
Cathodic equilibrium potential	E_{0c}	Equation (3.4)	V_{SCE}
Cathodic Tafel constant	b_c	Equation (3.6)	V/dec
Limiting current density	i_{lim}	Equation (3.8)	A/m^2

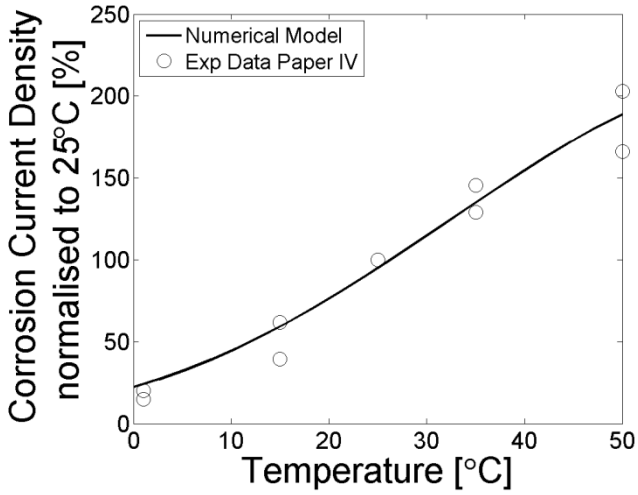

Figure 3.8 *Comparison of experimental and numerical data on the impact of temperature on the corrosion current density.*

Results presented in Figure 3.8 show a very good agreement between the experimental and numerical data, which indicates that the model is capable of simulating the short-term effect of temperature on the kinetics of the corrosion process.

3.3.2.3 Oxygen

As mentioned previously, the reduction of oxygen is one of the main half-cell reactions taking place under natural conditions in reinforced concrete structures (other cathodic reactions may also take place under certain conditions, see e.g. [*Küter 2009, Toro et al. 2012*]). Depletion of oxygen in the vicinity of the reinforcement will cease the cathodic half-cell reaction and subsequently the corrosion process itself. The effect is quantified by Equation (3.8) in the corrosion model, which relates the oxygen concentration at the steel surface to the limiting current density. The limiting current density directly affects the polarisation behaviour of the cathode and ultimately the corrosion current density. A graphical relation between the limiting current density and the corrosion current density for the simplified model is given in Figure 3.9.

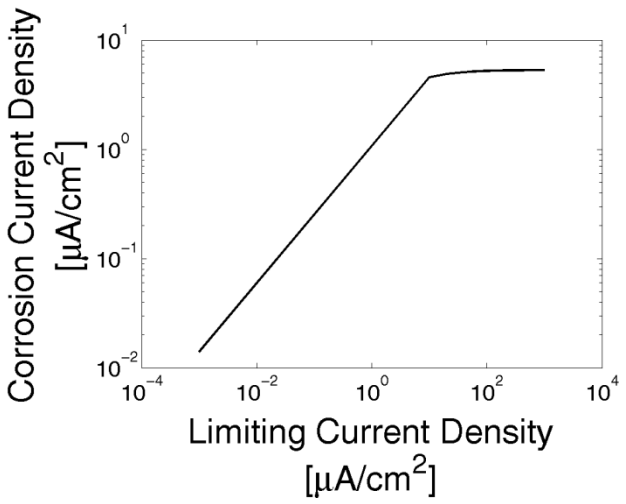

Figure 3.9 *Relation between limiting current density and corrosion current density for the simplified model geometry.*

Experimental results on the impact of oxygen on the corrosion process are presented in e.g. [*Raupach 1996*], who studied the kinetics of the corrosion process for specimens under different storage conditions. Among others, Raupach [*Raupach 1996*] investigated specimens that were stored under water for one year prior to electrochemical testing. To study the effect of oxygen on the corrosion rate, Raupach [*Raupach 1996*] polarised the steel surface to enhance the corrosion process and ensure oxygen reduction is the governing half-cell reaction at the cathodic sites. Results of the experimental investigations are illustrated in Figure 3.10. Initially, a considerable corrosion current density of approximately 2.5μA/cm^2 (1000μA) was measured, which decreased after a short period of time. The initial increase in corrosion current density was attributed to the presence of dissolved oxygen in the vicinity of the steel surface, which was rapidly consumed by the cathodic half-cell reaction leading to a depletion of oxygen and subsequent reduction of the corrosion rate.

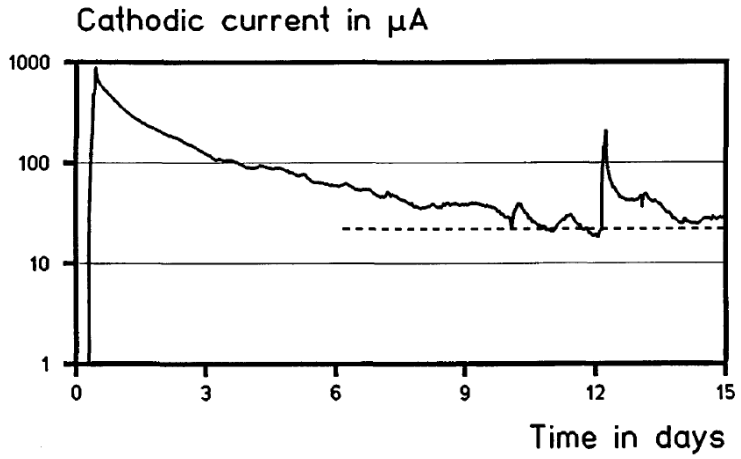

Figure 3.10 *Influence of oxygen availability on the cathodic reaction (oxygen reduction) and corrosion current density of submerged specimens, from [Raupach 1996].*

Similar results, found from numerical simulations, are presented in Figure 3.11 for the simplified model geometry. Initially, a considerable corrosion current density is obtained due to the presence of dissolved oxygen in the vicinity of the steel surface. With progressing time, the oxygen is consumed by the cathodic half-cell reaction, which leads to a depletion of the oxygen and a reduction of the corrosion current density to negligible values. The model parameters for the numerical simulation to investigate the influence of oxygen on kinetics of the corrosion process are given in Table 3.4. In addition, the development of the limiting current density and the oxygen concentration at the reinforcement surface (for different distances from the anode) are presented in Figure 3.12 and Figure 3.13, respectively.

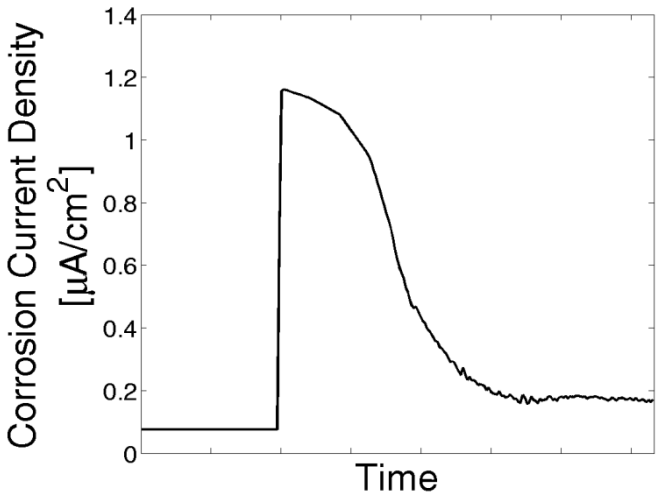

Figure 3.11 *Development of corrosion current density for the simplified model geometry under submerged conditions.*

Table 3.4 *Model parameters for numerical simulations to investigate the availability of oxygen at the cathode on the corrosion current density under submerged storage conditions (T 20°C).*

Model Parameter	Symbol	Value	Unit
Concrete resistivity	ρ_{conc}	20	Ωm
Anodic exchange current density	i_{0a}	1.88E-04	A/m^2
Anodic equilibrium potential	E_{0a}	-0.78	V_{SCE}
Anodic Tafel constant	b_a	0.06	V/dec
Cathodic exchange current density	i_{0c}	6.25E-06	A/m^2
Cathodic equilibrium potential	E_{0c}	0.16	V_{SCE}
Cathodic Tafel constant	b_c	0.16	V/dec
Oxygen concentration	c_{O2}	0.278	mol/m^3
Limiting current density	i_{lim}	2.14E-02	A/m^2

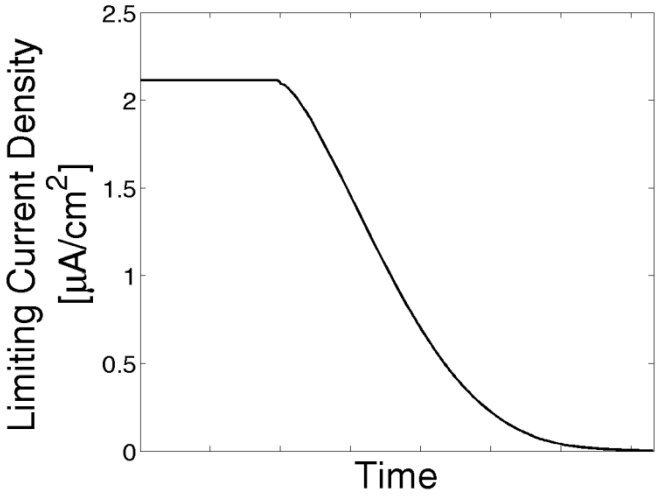

Figure 3.12 *Change of limiting current density under submerged conditions (for the simplified model geometry).*

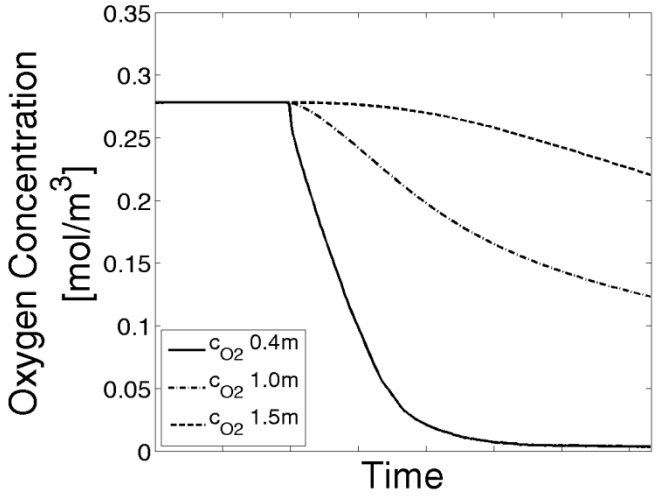

Figure 3.13 *Change of oxygen concentration (at reinforcement surface) at different distances from the anode under submerged conditions (for the simplified model geometry).*

3.3.3 Comparison to experimental tests

To demonstrate the capability of the reinforcement corrosion model presented in this chapter, Paper III, and Paper IV, numerical simulations of the reinforcement corrosion process are compared to experimental investigations presented in [*López et al. 1993a*].

López et al. [*López et al. 1993a*] investigated the influence of the degree of saturation on the resistivity of mortar specimens and the corrosion rate of carbon steel reinforcement. Two sets of specimen with mixed-in chlorides (2% by weight of cement) were prepared; one set for resistivity measurements ($8\times8\times2\text{cm}^3$ mortar prisms) and another for electrochemical measurements ($8\times5.5\times2\text{cm}^3$ mortar prisms). The specimens for the electrochemical measurements were prepared with two carbon steel reinforcement bars (working electrode), which were symmetrically embedded around a centred stainless steel rebar (counter electrode). The specimens were cured for 40 days at 23°C and afterwards exposed for 60 days to a relative humidity higher than 90%. Finally, the mortar prisms were stored at 50°C and 50% relative humidity for 500 days. More detailed information on the materials, conditioning, and geometry of the specimens as well as measurement techniques can be found in [*López et al. 1993, López et al. 1993a*].

Details on the model parameters are provided in Table 3.5 and the model geometry and mesh for the numerical simulations are shown in Figure 3.14. Geometry and material properties, such as mortar resistivity as a function of degree of saturation, were taken from the experimental data provided in [*Lopez et al. 1993a*]. Electrochemical parameters for the numerical model were derived from the thermodynamic and kinetic principles presented in the previous section.

Table 3.5 *Model parameters for numerical simulations to compare numerical results with experimental results obtained by [Lopez et al. 1993a].*

Model Parameter	Symbol	Value	Unit
Mortar resistivity	ρ_{mor}	[*López et al. 1993a*]	Ωm
Anodic exchange current density	i_{0a}	Equation (3.12)	A/m^2
Anodic equilibrium potential	E_{0a}	Equation (3.4)	V_{SCE}
Anodic Tafel constant	b_a	Equation (3.6)	V/dec
Cathodic exchange current density	i_{0c}	Equation (3.12)	A/m^2
Cathodic equilibrium potential	E_{0c}	Equation (3.4)	V_{SCE}
Cathodic Tafel constant	b_c	Equation (3.6)	V/dec
Limiting current density	i_{lim}	Equation (3.8)	A/m^2

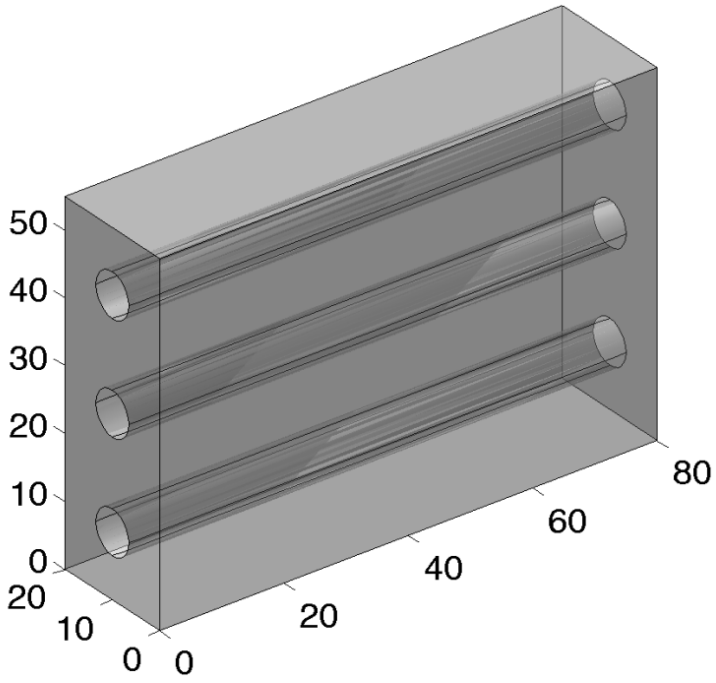

(a)

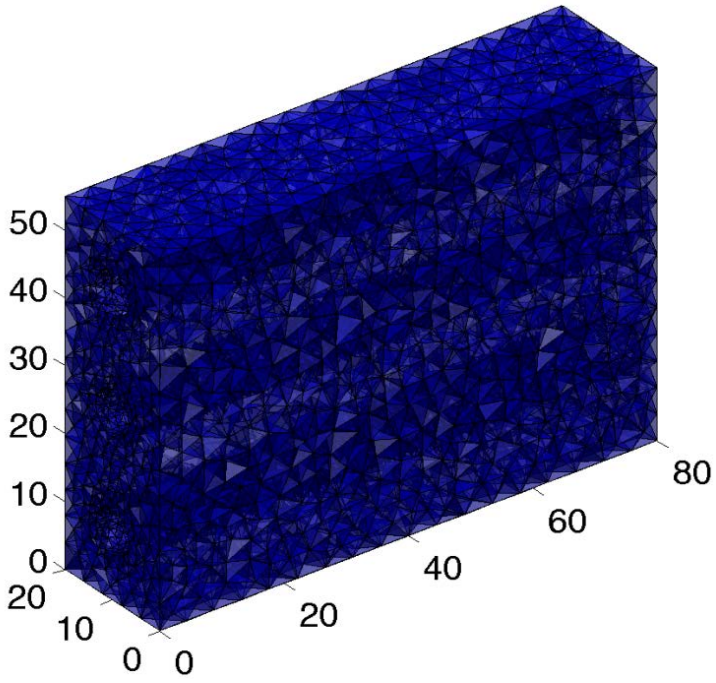

(b)

Figure 3.14 *(a) geometry and (b) mesh of numerical model for comparison with experimental investigations presented in [Lopez et al. 1993a] (all dimensions in mm).*

Results of the numerical simulations and presented in [*Lopez et al. 1993a*] are illustrated in Figure 3.15 highlighting the impact of varying degree of saturation on the corrosion current density. It is evident from the presented results that the corrosion model can accurately simulate the experimental conditions and corrosion current density presented in [*Lopez et al. 1993a*]. Furthermore, the impact of the various polarisation mechanisms controlling the corrosion process becomes clear from the results presented in Figure 3.15. At lower degrees of saturation (below approximately 30%), very low corrosion current densities are measured and predicted by the corrosion model. The results indicate that in this area resistance polarisation is mainly controlling the corrosion mechanism, which is attributed to the high mortar resistivity. In particular, the influence of the moisture content on the resistivity is considerable [*Tuutti 1982, Larsen 2007*]. With increasing degree of saturation the mortar resistivity is decreasing rapidly, which is consequently leading to an increase in the corrosion current density. Between approximately 60 and 80% degree of saturation, a limited increase in corrosion current density is observed, although the mortar resistivity is still decreasing. Within that area, the corrosion process is assumed to be controlled by a combination of activation and resistance polarisation. Finally, a decrease in corrosion current density is observed for values higher than approximately 85% degree of saturation. As presented in the previous section, the moisture content has considerable effects on the mass transport of species, which are relevant for the corrosion process. In this area (from approximately 85 to 100% degree of saturation), the corrosion process is mainly controlled by concentration polarisation due to a lack of oxygen ceasing the cathodic half-cell reaction. All these different polarisation phenomena, i.e. activation, concentration, and resistance polarisation, are captured very well by the reinforcement corrosion model indicating that it is indeed capable of simulating the kinetics of the corrosion process.

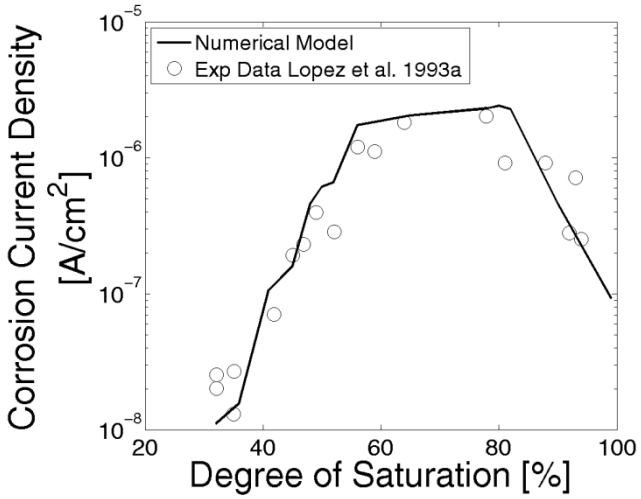

Figure 3.15 *Comparison between experimentally measured corrosion current density and numerically modelled corrosion current density (experimental data reproduced from [Lopez et al. 1993a]).*

3.4 Impact of cracks

Within the past decades numerous investigations on the impact cracks have on the ingress of corrosion initiating substances and reinforcement corrosion have generally concluded that cracks facilitate rapid ingress of aggressive substances, see e.g. [*Jacobsen et al. 1996, Aldea et al. 1999, Edvardsen 1999, Rodriguez 2003, Pease et al. 2009, Pease 2010*] and subsequently reduce the corrosion initiation time. Both laboratory studies (see e.g. [*Gautefall et al. 1983, Berke et al. 1993, Arya et al. 1996*]) and in-situ observations (see e.g. [*Rehm et al. 1964, Schießl 1976, Schießl et al. 1997*] have noted an expedited corrosion initiation in cracked concrete compared to pristine concrete. Commonly used approaches attempt to relate corrosion initiation and propagation to the concrete surface crack width (see e.g. [*Gautefall et al. 1983, Berke et al. 1993, Schießl 1976, Schießl et al. 1997*]). Hence, controlling concrete surface crack widths has become the norm to attempt to minimize the impact of cracks on corrosion-induced deterioration in structural design codes and recommendations, see e.g. [*ACI Committee 224 2001, DAfStb 2003, Eurocode 2 2004*]. Various probabilistic, empirical, and quasi-analytical cracking models are utilized in structural design codes to predict crack widths based upon numerous geometric and stress (or strain) parameters. However, predicted and observed crack widths can vary significantly. Further, a number of studies (both from laboratory and in-situ conditions) indicate that the concrete surface crack width alone cannot accurately assess the impact of cracks on reinforcement corrosion as other factors, such as concrete cover thickness [*Schießl et al. 1997, Schießl 1976*], concrete composition (specifically water-to-cement ratio [*Berke et al. 1993, Schießl et al. 1997, Miyazato et al 2005, Otieno et al. 2010, Makita et al. 1980*] and addition of supplementary cementitious materials [*Gautefall et al. 1983, Marcotte et al. 2003,Scott et al. 2007*]), stress level in the reinforcement [*Yoon et al. 2004*], and crack orientation [*Poursaee et al. 2008*] alter the influence of the crack width on reinforcement corrosion.

One possible explanation for the lacking relationship between concrete surface crack width and reinforcement corrosion behaviour is that the surface crack width alone does not reliable describe the condition of the concrete-reinforcement interface [*Tammo et al. 2009, Pease 2010*]. The condition of the concrete-reinforcement interface appears to be a more fundamental issue than the concrete surface crack width influencing the corrosion protection ordinarily provided by concrete. Several references report accelerated corrosion initiation and relatively excessive cross-sectional reductions (compared to reinforcement with good cohesion with concrete) taking place at sites of various interfacial defects, including entrapped or cast-in voids [*Buenfeld et al. 2004, Nygaard et al. 2005*], spalled concrete [*O'Neil 1980*], and interfacial slip and separation caused by mechanical loading [*Pease et al. 2011*]. The presence of voids at the concrete-reinforcement interface reduces the critical chloride threshold for corrosion initiation as studied and presented by [*Buenfeld et al. 2004, Nygaard et al. 2005*]. This, coupled with the increased ingress rate of corrosion-initiating substances in the

presence of concrete cracks as described above, clearly illustrates the potential deleterious impact of concrete cracks on reinforced concrete structures.

Paper VIII presents experimental studies investigating the relation between damage at the concrete-reinforcement interface and initiation of reinforcement corrosion in plain and fibre reinforced concrete. Main focus of the study was to test the hypothesis that controlling the concrete-reinforcement interfacial condition can be used as a reliable indicator for the impact of cracks on the risk of corrosion initiation along the reinforcement. The relation between interfacial damage and risk of corrosion initiation along the reinforcement was investigated for plain (PC) and steel fibre reinforced concrete (SFRC) beams subjected to flexural loading. A numerical model, developed and calibrated in Paper VI and Paper VII, provided estimates on the extent of the interfacial damage for the applied loads and measured surface crack widths. The impact of concrete cover thickness, concrete composition, stress level in the reinforcement and crack orientation on the mechanical response of the beam, i.e. cracking and interfacial damage, is directly accounted for in the numerical model. Location- and time-dependent corrosion measurements along the reinforcement were performed using recently developed "instrumented rebars", which have a largely similar mechanical behaviour as conventional reinforcement [*Pease et al. 2011*]. A sketch of the design of the instrumented rebar is illustrated in Figure 3.16. The applicability of the instrumented rebar to monitor time- and location-dependent corrosion potentials in concrete, while having a similar mechanical behaviour as a conventional rebar, was tested and presented in [*Pease et al. 2011*]. Figure 3.17 illustrates the customized steel cracking frames, which were used to hold open cracks and interfacial damage after the beams were pre-cracked using a standard loading machine. During pre-cracking, load was applied to estimated cracking loads predicted by the numerical cracking model described in Paper VI and Paper VII. More detailed information on the material properties, specimen geometry, and mechanical and electrochemical testing procedures are provided in Papers VI - VIII.

For each beam tested, the corrosion potential was measured at 17 locations and the corrosion current at 8 locations along the instrumented rebar. Contour plots illustrating results of all sensor locations along the instrumented rebar for plain reinforced concrete (PC) and steel fibre reinforced concrete (SFRC) are shown in Figure 3.18, Figure 3.19, and Figure 3.20. Results are given as a function of the exposure time (in days) and location from the crack (in mm) as well as corrosion potential (in V_{SCE}) and corrosion current (in μA), which are indicated by a colour scale. Comparisons of the contour plots presented in Figure 3.18, Figure 3.19, and Figure 3.20, show similar corrosion potentials for all three materials tested at the beginning of exposure, indicating passive corrosion state of the reinforcement. Similar values for passive reinforcement are reported in the literature (see e.g. [*Küter 2009, Pease et al. 2011*]). With progressing time, an either gradual decrease or sudden drop in the corrosion potential was observed for sensors along the instrumented rebar for all beams tested indicating that

active corrosion is thermodynamically favoured. Signs of active corrosion were observed for potential differences ranging from approximately 0.1 to 0.4 V_{SCE} for the various materials tested. Active corrosion was additionally confirmed by corrosion current measurements and destructive visual observations after testing was finished. However, time to corrosion initiation and extent of corrosion varied for the tested PC and SFRC beams.

The results facilitate the hypothesis that the concrete-reinforcement interfacial condition can be used as a reliable indicator to quantify the impact of mechanically induced cracks on the risk of corrosion initiation along the reinforcement. Very good agreements between the simulated interfacial damage, in particular the separation between reinforcement and concrete, and extent of active corrosion along the instrumented rebar indicated by the electrochemical measurements were obtained for all materials tested. Similar to the interfacial damage, a good correlation between the crack width at the concrete surface and extent of corrosion along the reinforcement was found for the three beams tested. However, for larger crack widths at the concrete surface the correlation between crack width and extent of corrosion may not hold true, especially with regards to the use of SFRC as the addition of steel fibres alter the extent of interfacial damage compared to PC as presented in Paper VI and Paper VII.

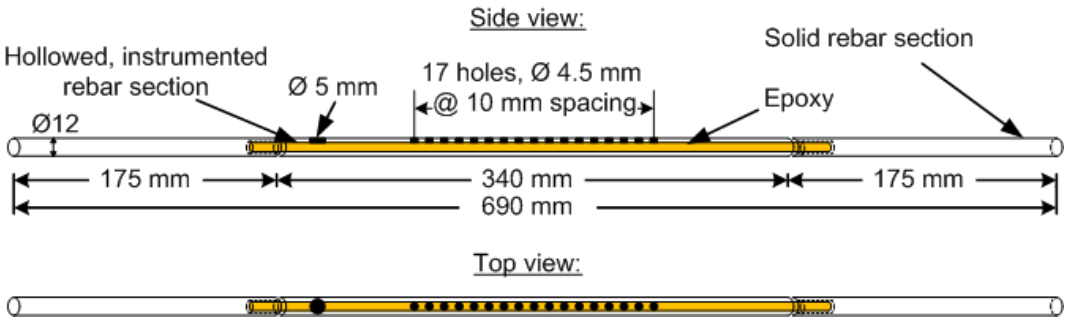

Figure 3.16 *Design of instrumented rebar for time- and location-dependent corrosion potential and corrosion current measurements (Note: ribs are not shown in sketch), after [Pease et al. 2011].*

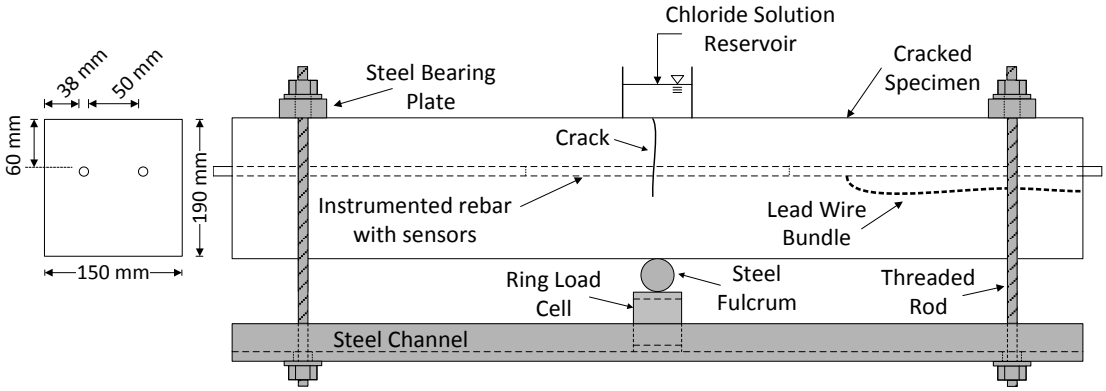

Figure 3.17 *Steel cracking frames for loading of beams illustrating the instrumented rebar and ponding reservoir, after [Pease et al. 2011].*

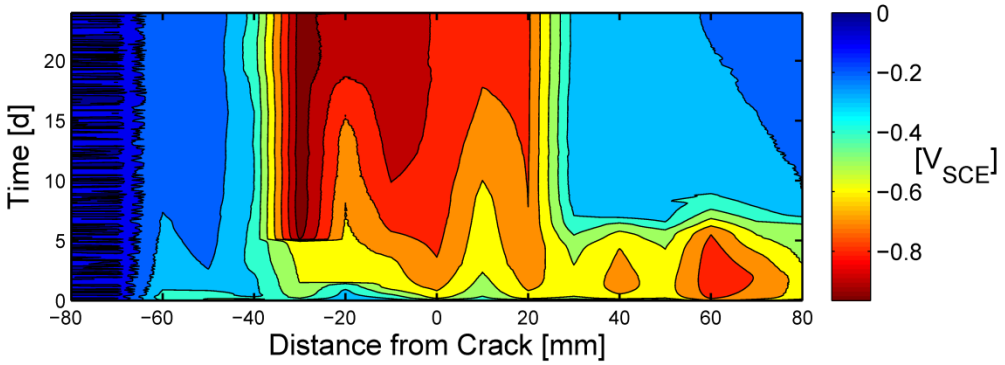

(a)

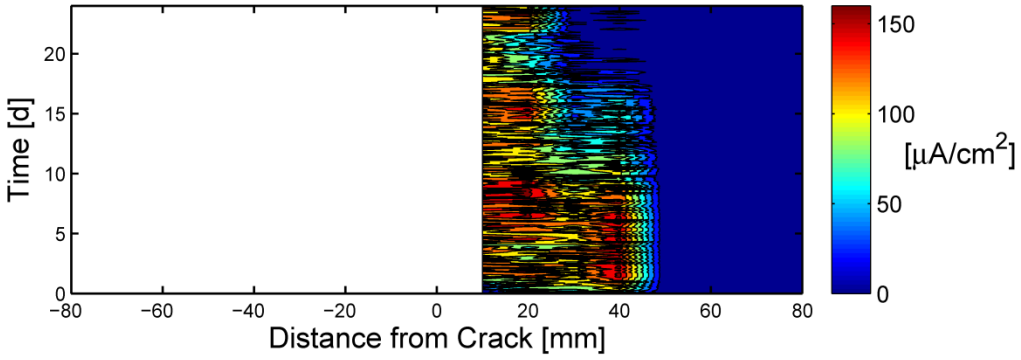

(b)

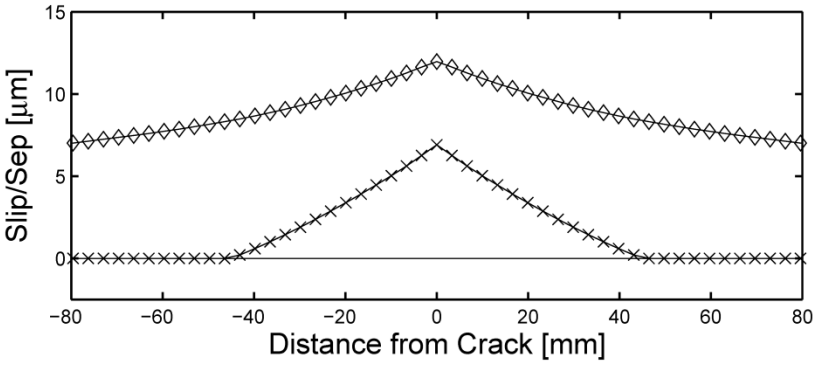

(c)

Figure 3.18 *Location- and time-dependent corrosion potential (a) and corrosion current density (b) (only for half of the sensors) measurements for plain concrete. (c) simulated extent of slip (diamond symbols) and separation (cross symbols) between concrete and reinforcement (crack width at concrete surface 0.069mm).*

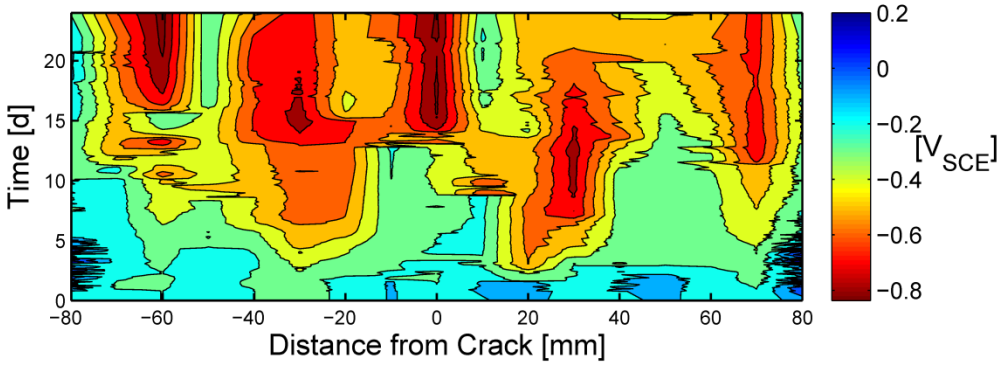

(a)

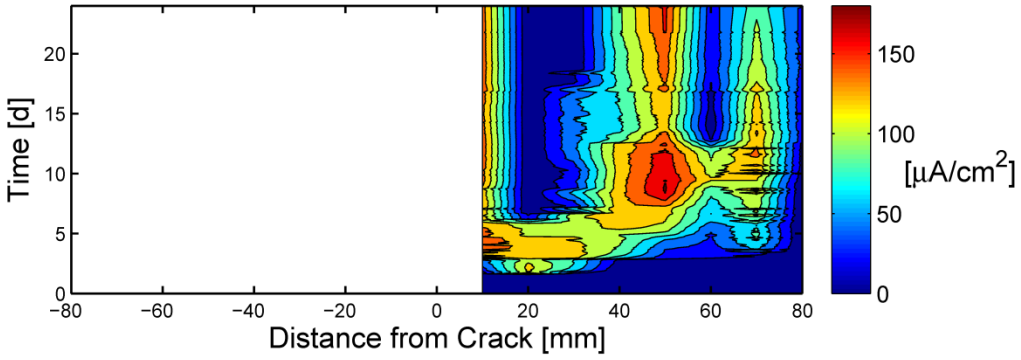

(b)

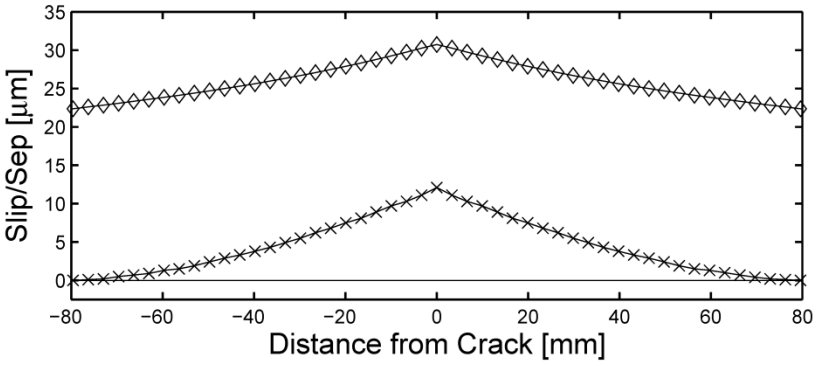

(c)

Figure 3.19 *Location- and time-dependent corrosion potential (a) and corrosion current density (b) (only for half of the sensors) measurements for steel fibre reinforced concrete (0.5 vol%). (c) simulated extent of slip (diamond symbols) and separation (cross symbols) between concrete and reinforcement (crack width at concrete surface 0.139mm).*

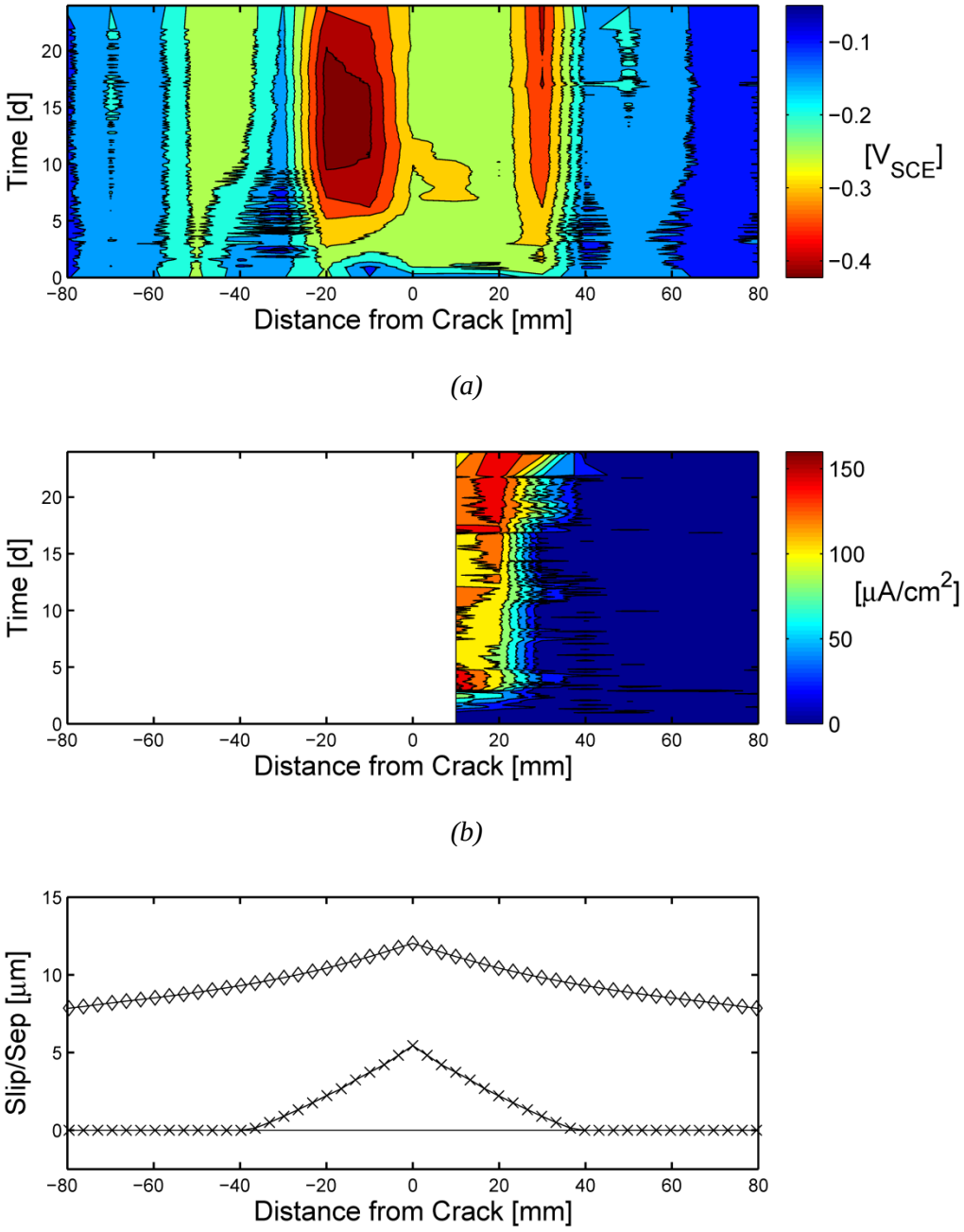

Figure 3.20 *Location- and time-dependent corrosion potential (a) and corrosion current density (b) (only for half of the sensors) measurements for steel fibre reinforced concrete (1.0 vol%). (c) simulated extent of slip (diamond symbols) and separation (cross symbols) between concrete and reinforcement (crack width at concrete surface 0.068mm).*

3.5 Service life prediction - an example

To demonstrate the potential use of the electrochemical corrosion model for service life prediction a numerical example is provided. The example accounts for heat and mass transfer of various species, which is described by the material and transport model introduced in Chapter 2. The heat and mass transfer is furthermore fully coupled to the reinforcement corrosion model presented in the previous sections of this chapter, which simulates the initiation and propagation of reinforcement corrosion. Corrosion is initiated when a critical chloride threshold at the reinforcement surface is reached (see Section 3.3.1). As mentioned previously, the critical chloride thresholds are distributed randomly along the reinforcement surface, hence anodic areas will also form randomly. The defined critical chloride thresholds are assumed constant throughout the complete simulation time. Varying climatic boundary conditions are applied, which will affect the thermodynamics and kinetics of reinforcement corrosion as presented in Sections 3.2 and 3.3. To demonstrate the impact of cracks on the service life prediction, the simulation is repeated and a crack is included in the geometry. The crack is considered to act as a free surface in terms of heat and mass transfer. Although, previously presented results (see Section 2.5) indicate that a portion of the crack inhibits the ingress of aggressive substances, such as moisture or chlorides, and obeys similar behaviour as the bulk material, the delayed ingress is negligible with respect to the service life of a reinforced concrete structure. In the presented experimental tests (see Section 2.5), the moisture front reached the bottom of the measurement area after a couple of hours. Model geometry and mesh for the numerical example are presented in Figure 3.21. Annual profiles of temperature, relative humidity, and chloride, applied as boundary conditions in the numerical simulation, are presented in Figure 3.22, Figure 3.23, and Figure 3.24. An overview of the modelling parameters for the simulation is given in Table 3.6. Selected results of the simulation include corrosion potential, corrosion current density, chloride concentration, and critical chloride thresholds along the reinforcement surface for different times as well as the development of cross sectional reduction of the reinforcement over a period of 100 years.

Figure 3.25 (a) and (b) illustrate the assigned critical chloride thresholds as well as chloride concentrations for various times in the uncracked and cracked beam geometry, respectively. The presented results clearly show the impact of the crack on the chloride ingress. Considerably higher chloride concentrations can be found in the vicinity of the reinforcement due to the presence of the crack, which leads to an earlier achievement of the assigned critical chloride thresholds in the vicinity of the crack. As soon as a critical chloride threshold is reached, corrosion is initiated as shown in Figure 3.26 by a decrease in corrosion potential. Comparing the uncracked and cracked geometry reveals, that corrosion is initiated considerably earlier in the cracked beam. After approximately 29.2 years of simulation time no decrease in corrosion potential is seen for the uncracked beam geometry, while the corrosion potential near the crack

is decreased to values indicating active corrosion of reinforcement for the cracked beam geometry. As the chloride concentration near the reinforcement is increasing with progressing time, more critical chloride thresholds are reached and anodic sites along the reinforcement are formed. The resulting corrosion current density along the reinforcement in the cracked and uncracked beam geometry is illustrated in Figure 3.27 for selected times. Similar to the development of the corrosion potential, the influence of the crack can be observed. After approximately 29.2 years, two distinct regions can be distinguished for the cracked beam geometry; an active region near the crack and passive regions at a certain distance from the crack. No active corrosion is observed in the uncracked beam geometry. The arrangement of anodic and cathodic sites in the cracked beam geometry results in a localized corrosion attack near the crack, with higher cross sectional reductions of the reinforcement compared to the uncracked beam geometry. Figure 3.28 shows the development of the cross sectional reduction of the reinforcement over a period of 100 years for both geometries. The impact of the crack on the cross sectional reduction can be clearly seen comparing Figure 3.28 (a) and (b). While up to approximately 30 years no corrosion is initiated in the uncracked beam, active corrosion is observed in the cracked beam almost right from the beginning. Comparison between the cross sectional reduction after approximately 100 years reveals that higher values can be found in the cracked beam geometry. A flattening of the cross sectional reduction curves towards the end of the simulations is observed for both geometries, which is attributed to the formation of large anodic areas along the reinforcement, rather than distinct anodic and cathodic areas. The corresponding corrosion current density is then considerably lower (see Section 3.3.2.1), resulting therefore in lower cross sectional reductions. Variations in the corrosion current density due to annual variations in temperature, chloride, and moisture are clearly visible in Figure 3.29 in which the cross sectional reduction between 33 and 35 years is plotted for the uncracked beam geometry and between 7 and 9 years for the cracked beam geometry.

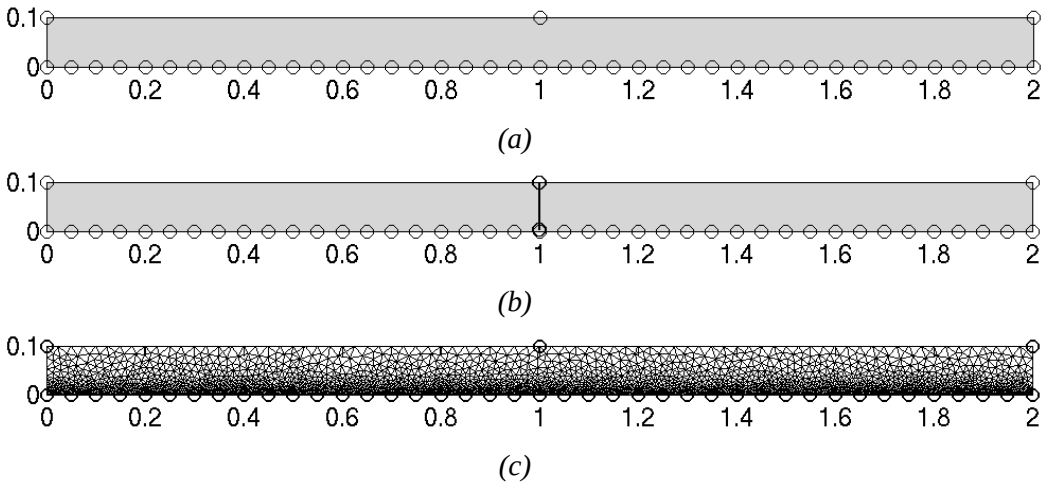

Figure 3.21 *Model geometry for (a) uncracked beam and (b) cracked beam and (c) mesh.*

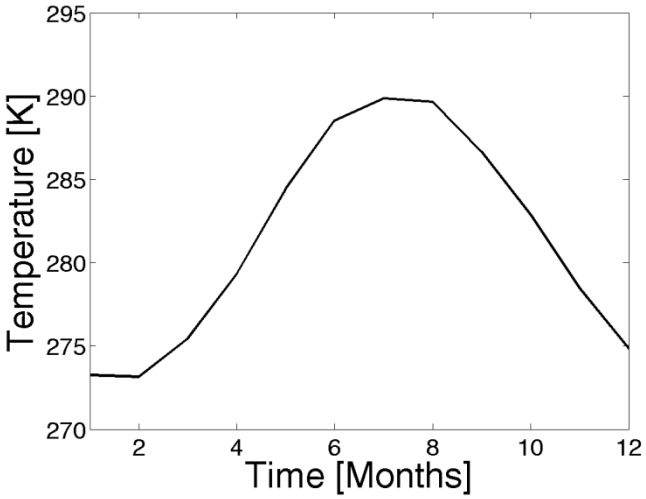

Figure 3.22 *Annual temperature profile (temperature profile is duplicated for 100 years).*

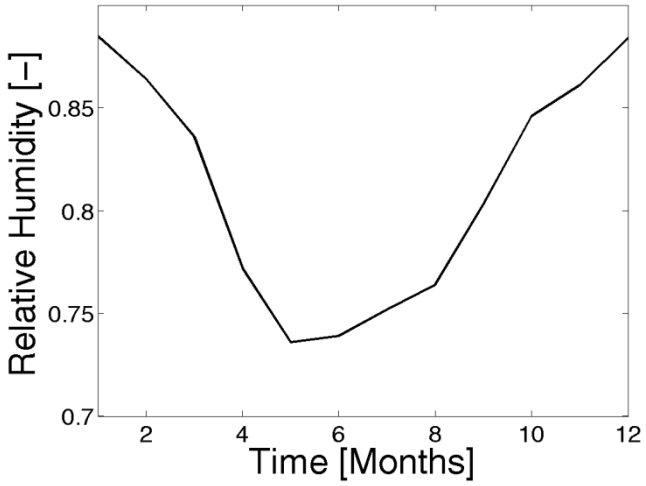

Figure 3.23 *Annual relative humidity profile (relative humidity profile is duplicated for 100 years).*

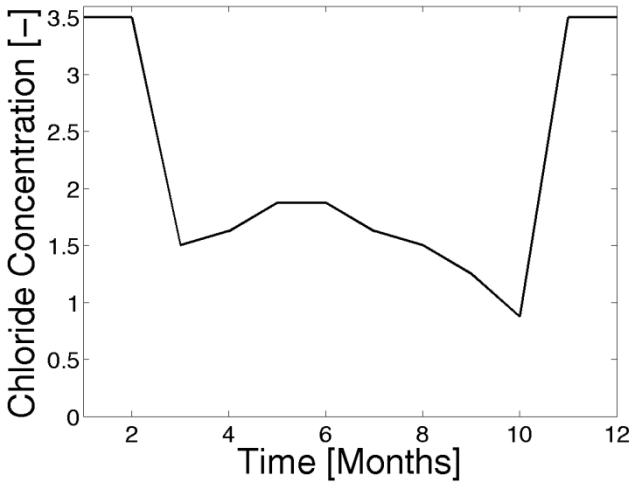

Figure 3.24 *Annual chloride profile (chloride profile is duplicated for 100 years).*

Table 3.6 *Model parameters for service life prediction of cracked and uncracked beam geometry.*

Model Parameter	Symbol	Value	Unit
Moisture transport coefficient	$k_{pC,T}$	Section 2.6	m/s
Ionic transport coefficient	D_i	Section 2.6	m^2/s
Heat transport coefficient	$k_{T,pC}$	Section 2.6	W/m^2K
Oxygen transport coefficient	D_{O2}	Paper IV	m^2/s
Concrete resistivity	ρ_{conc}	Paper IV	Ωm
Anodic exchange current density	i_{0a}	Equation (3.12)	A/m^2
Anodic equilibrium potential	E_{0a}	Equation (3.4)	V_{SCE}
Anodic Tafel constant	b_a	Equation (3.6)	V/dec
Cathodic exchange current density	i_{0c}	Equation (3.12)	A/m^2
Cathodic equilibrium potential	E_{0c}	Equation (3.4)	V_{SCE}
Cathodic Tafel constant	b_c	Equation (3.6)	V/dec
Limiting current density	i_{lim}	Equation (3.8)	A/m^2

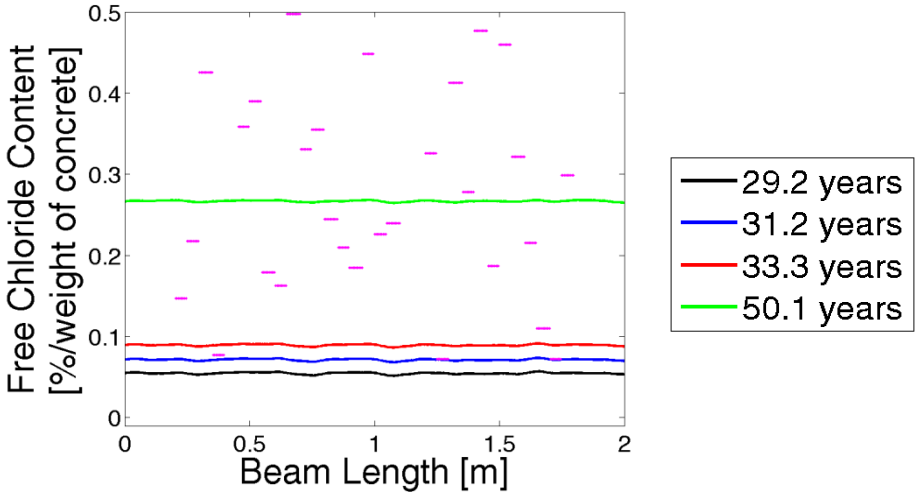

(a)

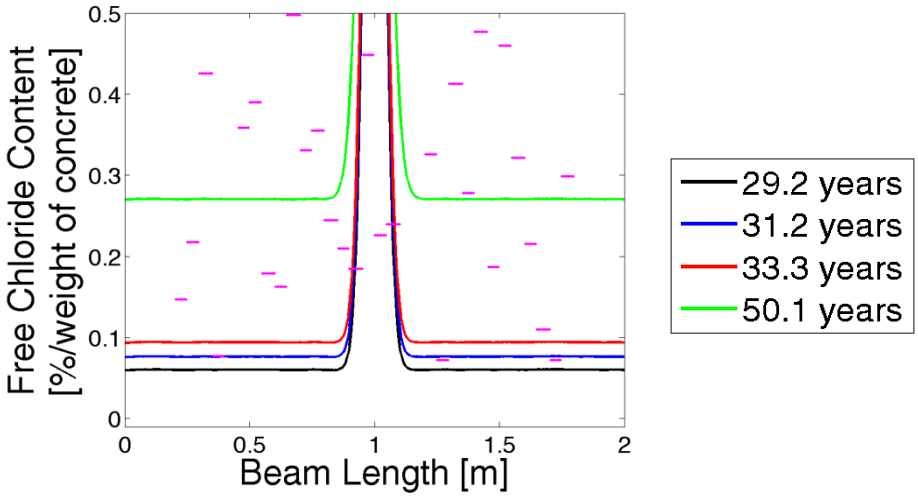

(b)

Figure 3.25 *Free chloride concentration and critical chloride threshold (magenta broken lines) at the reinforcement surface for (a) uncracked beam and (b) cracked beam geometry at selected times.*

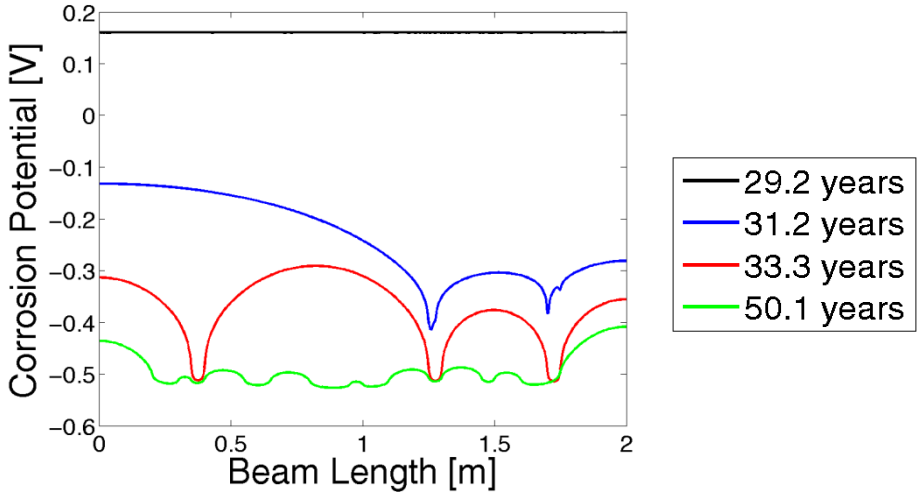

(a)

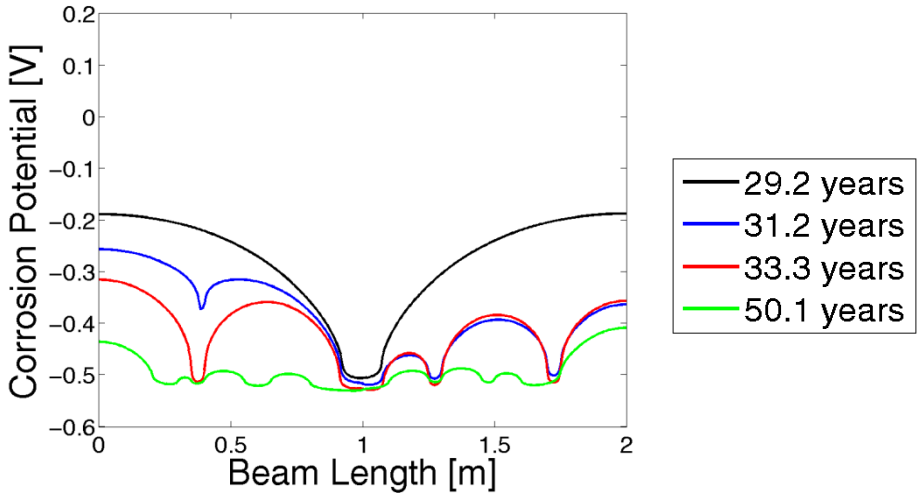

(b)

Figure 3.26 *Corrosion potential at the reinforcement surface for (a) uncracked beam and (b) cracked beam geometry at selected times.*

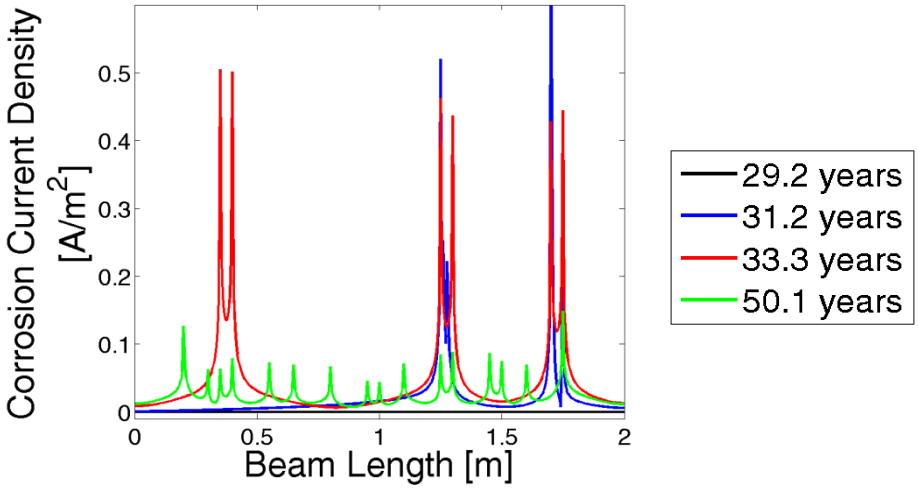

(a)

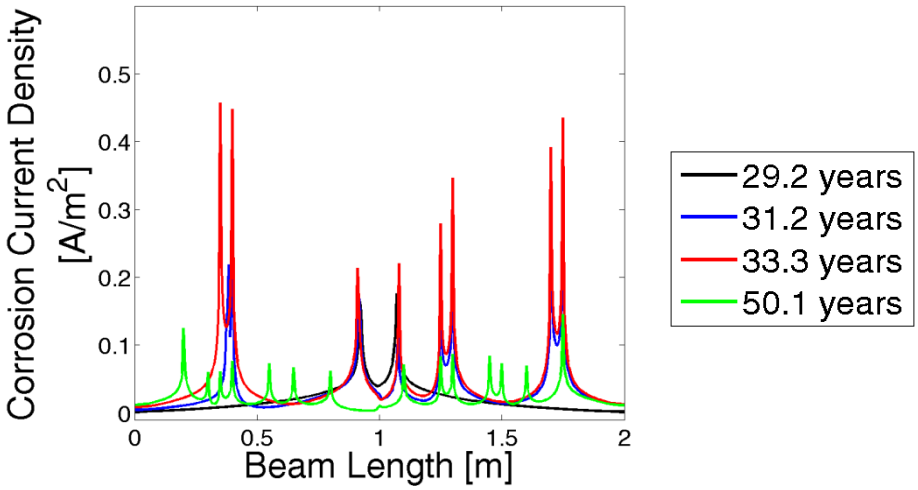

(b)

Figure 3.27 *Corrosion current density at the reinforcement surface for (a) uncracked beam and (b) cracked beam geometry at selected times.*

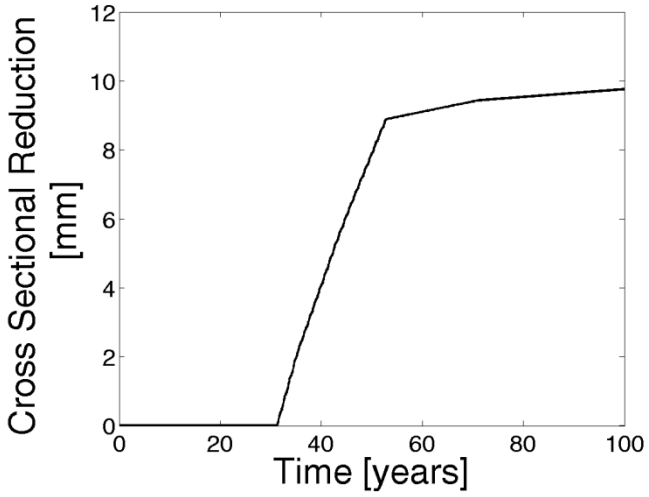

(a)

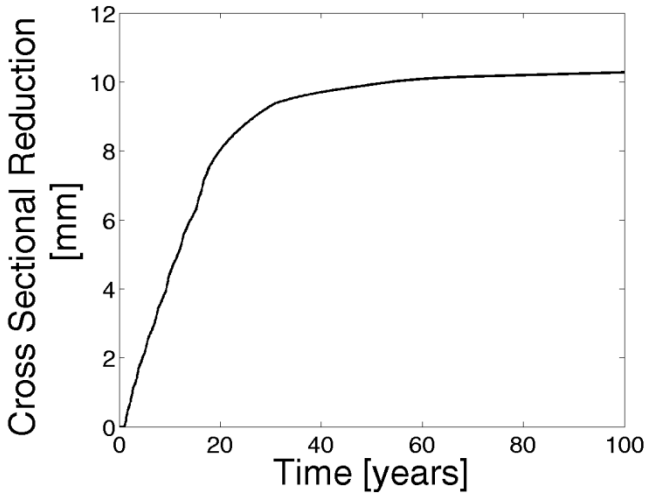

(b)

Figure 3.28 *Heaviest cross sectional reduction of reinforcement for (a) uncracked beam and (b) cracked beam geometry.*

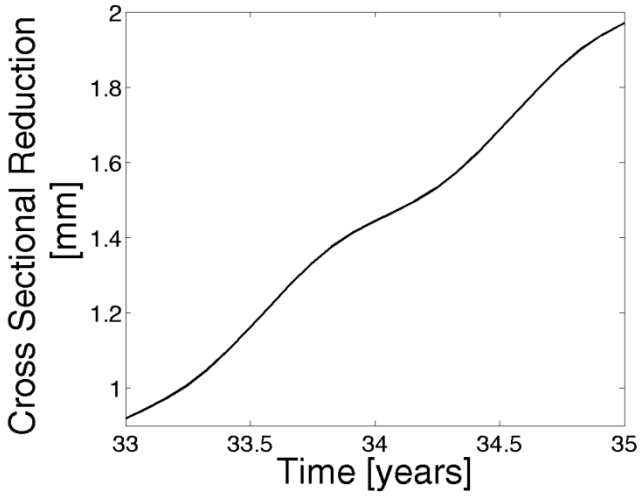

(a)

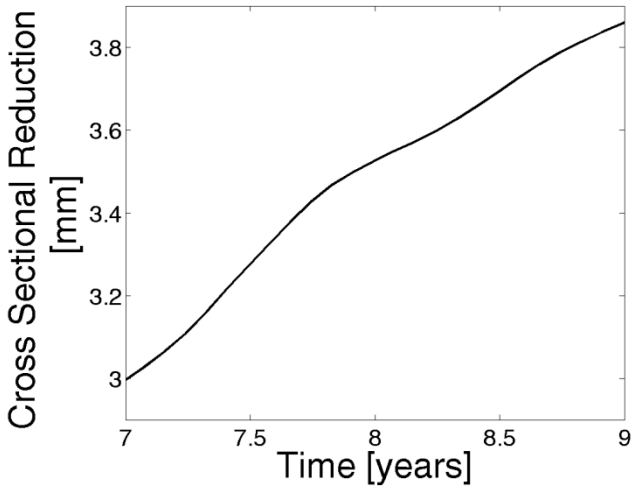

(b)

Figure 3.29 *Influence of annual temperature, chloride, and moisture variations on the cross sectional reduction of reinforcement for (a) uncracked beam and (b) cracked beam geometry.*

3.6 Summary and conclusions

Chapter 3 dealt with the numerical simulation of the corrosion process in reinforced concrete, which is indispensible for a service life prediction of reinforced concrete associated with chloride-induced corrosion. A numerical model to describe the corrosion process of steel in concrete was presented taking into account basic thermodynamic and kinetic principles of the reinforcement corrosion process. The model accounts further for the impact of various polarisation phenomena, heat, and mass transport of different species on the corrosion process.

The influence of individual parameters on the kinetics of the corrosion process was dealt with in Section 3.3.2 and results of numerical simulations were compared to experimental data. Initially, the impact of the geometrical arrangement of anodic and cathodic areas along the reinforcement on the corrosion current density was investigated. Numerical results dealing with the impact of temperature on the corrosion process were compared to experimental investigations carried out in connection with this Ph.D. study (presented in Paper V). Furthermore, it was shown that the model can accurately capture the effect of concentration polarisation on the corrosion process comparing model results to experimental results provided in the literature. Finally, the applicability of the model using basic thermodynamic and kinetic principles to model the corrosion process accounting for the impact of various polarisation phenomena was illustrated comparing numerical simulations to experimental results presented in [*López et al. 1993a*].

The influence of cracks on the risk of corrosion initiation in plain reinforced concrete and steel fibre reinforced concrete was presented in Section 3.4 and Paper VIII. Results of electrochemical measurements (corrosion potential and corrosion current), mechanical simulations (predictions of the extent of slip and separation between concrete and reinforcement) and destructive visual observations (extent of chloride ingress and corrosion along the conventional and instrumented reinforcement) were presented.

To demonstrate the potential use of the electrochemical model for service life prediction, a numerical example was given, in which a simple beam geometry with and without a crack was studied. The electrochemical model was fully coupled to the heat and mass transfer model presented in Chapter 2, to account for impact of temperature, moisture, and chloride on the initiation and propagation of reinforcement corrosion.

From the work presented in this chapter the following conclusion can be drawn:

- Basic thermodynamic and kinetic principles can be used to describe the corrosion process of reinforcement in concrete, which was verified comparing results of numerical simulations to experimental investigations either provided in the literature or conducted throughout the Ph.D. study.

- The presented corrosion model holds the potential to investigate the influence of individual parameters on the corrosion process. This may be used for design purposes estimating the service life of new structures, maintenance planning, and determination of the residual service life of existing structures or to evaluate the potential of repair methods, e.g. replacement of concrete cover. For instance, the influence of geometrical parameters, such as arrangement of reinforcement or increase/decrease of concrete cover thickness, as well as the influence of specific material properties, such as the resistivity, may be investigated with the model and related to the service life of a reinforced concrete in terms of initiation and propagation of reinforcement corrosion.
- The hypothesis that the concrete-reinforcement interfacial condition is a reliable indicator to quantify the impact of mechanically induced cracks on the risk of corrosion initiation along the reinforcement was reinforced. Very good agreements between simulated interfacial damage, in particular the separation between reinforcement and concrete, and extent of active corrosion along the instrumented rebar (indicated by electrochemical measurements) were obtained for all materials tested. The extent of interfacial damage due to load-induced cracking may be determined by mechanical finite element models, which directly account for the impact of various parameters (e.g. concrete cover thickness, concrete composition, stress level in the reinforcement and crack orientation) on the mechanical response (extent and magnitude of slip and separation between reinforcement and concrete). Such models may further be directly coupled to corrosion models providing important information on the interfacial conditions along the reinforcement enhancing service life predictions for reinforced concrete.

Chapter 4

Corrosion-induced concrete damage

4.1 Introduction

This chapter deals with corrosion-induced damage in cementitious materials, in particular cover cracking in reinforced mortar and concrete samples. The chapter is comprised of several sections. In Section 4.2, the modelling approach for a finite element (FEM) based model is introduced that is capable of simulating corrosion-induced deformations. The model is based on non-linear elastic fracture mechanics in which fracture mechanical properties are described by the effective cohesive relationship of the cementitious material. A more detailed description of the developed model is given in Paper IX. A review of basic fracture mechanics is not included in this chapter as this is not within the scope of this Ph.D. thesis and can be found elsewhere in the literature, see e.g. [*Shah et al. 1995, Karihaloo 1995, van Mier 1997, Anderson 2005*].

Section 4.3 presents results of x-ray attenuation measurements to quantify the penetration of corrosion products in cementitious materials. Detailed information on the applicability of x-ray attenuation measurements to determine the penetration of corrosion products can be found in Paper X, while results of an experimental study are presented in Paper XI. Results of x-ray attenuation measurements are then used to develop a concept to describe the penetration of solid corrosion products in cementitious materials and further develop the FEM based cracking model in Section 4.4. Further details on the FEM based model including the penetration of solid corrosion products and other time-dependent phenomena can be found in Paper XII. Finally, a brief summary is provided and conclusions are drawn in Section 4.5.

4.2 Modelling approach

Once corrosion is initiated, electrochemical half-cell reactions are taking place along the reinforcement. While at the anode an oxidation of iron is occurring, a reduction reaction (e.g. reduction of oxygen) is taking place at the cathodic sites along the reinforcement. The ionic reaction products of these half-cell reactions may then further react and form solid corrosion products in the vicinity of the reinforcement. As presented in the previous chapter, the kinetics (i.e. the rate) of these reactions and therefore the formation of the latter corrosion products, are dependent on numerous factors (see Section 3.3). Moreover, the type of corrosion product is dependent on the thermodynamical conditions present in the vicinity of the reinforcement [*Küter 2009*]. Solid corrosion products, which may form as a result of chloride-induced corrosion, are given in Table 4.1 [*Koleva et al. 2006, Marcotte et al. 2007, Caré et al 2008*]. Apart from the solid corrosion products presented in Table 4.1, soluble iron-chloride complexes (also referred to as green rust) may form in an oxygen-deprived environment in which chlorides are present [*Refait et al. 1998, Génin et al. 2001, Koleva et al. 2006, Küter 2009*]. Such soluble iron-chloride complexes may not necessarily form in the vicinity of the reinforcement surface, as shown e.g. by [*Küter 2009*]. In the present thesis, the formation of such soluble corrosion products is neglected and only the formation of solid iron oxides in the vicinity of the reinforcement surface is assumed.

Independent of the type of iron oxides formed as a result of active corrosion, the iron oxides occupy a larger volume than the initial iron that is consumed during the corrosion reaction, see e.g. [*Alonso et al., 1998, Marcotte et al. 2007*]. The increased volume of the corrosion products causes tensile stresses in the surrounding concrete and may lead to concrete cracking, spalling or delamination if the tensile strength of the concrete is exceeded. Formation of cracks in the concrete cover as well as cross sectional reduction of reinforcement area is affecting strength and serviceability of reinforced concrete structures. Hence, the description of the corrosion process (see Chapter 3) as well as the subsequent formation and propagation of corrosion-induced cracking is of major importance for the prediction of (residual) service life and/or support of maintenance planning of reinforced concrete structures.

Table 4.1 *Expansion coefficients of selected corrosion products, from [Caré et al. 2008]*.

Name	Chemical symbol	Volume expansion coefficient
Magnetite	Fe_3O_4	2.08
Hematite	Fe_2O_3	2.12
Goethite	α-FeOOH	2.91
Lepidocrocite	$Fe_2O_3 \cdot H_2O$	6.40

A variety of models dealing with corrosion-induced concrete cover cracking can be found in the literature. The available models can be broadly divided into empirical, see e.g. [*Alonso et al. 1998*], analytical, see e.g. [*Bazant 1979, Chernin et al. 2010*], and numerical models, see e.g. [*Molina et al. 1993, Andrade et al. 1993, Val et al. 2009*]. Paper IX introduces the concept of a combined modelling approach to simulate corrosion-induced concrete cover cracking in reinforced concrete. While an electrochemical model (see Chapter 3) is employed to describe the rate of corrosion and subsequent formation of corrosion products, a fracture mechanics model is used to simulate the formation of corrosion-induced cracks. The model assumes uniform corrosion along the reinforcement for which the mechanical analysis can be formulated in a 2D plain strain problem. Basic geometrical considerations, assumed crack propagation, and methodology of load application in the finite element method (FEM) model are illustrated in Figure 4.1 and Figure 4.2. For the determination of the corroded reinforcement section (see Figure 4.1), Faraday´s law is used, which describes the relation between thickness reduction per time and corrosion current density, predicted by the corrosion model described in the previous chapter:

$$X(t) = \frac{M_{Fe}}{zF\rho_{Fe}} \int_0^t i_{corr}\,(t)dt \qquad (4.1)$$

where *X(t)* is the cross sectional reduction of the reinforcement as a function of time, *t*, M_{Fe} the molar mass of iron, and ρ_{Fe} the density of iron.

To model the expansive nature of corrosion products a thermal analogy was used, in which a thermal load was applied to the corroded reinforcement section (see Figure 4.1) to mimic the increased volume of corrosion products. Assuming a constant coefficient of thermal expansion, the applied temperature increment was then representing the solid corrosion product. Assuming further isotropic material properties of the corrosion products, the linear expansion coefficient may be obtained as one third of the volume expansion coefficient. For instance, assuming the formation of Lepidocrocite with a volume expansion coefficient of 6.4 (see Table 4.1); a linear expansion coefficient of 2.13 was applied in the FEM model.

To demonstrate the applicability of the model, numerical simulations are compared to experimental data presented in [*Vu et al. 2005*]. Vu et al. [*Vu et al. 2005*] monitored corrosion-induced crack formation in reinforced concrete slabs under accelerated conditions, i.e. a constant current was applied to polarise the steel and enforce active corrosion. Throughout the experiments, a constant corrosion current density of 100 $\mu A/cm^2$ was applied. Assuming 100% current efficiency, i.e. all current applied is used for the formation of corrosion products, and uniform corrosion, Equation 4.1 yields the cross sectional reduction of the reinforcement. An overview of the material properties (provided in [*Vu et al. 2005*]) used for the simulation of the experiments is given in Table 4.2.

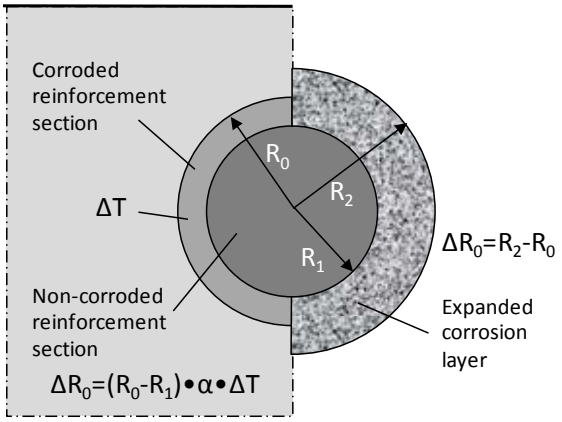

Figure 4.1 *Load application and geometrical considerations in FEM model to simulate corrosion-induced concrete cracking, from [Michel et al 2010a].*

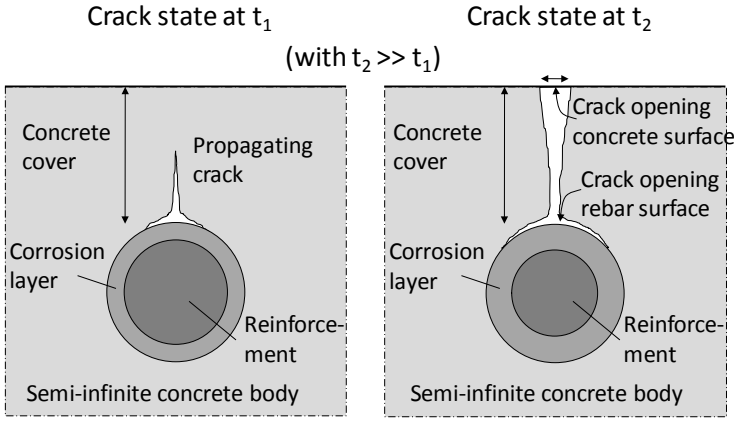

Figure 4.2 *Assumed crack propagation in FEM model to simulate corrosion-induced concrete cover cracking, from [Michel et al. 2010a].*

A comparison of the experimental and numerical results is shown in Figure 4.3. It appears that the model can accurately simulate the experimental data once a certain crack width is reached. However, the time-to-crack initiation and the initial crack propagation is considerably overestimated by the model (please note the logarithmic time scale in Figure 4.3). This discrepancy between the experimental data and numerical results may be attributed to the penetration of part of the corrosion products into open pore space/voids of the surrounding concrete. The next section deals with this phenomenon and introduces a measurement technique that allows for a direct quantification of the size of the so-called corrosion accommodating region (CAR).

Table 4.2 *Material properties to simulate corrosion-induced concrete cover cracking under accelerated conditions, from [Vu et al. 2005].*

Name	Symbol	Value	Unit
Young's modulus concrete	E_c	42.25	GPa
Tensile strength concrete	$f_{t,c}$	3.94	MPa
Young's modulus corrosion products	E_{corr}	2.1	GPa
Volume expansion coefficient corrosion products	η_{vol}	2.94	-

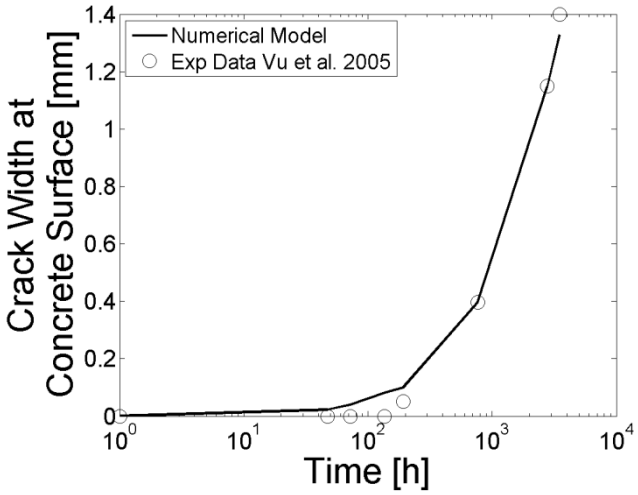

Figure 4.3 *Comparison between experimentally measured and numerically predicted concrete cracking under accelerated corrosion conditions (experimental data reproduced from [Vu et al. 2005]).*

4.3 Penetration of corrosion products

The corrosion accommodation region (CAR) (also referred to as “diffusion” or “porous” zone) is a key parameter in corrosion-induced concrete cracking models. The CAR describes a region of concrete around the reinforcement, which can accommodate expansive corrosion products delaying stress development in the concrete. This region has a major influence on the predicted time-to-crack initiation and the crack propagation behaviour [*Liu et al. 1998, Caré et al. 2008, Val et al. 2009*]. Inconsistent values are cited for the CAR, ranging from 0.002 to approximately 0.12 mm in thickness [*Chernin et al. 2010*]. In some cases, the size of the CAR is “determined” as a fitting parameter to provide model outputs in line with experimental results [*Liu et al. 1998, El Maaddawy 2009, Val et al. 2009*]. Previous experimental efforts to physically measure the thickness of the CAR included cutting, sawing, and impregnating samples [*Caré et al. 2008*]. These destructive methods are potentially invasive, causing possible movement or washing away of corrosion products and hindering reliable measurements. Paper X presents the applicability of the x-ray attenuation method to monitor corrosion products as well as the formation and propagation of cracks in cementitious materials in a non-destructive manner.

Selected experimental results from an initial study on reinforced mortar samples in form of contour plots are presented in Figure 4.4. The contour plots were obtained by image analysis of the original x-ray images including location- and time-dependent information on the concentration of corrosion products as well as corrosion-induced cracks. For further details about geometry and material of the specimens tested as well as the x-ray attenuation measurement technique and subsequent image analysis reference is made to Paper X and [Pease 2010].

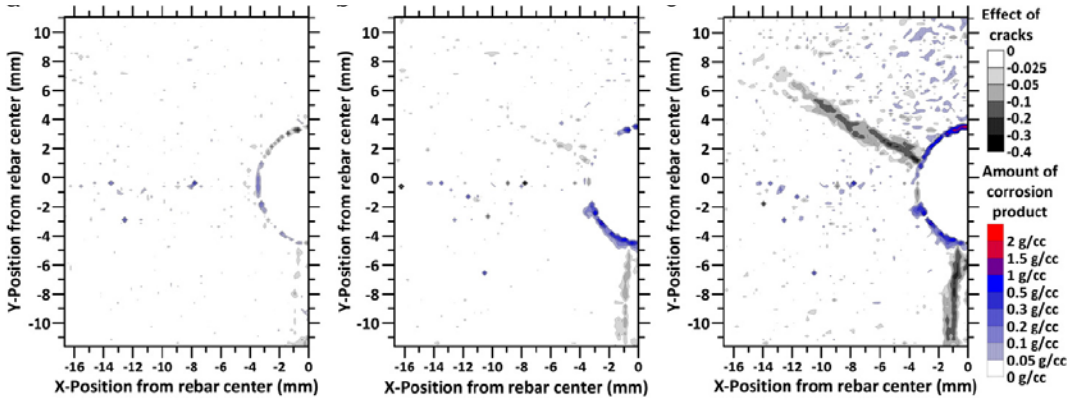

Figure 4.4 *Contour plots with location- and time-dependent information on corrosion-induced cracks (grey in colour) and concentration of corrosion products (blue in colour) after 14 hours (left), 71 hours (middle), and 119 hours (right) of accelerated corrosion testing, from [Michel et al. 2011].*

To further study the corrosion accommodating region (CAR) and potential influences of concrete properties (e.g. water-to-cement ratio) and corrosion current density on the movement of corrosion products, a parametric study was conducted. Throughout the study, the influence of corrosion current density and water-to-cement ratio (w/c) on the CAR as well as the formation and propagation of corrosion-induced cracks in reinforced cementitious materials was investigated. The applied corrosion current densities were in the range of 10 μA/cm^2 to 100 μA/cm^2, in which 10 μA/cm^2 was reported as a realistic corrosion current density for actual structures subjected to corrosion, see e.g. [*Tuutti 1982*]. While selected results of the study are presented in Figure 4.5 and Figure 4.6, detailed information on the geometry and mix design of the specimens, measurement technique, and results can be found in Paper XI.

In general, it is observed that the amount of corrosion products is increasing and further penetrating into the cementitious material as time progresses, independent of w/c and applied corrosion current density. Furthermore, the results indicate (see Figure 4.5 and Figure 4.6) that the depth of penetration of corrosion products is varying for the different w/c and applied corrosion current densities. While with decreasing corrosion current density the depth of penetration of corrosion products is increased, the results indicate that the depth of penetration is reduced as the w/c is reduced for the same corrosion current density.

Results of the experimental study presented in Paper XI provided pertinent information for the further development and verification of the corrosion-induced cracking model introduced in the previous section. The basic concept to incorporate the movement of solid corrosion products into corrosion-induced cracking models is presented in the next section.

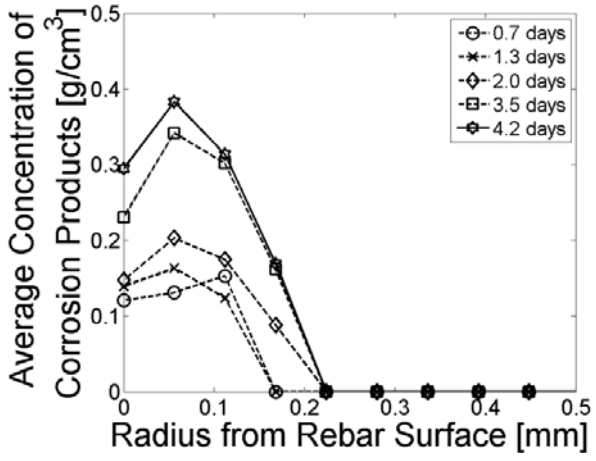

(a)

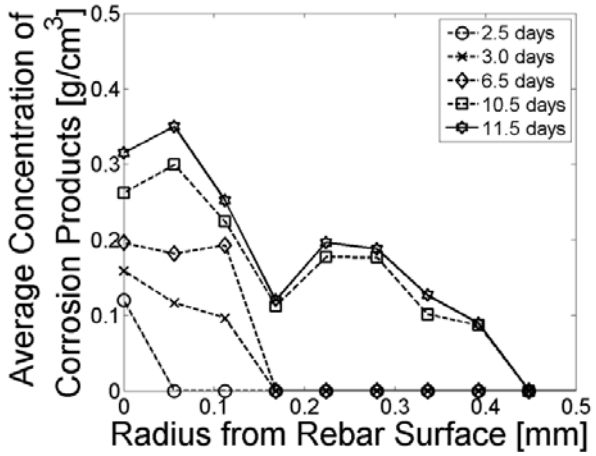

(b)

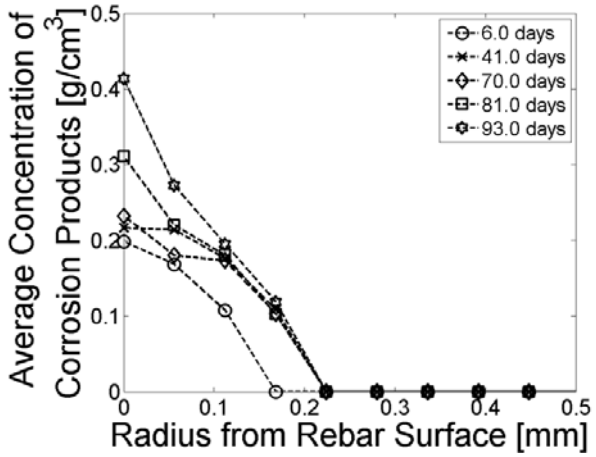

(c)

Figure 4.5 *Average concentration of corrosion products as a function of radius from the rebar surface at varying times for specimens with a w/c of 0.5 subjected to (a) 100 μA/cm^2, (b) 50 μA/cm^2, and (c) 10 μA/cm^2 corrosion current density. The solid line indicates the time when a crack was first observed (please note: no cracks were observed for the specimen subjected to 10 μA/cm^2 until the test was terminated).*

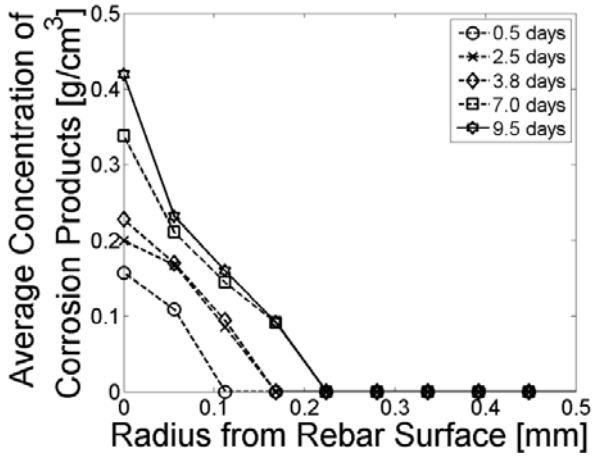

(a)

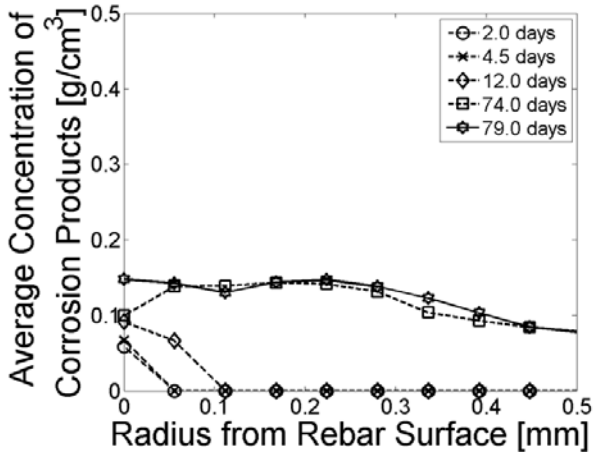

(b)

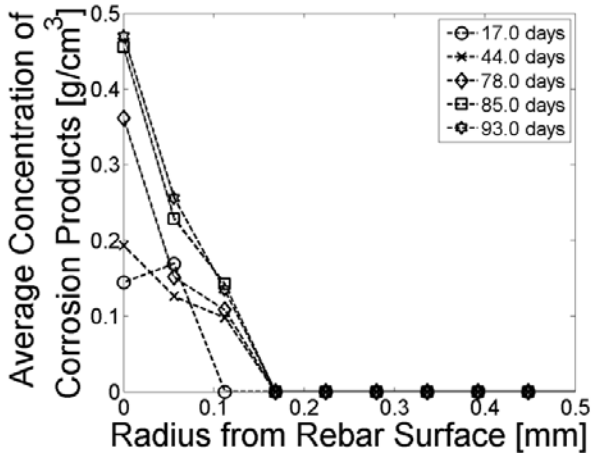

(c)

Figure 4.6 *Average concentration of corrosion products as a function of radius from the rebar surface at varying times for specimens with a w/c of 0.3 subjected to (a) 100 µA/cm^2, (b) 50 µA/cm^2, and (c) 10 µA/cm^2 corrosion current density. The solid line indicates the time when a crack was first observed (please note: no cracks were observed for the specimen subjected to 10 µA/cm^2 until the test was terminated).*

4.4 Corrosion-induced cracking model

As presented in the previous sections, the penetration of solid corrosion products has considerable effects on the time-to-crack initiation in reinforced concrete. Paper XII introduces a finite element (FEM) based corrosion-induced cracking model taking into account the penetration of solid corrosion products into the pore spaces/voids of cementitious materials. The introduced FEM model is based on the modelling approach presented in Section 4.2 taking into account the experimental results on penetration of solid corrosion products shown in Section 4.3.

A conceptual schematic to include the penetration of solid corrosion products in the FEM model is shown in Figure 4.7. Based on the experimental results presented in the previous section and Paper XI, it is assumed that an initial corrosion accommodating region (CAR) around the reinforcement exists, denoted CAR_0, which delays stress formation while filling with solid corrosion products. Once this initial CAR_0 is filled with corrosion products, tensile stresses in the surrounding cementitious material will increase and potentially lead to the formation of micro-cracks. These micro-cracks allow solid corrosion products to penetrate additional pore spaces and further delay corrosion-induced stresses. At some point a maximum size of the CAR, denoted as CAR_{MAX}, is reached. No corrosion products can penetrate the matrix of the cementitious material beyond that point and all additionally formed corrosion products will introduce tensile stresses and potentially lead to the formation of a macro-crack.

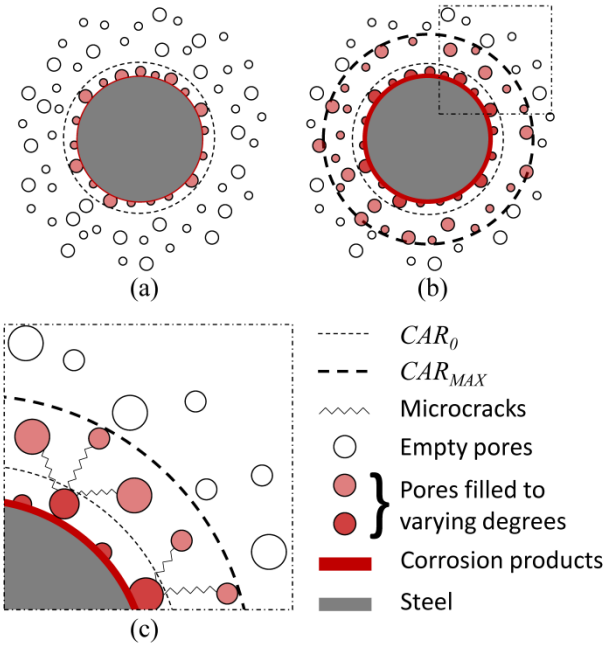

Figure 4.7 *Conceptual schematic to describe the penetration of solid corrosion products, where (a) shows the initial CAR_0, (b) the increase in CAR size to a maximum, and (c) the formation of micro-cracks between pores, from [Pease et al. 2012a].*

To demonstrate the applicability of the developed FEM model to predict corrosion-induced deformations and subsequent crack formation, numerical simulations are compared to two experimental studies:

1. The experimental investigations conducted by [*Vu et al. 2005*] (see Section 4.2).
2. Photogrammetric investigations of reinforced specimens subjected to accelerated corrosion presented in Paper XII.

Figure 4.8 illustrates a comparison of the experimental data provided in [*Vu et al. 2005*] and numerical predictions (taking into account the penetration of solid corrosion products and neglecting the penetration of solid corrosion products). While the initial CAR size and growth was estimated from experimental data presented in Paper XI, material properties were applied as presented in Table 4.2. It is evident from the results that the presented model can very precisely describe the experimental observations presented in [*Vu et al. 2005*] including the time-to-crack initiation and the subsequent crack propagation when the penetration of solid corrosion products is accounted for.

Paper XII introduces digital image correlation (DIC) for corrosion-induced deformation measurements. Reinforced specimens were subjected to accelerated corrosion and monitored by means of DIC, which allowed for deformation measurements in the sub-micron scale between reinforcement and cementitious material. For further details about geometry and mix design of the specimens as well as DIC measurement technique reference is made to Paper XII. Selected results of the experimental study are presented in Figure 4.9 and compared to numerical predictions in Figure 4.10.

Figure 4.9 shows corrosion-induced deformations between the steel and cementitious material at various positions around the reinforcement determined from DIC measurements. While at some locations an increase in deformation with progressing time is measured (indicating presence and formation of solid corrosion products), decreasing deformations are obtained for other locations. The results indicate that the formation of corrosion products is non-uniform around the reinforcement, although a direct current was applied enforcing corrosion to occur.

Although the results indicate non-uniform corrosion around the steel circumference, the FEM model was used to simulate the experiments. A comparison of modelled and measured deformations is provided in Figure 4.10 after three days of accelerated testing. Despite the fact that the FEM model assumes a uniform deposition of corrosion products and therefore cannot accurately model all measured corrosion-induced deformations, Figure 4.10 illustrates the model can accurately describe certain locations and appears to capture important processes of the corrosion-induced deformation process.

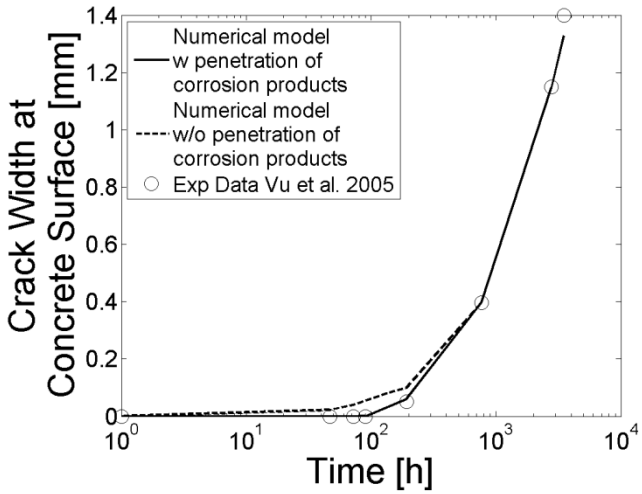

Figure 4.8 *Comparison between experimentally measured and numerically predicted concrete cracking under accelerated corrosion conditions (100 μA/cm^2) taking into account the penetration of solid corrosion products (experimental data reproduced from [Vu et al. 2005]).*

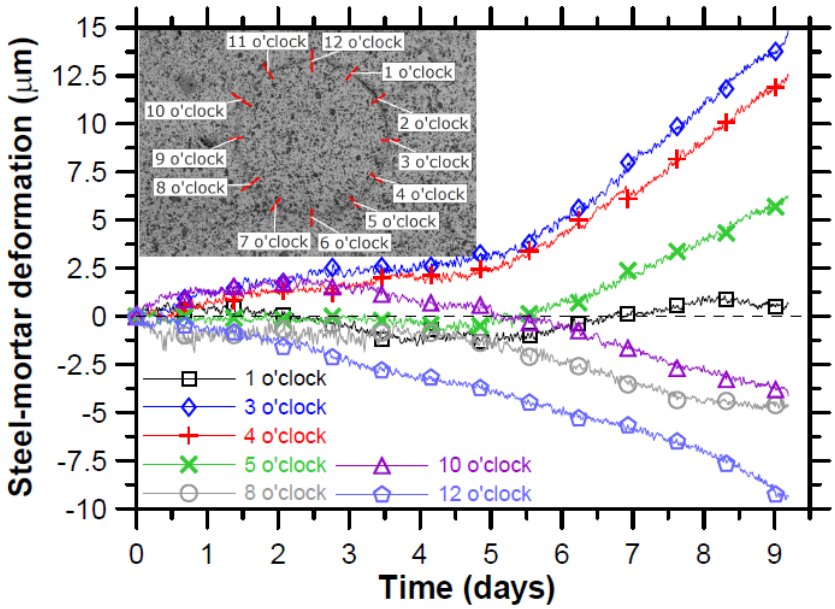

Figure 4.9 *Corrosion-induced deformations measured between steel and mortar at varying locations identified in the inset image using DIC, from [Pease et al. 2012a].*

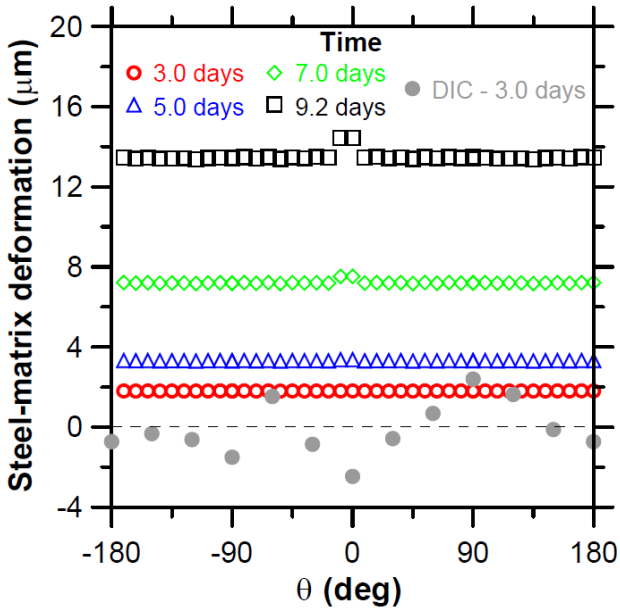

Figure 4.10 *Modelled corrosion-induced deformations between steel and cementitious matrix at varying locations of the steel surface expressed as polar coordinates. For DIC measurements – clockwise from 12 to 6 o'clock corresponds to 0 to +180°, counter clockwise from 12 to 6 o'clock corresponds to 0 to -180°, from [Pease et al. 2012a].*

4.5 Summary and conclusions

Chapter 4 of this Ph.D. thesis dealt with corrosion-induced damages, in particular the formation and propagation of cracks in reinforced mortar and concrete specimens. A finite element based modelling approach was presented in Section 4.2 and Paper IX that allows for the simulation of corrosion-induced deformations utilising a thermal analogy. In Section 4.3, the influence of solid corrosion products penetrating into cementitious materials on the time-to crack initiation was discussed. While Paper X introduced x-ray attenuation as a measurement technique to quantify the penetration of corrosion products, an experimental study on the impact of water-to-cement ratio and corrosion current density on the corrosion accommodating region was presented in Paper XI. These experimental results were used in Section 4.4 and Paper XII to further develop the finite element based cracking model to include the penetration of solid corrosion products into cementitious materials.

From the work presented in this chapter the following conclusion can be drawn:

- The finite element based cracking model can be used to describe corrosion-induced deformations in reinforced cementitious materials, which was verified comparing numerical simulations and experimental investigation either presented in literature or conducted during the Ph.D. study.

- The used thermal analogy to describe the increased volume of solid corrosion products holds the potential to mimic any type of solid corrosion product that is formed. Further, the developed model can be used to investigate the impact of varying geometrical parameters (e.g. concrete cover thickness or rebar diameter) and material properties (concrete tensile strength, concrete softening behaviour) on the formation and propagation of cracks. In particular, the concrete softening behaviour, i.e. the ability to transfer stresses once cracked, is of interest with respect to the use of fibre reinforced cementitious materials.
- The penetration of corrosion products into cementitious materials has a considerable influence on the time-to-crack initiation and propagation. X-ray attenuation measurements can be used to obtain location- and time-dependent information on the penetration of corrosion products. Such measurements were used to develop a concept to describe the penetration of solid corrosion products in a finite element based cracking model.

Chapter 5

Summary and discussion

5.1 Summary

The objective of this Ph.D. study was to establish, test, and demonstrate a theoretical framework to describe reinforcement corrosion in concrete using numerical methods. To limit the scope of the work, focus was placed on chloride-induced reinforcement corrosion and subsequent mechanical analysis of corrosion-induced cracking in structural members. The framework was based on the analysis of the ingress of aggressive substances, electrochemical processes, and corrosion-induced damages (see Figure 1.3). The study included numerical and experimental work on heat and mass transport, electrochemical processes, and corrosion-induced damages in reinforced cementitious materials. The applicability of the individual models was verified comparing numerical predictions with experimental results either obtained as part of the Ph.D. study or provided in the literature.

5.2 Discussion

5.2.1 Modelling reinforcement corrosion

Reinforcement corrosion processes in concrete structures are highly complex and affected by interactions of the steel and concrete with ambient conditions. The electrochemical half-cell reactions of the active (anode) and the passive reinforcement surface (cathode) as well as the heat and mass transfer of various species are controlling the reinforcement corrosion process. Previous models simulating the reinforcement corrosion process in reinforced concrete, see e.g. [*Jäggi 2001, Kranc et al. 2001,*

Maruya et al. 2003, Ouglova et al. 2005, Isgor et al. 2006, Osterminski et al. 2006, Warkus et al. 2006, Warkus et al. 2008] were limited to either the initiation or the propagation phase and often based on oversimplified assumptions concerning material parameters and structural detailing.

While the developed set of models allow for the combined simulation of initiation and propagation of reinforcement corrosion, the application is at present limited to chloride-induced corrosion with preselected anodic and cathodic half-cell reactions. To describe chloride-induced corrosion initiation, a conditional statement is defined along the reinforcement surface, which comprises the definition of a critical chloride threshold for elements along the reinforcement surface (see Section 3.3.1). The defined critical chloride thresholds are varied randomly along the reinforcement surface to account for the influence of various parameters and represent a realistic structure with defects and voids present at the concrete steel interface as was shown in e.g. [*Buenfeld et al. 2004, Nygaard et al. 2005, Angst et al. 2009*]. Further, the influence of various parameters on the kinetics of the corrosion process is included in the developed model and was studied by means of a parametric study. Within the parametric study, the effects of anode-to-cathode area ratio, oxygen, temperature, and moisture content on the corrosion current density were investigated (see Section 3.3.2). It was shown that the developed corrosion model, based on generally accepted physical laws describing thermodynamics and kinetics of electrochemical processes, can capture the influence of the investigated parameters comparing experimental and numerical data. This allows the corrosion model (when coupled to the heat and mass transport model) to include the impact of varying exposure conditions, material properties, and structural detailing on the corrosion process and enhance predictions of the initiation of reinforcement corrosion and the corrosion rate over time.

Although, the potential of the model to describe the thermodynamics and kinetics of the reinforcement corrosion process could be shown comparing experimental and numerical data, further validation is needed. In particular, long-term in-situ data of reinforced concrete structures is needed to validate the ability of the developed set of models to provide accurate predictions of corrosion state and rate under varying exposure conditions.

5.2.2 Impact of cracks

5.2.2.1 Ingress of aggressive substances

Current recommendations, standards, and service life models, see e.g. [*fib Bulletin 34 2006, Life-365 Consortium II 2010, Jäggi 2001, Kranc et al. 2001, Maruya et al. 2003, Ouglova et al. 2005*] assume an initial pristine state for the determination of the (residual) service life of reinforced concrete structures. Research and experiments conducted throughout this Ph.D. study showed that cracks facilitate rapid ingress of

aggressive substances [*Jacobsen et al. 1996, Aldea et al. 1999, Edvardsen 1999, Rodriguez et al. 2003, Lindquist et al. 2006, Pease et al. 2009*], and cause considerable reductions in the time to corrosion initiation [*Schießl 1976, Schießl et al. 1997, Otieno et al. 2010, Pease et al. 2011*].

To account for the impact of cracks on the ingress of aggressive substances, a numerical model was presented in this Ph.D. thesis. The model is based on experimental work presented in [*Pease 2010*] and assumes that the total crack length can be divided into two parts; 1) a coalesced crack length that behaves as a free surface for moisture ingress, and 2) an isolated micro-cracking length that resists ingress similarly to the bulk material. Experimental and numerical results were presented illustrating that the model can accurately describe the ingress behaviour in cracked wedge splitting test (WST) specimens. This allows the heat and mass transport model to account for the impact of cracks on the ingress of potential corrosion-initiating substances and provide more realistic predictions on the initiation and propagation of reinforcement corrosion (when coupled to corrosion model).

However, potential self-healing of cementitious materials, closure of cracks due to stress relaxation or pumping effects due to opening and closing of cracks are not considered in the present model. These effects may have a considerable impact hindering the ingress of aggressive substances and subsequently affecting the reinforcement corrosion process.

5.2.2.2 Reinforcement corrosion

Although a number of studies (both from laboratory and in-situ conditions) indicate that the concrete surface crack width alone cannot accurately assess the impact of cracks on reinforcement corrosion, (see e.g. [*Schießl et al. 1997, Schießl 1976, Berke et al. 1993, Schießl et al. 1997, Miyazato et al 2005, Otieno et al. 2010, Makita et al. 1980*]), the concrete surface crack width is commonly related to corrosion initiation and propagation (see e.g. [*Gautefall et al. 1983, Berke et al. 1993, Schießl 1976, Schießl et al. 1997*]).

Experimental results presented in this Ph.D. study facilitate the hypothesis that the concrete-reinforcement interfacial condition can be used as a reliable indicator to quantify the impact of mechanically induced cracks on the risk of corrosion initiation along the reinforcement. In particular, the separation between reinforcement and concrete appears to be a reliable indicator for the extent of active corrosion along the reinforcement. To predict the interfacial damage due to load-induced cracking a mechanical finite element model was used, which directly accounts for the impact of various parameters (e.g. concrete cover thickness, concrete composition, stress level in the reinforcement, and crack orientation) on the mechanical response (extent and magnitude of slip and separation between reinforcement and concrete). The developed finite element model, capable to describe the interfacial damage due to mechanical loading,

may be used to enhance present service life models providing valuable information on the risk for reinforcement corrosion based on a single reliable indicator.

Although, very good agreements between experimental and numerical results were found in this study further investigations are needed. The penetration of solid corrosion products into cracks as well as dynamic loading are not dealt within the present model, which may alter the impact of cracking over time.

5.2.3 Modelling corrosion-induced damages

As a result of active reinforcement corrosion, solid corrosion products may form and lead to concrete cracking, spalling, and delamination. The formation and propagation of corrosion-induced damages can be modelled using finite element models based on fracture mechanics of concrete as previously shown, see e.g. [*Alonso et al. 1998, Bazant 1979, Chernin et al. 2010, Molina et al. 1993, Andrade et al. 1993, Val et al. 2009*]. A key parameter in modelling corrosion-induced damages is the corrosion accommodation region (CAR) (also referred to as “diffusion” or “porous” zone), which has a major influence on the predicted time-to-crack initiation and the crack propagation behaviour [*Liu et al. 1998, Caré et al. 2008, Val et al. 2009*].

To simulate corrosion-induced concrete cracking a finite element based model was presented using a thermal analogy to describe the expansive nature of solid corrosion products. Possible formation of soluble corrosion products, such as iron-chloride compounds, is not included in the model. The model further assumed that solid corrosion products are uniformly deposited around the circumference of the reinforcement. In contrast to previous attempts, the description of the CAR is based on non-destructive experimental observations by means of x-ray attenuation measurements. Results of x-ray attenuation measurements allowed for the development of a concept to describe the penetration of solid corrosion products into the available pore space of cementitious materials. The applicability of the developed model to accurately describe corrosion-induced cracking was shown comparing experimental data and numerical predictions of accelerated corrosion tests. In combination with the corrosion model (providing information on the rate of formation of solid corrosion products), the cracking model holds the potential to describe corrosion-induced cracking in reinforced concrete members under varying exposure conditions.

However, results of additional photogrammetric experiments clearly indicated that corrosion products form in a non-uniform manner around the circumference of the reinforcement. The non-uniform formation of corrosion products may have a considerable impact on the time-to corrosion cracking and propagation of corrosion-induced cracking. Although, the developed model does not include non-uniform corrosion yet, adjustments may be made to study this phenomenon.

5.2.4 Service life model

Due to increasing service life requirements for modern concrete structures (up to 100 or even 200 years of expected service life), the design and dimensions (e.g. water-to-cement ratio or concrete cover thickness) of reinforced concrete structures in aggressive environments is at present mainly governed by durability issues. However, the design of reinforced concrete structures is typically realised using standards, codes or simply expertise, which are often based on oversimplified assumptions and do not account for important phenomena affecting the service life. This is mainly because tools for a quantitative service life prediction are lacking. In this thesis, a general framework for the service life prediction of reinforced concrete associated with chloride-induced corrosion was proposed. The model includes heat and mass transfer in porous media and electrochemical corrosion processes in cracked and uncracked reinforced concrete. The model further allows for subsequent mechanical analysis of corrosion-induced damages.

The potential use of the proposed model for the service life prediction of reinforced concrete was presented in Section 3.5, in which a simple beam geometry with and without a crack was studied. The coupled transport and corrosion model allowed for the simulation of initiation and propagation of chloride-induced corrosion in reinforced concrete. Further, the impact of cracks on the ingress of aggressive substances and the initiation and propagation of reinforcement corrosion could be clearly shown (see Figure 5.1). Hence, the proposed model can be used to predict the service life of reinforced concrete if a certain limit state, e.g. initiation of corrosion or certain cross sectional reduction, is set. Moreover, governing parameters controlling the corrosion process can be easily assessed with the proposed service life model and used in the design phase to optimise structures in terms of service life. For instance, the concrete resistivity has a considerable impact on the corrosion current density (see Figure 3.15). Materials with supplementary cementitious materials are well known to have an increased resistivity [*Larsen 2007*], which can be beneficial in terms of service life as the corrosion current density may be considerable reduced. Furthermore, the model can be easily used to support maintenance planning of existing structures or to evaluate repair methods, such as replacement of the concrete cover, as time-to corrosion initiation (see Figure 5.1) or subsequent corrosion-induced damages (see Figure 4.8) can be determined within acceptable limits. The model may be further used in a probabilistic framework assessing the influence of varying geometrical or material properties. However, while the influence of varying geometrical parameters, such as variations in the concrete cover or position of reinforcement, may be easy to investigate, as the geometrical parameters can be considered independent of each other, investigations of variations in materials properties may be more difficult if not impossible to evaluate. For instance variations in the concrete mix design, may affect the microstructure, which is related to moisture fixation and transport and subsequently to transport of ions. The dependencies between these key parameters of service life

modelling should be investigated and evaluated before a probabilistic framework is used for service life prediction of reinforced concrete structures.

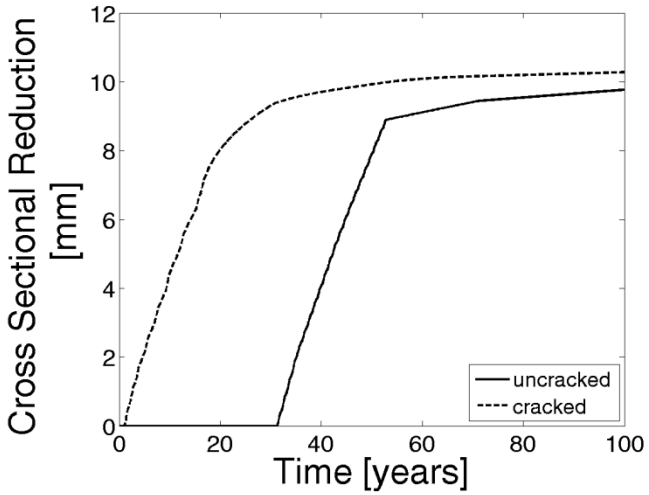

Figure 5.1 *Comparison between numerical predictions of cross sectional reduction in a cracked and uncracked beam (for a specific geometry and material properties (see Section 3.5)).*

5.2.5 Limit states for end of service life

Limit states defining the end of service life for a structure are typically set by the owner and based on the criteria that the structure fulfils a certain functionality within the service life. Typical limit states are for instance the initiation of corrosion, the appearance of rust stains, the formation of corrosion-induced cracks or failure of the structure. While limit states, such as failure or corrosion-induced cracking are clearly visible and comparably easy to evaluate, initiation of reinforcement corrosion is much more difficult to determine by means of monitoring. Nevertheless, the most common limit state used by consultants and design engineers is depassivation/initiation of corrosion, which in case of chloride-induced corrosion is associated with a critical chloride threshold. As illustrated in this Ph.D. work and presented in earlier work [*Buenfeld et al. 2004, Nygaard et al. 2005, Pease 2010*] interfacial damages, such as defects, voids, slip, and separation, have a considerable impact on the risk of corrosion initiation. In particular, in the presence of load-induced or shrinkage cracks, the concept of a critical chloride threshold is not valid, as the protection by concrete is no longer given. Service life predictions with the presented numerical model and experimental investigations on the ingress of aggressive substances and the corrosion process in cracked concrete reinforced this hypothesis (see Figure 3.18, Figure 3.19, Figure 3.20, and Figure 3.28). Even in uncracked concrete, rather short service life predictions were obtained (see Figure 3.28 and Figure 5.1), when varying chloride thresholds along the reinforcement were included in the model (for the chosen model geometry and material properties). The assumption of varying critical chloride thresholds along the reinforcement appears to be reasonable as interfacial voids or defects

along the reinforcement/concrete interface are inevitable (see Section 3.3.1). Hence, to obtain a defined limit state of 100 years or more, either the design of a reinforced concrete structure is to be changed, considerable maintenance and repair efforts are needed or acceptance of different limit states is required.

Combining the corrosion-induced cracking model and predictions of the coupled transport and corrosion model allows for a description of the corrosion current density and subsequent formation of solid corrosion products. Both analyses may be used to determine an allowable corrosion-induced damage, which can be easily assessed by means of monitoring. Paper XIII introduces limit states for the service life of reinforced concrete structures in terms of allowable corrosion-induced damage. Considerable service times may thereby be gained allowing for minor corrosion-induced damages as presented in Paper XIII.

Chapter 6

Conclusions and recommendations for further work

The main conclusions of this Ph.D. thesis are presented in the following. Conclusions are drawn for experimental work and the proposed framework for service life prediction of reinforced concrete structures subjected to chloride-induced corrosion. In addition, recommendations for future work are given.

6.1 Conclusions

Transport of mass and heat in porous media

Chapter 2 dealt with the heat and mass transport in porous media. A numerical model to describe the state and transport of various substances was presented taking into account the influence of temperature and chloride ions on the moisture state and transport. The model further included the impact cracks have on moisture ingress.

From the work presented in Chapter 2 the following conclusion can be drawn:

- The employed heat and mass transport model allows for the simulation of chloride ingress in concrete. Good correlations were found between experimental observations and simulations on the ingress of chloride in a concrete wall element placed in the tidal zone of the Trondheim Fjord.
- The impact of chloride ions on the moisture sorption can be described by Raoult's law. Good correlations were found between experimental data provided in the literature and Raoult's law for chloride concentrations up to approximately 4.5 mol/L.

- The impact of temperature on the moisture state in cementitious materials can be determined using time domain reflectometry (TDR) measurements in combination with multi-layer adsorption theory.

Corrosion of steel in concrete

Chapter 3 dealt with the numerical simulation of the corrosion process in reinforced concrete. A numerical model to describe the corrosion process of steel in concrete was presented taking into account the impact of various polarisation phenomena and the influence of bending cracks on corrosion initiation.

From the work presented in Chapter 3 the following conclusion can be drawn:

- Comparisons between experimental observations and numerical simulations showed that basic thermodynamic and kinetic principles can be used for the simulation of corrosion processes of reinforcement in concrete.
- Experimental observations showed that the concrete-reinforcement interfacial condition can be used as an indicator to quantify the impact of mechanically induced cracks on the risk of corrosion initiation along the reinforcement.

Corrosion-induced concrete damage

Chapter 4 of this Ph.D. thesis dealt with corrosion-induced damages. A finite element based modelling approach was presented that allows for the simulation of corrosion-induced deformations utilising a thermal analogy. The model further accounted for the penetration of solid corrosion products into cementitious materials.

From the work presented in Chapter 4 the following conclusion can be drawn:

- Comparisons between experimental and numerical results showed that the finite element based cracking model can be used to describe corrosion-induced deformations in reinforced cementitious materials.
- The applied thermal analogy, to describe the expansive nature of solid corrosion products, can be used to mimic any solid corrosion product that is formed.
- X-ray attenuation measurements can be used to obtain location- and time-dependent information on the penetration of corrosion products into the available pore space/voids of cementitious materials.
- Considerable service times can be gained (up to approximately 50 years depending among others on the corrosion rate, material, and geometrical properties) allowing for minor corrosion-induced damages, i.e. corrosion-induced concrete cover cracking with crack width openings at the concrete surface of 0.2 mm.

Service life prediction

A numerical example was provided in Chapter 3 of this Ph.D. thesis to demonstrate the potential use of the proposed framework for service life prediction. In the example, a simple beam geometry subjected to varying exposure conditions (i.e. temperature, moisture, and chloride) with and without a crack was studied.

From the example the following conclusion can be drawn:

- In combination with the heat and mass transport model, the corrosion model can be used to determine the time-to initiation and propagation of reinforcement corrosion. To define the time-to reinforcement corrosion initiation a conditional statement, e.g. critical chloride threshold or concrete carbonation, can be used.
- Individual parameters (as well as coupling between individual parameters), e.g. temperature, moisture content, concrete resistivity, concrete cover thickness, transport properties of various species, etc., affecting the corrosion process can be investigated with the proposed framework and potentially used for design purposes estimating the service life of new structures, maintenance planning, and determination of the residual service life of existing structures.
- Further coupling, i.e. combined analyses of ingress of aggressive substances, electrochemical, and mechanical processes, can be used to model corrosion-induced concrete damages.
- Similar to the combined transport and corrosion model, the influence of individual parameters (as well as coupling between individual parameters), e.g. concrete cover thickness, rebar diameter, concrete tensile strength, concrete softening behaviour, porosity, etc., on the formation and propagation of corrosion-induced cracks can be investigated.

6.2 Recommendations for further work

Based on the findings and conclusions of this Ph.D. study, the following recommendations for further work are listed:

Transport of mass and heat in porous media

Although, the capability of the heat and mass transport model to describe the moisture and chloride ingress behaviour in (cracked) cementitious materials could be shown further development is recommended.

- To include potential changes in the microstructure due to the interaction of chloride (and other) ions with the solid phases of cementitious materials, more advance chloride binding models are needed.

- The impact of sorption hysteresis on the moisture state is not included in the present model, which may affect the moisture state and transport, and subsequently the transport of ions, thermodynamics, and kinetics of the electrochemical half-cell reactions.

Corrosion of steel in concrete

Despite the fact that, the results presented in Chapter 3 clearly indicate the potential of the model to describe the corrosion process in reinforced cementitious materials further development is needed.

- Future development is to include a more detailed thermodynamic description of the electrochemical half-cell reactions for the anodic and cathodic regions. So far, the model is limited to describe chloride-induced corrosion with predefined anodic (oxidation of iron) and cathodic (reduction of oxygen) half-cell reactions. Although, these reactions are most typically found under natural exposure conditions other half-cell reactions are certainly possible and must be taken into consideration for a complete evaluation of the corrosion process.
- Further studies on the impact cracks have on the corrosion process in reinforced cementitious materials are needed. In particular, the self-healing of cementitious materials, penetration of solid corrosion products into cracks, and closure of cracks due to stress relaxation should be further investigated. These phenomena may hinder the transport of aggressive substance through the crack and slow down or even cease the corrosion process.

Corrosion-induced concrete damage

Although, comparisons between experimental and numerical results presented in Chapter 4 indicate that the model is capable describing corrosion-induced cracking in reinforced cementitious materials further development is needed.

- In particular, experimental investigations conducted by means of digital image correlation indicate non-uniform corrosion-induced deformations and hence formation of corrosion products around the reinforcement circumference. The non-uniformity may have a considerable impact on the formation and propagation of cracks and must be further investigated. Further studies, may also focus on the potential formation of soluble corrosion products that may not precipitate at the reinforcement steel interface.
- Further development is to include, additional concrete damage types, i.e. concrete spalling and delamination, and the impact of corrosion on the bond strength between reinforcement and concrete (including different geometries e.g. more rebars and the influence of rebar spacing). Also, the extension of the corrosion-induced cracking model to 3D is recommended including information on the initiation and propagation of active corrosion from the service life model presented in Section 3.5.

Bibliography

ACI Committee 224, (2001), ‘Control of cracking in concrete structures’, American Concrete Institute, Farmington Hills, MI, USA.

Adolphs, J. & Setzer, M.J. (1996), ‘A Model to Describe Adsorption Isotherms’, *Journal of Colloid and Interface Science*, 180:70-76.

Aldea, C.-M. Shah, S.P. & Karr, A. (1999), ‘Permeability of cracked concrete’, *Materials and Structures*, 32(219):370-376.

Alonso, C., Andrade, C., Rodriguez, J., & Diez, J.M. (1998), ‘Factors controlling cracking of concrete affected by reinforcement corrosion’, *Materials and Structures*, 31(211):435-441.

Anderson, T.L. (2005), *Fracture Mechanics: Fundamentals and Applications*, CRC Press.

Andrade, C., Alonso, C., & Molina, F.J. (1993), ‘Cover cracking as a function of bar corrosion: Part 1 - Experimental test’, *Materials and Structures*, 26(8):453-464.

Angst, U., Elsener B., Larsen, C.K. & Vennesland, Ø. (2009), ‘Critical chloride content in reinforced concrete - A review’, *Cement and Concrete Research*, 39(12):1122-1138.

Arup, H. (1983), *The mechanisms of protection of steel by concrete*, In Crane, A. P., editor, Corrosion of Reinforcement in Concrete Construction, pp. 151-157. Society of chemical industry, Ellis Horwood Limited.

Arya, A. & Ofori-Darko, F. (1996), ‘Influence of crack frequency on reinforcement corrosion in concrete’, *Cement and Concrete Research*, 26(3):345-353.

Bardal, E. (2004), *Corrosion and Protection*, Springer-Verlag, London, UK.

Baroghel-Bouny, V., Thiéry, M. & Wang, X. (2011), ‘Modelling of isothermal coupled moisture - ion transport in cementitious materials’, *Cement and Concrete Research*, 41(8):828-841.

Basett, J., Denney, R.C., Jeffery, G.H. & Mendham, J. (1978), *Vogel's textbook of quatitative inorganic analysis - Fourth edition*, Longman Group Limited, London, UK.

Bastidas-Arteaga, E., Chateauneuf, A., Sánchez-Silva, M., Bressolette, P. & Schoefs, F. (2011), ‘A comprehensive probabilistic model of chloride ingress in unsaturated concrete’, *Engineering Structures*, 33:720-730.

Bazant, Z.P. (1979) ‘Physical model for steel corrosion in concrete sea structures - Application’, *Journal of the Structural Division - ASCE*, 105(6):1155-1166.

Bear, J. & Bachmat, Y. (1991), *Introduction to modeling of transport phenomena in porous media*, Kluwer Academic Publishers, Dordrecht, Netherlands.

Berke, N., Dallaire, M., Hicks, M. & Hoopes, R. (1993), ‘Corrosion of steel in cracked concrete’, *Corrosion Engineering*, 49(11):934-943.

Birnin-Yauri, U. & Glasser, F. (1998), ‘Friedel's salt, $Ca_2Al(OH)_6(Cl,OH)\cdot 2H_2O$: Its solid solutions and their role in chloride binding’, *Cement and Concrete Research*, 28(12):1713-1723.

Bonnet, S. (1997), 'Influence of chloride on equilibrium behaviour and on transfer properties of civil engineering materials', (in French), *Ph.D. thesis*, INSA, Toulouse, France.

Böhni, H. (2005), *Corrosion in reinforced concrete structures*, Woodhead Publishing Ltd.

Buchwald, A. (2000), 'Determination of the ion diffusion coefficient in moisture and salt loaded masonry materials by impedance spectroscopy', *In: Proceedings for Third international symposium,* Vienna, Austria.

Buenfeld, N., Glass, G., Reddy, B., & Viles, F. (2004), 'Process for the Protection of Reinforcement in Reinforced Concrete', *United States Patent 6685822*, USPTO, Alexandria, VA, USA.

Caré, S., Nguyen, Q.T., L´Hostis, V. & Berthaud, B. (2008), 'Mechanical properties of the rust layer induced by impressed current method in reinforced mortar', *Cement and Concrete Research*, 38(8-9):1079-1091.

Caré, S. (2008), 'Effect of temperature on porosity and on chloride diffusion in cement pastes', *Construction and Building Materials*, 22:1560-1573.

Carmeliet, J. & Roels, S. (2002), 'Determination of the moisture capacity of porous building materials', *Journal of Thermal Envelope and Building Science*, 25(3):209-237.

Chernin, L., Val, V.D. & Volokh K.Y. (2010), 'Analytical modelling of concrete cover cracking by corrosion of reinforcement', *Materials and Structures*, 43(4): 543-556.

DAfStb (2003) , 'Guideline waterproof concrete constructions', Deutscher Ausschuss für Stahlbeton.

De Vries, A.D. (1958), 'Simultaneous trasnfer of heat and moisture in porous media', *Transactions of the American Geophysical Union*, 39:909-916.

De Weerdt, K. & Geiker, M.R. (2012), 'Changes in the Phase Assemblage of Concrete Exposed to Seawater - Case Study', *In: Proceedings for ICDC (International Congress on Durability of Concrete)*, Trondheim, Norway.

Dobson, M.C., Ulaby, F.T., Hallikainen, M.T. & El-Rayes, M.A. (1985), 'Microwave dielectric behaviour of wet soil, II. Dielectric mixing models', *IEEE Transactions on Geoscience and Remote Sensing*, GE-23(1):35-46.

DS/EN 1504, 'Products and systems for the protection and repair of concrete structures. Definitions, requirements, quality control and evaluation of conformity', Standard, DS/EN 1504 1-10, Dansk Standard (DS), Charlottenlund, Denmark.

Dullien, F.A.L. (1979), *Porous Media - Fluid Transport and Pore Structure*, Academic Press, New York, USA.

DuraCrete (2000), 'General guidelines for durability design and redesign', *Tech. Rep. Report BE95-1347/R15*, European Union, Luxembourg, part of the Brite-EuRam III Project BE95-1347 Probabilistic Performance based Durability Design of Concrete Structures, 109 pp.

Edvardsen, C. (1999), 'Water permeability and autogenous healing of cracks in concrete', *ACI Materials Journal*, 96(4):448-454.

Ehlen, M.A., Thomas, M.D.A. & Bentz, E.C. (2009), 'Life-365 service life prediction model version 2.0 - widely used software helps assess uncertainties in concrete service life and life-cycle costs', *Concrete International - the Magazine of the American Concrete Institute*, 31(5), 41.

El Maaddawy, T. & Soudki, K. (2007), 'A model for prediction of time from corrosion initiation to corrosion cracking', *Cement and Concrete Composites*, 29 (3):168–175.

Eurocode 2 (2004), 'Design of concrete structures, Part 1, General rules and rules for buildings', BS EN 1992-1-1.

fib Bulletin 183 (1992), 'Durable Concrete Structures', *Tech. Rep. fib Bulletin 34*, International Federation for Structural Concrete (fib), Lausanne, Switzerland, 2nd edition. 112 pp.

fib Bulletin 34 (2006), 'Model code for service life design', *Tech. Rep. fib Bulletin 34*, International Federation for Structural Concrete (fib), Lausanne, Switzerland, 126 pp.

Fontana, M.G. & Greene, N.D. (1978), *Corrosion engineering*, McGraw-Hill.

Frederiksen, J. & Poulsen, E. (1997), 'Hetek: Chloride penetration into concrete - manual', *Tech. Rep. Report No. 123*, Road Directorate, Danish Ministry of Transport.

Gautefall, O. & Vennesland, Ø. (1983), 'Effects of cracks on the corrosion of embedded steel in silicaconcrete compared to ordinary concrete', *Nordic Concrete Research*, 2:17-28.

Génin, J.-M.R., Refaita, P., Bourriéb, G., Abdelmoulaa, M., & Trolard, F. (2001), 'Structure and stability of the Fe(II)–Fe(III) green rust "fougerite" mineral and its potential for reducing pollutants in soil solutions', *Applied Geochemistry*, 16(5):559-570.

Ghods, P., Isgor, O.B. & Pour-Ghaz, M. (2007), 'A practical method for calculating the corrosion rate of uniformly depassivated reinforcing bars in concrete', *Materials and Corrosion*, 58(5):265-272.

Glass, G.K. & Buenfeld, N.R. (2000), 'The influence of chloride binding on the chloride induced corrosion risk in reinforced concrete' *Corrosion Science*, 42:329-344.

Hagymassy, J.J.R., Brunauer, S. & Mikhail, R.S.H. (1969), 'Pore structure analysis by water vapour adsorption - t-curves for water vapour', *Journal of Colloid and Interface Science*, 29(3):485-491.

Hansen, E.J. & Saouma, V.E. (1996), 'Numerical simulation of reinforced concrete deterioration - Part I: Chloride diffusion', *ACI Materials Journal*, 96:173-180.

Hasegawa, Y., Miyazato, S. & Oyamoto, T. (2004), 'Proposal for Corrosion Rate Analytical Model of Reinforced Concrete', In: *Proceedings of 29th Conference on OUR WORLD IN CONCRETE & STRUCTURES*, Singapore, Republic of Singapore.

Huet, B., L´hostis, V., Santarini, G., Feron, D. & Idrissi, H. (2007), 'Steel corrosion in concrete: Deterministic modeling of cathode reaction as a function of water saturation degree', *Corrosion Science*, 49:1918-1932.

Hundt, J. & Kantelberg, H. (1978), ‘Sorptionsuntersuchungen an Zementstein, Zementmörtel und Beton‘, *Deutscher Ausschuss für Stahlbeton*, 297:25-39.

Hurlen, T. (1960), ‘Heat of Activation in Electrode Kinetics’, *Acta Chemica Scandinavica*, 14:1564-1570.

Isgor, B.O. & Razaqpur, G.A. (2006), ‘Modelling steel corrosion in concrete structures’, *Materials and Structures*, 39(287): 291-302.

Ishida, T., Maekawa, K. & Kishi, T. (2007), ‘Enhanced modeling of moisture equilibrium and transport in cementitious materials under arbitrary temperature and relative humidity history’, *Cement and Concrete Research*, 37:565-578.

Jacobsen, S., Marchand, J. & Boisvert, L. (1996), ‘Effect of cracking and healing on chloride transport in OPC concrete’, *Cement and Concrete Research*, 26(6):869-881.

Jäggi, S. (2001), ‘Experimentelle und numerische Modellierung der lokalen Korrosion von Stahl in Beton unter besonderer Berücksichtigung der Temperaturabhängigkeit’, *Ph.D. thesis*, Eidgennössische Technische Hochschule Zürich, Zürich, Switzerland.

Janssen, H., Blocken, B. & Carmeliet, J. (2007), ‘Conservative modelling of the moisture and heat transfer in building components under atmospheric excitation’, *International Journal of Heat and Mass Transfer*, 50:1128-1140.

Justnes, H. (1998), ‘A review of chloride binding in cementitious systems’, *Nordic Concrete Research*, 21:1-6.

Justnes, H. (2002), ’Utvikling av miljøvennlig korrosjonsinhibitor basert på kalsiumnitrat. Del 2: Betong. Aktivitet 2a: Støping og instrumentering av veggelementer’, SINTEF Bygg og miljø- Sement og betong, Trondheim.

Karihaloo, B.L. (1995), *Fracture Mechanics & Structural Concrete*, Concrete Design and Construction Series, Longman Scientifc & Technical, Essex, England.

Krischer, O. (1978), *Die wissenschaftlichen Grundlagen der Trocknungstechnik*, 3. Auflage, Springer Verlag Berlin.

Koleva, D.A., Hu, J., Fraaij, A.L.A., Stroeven, P., Boshkov, N., & de Wit, J.H.W. (2006), ‘Quantitative characterisation of steel/cement paste interface microstructure and corrosion phenomena in mortars suffering from chloride attack’, *Corrosion Science*, 48(12):4001-4019.

Koniorczyk, M. & Wojciechowski M. (2009), ‘Influence of salt on desorption isotherm and hygral state of cement mortar - Modelling using neural networks’, *Construction and Building Materials*, 23:2988-2996.

Koryta, J., Dvořák, J., & Boháčková, V. (1970), *Electrochemistry*, Methuen & CO Ltd.

Kranc, S.C. & Sagüés, A.A. (2001), ‘Detailed modeling of corrosion macrocells on steel reinforcing in concrete’, *Corrosion Science*, 43(7):1355-1372.

Krus, M. (1995), ‘Feuchtetransport- und Speicherkoeffizienten poröser mineralischer Baustoffe‘, *Ph.D. thesis*, Universität Stuttgart, Stuttgart, Germany.

Küter, A. (2009), 'Management of reinforcement corrosion: a thermodynamical approach', *Ph.D. thesis*, Technical University of Denmark, Kgs. Lyngby, Denmark.

Larsen, C.K., Østvik, J.-M. & Bjøntegaard, Ø. (2007), ' Compilation of 5 papers on (1) Electrical resistivity as a durability indicator and (2) Cracking tendency in hardening concrete', *Technology Report 2482*, Norwegian Public Roads Administration, Directorate of Public Roads, Technology Department.

Li, V. (2004), 'A New Research Framework for Sustainable Infrastructures', *Seminar*, Department of Civil Engineering, Technical University of Denmark.

Life-365 Consortium II (2010), 'Life-365 Service life prediction model and computer program for predicting the service life and life-cycle cost of reinforced concrete exposed to chlorides'.

Lindquist, W.D. Darwin, D, Browning, J.-A. & Miller, G. (2006), 'Effect of cracking on chloride content in concrete bridge decks', *ACI Materials Journal*, 103(6):467-473.

Liu, Y. & Weyers, R.E. (1998), 'Modeling the time-to-corrosion cracking in chloride contaminated reinforced concrete structures', *ACI Materials Journal*, 95(5):675-681.

López, W, González, J.A. & Andrade, C. (1993), 'Influence of Temperature on the Service Life of Rebars', *Cement and Concrete Research*, 23:1130-1140.

López, W & González, J.A. (1993a), 'Influence of the Degree of Pore Saturation on the Resistivity of Concrete and the Corrosion Rate of Steel Reinforcement', *Cement and Concrete Research*, 23: 368-376.

Luping, T. & Nilsson, L.-O. (1993), 'Chloride binding capacity and binding isotherms of OPC pastes and mortars', *Cement and Concrete Research*, 23(2):247-253.

Lykow, A.W. (1958), *Transporterscheinungen in kapillarporösen Körpern*, Akademie Verlag Berlin.

Maekawa, K., Kishi, T. & Chaube, R.P. (1999), *Modelling of Concrete Performance*, E&FN Spon.

Makita, M., Mori, Y. & Katawaki, K. (1980), 'Marine corrosion behavior of reinforced concrete exposed at tokyo bay', In: *ACI Special Publication*, 65:271-290.

Marcotte, T. & Hansson, C. (2003), 'The influence of silica fume on the corrosion resistance of steel in high performance concrete exposed to simulated sea water', *Journal of Material Sciences*, 28:4765-4776.

Marcotte, T. & Hansson, C. (2007), 'Corrosion products that form on steel within cement paste', *Materials and Structures*, 40(3):325-340.

Marques, P.F. & Costa, A. (2010), 'Service life of RC structures: Carbonation induced corrosion. Prescriptive vs. performance-based methodologies', *Construction and Building Materials*, 24(3):258-265.

Marsavina, L., Audenaert, K., De Schutter, G., Faur, N. & Marsavina, D. (2009), 'Experimental and numerical determination of the chloride penetration in cracked concrete', *Construction and Building Materials*, 23(1):264-274.

Martín-Pérez, B. (1999), 'Service Life Modelling of R.C. Highqay Structures Exposed to Chlorides', *Ph.D. thesis*, University of Toronto, Toronto, Canada.

Maruya, T., Hsu, K., Takeda, H. & Tangtermsirikul, S. (2003), 'Numerical Modeling of Steel Corrosion in Concrete Structures due to Chloride Ion, Oxygen and Water Movement', *Journal of Advanced Concrete Technology*, 1(2):147-160.

Michel, A., Geiker, M.R., Stang, H. & Olesen, J.F. (2010), 'Numerical modelling of reinforcement corrosion in concrete structures', *In: Proceedings for 8th fib PhD Symposium*, Kgs. Lyngby, Denmark.

Michel, A., Solgaard, A.O.S., Geiker, M.R., Stang, H. & Olesen, J.F. (2010a), 'Modeling Formation of Cracks in Concrete Cover due to Reinforcement Corrosion', In: *Proceedings of FraMCos 7 (7th International Conference on Fracture Mechanics of Concrete and Concrete Structures)*, Jeju, South Korea.

Michel, A., B.J. Pease, Geiker, M.R., Stang, H. & Olesen, J.F. (2011), 'Monitoring reinforcement corrosion and corrosion-induced cracking using non-destructive x-ray attenuation measurements', *Cement and Concrete Research*, 41:1085-1094.

Miyazato, S. & Hiraishi, Y. (2005), 'Transport properties and steel corrosion in ductile fiber reinforced cement composites, *In: Proceedings of the 11th international conference on Fracture*, Turin, Italy.

Moffitt, L.R. (1964), 'Time domain reflectometry - theory and applications', *Engineering Design News*, 38-44.

Molina, F.J., Alonso, C., & Andrade, C. 1993, 'Cover cracking as a function of rebar corrosion: part 2 - numerical model', *Materials and Structures*, 26:532-548.

Moreno, M., Morris, W. Alvarez, M. & Duff, G. (2004), 'Corrosion of reinforcing steel in simulated concrete pore solutions effect of carbonation and chloride content', *Corrosion Science*, 46(11):2681-2699.

Mualem, Y. (1976), 'A new model for predicting the hydraulic conductivity of unsaturated porous media', *Water Resource Research*, 12:513-522.

Nilsson, L.O., Poulsen, E., Sandberg, P., Sørensen, H.E. & Klinghoffer, O. (1996), 'Hetek, chloride penetration into concrete state-of-the-art - transport processes, corrosion initiation, test methods and prediction models', *Technical Report: Report No. 53*, The Danish Road Directorate.

Noghabai, K. (1999), 'FE-Modelling of cover splitting due to corrosion by use of inner softening band', *Materials and Structures*, 32(221):486-491.

Nygaard, P.V. & Geiker, M.R. (2005), 'A method for measuring the chloride threshold level required to initiate reinforcement corrosion in concrete', *Materials and Structures*, 38:489-494.

O'Neil, E.F. (1980), 'Study of reinforced concrete beams exposed to marine environment, *In: ACI Special Publication*, 65:113-132.

Osterminski, K., Schießl, P., Volkwein, A. & Maye, T.F. (2006), 'Modelling reinforcement corrosion - usability of a factorial approach for modelling resistivity of concrete', *Materials and Corrosion*, 57(12):926-931.

Østnor, T.A. (2011), 'Renewed corrosion inhibitor test of field station concrete', SINTEF Building and Infrastructure, Trondheim, Norway.

Otieno, M.B, Alexander M.G. & Beushausen, H.-D. (2010), 'Corrosion in cracked and uncracked concrete - Influence of crack width, concrete quality and crack reopening', *Magazine of Concrete Research*, 62(6):393-404.

Ouglova, A., Raharinaivo A., Berthaud Y., Petre-Lazar, I. & Bouk-henfouf, H. (2005), 'Numerical simulation of potential distribution due to the corrosion of reinforcement in concrete structures', *Materials and Structures*, 38(281):711-719.

Ouglova, A. Berthaud, Y. Francois, M. & Foct, F. (2006), 'Mechanical properties of an iron oxide formed by corrosion in reinforced concrete structures', *Corrosion Science*, 48(12):3988-4000.

Pease, B., Couch, J., Geiker, M., Stang, H. & Weiss, J. (2009), 'Assessing the portion of the crack length contributing to water sorption using X-ray absorption measurements on concrete wedge splitting specimens', *In: Proceedings of ConcreteLife '09: 2nd International RILEM Workshop on Concrete Durability and Service Life Planning*, Haifa, Israel.

Pease, B. (2010), 'Influence of concrete cracking on ingress and reinforcement corrosion', *Ph.D. thesis*, Technical University of Denmark, Kgs. Lyngby, Denmark.

Pease, B., Geiker, M., Stang, H. & Weiss, J. (2011), 'The design of an instrumented rebar for assessment of corrosion in cracked reinforced concrete', *Materials and Structures*, 44(7):1259-1271.

Pease, B. J., Michel, A., Geiker, M. R. & Stang, H. (2012), 'Modelling Moisture Ingress through Simplified Concrete Geometries', *In: Proceedings for ICDC (International Congress on Durability of Concrete)*, Trondheim, Norway.

Pease, B.J., Michel, A, Thybo, A.E.A. & Stang, H. (2012a), 'Estimation of elastic modulus of reinforcement corrosion products using inverse analysis of photogrammetric measurements for input in corrosion-induced cracking model', *In: Proceedings of IABAMAS 2012 (6th International Conference on Bridge Maintenance, Safety and Management)*, Villa Erba, Italy.

Pel, L. (1995), 'Moisture transport in building materials', *Ph.D. thesis*, Eindhoven University of Technology, Eindhoven, Netherlands.

Perez, N (2004), *Electrochemistry and Corrosion Science*, Kluwer Academic Publishers, Boston.

Phillipson, M.C., Baker, P.H., Davies, M., Ye, Z., Galbraith, G.H. & McLean, R.C. (2008), 'Suitability of time domain reflectometry for monitoring moisture in building materials', *Building Services Engineering Research & Technology*, 29(3):261-272.

Philip, J.R. & de Vries, A.D. (1957), 'Moisture Movement in Porous Materials under Temperature Gradients', *Transactions of the American Geophysical Union*, 38:223-232.

Pihlajavaara, S.E. (1965), 'On the main feature and methods of investigation of drying and related phenomena in concrete', *Ph.D. thesis*, University of Helsinki, Helsinki, Finland.

Poyet, S. (2009), 'Experimental investigation of the effect of temperature on the first desorption isotherm of concrete', *Cement and Concrete Research*, 39():1052-1059.

Poursaee, A & Hansson, C.M. (2008), 'The influence of longitudinal cracks on the corrosion protection afforded reinforcing steel in high performance concrete', *Cement and Concrete Research*, 38(8-9):1098-1105.

Radjy, F., Sellevold, E.J. & Hansen, K.K. (2003), 'Isosteric vapor pressure - temperature data for water sorption in hardened cement paste: enthalpy, entropy and sorption isotherms at different temperatures', *Report BYG-DTU R057*, Technical University of Denmark (DTU), Kgs. Lyngby, Denmark.

Raupach, M. (1996), 'Investigations on the influence of oxygen on corrosion of steel in concrete - Part l', *Materials and Structures*, 29:174-184.

Refait, P., Abdelmoula, M., & Genin, J.-M. (1998), 'Mechanisms of formation and structure of green rust one in aqueous corrosion of iron in the presence of chloride ions', *Corrosion Science*, 40(9):1547:1560.

Rehm, G. & Moll, H.L. (1964), 'Versuche zum Studium des Einflußes der Rissbreite auf die Rostbildung an der Bewehrung von Stahlbetonbauteilen', *Deutscher Ausschuss für Stahlbeton*, 169.

Rendell, F., Jauberthie, R. & Grantham, M. (2002), *Deteriorated Concrete - Inspection and physicochemical analysis*, London, UK, Thomas Telford, 1st edition.

RILEM TC 154-EMC (2003), 'Recommendations of RILEM TC 154-EMC: Electrochemical techniques for measuring metallic corrosion Half-cell potential measurements - Potential mapping on reinforced concrete structures', *Materials and Structures*, 36(261):461-471

Rode, C. (1990), 'Combined heat and moisture transfer in building constructions', *Ph.D. thesis*, Technical University of Denmark, Kgs. Lyngby, Denmark.

Rodriguez, O. & Hooton, R. (2003), 'Influence of cracks on chloride ingress into concrete," *ACI Materials Journal*, 100(2):120-126.

Saetta, A.V., Scotta, R.V. & Vitaliani, R.V. (1993), 'Analysis of chloride diffusion into partially saturated concrete', *ACI Materials Journal*, 90(5):441-45.

Samson, E. & Marchand, J. (2007), 'Modeling the transport of ions in unsaturated cement-based materials', *Computers and Structures*, 85:1740-1756.

Scheffler, G.A. (2009), 'Validation of hygrothermal material modelling under consideration of the hysteresis of moisture storage', *Ph.D. thesis*, Technische Universität Dresden, Dresden, Germany.

Scheffler, G.A & Plagge, R.A. (2010), 'Whole range hygric material model: Modelling liquid and vapour transport properties in porous media', *International Journal of Heat & Mass Transfer*, 53:286-296.

Schießl, P. (1976), 'Zur Frage der zulässigen Rissbreite und der enforderlichen Betondeckung im Stahlbetonbau unter besonderer Berücksichtigung der Karbonatisierung des Betons', *Deutscher Ausschuss für Stahlbeton 255*.

Schießl, P. (Ed.) (1988), '*Corrosion of steel in concrete*', Report of the Technical Committee 60 CSC, RILEM, Chapman and Hall, 1988.

Schießl, P. & Raupach, M. (1997), 'Laboratory studies and calculations on the influence of crack width on chloride-induced corrosion of steel in concrete', *ACI Materials Journal*, 94(1):56-62.

Schirmer, R. (1938), 'Die Diffusionszahl von Wasserdampf-Luftgemischen und die Verdampfungsgeschwindigkeit', *VDI Beiheft Verfahrenstechnik*, 2:170-177.

Scott, A. & Alexander, M. (2007), 'The influence of binder type, cracking and cover on corrosion rates of steel in chloride contaminated concrete', *Magazine of Concrete Research*, 59(7):495-505.

Shah, S.P., Swartz S.E. & Ouyang, C. (1995), *Fracture Mechanics of Concrete*, John Wiley & Sons, Inc..

Shreir, L.L. (1994), 'Corrosion in Aqueous Solutions', In Shreir, L.L., Jarman, R.A. & Burstein, G.T. editors, Corrosion Volume 1 Metal/Environment Reactions, Butterworth-Heinemann, Boston.

Stern, M. & Geary, A.L. (1957),' Electrochemical polarization I. A theoretical analysis of the shape of polarization curves', *Journal of the Electrochemical Society*, 104:56-63.

Synder, K.A. (2001), *Validation and modification of the 4sight computer program*, National Institute of Standards and Technology (NIST), Gaithersburg, Maryland.

Tammo, K. & Thelandersson, S. (2009), 'Nonlinear analysis of crack widths in reinforced concrete', *Magazine of Concrete Research*, 61(1):23-34.

Tanaka, N. & Tamamushi R. (1964), 'Kinetic Parameters of Electrode Reactions', *Elcctrochimica Acta*, 9:963-989.

Tang, L. & Nilsson, L.-O. (1993), 'Chloride binding capacity and binding isotherms of OPC pastes and mortars', *Cement and Concrete Research*, 23(2):247-253.

Topp, G.C., Davis, J.L. & Annan, A.P. (1980), 'Electromagnetic determination of soil water content: measurements in coaxial transmission lines', *Water Resource and Research*, 16:574-582.

Toro, L., Andrade, C., Fullea, J., Martínez, I. & Rebolledo, N. (2012), 'Steel Corrosion in a Chloride Contaminated Concrete Pore Solution with Low Oxygen Availability', In: Andrade, C. & Gulikers, J. editors, Advances in Modeling Concrete Service Life: Proceedings of 4th International RILEM PhD Workshop held in Madrid.

Tuutti, K. (1982), '*Corrosion of Steel in Concrete*', Swedish Cement and Concrete Research Institute at the Institute of Technology, Stockholm, 4-82.

Val, D.V., Chernin, L. & Stewart, M.G. (2009), 'Experimental and numerical investigation of corrosion-induced cover cracking in reinforced concrete structures', *Journal of Structural Engineering*, 135(4):376-385.

van Mier, J.G.M. (1997), '*Fracture Processes in Concrete Assessment of Material Parameters for Fracture Models*', CRC Press.

Vidal, T., Castel, A. & Francois, R. (2007), 'Corrosion process and structural performance of a 17 year old reinforced concrete beam stored in chloride environment', *Cement and Concrete Research*, 37(11):1551-1561.

Villmann, B., Bretschneider, N., Slowik, V. & Michel, A. (2006), 'Bestimmung von Materialeigenschaften zementgebundener Werkstoffe mittles inverser Analyse', *Bautechnik*, 83(11):747-753.

Vu, K., Stewart, M.G. & Mullard, J. (2005), 'Corrosion-Induced Cracking: Experimental Data and Predictive Models', *ACI Materials Journal*, 102(5):719-726.

Warkus, J., Raupach, M. & Gulikers, J. (2006), 'Numerical modeling of corrosion - Theoretical backgrounds -', *Materials and Corrosion*, 57: 614-617.

Warkus, J & Raupach, M. (2008), 'Numerical modelling of macrocells occurring during corrosion of steel in concrete', *Materials and Corrosion*, 59(2):120-133.

Xi, Y. & Bazant, Z. (1999), 'Modeling chloride penetration in saturated concrete', *Journal of Materials in Civil Engineering*, 11(1):58-65.

Xu, K., Daian J.-F. & Quenard, D. (1997), 'Multiscale Structures to Describe Porous Media Part I: Theoretical Background and Invasion by Fluids', *Transport in Porous Media*, 26:51-73.

Yoon, S., Wang, K., Weiss, J. & Shah, S. (2000), 'Interaction between Loading, Corrosion, and Serviceability of Reinforced Concrete', *ACI Materials Journal*, 97(6):637-644.

Yuan, Q., Shi, C., De Schutter, G., Audenaert, K. & Deng, D. (2009), 'Chloride binding of cementbased materials subjected to external chloride environment – a review', *Construction and Building Materials*, 23:1-13.

Zibara H. (2001), 'Binding of external chlorides by cement pastes', *Ph.D. thesis*, University of Toronto, Toronto, Canada.

Part II

Appended Papers

Paper I A. Michel, H. Sobczuk, M.R. Geiker, 'Application of time domain reflectometry (TDR) to determine the impact of temperature on the moisture sorption of cementitious materials', *Cement and Concrete Research*, accepted for publication.

Paper II B.J. Pease, A. Michel, M.R. Geiker, H. Stang, 'Modelling Moisture Ingress through Simplified Concrete Geometries', *In: Proceedings of ICDC (International Congress on Durability of Concrete)*, June 17-21, 2012, Trondheim, Norway, (2012).

Paper III A. Michel, M.R. Geiker, H. Stang, J.F. Olesen, 'Numerical modelling of reinforcement corrosion in concrete structures', *In: Proceedings of 8th fib PhD Symposium*, June 20-23, 2010, Kgs. Lyngby, Denmark, (2010).

Paper IV A. Michel, M.R. Geiker, H. Stang, J.F. Olesen, 'Modelling Reinforcement Corrosion in Concrete', *In: Proceedings of MicroDurability*, April 11-13, Amsterdam, Netherlands, (2012).

Paper V A. Michel, P. Nygaard, M.R. Geiker, 'Experimental investigation on the short-term impact of temperature and moisture on reinforcement corrosion', *Corrosion Science*, Vol. 72, pp. 26-34, (2013).

Paper VI A.O.S. Solgaard, A. Michel, H. Stang, 'Debonding at the Concrete/steel Interface in Reinforced Concrete Beams - Experimental Investigations: Part I', *Materials and Structures*, submitted.

Paper VII A.O.S. Solgaard, A. Michel, H. Stang, 'Debonding at the Concrete/Steel Interface in Reinforced Concrete Beams - Numerical Simulations: Part II', *Materials and Structures*, submitted.

Paper VIII A. Michel, A.O.S. Solgaard, B.J. Pease, M.R. Geiker, H. Stang, J.F. Olesen, 'Experimental investigation of the relation between damage at the concrete-steel interface and initiation of reinforcement corrosion in plain and fibre reinforced concrete', *Corrosion Science*, Vol. 77, pp. 308-321, (2013).

Paper IX A. Michel, A.O.S. Solgaard, M.R. Geiker, H. Stang, J.F. Olesen, 'Modeling Formation of Cracks in Concrete Cover due to Reinforcement Corrosion', *In: Proceedings of FraMCos 7 (7th International Conference on Fracture Mechanics of Concrete and Concrete Structures)*, May 23-28, 2010, Jeju, Korea, (2010).

Paper X A. Michel, B.J. Pease, M.R. Geiker, H. Stang, J.F. Olesen, 'Monitoring reinforcement corrosion and corrosion-induced cracking using non-destructive x-ray attenuation measurements', *Cement and Concrete Research*, Vol. 41, pp. 1085 - 1094, (2011).

Paper XI A. Michel, B.J. Pease, A. Peterová, M.R. Geiker, 'Experimental Determination of the Penetration Depth of Corrosion Products and Time to Corrosion-Induced Cracking in Reinforced Cement Based Materials', *In: Proceedings of ICDC (International Congress on Durability of Concrete)*, June 17-21, 2012, Trondheim, Norway, (2012).

Paper XII B.J. Pease, A. Michel, A.E.A. Thybo, H. Stang, 'Estimation of elastic modulus of reinforcement corrosion products using inverse analysis of photogrammetric measurements for input in corrosion-induced cracking model', *In: Proceedings of IABAMAS 2012 (6th International Conference on Bridge Maintenance, Safety and Management)*, July 8-12, Villa Erba, Italy, (2012).

Paper XIII A.O.S. Solgaard, A. Michel, M.R. Geiker, H. Stang, 'Concrete cover cracking due to uniform reinforcement corrosion', *Materials and Structures*, DOI 10.1617/s11527-013-0016-6.

Additional publications (not included in the thesis)

Paper A A. Michel, A.O.S. Solgaard, M.R. Geiker, H. Stang, J.F. Olesen, 'Numerical modelling of reinforcement corrosion, influence of steel fibres and moisture content on resistivity and corrosion current density', *In: Proceedings of 3rd Int. PhD Workshop on Modelling the Durability of reinforced Concrete*, October 22-24 2009, Guimarães, Portugal, (2009).

Paper B A.O.S. Solgaard, A. Michel, H. Stang, M.R. Geiker, 'The influence of electrical conductive fibres on the resistivity of concrete composites', *In: Proceedings of 3rd Int. PhD Workshop on Modelling the Durability of reinforced Concrete*, October 22-24, 2009, Guimarães, Portugal, (2009).

Paper C A. Michel, A.O.S. Solgaard, M.R. Geiker, H. Stang, J.F. Olesen, 'Modelling the Influence of Resistivity on the Corrosion of Reinforcement in Concrete', *In: Proceedings of CONMOD'10*, June 22-25, 2010, Lausanne, Switzerland, (2010).

Paper D A.O.S. Solgaard, A. Michel, H. Stang, M.R. Geiker, C. Edwardsen, A. Küter, 'Numerical modeling of cracking of concrete due to corrosion of reinforcement - Impact of cover thickness and concrete toughness', *In: Proceedings of FraMCos 7 (7th International Conference on Fracture Mechanics of Concrete and Concrete Structures)*, May 23-28, 2010, Jeju, Korea, (2010).

Paper E B.J. Pease, A. Michel, H. Stang, 'Quantifying Movements of Corrosion Products in Reinforced Concrete Using X-Ray Attenuation Measurements', *In: Proceedings of MicroDurability*, April 11-13, Amsterdam, Netherlands, (2012), accepted.

Paper F M.M. Flint, A. Michel, A. Gussiås, C.K. Larsen, J.-M. Østvik, S.L. Billington, M.R. Geiker, 'Overview of US-Norway Collaboration on Bridge Repair Sustainability', *In: Proceedings of ICDC (International Congress on Durability of Concrete)*, June 17-21, 2012, Trondheim, Norway, (2012).

Paper G M.M. Flint, A. Michel, S.L. Billington, M.R. Geiker, 'Influence of Temporal Resolution of Boundary Conditions on the Moisture, Temperature and Ion Distributions in Concrete', *Materials and Structures*, DOI 10.1617/s11527-013-0091-8.

Paper H A. Michel, B.J. Pease, A. Peterová, M.R. Geiker, H. Stang, A.E.A. Thybo, 'Penetration of corrosion products and corrosion-induced cracking in reinforced cementitious materials: Experimental investigations and numerical simulations', *Cement and Concrete Composites*, Article in press, (2013).

Paper I

”Application of time domain reflectometry (TDR) to determine the impact of temperature on the moisture sorption of cementitious materials”

A. Michel, H. Sobczuk & M.R. Geiker

Accepted for publication in: *Cement and Concrete Research.*

Application of time domain reflectometry (TDR) to determine the impact of temperature on the moisture sorption of cement based materials

Alexander Michel[a,c], Henryk A. Sobczuk[b], Mette R. Geiker[a,c]

[a)] *Technical University of Denmark (DTU), Department of Civil Engineering, Kgs. Lyngby, Denmark*
+45 4525 1656, +45 4588 3282, almic@byg.dtu.dk, http://www.dtu.dk

[b)] *Lublin University of Technology, Department of Environmental Engineering, Lublin, Poland*

[c)] *Norwegian University of Science and Technology (NTNU), Department of Structural Engineering, Trondheim, Norway*

Abstract

Although recognised, the influence of temperature on the moisture sorption of cement based materials is poorly investigated. In particular with respect to many deterioration mechanisms and moisture driven volume changes, an accurate determination of the amount of moisture is of major importance. In this study sealed concrete and calcium silicate specimens with constant moisture contents were subjected to varying temperatures and monitored by means of time domain reflectometry (TDR). The different dielectric constants of free and physically bound water allowed for tracking of changes of the moisture state in the specimens.

The results of the TDR measurements in combination with multilayer adsorption theory were used to model the impact of temperature on the amount of adsorbed water in cement based materials. Comparison of predicted and measured water vapour sorption isotherms presented in the literature for concrete, mortar, and cement paste coincided for moisture contents up to approximately 75 % RH.

Keywords: Temperature; Physical Properties; Transport Properties; Concrete; Modeling

1 Introduction

A number of service life models (e.g., *fib* [1,2] and Life-365 [3,4]) have been developed to address durability issues of reinforced concrete structures and provide tools to estimate the length of time during which a desired level of functionality is maintained. In particular, an accurate determination of the moisture transport and the state and amount of moisture in (reinforced) concrete structures is of major importance for prediction of many deterioration mechanisms [5] and moisture induced volumes changes.

In the hygroscopic range, the state of moisture is either adsorbed (bound) or capillary condensed (free). Although recognised, the influence of temperature on the moisture sorption of cement based materials is poorly investigated. Gravimetrical sorption measurements of cement based materials are very time consuming and only a limited amount of experimental studies can be found in the literature on the impact of temperature, see e.g. [6-12]. Among the few experimental studies, Radjy et al. [9] investigated one year old water-cured hardened cement paste sample with a water-to-cement ratio (w/c) of 0.5 for temperatures between 0 and 40 °C as well as approximately 2 years old (steam-cured) hardened cement paste samples with w/c of 0.35 and 0.45 for temperatures between 0 and 60 °C. Within the investigated temperature range, a limited influence of the temperature on the moisture sorption (for both steam and water-cured specimens) was observed by Radjy et al. [9], which could be described by the enthalpy of adsorbed water. In general, it was observed that with increasing temperature the moisture content in the hygroscopic region was decreased. These observations are in good agreement with results presented in [11,12].

Considerable higher impacts of temperature on the moisture sorption of cement based materials were observed in other studies, see e.g. [6-8,10]. Hundt and Kantelberg [10] investigated the impact of temperature on the moisture sorption for 3.6 year old concrete specimens with a w/c of 0.565 and 0.575 at four different temperatures (20, 45, 57.5 and 70 °C). Furthermore, results were presented in [10] for mature mortar specimens with a w/c of 0.5 and hardened cement paste with w/c of 0.4, 0.45, 0.5 and 0.55. Selected results from [10] are reproduced and presented in Figure 1. For all materials described in [10] a similar impact of the temperature on the moisture sorption can be seen; as temperature is increasing, the moisture content is decreasing in the hygroscopic range. A comparison between the experimental studies presented in [6,7,10] and [9,11,12] is given in Figure 2. The results are presented as change in relative humidity per degree Celsius against the relative humidity at reference temperature. It can be seen from the data presented in Figure 2 that for higher relative humidities (above approximately 80%) similar results are obtained for all experimental data, however, for lower relative humidities the impact of temperature is considerably higher for the data presented in [6,7,10]. While thermodynamics (enthalpy) of sorption could be used successfully to describe the impact of temperature in [9], only a limited applicability of the enthalpy of sorption is found for experimental data presented in [6-8,10] (see Figure 2). Therefore, the present study focuses on the experimental data presented in [6-8,10]. Figure 3 illustrates the relative change in moisture content (compared to the reference temperature of 20°C). The results show that for the investigated temperatures the relative change in moisture content was very similar for all investigated materials in [10], i.e. concrete, mortar and cement paste with varying w/c ratios. This indicates that a common physical phenomenon is related to the process.

In the present study sealed concrete and calcium silicate specimens with constant moisture contents were subjected to various ambient temperatures and monitored by means of time domain reflectometry (TDR). TDR was originally developed to detect defects in telecommunication cables and electrical wires [13]. More recently, the TDR technique was applied to other porous media, such as soil or masonry, to determine and monitor moisture contents [14-16]. Advantages of the TDR technique include the high spatial resolution, the non-destructive nature of the measurement technique, the general applicability (in-situ as well as laboratory), and the high precision and stability. The high precision and stability of the TDR technique allow for determination of very small changes in moisture contents (0.01 cm^3/cm^3). This in combination with the different dielectric

constants of free and physically bound water is used in the present study to track changes in the amount of adsorbed water in specimens subjected to temperature variations.

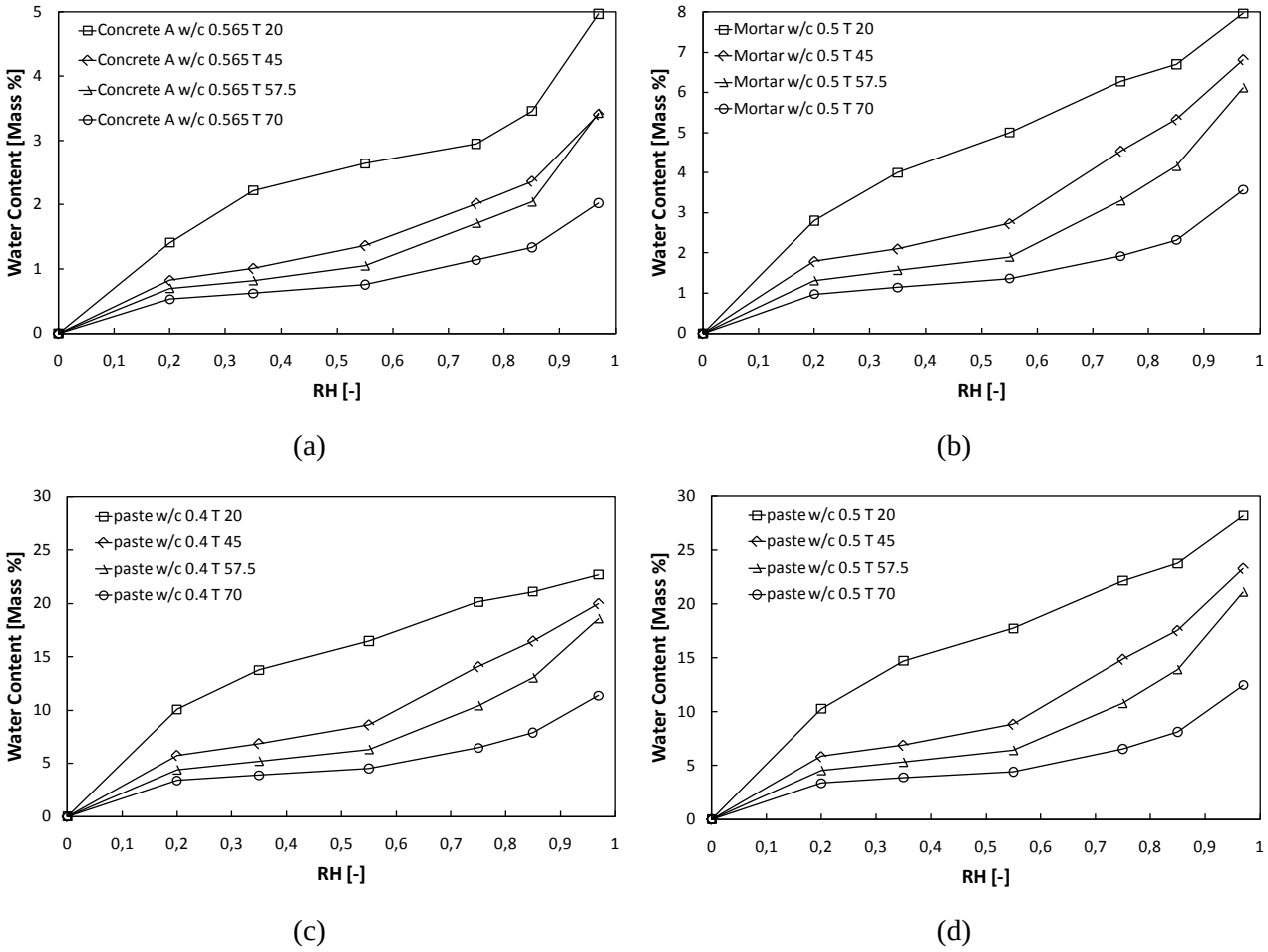

Figure 1: Sorption isotherms for concrete (a), mortar (b) and cement paste (c und d) at various temperatures (reproduced from data presented in [10]).

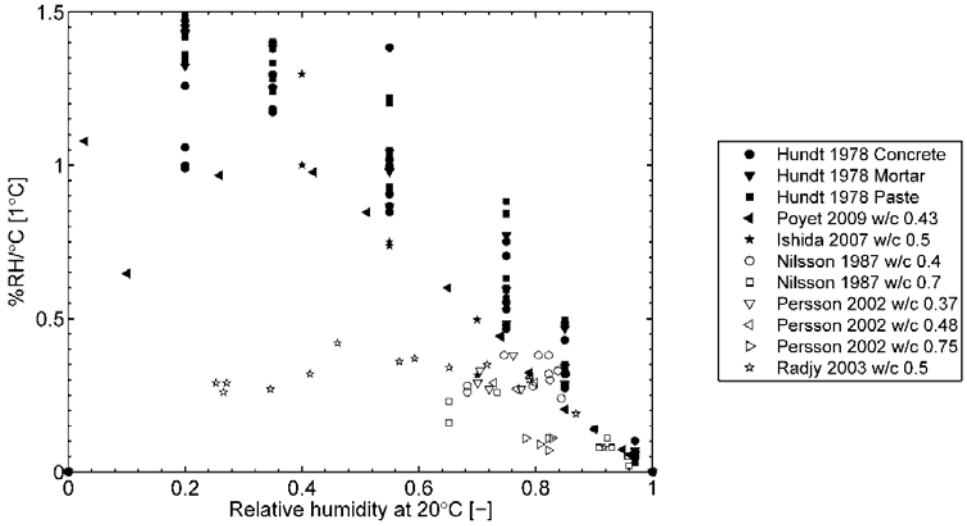

Figure 2: Change in relative humidity per degree of Celsius against relative humidity at reference temperature for various materials from [6-12] (reproduced from data presented in [9,11,12] and [6,7,10]).

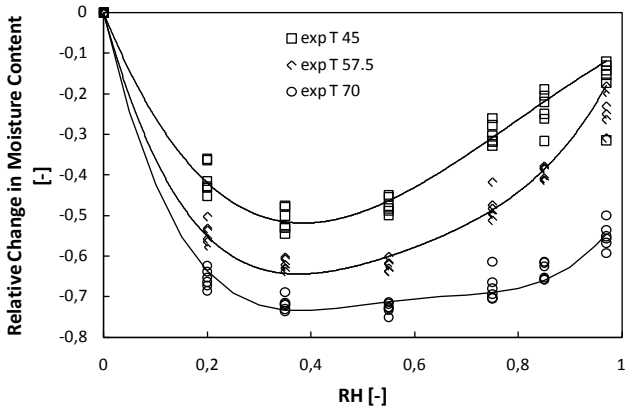

Figure 3: Relative change in moisture content for all materials presented in [10] (note: experimental data is illustrated by markers, solid lines are only for visual support; reference temperature 20°C).

2 Experimental studies

2.1 Materials and specimen preparation

Aalborg Rapid® Portland cement (Type 52.5N cement [17]) was used. The mix contained 375 kg/m^3 cement, 760 kg/m^3 fine aggregates (0 - 4 mm), 56 kg/m^3 aggregates (4 - 8 mm), 1025 kg/m^3 coarse aggregates (8 - 16 mm) (in accordance with [18]), and had a water-to-cement ratio (w/c) of 0.42. After casting the specimens were stored for 24 hours under a plastic sheet in laboratory conditions (i.e., 20 ±2 °C) and were then demolded. Upon demolding, the specimens were stored in saturated lime water for additional 2 days at 20 ±2 °C. At the age of 3 days, 2 holes (each with a diameter of 2 mm) were drilled in each specimen to insert a TDR probe and filled with cement paste (w/c 0.42). Subsequently, the specimens were again stored for 28 days in saturated lime water at 20 ±2 °C. Finally, all specimen surfaces were sealed, the top surface with epoxy resin and the remaining surfaces with multiple layers of aluminium tape to maintain the moisture content of the specimens throughout the experimental procedure. The final moisture content was measured after termination of the experimental investigations by means of the weigh-dry-weigh method (oven 100 °C) and corresponded to a relative humidity (RH) of 98 % (determined from conventional gravimetrical sorption measurements).

Figure 3 illustrates a finalized specimen as well as a sketch of a specimen with a TDR probe and the volume of material that is influenced by the TDR measurements, which is depended on the TDR probe geometry. In the present study a 2 wire probe was used, for which the volume of interaction can be assumed to be twice the distance between the wires of the probes [19], i.e. a cylinder with the length of the probe (120 mm) and a diameter of 40 mm. More detailed information on the interaction between the investigated material and the TDR probe geometry can be found in e.g. [19].

In addition to the concrete specimens, calcium silicate specimens with TDR probes were prepared. In contrast to the concrete specimens, the TDR probes were pushed in the calcium silicate specimens and stored for 28 days at 50 ±5 % RH. Finally, all surfaces were sealed in the same way as the concrete specimens.

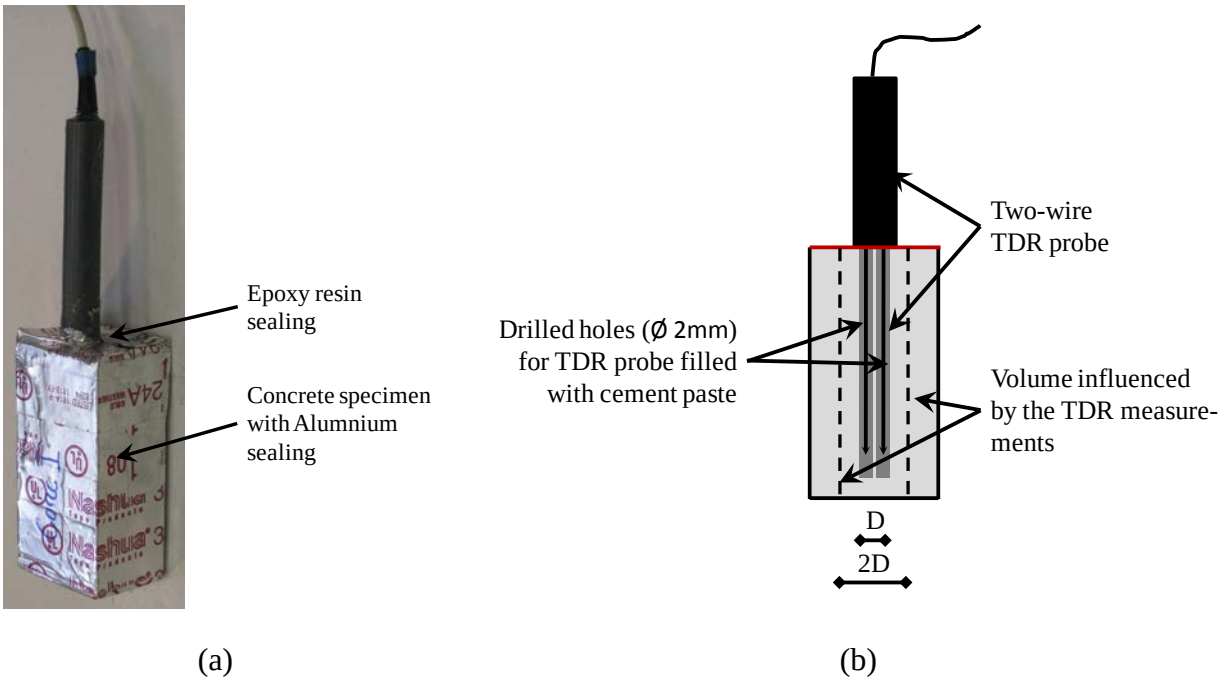

Figure 4: (a) Sealed specimen with TDR probe and (b) sketch of a specimen indicating two-wire TDR probe, drilled holes filled with cement paste as well as aluminium and epoxy resin surface sealing. The interacting volume is indicated by the broken line (Please note: Sketch is not in scale).

2.2 Testing procedure

The experimental set up used in the present study is illustrated in Figure 4 and consisted of the sealed specimens with TDR probes, TDR monitoring equipment and a temperature controlled unit (accuracy ±1 °C). Throughout the experimental studies the prepared and sealed specimens were in a temperature controlled chamber subjected to various ambient temperatures, in the range from 20 °C to 50 °C. The temperature in the chamber was changed by 1 °C every four hours to allow for the samples to equilibrate with the ambient temperature. One complete cycle of temperature change took 124 hours. During this time automatic TDR measurements of the concrete and calcium silicate samples were taken every 30 minutes. The cycle of measurement was repeated four times to investigate the stability of the readout from each sample and to confirm that the sample properties did not change during the heating and cooling cycles.

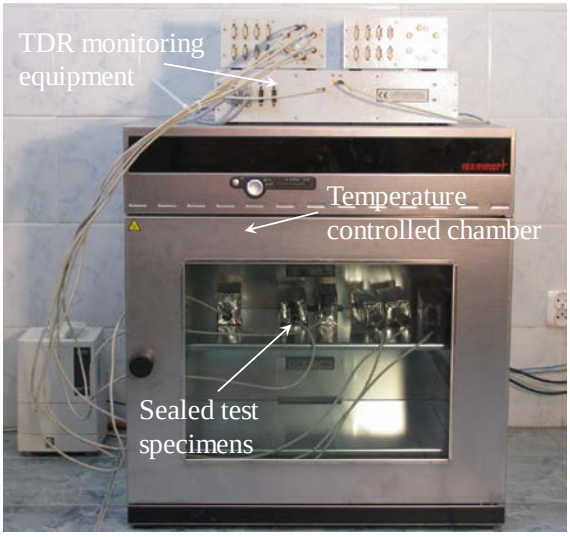

Figure 5: Experimental set up for TDR measurements illustrating the sealed specimens, TDR monitoring equipment and temperature controlled chamber.

3 Time domain reflectometry (TDR)

3.1 Physical basis

The dielectric permittivity of a material can be calculated from the travel time of an electric pulse in the material. And the travel time can be measured by the time domain reflectometry (TDR), i.e. measurement of a reflected pulse delay with respect to the incident pulse. The delay of the pulse depends linearly on the square root of dielectric permittivity, ε_r, of the investigated material [19]

$$\sqrt{\varepsilon_r} = \frac{ct}{2D} \qquad \text{Eq. (1)}$$

where c is the speed of light, t the travel time of the pulse measured by TDR and $2D$ the length of the pulse travel within the investigated material.

If the travel time of the pulse for a given distance is known, the dielectric permittivity of the investigated material can be calculated according to Eq. 1. TDR allows for measurements of the pulse travel time within the range of a few picoseconds accuracy by interpretation of the reflected pulses visible on the trace of the probes in the material. This corresponds to tenths of percent of volumetric water content.

A typical probe signal with characteristic features for the investigated concrete specimens is shown in Figure 5. At *(a)* (see Fig. 5) a distinct minimum in the amplitude can be seen representing a time marker to measure the delay time of the further reflected pulse. Afterwards a maximum *(b)* (see Fig. 5) in the amplitude can be observed, which represents the reflected pulse at the beginning of the investigated material and a second maximum *(c)* (see Fig. 5), which is the reflection from the end of the probe. The measurement time is equal to the delay of the second maximum with respect to the first maximum, which varies according to the dielectric permittivity of the investigated material.

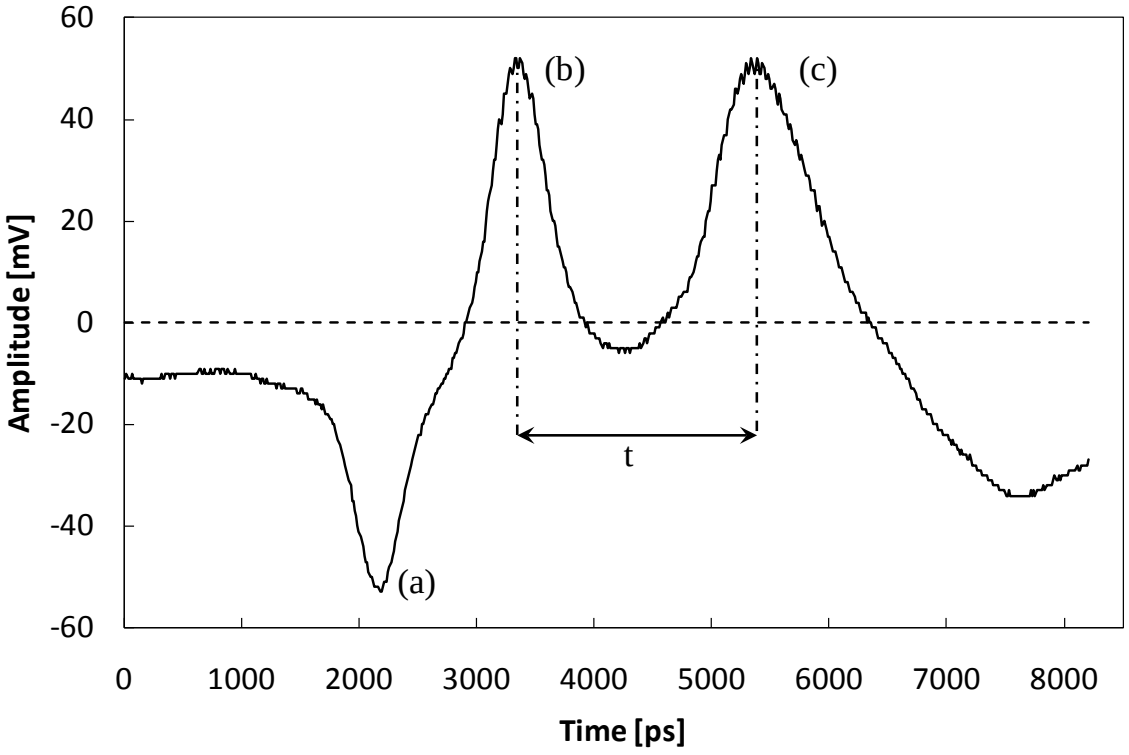

Figure 6: Typical TDR probe trace obtained from concrete specimen.

The reflection coefficient, R_{12}, for the pulse at the entrance of the investigated material can be given as follows

$$R_{12} = \frac{z_2 - z_1}{z_2 + z_1} \quad \text{Eq. (2)}$$

where z_1 is the impedance of the long line [19] where the pulse actually travels and z_2 the impedance of the line where the pulse enters. The value of the impedance $z_1$is constant for a given probe configuration while the value of the impedance z_2 depends on the properties of the investigated material and probe geometry. For a two wire TDR probe, as used in the present study (see Fig. 3 (b)), the impedance z_2 may be calculated as follows

$$z_2 = \frac{z_{02}}{\sqrt{\varepsilon_r}} \quad \text{Eq. (3)}$$

where z_{02} is the characteristic impedance of the probe surrounded by air. z_{02} depends only on the geometry of the probe and not on the dielectric permittivity of the investigated material. For a two wire probe the characteristic impedance can be determined as follows

$$z_{02} = 120\ ln\left(\frac{l}{r} + \sqrt{\left(\frac{l}{r}\right)^2 - 1}\right) \quad \text{Eq. (4)}$$

where l is half the distance between the probe rods and r the rod radius. For the present TDR probe geometry z_{02} = 307 Ω and z_1 = 50 Ω. As $z_2 > z_1$, the reflected pulse will have a positive amplitude, marked as (b) in Figure 5. Assuming an incident pulse with the amplitude $A0$, the amplitude of the first reflected pulse, $A1$, which can be observed at the receiver, can be determined as follows

$$A1 = A0R_{12} \quad \text{Eq. (5)}$$

Combining Eq. 2 and Eq. 3 yields Eq. 6 allowing for the determination of the reflected pulse $A1$ as a function of dielectric permittivity of the investigated material

$$A1 = A0\frac{z_{02} - z_1\sqrt{\varepsilon_r}}{z_{02} + z_1\sqrt{\varepsilon_r}} \quad \text{Eq. (6)}$$

3.2 Mixture theory and temperature dependence

A number of mixture models can be found in the literature to describe the dielectric permittivity of porous materials, an overview of various models proposed can be found e.g. in [19]. In general, all models can be represented in the following form

$$\epsilon_{app} = F(\epsilon_i, x_i) \quad \text{Eq. (7)}$$

where, ϵ_{app} is the apparent (effective) value of the dielectric permittivity of the mixture, ϵ_i is the dielectric permittivity of the *i-th* constituent and x_i is the volume fraction of the *i-th* constituent.

Assuming a temperature dependent behaviour of all volume fractions considered as well as the corresponding dielectric permittivity's Eq. (7) yields (assuming a closed system)

$$\epsilon_{app}(T) = F(\epsilon_i(T), x_i(T)) \quad \text{Eq. (8)}$$

The effective value of the dielectric permittivity might be approximated with a truncated Taylor series assuming small temperature variations

$$\epsilon_{app}(T) \cong F\big(\epsilon_i(T_0), x_i(T_0)\big) + \frac{dF\big(\epsilon_i(T_0), x_i(T_0)\big)}{dT}\Delta T \qquad \text{Eq. (9)}$$

Reformulation of the second term in Eq. (9) yields

$$\frac{dF\big(\epsilon_i(T_0), x_i(T_0)\big)}{dT} = \sum_i \frac{\partial F\big(\epsilon_i(T_0), x_i(T_0)\big)}{\partial \epsilon_i}\frac{d\epsilon_i}{dT} + \frac{\partial F\big(\epsilon_i(T_0), x_i(T_0)\big)}{\partial x_i}\frac{dx_i}{dT} \qquad \text{Eq. (10)}$$

with

$$\sum \frac{dx_i}{dT} = 0 \qquad \text{Eq. (11)}$$

For the given assumptions, i.e. small temperature variations within the volume fractions, any theoretical mixture formula can be considered in a simplified, linear form, which is form dependent on the applied theoretical mixture formula

$$\Delta F\big(\epsilon_i(T_0), x_i(T_0)\big) = \Delta T\left(\sum_i F_{\epsilon_i}\,\frac{d\epsilon_i}{dT} + F_{x_i}\frac{dx_i}{dT}\right) \qquad \text{Eq. (12)}$$

with

$$F_{\epsilon_i} = \frac{\partial F\big(\epsilon_i(T_0), x_i(T_0)\big)}{\partial \epsilon_i} \quad \text{and} \quad F_{x_i} = \frac{\partial F\big(\epsilon_i(T_0), x_i(T_0)\big)}{\partial x_i} \qquad \text{Eq. (13)}$$

where F_{ϵ_i} and F_{x_i} can be considered constant without a major loss of accuracy.

The factors $d\epsilon_i/dT$ and dx_i/dT are material properties that depend on the type of constituent in the mixture as well as their temperature properties, and thus can be fit to experimental data. In particular, the volume fractions of physically bound (adsorbed) and free (capillary condensed) water in the mixture were of interest in the present study.

3.3 Water content measurements with TDR in porous media

The apparent dielectric permittivity is a function of the dielectric properties of the mixture volume, i.e. solid, liquid and gaseous phases, the TDR probe is installed in. To determine the volumetric water content of a porous medium the relation between the measured apparent dielectric constant and the moisture content must be known. A number of such relations have been proposed and can be found in the literature, e.g. [20-23]. In general, the proposed mixing models can be divided into models based on the mixture theory, see e.g. [14,24,25] and empirical models [15,26,27].

For the present study a mixing rule proposed in [14] is used to investigate the moisture state in the specimens tested. The approach describes the apparent dielectric constant as a function of four phases, i.e. the solid phase, the gaseous phase, and the liquid phase, which is further divided into a free (capillary condensed) and physically bound (adsorbed) water phase.

$$\varepsilon_{app} = \left((\theta-\theta_{bw})\varepsilon_{fw}{}^{\eta} + \theta_{bw}\varepsilon_{bw}{}^{\eta} + (1-\varphi)\varepsilon_s{}^{\eta} + (\varphi-\theta)\varepsilon_a{}^{\eta}\right)^{1/\eta} \qquad \text{Eq. (14)}$$

with

$$\theta_{bw} = l_{naw} S_{eff} \delta_{H2O} \qquad \text{Eq. (15)}$$

In Eq. (14) ε_{app} is the apparent dielectric constant of the mixture, θ the total moisture content in g/cm^3, θ_{bw} the amount of physically bound water in g/cm^3, ε_{fw} the dielectric constant of free water, ε_{bw} the dielectric constant of physically bound water, ε_s the dielectric constant of the solid matrix, ε_a the dielectric constant of the gaseous phase, φ the porosity present in the mixture, l_{naw} the number of adsorbed monomolecular water layers, S_{eff} the specific surface area, and δ_{H2O} the statistical average thickness of one monomolecular water layer. The parameter η describes the orientation of the layered system. Values between 1 (electrical field is parallel to layering) and -1 (electrical field is perpendicular to layering) were identified in literature, see e.g. [28].

Due to the high binding forces (van der Waal's forces), between the inner surface and physically bound (adsorbed) water, the dielectric properties of the physically bound water vary significantly from the dielectric properties of free water (see Table 1). This phenomenon is used to determine the amount of free and physically bound water in the specimens under varying ambient temperatures while the total moisture content is kept constant. Furthermore, it was assumed that within the range of applied temperatures the dielectric properties of the gaseous and solid phase do not show a temperature dependent behaviour [29], and that the volume fractions of the constituents (i.e. solid and porous phase as well as the total amount of water present in the mixture) stay constant throughout the experiment, which was confirmed by weight measurements. Based on the assumptions presented in Section 3.2 and assuming that only ε_{fw} and θ_{bw} vary with temperature, Eq. (14) may be reformulated to describe variations of the apparent dielectric constant of the mixture with temperature:

$$\Delta\varepsilon_{app} = \frac{1}{\eta}\varepsilon_{app}^{1-\eta}\left(\eta(\theta-\theta_{bw})\varepsilon_{fw}{}^{\eta-1}\frac{d\varepsilon_{fw}}{dT} + \left(\varepsilon_{bw}{}^{\eta} - \varepsilon_{fw}{}^{\eta}\right)\frac{d\theta_{bw}}{dT}\right)\Delta T \qquad \text{Eq. (16)}$$

To describe the impact of temperature on the dielectric constant of free water Eq. (17) [30] was used, which can be written as follows (reference temperature of 25 °C).

$$\varepsilon_{fw} = 78.54(1 - 4.579\cdot 10^{-3}\Delta T + 1.19\cdot 10^{-5}\Delta T^2 - 2.8\cdot 10^{-5}\Delta T^3) \qquad \text{Eq. (17)}$$

4 Results

4.1 Change in dielectric permittivity of the mixture

Figure 6 illustrates the experimentally measured apparent dielectric constant of the concrete and calcium silicate specimens as a function of temperature. It can be clearly seen that the dielectric properties of the materials differ. The apparent dielectric constant of concrete is more than twice as high as the one for the investigated calcium silicate. Furthermore, the dielectric properties of the concrete specimen show a pronounced temperature dependence (see Fig. 6 (a)). Within the investigated temperature range, the apparent dielectric constant of the concrete specimens is around 8% higher for 50 °C compared to the dielectric constant at 20 °C. The results of the experimentally measured apparent dielectric constant of calcium silicate show no major dependence on the temperature (see Fig. 6 (b)).

Similar observations were made for different soil types subjected to varying temperatures, see e.g. [31,32]. The behaviour observed for the concrete specimens might be explained by a change in the amount of free and physically bound water fractions (see Eq. (14)) and the assumptions presented in Section 3.2. For further interpretations, only the results of the investigated concrete specimens were dealt with as the temperature dependent behaviour was not observed for the calcium silicate specimens.

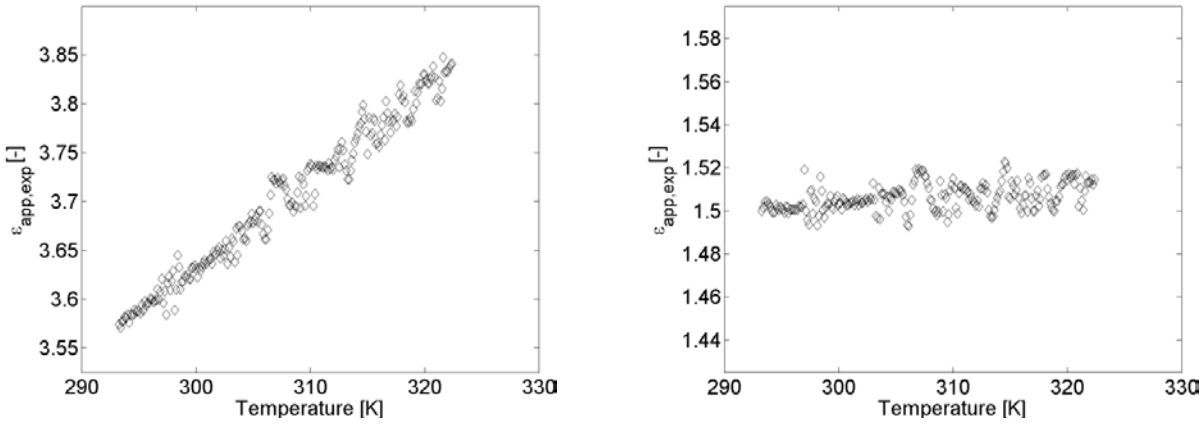

(a) (b)

Figure 7: Measured apparent dielectric constant as a function of temperature for concrete (a) and calcium silicate (b).

4.2 Determination of physically bound water fraction and impact of temperature

Equation (14) was used to determine the amount of free (capillary condensed) and physically bound (adsorbed) water in the concrete specimens as a function of the measured apparent dielectric constant. An overview of the parameters used in Eq. (14) is given in Table 1. The total moisture content was measured by means of the weigh-dry-weigh method (oven 100 °C) of capillary saturated samples. Values for the dielectric constant of the gaseous and solid phase were taken from literature, see e.g. [28,33]. The dielectric constant of physically bound water was determined from the experimentally measured apparent dielectric constant of the mixture at the reference temperature, i.e. 20 °C. The parameter η was determined to be 0.56, which is in good agreement with values reported in the literature for isotropic materials [14,24], while the porosity of the mixture was determined to be 0.106. Both parameters, i.e. η and the porosity, were also determined from the experimentally measured apparent dielectric constant of the mixture at the reference temperature.

The impact of temperature on the calculated amount of physically bound water present in the concrete specimens is given in Figure 7 (a). In addition, the experimentally measured and fitted apparent dielectric constants (Eq. (14)) of the mixture are presented in Figure 7 (b). It is evident from obtained results (see Figure 7 (a)) that the physically bound water fraction in the concrete specimens is decreasing with increasing temperature. Extrapolation of the obtained relation between temperature and amount of physically bound water yields zero at 100 °C, which is in agreement with experimental observations, i.e. all adsorbed water is released. Furthermore, similar water content fractions, i.e. capillary water and (physically) bound water, were measured by [34] for the reference temperature of 20 °C. In addition, the number of adsorbed monomolecular water layers, l_{naw}, as a function of the investigated temperature is given in Fig. 7 (c). For the determination of l_{naw} Eq. (15) was used with a specific inner surface of 35.48 m^2/g (determined from water vapour sorption experiments) and a statistical average thickness of one monomolecular water layer of 3.04 Å.

Table 1: Parameters for mixing theory model (Eq. (14)) to determine the amount of physically bound water.

Parameter	Symbol	Value	Unit
Total moisture content	Θ	0.045	[g/cm3]
Volume fraction of physically bound water at reference temperature	$\theta_{bw,20}$	0.044	[g/cm3]
Volume fraction of free water at reference temperature	$\theta_{fw,20}$	0.001	[g/cm3]
Dielectric constant of free water	ε_{fw}	Eq. 16	[-]
Dielectric constant of solid matrix	ε_s	3.75	[-]

Dielectric constant of the gaseous phase	ε_a	1	[-]
Dielectric constant of physically bound water	$\varepsilon_{bw,20}$	2.1	[-]
Porosity	φ	0.106	[-]
Semi-empirical	η	0.56	[-]

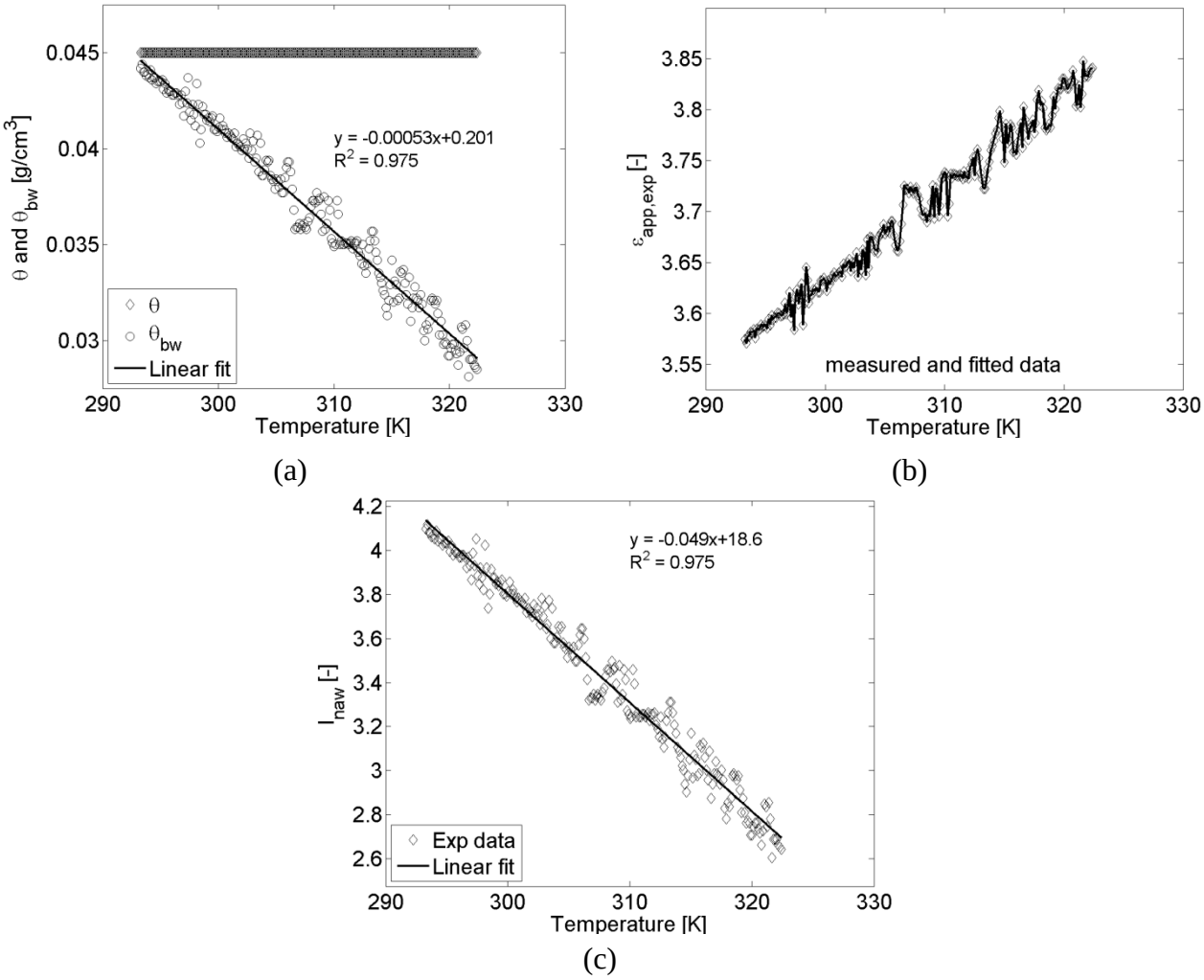

Figure 8: (a) Amount of physically bound and total water content in concrete specimens as a function of temperature determined with Eq. (14), (b) experimentally measured and fitted apparent dielectric constant and (c) number of adsorbed water layers as a function of temperature.

5 Discussion and interpretation of results

Experimental investigations of sealed concrete specimens with known moisture contents subjected to various temperatures revealed a temperature dependent behaviour of the specimens. Measurements of the apparent dielectric constant of the mixture by means of TDR indicated an increase in the dielectric constant, which is directly related to the moisture content (see Eq. (14)).

Similar observations were made by [29,31,32,35] for different soil types subjected to varying temperatures and known water contents. Depending on the amount of free (capillary condensed) and physically bound (adsorbed) water present in the specimens, either an increase or decrease in the apparent dielectric constant of the mixture was measured. For soils with a high content of free water a decrease in apparent dielectric constant was measured for the mixture with increasing temperature and vice versa for soils with a large amount of physically bound water. According to [29,31,32,35], the behaviour can be explained by the impact of two competing phenomena on the apparent dielectric constant of the mixture with increasing temperature. On the one hand, the

dielectric constant of free water is decreasing with increasing temperature as shown in e.g. [30,36,37] (see Eq. (16)). On the other hand, the temperature increase induces kinematic energy allowing for a change of physically bound water into free water resulting in an increase in the apparent dielectric constant of the mixture. Physically bound water is strongly fixed to the solid surfaces resulting in a significantly lower dielectric constant compared to free water, as the physically bound water is released the hindered movement of the physically bound water molecules is vanished resulting in the same dielectric properties of free water.

This effect (release of physically bound water due to an increased temperature) may be used to determine the impact of temperature on the moisture sorption of cement based materials assuming that:

1. The amount of physically bound water is significanly higher than the amount of free water for the complete relative humidity (RH) range.
2. The release of physically bound water is independent of the RH.
3. The average thickness of the adsorbed water layer is known in the relevant RH range (for a reference temperature).
4. The specific surface area of the investigated material is known.

Baroghel-Bouny investigated water vapour sorption isotherms of well cured samples with various concrete types and hydrated cement pastes with varying binder compositions [5]. Among others, Baroghel-Bouny investigated the average statistical thickness of the adsorbed water on the solid phase (which can be obtained from the adsorbed moisture volume and the specific surface area of the investigated material) and compared the results to the ‘‘t-curve’’ proposed by Hagymassy et al. [38] for non-porous adsorbents. The comparison revealed a very good agreement up to 63% RH for all investigated materials. Baroghel-Bouny concluded that for all investigated materials the increase in water content is statistically equivalent to an increase in adsorbed multilayer water molecules on the solid phase up to a RH of 63%. For RH above 63% the determined average statistical thickness of adsorbed water is deviating from the “t-curve”. Deviations were attributed to either capillary condensation (adsorbed moisture volume lies above the “t-curve”) or limited pore sizes hindering the build-up of additional adsorbed monomolecular water layers (adsorbed moisture volume lies below the “t-curve”). However, the deviation from the “t-curve” was small for all investigated materials, indicating that the amount of free water was low compared to the amount of physically bound water.

The “t-curve” determined by Hagymassy et al. is illustrated in Figure 8 along with the calculated average statistical thickness of the adsorbed water layer of selected materials presented in [10]. Similar to the results presented by Baroghel-Bouny in [5], a very good agreement with the “t-curve” proposed by Hagymassy et al. [38] can be seen for all materials up to approximately 75 % RH. The results indicate that for the materials described in [10], the increase in water content at increasing RH can be described by the theory of multilayer water adsorption on solid phases up to a RH of approximately 75 %. For RH above approximately 75 % the “t-curve” was overestimating the moisture content, which may be attributed to limited pore sizes as mentioned before. Nevertheless, to model the impact of temperature on the moisture sorption in the present study the “t-curve” proposed by Hagymassy et al. [38] was used for the complete moisture range, which is expected to result in an overestimation of the impact of temperature on water content for RH above approximately 75 %.

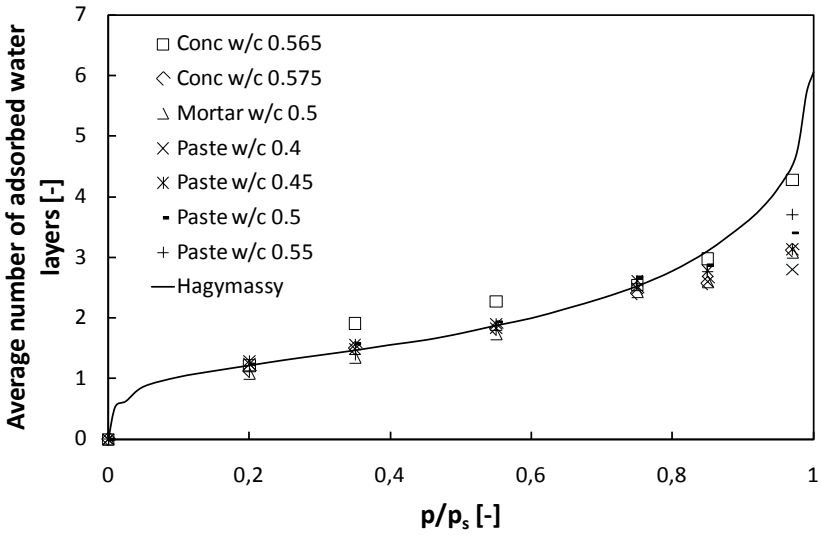

Figure 9: Comparison between the average statistic number of adsorbed water layers for various materials presented in [10] and the "t-curve" presented in [38].

The proposed scheme to model the influence of temperature on the physically bound (adsorbed) water of cement based materials is given in Figure 9. Initially, results of the TDR measurement are used along with the "t-curve" proposed by Hagymassy et al. [38] to describe the general impact of temperature on the number of adsorbed monomolecular water layers. Conventional gravimetrical sorption measurements at a reference temperature provide information on the specific surface area of the investigated material. Finally, the specific surface area (determined at a reference temperature) along with the results of the TDR measurements and the "t-curve" are used to model water vapour sorption isotherms of the investigated material at various temperatures. To determine the specific surface area of the different materials the excess surface work model proposed by [39] may be used.

The calculated specific surface areas for all materials are given in Table 2 using the water vapour sorption isotherms determined at 20 °C [10]. However, it should be mentioned that for the determination of the specific surface area a stable porous matrix was assumed, i.e. irreversible effects altering the specific surface area, see e.g. [5,40], are not taken into account. Results of the modelled and experimentally obtained water vapour sorption isotherms are presented in Figures 10, 11 and 12 for concrete, mortar and cement paste. As mentioned earlier, the impact of temperature on the capillary condensed water is not considered in the model and the possible capillary condensed water is treated as adsorbed water, which leads to a possible overestimation of the impact of temperature on the water content above approximately 75 % RH.

As expected, a good agreement between modelled and experimental results was found for RH up to approximately 75 % for all materials. For the concrete investigated in [10] (see Fig. 10), the comparison between modelled and experimental water vapour sorption isotherms revealed a very good agreement for the complete hygroscopic moisture range and all temperatures. Especially, for higher temperatures an almost perfect agreement between modelled and experimental results was found.

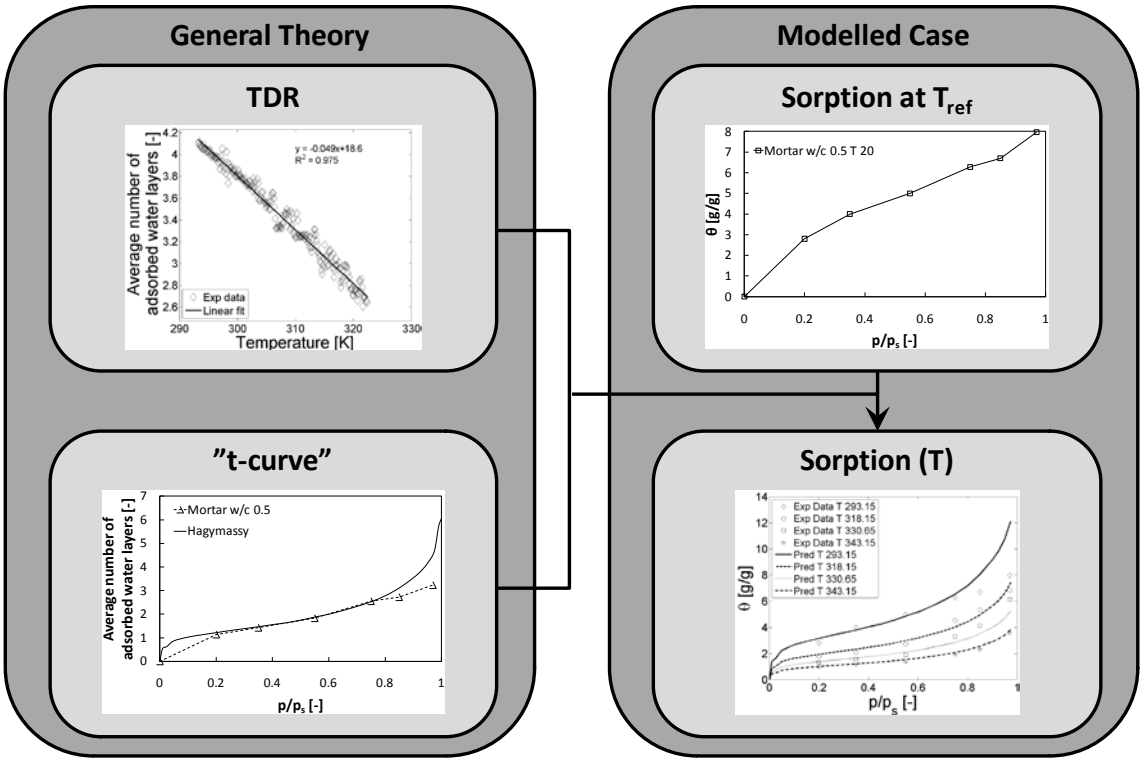

Figure 10: Proposed model scheme to predict the impact of temperature on the moisture sorption of cement based materials.

Figure 11 illustrates the experimental and modelled results for mortar. Up to approximately 75 % RH a very good agreement between the experimental and modelled results was found for the reference temperature (20 °C / 293.15 K). As mentioned earlier, the overestimation of the water content for RH above 75 % at the reference temperature is most likely attributed to limited pore sizes hindering the build-up of additional adsorbed monomolecular water layers (see Fig. 8). However, with increasing temperature, good correlations between the experimental and modelled results can be also seen for RH above 75 % indicating that the water uptake can be described by multilayer adsorption theory. Similar observations can be seen for the experimental and modelled water vapour sorption isotherms of cement paste presented in Figure 12 for different temperatures.

Table 2: Specific surface areas of various materials presented in [10] calculated by means of the excess surface work model presented in [39].

Material	w/c [-]	Specific surface area [m^2/g]
Concrete	0.565	38
	0.575	46
Mortar	0.5	84
Cement paste	0.4	267
	0.45	266
	0.5	272
	0.55	270

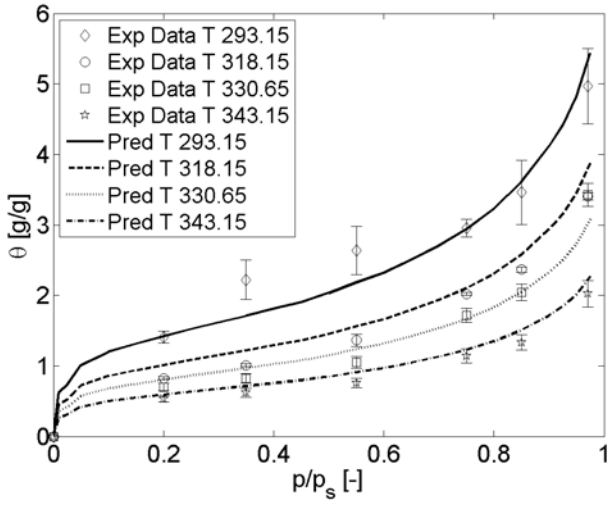

Figure 11: Comparison between modelled (lines) and experimental (markers) sorption isotherms at various temperatures for concrete with a w/c of 0.565 presented in [10].

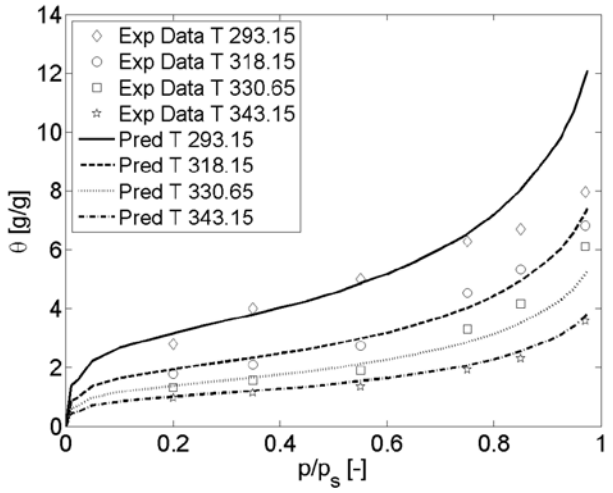

Figure 12: Comparison between modelled (lines) and experimental (markers) sorption isotherms at various temperatures for mortar with a w/c of 0.5 presented in [10].

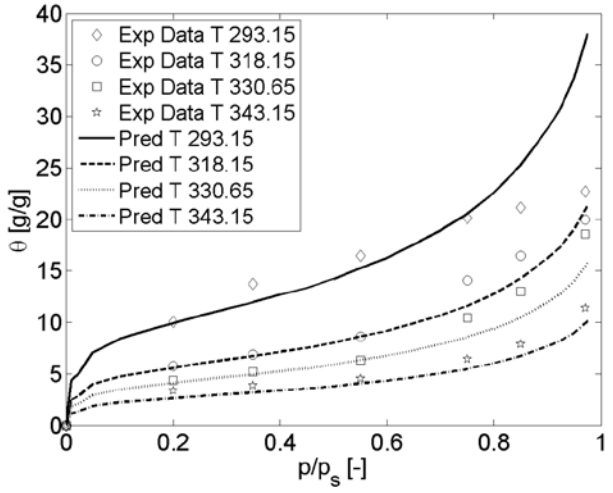

Figure 13: Comparison between modelled (lines) and experimental (markers) sorption isotherms at various temperatures for cement paste with a w/c of 0.4 presented in [10].

6 Conclusions

In the present study, sealed concrete and calcium silicate specimens with constant water contents were subjected to varying temperatures and monitored by means of time domain reflectometry (TDR). Results of the TDR measurements showed a temperature dependent behaviour for the investigated concrete samples, i.e. an increase in apparent dielectric constant of the mixture corresponding to an apparent increase in moisture content. Similar observations were earlier reported for certain soil types. The increase in apparent dielectric constant of the mixture is a result of two competing phenomena related to the temperature changes; a decrease in dielectric constant of free (capillary condensed) water and induced kinematic energy as the temperature increases resulting in a release of physically bound (adsorbed) water. Results illustrated in the present study indicate that the TDR measurements can be used to determine the impact of temperature on the water vapour sorption isotherm of a given cement based material. To determine the impact of temperature, results of TDR measurements in combination with the average number of adsorbed water layers can be used. The specific surface area can be determined from conventional sorption measurements and the average number of adsorbed water layers can be determined from the so called “t-curve” at a reference temperature.

Comparisons between modelled and experimental water vapour sorption isotherms from the literature showed a very good agreement for all investigated cement based materials up to approximately 75 % RH at 20 °C, which is the RH range in which the water uptake is described by multilayer adsorption theory. Deviations for higher RH are most likely attributed to limited pore sizes hindering the build-up of additional adsorbed monomolecular water layers. Further studies are required to investigate the observed phenomena, i.e. a release of physically bound water at increased temperature, for different water contents to reinforce the hypothesis that TDR measurements can be used to describe the impact of temperature on the sorption behaviour of cement based materials.

Acknowledgements

The first author gratefully acknowledges the financial support of Femern Bælt A/S, Sund & Bælt Holding A/S and The Danish Agency for Science, Technology and Innovation as well as COIN (COncrete INnovation centre, www.coinweb.no) and its partners for facilitating the research behind this paper.

References

1. *fib* Bulletin 34, Model code for service life design, Int. Fed. structural concrete (fib), 2006.
2. *fib* Bulletin 55, Model code 2010, Int. Fed. structural concrete (fib), 2010.
3. M.A. Ehlen, M. D. A. Thomas, E. C. Bentz, Life-365 Service Life Prediction Model Version 2.0 - Widely used software helps assess uncertainties in concrete service life and life-cycle costs, Conc. Int. 31 (2009) 41-46.
4. Life-365 Consortium II, Life-365 Service life prediction model and computer program for predicting the service life and life-cycle cost of reinforced concrete exposed to chlorides, 2010.
5. V. Baroghel-Bouny, Water vapour sorption experiments on hardened cementitious materials Part I: Essential tool for analysis of hygral behaviour and its relation to pore structure, Cem. Concr. Res. 37 (2007) 414-437.
6. S. Poyet, Experimental investigation of the effect of temperature on the first desorption isotherm of concrete, Cem. Concr. Res. 39 (2009) 1052-1059.
7. T. Ishida, K. Maekawa, T. Kishi, Enhanced modeling of moisture equilibrium and transport in cementitious materials under arbitrary temperature and relative humidity history, Cem. Concr. Res. 37 (2007) 565-578.

8. S. E. Pihlajavaara, On the main feature and methods of investigation of drying and related phenomena in concrete, PhD Thesis, University of Helsinki, (1965).
9. F. Radjy, E.J. Sellevold, K.K. Hansen, Isosteric vapor pressure - temperature data for water sorption in hardened cement paste: enthalpy, entropy and sorption isotherms at different temperatures, Report BYG-DTU R057, Technical University of Denmark (DTU), Lyngby, Denmark, (2003).
10. J. Hundt, H. Kantelberg, Sorptionsuntersuchungen an Zementstein, Zementmörtel und Beton, Deutscher Ausschuss für Stahlbeton 297 (1978) 25-39.
11. L-O. Nilsson, Temperature Effects in Relative Humidity Measurements on Concrete – Some Preliminary Studies, The Moisture Group, Report 1987:1. BFR, 84, (1987).
12. B. Persson, Self-desiccation and chloride migration, Report TVBM-3104, Lund University, Division of Building Materials, Sweden, (2002) 175-194.
13. L. R. Moffitt, Time domain reflectometry - theory and applications, Eng. Design News, (1964) 38-44.
14. M. C. Dobson, F. T. Ulaby, M. T. Hallikainen, M. A. El-Rayes, Microwave dielectric behaviour of wet soil, II. Dielectric mixing models, IEEE Transactions on Geoscience and Remote Sensing GE-23(1) (1985) 35-46.
15. G.C. Topp, J. L. Davis, A. P. Annan, Electromagnetic determination of soil water content: measurements in coaxial transmission lines, Water Resourc. Res. 16 (1980) 574-582.
16. M. C. Phillipson, P.H. Baker, M. Davies, Z. Ye, G. H. Galbraith, R. C. McLean, Suitability of time domain reflectometry for monitoring moisture in building materials, Building Services Engineering Research & Technology 29(3) (2008) 261-272.
17. DS/EN 197-1, Cement - part 1: composition, specification and conformity criteria for common cements, Tech. rep, Danish Standards Association, (2001).
18. DS-2426, Concrete - materials - rules for application EN 206-1 in Denmark, Tech. rep, Danish Standards Association, (2004).
19. H. Sobczuk, R. Plagge, Time domain reflectometry method in environmental measurements, Polskiej Akademii Nauk, Vol. 39, Lublin, Poland, (2007).
20. W. R. Tinga, W. A. G. Voss, D. F. Blossey, Generalized approach to multiphase dielectric mixture theory, J. Hydrology 236 (1973) 252-258.
21. K. Roth, H. Schulin, H. Flüher, W. Attinger, Calibration of Time Domain Reflectometry for water content measurements using a composite dielectric approach, Water Resourc. Res.. 26(10) (1990) 2267-2273.
22. W.R. Walley, Considerations on the use of Time Domain Reflectometry (TDR) for measuring soil-water content, J. Soil Sci. 44(1) (1993) 1-9.
23. J.L. Davis, W. J. Chudobiak, In-situ meter for measuring relative permittivity of soils, Geological Survey of Canada, Paper 75-1A (1975) 75-79.
24. J.R. Birchak, C. G. Gardner, J. E. Hipp, J. M. Victor, High dielectric constant microwave probes for sensing soil moisture, Proceedings of the IEEE 62(1) (1974) 93-98.
25. G.P. de Loor, Dielectric properties of heterogeneous mixtures containing water, J. Microwave Power 3(2) (1968) 67-73.
26. C.H. Roth, M. A. Malicki, R. Plagge, Empirical evaluation of the relationship between soil dielectric constant and volumetric water content as the basis for calibrating soil moisture measurements by TDR, J. Soil Science 43(1) (1992) 1-13.
27. M.A. Malicki, W. M. Skierucha, A manually controlled TDR soil moisture meter operating with 300 ps rise-time needle pulse, Irrigation Science 10(2) (1989) 153-163.

28. W.F. Brown, Dielectrics, In: Encyclopedia of Physics, Vol. 17, Berlin, Springer, (1956).
29. T. Schanz, W. Baille, L. N. Tuan, Effects of Temperature on Measurements of Soil Water Content with Time Domain Reflectometry, Geotechn. Test. J. 34(1) (2010) 1-8
30. R. Weast, M.J. Astle, W.H. Beyer, CRC Handbook of Chemistry and Physics, CRC Press, Inc., Boca Raton, FL, (1986).
31. L.W. Petersen, O. Jacobsen, F. Plauborg, M. Andersen, D. Rolston, The Effects of Temperature on the Determination of Soil Water Content by Time-Domain Reflectometry, Soil Science Society of America Annual Meeting, St. Louis, MO, October 29-Novemeber 3, (1995).
32. J.M. Wraith, D. Or, Temperature Effects on Soil Bulk Dielectric Permittivity Measured by Time Domain Reflectometry: Experimental Evidence and Hypothesis Development, Water Resour. Res. 35(2) (1999) 361-369.
33. F.W. Sears, M.W. Zemansky, H.D. Young, University Physics, 6th Ed., Addison-Wesley, (1982).
34. A. C. A. Muller, K. L. Scrivener, A. M. Gajewicz, P. J. McDonald, Use of bench-top NMR to measure the density, composition and desorption isotherm of C-S-H in cement paste, Micropor. Mesopor. Mater. (2013), http://dx.doi.org/10.1016/j.micromeso.2013.01.032.
35. W. Skierucha, Temperature Dependence of Time Domain Reflectometry - Measured Soil Dielectric Permittivity, J. Plant Nutrition and Soil Sci. 172(2) (2009) 186-193.
36. S. Pepin, N. J. Livingston, W. R. Hook, Temperature-Dependent Measurement Errors in Time Domain Reflectometry Determinations of Soil Water, Soil Sci. Soc. Am. J. 59(1) (1995) 38-43.
37. M. Persson, Soil Solution Electrical Conductivity Measurements Under Transient Conditions Using Time Domain Reflectometry, Soil Sci. Soc. Am. J. 61(4) (1997) 997-1003.
38. J. J. R. Hagymassy, S. Brunauer, R. S. H. Mikhail, Pore structure analysis by water vapour adsorption - t-curves for water vapour, J. Colloid Interface Sci. 29(3) (1969) 485-491.
39. J. Adolphs, M. J. Setzer, A Model to Describe Adsorption Isotherms, J. Colloid and Interface Sci. 180 (1996) 70-76.
40. R. F. Feldman, Sorption and length-change scanning isotherms of methanol and water on hydrated portland cement, in: Proceedings of 5th International Congress on the Chemistry of Cement, Cem. Assoc. of Japan, Tokyo, Volume 3 (1968) 53-66.

Paper II

” Modelling Moisture Ingress through Simplified Concrete Crack Geometries”

B.J. Pease, A. Michel, M.R. Geiker & H. Stang

Published in: *Proceedings of ICDC (International Congress on Durability of Concrete), June 17-21, 2012, Trondheim, Norway.*

2012 ICDC
INTERNATIONAL CONGRESS on DURABILITY of CONCRETE

MODELLING MOISTURE INGRESS THROUGH SIMPLIFIED CONCRETE CRACK GEOMETRIES

Brad J. Pease[1], Alexander Michel[1], Mette Geiker[1,2] and Henrik Stang[1]

[1]Technical University of Denmark, Department of Civil Engineering, Kgs. Lyngby, Denmark
[2]Norwegian University of Science and Technology, Department of Structural Engineering, Trondheim, Norway

ABSTRACT

This paper introduces a numerical model for ingress in cracked steel fibre reinforced concrete. Details of a simplified crack are preset in the model's geometry using the cracked hinge model (CHM). The total crack length estimated using the CHM was, based on earlier work on conventional concrete, considered to have two parts; 1) a coalesced crack length which behaves as a free-surface for moisture ingress, and 2) an isolated microcracking length which resists ingress similarly to the bulk material. Transport model results are compared to experimental results from steel fibre reinforced concrete wedge splitting specimens conditioned to 50% relative humidity, cracked to varying crack geometries, and exposed to liquid water. Water sorption was monitored by recording x-ray attenuation images over time. Comparisons of results indicate the simplified crack geometry can accurately assess the impact cracks have on moisture ingress. Results from the transport model indicate the length of the isolated microcracks was approximately 19 mm for the investigated concrete composition.

Key-words: X-ray attenuation; numerical model; cracks; moisture ingress

INTRODUCTION

Several service life models (e.g., *fib* [1,2] and Life-365 [3,4]) have been developed to provide tools to estimate the length of time during which a reinforced concrete structure maintains a desired level of functionality. Fig. 1 illustrates the typical approach utilized by these models, initially developed by Tuutti in [5]. Two phases comprise the service life of a structure (Fig. 1); 1) the initiation phase when aggressive substances penetrate into the concrete cover, eventually causing, e.g. initiation of reinforcement corrosion (illustrated by a lower rate of deterioration in Fig. 1), and 2) the propagation phase when continued reinforcement corrosion-induced damage causes the increased rate of deterioration. Certain service life models consider the propagation phase (e.g., Life-365), although only as a fixed length of time [4]. More typically the end of the initiation phase, here corrosion initiation, marks the end of the service life and the propagation phase is ignored as indicated by the blue dot in Fig. 1. Fig. 1 also presents a modified service life modelling approach, similar to the approach suggested by Tuutti [5], which considers the impact of concrete cracking, caused by hygral/thermal shrinkage, self-weight and construction loads,

etc., on the service life of concrete structures. Hence, this modified approach takes into account more realistic initial conditions of concrete structures, as indicated by the imperfect structural condition at the beginning of the structure's lifetime (broken red line in Fig. 1). Concrete cracks facilitate rapid local ingress of aggressive substance regardless of the controlling ingress mechanism(s) [6-11], and cause potentially drastic reductions in the time to corrosion initiation [12-14]. Active corrosion has commenced after only weeks under experimental conditions [12-14] and within one year under field conditions [15]. Therefore, the propagation phase must be included in service life models, as indicated by the red block in Fig. 1, to represent realistic scenarios for reinforced concrete structures. Extensive experimental and modelling work has been conducted concerning deterioration during corrosion propagation, including reduced capacity due to reinforcement cross-section reduction [16] and corrosion-induced damage to covering concrete [17-20]. Nevertheless, several key issues remain that must be included in service life modelling, including but not limited to quantifying and modelling the impact cracks have on ingress and corrosion as well as accurate models for corrosion-induced damage during the propagation phase of corrosion to determine acceptable limits of deterioration causing ('safe') structural damage.

This paper presents a combined experimental and modelling investigation on one key issue discussed above, the impact of cracks on ingress behaviour. Concrete cracks typically have complex morphologies including a crack mouth opening, possible crack branching, tortuosity, isolated microcracking, etc., which may impact ingress rates in cracked concrete [6-11]. Detailed fracture mechanics models are capable of modelling such details of cracks [21], however, computation times can be extensive and are likely unrealistic currently for actual reinforced concrete structures. Previous work presented in [11,22] hypothesized ingress in a crack in ordinary concrete could be accurately estimated by assuming a simple crack morphology where the total crack length consists of a region of isolated microcracks near the crack tip, which has a constant length and minimal impact on moisture ingress, and a coalesced crack that behaves as a free surface. Results presented here indicate this simplified crack morphology can be used to accurately model moisture ingress in cracked steel fibre reinforced concrete, and may be useful in the development of service life models that account for initial cracking of concrete.

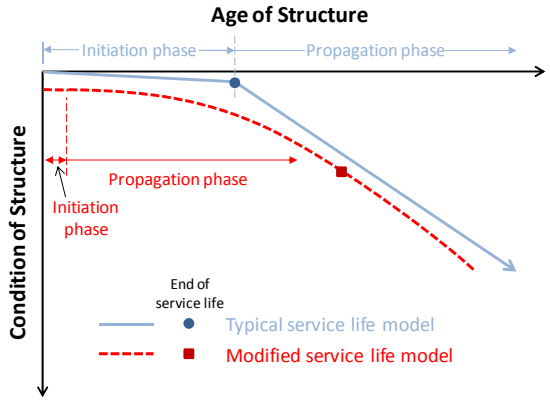

Figure 1 – Schematic of the typical Tuutti service life modelling approach, after [5], shown by the solid blue line, and a modified approach considering concrete cracks, shown by the broken red line. The end of service life depends on the defined limit state.

EXPERIMENTAL APPROACH

Mixture Proportions and Specimen Preparation

Aalborg white portland cement was used with an estimated Bogue composition of 78.8% C_3S,

10.5% C_2S, 4.9% C_3A, 1.0% C_4AF, 0.6% MgO, 2.1% SO_3, and an Na_2O equivalent alkali content of 0.19%. The aggregate was washed Class E 0-4 mm sea-sand and Class A 4–8 mm sea-gravel (in accordance with [23]). A water-to-cement ratio of 0.50 was used with a cement content of 330 kg/m^3, 764 kg/m^3 fine aggregate, 1,099 kg/m^3 coarse aggregate (71.5% aggregate by volume), and 19 kg/m^3 steel fibres (0.25% fibre by volume). The steel fibres had a length of 12.5 mm, diameter of 0.4 mm, elastic modulus of 200 GPa, and tensile strength of 1300 MPa. The concrete was mixed using a standard pan mixer with a 120 l capacity. The fine and coarse aggregate were first mixed dry for 1 min, followed by 3 min mixing with one third of the mixing water. Mixing was stopped for 2 min prior to adding and mixing the cement for 1 min. The remaining water was then added and mixing continued for 3 min after addition of water, during which time the steel fibres were added. The mixer was then opened and the pan and blades were scraped, followed by 1 additional minute of mixing.

Concrete was placed, and compacted by combined rodding and vibration in specialty wedge split test (WST) specimen moulds consisting of a 100 x 100 x 100 mm^3 prism with a 30 x 32 x 100 mm^3 recessed centre on the specimen's top (see Fig. 2(a)). After casting, specimens were stored in laboratory conditions (i.e., 18° ±2°C) covered with wet burlap and plastic sheets for 24 hours. The specimens were cured sealed in multiple layers of plastic at 20° ±2°C for 6 days before placing the still sealed samples in an oven at 45° ±2°C until samples reached a maturity age of 1 year. After accelerated curing specimen were unsealed, a 28 mm notch was cut resulting in a height, h (see Fig. 2(a)) of 50 mm and halved yielding two 50 mm thick specimen. All cuts were made using a water-cooled concrete saw. After cutting, specimens were conditioned at 50% ±3% relative humidity for no less than 1 year.

Splitting load was applied to the WST specimens via a rigid wedge with crack mouth opening displacement (CMOD) control. Three samples were cracked to a CMOD of 1.8 mm for estimation of materials properties using the technique described in the following section, while other samples were loaded or cracked to 70% and 90% of peak load, peak load, and 0.10 mm CMOD. After loading/cracking of the SFRC WST specimens aluminium tape was used to seal all specimen sides except the top surface, which simultaneously provided simple boundary conditions and a pond for exposure to water via the cast-in recess and cut notch. Additional details on the mixture design, curing and conditioning regimes, specimen preparation, and wedge split test method are available in the literature [22].

Inverse Analysis with the Cracked Hinge Model

Fig. 2 shows an implementation of the cracked hinge model (CHM), developed in [24,25], to the WST geometry. The CHM simulates the area directly surrounding the propagation crack using the loading and deformation shown in Fig. 2(b) and the stress distribution in Fig. 2(c). The rigid boundaries of the cracked hinge provide a joint to the bulk (uncracked) specimen, which is controlled by Hooke's law. An inverse analysis approach, developed in [26] and extended in [21], allows for estimation of the concrete's tensile strength, f_t, elastic modulus, E, and cohesive crack relationship, $g(w)$ by comparison and minimization of differences between experimental results and outputs of the CHM. Stresses transferred across the cracked hinge are controlled by Eq. 1:

$$\sigma = \begin{cases} \sigma(\varepsilon) = E \cdot \varepsilon & \text{Pre-cracked state} \\ \sigma_w(w) = g(w) \cdot f_t & \text{Cracked state} \end{cases} \quad \text{Eq. 1}$$

where a tri-linear cohesive crack relationship, $g(w)$ controls the stress transferred across a crack with width, w as:

$g(w) = b_i - a_i \cdot w$ where $w_{i-1} < w < w_i$ and $i = 1 \rightarrow 3$ Eq. 2

where $a_{1\text{-}3}$ are slopes and $b_{1\text{-}3}$ are intercepts describing the cohesive relationship of the steel fibre reinforced concrete (SFRC). Once cracking occurs, the estimated crack width profile, *w(y)* can be computed using Eq. 3:

$$w(y) = \frac{2\varphi(y-y_0)-\zeta_i}{1-\beta_i} \quad \text{Eq. 3}$$

where φ describes the rotation of the cracked hinge, y and y_0 the incremental and initial, respectively, location on the cracked hinge (see Fig. 2(b)), and β_i and ζ_i are dimensionless factors defined as:

$$\beta_i = \frac{f_t \cdot a_i \cdot s}{E} \text{ and } \zeta_i = \frac{f_t \cdot b_i \cdot s}{E} \quad \text{Eq. 4}$$

where s is the width of the cracked hinge, which is equal to $0.5 \cdot h$. Additional details on the CHM and the inverse analysis approach are available in the literature [21,22,25,26].

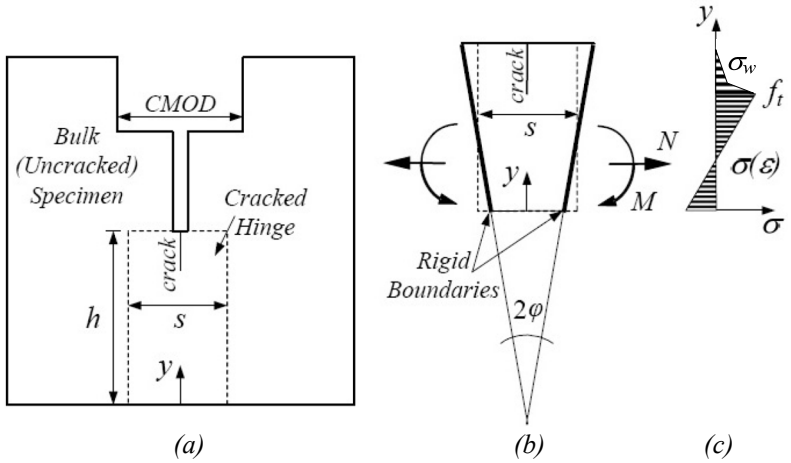

Figure 2 – (a) The wedge split test specimen with the cracked hinge model applied (after [26]), (b) loading and deformation of the hinge (after [25]), and (c) the assumed stress distribution (after [25]).

X-ray Attenuation Measurement Technique

A GNI x-ray attenuation measurement system located at the Technical University of Denmark [27] was used to monitor water sorption in the SFRC WST specimens, shown in Figure 3(a). A polychromatic x-ray source and a 25 mm x 25 mm x-ray camera are housed in a programmable, moveable frame. X-ray source energy settings of 110 keV and 15 μA were used for all measurements. Commonly, the composite system shown in Fig. 3(b) is used to derive Eq. 5 [22,27,28], which relates the reduction in x-ray photons passing through an initially conditioned specimen, I_{dry} caused by ingress of liquid water, I_{wet} to the change in moisture content, Δw.

$$\Delta w = -\frac{\rho_w}{\mu_{eff,w} \cdot t} ln\left(\frac{I_{wet}}{I_{dry}}\right) \quad \text{Eq. 5}$$

where ρ_w is the density of water, $\mu_{eff,w}$ is the effective attenuation coefficient of water (i.e., the attenuation coefficient of water as measured through the 50 mm SFRC WST specimens), and t is the specimen thickness. A recent study has indicated that the material type and thickness of the specimen affects the attenuation coefficient of water, necessitating the use of $\mu_{eff,w}$ as opposed to the linear attenuation coefficient or the attenuation coefficient measured through water alone [29]. The 25 mm x 25 mm x-ray camera captured images a total of 15 locations, providing data from an 80 mm x 55 mm region from the WST specimens. The measured region was centred

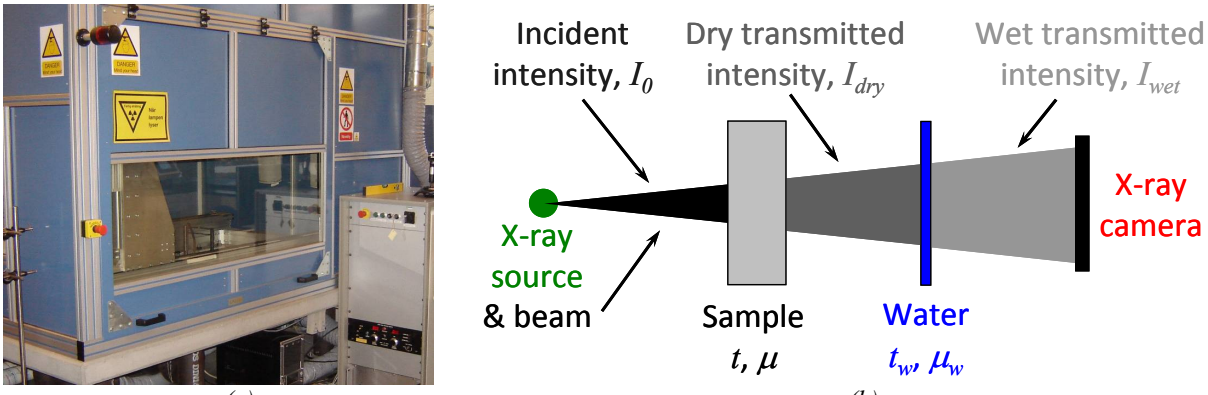

(a) (b)

Figure 3 – (a) X-ray attenuation equipment and (b) schematic of moisture ingress measurement described as a composite system of a conditioned sample and a thickness of water.

horizontally with the notch and vertically the measurement area began approximately 5 mm above the specimen bottom. At each measurement location a total integration time of 60 seconds (60 images with 1 second exposure time) were captured and summed. Fig. 4(b) shows typical images from the 15 measurement locations. Steel fibres are clearly present and the black areas on the parameter of the measurement area and at the notch caused by a 6 mm thick steel shield. Additional details on the x-ray attenuation equipment used and the measurement technique are available in the literature [11,20,22,27-29].

Fig. 4(a) describes an issue with the x-ray attenuation measurement technique, namely that slight variability in the number of x-ray photons detected by the x-ray camera over time occurs. For example, the highlighted regions in images 0 and 1 are the same location on the WST; however, the average number of x-ray photons detected within the regions varies from 35,847.5 counts in image 0 to 35,311.0 counts in image 1. These overlapping regions were utilized to provide a local normalization factor, f_i described by Eq. 6:

$$f_i = \frac{\mu_{A,i-1}}{\mu_{B,i}} \text{ for } i = 1 < n \qquad \text{Eq. 6}$$

where, $\mu_{A,i-1}$ and $\mu_{B,i}$ are the mean x-ray photon count from the overlapping regions of images *i-1* and *i* and *n* is the number of locations. The normalization factor, f_i was then applied to all pixels of image *i*, as shown in Fig. 4(a) and the subsequent image, *i+1* is normalized by the same approach. Fig. 4(b) shows the locations of overlapping regions used for the local normalizations. A batch code for the software package 'ImageJ', described in [11], was modified to assess the direction of the x-ray source/camera movement, assign the appropriate coordinates of overlapping regions depending on movement direction, measure $\mu_{A,i-1}$ and $\mu_{B,i}$ values, perform

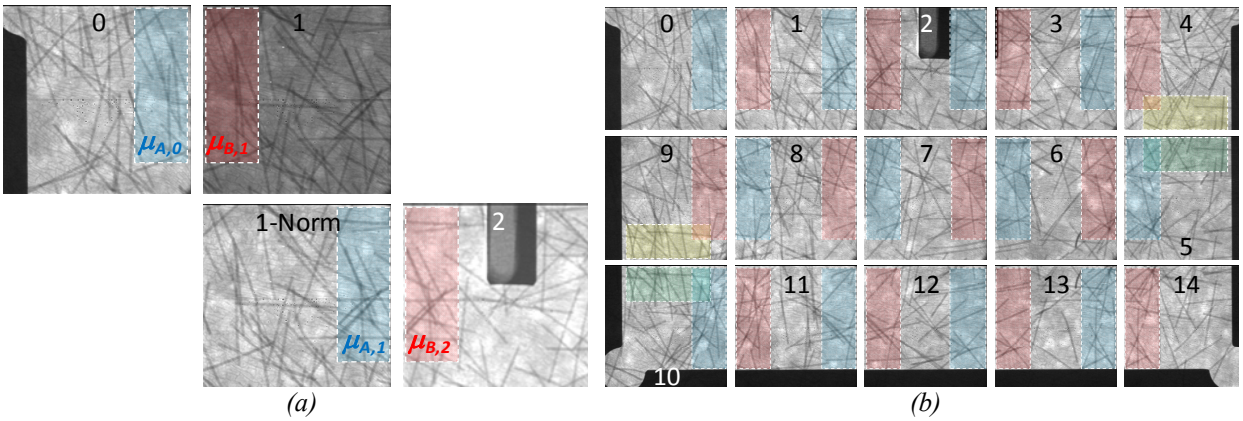

(a) (b)

Figure 4 – (a) Description of the local normalization using overlapping regions of individual images (note that contrasts have been changed to emphasize measurement variability) and (b) an example of 15 summed images making up a single measurement, with overlapping regions used for local normalization indicated.

the normalization of summed images, and translate individual images to stitch together an image of the entire measurement area with the propagated local normalization. Three initial measurements (I_{dry}) were averaged from the dry specimens, with 'I_{wet}' measurements taken 3, 30 minutes, 1, 1.5, 2, 3, 4, 6 and 7 hours after exposure to liquid water. Global normalization (i.e., normalization of stitch images taken at different times), also required due to measurement variability, was realized by measuring the mean x-ray photon count from identical regions from all images where the concrete remained in the initial condition after 7 hours.

TRANSPORT MODELLING APPROACH

The following moisture transport model was applied to the WST geometry, assuming an initial condition within the SFRC of 50% relative humidity. Sealed conditions were used for all surfaces except for the recess, notch, and crack and the top surface of the specimen. The recess, notch, and crack were exposed to liquid water at atmospheric pressure. The top of the WST specimen was left unsealed during x-ray measurements; therefore, a boundary condition of 65% relative humidity (based on measured relative humidity in the x-ray chamber during testing) was used. The crack geometry was determined by the CHM (Eq. 4) with the assumption that a constant length from the crack tip of the estimated crack consisted of isolated microcracking. Moisture ingress in this region is assumed to be identical to the bulk concrete. The remaining crack length is assumed to be a coalesced crack, which behaved as a free surface for moisture ingress.

Eq. 7 describes the coupled vapour and liquid water flow, which together yield the total moisture flow in the steel fibre reinforced concrete.

$$\frac{\partial m_{l+v}}{\partial t} = -C\frac{\partial p_c}{\partial t} = -\nabla\left(\frac{\mathrm{D_v(\Theta_l)}}{\mathrm{R_v T}}\nabla \mathrm{p_v} + \mathrm{K_l(\Theta_l)}\nabla \mathrm{p_c} + \rho_\mathrm{w} g\right) \quad \text{Eq. 7}$$

where, m_{l+v} is the sum of the water vapour and liquid water content, C is the moisture capacity, p_c is capillary pressure, D_v is the vapour diffusion coefficient, θ_l is moisture content, R_v is the gas constant of water vapour, T is temperature, p_v is vapour pressure, K_l is the liquid conductivity coefficient, ρ_w is density of water, g is gravity, and t is time. Using capillary pressure, p_c as the common driving potential for vapour and liquid water transport, Eq. 7 yields Eq. 8:

$$\frac{\partial m_{l+v}}{\partial t} = -C\frac{\partial p_c}{\partial t} = -\nabla\left(\frac{\mathrm{D_v(\Theta_l)}}{\mathrm{R_v T}}\frac{\mathrm{p_{v,sat}}\phi}{\rho_\mathrm{l}\mathrm{R_v T}}\nabla \mathrm{p_c} + \mathrm{K_l(\Theta_l)}\nabla \mathrm{p_c} + \rho_\mathrm{w} g\right) \quad \text{Eq. 8}$$

where $p_{v,sat}$ is the saturation vapour pressure and φ is relative humidity. The derivation of the mass balance equation for isothermal moisture transport (Eqs. 7 and 8) along with the corresponding constitutive equations can be found in the literature (see e.g., [30-34]). To solve Eq. 7, specific information on 1) the capillary pressure curve describing the moisture storage of the SFRC, 2) the vapour diffusion coefficient, and 3) the liquid water conductivity are needed.

1) In the present model the capillary pressure curve is described by a bimodal function of a van Genuchten type [35]:

$$\mathrm{\Theta_l} = w_{cap}\sum_{i=1}^{k}\frac{l_i}{\left(1+(a_i p_c)^{n_i}\right)^{m_i}} \text{ with } \mathrm{m_i} = 1 - \frac{1}{n_i} \quad \text{Eq. 9}$$

where w_{cap} is the capillary moisture content, a, n and m are shape parameters and l a weighing factor. The chosen parameters for the present model are given in Table 1. The pore volume distribution of the porous media can be obtained from the derivation of Eq. 9 with respect to the capillary pressure and use of Young's - Laplace equation to relate capillary pressure, p_c and pore radius, r:

$$p_c = \frac{2\gamma\cos\theta}{r} \quad \text{Eq. 10}$$

where γ is surface tension and θ is the wetting angle.

2) Vapour flow transport is described as:

$$D_v(\Theta_l) = \frac{D_{v,air}}{\mu_{dry}} f_v(\Theta_l) \quad \text{Eq. 11}$$

where $D_{v,air}$ is the vapour diffusion coefficient of air, μ_{dry} the vapour diffusion resistance number and $f_v(\theta_l)$ the vapour diffusion scaling function. The vapour diffusion coefficient of air is described by the relation given in [36]:

$$D_{v,air} = 0.083 \frac{p_0}{p} \left(\frac{T}{273.15}\right)^{1.81} \quad \text{Eq. 12}$$

where p_0 is the reference gas pressure. The applied vapour diffusion scaling function has been proposed by Scheffler & Plagge [37] and is based on a mechanistic modelling approach taking into account the impact of moisture content and the microstructure of the porous media on vapour diffusion. The vapour diffusion scaling function is given as:

$$f_v(\Theta_l) = \frac{1-\frac{\theta_l}{\theta_{por}}}{\left(\frac{\theta_l}{\theta_{por}}\right)^{n_{sp}} + \left(1-\frac{\theta_l}{\theta_{por}}\right)^2 \left(1-\left(\frac{\theta_l}{\theta_{por}}\right)^{n_{sp}}\right)} \quad \text{Eq. 13}$$

where θ_{por} is porosity and n_{sp} a modelling parameter.

3) Liquid moisture flow is described as:

$$K_l(\Theta_l) = K_{l,rel}(\Theta_l) f_l(\Theta_l) K_{l,sat} \quad \text{Eq. 14}$$

where $K_{l,rel}$ is the relative liquid conductivity containing information on the SFRC pore structure, $K_{l,sat}$ the liquid conductivity at saturation and $f_l(\theta_l)$ a liquid flow scaling function, which is similar to the vapour flow scaling function based on a mechanistic modelling approach proposed by Scheffler & Plagge [37]. For the determination of the relative liquid conductivity the approach derived by Mualem [38], is employed as:

$$K_{l,rel}(\Theta_l) = \left[\frac{\int_0^{\Theta_l} p_c(\theta)^{-1} d\theta}{\int_0^{\Theta_{por}} p_c(\theta)^{-1} d\theta}\right]^2 \quad \text{Eq. 15}$$

Instead of the tortuosity factor proposed in [38], a liquid flow scaling function [37,39] is used, which is described as:

$$f_l(\Theta_l) = \frac{\left(\frac{\theta_l}{\theta_{por}}\right)^{n_{sp}}}{\left(\frac{\theta_l}{\theta_{por}}\right)^{n_{sp}} + \left(1-\frac{\theta_l}{\theta_{por}}\right)^2 \left(1-\left(\frac{\theta_l}{\theta_{por}}\right)^{n_{sp}}\right)} \quad \text{Eq. 16}$$

Table 1: Parameters for capillary suction curve, values from [40].

Parameter	i	
	1	2
Capillary moisture content, kg/m^3	116	
l_i	0.426	0.574
a_i	2.4 E-08	2.1 E-07
n_i	2.34	2.68

Typical moisture transport input parameters, i.e. the moisture storage function and its derivation, the pore size distribution, along with the vapour and liquid flow transport coefficients, for concrete are presented in Fig. 5. More detailed information on the mechanistic model and the derivation of the liquid and vapour flow scaling functions can be found in [37,39].

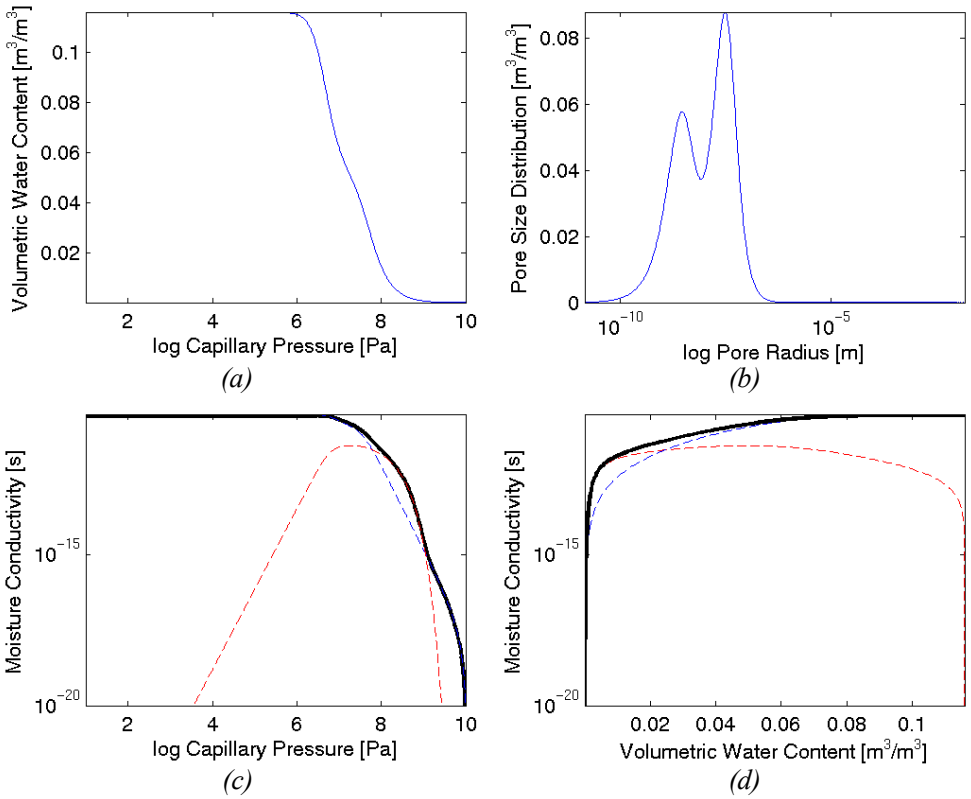

Figure 5 – Transport properties for modelling of coupled vapour and liquid moisture transport in the steel fibre reinforced concrete: (a) moisture storage function, (b) pore size volume distribution derived from the moisture storage function. Moisture conductivity (solid black line indicates sum of liquid (broken blue line) and vapour (broken red line) conductivity) as a function of (c) logarithm of capillary pressure and (d) volumetric water content.

RESULTS

Cracked hinge model inverse analysis estimates of the material properties of the SFRC are listed in Table 2, with the estimated crack profiles at various loads/CMOD's shown in Fig. 6. The CHM estimates the total crack opening displacement (COD) below the WST specimen notch, but is unable to consider details of the cracks such as isolated microcracking, crack branching, etc. All crack profiles are maximal at the crack edge (i.e., bottom of notch) and the COD's decrease linearly to the crack tip. Estimates indicate cracking has occurred at 70% of the peak load, although only a minute crack is formed with a length of 4.8 mm and a maximum COD of approximately 0.9 μm. Additional deformation causes the estimated crack length and COD's to increase to a maximum of 34 mm and 0.043 mm, respectively for the 0.1 mm CMOD specimen.

Fig. 7 illustrates the impact of the local normalization approached for computed x-ray attenuation images (Eq. 5). Fig. 7(a) and (b) show typical results without and with the local normalization, respectively. The images lower threshold was set to 0 g/cm^3 of water, meaning any grey-to-white-scales indicate the presence of moisture while black indicates either 0 or a negative number. Without the local normalization, boundaries between individual measurement locations are clearly visible and in certain cases neighbouring locations provide highly different assessments of the moisture conditions. For example, in Fig. 7(a) the moisture front appears to end abruptly at the boundary of the second and third row of images. In the first author's

Table 2: Estimated material properties of SFRC by inverse analysis of CHM.

E [GPa]	31
f_t [MPa]	3.3
a_1 [MPa/MPa/mm]	11.3
b_1 [MPa/MPa]	1
a_2 [MPa/MPa/mm]	1.62
b_2 [MPa/MPa]	0.435
a_3 [MPa/MPa/mm]	0.101
b_3 [MPa/MPa]	0.104

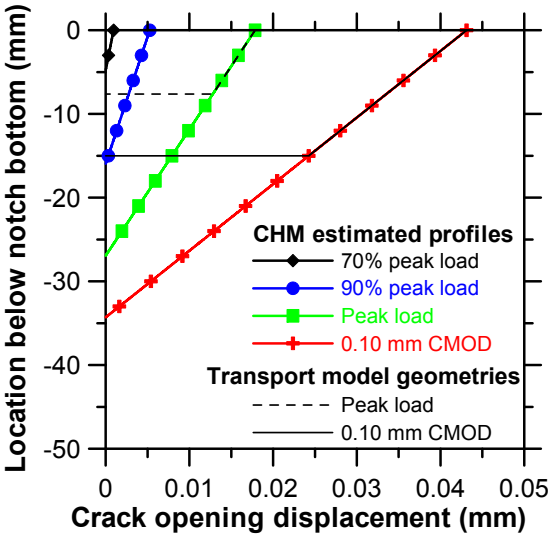

Figure 6 – Estimated crack profiles from the CHM for SFRC WST specimens at varying load/CMOD's. Crack geometries used in transport modelling are shown for peak load and 0.10 mm CMOD specimens.

experience this issue has caused extreme difficulty in analyzing and interpreting results from x-ray attenuation measurements of large specimens that require stitching together of multiple images. The problem is likely caused by compounding calculation error due to logarithmic subtraction in Eq. 5 and local (i.e., from one measurement location to next) and global (i.e., from measurement of 'I_{dry}' to 'I_{wet}') measurement variability. Fig. 7(b) and results presented below indicate local normalization provides a repeatable method to mitigate measurement variability.

Figs. 8-11 provide contour plots of the moisture content in the 50 mm thick WST specimen determined from images similar to that shown in Fig. 7(b) calculated after various times of exposure to liquid water to the loaded/cracked SFRC WST specimens. The black boxes on the contour plots identify the location of the notch and a steel shield that was used to cover the notch. The steel shield causes a small area near the notch to be incalculable due to the intense attenuation provided by 6 mm of steel plus 50 mm of concrete. The steel shield and notch can be seen in Fig. 7(b). An additionally artefact in the contour plots is the false indication of water. In nearly all the contour plots, there are at least small areas where moisture is indicated, but likely not actually present. For example, Fig. 8(a) indicates small amounts of water particularly below -25 mm below the notch. As water is introduced only through the notch, it is unlikely water reached these locations after only 3 minutes of exposure. These false indications of moisture can quantity in the WST specimens over time. The SFRC, which was conditioned to 50% relative humidity, rapidly absorbs moisture. After 7 hours the minimum moisture contour (0.30 g/cm^3) reached the extents of the x-position in most cases. For selected specimens a final x-ray make

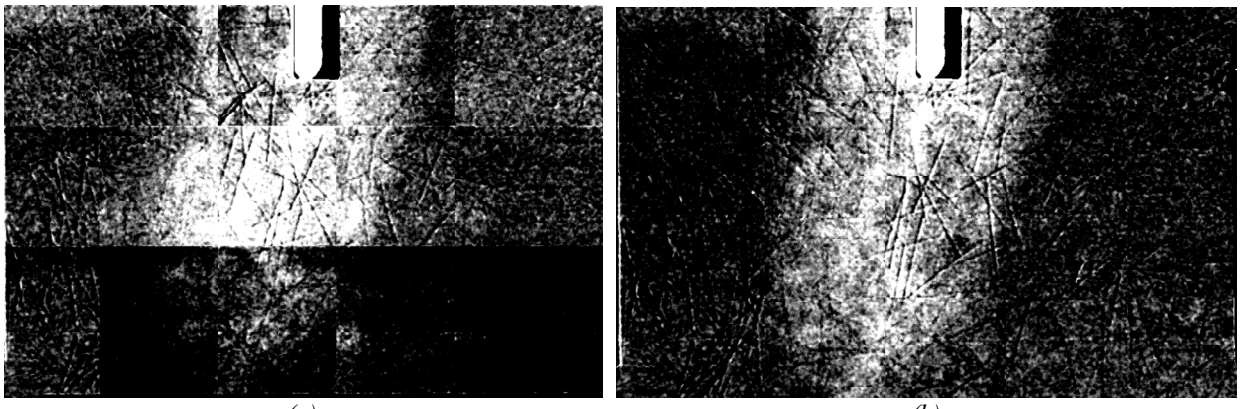

(a) *(b)*

Figure 7 – Calculated images (Eq. 5) (a) without and (b) with local normalization approach applied.

distinguishing the moisture front difficult in extreme cases, as most clearly seen in Figs. 8(f), 9(d,g), 10(d), and 11(h). False indications are likely caused by measurement variability and could likely be minimized, if not avoided, by increasing the integration times or altering x-ray source settings in future studies. Nevertheless, in many cases the moisture front is clear and by repeating measurements at various times, trends can be extracted.

Comparison of the various figures indicates moisture advances further and typically in increased attenuation measurement taken after 24 hours indicated the moisture front had moved beyond the measured area. The impact of the load level or CMOD is apparent, particularly in Figs. 10 and 11. Ingress occurs more rapidly in the y-direction of the peak load and 0.10 mm CMOD specimens with the minimum moisture contour reaching depths of approximately 10 mm and 17 mm below the notch, respectively compared to only approximately 7 mm below the notch for the 70% peak load specimen after 3 minutes (Figs. 8-11(a)). The trend continues at later times, e.g.

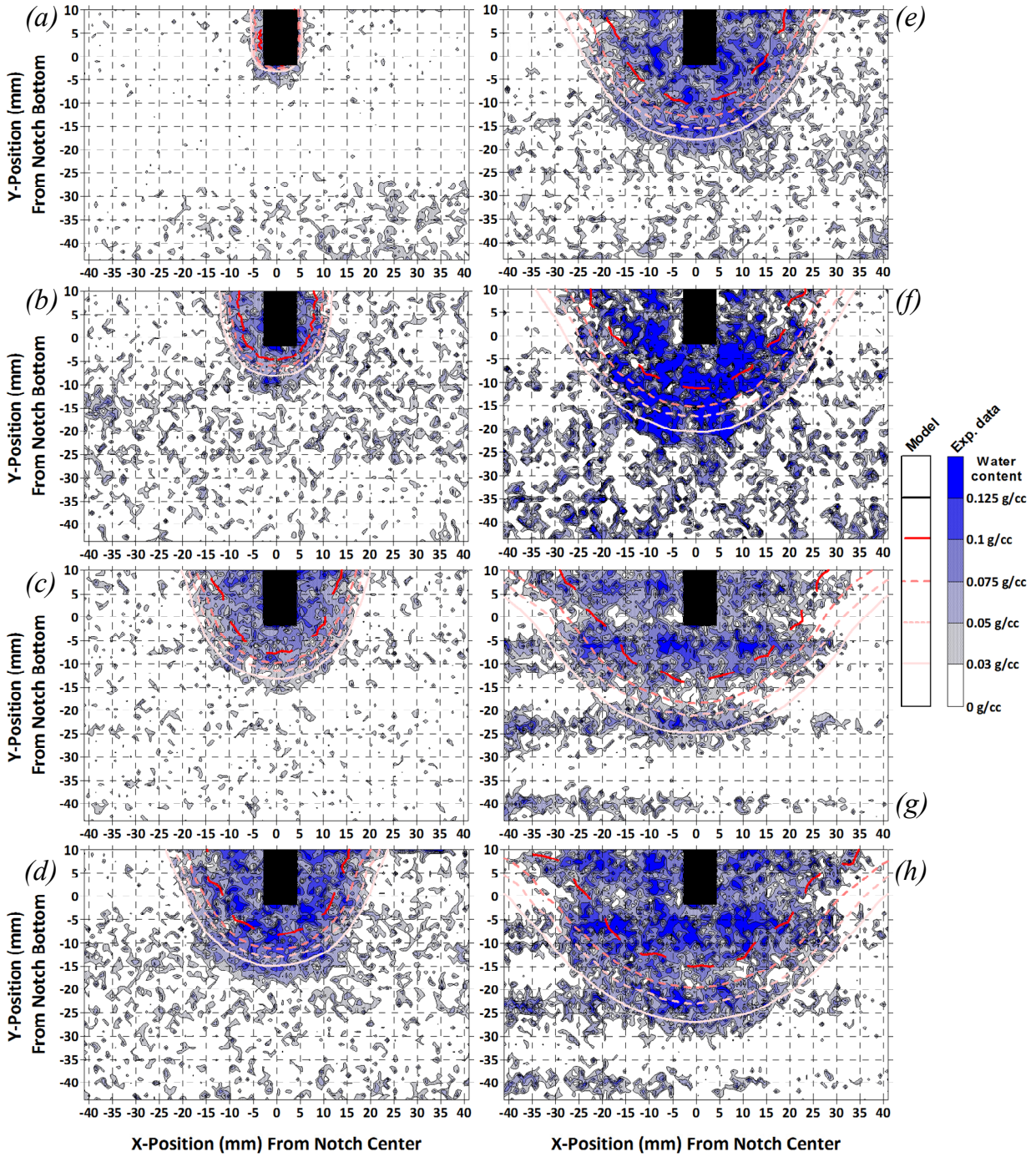

Figure 8 – Experimental and modelled ingress results for 70% peak load WST specimen after (a) 3, (b) 30 minutes, (c) 1.5, (d) 2, (e) 3, (f) 4, (g) 6, and (h) 7 hours of exposure to liquid water.

after 4 hours (Figs. 8-11(f)) of exposure moisture reached approximately 20 mm below the notch for the 90% peak load specimen, 25 mm for the peak load specimen, and 35 mm for the 0.10 mm CMOD specimen. Lateral ingress, however, appears to be unaffected by cracking of the SFRC WST specimens, e.g. after 1.5 hours (Figs. 8-11(c)) x-ray attenuation measurements indicate the lateral ingress reached a maximum of between ±18-20 mm from the notch centre for all specimens.

COMPARISON OF EXPERIMENTAL AND TRANSPORT MODEL RESULTS

Figs. 8-11 also provide modelled results of ingress as the various isolines that match the contour lines of the experimental data. Data presented in Fig. 8 (70% peak load sample) was used to

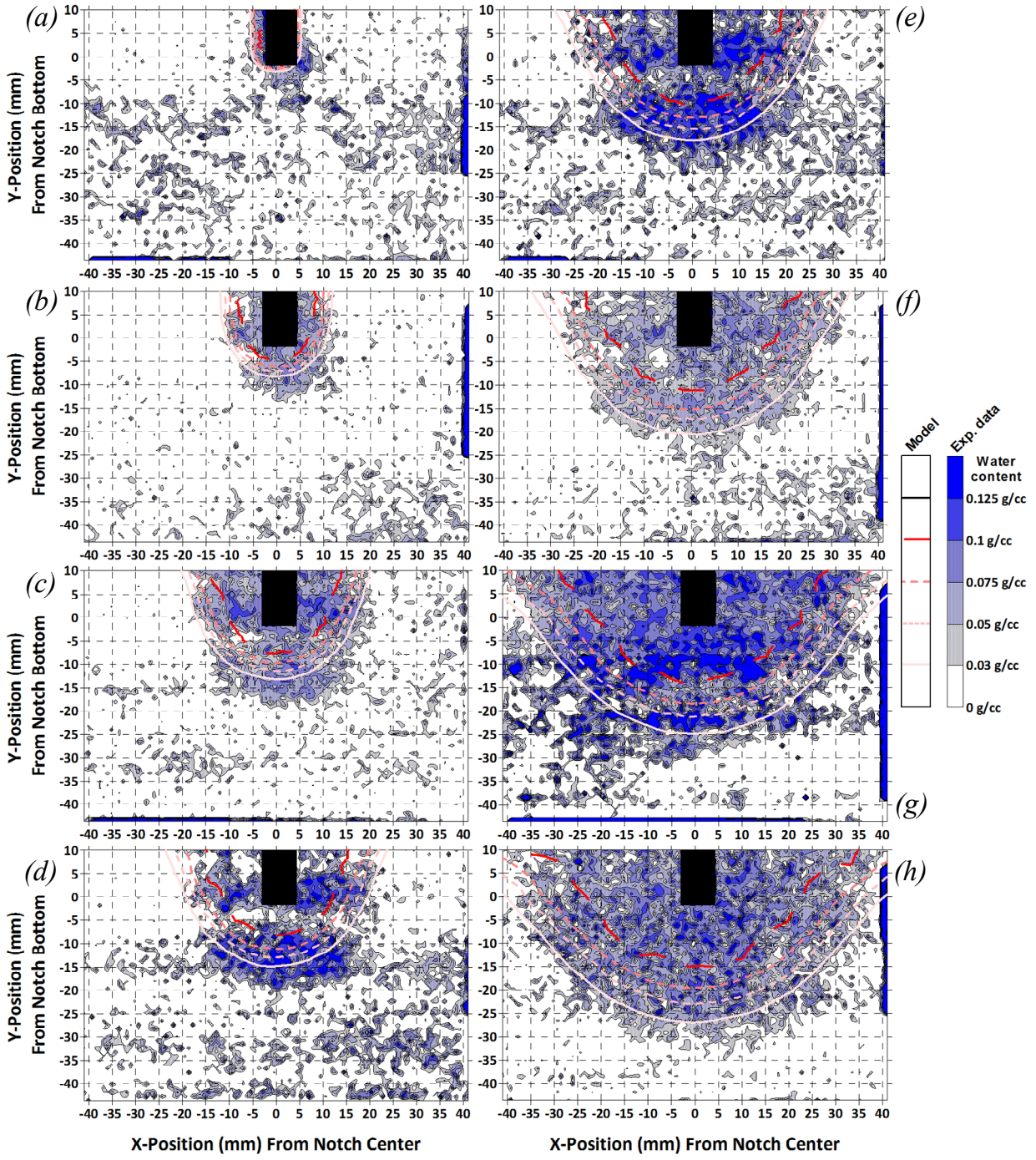

Figure 9 – Experimental and modelled ingress results for 90% peak load WST specimen after (a) 3, (b) 30 minutes, (c) 1.5, (d) 2, (e) 3, (f) 4, (g) 6, and (h) 7 hours of exposure to liquid water.

determine three model parameters, n_{sp}, μ, and $K_{l,sat}$ which were found to be 1 (unitless), 30 (unitless), and 3.5 x 10^{-7} m/sec, respectively, and were held constant. Similar values for liquid conductivity at saturation, $K_{l,sat}$ have been reported in the literature, see e.g., 1.5 x 10^{-6} m/sec for 0.3 water-to-cement ratio cement paste [41], and permeability values for mortar presented in [40]. As previously stated, the model geometry of the crack was determined using the CHM and assuming a constant length from the crack tip of the estimated crack consisted of isolated microcracking that does not impact the moisture ingress behaviour. Using the transport model, a constant length of the isolated microcracking of 19.3 mm was used, which compares well to previous determinations through epoxy impregnation for ordinary concrete measured between 16.5-18.5 mm [22]. Fig. 6 shows the crack geometries used for modelling ingress in the cracked SFRC WST specimens. The estimated crack lengths for the 70% and 90% peak load specimens did not reach a total length of 19.3 mm; therefore, ingress was modelled in both cases

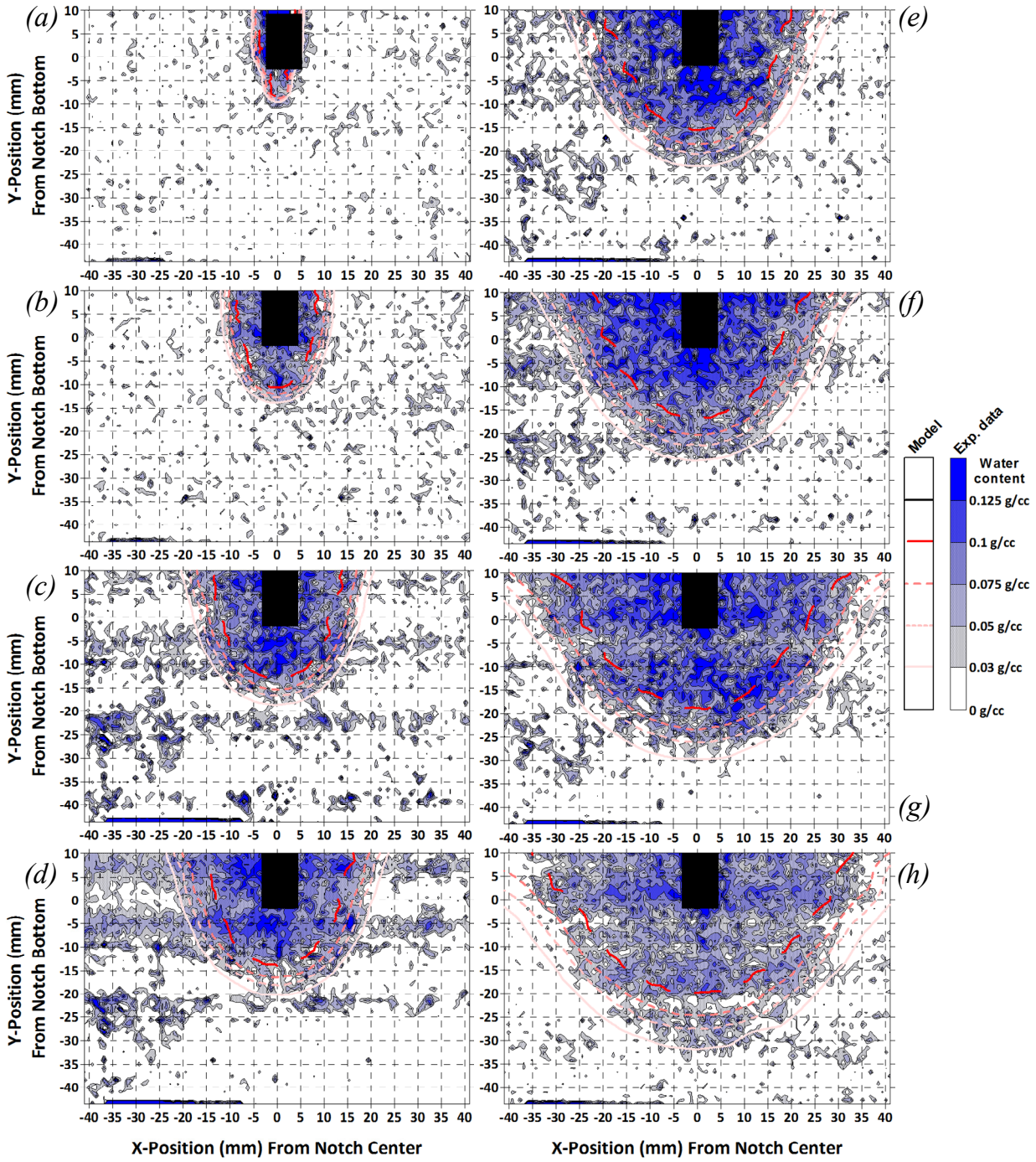

Figure 10 – Experimental and modelled ingress results for peak load WST specimen after (a) 3, (b) 30 minutes, (c) 1.5, (d) 2, (e) 3, (f) 4, (g) 6, and (h) 7 hours of exposure to liquid water.

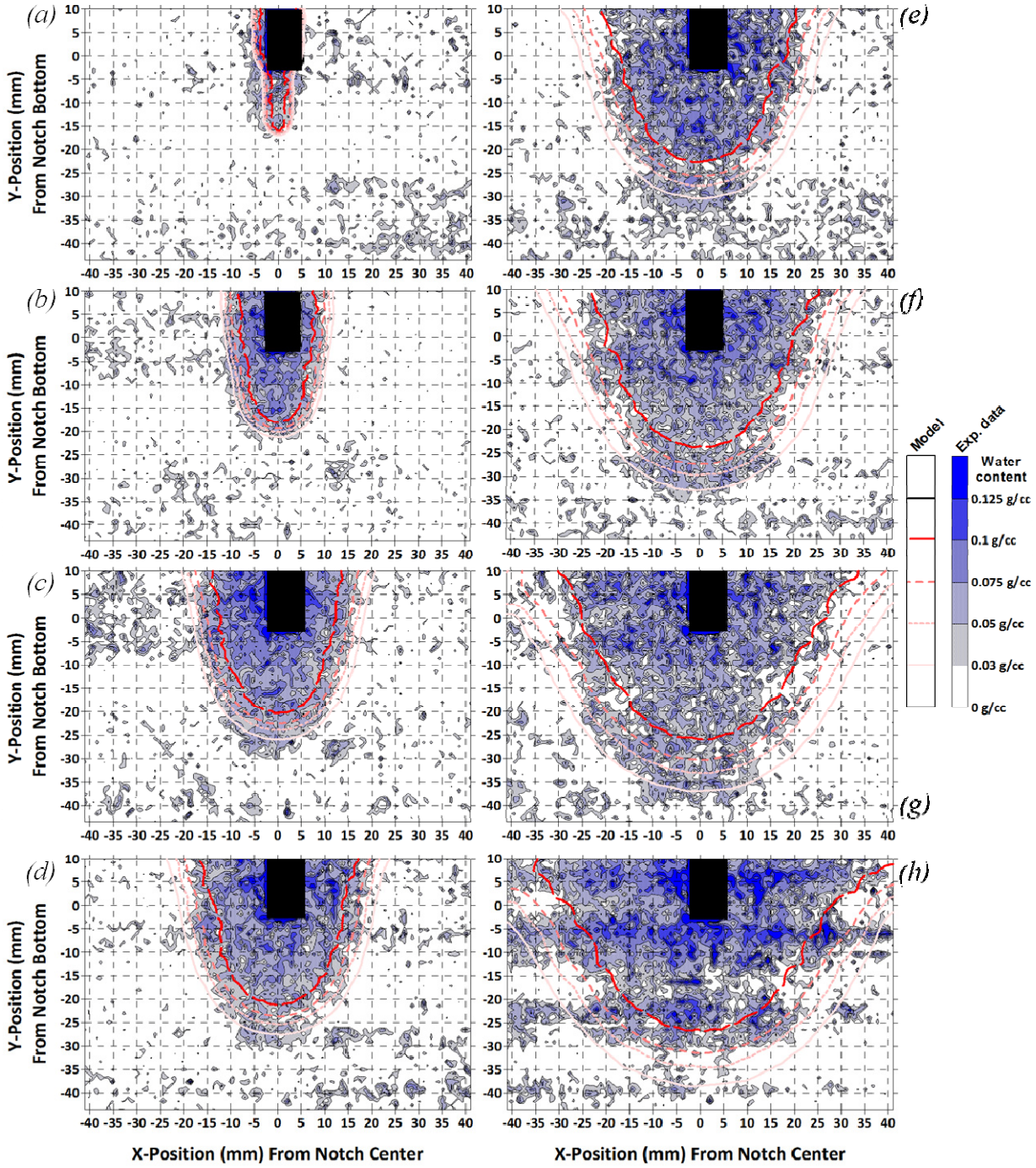

Figure 11 – Experimental and modelled ingress results for 0.10 mm CMOD WST specimen after (a) 3, (b) 30 minutes, (c) 1.5, (d) 2, (e) 3, (f) 4, (g) 6, and (h) 7 hours of exposure to liquid water.

without a crack. The transport model appears to accurately estimate the impact of cracking in the SFRC on the extent, both vertically and horizontally, of moisture ingress using the simplified crack geometries. Location variations in the moisture content, characteristic of the experimental data, were not found in the model results. This contradiction is due to the use of a homogeneous moisture storage function in the model, while the cement content (or inversely, aggregate content) of the SFRC varies naturally with location in the experimental specimens.

SUMMARY AND CONCLUSIONS

This paper, which presents a combined experimental and modelling investigation on moisture

ingress in steel fibre reinforced concrete wedge split test specimen deformed to various states (70% and 90% of peak load, peak load, and 0.10 mm crack mouth opening displacement) and conditioned to 50% relative humidity, has concluded:

- The impact of cracks on extent of moisture ingress can, in this case, be accurately modelled using a simplified crack geometry, which consists of:
    - A coalesced crack length, which behaves as a free-surface for moisture ingress
    - An isolated microcracking portion of constant length of approximately 19 mm, which resists ingress similarly to the bulk material.
- The extent of ingress into the depth of the steel fibre reinforced concrete increased with increased crack deformation at a given time; however, the extent of lateral ingress at a given time remained relatively constant for all load/crack states.
- The steel fibre reinforced concrete has a varying moisture storage capacity due to natural variations in cement content. The current model assumes a homogeneous moisture storage capacity and therefore is unable to account for such variations.

ACKNOWLEDGEMENT

Financial contributions from the Danish Expert Centre for Infrastructure Constructions and the project 'Sustainable Rehabilitation of Civil and Building Structures' funded by Nordic Innovation Centre, project no. 08190 SR are greatly appreciated. The second author gratefully acknowledges the financial support of Femern Bælt A/S, Sund & Bælt Holding A/S, and The Danish Agency for Science, Technology and Innovation. Additionally, the assistance of Oldrich Svec is appreciated in altering the 'ImageJ' batch code used here.

REFERENCES

1. *fib* Bulletin 34, "Model code for service life design," Int. Fed. structural concrete (*fib*), 2006.
2. *fib* Bulletin 55, "Model code 2010," Int. Fed. structural concrete (*fib*), 2010.
3. Ehlen, M.A., et al., "Life-365 Service Life Prediction Model Version 2.0 - Widely used software helps assess uncertainties in concrete service life and life-cycle costs," Conc. Int. **31** 41-46, 2009.
4. Life-365 Consortium II, "Life-365 Service life prediction model and computer program for predicting the service life and life-cycle cost of reinforced concrete exposed to chlorides," 2010.
5. Tuutti, K., "Corrosion of Steel in Concrete," Swedish Cement and Concrete Research Institute at the Institute of Technology, Stockholm, 4-82, 1982.
6. Jacobsen, S., et al., "Effect of cracking and healing on chloride transport in OPC concrete," Cem. Con. Res. **26** 869-881, 1996.
7. Aldea, C.-M., et al., "Permeability of cracked concrete," Mat. & Struct. **32** 370-376, 1999.
8. Edvardsen, C., "Water permeability and autogenous healing of cracks in concrete," ACI Mat. J. **96** 448-454, 1999.
9. Rodriguez, O., Hooton, R., "Influence of cracks on chloride ingress into concrete," ACI Mat. J. **100** 120-126, 2003.
10. Lindquist, W.D., et al., "Effect of cracking on chloride content in concrete bridge decks," ACI Mat. J. **103** 467-473, 2006.
11. Pease, B., et al., "Assessing the portion of the crack length contributing to water sorption using x-ray absorption measurements on concrete wedge splitting specimens," ConcreteLife'09: 2nd Int. RILEM Workshop on Conc. Durability and Service Life Planning, Haifa, Israel, 2009.
12. Schießl, P., Raupach, M., "Laboratory studies and calculations on the influence of crack width on chloride-induced corrosion of steel in concrete," ACI Mat. J. **94** 56-62, 1997.
13. Otieno, M., et al., "Corrosion in cracked and uncracked concrete - Influence of crack width, concrete quality and crack reopening," Mag. Conc. Res. **62** 393-404, 2010
14. Pease, B., et al., "The design of an instrumented rebar for assessment of corrosion in cracked reinforced concrete," Mat. & Struct. **44** 1259-1271, 2011

15. Schießl, P., “Zur frage der zulassigen Rissbreite und der enforderlichen Betondeckung im Stahlbetonbau unter besonderer Berucksichtigung der Karbonatisierung des Betons,” Deutscher Ausschuss für Stahlbeton **255**, 1976.
16. Isgor, O.B., Razaqpur, A.G., “Modelling steel corrosion in concrete structures,” Mat. & Struct. **39** 259-270, 2006.
17. Liu, Y., Weyers, R., “Modeling the time-to-corrosion cracking in chloride contaminated reinforced concrete,” ACI Mat. J. **95** 675-681, 1998.
18. Vu, K., et al., “Corrosion-induced cracking: Experimental data and predictive models,” ACI Struct. J. **102** 719-726, 2005
19. Li, C.-Q., et al., “Prediction of reinforcement corrosion in concrete and its effects on concrete cracking and strength reduction,” ACI Mat. J. **105** 3-10, 2008.
20. Michel, A., et al., “Monitoring reinforcement corrosion and corrosion-induced cracking using non-destructive x-ray attenuation measurements,” Cem. Conc. Res. **41** 1085-94, 2011.
21. Skoček, J., “Fracture propagation in cementitious materials: Multi-scale approach - measurements and modeling,” Ph.D. thesis, Technical University of Denmark, Kgs. Lyngby, Denmark, 2010.
22. Pease, B., “Influence of concrete cracking on ingress and reinforcement corrosion,” Ph.D. thesis, Technical University of Denmark, Kgs. Lyngby, Denmark, 2010.
23. DS-2426, “Concrete—Materials—Rules for application EN 206-1 in Denmark,” Danish Standards Association, 2004.
24. Ulfkjaer, J.P., et al., “Analytical model for fictitious crack propagation in concrete beams,” J. of Enging. Mech. **121** 7-15, 1995.
25. Olesen, J.F., “Fictitious crack propagation in fiber-reinforced concrete beams,” J. Enging. Mech. **127** 272-280, 2001.
26. Østergaard, L., “Early-age fracture mechanics and cracking of concrete - Experiments and modelling,” Ph.D. thesis, Technical University of Denmark, Kgs. Lyngby, Denmark, 2003
27. Hansen, K., et al., “Dual-energy x-ray absorptiometry for the simultaneous determination of density and moisture content in porous structural materials,” Proc. 5th Symp. on Building Physics in the Nordic Countries **1** 281-288, 1999.
28. Roels, S., Carmeliet, J., “Analysis of moisture flow in porous materials using microfocus x-ray radiography,” Int. J. Heat & Mass Transfer **49** 4762-4772, 2006.
29. Pease, B., Scheffler, G.A., Janssen, H., “Monitoring moisture movements in building materials using x-ray attenuation: Influence of beam-hardening of polychromatic x-ray photon beams,” Submitted to Construction and Building Materials, 2011.
30. P. Häupl, et al., “Coupled heat air and moisture transfer in building structures,” Int. J. Heat & Mass Transfer **40** 1633-1642, 1997.
31. J.R. Philip, D.A. de Vries, “Moisture movement in porous materials under temperature gradients,” Trans. Am. Geophys. Union **38** 222-232, 1957.
32. F.A.L. Dullien, “Porous Media – Fluid Transport and Pore Structure,” Academic Press, 1979.
33. S. Whitaker, “Flow in porous media I: A theoretical derivation of Darcy’s law,” Transport Porous Med. 1 pp. 3-25, 1986.
34. J. Bear, Y. Bachmat, “Introduction to modeling of transport phenomena in porous media,” Kluwer Academic Publishers, Dordrecht, 1991.
35. Carmeliet J, Roels S. “Determination of the moisture capacity of porous building materials,” J Therm Envelope Build Sci. **25** 209-237, 2002.
36. R. Schirmer, “Die Diffusionszahl von Wasserdampf-Luftgemischen und die Verdampfungsgeschwindigkeit,” VDI Beiheft Verfahrenstechnik **2** 170-177, 1938.
37. Scheffler, G.A., Plagge, R.A, “Whole range hygric material model: Modelling liquid and vapour transport properties in porous media,” Int. J. Heat & Mass Transfer **53** 286-296, 2010.
38. Y. Mualem, “A new model for predicting the hydraulic conductivity of unsaturated porous media,” Water Resour. Res. **12** 513-522, 1976.
39. Scheffler, G.A., “Validation of hygrothermal material modelling under consideration of the hysteresis of moisture storage,” Ph.D. thesis, Technische Universität Dresden, Germany, 2009.
40. Derluyn, H., et al., “Influence of the nature of interfaces on the capillary transport in layered materials,” Const. and Build. Mat. **25** 3685-3693, 2011.
41. Pour-Ghaz, M., et al., “Numerical and experimental assessment of unsaturated fluid transport in saw-cut (notched) concrete elements,” ACI SP 266, 73-83, 2009.

Paper III

” Numerical modelling of reinforcement corrosion in concrete structures”

A. Michel, M.R. Geiker, H. Stang & J.F. Olesen

Published in: *Proceedings of 8th fib PhD Symposium, June 20-23, 2010, Kgs. Lyngby, Denmark.*

Numerical modelling of reinforcement corrosion in concrete structures

A. MICHEL, M. R. GEIKER, H. STANG AND J. F. OLESEN

Technical University of Denmark
Brovej, Building 118, Dk-2800 Kgs. Lyngby, Denmark
almic@byg.dtu.dk

Abstract
An overview of an ongoing research project related to service life prediction of concrete structures is presented. Focus is placed on numerical modelling of the propagation of macro cell corrosion. The applied modelling approach is physio-chemical taking into account materials properties and characteristics (including cracks and other defects), structural detailing and varying boundary conditions. The approach combines the modelling of electrochemical processes, transport processes and mechanical performance.

To demonstrate the potential use of the modelling approach a numerical example is provided; the influence of three exposure scenarios on the corrosion rate of steel in concrete is illustrated

1. Motivation

Each year, large sums are used to ensure the durability of concrete structures, especially towards reinforcement corrosion. Improved durability provides increased structural reliability, economical improvements in form of less need for maintenance and repair, and increased energy and resource efficiency leading to improved sustainability. Much focus is placed on means of ensuring a long service life of cracked reinforced concrete structures. The effectiveness of service life enhancing solutions is, however, difficult to evaluate based on current service life models, as these models a) are not based on a detailed description of the corrosion processes, and b) do not take the presence of cracks and other defects into account. Also, experimental investigations of initiation and propagation of reinforcement corrosion are very time consuming and due to the complexity of the concrete-steel system the results are difficult to generalize.

So far, numerical investigations to determine the influence of defects on concrete properties and corrosion are very limited (see e.g. [1], [2], and [3]).

The objective of the PhD project is to establish, test and demonstrate the applicability of a theoretical framework for the modelling of rebar corrosion in reinforced concrete structures. The applied modelling approach is physio-chemical taking into account materials properties and characteristics (including cracks and other defects), structural detailing and boundary conditions. The approach combines the modelling of electrochemical processes, transport processes and mechanical performance.

In the present paper the theoretical framework for the proposed modelling approach is summarised. Furthermore, selected results are given illustrating the potential use of the applied proposed modelling approach.

2. Modelling approach

The basic concept of the modelling approach is illustrated in Fig. 1 a). The approach takes into account electrochemical processes (corrosion model), structural defects (mechanical models) as well as transport phenomena of potentially aggressive media in concrete (material

and transport models). To model the propagation of reinforcement corrosion in concrete structures a physio-chemical, FEM based corrosion model has been established. The corrosion combines electrochemical corrosion processes with fundamental transport mechanisms and structural defects to allow simulation of the propagation of macro cell corrosion in a concrete-steel system. The anodic and cathodic areas of the reinforcement are prescribed since the present model is dealing with propagation of reinforcement corrosion. The proposed system to model propagation of reinforcement corrosion is illustrated in Fig. 1 b).

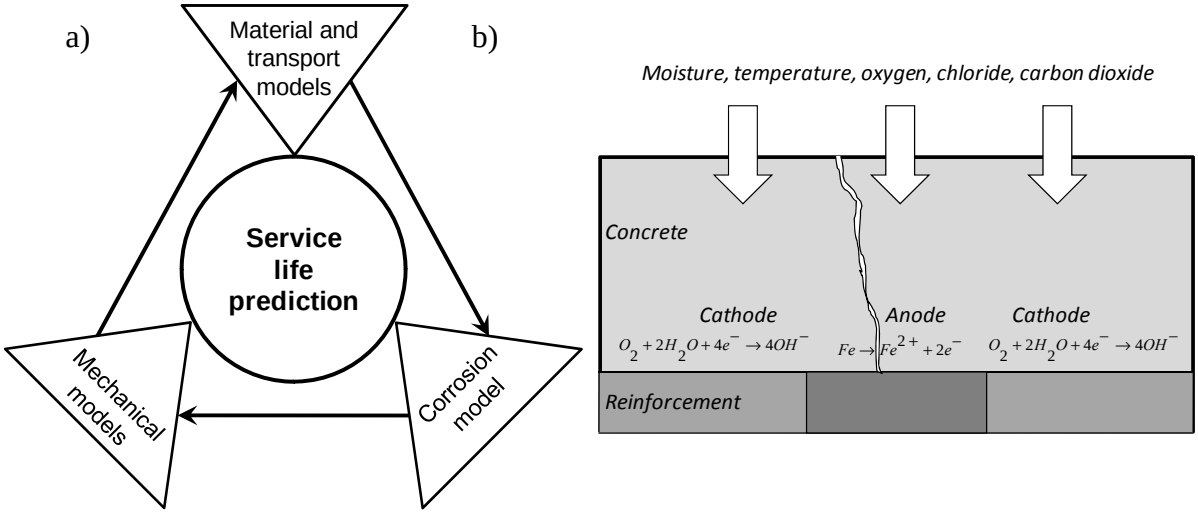

Figure 1: a) approach of the proposed service life prediction model, and b) concrete-steel system to model propagation of reinforcement corrosion.

2.1 Corrosion model

To describe the electrochemical processes and determine the corrosion rate of steel embedded in concrete two physical laws are used. The first one is Laplace's equation (Eq. (7) in Fig. 2) describing the electric potential distribution in the concrete assuming electrical charge conservation and isotropic conductivity. The second is Ohm's law (Eq. (6) in Fig. 1), which can be used to determine the corrosion current density if the potential distribution and the resistivity of the electrolyte are known [1]. Subsequently, the rate of dissolution of iron on the steel surface in concrete can be calculated using Faraday's law as follows

$$X(t) = \frac{M}{zF\rho} \int_0^t i_{corr}(t) dt \tag{1}$$

where $X(t)$ = thickness reduction, $i_{corr}(t)$ = corrosion current density, M = mol mass of the metal, z = number of electrons in the reaction equation for the anodic reaction and ρ = density of the metal. An overview of the proposed solution procedure for the corrosion model is given in Fig. 2. To solve Laplace's equation appropriate boundary conditions are needed. So called polarisation curves are used as boundary conditions describing the kinetics of the corrosion process or in other words quantifying the relation between production and consumption of current as a function of the potential at the steel surface. For the anodic and cathodic regions of the steel surface, the polarisation curves can be defined by Eq. (2) and Eq. (3) given in Fig. 2, taking into account the effects of activation and concentration polarisation. Additional information on the theory of polarisation phenomena of metals in an electrolyte are given in e.g. [4] and [5]. A more detailed description of the applied finite element method corrosion model and the underlying materials and electrochemical properties models can be found in [6].

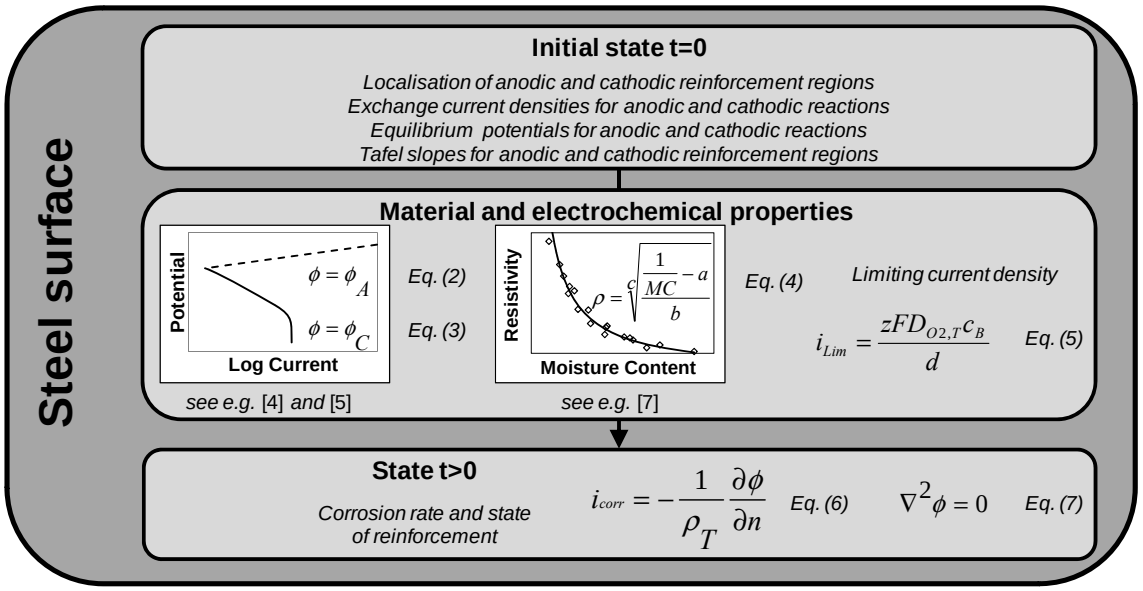

Symbols

ϕ	electric potential	i_{Lim}	limiting current density
ϕ_A	anodic electric potential	z	number of transferred electrons
ϕ_C	cathodic electric potential	F	Faraday's number
ρ	concrete resistivity at reference temperature	$D_{O2,T}$	oxygen transport function
MC	moisture content	c_B	O_2 concentration at concrete surface
a	non-physical fitting parameter	d	concrete cover thickness
b	non-physical fitting parameter	ρ_T	concrete resistivity
c	non-physical fitting parameter	n	direction normal to the rebar surface

Figure 2: Proposed corrosion model.

2.2 Material and transport models

The corrosion processes and electrochemical parameters, such as anodic and cathodic electric potentials, the polarisation of the steel surface and the concrete resistivity, are influenced by the exposure conditions and the materials properties of the reinforced concrete.

Temperature, oxygen and chloride ion concentration mainly affect the polarisation behaviour of steel in concrete while the moisture content and possible addition of conductive fibres strongly influence the concrete resistivity. The effect of chloride ions and temperature on the concrete resistivity seems minor compared to moisture and fibre content (see e.g. [8] and [9]). An overview of the proposed model to determine the time dependent distribution of temperature, chloride ions, oxygen and moisture is illustrated in Fig. 3.

The time dependent distribution of the considered species in the concrete domain and along the concrete-steel interface is obtained by solution of a quasi-harmonic equation (Eq. (8) in Fig. 3). Application of appropriate boundary conditions as well as coefficients describing material properties and transport functions of the concrete to Eq. (8) allow prediction of the time dependent distributions of potentials such as temperature, moisture, oxygen and chloride. A more detailed description of the applied material and transport model can be found in [4].

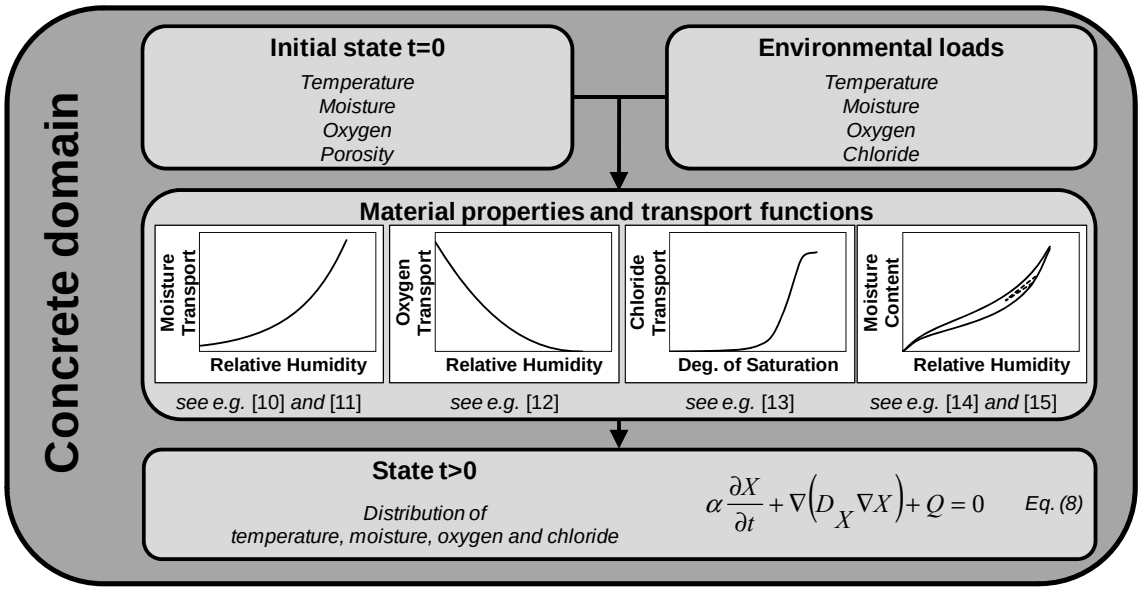

Symbols

α	coefficient representing material properties	X	potential
D_X	corresponding transport function for potential X	t	time
Q	sink term for negative values and source term for positive values		

Figure 3: Proposed transport models.

2.3 Impact of possible defects

Current service life models (see e.g. [16]) assume in most cases that the structure is a homogeneous defect-free system. In real structures, however, cracks and other defects can be found. These defects have a major impact on the concrete durability. Cracks provide easy access to aggressive substances and voids affect the critical chloride content initiating corrosion [17].

In connection with the ongoing project an experimental study to investigate the impact of cracks on the initiation and propagation phase of corrosion in ordinary and fibre reinforced concrete is initiated. The main focus of the investigations is placed on the effect of debonding between concrete and steel since it is believed that the amount of damage at the concrete-steel interface is the major driving force for initiation and propagation of corrosion in concrete structures. The experimental program covers mechanical as well as electrochemical tests. Mechanical investigations are carried out to study the relation between debonding and geometrical parameters, material parameters as well as load. For the electrochemical measurements so-called instrumented rebars are used, which allow location dependent electric potential and current measurements while acting mechanically similar to a standard rebar [18].

3. Numerical example

For the numerical example the impact of varying relative humidity, temperature and oxygen content on the corrosion current density was studied. The input parameters for the numerical simulation and more details on the three exposure scenarios are given in Table 1. The chosen model geometry and the results of the numerical modelling are illustrated in Figure 4. The most pronounced effect can be observed for Exposure Scenario 1, following the changing moisture content in the concrete due to the applied boundary conditions and moisture transport function. The impact of the Exposure Scenarios 2 and 3 appears to be less pronounced for the investigated geometry and boundary conditions.

Table 1: Input parameters and exposure scenarios for the numerical example.

Parameter	Value	Unit	Parameter	Value	Unit
Anodic exchange current density at equilibrium	1.88 E-04	[A/m^2]	Concrete resistivity	Eq. (3)	[ohm m]
Anodic equilibrium potential	-0.78	[V]	Initial bulk humidity	0.9	[-]
Anodic Tafel constant	0.06	[V/dec]	Moisture transport	Eq. (6)	[m/s^2]
Cathodic exchange current density at equilibrium	6.25 E-06	[A/m^2]	Limiting current density	Eq. (4)	[A/m^2]
Cathodic equilibrium potential	0.16	[V]	Oxygen transport	Eq. (6)	[m/s^2]
Cathodic Tafel constant	0.16	[V/dec]	Temperature	Eq. (6)	[K]

Scenario	Relative humidity [-]	Oxygen [mol/m^3]	Temperature [K]
1	0.72 - 0.91	1	295
2	0.8	1	275 - 295
3	0.72	0.2 - 1	295

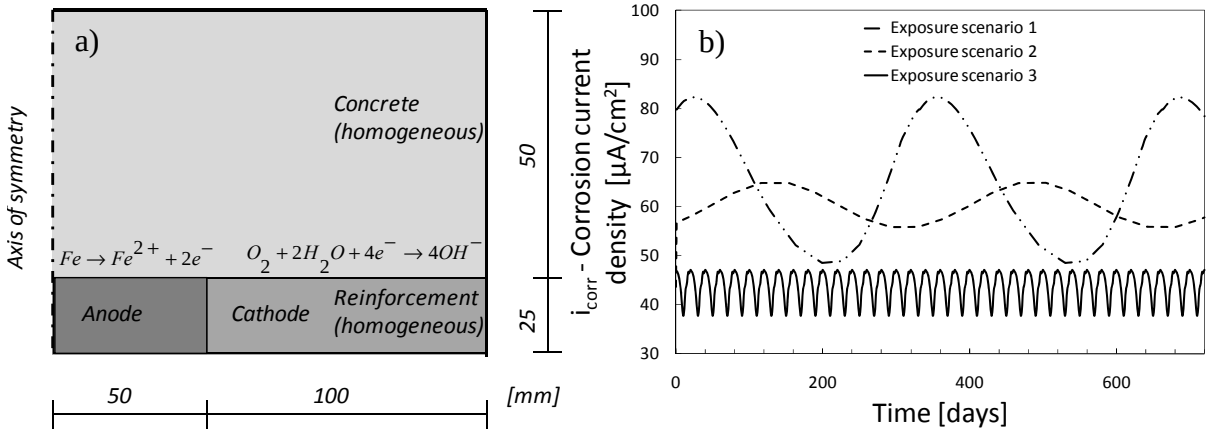

Figure 4: a) geometry modelled and b) corrosion current density for the numerical example.

4. Summary and conclusions

The basic concept for a numerical modelling approach, which allows the prediction of the corrosion rate of reinforcement in concrete structures, was given. The proposed model combines modelling of electrochemical corrosion processes and transport mechanisms to allow simulation of the propagation of macro cell corrosion in a concrete-steel system. The applied approach takes into account materials properties and characteristics (including cracks and other defects), structural detailing and boundary conditions.

To demonstrate the potential use of the proposed modelling approach a numerical example was presented. In the example the influence of varying exposure scenarios on the corrosion current density and hence the corrosion rate of the reinforcement were investigated. The presented results illustrate the major impact of the exposure conditions on the corrosion current density. To take into account the effect of structural defects on the propagation phase of steel corrosion in future simulations an experimental study has been initiated. The results of the experimental investigations will be used to extend the present corrosion and transport model.

5. Acknowledgments

The first author gratefully acknowledges the financial support of Femern Bælt A/S, Sund & Belt Holding A/S and The Danish Agency for Science, Technology and Innovation.

References

[1] B.O. Isgor & G. A. Razaqpur, “Modelling steel corrosion in concrete structures”, *Materials and Structures* vol. 39, pp. 291-302, 2006.

[2] Y. Hasegeva, S. Miyazato & T. Oyamoto, “Proposal for Corrosion Rate Analytical Model of Reinforced Concrete”, *29th Conference on OUR WORLD IN CONCRETE & STRUCTURES*, 25-26 August, Singapore, 2004.

[3] A. Ouglova, A. Raharinaivo, Y. Berthaud, I. Petre-Lazar & H. Boukhenfouf, “Numerical simulation of potential distribution due to the corrosion of reinforcement in concrete structures”, *Materials and Structures* vol. 38, pp. 711-719, 2005.

[4] M. Stern & A. L. Geary, “Electrochemical polarization I. A theoretical analysis of the shape of polarization curves”, *Journal of the Electrochemical Society* vol. 104, pp. 56-63, 1957.

[5] E. Bardal, “Corrosion and Protection”. *Engineering Materials and Processes* London, UK: Springer, 1st edition, 2004.

[6] A. Michel, A. O. S. Solgaard, M. R. Geiker, H. Stang & J. F. Olesen, “Numerical modelling of reinforcement corrosion, influence of steel fibres and moisture content on resistivity and corrosion current density”, *Proceedings of 3rd Int. PhD Workshop on Modelling the Durability of reinforced Concrete*, Oct. 22-24 Guimarães, Portugal, 2009.

[7] C. Hötte, “Bestimmung des Feuchtezustandes von Mauerwerk mit Hilfe von Multiring-Elektroden - Untersuchungen zum Ankoppelungsmörtel und an Probewänden”, *Diplomarbeit*, Technische Hochschule Aachen, Institut für Bauforschung, 2003.

[8] K. Tuutti, “Corrosion of steel in concrete”, *Report 4-82*, Swedish Cement and Concrete Research Institute, 1982.

[9] A. Michel, A. O. S. Solgaard, M. R. Geiker, H. Stang and J. F. Olesen, “Influence of Resistivity on the Corrosion of Reinforcement in Concrete”, *Proceedings of CONMOD’10*, June 22-25, Lausanne, Switzerland, 2010.

[10] Z. P. Bazant, “Physical model for steel corrosion in concrete sea structures - Application”, *Journal of the Structural Division* vol. 105, pp. 1155-1166, 1994.

[11] L. Pel, “Moisture transport in building materials”, *PhD Thesis*, Eindhoven University of Technology, 1995.

[12] V. G. Papadakis, C. G. Vayenas & M. N. Fardis, “Physical and Chemical Characteristics Affecting the Durability of Concrete”, *ACI Materials Journal* vol. 8, pp. 186-196, 1991.

[13] E. P. Nielsen & M. R. Geiker, “Chloride diffusion in partially saturated cementitious material”, *Cement and Concrete Research* vol. 33, pp. 133-138, 2003.

[14] H. L. Frandsen, S. Svensson & L. Damkilde, “A hysteresis model suitable for numerical simulation in wood”, *Holzforschung* vol. 61, pp. 175-181, 2007.

[15] B. Johannesson & M. Janz, “A two-phase moisture transport model accounting for sorption hysteresis in layered porous building constructions”, *Building and Environment* vol. 44, pp. 1285-1294, 2009.

[16] fib, “Model Code for Service Life Design”, *International Federation for Structural Concrete (fib)*, Lausanne, Switzerland, 1st edition, 126 pp., 2006.

[17] N. Buenfeld, G. Glass, B. Reddy, & F. Viles, “Process for the Protection of Reinforcement in Reinforced Concrete”, *United States Patent 6685822*, 30 pp., 2004.

[18] B. Pease, M. Geiker, H. Stang & J. Weiss, “Development of an instrumented rebar for assessment of corrosion risk in cracked reinforced concrete beams”, *in preparation*.

Paper IV

” Modelling Reinforcement Corrosion in Concrete”

A. Michel, M.R. Geiker, H. Stang & J.F. Olesen

Published in: *Proceedings of MicroDurability, April 11-13, 2012, Amsterdam, Netherlands.*

MODELLING REINFORCEMENT CORROSION IN CONCRETE

A. Michel (1), M. R. Geiker (1), (2), H. Stang (1) and J. F. Olesen (1)

(1) Department of Civil Engineering, Technical University of Denmark, Kgs. Lyngby, Denmark

(2) Department of Structural Engineering, Norwegian University of Science and Technology, Trondheim, Norway

Abstract

A physio-chemical model for the simulation of reinforcement corrosion in concrete structures was developed. The model allows for simulation of initiation and subsequent propagation of reinforcement corrosion. Corrosion is assumed to be initiated once a defined critical chloride threshold is reached causing the formation of anodic and cathodic regions along the reinforcement. Critical chloride thresholds, randomly distributed along the reinforcement surface, link the initiation and propagation phase of reinforcement corrosion.

To demonstrate the potential use of the developed model, a numerical example is presented, that illustrates the formation of corrosion cells as well as propagation of corrosion in a reinforced concrete structure.

Keywords: Corrosion, Concrete, Numerical simulation.

1. INTRODUCTION

Within the past decades, models as well as standards and recommendations, see e.g. [1-3], have been developed to facilitate service life prediction of reinforced concrete structures. Numerous models have been developed describing the initiation and propagation of reinforcement corrosion. Commonly, the initiation phase of reinforcement corrosion is described by the transport of aggressive substances in the concrete, either chloride ions, see e.g. [4-6], or carbon dioxide, see e.g. [7], leading to initiation of corrosion. Models dealing with the propagation of reinforcement corrosion include often the impact of environmental conditions on the corrosion behaviour; see e.g. [8-10]. To the authors' knowledge, all of the proposed models treat either the initiation or propagation phase of reinforcement corrosion in concrete structures explicitly.

The present paper introduces a physio-chemical model, which is capable of simulating both initiation and propagation of reinforcement corrosion. To demonstrate the potential use of the model, a numerical example is presented, which illustrates the formation of corrosion cells as well as propagation of corrosion in a reinforced concrete structure exposed to chloride. Future development is to include a more detailed thermodynamic description of the electrochemical reactions for the anodic and cathodic regions as well as the impact of defects, such as cracks in the concrete as well as defects along on the concrete-steel interface, on the initiation and propagation phase of the corrosion.

2. EQUATIONS USED IN NUMERICAL MODELLING

The equations describe transport properties (Sections 2.1-2.4) and reinforcement corrosion (Section 2.5).

2.1 Heat transfer

Heat transfer within the concrete domain is described by Fourier's law as follows:

$$\frac{\partial T}{\partial t} = -\frac{\lambda(\theta_l)}{\rho C_p}\nabla T \qquad \text{With} \qquad \lambda(\theta_l) = \lambda_{conc} + \lambda_w \theta_l \tag{1}$$

where, T is the temperature, $\lambda(\theta_l)$ the thermal conductivity of concrete, λ_{conc}, and water, λ_w, depending on the moisture content θ_l, ρ the mass density and C_p the specific heat capacity.

2.2 Moisture transport

Coupled vapour and liquid water flow, which together yields the total moisture flow, is described as follows:

$$\frac{\partial m_{l+v}}{\partial t} = -C_w \frac{\partial p_c}{\partial t} = -\nabla\left(\frac{D_v(\theta_l)}{R_v T}\nabla p_v + K_l(\theta_l)\nabla p_c + \rho_w g\right) \tag{2}$$

where, m_{l+v} is the sum of the water vapour and liquid water content, C_w the moisture capacity, p_c the capillary pressure, D_v the vapour diffusion coefficient, θ_l the moisture content, R_v the gas constant of water vapour, T the temperature, p_v the vapour pressure, K_l the liquid conductivity coefficient, ρ_w the density of water, g the gravity, and t the time. Using capillary pressure as the common driving potential for vapour and liquid water transport, Eq. 2 yields Eq. 3:

$$\frac{\partial m_{l+v}}{\partial t} = -C_w \frac{\partial p_c}{\partial t} = -\nabla\left(\frac{D_v(\theta_l)}{R_v T}\frac{p_{v,sat}\varphi}{\rho_l R_v T}\nabla p_c + K_l(\theta_l)\nabla p_c + \rho_w g\right) \tag{3}$$

where $p_{v,sat}$ is the saturation vapour pressure and φ is relative humidity. The derivation of the mass balance equation for isothermal moisture transport (Eqs. 2 and 3) along with the corresponding constitutive equations can be found in the literature (see e.g., [11-12]).

Furthermore, a more thorough description of the moisture transport model implemented in the present model can be found in [13] along with information on the chosen capillary pressure curve describing the moisture storage [14], vapour transport coefficient and liquid water conductivity [15-17].

2.3 Multi-ion transport

Transport of ions is described by Nernst-Planck equation taking into account transport due to diffusion, migration and convection:

$$\frac{\partial c_i}{\partial t} = \nabla\left(D_i \nabla c_i + z_i u_{mi} F c_i \nabla\varphi - c_i u\right) \tag{4}$$

where c_i is the ionic concentration, D_i the diffusion coefficient, z_i the charge number of the ionic species, u_{mi} the ionic mobility, F Faraday's constant, φ the electric potential and u the

velocity of the solvent. To account for the impact of the moisture content on the diffusion of the various ions, the following relation proposed by [18] is used:

$$D_i\left(S_l\right) = D_i^0 S_l{}^{\beta} \tag{5}$$

where D_i^0 is the free diffusion coefficient in bulk water, S_l the degree of saturation and β a model parameter. Chloride binding is described through an apparent diffusion coefficient for chloride ions as follows:

$$D_{cl,bind}\left(S_l\right) = D_{cl}\left(S_l\right)\frac{1}{1+\alpha_{bind}\left/\theta_l\left(1+\beta_{bind}c_{cl}\right)^2\right.} \tag{6}$$

where α_{bind} and β_{bind} are model parameters

2.4 Oxygen transport

Transport of oxygen within the model is described by a relation proposed by [19] and can be written as follows:

$$D_{O_2} = 1.92\cdot 10^{-6}\theta_{por}\left(1-RH\right)^{2.2} \tag{7}$$

where θ_{por} is porosity and RH the relative humidity.

2.5 Reinforcement corrosion

The electric potential distribution is described by Laplace's equation and Ohm's law is used to determine the rate of dissolution of iron within the model:

$$\nabla^2\varphi = 0 \tag{8}$$

$$i_{corr} = \frac{1}{\rho_{el}}\frac{\partial\varphi}{\partial n} \tag{9}$$

where ρ_{el} is the concrete resistivity and n the direction normal to the steel surface. Butler - Volmer equations are used to describe the electrochemical kinetics for the anodic and cathodic regions of the steel surfaces, respectively. Assuming that the electrochemical reactions take place at separate electrodes and polarization is high, the Butler - Volmer equations can be replaced by Tafel equations for the anodic and cathodic regions. Taking into account the effects of activation and concentration polarization [20-21] the Tafel equations can be written as follows:

$$i_A = i_{0,A}\gamma_A \qquad \text{with} \qquad \gamma_A = \exp\left(\ln 10\frac{\varphi_A-\varphi_{0,A}}{b_A}\right) \tag{10}$$

$$i_C = i_{0,C}\frac{1-\gamma_C}{1+i_{0,C}\left/i_{Lim}\gamma_C\right.} \qquad \text{with} \qquad \gamma_C = \exp\left(-\ln 10\frac{\varphi_C-\varphi_{0,C}}{b_C}\right) \tag{11}$$

where $i_{0,A}$, $i_{0,C}$ is anodic and cathodic exchange current density, respectively, i_{Lim} the limiting current density, φ_A, φ_C the anodic and cathodic potential, respectively, $\varphi_{0,A}$, $\varphi_{0,C}$ the anodic and cathodic equilibrium potential, respectively and b_A, b_C the anodic and cathodic Tafel con-

stant, respectively. Combining Faraday's law with Fick's law, the limiting current density accounting for a lack of oxygen at the cathodic regions of the steel surface can be given as follows:

$$i_{Lim} = \frac{zFD_{O_2}}{\delta} c_{O_2} \tag{12}$$

where δ is the diffusion layer thickness and c_{O2} the oxygen concentration. To account for the impact of temperature on Eq. 10 and 11, the Tafel constants, b_A and b_C, are described as follows [20]:

$$b_A = \frac{RT}{F(1-\alpha_A)} \quad \text{and} \quad b_C = \frac{RT}{F(1-\alpha_C)} \tag{13}$$

where α_A, α_C is the anodic and cathodic charge transfer coefficient, respectively.

To describe the moisture dependence of the concrete resistivity a power law is used in the present model:

$$\rho_{el} = \sqrt[c]{\frac{1/\theta_l - a}{b}} \tag{14}$$

where *a*, *b* and *c* are modelling parameters.

To link corrosion initiation, i.e. the formation of anodic regions at the reinforcement surface, and subsequent propagation of reinforcement corrosion a conditional statement is defined along the reinforcement surface. Since the present model is dealing with chloride-induced corrosion the conditional statement comprises the definition of a critical chloride threshold for elements along the reinforcement surface, which might be defined as follows:

$$BC_{Steel} = \begin{cases} i_A & for \; c_{cl} \geq c_{crit} \\ i_C & c_{cl} < c_{crit} \end{cases} \tag{15}$$

where BC_{steel} defines the boundary condition along the steel surface, c_{cl} is the chloride concentration along the reinforcement and c_{crit} the critical chloride threshold defined along the reinforcement elements. Within the literature varying chloride threshold values can be found, ranging from 0 to around 0.4 % of weight cement [22], mainly influenced by the defects [23-24] present along the reinforcement as well as the electrochemical potential [22]. In the present model, the critical chloride threshold is varied randomly, ranging from 0 to 0.4 % of weight cement, along the reinforcement surface to represent an actual structure with defects present at the concrete steel interface. Also, possible impacts due to corrosion induced damages are not considered.

3. NUMERICAL EXAMPLE

3.1 Geometry and boundary conditions

To illustrate the potential use of the presented model, a simple beam geometry is modelled, see Fig. 1. The applied boundary conditions, i.e. annual variations of relative humidity, temperature, chloride concentration and oxygen concentration at the concrete surface, are given in Fig. 2.

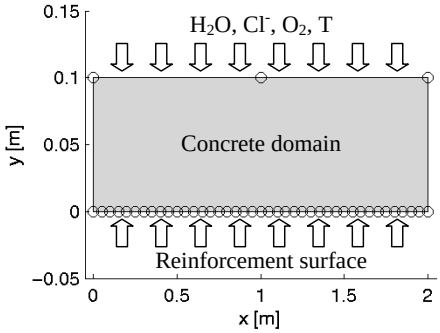

Figure 1: Model geometry with environmental boundary conditions and model domains.

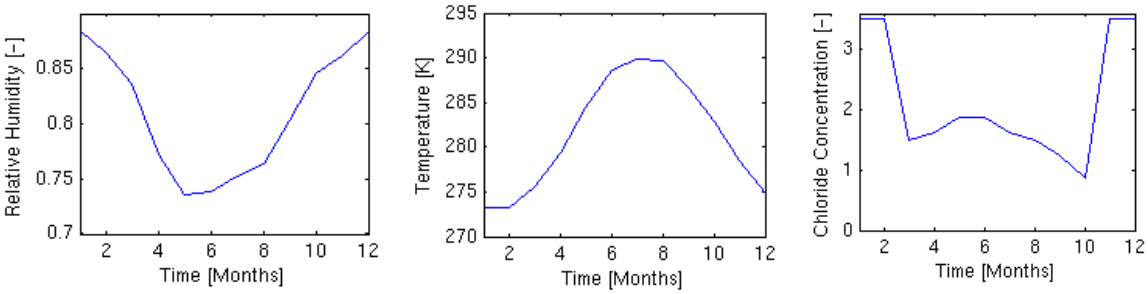

a) b) c)

Figure 2: Environmental boundary conditions applied in the model, annual variation of a) relative humidity, b) temperature and c) chloride ions. The oxygen concentration is assumed to be constant at the concrete surface.

3.2 Material properties

An overview of the most important material properties, for the present numerical example, is given in Fig. 3 and 4. Information on the transport and material properties, i.e. transport coefficients, moisture storage and microstructure is shown in Fig. 3. Oxygen and chloride transport coefficients are presented in Fig.4 along with the electrochemical properties of the steel and concrete.

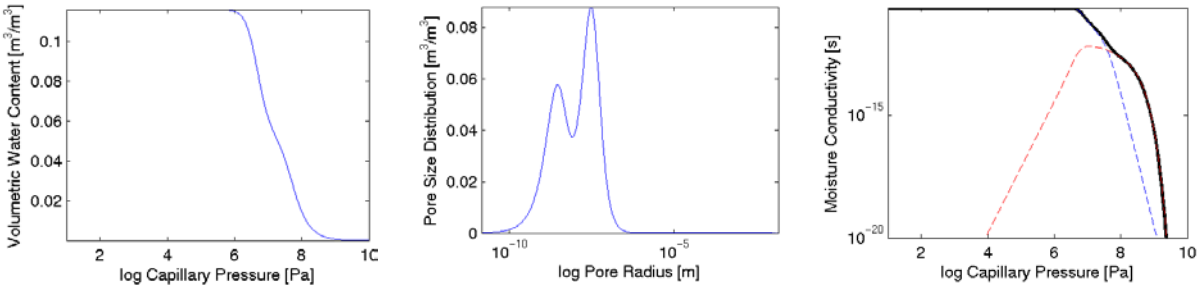

a) b) c)

Figure 3: Moisture transport properties, a) bi-modal moisture storage function, b) pore size distribution (derived from a)) and c) moisture conductivity.

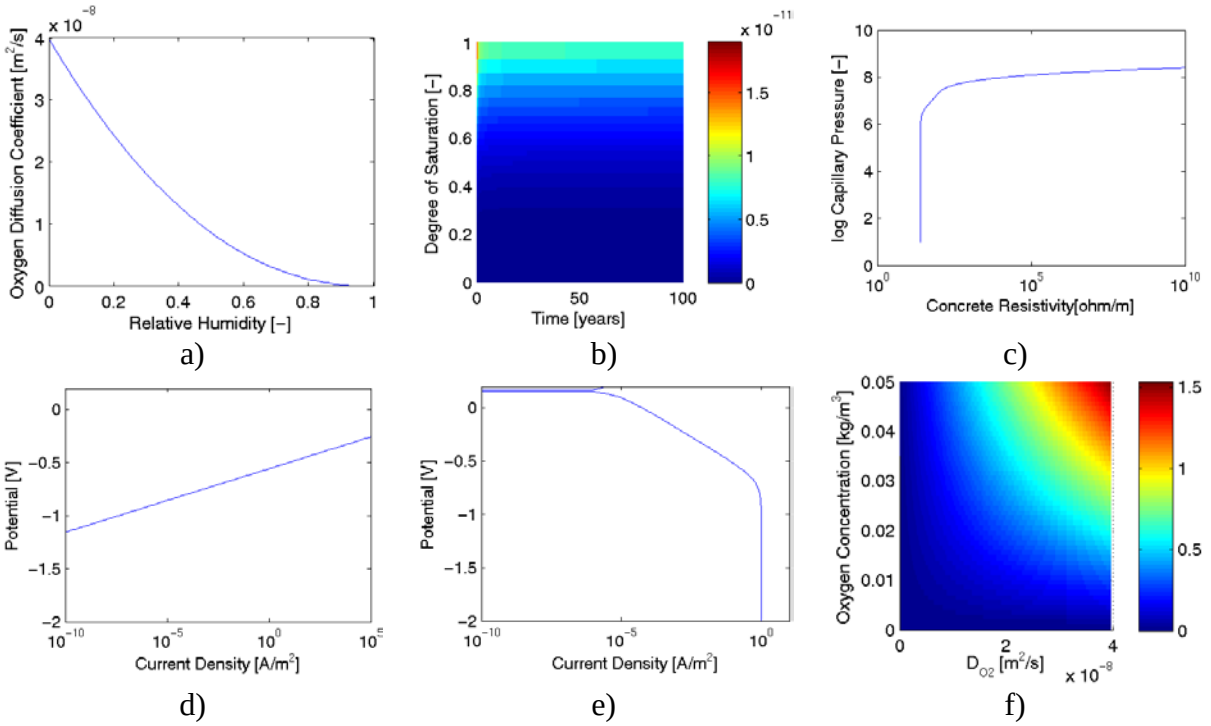

Figure 4: Transport and electrochemical properties, a) oxygen diffusion coefficient, b) chloride diffusion coefficient in [m^2/s], c) concrete resistivity, d) anodic polarization curve, e) cathodic polarization curve and f) limiting current density in [A/m^2].

3.3 Results and discussion

Results of the numerical model are given in Fig. 5 for selected times (in all plots the colours relate to the following times: black - 18.6 years, blue - 21.8 years, red - 24.8 years and green - 37.3 years). Fig. 5 a) illustrates the potential distribution and Fig. 5 c) the chloride concentration together with the defined critical chloride threshold along the reinforcement surface for selected times. From the results presented it can be clearly seen how anodic areas are forming along the reinforcement at different times as the critical chloride threshold is reached.

Fig. 5 b) illustrates the corrosion current density along the reinforcement for the selected times. Finally, the accumulated cross sectional reduction for the worst area of the reinforcement is given for the complete simulation time, i.e. 100 years, in Fig 5 d). It can be seen that within the initial 21 years, no cross sectional reduction is happing, as no corrosion has been initiated yet. After, initiation of corrosion an increase in the cross sectional reduction can be seen, which is mainly influenced by the environmental conditions, i.e. the moisture content and oxygen availability at the reinforcement surface. To illustrate the impact of the annual variations on the cross sectional reduction the subplot in Fig 5 d) gives the results obtained between 30 and 32 years of simulation. The impact of the environmental boundary conditions can be clearly seen in the subplot of Fig. 5 d) as the cross sectional reduction is varying within the selected simulation time. Finally, a significantly reduced corrosion rate can be seen for the last 30 years, since all of the reinforcement is acting anodic and very slow micro cell corrosion is governing the cross sectional reduction now.

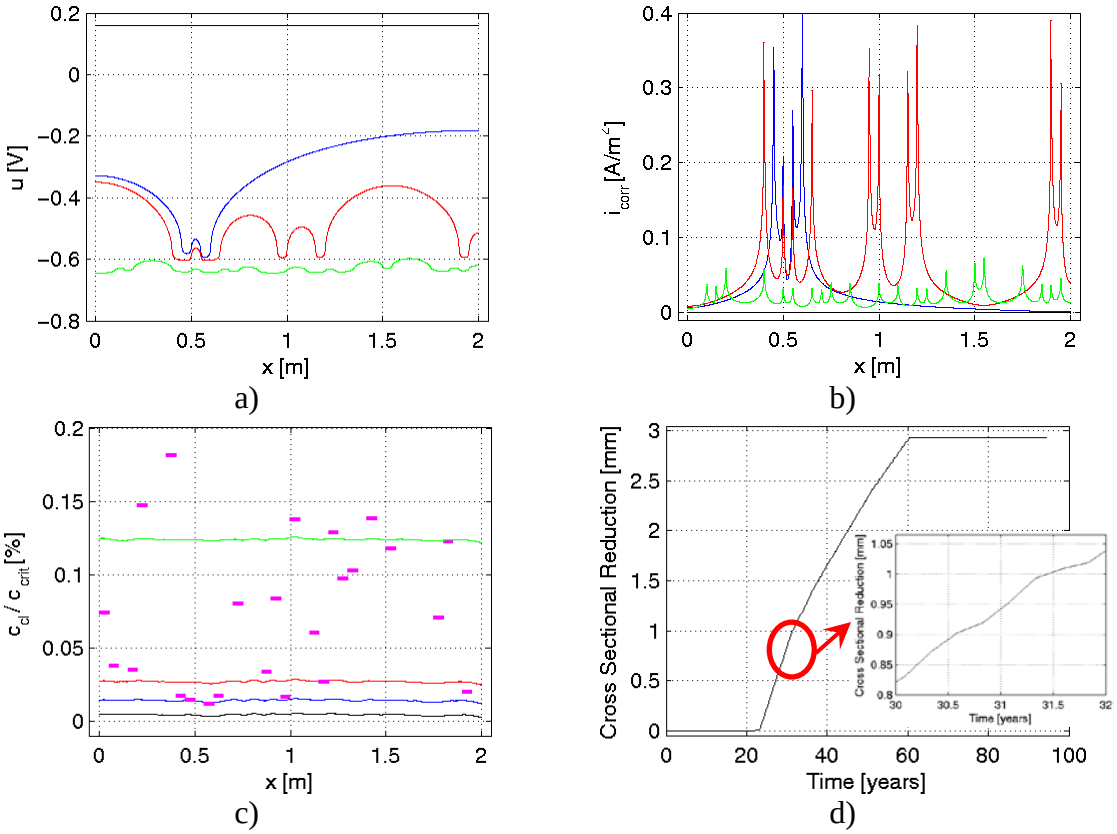

Figure 5: Results from numerical simulation along the reinforcement surface for selected times (black - 18.6 years, blue - 21.8 years, red - 24.8 years and green - 37.3 years), a) potential distribution, b) corrosion current density, c) critical chloride threshold and chloride concentration and d) cross sectional reduction over 100 years of simulation time.

4. CONCLUSIONS

A numerical model was described which allows for simulation of initiation and propagation of reinforcement corrosion in concrete structures. Corrosion is assumed to be initiated once a defined critical chloride threshold is reached causing the formation of anodic and cathodic regions along the reinforcement. Critical chloride thresholds, randomly distributed along the reinforcement surface, link the initiation and propagation phase of reinforcement corrosion. To demonstrate the potential use of the model, an example was given illustrating the impact of environmental boundary conditions on the initiation and propagation of reinforcement corrosion.

Future development is to include a more detailed thermodynamic description of the electrochemical reactions for the anodic and cathodic regions as well as the impact of defects, such as cracks in the concrete as well as defects along on the concrete-steel interface, on the initiation and propagation phase of the corrosion.

ACKNOWLEDGEMENTS

The first author gratefully acknowledges the financial support of Femern Bælt A/S, Sund & Belt Holding A/S and The Danish Agency for Science, Technology and Innovation.

REFERENCES

[1] *fib* Bulletin 34, "Model code for service life design," Int. Fed. structural concrete (fib), 2006.
[2] *fib* Bulletin 55, "Model code 2010," Int. Fed. structural concrete (fib), 2010.
[3] Duracrete, "Probabilistic performance based durability design of concrete structures," The European Union-Brite EuRam III, 2000.
[4] Bastidas-Arteaga, E., et al., "A comprehensive probabilistic model of chloride ingress in unsaturated concrete," Engineering Structures 33 720-730, 2011.
[5] Marsavina, L., et al., "Experimental and numerical determination of the chloride penetration in cracked concrete," Construction and Building Materials 23 264-274, 2009.
[6] Hansen, E. J., et al., "Numerical simulation of reinforced concrete deterioration - Part I: Chloride diffusion," ACI Materials Journal 96 173-180, 1996.
[7] Marques, P. F., et al., "Service life of RC structures: Carbonation induced corrosion. Prescriptive vs. performance-based methodologies," Construction and Building Materials 24 258-265, 2010.
[8] Bazant, Z. P., "Physical model for steel corrosion in concrete sea structures - Application," Journal of the Structural Division 105 1155–1166, 1979.
[9] Isgor, B. O., et al., "Modelling steel corrosion in concrete structures," Materials and Structures 39 291-302, 2006.
[10] Warkus, J., et al., "Numerical modeling of corrosion - Theoretical backgrounds -," Materials and Corrosion 57 614-617, 2006.
[11] Häupl P., et al., "Coupled heat air and moisture transfer in building structures," Int. J. Heat & Mass Transfer 40 1633-1642, 1997.
[12] Philip, J.R., et al., "Moisture movement in porous materials under temperature gradients," Trans. Am. Geophys. Union 38 222-232, 1957.
[13] Pease, B., et al., "Modelling moisture ingress through simplified concrete crack geometries," In: Proceedings of International Congress on Durability of Congress, Trondheim, 2012.
[14] Derluyn, H., et al., "Influence of the nature of interfaces on the capillary transport in layered materials," Const. and Build. Mat. 25 3685-3693, 2011.
[15] Schirmer, R., "Die Diffusionszahl von Wasserdampf-Luftgemischen und die Verdampfungsgeschwindigkeit," VDI Beiheft Verfahrenstechnik 2 170-177, 1938.
[16] Scheffler, G.A., et al., "Whole range hygric material model: Modelling liquid and vapour transport properties in porous media," Int. J. Heat & Mass Transfer 53 286-296, 2010.
[17] Mualem, Y., "A new model for predicting the hydraulic conductivity of unsaturated porous media," Water Resour. Res. 12 513-522, 1976.
[18] Buchwald, A., "Determination of the ion diffusion coefficient in moisture and salt loaded masonry materials by impedance spectroscopy," In: Third international symposium, Vienna, 475-482, 2000.
[19] Papadakis, V. G., et al., "Physical and Chemical Characteristics Affecting the Durability of Concrete," ACI Materials Journal 8 186-196, 1991.
[20] Stern, M., et al., "Electrochemical polarization I. A theoretical analysis of the shape of polarization curves," Journal of the Electrochemical Society, 104 56–63, 1957.
[21] Bardal, E., "Corrosion and Protection," Engineering Materials and Processes, London, UK, Springer, 1st edition, 336 pp., 2004.
[22] Angst, U., et al., "Critical chloride content in reinforced concrete - A review," Cement and Concrete Research 39 1122-1138, 2009.
[23] Nygaard, P.V., et al., "A method for measuring the chloride threshold level required to initiate reinforcement corrosion in concrete," Materials and Structures 38 489-494, 2005.
[24] Buenfeld, N., et al., "Process for the Protection of Reinforcement in Reinforced Concrete," United States Patent 6685822, 2004.

Paper V

” Experimental investigation on the short-term impact of temperature and moisture on reinforcement corrosion”

A. Michel, P. Nygaard & M.R. Geiker

Published in: *Corrosion Science.*

Volume 72, July 2013

ISSN 0010-938X

ELSEVIER

CORROSION SCIENCE

The Journal on Environmental Degradation of Materials and its Control

Editor-in-Chief: G. T. BURSTEIN, University of Cambridge, U.K.

An Official Journal of the Institute of Corrosion

CONTENTS

Contents continued on outside back cover

http://www.elsevier.com/locate/corsci

Corrosion Science 72 (2013) 26–34

Contents lists available at SciVerse ScienceDirect

Corrosion Science

journal homepage: www.elsevier.com/locate/corsci

Experimental investigation on the short-term impact of temperature and moisture on reinforcement corrosion

A. Michel [a,c,*], P.V. Nygaard [b], M.R. Geiker [a,c]

[a] Technical University of Denmark (DTU), Department of Civil Engineering, Kgs. Lyngby, Denmark
[b] Swiss Federal Laboratories for Materials Science and Technology (EMPA), Abteilung Beton/Bauchemie, Dübendorf, Switzerland
[c] Norwegian University of Science and Technology (NTNU), Department of Structural Engineering, Trondheim, Norway

ARTICLE INFO

Article history:
Received 22 May 2012
Accepted 26 February 2013
Available online 7 March 2013

Keywords:
A. Steel reinforced concrete
B. Polarization
C. Atmospheric corrosion

ABSTRACT

In this study, reinforced concrete specimens with and without mixed-in chlorides were conditioned at different relative humidities and subsequently subjected to varying temperatures. Results of the study confirmed that neither temperature nor moisture content have a major impact on the corrosion state and rate of passively corroding reinforcement. For actively corroding reinforcement, a temperature and moisture dependent corrosion rate was observed. The temperature dependency could be described by the Arrhenius equation with moisture dependent activation energies of approximately 10 kJ/mol at 75% RH and 35–40 kJ/mol above 85% RH.

1. Introduction

The design, e.g. water-to-cement ratio and concrete cover, of reinforced concrete structures in aggressive environments is mainly governed by durability issues. In particular, the ingress of aggressive substances, such as chloride ions or carbon dioxide potentially leading to corrosion initiation, is controlling the design of reinforced concrete structures. In sound concrete, the reinforcement is protected by a thin oxide layer, the so-called passive film, which is formed due to the alkaline environment in the concrete [1–4]. However, if this passive film is destroyed active corrosion can initiate. Especially, the penetration of chloride ions through the protecting concrete cover and its accumulation beyond a certain critical concentration can result in the destruction of the passive film [5,6]. Carbonation and the subsequent pH reduction of the concrete due to the penetration of carbon dioxide and depletion of the hydration products may also result in the loss of passivity [7,8].

Once corrosion is initiated, the rate is mainly influenced by a number of material properties and environmental factors. Temperature, concrete resistivity, moisture content, and oxygen availability are considered to be the predominant factors controlling the kinetics of the corrosion process [9,10]; however, corrosion may also take place in oxygen deprived environments [11,12]. A number of studies can be found in the literature dealing with the influence of material properties and environmental exposure on the corrosion state and rate of reinforcement. Among others, studies were conducted on the influence of carbonation, temperature, relative humidity, and resistivity under controlled laboratory conditions, see e.g. [13–16], as well as on-site conditions, see e.g. [17–22]. Although the presented results have contributed to a better understanding of these influencing parameters, the findings are difficult to compare as various materials (e.g. reinforced mortar or concrete samples) with different compositions and geometries were studied. Furthermore, varying electrochemical measuring techniques were applied to determine the corrosion rate and state of embedded reinforcement. Moreover, the quantification of the impact of individual parameters on the kinetics of the corrosion process, such as temperature or relative humidity, may be difficult to determine from studies conducted under on-site conditions. For instance, recent investigations of reinforced concrete specimens exposed to varying environmental conditions concluded, "*Despite numerous analyses of the data, considering the test issues, the concrete states, and so on, no correlation was found between the corrosion rate and the relative humidities. From previous studies no Arrhenius law considering the temperature issue, was found either. In conclusion, it appears that both parameters, temperature and humidity, interact with each other and that this influences the corrosion results.*" [23]. Therefore, it is important to conduct additional studies to aid the evaluation of underlying processes affecting the corrosion rate and state of reinforcement and furthermore help to better understand experimental results and their limitations.

* Corresponding author at: Technical University of Denmark (DTU), Department of Civil Engineering, Kgs. Lyngby, Denmark. Tel.: +45 4525 1656; fax: +45 4588 3282.
E-mail address: almic@byg.dtu.dk (A. Michel).
URL: http://www.dtu.dk (A. Michel).

0010-938X/$ - see front matter © 2013 Elsevier Ltd. All rights reserved.
http://dx.doi.org/10.1016/j.corsci.2013.02.006

To investigate the combined (short-term) impact of temperature and relative humidity on the corrosion process, concrete specimens with partly embedded reinforcement (passively and actively corroding) were conditioned at different relative humidities and subsequently subjected to varying temperatures in this study. Potentiodynamic linear polarization resistance and galvanostatic pulse measurements were used to measure and determine the free corrosion potential, polarization and ohmic resistance. From that, the corrosion rate of each reinforcement bar in the specimens was calculated. The results were finally used to determine the activation energy of the corrosion process and describe the (short-term) impact of temperature and relative humidity on the kinetics of the corrosion process in reinforced concrete.

2. Experimental investigations and set up

For the experimental investigations six concrete specimens, each with ten partly embedded reinforcement bars, were cast from concrete with and without mixed-in chloride, i.e. three specimens with and three specimens without mixed-in chlorides. Upon casting, curing, and preparation, the specimens were placed in three different climate chambers with different relative humidities and temperatures (measurement step 1) given in Table 1, i.e. one specimen with and one specimen without chloride were placed in each of the three climate chambers. Hence, three specimens with passively corroding reinforcement (series S1) and three specimens with actively corroding reinforcement (series S2), corroding at different rates due to the different exposure conditions, were obtained.

Table 1
Relative humidity and temperature for each measurement step. During conditioning (approximately 4 years) the specimens were stored at relative humidities and temperatures given for measurement step 1 (one specimen with passively and one specimen with actively corroding reinforcement bars for each relative humidity).

Relative humidity (%)	Measurement step						Unit
	1	2	3	4	5	6	
75	25	35	50	1	15	25	°C
85	35	25	50	1	15	35	°C
96	15	1	50	35	25	15	°C

After approximately 4 years of constant exposure (measurement step 1 in Table 1), the corrosion state and rate of the reinforcement bars in each of the six specimens was measured. Following this, the temperature in each of the three climate chambers was changed to the value of measurement step 2 (see Table 1) and the corrosion state and rate measurements repeated. The procedure was repeated for all measurements steps given in Table 1 and the combined (short-term) effect of the temperature and relative humidity on the corrosion process determined. Finally, the specimens were split-opened using chisel and hammer to allow for visual inspection of the extent of corrosion along the embedded reinforcement and to determine the carbonation depth.

As the experimental setup was used earlier in a research project on the use of non-destructive electrochemical techniques for monitoring of reinforcement corrosion, parts of the description in this section can also be found in [24]. However, for completeness all details of the experimental work are included and described in the following section.

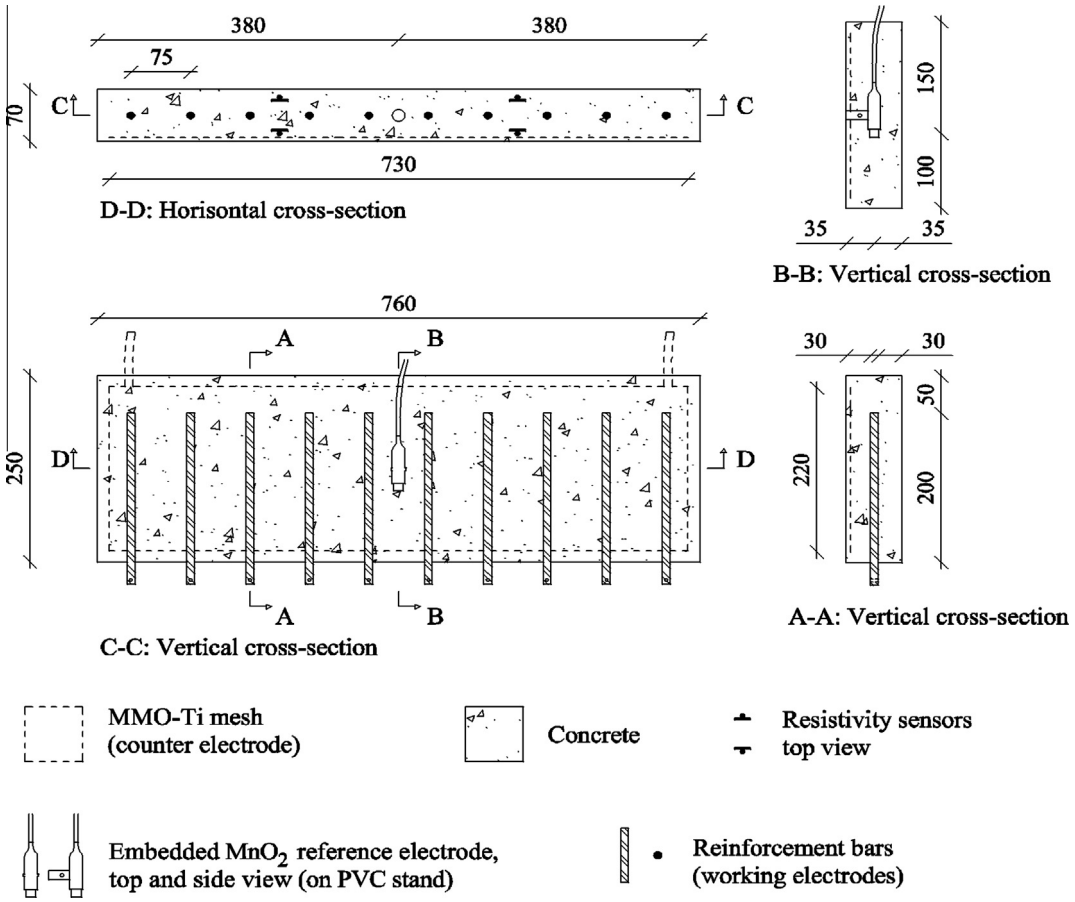

Fig. 1. Geometry of specimens (all measurements are given in mm). From [24].

2.1. Materials and specimen preparation

The geometry of the specimens is shown in Fig. 1. Each specimen consisted of a rectangular concrete specimen (760 mm × 250 mm × 70 mm) with ten smooth carbon steel reinforcement bars (10 mm diameter). Each bar had a length of 230 mm of which 200 mm were embedded in the concrete. The chemical composition of the reinforcement bars is given in Table 2. Along with the reinforcement bars, one mixed metal oxide titanium (MMO-Ti) mesh (730 mm × 220 mm), a manganese dioxide (MnO_2) reference electrode, and two resistivity sensors were embedded in each specimen. The MMO-Ti mesh was placed 5 mm below the concrete surface (250 mm × 760 mm) and the reference electrode centred in the specimen. Both resistivity sensors, each consisting of two parallel rectangular MMO-Ti plates (20 mm × 75 mm) with a spacing of 35 mm, were placed symmetrically around the centre of the specimen with a distance of 300 mm between the sensors. An accurate positioning of the reinforcement bars and the resistivity sensors was secured fixing these in the bottom plate of the mould whereas the reference electrode and the MMo-Ti mesh were mounted on PVC inserts fixed to the mould side.

Concrete with a w/c of 0.5 was used for the study. The mix composition and selected concrete properties of series S1 and S2 are given in Tables 3 and 4, respectively. To initiate corrosion in specimens of series S2, i.e. with actively corroding reinforcement bars, 4% chloride by mass of cement was added. The cement used was Danish white Portland cement (CEM I 52.5 R). The chemical composition of the cement can be found in [24]. Prior to casting, all reinforcement bars were cleaned in a 10% inhibited hydrochloride acid until they appeared with a uniform grey surface, rinsed in distilled water, and dried with hot air.

Table 2
Chemical composition of reinforcement bars (mass%). Tested in accordance with [25].

C	Si	Mn	P	S	Cr	Mo	Ni	Al
0.11	0.18	0.67	0.006	0.019	0.027	0.001	0.029	0.002
Co	Cu	Ti	V	Sn	Mg	N	Fe[a]	
0.014	0.005	0.002	0.009	0.002	0.0002	0.0	99	

[a] Calculated as remained.

Table 3
Concrete mix design.

Property		Amount	Unit
Cement		325	kg/m^3
Water		162.5	kg/m^3
Aggregate	0–4 mm	814	kg/m^3
Aggregate	4–8 mm	1079	kg/m^3
Paste content		26.6	vol.%
Chloride	Series S1	0	mass% of cement
	Series S2	4	mass% of cement

Table 4
Selected fresh and hardened properties of the concrete mixes used for the specimens.

Property	Method	Series		Unit
		S1	S2	
Slump	EN 12350-2 [26]	70	50	mm
Air content	EN 12350-7 [27]	2.1	2.0	vol.%
Density, hardened	EN 12390-7 [28]	2280	2380	kg/m^3
Compressive strength	EN 12390-3 [29]	40	35	MPa
Electrical resistivity	APM 219 [30]	7.6	4.0	kΩ cm

After casting, the specimens were kept in the moulds for one day, demoulded, sealed in plastic, and cured at 20 ± 2 °C. After curing for 28 days, the specimens were unwrapped and an epoxy coating applied to the four edges and the first 30 mm of each protruding reinforcement bar. This was done to prevent corrosion on the protruding parts of the embedded reinforcement bars and to obtain a unidirectional moisture transport through the surfaces parallel to the reinforcement bars. Prior to application of the epoxy coating, the protruding ends of the reinforcement bars were sandblasted to remove any cement paste and corrosion products formed during curing. The specimens were then placed in climate chambers at initial relative humidities and temperatures given in Table 1 (measurement step 1) and kept under these conditions until testing was started.

2.2. Testing

After approximately 4 years of conditioning at the initial temperatures and relative humidities (measurement step 1), testing was started measuring the free corrosion potential, E_{corr}, and the polarization resistance, R_P, of all reinforcement bars in the six specimens. Following this, the temperature in each of the three climate chambers was changed to the values of measurement step 2 (Table 1) and the specimens allowed to equilibrate for three days before E_{corr} and R_P measurements were repeated. This procedure was repeated for all measurement steps. In the following section, the procedures used to measure E_{corr} and R_P are described in detail.

2.2.1. Determination of free corrosion potential, polarization and ohmic resistance

Each measurement was initiated monitoring the free corrosion potential, E_{corr}, of the selected reinforcement bar versus the MnO_2 reference electrode. When a potential drift smaller than 3 mV over a 3 s period was obtained, the free corrosion potential, E_{corr}, was measured for a period of 2 s. For the determination of the ohmic resistance, R_Ω, a current pulse, I_{CE}, of 25 μA and 4 s duration was then applied from the counter electrode polarizing the reinforcement bar in cathodic direction. Due to the double layer capacitance (with a low-pass filter behaviour in electronic terms), the resistance over the double layer is zero at the very moment the current is applied. Thus, the non-controlled potential response corresponds to the ohmic resistance (Ohm's law). Before and during the current pulse, the potential of the reinforcement was measured with a frequency of 10 Hz. After the pulse, the potential was actively drawn to the initially measured free corrosion potential, E_{corr}, (measured as average of the 2 s period). Additional details on the application of the galvanostatic pulse technique to determine the ohmic resistance can be found in e.g. [31,32].

As the point between the almost vertical potential drop, E_Ω, (caused by the ohmic resistance, R_Ω) and the subsequent potential transient, E_P, i.e. the charging curve, could not be determined with sufficient precision, the ohmic potential drop, E_Ω, was estimated as follows. The ohmic potential drop, E_Ω, was determined subtracting the mean free corrosion potential, E_{corr} (recorded during the 2 s before applying the pulse), from the mean of the potential values recorded during the first half second after initiating the pulse. The ohmic system resistance, R_Ω, was then determined using Ohm's law.

The potentiodynamic linear polarization resistance measurement was then started polarizing the reinforcement 15 mV in cathodic direction versus the free corrosion potential, E_{corr}, after which the reinforcement was polarized 30 mV in anodic direction, i.e. to a value 15 mV more positive than the free corrosion potential, E_{corr}. In both cathodic and anodic direction, a sweep rate of 10 mV per minute was used. During the measurement, the polarization current was recorded for each mV with a resolution of

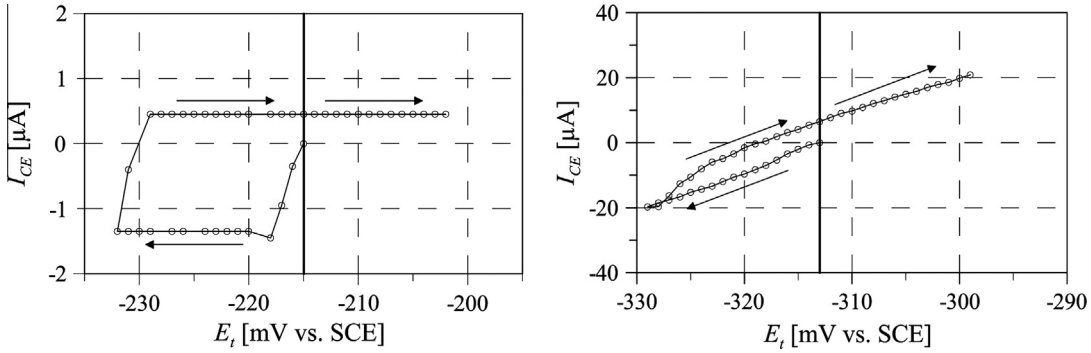

Fig. 2. Typical polarization curves from potentiodynamic linear polarization resistance measurements on passively (left) and actively (right) corroding reinforcement bars in specimens of series S1 and S2, respectively.

50 nA. Typical polarization curves obtained from the measurements on the passively and actively corroding reinforcement bars are presented in Fig. 2, left and right graph, respectively.

For the actively corroding reinforcement bars in series S2, where very similar anodic and cathodic polarization curves were observed (i.e. a relatively small hysteresis, see Fig. 2, right graph) the polarization resistance, R_P, was calculated using data from the anodic polarization curve only, i.e. from −15 mV to +15 mV versus the free corrosion potential, E_{corr}. After compensating the recorded potentials for the ohmic resistance, R_Ω, determined prior to the measurement (see above) a straight line was fitted to the anodic polarization curve (current as function of the potential). The polarization resistance, R_P, was then calculated as the reciprocal slope of the fitted line multiplied with a steel area, A, of 62.8 cm^2, corresponding to the reinforcement length of 20 cm and diameter of 1 cm.

The same mathematical procedure was used for polarization curves obtained from the passively corroding reinforcement bars of series S1. However, due to the observed hysteresis between the cathodic and anodic polarization curves (see Fig. 2, left graph), only the linear part of the anodic polarization curve from approximately −13 mV to +15 mV versus the free corrosion potential, E_{corr}, was used in the calculation. This part of the polarization curve was assumed to give the best approximation of the polarization resistance, R_P. The assumption was based on the work in [33], in which the current response of passively corroding steel to a triangular potential sweep was considered.

Finally, the corrosion current densities, i_{corr}, were calculated from the determined polarization resistances, R_P, using the Stern-Geary equation [34] given in Eq. (1). For the passively corroding reinforcement bars (series S1), a proportionality factor, B, of 52 mV was used, whereas a value of 26 mV was used for the actively corroding reinforcement bars (series S2) [35]:

$$i_{corr} = \frac{B}{R_P A} \quad (1)$$

Upon analysing all measurements, the mean and standard deviation of the R_P and i_{corr} values were calculated for the reinforcement bars in each specimen omitting values deviating more than three standard deviations from the mean.

2.2.2. Impact of temperature on moisture state

As saturated salt solutions were used for maintaining the relative humidities in the climate chambers, a variation was expected when the temperatures were varied. In the climate chamber with a relative humidity (RH) of 75%, sodium chloride was used, for which a variation between 74% and 75% RH was expected within the applied temperature range of 1–50 °C [36]. Higher variations were anticipated for the climate chambers where potassium chloride (85% RH at 25 °C) and potassium nitrate (94% RH at 25 °C) were used. The relative humidity was expected to vary from 81% to 88% RH and 85% to 96% RH for the investigated temperatures for potassium chloride and potassium nitrate [36], respectively. However, due to the relatively short duration at each temperature step the moisture content in the concrete specimens at the depth of the reinforcement bars was assumed not to be affected by the variations.

3. Results and discussion

Experimental results on the combined (short-term) impact of varying temperature and relative humidity on the corrosion process of passively and actively corroding reinforcement bars are presented in the following. Results include information on the free corrosion potential, polarization and ohmic resistance, corrosion current density, and activation energy. For all specimens the mean values of measurements on ten reinforcement bars are presented along with standard deviations. In addition, with measurement steps 2–6 (see Table 1) measurement step 1 is presented for all results. Finally, results of destructive visual investigations are presented including the extent of corrosion along the embedded reinforcement bars and carbonation depth.

3.1. Visual observations

After the electrochemical measurements were finalised, destructive visual investigations were performed on a number of specimens to investigate the carbonation depth and extent of corrosion along the embedded reinforcement bars. The carbonation depth was measured by means of the pH indicator phenolphthalein, which was applied to a freshly broken concrete surface. To open the test specimens, a 15 mm deep notch was cut and subsequently the test specimens were split-opened using chisel and hammer. Results for a specimen of series S1 (75% RH and 25 °C for approximately 4 years) are presented in Fig. 3 indicating that only the outer layer of the concrete cover was carbonated. Based

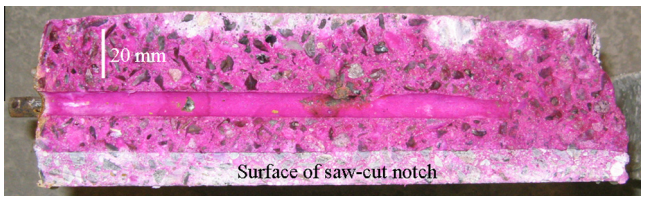

Fig. 3. Carbonation depth (indicated by lighter colour) of specimen exposed to 75% RH and 25 °C for approximately 4 years.

Fig. 4. Passively corroding reinforcement bar of series S1 (96% RH and 15 °C for approximately 4 years). Please note: Rebar was bent during removal from specimen.

Fig. 5. Actively corroding reinforcement bars of series S2, exposed to (a) 75% RH and 25 °C, (b) 85% RH and 35 °C, and (c) 96% RH and 15 °C for approximately 4 years.

on the results presented in Fig. 3, it was assumed that the remaining test specimens were carbonated to a similar extent or less (in case of storage in higher relative humidities or lower temperatures hindering the ingress of carbon dioxide and thereby the carbonation process).

In addition, test specimens of series S1 and S2, i.e. passively and actively corroding, were split-opened, the reinforcement bars removed, and the extent of reinforcement corrosion investigated. Exemplary results of a passively corroding reinforcement bar of series S1 are presented in Fig. 4. No signs of corrosion were found along the reinforcement bar surface (for all storage conditions, see Table 1), which is in agreement with the electrochemical measurements presented in the proceeding sections. Exemplary reinforcement bars retrieved from specimens of series S2 are given in Fig. 5. For all storage conditions, signs of active corrosion were found. Specimens that were exposed to relative humidities of 85% and 96% showed signs of extensive general corrosion along the entire reinforcement bar (see Fig. 5b and c). In contrast to specimens stored at 85% and 96% RH, distinct anodic and cathodic regions were found along the reinforcement bar surface of specimens exposed to 75% RH (see Fig. 5a), although 4% chloride by mass of cement were added to the concrete mix (see Table 3). Visual examination of 10 reinforcement bars concluded that approximately 30–50% of the reinforcement bar surface was corroded. Based on the visual observations, the corroding area for specimens of series S2 was adjusted [37] to determine the corrosion current density from linear polarization resistance measurements (see Eq. (1)). For specimens of series S2 conditioned at 85% and 96% RH, a corroding area of 62.8 cm^2 was assumed, while a corroding area of approximately 30 cm^2 was assumed for specimens conditioned at 75% RH.

3.2. Free corrosion potential

Results of the free corrosion potential, E_{corr}, measurements are given in Figs. 6 and 7 for specimens with passively and actively corroding reinforcement bars, respectively. To convert the free corrosion potentials from mV_{MnO2} to mV_{SCE}, 152 mV were added to the measured free corrosion potentials [1]. The influence of junction potentials, which may be created at interfaces between solutions of different composition (chloride content, pH, etc.) due to varying ion mobility of ions present, was assumed to be negligible with respect to the variability of the measured and presented corrosion potentials.

E_{corr} values between approximately −250 and −150 mV_{SCE} were measured for the passively corroding reinforcement bars, which is

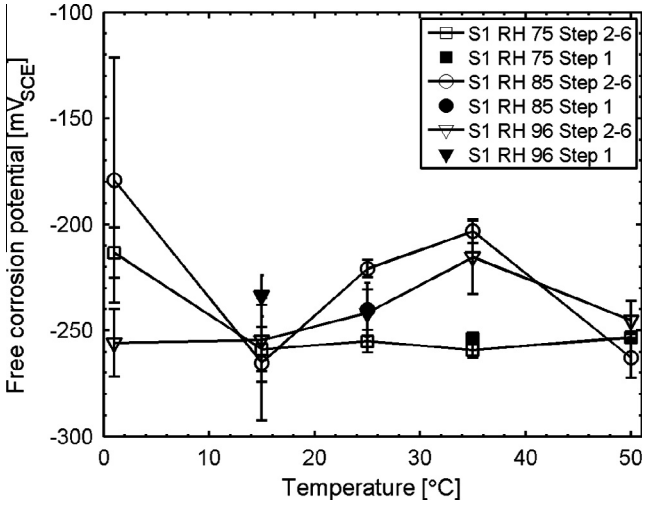

Fig. 6. Free corrosion potential, E_{corr}, at different temperatures and relative humidities for passively corroding reinforcement bars (series S1).

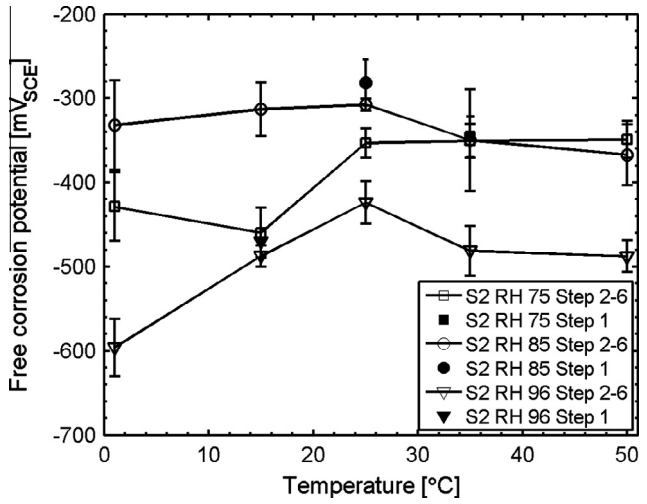

Fig. 7. Free corrosion potential, E_{corr}, at different temperatures and relative humidities for actively corroding reinforcement bars (series S2).

in agreement with typical E_{corr} values reported in literature for passively corroding reinforcement, see e.g. [11,38]. More negative corrosion potentials, in the range from −600 to −300 mV_{SCE}, were obtained for the actively corroding reinforcement bars of series S2. Similar values have been reported in the literature for actively corroding reinforcement, see e.g. [39,40]. No considerable influence of either temperature or relative humidity on the free corrosion potentials, E_{corr}, of the actively and passively corroding reinforcement was seen.

3.3. Polarization resistance

The polarization resistances, R_P, determined from potentiodynamic linear polarization resistance measurements are given in Figs. 8 and 9. Results for the passively corroding reinforcement bars are shown in Fig. 8 with values ranging from approximately 500 to 2500 kΩ cm^2. No systematic influence of either temperature or moisture was observed for passively corroding reinforcement bars embedded in specimens of series S1.

Significantly lower R_P values were obtained for actively corroding reinforcement bars ranging from 20 to 200 kΩ cm^2 as shown in

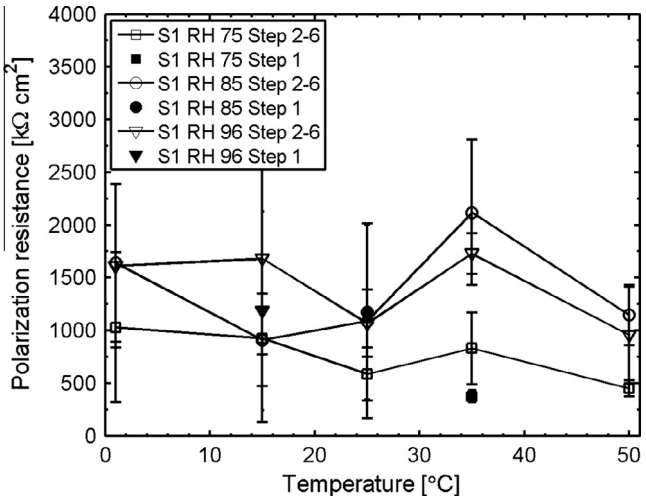

Fig. 8. Polarization resistance, R_p, at different temperatures and relative humidities for passively corroding reinforcement bars (series S1).

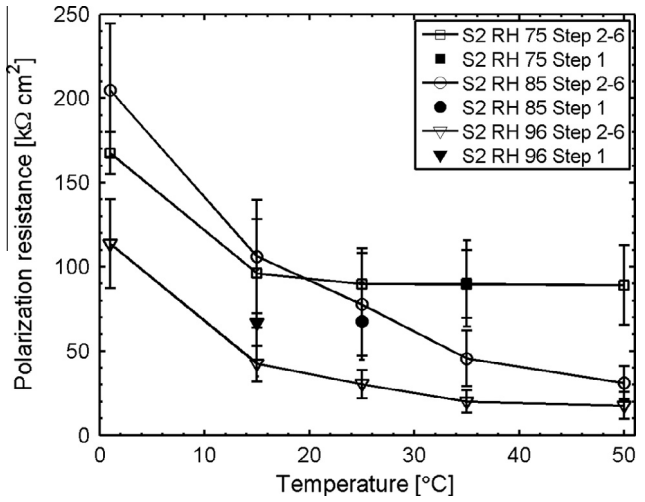

Fig. 9. Polarization resistance, R_p, at different temperatures and relative humidities for actively corroding reinforcement bars (series S2).

Fig. 9. In contrast to the passively corroding reinforcement bars, a continuous decrease of the polarization resistance, R_P, was observed for all actively corroding reinforcement bars (see Fig. 9) with increasing temperature. Furthermore, a moisture dependent behaviour was seen for the actively corroding reinforcement (series S2); with increasing relative humidity, a decrease in the polarization resistance, R_P, was observed.

3.4. Ohmic resistance

The ohmic resistances, R_Ω, determined from galvanostatic pulse measurements for actively corroding reinforcement bars are shown in Fig. 10. No ohmic resistances were determined for passively corroding reinforcement bars (series S1). However, as the polarization resistance, R_P, is much higher than R_Ω, for specimens of series S1 (see Fig. 9), it can be assumed that the introduced error in the uncompensated R_P and i_{corr} values is negligible, see e.g. [24,41].

For all actively corroding reinforcement bars (series S2), a temperature and moisture dependent behaviour of the ohmic resistance, R_Ω, was observed. For specimens conditioned at 75% relative humidity, R_Ω values ranging from approximately 35 to 80 kΩ cm^2 were measured. Moreover, for specimens conditioned at 85% and 96% relative humidity, R_Ω values between 25 and 60 kΩ cm^2 and 15 and 40 kΩ cm^2 were obtained, respectively.

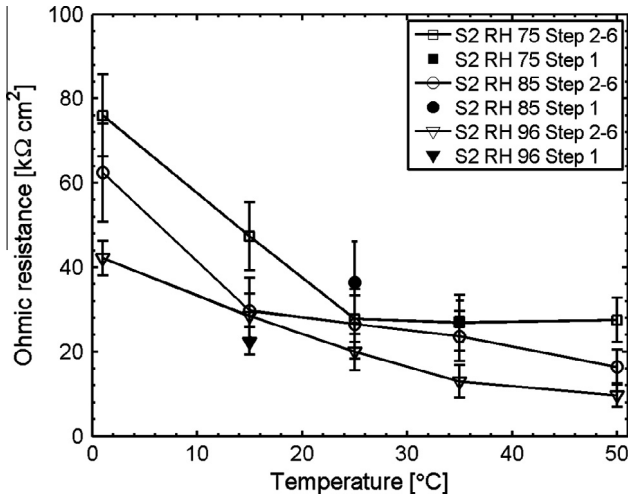

Fig. 10. Ohmic resistance, R_Ω, at different temperatures and relative humidities for actively corroding reinforcement bars (series S2).

3.5. Corrosion current density

Results of the calculated corrosion current density, i_{corr}, for passively and actively corroding reinforcement bars are given in Figs. 11 and 12, respectively. For the passively corroding reinforcement bars (series S1) corrosion current densities, i_{corr}, in the range from 0.05 to 0.15 μA/cm^2 were determined. Similar values have been proposed in the literature for passively corroding reinforcement, see e.g. [41–43]. Further, no influence of either temperature or relative humidity on the corrosion current density, i_{corr}, of the passively corroding reinforcement bars (series S1) was found.

For the actively corroding reinforcement bars (series S2), an increase in corrosion current density, i_{corr}, with increasing temperature was observed for specimens conditioned at 85% and 96% relative humidity, see Fig. 12. No considerable increase in i_{corr} was observed for actively corroding reinforcement bars embedded in the specimen conditioned at 75% relative humidity. Corrosion

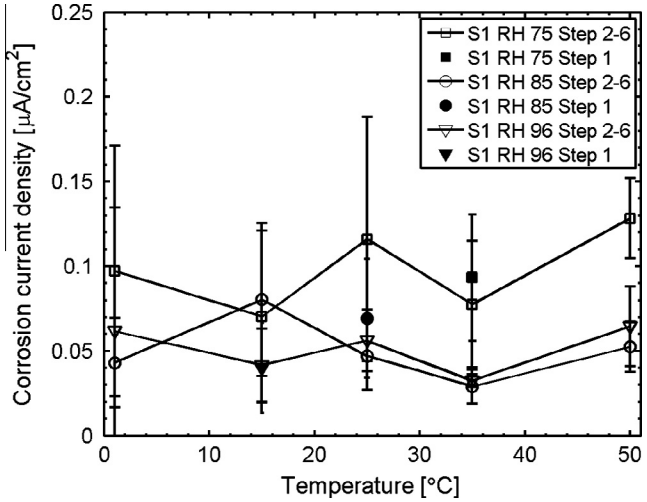

Fig. 11. Corrosion current density, i_{corr}, at different temperatures and relative humidities for passively corroding reinforcement bars (series S1).

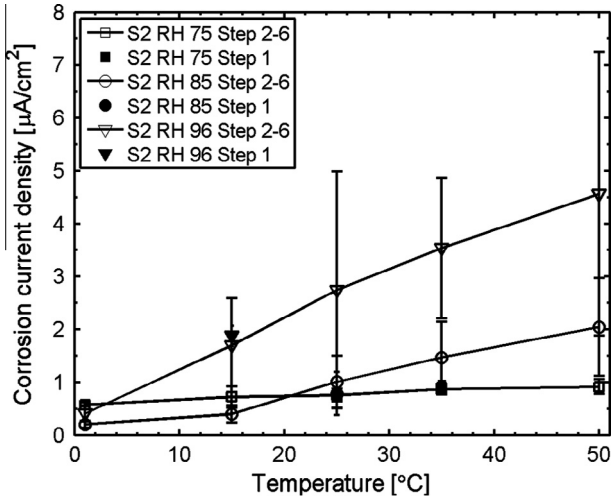

Fig. 12. Corrosion current density, i_{corr}, at different temperatures and relative humidities for actively corroding reinforcement bars (series S2).

current densities, i_{corr}, from approximately 0.5 to 0.9 µA/cm^2 were obtained for reinforcement bars of the specimen conditioned at 75% relative humidity. Higher corrosion current densities, i_{corr}, were obtained for reinforcement bars embedded in specimens conditioned at 85% and 96% relative humidity, with values ranging from 0.2 to 2 µA/cm^2 and 0.2 to 4.5 µA/cm^2, respectively. The determined corrosion current densities for the actively and passively corroding reinforcement bars were in good agreement with the trends observed by the destructive visual observations. No signs of active corrosion were found in specimens of series S1, i.e. passively corroding reinforcement bars. Signs of active corrosion were found for all reinforcement bars embedded in specimens of series S2. Considerable higher signs of active corrosion were observed for specimens conditioned at 85% and 96% relative humidity compared to reinforcement bars embedded in the specimen conditioned at 75% relative humidity.

In addition, the calculated i_{corr} values for the actively corroding reinforcement bars (series S2) are plotted against the corresponding ohmic resistances, R_Ω, and presented in Fig. 13. A good correlation between i_{corr} and R_Ω was only found for the specimen conditioned at a relative humidity of 96%. For the other actively corroding reinforcement bars, no distinct correlation between i_{corr} and R_Ω was found for the temperatures and relative humidities investigated in this study. The results presented in Fig. 13 indicate that R_Ω is inadequate as a single quantitative parameter to describe the corrosion rate. For instance, for an ohmic resistance, R_Ω, of approximately 27 kΩ cm^2 corrosion current densities in the range from approximately 0.2 to 2.2 µA/cm^2 were obtained depending on the temperature and relative humidity. To determine the corrosion current density, the impact of individual parameters, such as temperature and relative humidity, on the kinetics of the corrosion process must be considered [13,15] and the rate controlling process(es) identified. In the present study, it is assumed that the corrosion rate may be governed by (a) activation polarization (of anode or cathode), which arises when the half-cell reaction at the metal-electrolyte interface itself is hindered (i.e. the mass or charge transfer through the electrical double layer is hindered), (b) resistance polarization, which is caused by the electrolyte, passive film or other materials that may provide a significant ohmic resistance or (c) a combination of activation and resistance polarization. To identify the rate controlling mechanism(s) for actively corroding reinforcement bars, the activation energy was calculated and is presented in the following section.

3.6. Activation energy of reinforcement corrosion

To determine the activation energy of the corrosion process for actively corroding reinforcement bars (series S2), results of the corrosion current densities, i_{corr}, are presented in an Arrhenius plot as illustrated in Fig. 14, where the natural logarithm of i_{corr} is plotted against the inverse of the temperature.

For actively corroding reinforcement bars, linear correlations between the calculated logarithm of i_{corr} and the reciprocal of the temperature were found (see Fig. 14). The calculated activation energies for the tested specimens are presented in Table 5 along with values reported in the literature. From Table 5 it can be seen that the results obtained in the present study are of the same order of magnitude as values reported in the literature. The scatter in the presented values (experimental data and literature) may be attributed to various measurement techniques, parameters, and setups used to determine the electrochemical properties of the specimens (linear polarization technique, sweep rates, commercial devices, etc.) and the assumptions made to determine the corrosion rate

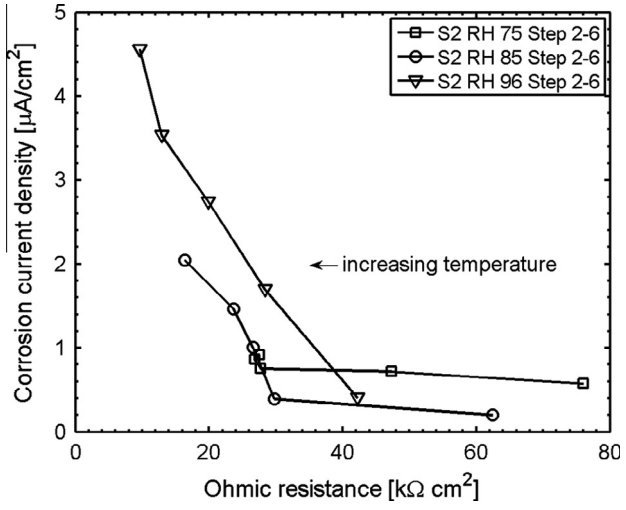

Fig. 13. Corrosion current density, i_{corr}, as a function of the ohmic resistance, R_Ω, at different temperatures and relative humidities for actively corroding reinforcement bars (series S2).

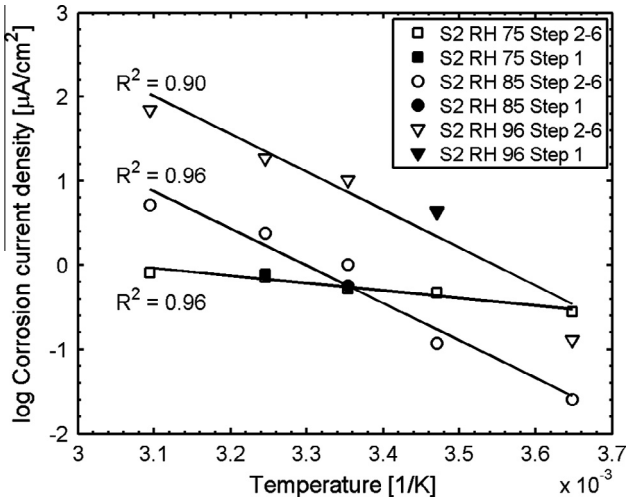

Fig. 14. Arrhenius plot at different temperatures and relative humidities for actively corroding reinforcement bars (series S2).

Table 5
Determined activation energies for actively corroding reinforcement bars (series S2) along with results reported in the literature.

Source	RH (%)	T (°C)	S2 (active) (kJ/mol)
Present study	75	1–50	7
	85	1–50	37
	96	1–50	39
Raupach [15]	70	20–61	32
	88	20–61	40
Bertolini and Polder [18]	80	12–30	30
López et al. [16]	90	0–50	29
	100	0–50	33

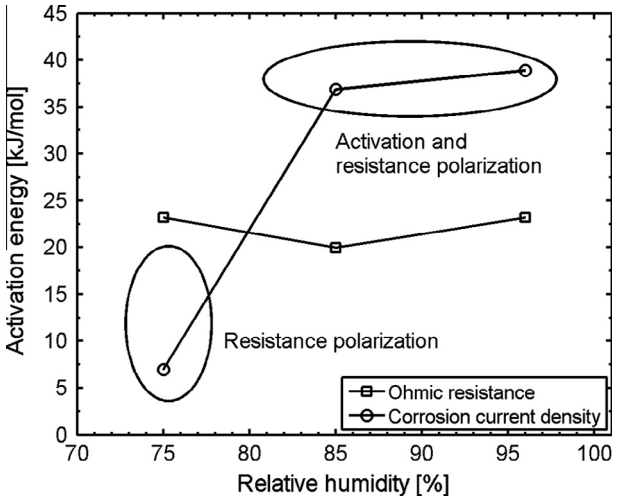

Fig. 15. Activation energy of i_{corr} and R_{Ω} as a function of relative humidity for actively corroding reinforcement bars (series S2).

(e.g. corroding area and B-values). Results from the present study (see Table 5), indicate, however, a moisture dependent behaviour of the activation energy for actively corroding reinforcement. Between 70% and 85% relative humidity, a steep increase in activation energy is observed, whereas above 85% relative humidity an almost constant activation energy is maintained.

The moisture dependency of the activation energy may be explained by the influence of different polarization mechanisms (activation and resistance polarization) [13,15]. Fig. 15 illustrates the determined activation energies of the corrosion current density, i_{corr}, along with the activation energies of the ohmic resistance, R_{Ω}. Results presented in Figs. 13 and 15 indicate that the activation energy of the corrosion process can be divided into two areas. At lower relative humidities (below approximately 80%), the corrosion process appears to be mainly controlled by resistance polarization, i.e. the concrete resistivity. No considerable increase in corrosion rate was observed for the specimen conditioned at 75% relative humidity although the ohmic resistance decreased due to increasing temperature (see Fig. 10). Similar observations were reported in e.g. [9]. For higher relative humidities (above approximately 80%), the results presented in Figs. 13 and 15 indicate that the corrosion rate is controlled by both resistance and activation polarization. With further decreasing ohmic resistance, activation polarization is assumed to become more important, i.e. it will take over as governing/limiting mechanism.

4. Summary and conclusions

In this study, specimens with partly embedded reinforcement bars conditioned at different relative humidities (75%, 85%, and 96%) were subjected to different temperatures, i.e. 1, 15, 25, 35, and 50 °C. Throughout the exposure period galvanostatic pulse and potentiodynamic linear polarization resistance measurements were performed. The electrochemical measurement techniques allowed for determination of the free corrosion potential, polarization and ohmic resistance, and corrosion rate. The calculated corrosion rates were used to determine the activation energy of the corrosion process and allowed for identification of rate controlling mechanisms.

No considerable impact of temperature and relative humidity on the corrosion rate of passively corroding reinforcement bars was found, which is in agreement with previously presented studies in the literature. Further, no considerable influence of the relative humidity and temperature on the electrochemical properties, i.e. free corrosion potential and polarization resistance, was observed for the passively corroding specimens. In contrast to passively corroding reinforcement bars, temperature and moisture dependent behaviour was observed for corrosion current density, polarization, and ohmic resistance of actively corroding reinforcement bars. The determined corrosion current densities for the actively and passively corroding reinforcement bars were in good agreement with the trends observed by the destructive visual observations. For actively corroding reinforcement bars, signs of active corrosion were found for all specimens. Considerable higher signs of active corrosion were observed for specimens conditioned at 85% and 96% relative humidity compared to reinforcement bars embedded in the specimen conditioned at 75% relative humidity. The observed temperature dependency could be described by the Arrhenius equation with a moisture dependent activation energy. For 75% relative humidity, an activation energy of approximately 10 kJ/mol was obtained in the present study. Above 85% relative humidity activation energies in the range of 35–40 kJ/mol were determined. The moisture dependency of the activation energy may be explained by the influence of different polarization (control) mechanisms (activation and resistance polarization). For lower relative humidities, the corrosion process appears to be governed by resistance polarization while with increasing relative humidity the corrosion current density is controlled by a combination of activation and resistance polarization.

Acknowledgements

The first author gratefully acknowledges the financial support of Femern Bælt A/S, Sund and Bælt Holding A/S and The Danish Agency for Science, Technology and Innovation as well as COIN (COncrete INnovation centre, www.coinweb.no) and its partners for facilitating the research behind this paper. Furthermore, the authors acknowledge the support of BSc students Anker Henriksen and Burak Demirci, DTU.

References

[1] E. Bardal, Corrosion and Protection. Engineering Materials and Processes, first ed., Springer, London, 2004.
[2] C. Andrade, P. Merino, X. Novoa, M. Perez, L. Soler, Passivation of reinforcing steel in concrete, Mater. Sci. Forum 192–194 (1995) 891–898.
[3] A. Poursaee, C. Hansson, Reinforcing steel passivation in mortar and pore solution, Cem. Concr. Res. 37 (2007) 1127–1133.
[4] P. Sandberg, Chloride Initiated Reinforcement Corrosion in Marine Concrete, PhD thesis, Lund Institute of Technology, Lund, Sweden, 1998.
[5] M. Montemor, A. Simoes, M. Ferreira, Chloride-induced corrosion on reinforcing steel: from the fundamentals to the monitoring techniques, Cem. Concr. Comp. 25 (2003) 491–502.
[6] M. Raupach, Chloride-induced macrocell corrosion of steel in concrete – theoretical background and practical consequences, Constr. Build. Mater. 10 (1996) 329–338.
[7] K.Y. Ann, S.-W. Pack, J.-P. Hwang, H.-W. Song, S.-H. Kim, Service life prediction of a concrete bridge structure subjected to carbonation, Constr. Build. Mater. 24 (2010) 1494–1501.

[8] L.J. Parrott, Study of carbonation-induced corrosion, Mag. Concr. Res. 46 (1994) 23–28.
[9] K. Tuutti, Corrosion of Steel in Concrete, Swedish Cement and Concrete Research Institute, Stockholm, Sweden, 1982.
[10] A.M. Neville, Properties of Concrete, fourth ed., Longman Group Limited, Harlow, 1995.
[11] A. Küter, Management of Reinforcement Corrosion: A Thermodynamical Approach, PhD thesis, Technical University of Denmark, Kgs. Lyngby, Denmark, 2009.
[12] A. Küter, M.R. Geiker, P. Møller, On the application of thermodynamics of corrosion for service life design of concrete structures, in: K. van Breugel, G. Ye, Y. Yuan (Eds.), 2nd International Symposium on Service Life Design for Infrastructures, RILEM Publications SARL, Delft, 2010, pp. 637–644.
[13] G.K. Glass, C.L. Page, N.R. Short, Factors affecting the corrosion rate of steel in carbonated mortars, Corros. Sci. 32 (1991) 1283–1294.
[14] S.G. Millard, D. Law, J.H. Bungey, J. Cairns, Environmental influences on linear polarisation corrosion rate measurements in reinforced concrete, NDT&E Int. 34 (2001) 409–417.
[15] M. Raupach, Effect of temperature on chloride induced steel corrosion in concrete, in: E. Bardal, (Ed.), Advances in Corrosion Control and Materials in Oil and Gas Production: Papers from Eurocorr '97 and Eurocorr '98 (European Federation of Corrosion Publications, 26), Maney Publishing, 1999, pp. 431–438.
[16] W. López, J.A. González, C. Andrade, Influence of temperature on the service life of rebars, Cem. Concr. Res. 23 (1993) 1130–1140.
[17] H.S. So, S.G. Millard, On-site measurements on corrosion rate of steel in reinforced concrete, ACI Mater. J. 104 (2007) 638–642.
[18] L. Bertolini, R. Polder, Concrete Resistivity and Reinforcement Corrosion Rate as a Function of Temperature and Humidity of the Environment, TNO Building and Construction Research, Delft, Netherlands, 1997.
[19] C. Andrade, M. Keddam, X.R. Nóvoa, M.C. Pérez, C.M. Rangel, H. Takenouti, Electrochemical behaviour of steel rebars in concrete: influence of environmental factors and cement chemistry, Electrochim. Acta 46 (2001) 3905–3912.
[20] C. Andrade, C. Alonso, J. Sarria, Influence of relative humidity and temperature on-site corrosion rates, Mater. Constr. 48 (1998) 5–17.
[21] C. Andrade, C. Alonso, J. Sarria, Corrosion rate evolution in concrete structures exposed to the atmosphere, Cem. Concr. Comp. 24 (2002) 55–64.
[22] C. Andrade, A. Castillo, Evolution of reinforcement corrosion due to climatic variations, Mater. Corros. 54 (2003) 379–386.
[23] V. Bouteiller, J.-F. Cherrier, V. L'Hostis, N. Rebolledo, C. Andrade, E. Marie-Victoire, Influence of humidity and temperature on the corrosion of reinforced concrete prisms, Eur. J. Environ. Civ. Eng. 16 (2012) 471–480.
[24] P.V. Nygaard, M.R. Geiker, Measuring the corrosion rate of steel in concrete – effect of measurement technique, polarisation time and current, Mater. Corros. 63 (2012) 200–214.
[25] ASTM E415-99a, Standard Test Method for Optical Emission Vacuum Spectrometric Analysis of Carbon and Low-Alloy Steel, ASTM International, 2005.
[26] DS/EN 12350-2, Testing Fresh Concrete – Part 2: Slump Test, European Committee for Standardization, 2002.
[27] DS/EN 12350-7, Testing Fresh Concrete – Part 2: Air Content – Pressure Methods, European Committee for Standardization, 2002.
[28] DS/EN 12390-3, Testing Hardened Concrete – Part 3: Compressive Strength of Test Specimens, European Committee for Standardization, 2002.
[29] DS/EN 12390-7, Testing Hardened Concrete – Part 3: Density of Hardened Concrete, European Committee for Standardization, 2002.
[30] APM 219, Concrete Testing – Hardened Concrete, Electrical Resistivity, AEC laboratory, Denmark, 1996.
[31] B. Elsener, Corrosion rate of steel in concrete – measurements beyond the Tafel law, Corros. Sci. 47 (2005) 3019–3033.
[32] B. Elsener, O. Klinghoffer, T. Frølund, E. Rislund, Y. Schiegg, H. Böhni, Assessment of reinforcement corrosion by means of galvanostatic pulse technique, in: A. Blankvoll (Ed.), International Conference Repair of Concrete Structures: From Theory to Practice in a Marine Environment, Norwegian Road Research Laboratory, 1997, pp. 391–398.
[33] C. Gabrielli, K. Keddam, H. Takenouti, The relationship between the impedance of corroding electrode and its polarisation resistance determined by a linear voltage sweep technique, Electrochim. Acta 24 (1979) 61–65.
[34] M. Stern, A.L. Geary, Electrochemical polarisation, i. a theoretical analysis of the shape of polarisation curves, J. Electrochem. Soc. 104 (1957) 56–63.
[35] C. Andrade, J.A. Gonzalez, Quantative measurements of corrosion rate of reinforcing steel embedded in concrete using polarisation resistance measurements, Werkst. Korros. 29 (1978) 515–519.
[36] DS/EN 12571, Hygrothermal performance of building materials and products. Determination of hygroscopic properties, European Committee for Standardization, 2000.
[37] A. Poursaee, C. Hansson, The influence of longitudinal cracks on the corrosion protection afforded reinforcing steel in high performance concrete, Cem. Concr. Res. 38 (2008) 1098–1105.
[38] B.J. Pease, M.R. Geiker, H. Stang, J. Weiss, The design of an instrumented rebar for assessment of corrosion in cracked concrete, Mater. Struct. 38 (2011) 1259–1271.
[39] P. Schießl, Zur Frage der zulässigen Rissbreite und der erforderlichen Betondeckung im Stahlbetonbau unter besonderer Berücksichtigung der Karbonatisierung des Betons, Deutscher Ausschuss für Stahlbeton, pp. 255, 1976 (in German).
[40] B. Elsener, C. Andrade, J. Gulikers, R. Polder, M. Raupach, Half-cell potential measurements – potential mapping on reinforced concrete structures, Mater. Struct. 36 (2003) 461–471.
[41] S.G. Millard, K.R. Gowers, R.P. Gill, Practical field measurement of reinforcement corrosion in concrete using linear polarisation methods, Brit. J. NDT 34 (1992) 444–452.
[42] H. Arup, The mechanisms of protection of steel by concrete, in: A.P. Crane (Ed.), Corrosion of Reinforcement in Concrete Construction, Ellis Horwood Limited, Chichester, 1983, pp. 151–157.
[43] J.A. Gonzalez, A. Molina, M.L. Escudero, C. Andrade, Errors in the electrochemical evaluation of very small corrosion rates – i. polarisation resistance method applied to corrosion of steel in concrete, Corros. Sci. 25 (1985) 917–930.

Paper VI

” Debonding at the Concrete/steel Interface in Reinforced Concrete Beams - Experimental Investigations: Part I”

A.O.S. Solgaard, A. Michel & H. Stang

Submitted to: *Materials and Structures.*

Debonding at the Concrete/steel Interface in Reinforced Concrete Beams - Experimental Investigations: Part I

Anders Ole Stubbe Solgaard [1&2]

Alexander Michel[2]

Henrik Stang[2]

1 COWI A/S Denmark, Kgs. Lyngby Denmark

2 Department of Civil Engineering, Technical University of Denmark, Kgs. Lyngby Denmark

Phone: +45 4525 5033

Fax: +45 4588 3282

aos@byg.dtu.dk

www.byg.dtu.dk

Abstract

The majority of degradation problems of reinforced concrete structures is related to corrosion of embedded reinforcement. Steel reinforcement is protected against depassivating substances such as Cl^- by the concrete cover, which acts as a physical barrier. However, due to mechanical loading cracks are often formed in the concrete cover and the ingress of hazardous substances is increased which in most cases lead to reduced durability of the embedded reinforcement. To take this into account in the re-assessment of concrete structures and the susceptibility of reinforcement corrosion it is of vital importance to analyse the relationship between the damage of the confining concrete and the formation of corrosion cells along the reinforcement. The most common approach previously used has been to establish a correlation between damage in the concrete cover and susceptibility has focused on the relationship between the crack width at the concrete surface and corrosion initiation along reinforcement. However, these models have proven insufficient and therefore other parameters affecting the corrosion initiation have been analysed. The present paper presents experimental observations by photogrammetry on the load-induced debonding at the concrete/steel interface, viz. slip and separation for different cementitious composites like plain concrete and fibre reinforced concrete. The scope of these investigations is to analyse the extent of damage at the concrete/steel interface for various concrete compositions, with difference fracture mechanical properties. The results from the experimental observations clearly show that the debonding at the concrete/steel interface and the crack propagation in the concrete cover are reduced significantly by the addition of fibres to the concrete. This could potentially be used guidelines for Service Life Design of reinforced concrete structures where fibre reinforced concrete is used for conventional reinforced concrete structures in order to minimize load-induced damage which could reduce the extent of possible spots for onset of corrosion along the reinforcement.

Keywords: Photogrammetry, Experimental Observations, Service Life Design, Debonding.

Introduction

Corrosion of embedded reinforcement is the main deterioration process of reinforced concrete structures and according to [*Rendell et al., 2002*] 90% of the deterioration problems are related to corrosion of embedded reinforcement. Annually, enormous sums are spent on maintenance and repair of reinforced concrete structures [*Mokhtar et al., 2008*]. Thus, the economical consequences of corrosion of reinforced concrete structures are considerable not only for the owners but also for the users of the structures, and the need for guidelines, concerning design of durable reinforced concrete structures, is urgent. Over the last decades recommendations for service life design (SLD) such as [*DuraCrete, 2000*], [*Fib, 2006*] and [*Darts, 2004*], have become an important tool for civil engineers to ensure that only limited repair is required within a given time frame, the so-called service life, to maintain the structural integrity of the construction. To comply with the aforementioned restrictions it is often specified that corrosion of embedded reinforcement is not allowed.

Reinforcement embedded in sound, un-contaminated concrete is protected against corrosion due to the formation of a passive layer on the surface of the reinforcement caused by the alkalinity (pH~13) of the concrete matrix [*Bertolini et al., 2004*]. However, due to the ingress of de-passivating substances such as eg Cl^-, corrosion of embedded reinforcement may be initiated. The ingress rate of de-passivating substances is increased significantly if cracks are present in the concrete cover as opposed to un-cracked concrete; since cracks act as rapid pathways for the hazardous substances previously explained by eg [*Jacobsen et al., 1996*], [*Wang et al., 1997*], [*Aldea et al., 1999*], [*De Schutter, 1999*], [*Edvardsen, 1999*], [*Rodriguez and Hooton, 2001*], [*Win et al., 2004*] and [*Küter et al., 2005*]. Consequently, the impact of cracks in the concrete cover, originating from eg shrinkage and/or mechanical loading, on the corrosion rate of embedded reinforcement has been the pivot of numerous experimental and numerical investigations eg [*Berke et al., 1993*], [*Schießl and Raupach, 1997*], [*Mohammed et al., 2001*], [*Pease et al., 2006*] and [*Pease, 2010*]. Different proposals for establishing a correlation between the crack mouth opening displacement (CMOD) at the concrete surface and the risk of reinforcement corrosion have been reported in the literature see eg [*Rehm and Moll, 1964*], [*Schießl and Raupach,*

1997] and [*Mohammed et al., 2001*]. Although, good correlations can be made for relatively short exposure, viz. less than approx. 3 years, between crack width and extent of reinforcement corrosion, other factors such as concrete cover thickness and concrete quality seems to have a major influence for longer exposure and some investigations show no correlation at all between crack width and risk of corrosion [*Kennedy, 1956*], [*Francois and Arliguie, 1998*]. In a SLD perspective, it is of vital importance to establish a proper basis for the connection between damage of the concrete cover and the risk of reinforcement corrosion, since service life for large infrastructural structures can be up to 150 years.

Given that the existing correlations concerning crack width and the risk of reinforcement corrosion have proven inadequate for long term predictions other approaches need to be investigated. Tammo suggested that one reason for the poor correlation between crack width and risk of corrosion is that surface crack width is poorly correlated with the crack width at the reinforcement level (due to, among other effects, the formation of concrete cones around the rebar) and that it is this latter crack width, which has the major influence on the risk of corrosion [*Tammo and Thelandersson, 2009a*] and [*Tammo and Thelandersson, 2009b*]. A somewhat similar approach concerns the correlation between the extent of damage at the concrete/steel interface and the risk of reinforcement corrosion. Experimental observations concerning ingress of chloride ions in cracked reinforced concrete have revealed that there is a substantial ingress of Cl^- along the reinforcement next to a concrete crack [*Win et al., 2004*]. Thus corrosion may be promoted along the reinforcement due to defects at the concrete/steel interface because of the increased ingress rate of de-passivating substances. The debonding, viz. slip (along the rebar) and separation (perpendicular to the rebar) at the concrete/steel interface, in reinforced concrete specimens subjected to flexural loading has been experimentally observed by eg Pease et al. [*Pease et al., 2006*] and Pedersen [*Pedersen, 2008*]. Pease et al. [*Pease et al., 2011*] developed an instrumented rebar for the assessment of location dependent open circuit potential measurements along the reinforcement while at the same time having similar mechanical properties as those of conventional reinforcement. Results published in [*Pease et al., 2011*] and [*Pease, 2010*] indicate that the damage at the concrete/steel interface may be linked to the risk of corrosion along the

reinforcement, and is more likely a unique indication of the risk of reinforcement corrosion than the crack width at the concrete surface.

Bearing these observations in mind it was decided to initiate a research program concerning the relationship between load-induced damage of reinforced concrete beams and the risk of corrosion along the reinforcement experimentally and numerically. The research program consists of three parts:

I) Experimental observations on the load-induced damage in reinforced concrete beams.
II) Numerical simulations of this load-induced damage.
III) Experimental observations concerning the correlation between this damage and the extent of corrosion along the reinforcement.

The research program comprises investigations on the influence of the ductility of the concrete on the crack initiation and propagation in the concrete cover and at the concrete/steel interface caused by mechanical loading. The latter has to a certain extent been experimentally investigated by Miyazato et al. [*Miyazato and Hiraishi, 2005*]. The ductility of the concrete is varied by testing different concrete compositions, viz. plain concrete (PC) and steel fibre reinforced concrete (SFRC).

The experimental investigations presented in this paper comprise, photogrammetric analyses of the extent of damage at the concrete/steel interface, viz. slip and separation, and measurements of the crack width at the tensile surface and at the level of the reinforcement as a function of the applied load, ie bullet I. Results from these observations are used for qualitative as well as quantitative descriptions of the formation and propagation of cracks around embedded reinforcement subjected to flexural loading and comparisons of the crack formation in PC and SFRC are presented.

The experimental observations presented in this paper are compared to numerical simulations of this load-induced damage formation in the concrete cover (bullet II). That numerical model, results from the numerical simulations and the comparisons with the experimental data are presented in a separate paper by Solgaard et al. [*Solgaard et al., 2012*].

Having described this load-induced damage formation experimentally (this paper) as well as numerically, [*Solgaard et al., 2012*], the final step of this research program is to describe the correlation between the cracking process and the risk of

corrosion along the embedded reinforcement (bullet III). The risk of corrosion along the reinforcement is measured by the use of a so-called instrumented rebar and the experiments are similar to those described by Pease et al. [*Pease et al., 2011*]. Results from these investigations are related to numerical simulations concerning the load-induced damage in the concrete cover to analyse the relationship between damage and risk of corrosion. Hence, fracture mechanical properties of the reinforced concrete beams are correlated to electrochemical observations of reinforcement corrosion. The experimental results concerning the risk of corrosion along reinforcement embedded in cracked concrete (PC or SFRC) and the correlation to the damage formation are presented by Michel et al. [*Michel et al., 2012*].

It is the authors' opinion that knowledge of the relationship between the crack width at the surface (CMOD) and at the level of the reinforcement (COD), and the corresponding damage along the concrete/steel interface is of utmost importance for the understanding of the risk of corrosion along embedded reinforcement. Moreover cross-disciplinary models combining fracture mechanical properties of reinforced concrete with electrochemical properties of the (steel) reinforcement allows for a new approach concerning service life design of reinforced concrete structures in the civil infrastructure. Results from the present paper may help to increase understanding of the aforementioned relationships, which potentially could lead to an optimization in terms of durability and sustainability of reinforced concrete structures.

Description of load induced damage along concrete/steel interface

Damage at the concrete/steel interface associated with tensile loading has been experimentally investigated by eg Goto [*Goto, 1971*] and is explained in the following from Figure 1. Damage along the reinforcement consists of two components, viz. slip and separation. Slip relates to the displacement discontinuity between the reinforcement and the surrounding concrete *parallel* to the reinforcement, while separation corresponds to the displacement discontinuity between the reinforcement and the surrounding concrete *perpendicular* (in the surface-plane) to the reinforcement. Slip and separation along the reinforcement are formed when the chemical adhesion between the reinforcement and the surrounding concrete is broken corresponding to the shear stress between reinforcement and concrete reaching a certain value.

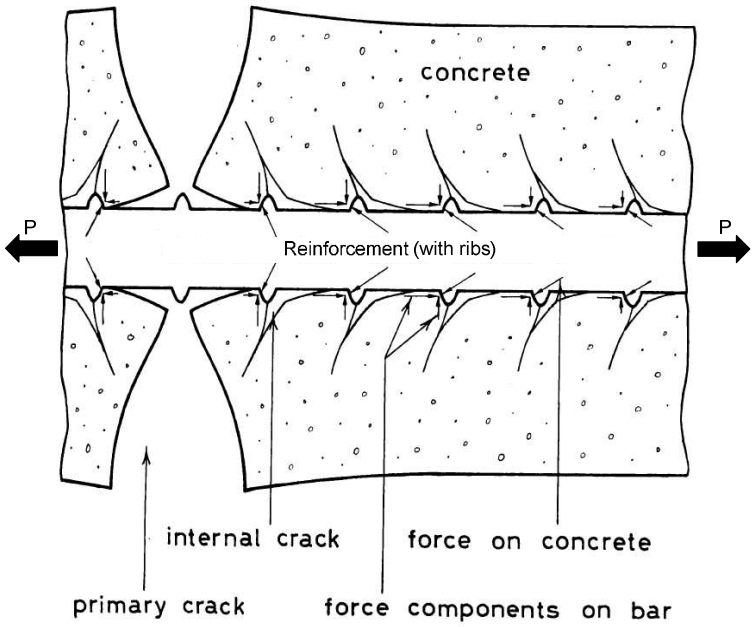

Figure 1: Schematic illustration of damage and cracking at concrete/steel interface under tensile loading. After [*Goto, 1971*].

Besides the slip and separation between the reinforcement and the surrounding concrete, which are formed when the concrete cracks, secondary cracks are formed, initiated from internal cracks (see Figure 1) and eventually resulting in concrete cones around the reinforcement (not shown in Figure 1) as presented by eg Tammo and Thelandersson [*Tammo and Thelandersson, 2009a*].

The deformations of the reinforced concrete associated with the applied tensile loading result in the formation of a primary transverse crack through the concrete cover, cf. Figure 1. The primary transverse crack is wider at the tensile surface, than at the level of the reinforcement due to – if the cracks are bending cracks, the crack opening profile, and – the restraining effect of the reinforcement and internal cracks and/or concrete cones formed at the ribs of the reinforcement [*Tammo and Thelandersson, 2009a*]. Secondary cracks through the concrete cover (not shown in Figure 1) may form from the internal cracks depending on the concrete cover thickness, the concrete quality and the load level among other factors [*ACI, 2001*]. The internal cracks are caused by the transfer of concentrated (compressive) load between the reinforcement and the surrounding concrete.

The bonding behaviour between reinforcement and concrete has been investigated numerically and experimentally and described in the literature as seen in the following. An overview of the topic is given in eg [*Fib, 2000*]. Experimental observations mainly concern the bond-behaviour of reinforcement embedded in PC [*Pedziwiatr, 2009*] [*Broms, 1965*]. The bond of conventional reinforcement embedded in SFRC has also been evaluated [*Ezeldin and Balaguru, 1990*], [*Rostásy and Hartwicht, 1988*]. Various models, either analytically or numerically based, for the bond-slip relationship are described in the literature [*Dörr, 1980*] and [*Schaefer, 1975*] of which some of the models show good correlation with experimental results. However, the bulk part of the existing experimental observations concerning the properties of the bond-slip relationship for reinforced concrete subjected to tensile loading is based on indirect measurements of the deformations between reinforcement and concrete. The aforementioned indirect measurements of the bond-slip relationship have been carried out eg by measuring the deformations at the surface of the investigated specimen while measuring the displacement of the reinforcement during loading and subsequently relate these deformations to slip at the concrete/steel interface. However, in order to relate these experimental observations a vast amount of assumptions, such as the overall mechanical response of the interface are required, before a so-called inverse analyse of the bond-slip can be carried out. Consequently, it is difficult to conclude on these observations as the results rely on the aforementioned assumptions. The experimental technique applied in this study, viz. photogrammetric analyses, allows for deformation measurements (eg cracks and

damage) within the micro range, viz. smaller than observable with the naked eye, and the technique is explained in more detail in a later section.

Description of experimental studies

The experimental observations presented in the paper concern direct measurements of the load induced damage in reinforced concrete specimens subjected to 3 point bending test (3PBT). These observations allow for:

- Measurements of the crack initiation and propagation at the concrete tensile surface due to applied flexural loading.
- Measurements of the slip and separation at the concrete/steel interface during loading.

The experimental observations are carried out for PC, 0.5 vol.-% and 1.0 vol.-% SFRC to quantify the possible beneficial effect on the crack- and damage formation from the addition of steel fibres. The fracture mechanical properties of those concrete compositions were determined from companion specimens (without conventional reinforcement) to those specimens used for the experimental observations described in this paper, cf. Figure 2. Those specimens were subjected to, three point bending tests according to standards [*Rilem, 2002*] and [*EN 14651, 2001*]. The fracture mechanical properties of the three concrete compositions have been determined by the use of inverse analysis of the experimental results. The procedure for inverse analysis described by Skoček and Stang [*Skoček and Stang, 2010*] was adapted for the analyses, and the experimental and numerical results are given in the results section.

The test matrix for the photogrammetric measurements is given in Table 1, along with the naming convention used for the specimens in the present paper.

Table 1: Test matrix for photogrammetric experiments.

	Concrete composition		
	PC	SFRC	
Fibre fraction [vol.-%]	0.0	0.5	1.0
	MSA3	**MSA8**	**MSA11**

The materials, specimens and experimental procedures of the research program are given in the following.

Materials and specimens

The experimental program comprises specimens cast from PC and SFRC (0.5 and 1.0 vol.-%). The mix designs for the three different mix compositions are shown in Table 2:

Table 2: Mix composition for the three mix designs (assumed s.s.d. of aggregates).

Constituent	Density	PC		SFRC 0.5 vol.-%		SFRC 1.0 vol.-%	
	[kg/m^3]	[kg/m^3]	[m^3/m^3]	[kg/m^3]	[m^3/m^3]	[kg/m^3]	[m^3/m^3]
Cement	3100	375	0.121	375	0.121	375	0.121
Water	1000	156	0.156	156	0.156	156	0.156
Sand	2540	760	0.299	755	0.297	750	0.295
Gravel	2625	56	0.021	56	0.021	56	0.021
Stones	2615	1025	0.392	1018	0.389	1011	0.387
Air	-	-	0.010	-	0.010	-	0.010
Fibres	7850	-	-	39	0.005	78	0.010

The cement type used for all mix compositions was Aalborg Portland RAPID cement, CEM I 52,5 N (MS/LA/≤ 2). Further information about the properties of RAPID cement is available in [*AAP, 2011*]. Aggregates were excavated sea bed materials natural rounded corresponding to Class E for sand (0-4 mm), class A for gravel (4-8 mm) and Class A for stones (8-16 mm) according to national standards [*DS-2426, 2004*]. Prior to mixing, the actual water content of the aggregates was determined by the use of the weigh-dry-weigh method in order to adjust the amount of mixing water to maintain the target w/c ratio.

The w/c ratio for the mix compositions given in Table 2 was 0.43. The cement paste content corresponds to 27.7 % of the total volume, and the aggregates corresponds to 71.2 %, 70.7 % and 70.2 % of the volume for PC, 0.5 vol.-% SFRC and 1.0 vol.-% SFRC, respectively.

The fibres used for the SFRC mixes were DRAMIX 65/35, viz. length 35 mm and diameter 0.55 mm (aspect ratio 65) manufactured by Bekaert NV. The fibres are hooked ended and manufactured from cold drawn black steel. More details about the fibres are available in [*Bekaert, 2011*]. As seen from Table 2 the content of aggregates was slightly reduced when fibres were added, compared to PC. The reduction of the aggregate content accounted for the addition of the fibres and the same grading of the aggregates was maintained for all three batches.

A standard pan mixer (capacity 300 l) was used for mixing of concrete.

For plain concrete, aggregates and sand were dry mixed for two min. Subsequently, water was added during the next minute under continuous mixing and the concrete was mixed for additional two minutes. Thus five minutes of total mixing time including two minutes of dry mixing

For SFRC mixes the aggregates and cement were dry mixed for two minutes. Subsequently, water was added under continuous mixing (one minute) and the SFRC was mixed for additional two minutes. Finally, the fibres were added under continuous mixing of the concrete, and this part of the mixing procedure lasted two minutes. Hence the total mixing time was seven minutes.

For each batch a slump test, in accordance with [*DS-12350-2, 2002*], was carried out after mixing. Results from the slump tests are given in Table 4.

The specimens were cast with two rebars (Ø12), viz. one conventional rebar and one special rebar. The arrangement of the conventional reinforcement is seen from Figure 2. The special rebar has mechanical properties similar to those of the instrumented rebar developed by Pease et al. [*Pease et al., 2011*], and has been used since the measurements form the basis of another experimental program concerning the risk of corrosion along the reinforcement in cracked concrete described in a separate paper [*Michel et al., 2012*]. It is assumed that the slightly different mechanical properties of the special rebar compared to those of conventional reinforcement do not have a significant influence on the crack and damage formation, as has been shown by Pease et al. [*Pease et al., 2011*] and this special rebar is not discussed any further in the present paper.

The specimens were cast in 290x310x650 mm moulds and vibrated by the use of a vibrating table. In order to avoid wall effect of fibre orientation, viz. 2D orientation of the fibres caused by the mould sides, the specimens were cast in oversize, and cut to the size of the test specimens prior to mechanical testing. The air content of the fresh concrete batches was measured by the use of a manual pressure meter and results are given in, Table 4.

After casting, the specimens were covered with plastic sheets to avoid moisture evaporation from the fresh concrete surface and left for curing for 24 h at laboratory conditions (20 ± 2 ºC) before demoulding. After demoulding the specimens were stored in lime rich water (minimum 28 days) until cutting and testing. The specimens were cut by the use of a water cooled diamond saw. Cutting of the specimens is presented in Figure 2, illustrating the specimen before

and after cutting. The final dimensions of the specimens were 150 x 140 x 650 mm (h x w x l).

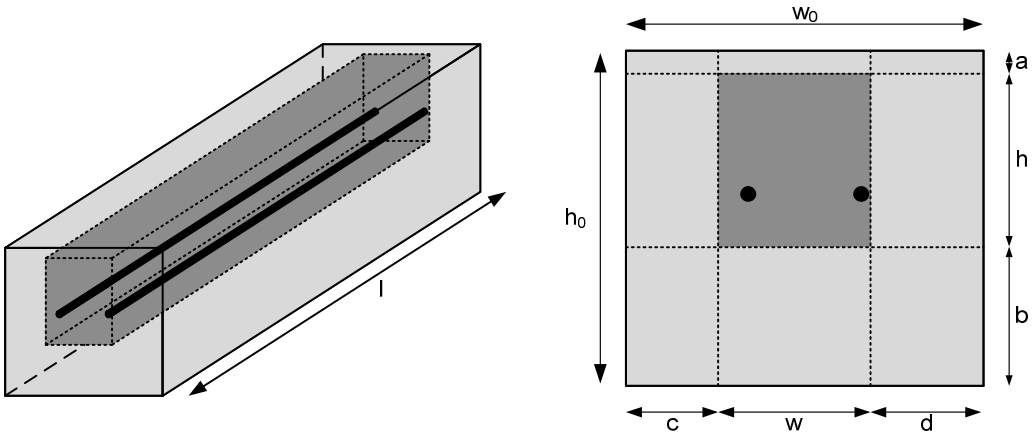

Figure 2: Specimen for photogrammetric observations of load induced damage. Left: Original specimen (light grey) and final specimen after cutting (dark grey). Right: Cross section of original specimen (light grey) and final specimen (dark grey) along with measures. The illustrations are not in scale.

The dotted lines in Figure 2 illustrate the cutting lines, and the dimensions given in the illustration are reproduced in Table 3:

Table 3: Dimensions of specimens before and after cutting.

H_o [mm]	290
w_o [mm]	315
a [mm]	40
b [mm]	100
c [mm]	80
d [mm]	95
h [mm]	150
w [mm]	140
l [mm]	650

The right cutting line shown in the right illustration of Figure 2 is approx. 2 – 4 mm from the rebar. Thus the rebar is covered by a minute concrete cover on the side. This is done in order to avoid damaging the concrete/steel interface during the cutting process.

Experimental Procedures

The experimental procedure and the techniques utilized for the photogrammetric analyses equipment are described in the following. The specimens are 650 mm long, cf. previous description, and the span during mechanical loading was 500 mm.

Photogrammetric measurements

The load-induced damage at the concrete/steel interface (slip and separation) and the initiation and formation of bending cracks in the concrete cover, were measured by the use of photogrammetric equipment monitoring the surface of the specimen. The photogrammetric measurements were carried out on the surface of the specimen with the rebar closest to the vertical surface, viz. the right vertical side of the specimen in Figure 2. The photogrammetric equipment consists of two CCD cameras positioned at the same level as the specimen. The set-up of the photogrammetric equipment is illustrated in Figure 3:

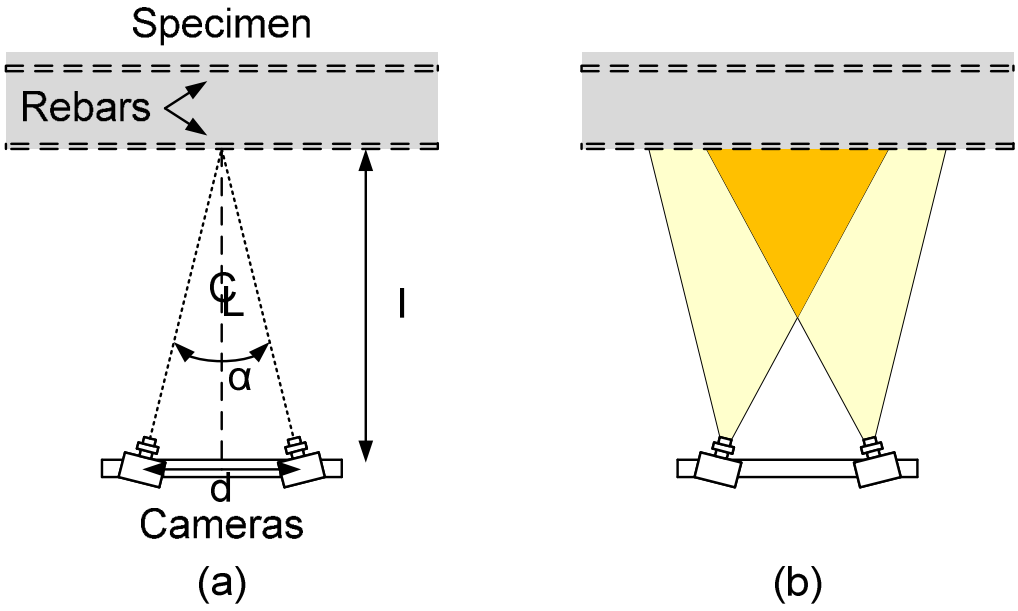

Figure 3: Top-view of set-up of photogrammetric equipment. (a) Alignment of cameras and specimen and (b) monitored surface at concrete specimen. The illustration is not in scale.

The cameras were positioned on a rig parallel to the concrete specimen and at a distance l. The cameras were placed at a mutual distance d and the angle between the cameras was constant α, cf. Figure 3a.

The area of the concrete surface of each camera is indicated with yellow in Figure 3b whereas the part of the concrete surface monitored by both cameras is indicated with orange in Figure 3b.

Prior to the mechanical testing, the monitored surface of the concrete specimen was painted and subsequently a random black pattern was applied, as shown in Figure 4.

Figure 4: Left: Concrete beam mounted in rig. Right: Surface of specimen showing original surface (left) and surface with applied random pattern (right).

The pattern applied to the monitored surface of the specimen was used for the post-processing of the photogrammetric observations; the deformations were calculated from a comparison of the random black pattern at the concrete surface during loading and the same pattern before loading, viz. the so-called reference picture. The frequency of data acquisition was 0.5 Hz.

The area of the specimen monitored by both cameras, was approx. 350 x 150 mm (l x h) and was positioned around the center of the specimen. The resolution of the CCD cameras used for the photogrammetric observations was 2 Megapixel.

Data from the photogrammetric observations were analysed by the use of the commercial available software ARAMIS. The analysis allows deformation and strain measurements to be undertaken in any point in the measurement area after the experiments have been carried out and the deformation and strain fields in the same area can be visualized. Furthermore, the technique allows identification of cracks as zones with localized strain. Further details on the photogrammetric equipment, ie software and the procedure for the subsequent analyses, are given in [*GOM, 2005*].

The reinforced concrete specimens were loaded in a load-controlled set-up, and the output of the experimental observations was corresponding load levels and strain and deformations at the concrete surface.

The slip and separation at the concrete/steel interface were determined by measuring the relative displacement, x and y, respectively, between points directly above and below the reinforcement for all load levels. The slip and separation at the concrete/steel interface were measured in various distances from the centre of the primary bending crack for all load levels.

Results and discussion

Casting of specimens

Results from the casting procedure of the different batches comprise both slump test and measurements of the air content of the fresh concrete. The results are given in Table 4.

Table 4: Measurements of air content and slump for batches.

		PC	**SFRC**	
Fibre content [vol-%]:		**0.0**	**0.5**	**1.0**
Slump [mm]	Average.	49	22	9
	St.dev.	3	6	5
Air [vol-%]	Average.	1.6	1.7	2.1
	St.dev.	0.4	0.6	0.3

It is seen from the results given in Table 4, that the slump is reduced with the addition of fibres. It is generally accepted that the slump is affected by the addition of fibres, where the amount and geometry of the fibres are some of the parameters influencing this phenomenon [*ACI, 1973*].

Concerning the air content of the fresh concrete, it is seen from the results given in Table 4 that there is no significant difference in the air content of the fresh concrete comparing PC and SFRC. In general, the addition of fibres leads to a higher air content and different porosity compared to PC, caused by among other factors, entrapment of air by the randomly dispersed fibres in the fresh concrete. The contradiction between the aforementioned general observations and the present experimental observations may be due to the fact that the SFRC specimens were vibrated for longer time than the PC specimens.

Fracture mechanical properties of concrete compositions

As previously mentioned, the fracture mechanical properties of the concrete compositions given in Table 2 were quantified experimentally from 3PBT. The load-deflection curves from the experimental observations (lines) and the inverse analyses (hollow symbols) are shown in Figure 5.

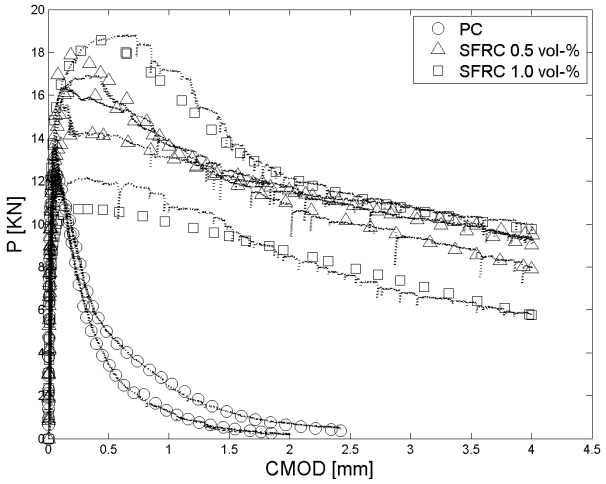

Figure 5: Load-deflection curves for all concrete compositions

Comparing the load-deflection curves for PC, 0.5 vol.-% SFRC and 1.0 vol.-% SFRC, it is clear that the addition of fibres changes the mechanical response significantly. The addition of fibres leads to a more ductile response of the material; viz. the post-peak branch of the P-CMOD relationship is less steep for SFRC as opposed to PC but the addition of fibres does not lead to a general increase in the peak load which is in line with the literature on this subject eg [*Löfgren et al., 2005*]. Furthermore, it is noted that there is a good correlation between experimental data and numerical simulations from inverse analysis.

Results from these inverse analyses cover the fracture energy, G_f, and the tensile strength, f_t, and are given in Table 5.

Table 5: G_f and f_t of the specimens determined by inverse analysis.

Composition	f_t		G_f	
	Average [Mpa]	St.dev. [Mpa]	Average [J/m^2]	St.dev. [J/m^2]
PC	1.8	0.1	569	55
0.5 vol.-% SFRC	1.7	0.1	4700	700
1.0 vol.-% SFRC	1.7	0.6	9000	2800

As seen from Table 5, the addition of fibres does not influence the tensile strength of the material significantly, which corresponds to the aforementioned observation concerning the peak load of the specimens. However, the fracture energy is significantly increased by the addition of fibres due to the post-crack load bearing capacity of SFRC. It is seen that the addition of fibres leads to a higher scatter in the experimental results, which is most pronounced for specimens containing 1.0

vol.-% of fibres. This may be caused by a larger variety in the composition of the materials, viz. decreased homogeneity of the material compared to PC as well as differences in the fibre orientation.

Visualization of the cracking

The deformations and strains are calculated by the use of the ARAMIS software associated with the photogrammetric equipment.

The visualizations given in Figure 6 and Figure 7 show the strain field for specimen MSA8 (SFRC 0.5 vol.-%) for two different load levels, viz. 20 KN and approx. 60 KN determined by the use of the photogrammetric equipment and the associated software. At the crack, "strain" is strictly speaking not an adequate term in this context. However, the illustrations are shown to visualize the positioning and extent of damage at the concrete/steel interface and in the concrete cover. Moreover, the pictures given in Figure 6 – Figure 7 serve as illustrations of the formation of cracks even smaller than observable by the naked eye, viz. in the micro range.

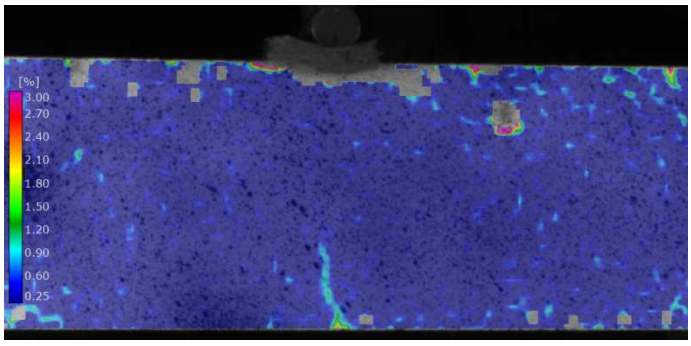

Figure 6: Visualization of the strain field of specimen MSA8 (SFRC 0.5 vol.-%) subjected to approx. 20 KN. CMOD ≈ 0.1 mm.

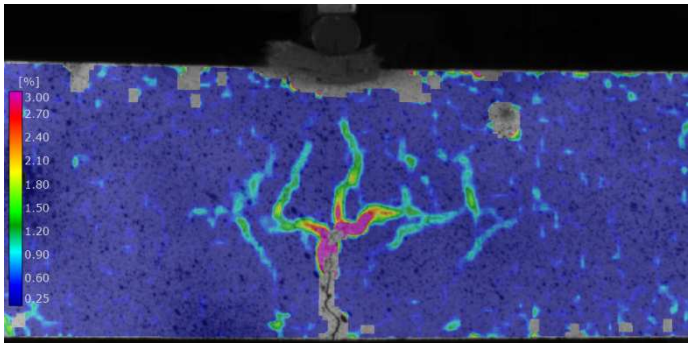

Figure 7: Visualization of the strain field of specimen MSA8 (SFRC 0.5 vol.-%) subjected to approx. 60 KN. CMOD ≈1.4 mm.

The grey areas in the visualizations in Figure 6 and Figure 7 are areas where the strain field cannot be calculated due to deformations exceeding the capacity of the analysis system. However, a thorough evaluation of the results from the photogrammetric analyses has revealed that all data relevant for the present study is available from the experimental observations.

Deformation measurements

The results from the investigations of the slip and separation at the concrete/steel interface are given in the following sub-sections. The naming convention for the specimens used in the following sections appears from Table 1.

The resolution of the photogrammetric equipment, 2 MegaPixel, corresponds to deformation measurements with an accuracy of the measurements being$1x10^{-4}$ times the dimensions of the area of the surface monitored by the cameras cf. the manual of the equipment [*GOM, 2005*]. Previous comparisons between measurements of the width of a crack formed in a concrete specimen during mechanical loading, by the use of a clip gauge and photogrammetric measurements presented in [*Pease et al., 2006*] revealed good correlation between the results obtained from the two different measuring techniques.

Relationship between CMOD and load

The relationships between crack width at the tensile surface of the concrete specimens and applied load are given in the following. Though multiple cracking occurred in most specimens during mechanical loading only results related to the primary bending crack are presented. The primary bending crack has been defined as the first crack being formed. For all specimens the primary bending crack is located at or very close to the centre of the specimen.

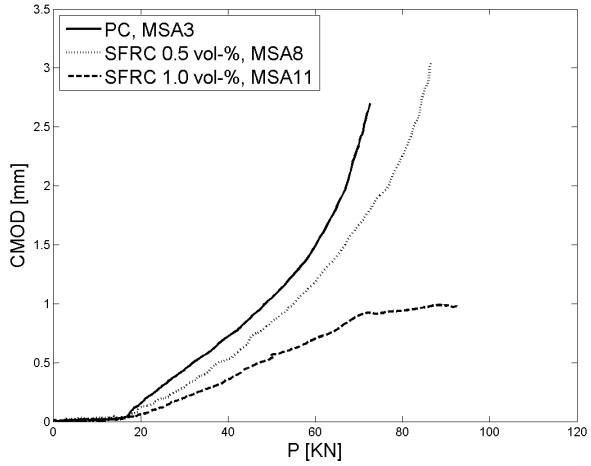

Figure 8: CMOD vs P relationship.

Figure 8 shows that the crack at the tensile surface is initiated at approximately the same load level applied, viz. 18 KN for all concrete compositions. However, once the crack is formed, the increase in crack width as a function of the applied load is significantly reduced for the steel fibre specimens compared to the plain concrete specimen. The reduction in CMOD as function of the load is more pronounced comparing 1.0 vol.-% SFRC with 0.5 vol.-% SFRC than 0.5 vol.-% SFRC with PC, ie 0 vol.-% of fibres.

Relationship between COD and load

The relationship between the crack opening displacement at the level of the reinforcement and the applied load is given in Figure 9:

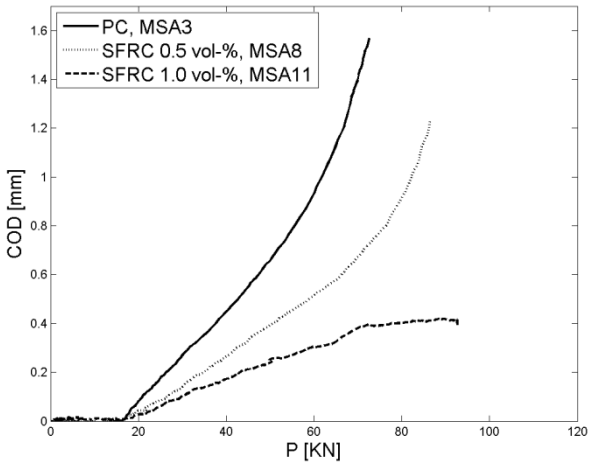

Figure 9: COD vs P relationship.

Figure 9 shows that the crack at the level of the reinforcement is initiated at the same load level for all specimens, viz. approx. 18 KN. Moreover it is seen that the addition of fibres reduce the increase in COD as a function of the applied load significantly.

Comparing Figure 8 and Figure 9 it is seen that once the crack is initiated at the concrete surface it propagates immediately to the level of the reinforcement. The results presented in Figure 8 and Figure 9 indicate that COD is proportional to CMOD. For small values of CMOD (CMOD < 0.3 mm) the same proportionality between CMOD and COD is seen for all the concrete compositions. However, for increasing values of CMOD, the SFRC specimens has a less steep increase in COD compared to PC, since the fibres bridge the crack and enable stress transfer across the crack.

Relationship between slip and load

The results given in Figure 10 – Figure 12 comprise the slip at various locations along the reinforcement as a function of the load applied, whereas the slip along the reinforcement and at the center of the primary bending crack at the reinforcement level is shown in Figure 13 – Figure 15 for selected COD and corresponding load levels. Finally the slip along the reinforcement is selected for all concrete compositions and the same (selected) COD in Figure 16 - Figure 17:

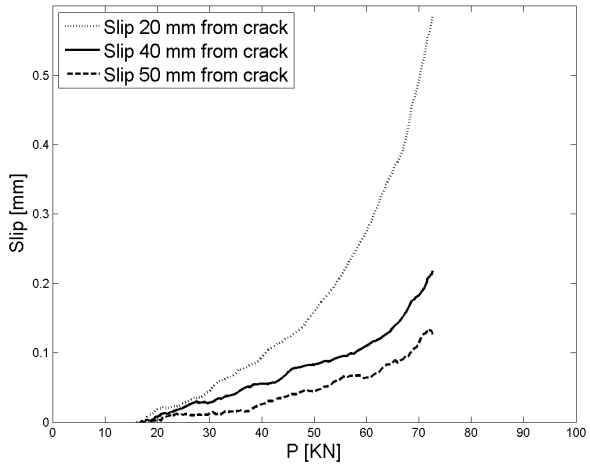

Figure 10: Slip vs load for PC (MSA3).

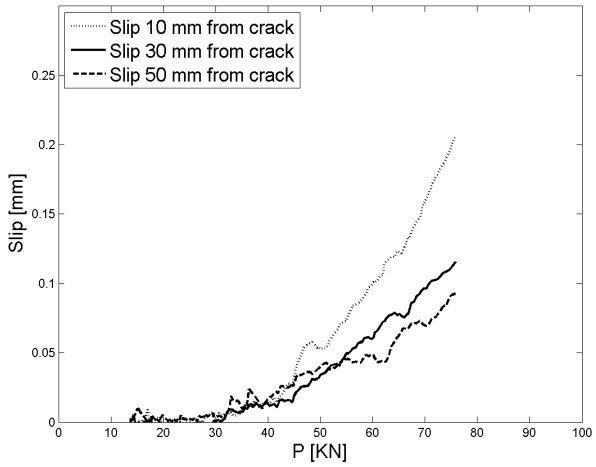

Figure 11: Slip vs load for 0.5 vol.-% SFRC (MSA8).

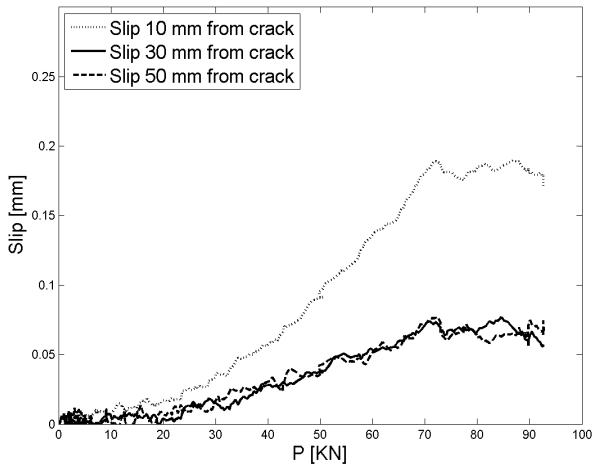

Figure 12: Slip vs load for 1.0 vol.-% SFRC (MSA11).

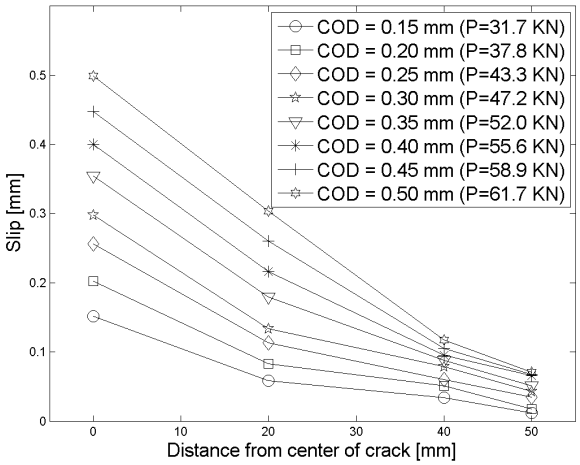

Figure 13: Slip vs. distance from center of main bending crack, PC (MSA3).

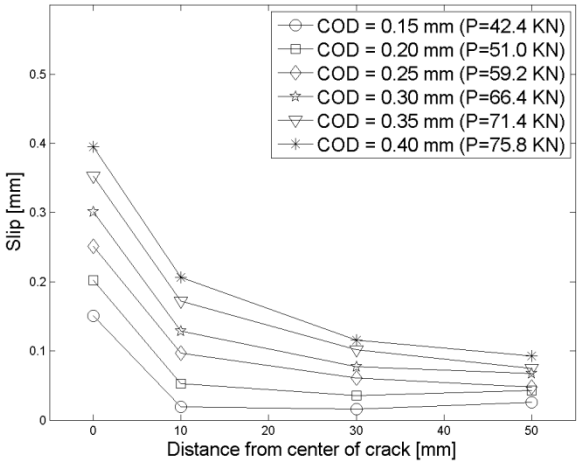

Figure 14: Slip vs. distance from center of main bending crack, 0.5 vol.-% SFRC (MSA8).

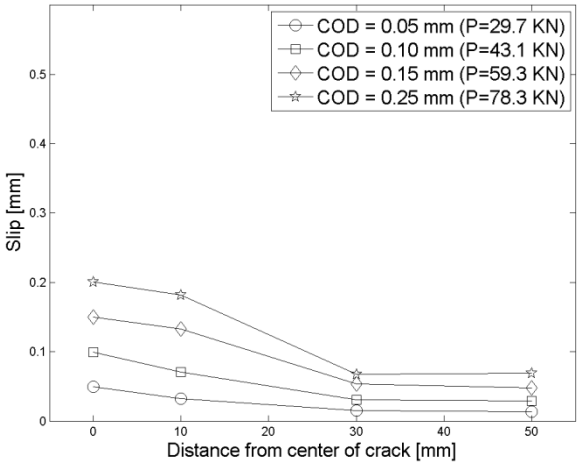

Figure 15: Slip vs. distance from center of main bending crack, 1.0 vol.-% SFRC (MSA11).

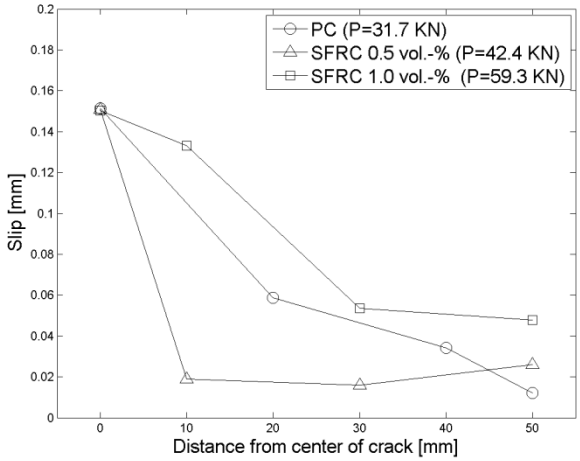

Figure 16: Slip vs. distance from center of main bending crack for all specimens, COD =0.15 mm.

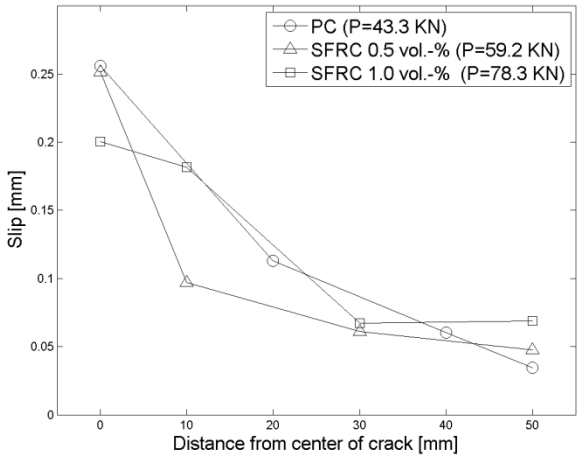

Figure 17: Slip vs. distance from center of main bending crack for all specimens, COD =0.25 mm.

For Figure 10 – Figure 12 the y-axis has been scaled whereas the same axes have been used for PC and SFRC in Figure 13 – Figure 15 to emphasize the substantial difference in the slip between PC and SFRC specimens.

The beneficial effect from the addition of fibres on the slip at the concrete/steel interface is obvious from Figure 10 – Figure 15. The slip is descending as a function of the distance from the main bending crack, cf. Figure 10 – Figure 15 as expected. More specifically, it is seen from Figure 10 – Figure 12 that the slip at a given load level is reduced approx. 50% comparing PC and 0.5 vol.-% SFRC, and additional 50% comparing 0.5 vol.-% SFRC and 1.0 vol.-% SFRC, as would be expected since the crack opening is reduced by the addition of fibres. Moreover, it is seen by comparisons of Figure 13 – Figure 15 that the level of slip along the reinforcement is similar for the three different concrete compositions for a specific

value of crack opening of the main transverse crack at the level of the reinforcement. This indicates, that the bond-slip relationship is independent by the addition of fibres. However, substantially different load levels are required to form a specific crack opening at the level of the reinforcement eg for COD = 0.15 mm 31.7, 42.4 and 59.3 KN are required for PC, 0.5 vol.-% SFRC and 1.0 vol.-% SFRC respectively.

However, it should be mentioned, that the extent of slip along the concrete/steel interface, viz. the length of the reinforcement where slip at the concrete/steel interface has occurred, cannot be directly quantified from the results given in Figure 10 – Figure 12.

The slip along the reinforcement for all specimens, is given for COD = 0.15 mm and COD = 0.25 mm, in Figure 16 and Figure 17, respectively. It is seen that for the same COD the slip along the reinforcement is similar for the different concrete compositions, as already explained. However, the load level required to create these specific values of COD is significantly increased by the addition of fibres.

Relationship between separation and load

Results concerning the separation at the concrete/steel interface are given in the following for various load levels, Figure 18 – Figure 20 and COD, Figure 21 – Figure 23. To ease the comparison between the three specimens, the separation along the reinforcement for specific values of COD for all specimens is presented in Figure 24 – Figure 25.

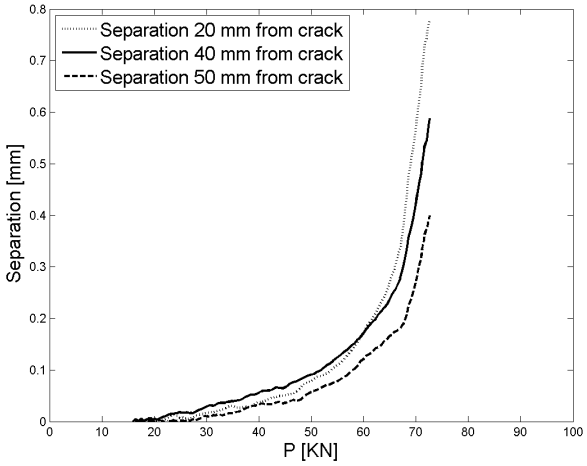

Figure 18: Separation vs load for PC (MSA3).

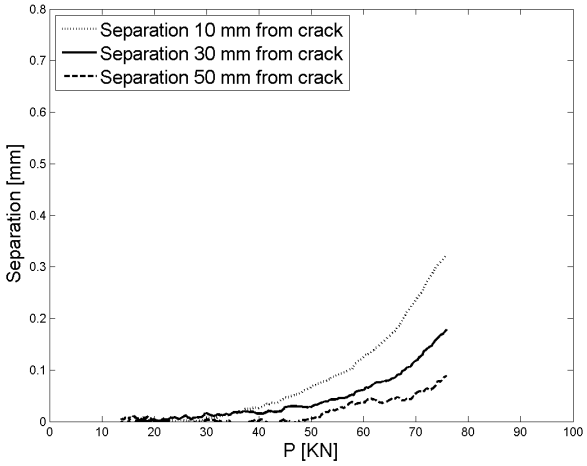

Figure 19: Separation vs load for 0.5 vol.-% SFRC (MSA8).

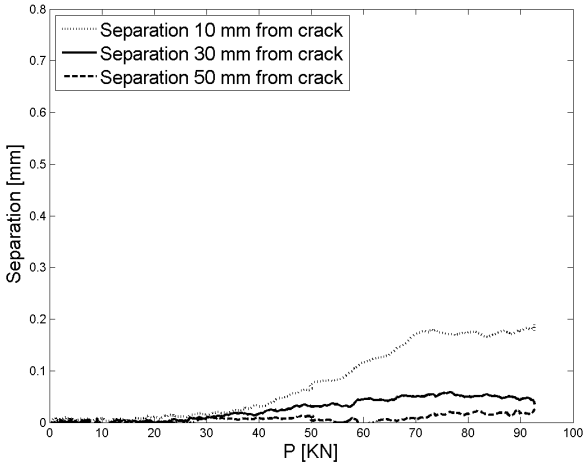

Figure 20: Separation vs load for 1.0 vol.-% SFRC (MSA11).

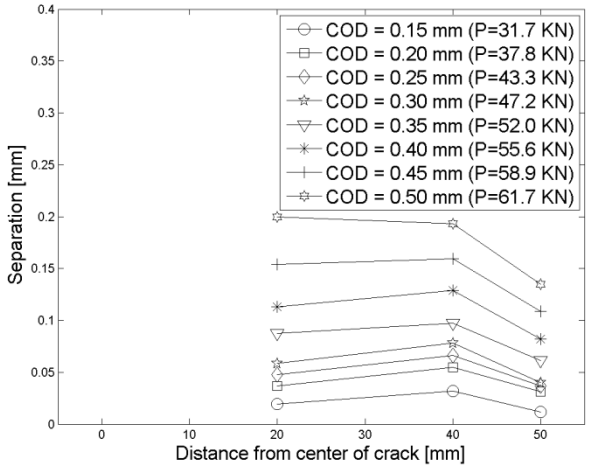

Figure 21: Separation vs. distance from center of main bending crack, PC (MSA3).

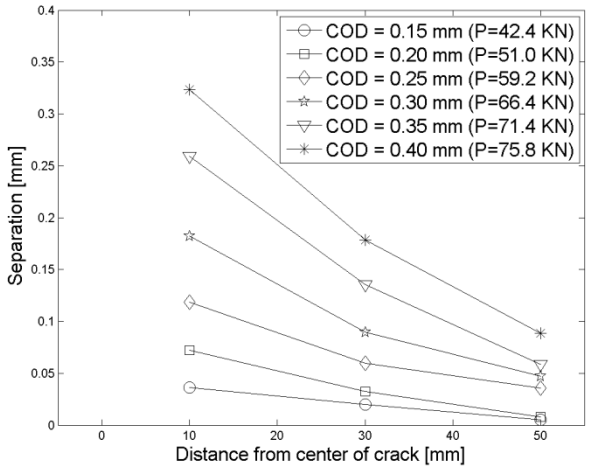

Figure 22: Separation vs. distance from center of main bending crack, 0.5 vol.-% SFRC (MSA8).

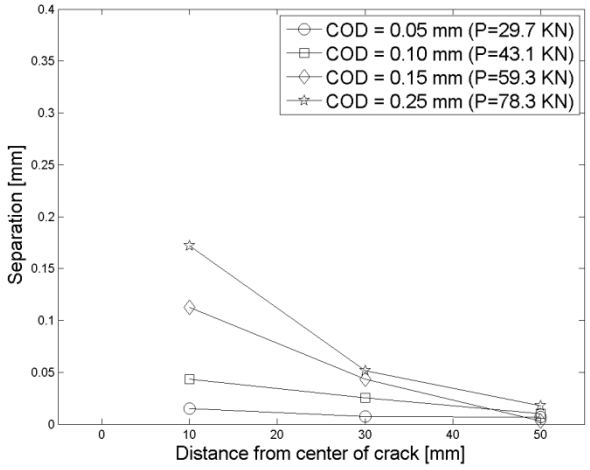

Figure 23: Separation vs. distance from center of main bending crack, 1.0 vol.-% SFRC (MSA11).

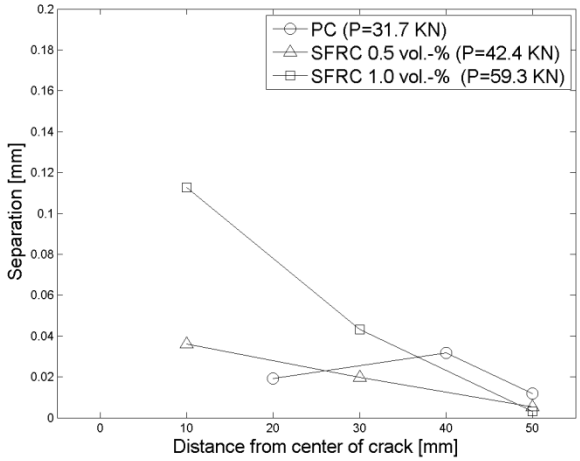

Figure 24: Separation vs. distance from center of main bending crack for all specimens, COD =0.15 mm.

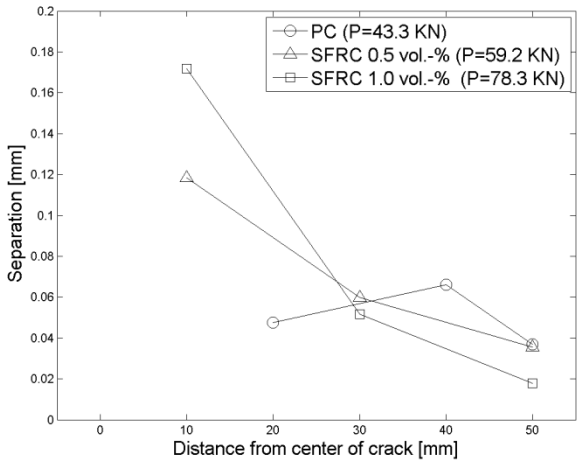

Figure 25: Separation vs. distance from center of main bending crack for all specimens, COD =0.25 mm.

The same axes have been used for Figure 18 – Figure 20 and Figure 21 – Figure 23 to ease comparisons of the separation for the different materials, and to emphasize the difference in the extent of separation at the concrete/steel interface for the different materials.

For PC, it is seen from Figure 18 and Figure 21 that the level of separation at the concrete/steel interface at various positions along the reinforcement is similar for a given COD, ie load level. This indicates that the separation along the reinforcement occurs instantaneously in the crack initiation phase. The same trend is seen for small values of COD for the two SFRC specimens, viz. 0.5 vol.-% SFRC (Figure 19 and Figure 22) and 1.0 vol.-% SFRC (Figure 20 and Figure 23). Based on these experimental results it is reasonable to conclude that the initiation of the separation occurs when the tensile capacity of the concrete matrix is exceeded. However, for increased load levels, viz. propagation of the separation,

the separation propagates faster closest to the main bending crack. This is seen for both SFRC compositions; cf. Figure 19 – Figure 20. The most reasonable explanation for this behavior is simple geometrical considerations.

Comparing Figure 18 – Figure 20 it is clear that the separation is prevented by the addition of fibers. Comparing the level of separation for PC and 0.5 vol.-% SFRC, Figure 18 and Figure 19 respectively, it is clear that the separation at different positions along the reinforcement is reduced by approx. 50% by the addition of only 0.5 vol.-% of fibres. The level of separation along the reinforcement is rather similar for 0.5 vol.-% SFRC and 1.0 vol.-% SFRC cf. a comparison of Figure 19 and Figure 20, suggesting that the increased addition of fibres only slightly has a beneficial effect on the separation. However it should be stressed that the separation for 1.0 vol.-% SFRC attains a somewhat constant level as opposed to the separation for 0.5 vol.-% SFRC where the separation is a constant increasing function of the applied load.

Comparing the figures concerning the separation along the reinforcement for various COD at the level of reinforcement (and thus various load levels), Figure 21 – Figure 23 it is clear that the level of separation is descending as a function of the distance from the main transverse crack for the SFRC specimens as opposed to PC. Moreover, it is seen that the level of separation at a given position along the reinforcement is not constant for the same COD at the level of reinforcement for the three specimens.

The results given in Figure 24 and Figure 25 concerning the separation at a given COD, 0.15 mm and 0.25 mm, respectively, indicate that the separation along the reinforcement is at the same level for all three concrete compositions for the same value of COD. However, as seen from the figures, the required load level to form the given values of COD is significantly increased by the addition of fibres.

Conclusions

This paper presents experimental observations, by means of photogrammetric measurements, of the formation and propagation of bending cracks and damage along the reinforcement in reinforced concrete beams subjected to 3 PBT. The experimental observations comprise specimens with 60 mm concrete cover and cast from PC, 0.5 vol.-% SFRC and 1.0 vol.-% SFRC, respectively.

The results and analyses presented in the paper contribute to an increased understanding of the mechanical performance of reinforced concrete structure subjected to flexural loading and based on these it can be concluded:

- The tensile strength of concrete, f_t, is not changed noticeable by the addition of fibres. However, the fracture energy, G_f, is increased by orders of magnitude due to the addition of fibres.
- The main bending crack is initiated at the tensile surface of the specimen at approx. the same load level regardless of the concrete composition. However, subsequently to crack initiation the increase in CMOD as function of the applied load is significantly reduced by the addition of fibres.
- The crack propagates fast from the tensile surface towards the compression zone, and the COD starts at the same load level as the CMOD regardless of the concrete composition.
- The evolution of the crack width at the level of the reinforcement as a function of the applied load is significantly reduced by the addition of fibres. Moreover, the same proportionality between COD and CMOD for the three concrete compositions for small values of CMOD (CMOD < 0.3 mm) can be seen. However, for larger values of CMOD the relationship is less steep for SFRC as opposed to PC indicating that the fibres hinder the crack width evolution.
- The slip at a given position at the concrete/steel surface is significantly reduced by the addition of fibres for a given load level; the slip is reduced approx. 50% and 75% comparing 0.5 vol.-% SFRC and 1.0 vol.-% SFRC with PC respectively. Results indicate that the extent of slip along the reinforcement is beneficially affected by the addition of fibres.
- The separation along the reinforcement is prevented by the addition of fibres, which is in accordance with the fracture mechanical properties, viz.

the fracture energy is increased significantly by the addition of fibres. More specifically, the results concerning separation at the concrete/steel interface indicate that the extent of separation is reduced by the addition of fibres for a given load level.

- Based on the experimental results given in the paper, it may be concluded that the addition of fibres can reduce the damage formation (slip and separation) at the level of the conventional reinforcement. This could potentially pave the way for further utilization of combined reinforcement systems, viz. fibres and conventional reinforcement, to improve the corrosion resistance from cracks of conventional reinforced concrete structures.

Future work

The results and analyses of the present paper reveal that the debonding at the concrete/steel interface is significantly reduced in SFRC as opposed to PC. However, further experimental observations are required in order to establish a relationship between the applied load and the damage along the reinforcement for other concrete compositions, concrete cover thicknesses, etc. The photogrammetric equipment described in the present paper is adequate for assessments of these results.

Acknowledgements

The first author gratefully acknowledge the full financial support of the Ph.D. study “Application of Fibre Reinforced in Civil Infrastructure” by the Danish Agency for Science, Technology and Innovation, COWI A/S, DTU, Bekaert NV, Grace, and the Danish Road Directorate.

References

[AAP, 2011] http://www.aalborgportland.dk/default.aspx?m=2&i=93, *Visited 18th October 2011.*

[ACI, 1973] ACI Committee 544 (1973), *State-of-the-Art Report on Fiber Reinforced Concrete*, American Concrete Institute, Farmington Hills, MI, USA.

[ACI, 2001] ACI Committee 224 (2001), *ACI 224.2R-92: Control of cracking in concrete structures*, American Concrete Institute, Farmington Hills, MI, USA.

[Aldea et al., 1999] Aldea, A.-M., Shah, S.P. and Karr, A. (1999), Effect of Cracking on Water and Chloride Permeability of Concrete, *Journal of Materials in Civil Engineering* **11** (3), 181-187.

[Bekaert, 2011] http://www.bekaert.com/~/media/Files/Download%20Files/Construction /Concrete%20reinforcement/Dramix%20General/Datasheet%20Dramix%20RC-6535-BN.ashx , *Visited 30th September 2011.*

[Berke et al., 1993] Berke, N., Dallaire, M., Hicks, M. and Hoopes, R. (1993), Corrosion of steel in cracked concrete, *Corrosion Engineering* **49** (11), 934-943.

[Bertolini, et al 2004] Bertolini, L., Elsener, B., Pedeferri, P. and Polder, R. (2004), *Corrosion of steel in concrete, Prevention, Diagnosis, Repair*, Wiley-VCH Verlag GmbH & Co. KGaA, Weinheim.

[Broms, 1965] Broms, B.B. (1965), Crack Width and Cack Spacing in Reinforced Concrete Members, *ACI Journal* **62** (10), 1237-1256.

[Darts, 2004] DARTS (2004), *The comprehensive decision tool*.

[De Schutter, 1999] De Schutter, G. (1999), Quantification of the Iifluence of Cracks in Concrete Structures on Carbonation and Chloride Penetration, *Magazine of Concrete Research* **51** (6), 427-435.

[Dörr, 1980] Dörr, K. (1980), *Ein Beitrag zur Berechnung con Stahlbetonscheiber unter besonderer Berücksichtigung des Verbundverhaltens*, PhD thesis. University of Darmstadt. Darmstadt, Germany.

[DS-12350-2, 2002] DS/EN-12350-2 (2002), *Testing fresh concrete – Part 2: Slump test*, Technical Report, Danish Standard Association.

[DS-2426, 2004] DS-2426 (2004), *Concrete-materials-rules for application EN 206-1 in Denmark*, Technical Report, Danish Standard Association.

[DuraCrete, 2000] DuraCrete (2000), *Probabilistic performance based durability design of concrete structures*, The European Union-Brite EuRam III.

[Edvardsen, 1999] Edvardsen, C. (1999), Water Permeability and Autogenous Healing of Cracks in Concrete, *ACI Materials Journal* **96** (4), 448-454.

[EN 14651, 2007] DS/EN 14651-+A1 (2007), *Test method for metallic fibre concrete – Measuring the flexural tensile strength (limit or proportionality (LOP), residual)*, Technical Report, Danish Standard Association.

[Ezeldin and Balaguru, 1990] Ezeldin, A.S. and Balaguru, P.N. (1990), Characterziation of bond between fiber concrete and reinforcing bars using nonlinear finite element analysis, *Computers and Structures* **37** (4), 569-584.

[Fib, 2000] Fib (2000), *Fib Bulletin 10, Bond of reinforcement in concrete*, State-of-the-art report, International Federation for Structural Concrete (fib).

[Fib, 2006] Fib (2006), *Fib Bulletin 34, Model code for service life design*, Tech. Rep. fib Bulletin 34, International Federation for Structural Concrete (fib).

[Francois and Arliguie, 1998] Francois, R. And Arliguie, G. (1998), Influence of service cracking on reinforcement steel corrosion, *Journal of Materials in Civil Engineering* **10** (1), 14-20.

[GOM, 2005] GOM Optical Measuring Techniques (2005), Aramis v5.4 User Manual, GOM mbh.

[Goto, 1971] Goto, Y. (1971), Cracks Formed in Concrete Around Deformed Tension Bars, *Journal of the American Concrete Institute*, **68** (4), 244-251.

[Jacobsen et al., 1996] Jacobsen, S., Marchand, J. and Boisvert, L. (1996), Effect of Cracking and Healing on Chloride Transport in OPC Concrete, *Cement and Concrete Research* **26** (6), 869-881.

[Kennedy, 1956] Kennedy, T.B. (1956), Tensile Crack Exposure Tests of Stressed Reinforced Concrete Beams, *ACI Journal* **56** (6), 1049-1063.

[Küter et al., 2005] Küter, A., Geiker, M.R., Olesen, J.F., Stang, H., Dauberschmidt, C. and Raupach M. (2005), Chloride Ingress of Concrete Cracks under Cyclic Loading, *Proceedings of ConMat'05*, Vancouver, Canada.

[Löfgren et al., 2005] Löfgren, I., Olesen, J.F. and Flansbjer, M. (2005), *Application of WST-method for fracture testing of fibre-reinforced concrete*, NT Technical Report, Norway.

[Michel et al.,2012] Michel, A., Solgaard, A.O.S., Pease, B.J., Geiker, M., Stang, H. and Olesen, J.F. (2012), Corrosion along the reinforcement – experimental analyses, submitted for *Materials and Structures* February 2012.

[Miyazato and Hiraishi, 2005] Miyazato, S. and Hiraishi, Y. (2005), Transport properties and steel corrosion in ductile fiber reinforced cement composites, *Proceedings of the 11th international conference on fracture*, Turin, Italy.

[Mohammed et al., 2001] Mohammed, T., Otsuki, N., Hisada, M. and Shibata, T. (2001), Effect of crack width and bar type on corrosion of steel in concrete, *Journal of Materials in Civil Engineering* **13** (3), 194-201.

[Mokhtar et al., 2008] Mokhtar, K.A, Loche, J.-M., Friedmann, H. Amiri, O. and Ammar, A. (2008), *Steel corrosion in reinforced concrete Report no. 2-2 Concrete in Marine Environment*, MEDACHS – Inerreg IIIB Atlantic Space – Project no. 197.

[Pease et al., 2006] Pease, B.J., Geiker, M., Stang, H. and Weiss, J. (2006), Photogrammetric assessment of flexure induced cracking of reinforced concrete beams under service loads, *Proceedings of the second international RILEM symposium – advances in concrete through science and engineering*.

[Pease, 2010] Pease, B.J. (2010), *Influence of concrete cracking on ingress and reinforcement corrosion*, Ph.D. thesis, Department of Civil Engineering,Technical University of Denmark, Lyngby, Denmark.

[Pease et al., 2011] Pease, B.J., Geiker, M., Stang, H. and Weiss, J. (2011), The design of an instrumented rebar for assessment of corrosion in cracked concrete, *Materials and Structures* **44** (7), 1259-1271.

[Pedersen, 2008] Pedersen, R.B. (2008), *Fracture mechanical analysis of reinforced concrete – Experiments and FEM modelling*, Master's thesis, Department of Civil Engineering,Technical University of Denmark, Lyngby, Denmark.

[Pedziwiatr, 2009] Pedziwiatr, J. (2009), The influence on the bond between concrete and reinforcement on thension stiffening effect, *Magazine of Concrete Research* **61** (6), 437-443.

[Rehm and Moll, 1964] Rehm, G. and Moll, H.L. (1964), *Versuche zum stadium des einflußes der rissbreite auf die rostbildung an der bewehrung von stahlbeton-bauteilen,* Deutscher Ausschuss für Stahlbeton 169.

[Rendell et al., 2002] Rendell, F, Jauberthie, R. and Grantham, M. (2002), *Deteriorated Concrete Inspection – Inspection and physiochemical analysis*, Thomas Telford, London.

[Rilem, 2002] Rilem TC-162 TDF (2002), Test and Design Methods for Steel Fibre Reinforced Concrete, *Materials and Structures* **35**, 579-582.

[Rodriguez and Hooton, 2003] Rodriguez, O.G. and Hooton, R.D. (2003), Influence of Cracks on Chloride Ingress into Concrete, *ACI Materials Journal* **100** (2), 120-126.

[Rostásy and Hartwicht, 1988] Rostásy, F.S. and Hartwicht, K. (1988), Bond of deformed reinforcing bar embedded in steel fibre reinforced concrete, *Composites and Lightweight Concrete* **10** (3), 151-158.

[Schaefer, 1975] Schaefer, H (1975), Contribution to the solution of contact problems with the aid of bond elements, *Computer Methods in Applied Mechanics and Engineering* **6** (3), 335-353.

[Schießl and Raupach, 1997] Schießl, P. and Raupach, M. (1997), Laboratory studies and calculations on the influence of crack width on chloride-induced corrosion of steel in concrete, *ACI Materials Journal* **94** (1), 56-62.

[Skoček and Stang, 2010] Skoček, J., and Stang, H. (2010), Application of optical deformation analysis system on wedge splitting test and its inverse analysis, *Materials and Structures* **43**, 63-72.

[Solgaard et al.,2012] Solgaard, A.O.S., Michel, A. and Stang, H. (2012), Debonding at the concrete/steel interface in reinforced concrete beams – Numerical simulations: Part II, submitted for *Materials and Structures* February 2012.

[Tammo and Thelandersson, 2009a] Tammo, K. and Thelandersson, S. (2009a), Nonlinear analysis of crack widths in reinforced concrete, *Magazine of Concrete Research* **61** (1), 23-34.

[Tammo and Thelandersson, 2009b] Tammo, K. and Thelandersson, S. (2009b), Crack widths near reinforcement bars for beams in bending, *Journal of the FIB* **10** (1), 27-34.

[Wang et al., 1997] Wang, K., Jansen, D.C., Shah, S.P. and Karr, A.F. (1997), Permeability Study of Cracked Concrete, *Cement and Concrete Research* **27** (3), 381-393.

[Win et al., 2004] Win, P.P., Watanabe, M. and Machida, A. (2004), Penetration Profile of Chloride Ion in Cracked Reinforced Concrete, *Cement and Concrete Research* **34**, 1073-1079.

Paper VII

” Debonding at the Concrete/Steel Interface in Reinforced Concrete Beams - Numerical Simulations: Part II”

A.O.S. Solgaard, A. Michel & H. Stang

Submitted to: *Materials and Structures.*

Debonding at the Concrete/Steel Interface in Reinforced Concrete Beams – Numerical Simulations: Part II

Anders Ole Stubbe Solgaard [1&2]

Alexander Michel[2]

Henrik Stang[2]

1 COWI A/S Denmark, Kgs. Lyngby Denmark

2 Department of Civil Engineering, Technical University of Denmark, Kgs. Lyngby Denmark

Phone: +45 4525 5033

Fax: +45 4588 3282

aos@byg.dtu.dk

www.byg.dtu.dk

Abstract

The formation of cracks in the concrete cover of reinforced concrete is often related to mechanical loading. Cracks may potentially promote the risk of reinforcement corrosion since the ingress rate of eg moisture and/or chlorides may increase. Corrosion initiation of reinforcement is often used as a limit state in guidelines for service life design. Though the formation of cracks is inevitable due to the brittle nature of concrete, they are not accounted for in such existing guidelines. To account for the influence of cracks and damage of the concrete cover in the service life design of a reinforced concrete structure it is of vital importance to determine the correlation between the risk of the initiation of reinforcement corrosion and the extent of damage associated to the load applied. Previous experimental studies of such damage formation have been presented in the literature. However, operational tools, eg numerical models, capable of correlating the applied load and the associated damage formation in the concrete cover are not available at the present moment.

The aim of this paper is to present a numerical model for the formation of tensile load-induced damage in concrete. The model simulates the formation of a bending crack through the concrete cover as well as the formation of damage at the concrete/steel interface. The numerical model is based on basic theories of fracture mechanics, viz. the so-called fictitious crack model, and the numerical simulations are compared to experimental data. The experimental data cover observations of flexural loading of conventional reinforcement embedded in plain concrete as well as steel fibre reinforced concrete (0.5 and 1.0 vol.-%).

Comparisons of the numerical and experimental results show, that the proposed model is capable of simulating all of the damage mechanisms, viz. the formation of a bending crack and – at the same time – the slip and separation at the concrete/steel interface very accurately. Values assigned to the input parameters used for the numerical model are all within reasonable levels. Based on those observations it may be concluded that the numerical model is based on correct physical assumptions.

The proposed numerical model may be an important tool for assessment of the relationship between applied load and the damage formation in reinforced concrete, which may be used for future guidelines for the service life design of reinforced concrete structures accounting for the formation of damage in the concrete cover.

Keywords: Numerical simulations, Fracture mechanics, Load-induced damage, Service Life Design, Fibre reinforced concrete.

Introduction

Reinforced concrete is the most widely used man-made construction material around the World for structures in the civil infrastructure. The serviceability of such structures is strongly related to the integrity, which is controlled by the durability. The deterioration of reinforced concrete structures is caused by a number of mechanisms such as freeze-thaw reactions, alkali-silica reactions and reinforcement corrosion, of which corrosion is the predominant deterioration mechanism [*Rendell et al., 2002*].

Corrosion of reinforcement occurs due to the ingress of de-passivating substances such as CO_2 and/or Cl^-. The ingress rate of those substances is strongly promoted by cracks in the concrete cover, which may be formed due to eg mechanical loading and/or shrinkage, since they act as pathways for the de-passivating substances [*Wang et al., 1994*], [*Edvardsen, 1999*] and [*Aldea et al., 1999*]. The formation of cracks in concrete is effectively inevitable due to the brittle nature of concrete.

The identification of the predominant role of cracks in the concrete on the transport of de-passivating substances led to different formulations of the correlation between the damage of the concrete and the risk of reinforcement corrosion. Such formulations are vitally necessary for proper design of durable reinforced concrete structures.

One of those formulations is based on the hypothesis that the risk of reinforcement corrosion is correlated to the crack mouth opening displacement (CMOD) at the concrete surface eg [*Schießl and Raupach, 1997*] and [*Mohammed et al., 2011*]. The proposed models for that relationship show rather good correlation for exposure times less than approx. three years. However, other experimental observations by eg Kennedy [*Kennedy, 1956*] and Francois and Arliguie [*Francois and Arliguie, 1998*] show no correlation at all between crack width and risk of reinforcement corrosion.

Bearing those observations in mind, it was proposed by Tammo and Thelandersson [*Tammo and Thelandersson, 2009a*] and [*Tammo and Thelandersson, 2009b*] that the risk of reinforcement corrosion is controlled by the crack opening displacement (COD) at the level of the reinforcement, which is poorly correlated with the CMOD eg due to the formation of concrete cones

around the reinforcement, cover thickness, rebar-concrete bond etc.. A similar approach for the formulation of the risk of reinforcement corrosion due to damage of the concrete cover was suggested by Pease et al. [*Pease et al., 2006*] and [*Pease et al., 2011*] proposing that the damage along the concrete/steel interface is a more fundamental measure than the CMOD at the concrete surface to describe the susceptibility of reinforcement corrosion. Results presented in [*Pease et al., 2011*] are supported by observations presented in [*Win et al., 2004*] showing that damage along the reinforcement results in a lateral ingress of chloride ions increasing the risk of reinforcement corrosion significantly.

Photogrammetric observations of the damage formation at the concrete/steel interface presented in [*Pease et al., 2006*] show that significant damage is induced at the concrete/steel interface, and similar observations are presented by Solgaard et al. [*Solgaard et al., 2012*] concerning reinforced concrete beams made from both plain concrete (PC) and Steel Fibre Reinforced Concrete (SFRC).

A numerical model for this damage formation is required to allow for design of durable reinforced concrete structures. The model should consider the formation of a bending crack through the concrete cover towards the reinforcement and damage at the concrete/steel interface caused by applied flexural load. The damage at the concrete/steel interface consists of *slip*, the displacement discontinuity parallel to the rebar surface and *separation*, the displacement discontinuity perpendicular to the rebar surface.

Previous work concerning formation of damage at the concrete/steel interface in conventional reinforced concrete beams subjected to mechanical loading has mainly focused on the slip behavior eg [*Tammo and Thelandersson, 2009a*] whereas the separation along the reinforcement has not investigated to the same extent.

The present paper describes a numerical FE based model for the prediction of load-induced damage of reinforced concrete specimens subjected to flexural load, viz. three point bending test (3 PBT). The numerical model describes the initiation and propagation of a main bending crack from the tensile surface of the concrete towards the reinforcement and the slip and separation at the concrete/steel interface. The presented numerical model is based on the fictitious crack model described by Hillerborg et al. [*Hillerborg et al., 1976*] taking the fracture mechanical properties of the concrete matrix into account. The numerical model is

compared to experimental results initially presented in [*Solgaard et al., 2012*]. Results from the numerical model may be used for further analysis of the relationship between load, CMOD and slip and separation along the reinforcement for reinforced concrete structures. Additionally, the results concerning the load-induced damage formation obtained by the use of this model were compared to the extent of corrosion along the reinforcement in cracked concrete (PC and SFRC) exposed to sea water by Michel et al. [*Michel et al., 2012*]. Results presented in that reference shows that the extent of damage along the reinforcement correlates with the area where corrosion is electrochemical favored. This observation may lead to a further understanding of the correlation between load-induced damage in reinforced concrete structures and the risk of corrosion along the reinforcement. Moreover, this could potentially lead to the formulation of models for service life design of reinforced concrete structures taking the correlation between load-induced damage formation and risk of corrosion into account.

Model description

The numerical model simulates slip and separation at the concrete/steel interface associated with crack formation in the concrete cover for reinforced concrete beams loaded in three point bending assuming 2D plain strain and discrete crack formation. The complete model is established by combining a serial and parallel model. The location of the main bending crack, viz. at the centre of the reinforced concrete beams, is predefined. The modelling approach for the main bending crack and the slip and separation at the concrete/steel interface is illustrated in Figure 1:

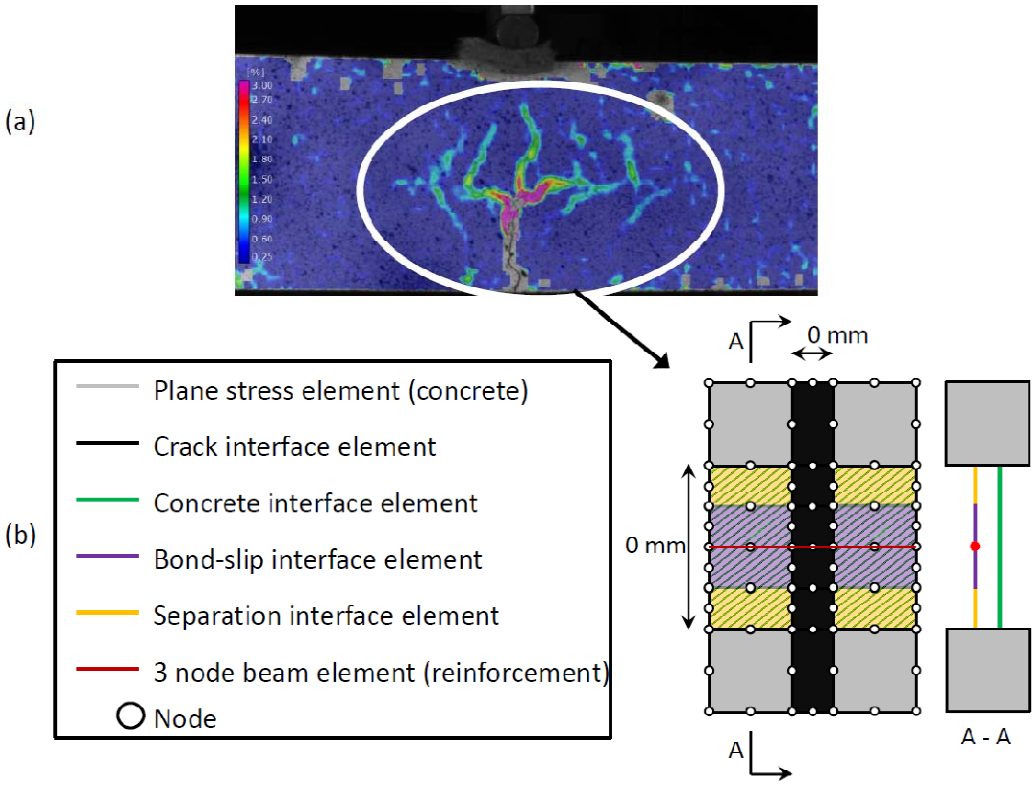

Figure 1: a) Illustration from photogrammetric assessment of the load-induced damage formation in reinforced concrete specimens [*Solgaard et al., 2012*]. b) Concept of the serial-parallel model simulating cracking, slip and separation at concrete/steel interface. The illustration is not in scale. Inspired by [*Olsen, 2010*].

A photogrammetric image of the reinforced concrete specimen is shown in Figure 1(a) whereas Figure 1(b) illustrates the details of the modelling approach at the centre of the specimen, viz. the serial-parallel model. To simulate the slip and separation at the concrete-reinforcement interface as well as cracking in the concrete domain a number of zero thickness interface elements (in serial and

parallel connection) are incorporated in the model, cf. Figure 1(b). The upper and lower parts of the concrete body are connected through a concrete interface at the reinforcement level. In addition, the reinforcement, represented by beam elements, is connected to the lower and upper concrete body respectively through a serial connection of bond-slip and separation interfaces. The reinforcement and the remaining part of the concrete domain have linear elastic properties assigned. The various interface elements shown in Figure 1(b) are described in the following.

Formation and propagation of the main bending crack in the concrete domain is based on the fictitious crack model [*Hillerborg et al., 1976*]. The mechanical properties of the "crack interface elements" in the concrete domain cf. Figure 1(b) are defined using a so-called cohesive relationship and described as follows:

$$\sigma = \begin{cases} \sigma_e(\varepsilon) = E_c \varepsilon & \text{Pre} - \text{cracked state} \\ \sigma_w(w) = g(w) f_t & \text{Cracked state} \end{cases} \tag{1}$$

where σ_ε is the elastic stress, E_c is the Young's modulus of concrete, ε is the elastic strain, $\sigma_w(w)$ the normal bridging stress as a function of the crack width w, $g(w)$ is the dimensionless cohesive relationship and f_t is the concrete tensile strength. Multi-linear softening relations adopted from [*Skoček and Stang, 2010*] are used to describe the dimensionless cohesive relationship, $g(w)$:

$$g(w) = b_i - a_i w \quad \text{with} \quad w_{i-1} < w < w_i \quad \text{and} \quad i = 1, \dots, n \tag{2}$$

where a_i describes the slopes of the cohesive branches, b_i the intercepts between the cohesive branches and w_i is defined as follows:

$$w_i = \frac{b_i - b_{i+1}}{a_i - a_{i+1}} \quad \text{with} \quad i = 1, \dots, n-1 \quad \text{and} \quad w_n = w_{crit} = \frac{b_n}{a_n} \tag{3}$$

where w_{crit} is the critical crack width. For $w > w_{crit}$ the crack is considered stress-free.

The concrete interface connecting the upper and lower concrete body, cf. Figure 1(b), is described by the same mechanical properties as the main bending crack given above. This concrete interface is incorporated in the model to account for the formation of radial cracks around the reinforcement which are not simulated

by the model. These radial cracks allow for the separation at the concrete/steel interface and consequently they have to be accounted for in the model to simulate the damage process.

The numerical model presented herein, is a 2D model, cf Figure 1, though the problem is 3D. In order to comply with this problem, the aforementioned concrete interface between the upper and lower parts of the concrete domain accounts for the properties in the remainder of the cross section where there is concrete.

Separation at the concrete/steel interface is described similar to the main bending crack, viz. by the use of a cohesive relationship describing the bridging stress and the crack width cf. Eq (1)-(3). However, for the separation interface elements the cohesive relationship is linear descending, n =1 in Eq. (2)-(3).

Finally, the bond-slip interface, which accounts for sliding at the concrete/steel interface, cf. Figure 1(b), is described by a cubic-relationship between the shear stress and slip, proposed by Dörr [*Dörr, 1980*]. For a given value of slip, the so-called constant slip value, dt^0, the relationship attains a constant relationship, cf. Eq. (4):

$$t_t = \begin{cases} f_t\left(1.4\left(\frac{dt}{dt^0}\right)^3 - 4.5\left(\frac{dt}{dt^0}\right)^2 + 5\left(\frac{dt}{dt^0}\right)\right) & \text{for} \quad 0 \le dt < dt^0 \\ 1.9 f_t & \quad dt \ge dt^0 \end{cases} \qquad (4)$$

where dt is the slip and t_t is the shear stress (bond).

Typical mechanical properties of the different interface elements, cf. Figure 1(b), are illustrated in Figure 2:

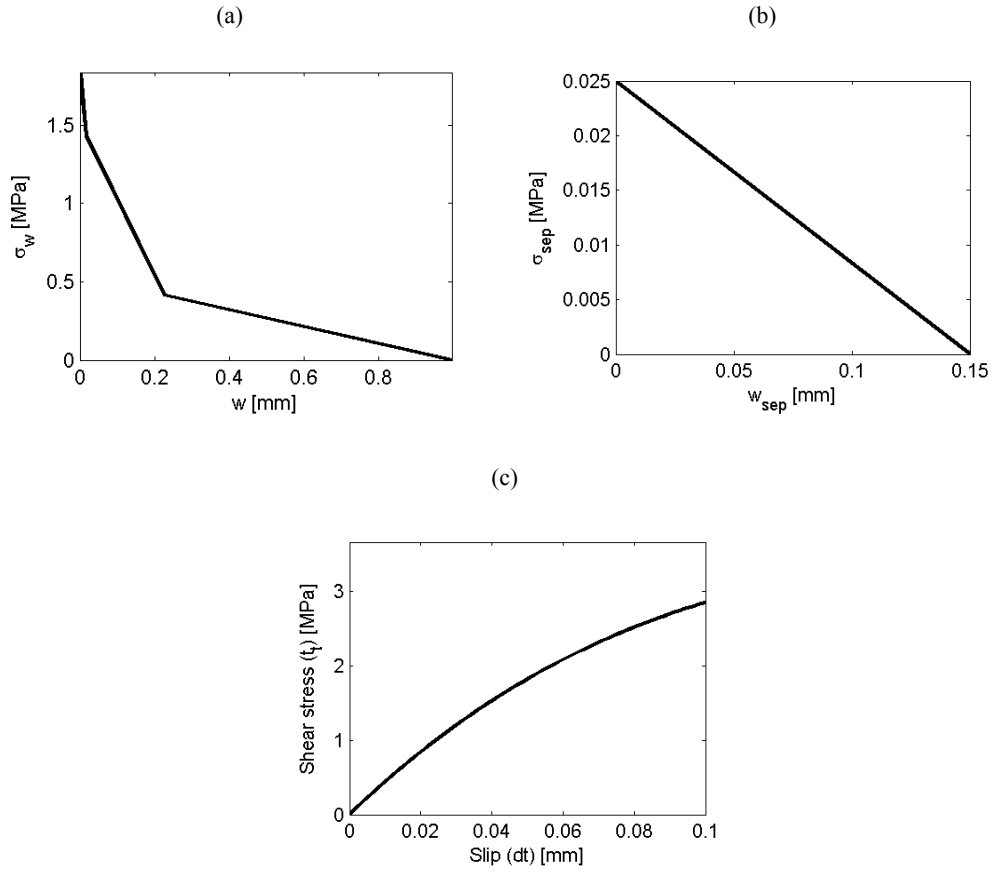

Figure 2: (a) normal stress-separation law for cracking in concrete domain, (b) normal stress-separation law for separation between concrete and reinforcement and (c) shear stress-slip relation between concrete and reinforcement.

The relationships of the various interface elements given in Figure 2(a)-(c) are not representative for all simulations described in the following sections. However, the illustration serves as a visual representation of Eq. (1)-(4).

The three latter interfaces, viz. the concrete interface between the upper and lower part of the concrete domain, the bond-slip relationship and the separation interface are modelled along the entire concrete/steel interface, while the crack interface is only located at the centre of the reinforced concrete specimen, cf. Figure 1.

The numerical model, viz. the serial-parallel model shown in Figure 1(b), was constructed, so that physical meaningful values can be assigned to the various interfaces to simulate cracking, slip and separation.

It is seen from Figure 1b and the descriptions given above, that the formation of slip and separation at the concrete/steel interface are modelled as two independent processes. The authors' are aware of the fact that this is not the case since these processes are linked in a so-called mixed-mode fracture behaviour. The mixed-

mode behaviour has been described by eg Carol et al. [*Carol et al., 1997*], Lourenco and Rots [*Lourenco and Rots, 1997*] and Nielsen et al. [*Nielsen et al., 2010*]. However, there still lacks a proper formulation of this mixed-mode behaviour which can be implemented in FEM simulations.

A description of the values assigned to various parameters such as dt^0 and β are given in a separate section along with sensitivity analyses of the influence of eg the strength of the separation interface $f_{t,sep}$.

Details on numerical model

Numerical simulations described in the present paper were carried out by the use of the commercially available FEM software package DIANA. Details on the numerical model such as the meshing, element types etc. are described in the following. Note that due to symmetry considerations only half of the reinforced concrete beam is modelled to reduce computational time. As previously mentioned, the numerical model is compared to experimental results concerning initiation of bending crack and formation of slip and separation along the reinforcement reported in [*Solgaard et al., 2012*]. The experimental observations were determined from flexural loading (3PBT) of 150 x 150 x 650 mm (h x w x l) reinforced concrete specimens.

The numerical model was solved by the use of the commercial available software DIANA with 1184 quadrangular elements and 2353 nodes. The interface accounting for the simulations of the main bending crack (black interface in Figure 1) is divided into two lines, viz. one below and one above the reinforcement, each consisting of 60 elements. The number of elements in the interface accounting for the bond-slip behaviour (purple interface in Figure 1) is 98, which is the same number of elements used for the interface accounting for the separation at the concrete/steel interface (yellow interface in Figure 1).

The number of elements in the three different interfaces, cf. Figure 1, has proven sufficient in a convergence analysis as will be seen in the following section.

Sensitivity and convergence analyses of the numerical model

The analysis given in the following concern convergence analyses of the number of elements utilized for the different interfaces given in the model, viz. interfaces accounting for main bending crack, bond-slip and separation behaviour, respectively. The maximum number of line divisions of an interface, and thereby maximum number of elements, is 98 in the FE software. Moreover, analyses concerning parameters, which are used to fit the experimental data, are presented in the following.

Material properties for SFRC with 1.0 vol.-% steel fibres were used for all the results from numerical simulations concerning the analyses given in the present section. The analyses presented in the following have been carried out for one load level, viz. 50 KN. However, other load levels have been investigated showing similar results.

Main bending crack interface

As previously described the interface for the main bending crack (black interface in Figure 1) consists of the same number of elements below and above the reinforcement, viz. 60 elements in each of those two interfaces summing up to a total of 120 elements. A convergence analysis of the number of elements below the reinforcement in the main bending crack is given in Figure 3.

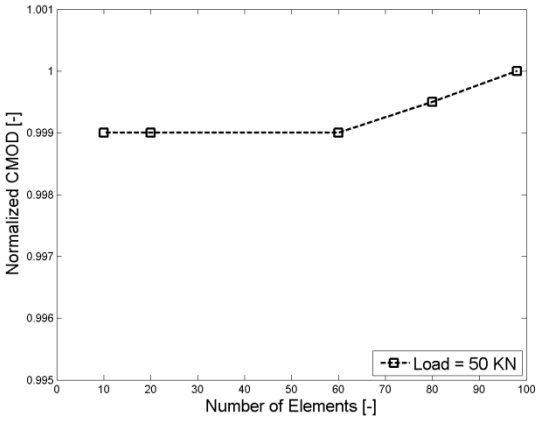

Figure 3: Normalized results from convergence analyses of number of elements in main bending crack.

Figure 3 shows the change in CMOD for a given number of elements normalized to the CMOD for 98 elements.

It is clear from the results presented in Figure 3 that the number of elements in the main bending crack interface has a minor influence on the results of the numerical simulations. The relative change is approx. 1‰ when decreasing the number of elements from 98 to 60. Thus it is concluded that the number of elements used for the numerical simulations presented in the following is sufficient.

Number of elements in the slip and separation interfaces

The number of elements in the slip and separation interfaces was varied in order to analyse the convergence of the model. The results from those simulations are given in Figure 4 and 5 for slip and separation, respectively.

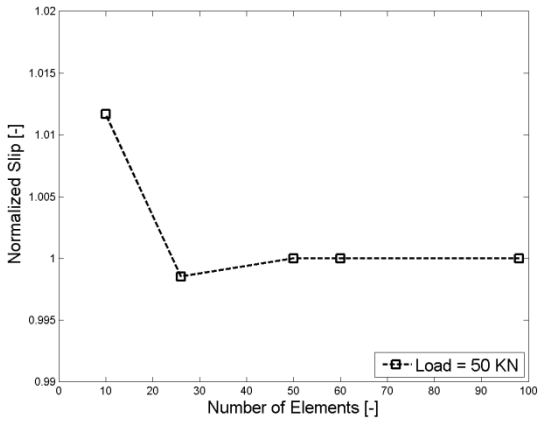

Figure 4: Normalized results from convergence analyses of the number of elements in the slip interface.

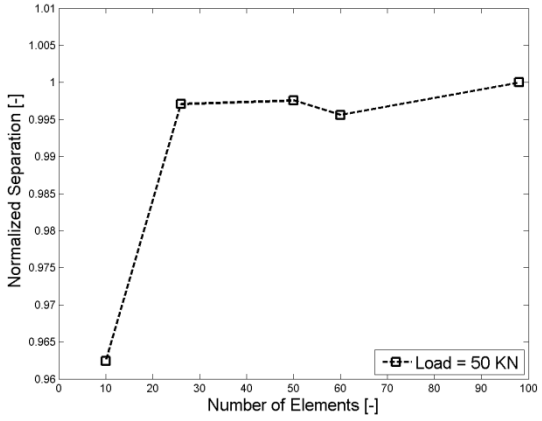

Figure 5: Normalized results from convergence analyses of the number of elements in the separation interface.

From Figure 4 it is seen that the slip does not change significantly when the number of elements in that interface is increased from 50 to 98. Consequently the number of elements used within this simulation approach is sufficient.
From Figure 5 it is seen, that the separation is changed less than 5 ‰ by increasing the number of elements from 60 to 98. Thus it is reasonable to conclude that the number of elements used for the numerical simulations, viz. 60, is sufficient.

Tensile strength of slip interface

The tensile strength of the slip interface (purple interface in Figure 1) was varied to analyse the influence on the slip along the reinforcement for various load levels. The slip 10 mm from the centre of the main bending crack at the level of the reinforcement is calculated for various values of this slip strength and shown in Figure 6 along with experimental results reported in [*Solgaard et al., 2012*]

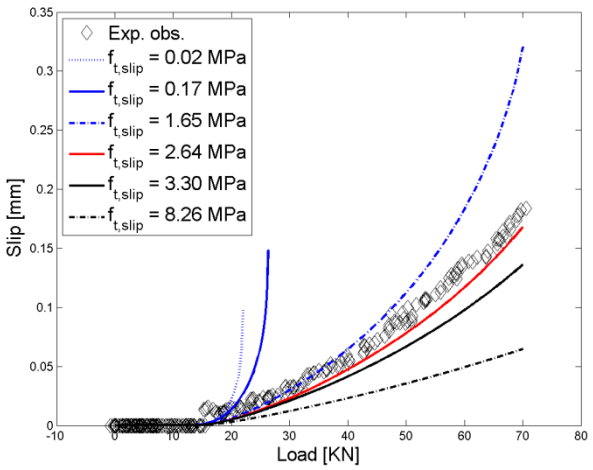

Figure 6: Slip 10 mm from centre of main bending crack, Numerical simulations for different values of $f_{t,slip}$ along with experimental results from 1.0 vol.-% SFRC reported in [*Solgaard et al., 2012*].

Results given in Figure 6 clearly indicate that the numerical model is capable of simulating the slip very accurate. Regardless of the value assigned to the tensile strength of the slip interface, $f_{t,slip}$, the slip is initiated for the same load level applied. However, it is also clear, that the propagation of the slip is very sensitive to changes in the value assigned to $f_{t,slip}$, cf. Figure 6.
Similar analysis of the influence of the tensile strength of the separation interface, $f_{t,sep}$, were carried out where similar results were observed. However, these convergence analyses are not given in the present paper.

Value of constant slip

As previously described, the slip at the concrete/slip interface is modelled by Dörr's model, cf. Eq. (4). It is seen from Eq. (4) that the shear stress-slip relationship attains a constant level for a given slip, dt^0. The influence of the magnitude of dt^0 was analysed assigning different values to dt^0 and model the corresponding slip at the concrete/steel interface. The results presented in the following correspond to the slip 10 mm from the centre of the main bending crack at the level of the reinforcement. The results from theses numerical simulations are presented in Figure 7 along with experimental data from 1.0 vol.-% SFRC reported in [*Solgaard et al., 2012*]:

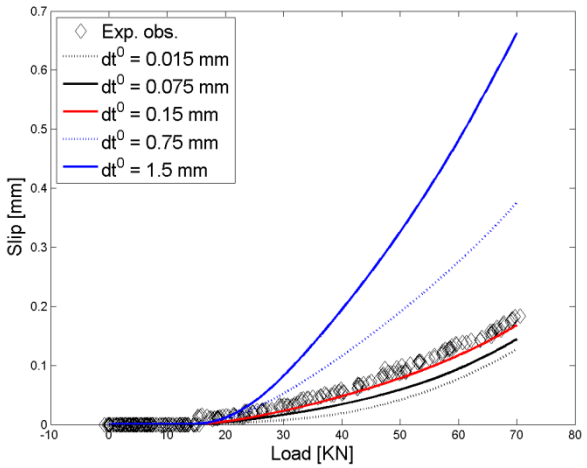

Figure 7: Slip 10 mm from centre of main bending crack, Numerical simulations for different values of dt^0 along with experimental results from 1.0 vol.-% SFRC reported in [*Solgaard et al., 2012*].

As seen in Figure 7 the numerical model is capable of simulating the slip 10 mm from the centre of the main bending crack accurately. Moreover it is clear that higher value assigned to dt^0 results in numerical simulations overestimating the slip, which is in accordance with the nature of the modelling approach of the slip behaviour given by Eq. (4).

Limitations for numerical simulations

The proposed numerical model is based on the fictitious crack model, which originally was proposed by Hillerborg et al. [*Hillerborg et al., 1976*]. Thus the numerical model is based on the assumption of discrete crack formation due to the applied load. As multiple cracking may occur, especially when considering SFRC, the results concerning the formation of the main bending crack predicted by the numerical model may be too conservative. However, as will be seen, the numerical model is capable of fitting the experimentally observed cracking details in a very convincing way.

The numerical model simulates the slip and separation, caused by the applied flexural load, along the reinforcement. Subsequently, the relative displacements of the elements of the different interfaces, cf. Figure 1, are evaluated to analyse the bond-slip and separation. Thus, the final results concerning the slip-length and separation-length are based on an interpretation of the deformations of the elements in the interfaces. The interpretations are based on the relative displacements between two nodes within an element at the interface for each load step. The bottom part of that element is connected to the reinforcement whereas the top part of that element is connected to the surrounding concrete. This is explained from Eq. (5)-(6) for slip and separation respectively:

$$\Delta u_x = \left|u_x^i - u_x^j\right| - \Delta u_{x,e} \tag{5}$$

$$\Delta u_y = \left|u_y^i - u_y^j\right| - \Delta u_{y,e} \tag{6}$$

where indices *i* and *j* refer to the node in the top and bottom of the element, respectively and indices *x* and *y* relate to the coordinate system. The x-axis of this coordinate system is aligned with the direction of the reinforcement. $\Delta u_{x,e}$ and $\Delta u_{y,e}$ are the elastic deformations in the two principle directions, ie parallel with and perpendicular to the reinforcement respectively. These elastic deformations are controlled by the elastic stiffness of the elements. A high value for the elastic stiffness has been assigned to these elements in the numerical model and consequently the elastic deformations are negligible (less than 1 μm). Consequently the elastic part of Eq. (5) and (6) vanish.

A non-physical fitting parameter has been applied to the simulations concerning the separation at the concrete/steel interface. This non-physical fitting parameter

does not influence the slip and the opening of the main bending crack, but has been incorporated to the model to account for the fact that the formation of the slip and the separation at the concrete/steel interface are linked processes (mixed mode fracture), whereas the numerical model simulates those as independent processes.

Parameters

The numerical model described in the present paper is tested by comparisons with experimental observations obtained by Solgaard et al. [*Solgaard et al., 2012*] concerning 3PBT of reinforced concrete beams cast from PC, 0.5 vol.-% SFRC and 1.0 vol.-% SFRC. The geometry of those beams is shown in Figure 8 and the dimensions of the specimen are given in Table 1.

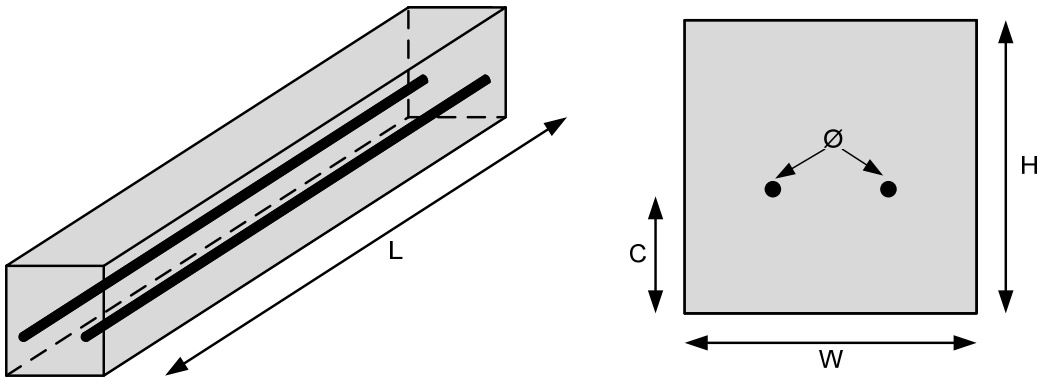

Figure 8: Geometry of specimens used for verification of numerical model: Left: Perspective view of reinforce concrete beam. Right: Cross section of reinforced concrete beam.

Table 1: Measures of specimens used for verification of numerical model.

H [mm]	150
W [mm]	150
C [mm]	60
$Ø$ [mm]	12
L [mm]	650

Experimental observations of CMOD, slip and separation caused by the flexural loading was measured by the use of photogrammetric equipment. The right side of the specimen was cut off leaving a minute concrete cover on the side of the reinforcement allowing for such measurements. Although these observations were

assessed from specimens slightly different than those used for the numerical simulations it is assumed that the load-induced damage in those two different specimens is somewhat similar. Further information about the properties of the concrete, casting procedure, experimental procedure, etc. is available in [*Solgaard et al., 2012*]. The fracture mechanical properties of the concrete matrix, which are used for the numerical simulations of load-induced damage formation in beams cast from PC or SFRC (0.5 and 1.0 vol.-%), are given in Figure 9 and

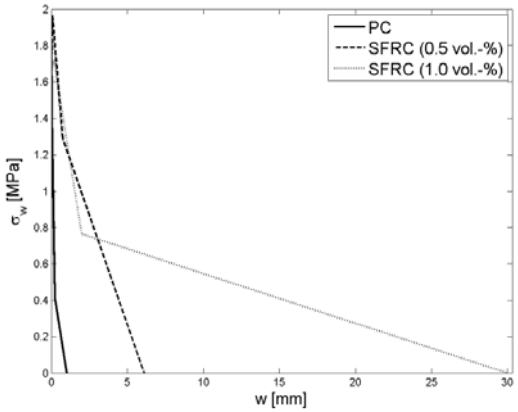

Figure 9: Cohesive relationships for PC and SFRC (0.5 and 1.0 vol.-%). From [*Solgaard et al., 2012*].

Table 2.

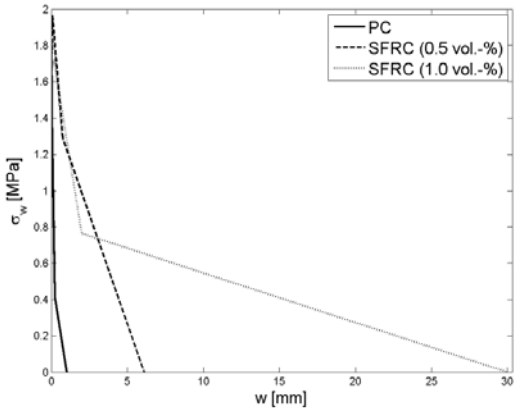

Figure 9: Cohesive relationships for PC and SFRC (0.5 and 1.0 vol.-%). From [*Solgaard et al., 2012*].

Table 2: Mechanical properties of "bending crack"-interface elements. Data from [*Solgaard et al., 2012*].

	PC	SFRC	
	0.0 vol.-%	0.5 vol.-%	1.0 vol.-%
f_t [MPa]	1.8	1.7	1.7
w_{crit} [mm]	1.0	6.1	30

G_f [J/m^2]	400	4700	13000

The tensile strength of the slip and separation interfaces and the constant slip are the only parameters fitted for the numerical simulations and the values assigned for those simulations are presented in Table 3:

Table 3: Mechanical properties of slip and separation interfaces.

	PC	SFRC	
	0.0 vol.-%	0.5 vol.-%	1.0 vol.-%
$f_{t,slip}$ [MPa]	2.57	1.10	2.31
$f_{t,sep}$ [MPa]	0.03	0.03	0.03
dt^0 [mm]	0.15	0.15	0.15

Results

Results of the numerical model for load-induced damage in the concrete cover and slip and separation in the concrete/steel interface presented above were compared to experimental observations. The section provides information concerning:

- CMOD at the concrete tensile surface vs. applied load
- Separation at concrete/steel interface vs. applied load
- Slip at concrete/steel interface vs. applied load
- Extent of slip and separation vs. applied load

for all concrete compositions previously described. All the numerical results are presented along with experimental results, originally published by Solgaard et al. [*Solgaard et al., 2012*], except for the simulations concerning the extent of slip and separation, since no experimental results are available for those observations. The numerical simulations and comparisons with the experimental results presented in the following correspond to the formation of the main bending crack up-to CMOD = 0.5 mm and a rebar stress of 192 MPa (PC), 131 MPa (SFRC 0.5 vol.-%) and 186 MPa (SFRC 1.0 vol.-%). Hence the rebar is in the elastic state. Results presented for the formation of slip and separation along the concrete/steel interface correspond to that load level. However, it should be noted, that numerical simulations have been carried out until failure of the specimen, and the results, though not presented here, correlate very well with the experimental results.

In general, the numerical simulations are presented by solid lines whereas the experimental results are presented by diamonds in the following figures. Moreover it is noted, that the same axes have been used for the three different concrete compositions to illustrate the differences in the CMOD, separation and slip caused by the addition of relatively small amounts of steel fibres.

Formation of the main bending crack

The experimental and numerical results concerning the CMOD vs. applied load for specimens from PC, 0.5 vol.-% SFRC and 1.0 vol.-% SFRC are presented in Figure 1010 - Figure 12.

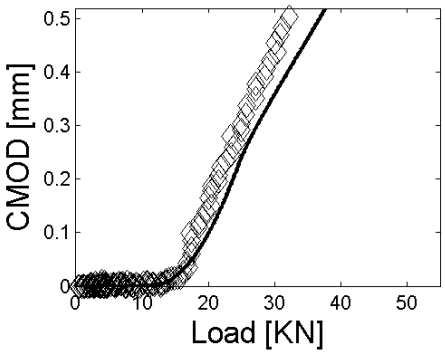

Figure 10: Numerical simulations and experimental results of the CMOD-load relationship for PC.

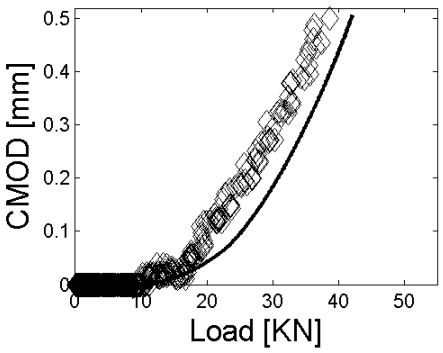

Figure 11: Numerical simulations and experimental results of the CMOD-load relationship for 0.5 vol.-% SFRC.

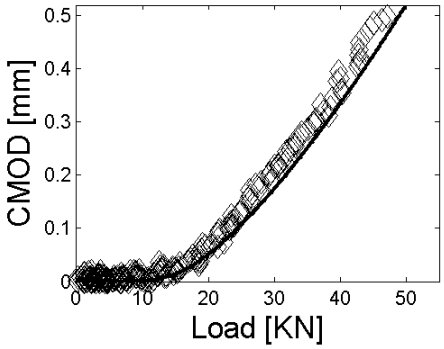

Figure 12: Numerical simulations and experimental results of the CMOD-load relationship for 1.0 vol.-% SFRC.

Separation at the concrete/steel interface

Numerical and experimental observations concerning the separation at the concrete/steel interface are illustrated in Figure 13 – Figure 15. The observations show the separation between concrete and reinforcement located 10 mm away from the main bending crack.

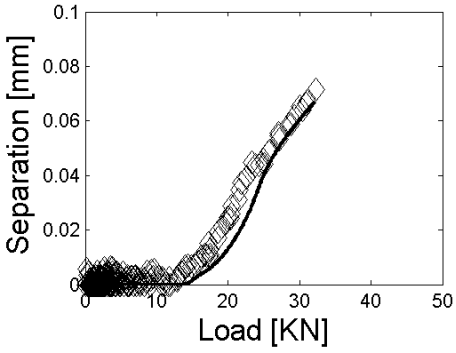

Figure 13: Numerical simulations and experimental results of the separation-load relationship for PC.

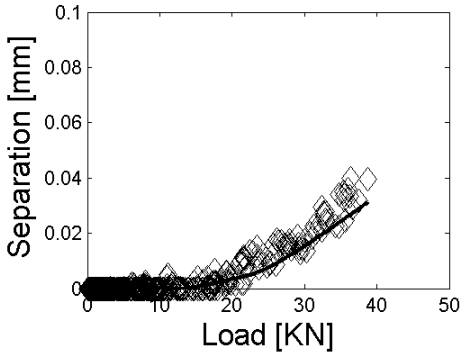

Figure 14: Numerical simulations and experimental results of the separation-load relationship for 0.5 vol.-% SFRC.

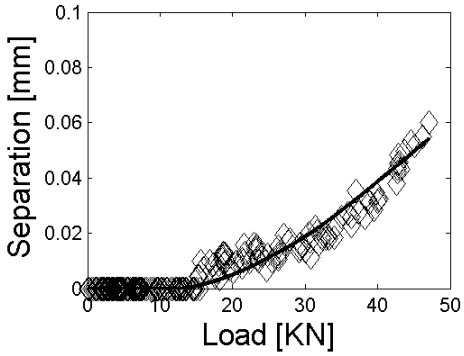

Figure 15: Numerical simulations and experimental results of the separation -load relationship for 1.0 vol.-% SFRC.

Slip at the concrete/steel interface

The slip at the concrete/steel interface as a function of the applied load (3PBT) is presented in Figure 16 – Figure 18. The presented simulations and experimental observations show the slip between concrete and reinforcement located 10 mm away from the main bending crack.

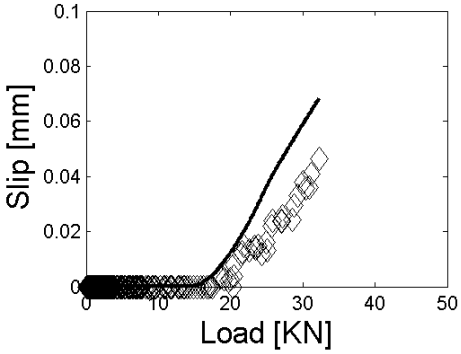

Figure 16: Numerical simulations and experimental results of the slip-load relationship for PC 10 mm from the main bending crack.

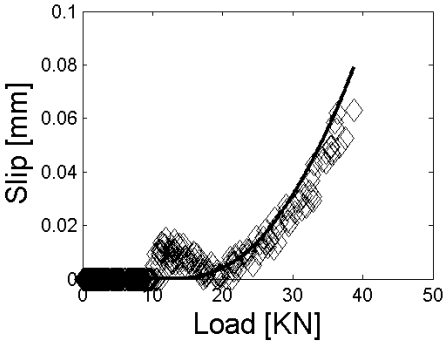

Figure 17: Numerical simulations and experimental results of the slip-load relationship for 0.5 vol.-% SFRC, 10 mm from the main bending crack.

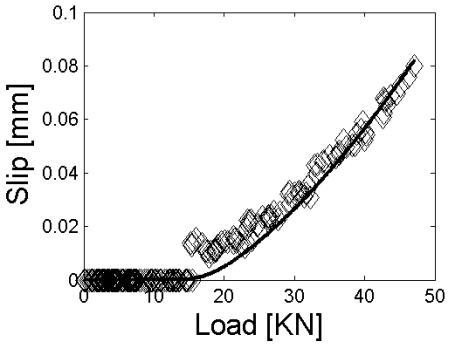

Figure 18: Numerical simulations and experimental results of the slip-load relationship for 1.0 vol.-% SFRC, 10 mm from the main bending crack.

Extent of separation along the concrete/steel interface

The extent of the separation along the concrete/steel interface is shown in Figures 19 - 21 for PC, 0.5 vol.-% SFRC and 1.0 vol.-% SFRC, respectively. Separation at the concrete/steel interface is assumed when the difference in the deformation between the top node and the bottom node of an element connected to the reinforcement and the surrounding concrete reaches Δu_y = 5 μm.

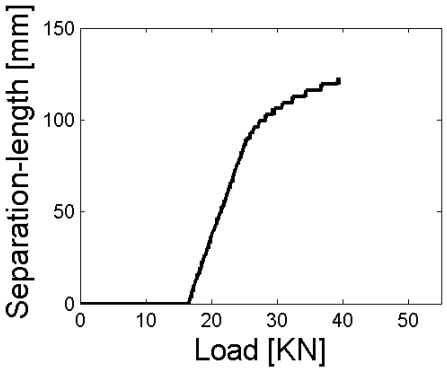

Figure 19: Numerical simulations of the extent of separation along the reinforcement for PC.

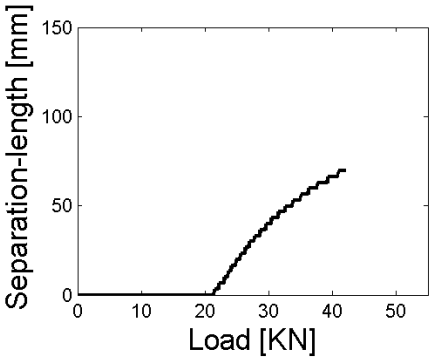

Figure 20: Numerical simulations of the extent of separation along the reinforcement for 0.5 vol.-% SFRC.

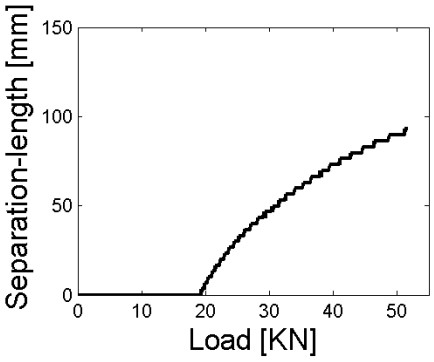

Figure 21: Numerical simulations of the extent of separation along the reinforcement for 1.0 vol.-% SFRC.

Extent of slip at the concrete/steel interface

The extent of slip along the concrete/steel interface has been simulated for all three concrete compositions. An element is considered "slipped" when the difference in the deformation in the y-direction between the top and bottom nodes of an interface element connecting the reinforcement and the surrounding concrete is Δu_x = 10 μm.

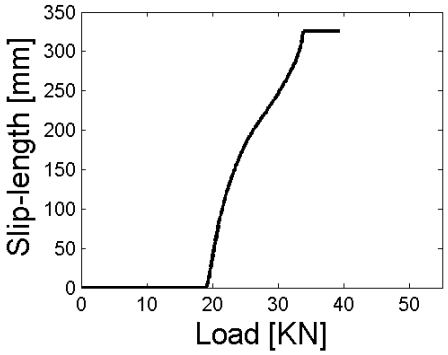

Figure 22: Numerical simulations of the extent of slip along the reinforcement for PC.

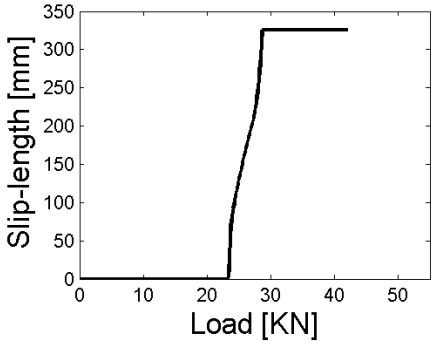

Figure 23: Numerical simulations of the extent of slip along the reinforcement for 0.5 vol.-% SFRC.

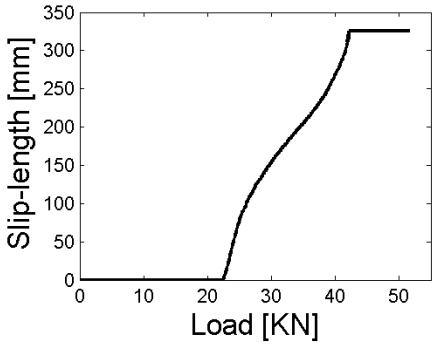

Figure 24: Numerical simulations of the extent of slip along the reinforcement for 1.0 vol.-% SFRC.

Note that the numerical simulations were carried out for half of the beam, ie the length is 325 mm. Thus the flat plateau which is eventually reached in Figure 22 – Figure 24 corresponds to full slip along the concrete/steel interface.

Discussion

The discussions presented in the following concern the correlation between the experimental observations and the numerical simulations for CMOD, slip and separation. Additionally, the approach for the simulations, ie the numerical model presented above, is discussed. The sensitivity of the numerical model is not discussed any further, since this was done previously.

Fracture mechanical properties

The fracture mechanical properties of the interfaces shown in Figure 1 are given in

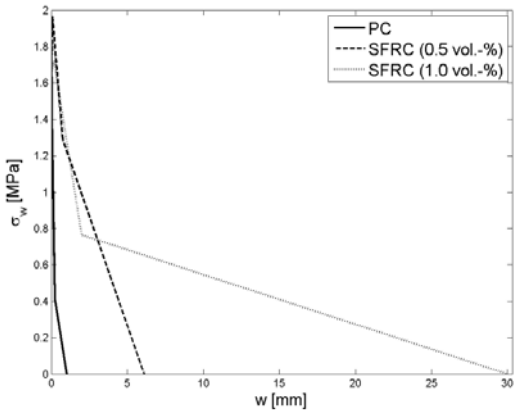

Figure 9: Cohesive relationships for PC and SFRC (0.5 and 1.0 vol.-%). From [*Solgaard et al., 2012*].

Table 2 and Table **3**. The properties given in

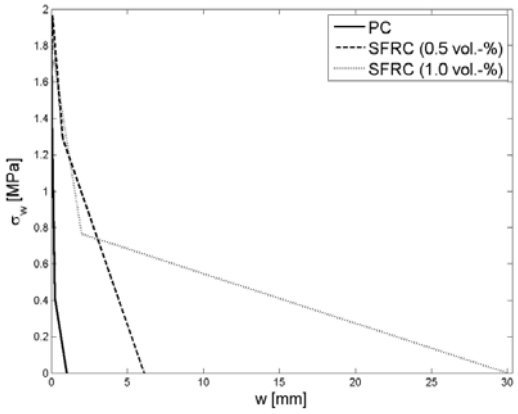

Figure 9: Cohesive relationships for PC and SFRC (0.5 and 1.0 vol.-%). From [*Solgaard et al., 2012*].

Table 2, ie the tensile strength of the concrete domain, the fracture energy and the critical crack width have been obtained from experimental analyses and it is clear

that the addition of fibres does not have a significant impact on the tensile strength of concrete, whereas the ductility, described from the fracture energy and the critical crack width are significantly increased by the addition of such relatively small amounts of fibres. The observations concerning the crack width and fracture energy are in accordance with observations presented by eg Löfgren et al. [*Löfgren et al., 2005*] and Kazemi et al [*Kazemi et al., 2007*].

The properties of the slip and separation interfaces are given in Table **3**. Those properties have been estimated by the numerical model to fit the experimental data. The values used for the tensile strength of the slip interface of the different concrete compositions are in the same order of magnitude (1.1 MPa – 2.57 MPa). However, there is no clear correlation between the fibre content and the fitted tensile strength of the slip-interface.

The strength of the separation interface is constant for all three concrete compositions investigated, viz. $f_{t,sep}$ = 0.03 MPa. The strength of the separation-interface is very low compared to that of the slip-interface and the tensile strength of the interface for the main bending crack. This separation interface describes the chemical bond between the concrete and steel and such values have to the best of the authors's knowledge not been described in the literature. Furthermore, numerical simulations on the impact of $f_{t,sep}$ showed no influence on the formation of the horizontal crack along the reinforcement. Hence the separation is controlled by the formation of internal cracks caused by local stress transfer from the reinforcement to the concrete via the ribs as previously described, and this is accounted for by the interface connecting the upper and lower parts of the concrete body, as previously described.

CMOD

The correlation between the main bending crack and the applied load, is well reproduced by the numerical model, cf. Figure 10 - Figure 12. In general, the model underestimates the CMOD-load relationship. However, the difference between the numerical and –experimental results is not significant. Comparing the experimental results for the three concrete compositions, it is seen that the crack is initiated for approx the same load level, viz. approx 15-18 KN. The numerical model is capable of fitting the crack initiation and the crack width increase as a function of the applied load for all the concrete compositions. Further, the

reduction in CMOD for the SFRC specimens compared to the PC specimen at the same load seen from the experimental observations is captured by the numerical model.

It is underlined that any differences between the numerical simulations and the experimental results may be caused by in-accuracies in the fracture mechanical properties of the concrete given in Table 2 and Figure 9. Those values are determined independently, from experimental observations, as previously described, and are not fitted within the present numerical model.

Separation

The formation of separation at the concrete/steel interface 10 mm away from the main bending crack is seen from Figure 13 - Figure 15. The relationship between the applied load and the slip observed from the numerical simulations is reproduced very accurately by the numerical model for all three concrete compositions. However, the numerical simulations for 0.5 vol.-% SFRC underestimate the separation-load relationship slightly.

Comparing the experimental results for the CMOD-load and the separation-load relationships for each concrete composition, it is seen that separation at the concrete/steel interface does not take place before the main bending crack has been initiated. It is also seen by comparisons of the same figures, that the numerical model simulates this phenomenon very well, though this relation has not been set as a prerequisite in the numerical model. This indicates that the numerical model reproduces the load-induced damage formation physically correct. Moreover, the experimental and the numerical results indicate that the separation at the concrete/steel interface is controlled by the rotation of the specimen caused by the applied load, since the initiation of the separation at the concrete/steel interface is only marginally affected by the addition of fibres. Finally, as previously explained, this separation is controlled by the properties of the interface connecting the upper and lower parts of the concrete body, as this accounts for the formation of internal cracks which are known to control the separation.

Slip

The slip formation at the concrete/steel interface 10 mm from the main bending crack is shown in Figure 16 - Figure 18. It is clear that the numerical simulations capture the experimental observations very well, though the relationship is slightly overestimated for PC, cf. Figure 16. The scatter in the experimental observations for 0.5 vol.-% SFRC is most likely due to the limited resolution of the experimental optical/digital technique. Moreover, it is seen by comparisons of the experimental results concerning the slip at the concrete/steel interface and the CMOD-load relationships, that slip does not take place at the concrete/steel interface before the main bending crack is initiated. The numerical model is capable of simulating the on-set of slip at the concrete/steel interface as well as the slip-propagation due to increased load applied.

Extent of separation and slip

The separation and slip along the reinforcement was simulated assuming threshold values of Δu_x = 10 μm and Δu_y = 5μm for the separation and slip, respectively, cf. Figure 19 - Figure 24. These values correspond to the resolution of experimental results obtained by the use of photogrammetric equipment, eg [*Solgaard et al., 2012*].

It is seen from Figure 19 - Figure 21 that the separation is not initiated for the same load level applied to the three concrete compositions, and that the separation propagates at approximately the same rate along the reinforcement in 0.5 vol.-% SFRC and 1.0 vol.-% SFRC whereas the separation rate along the reinforcement is higher for PC. It can be assumed, based on those observations that separation at the concrete/steel interface does not initiate before the main bending crack reaches the reinforcement. Comparing the three figures it may be concluded that the addition of fibres leads to a decrease in the propagation rate of the separation along the reinforement.

The analysis concerning the extent of slip along the concrete/steel interface, cf. Figure 22 - Figure 24, reveal that the slip is initiated for the same load level for SFRC whereas the load level required to form slip in PC is slightly lower. Once the slip at the concrete/steel is initiated the propagation of the slip along the reinforcement is lower for SFRC compared to PC. That may indicate that the addition of fibres prevent the slip formation at the interface.

The numerical simulations are not verified with experimental data, as that is not available and given that the results presented in Figure 19 - Figure 24 solely depends on the limits for the interpretation of whether an element is slipped or separated the results cannot be discussed any further. Conseqeuntly the results presented in Figure 19 - Figure 24 should be interpreted with precaution since they are not supported by experimental observations.

General discussion

The numerical simulations and the experimental results presented and discussed reveal that the separation and slip along the concrete/steel interface are not two independent phenomena as proposed by the numerical model, cf. Figure 1. The fracture process is a mixed-mode process, ie the two processes are linked as previously discussed. A non-physical fitting parameter was implemented in the model to account for this problem. The same value was assigned to this non-physical fitting parameter for all of the numerical simulations presented. This indicates that this parameter accounts for a problem related to the basis of the model since its value is constant regardless of the concrete properties.

Conclusion

Based on the numerical simulations and the comparisons of those with experimental data it can be concluded:

- A numerical model for the formation of load-induced damage of reinforced concrete subjected to 3PBT has been established. The numerical model simulates the formation of a main bending crack through the concrete cover and damage along the reinforcement (separation and slip) and is based on non-linear fracture mechanics (fictitious crack model and general cohesive fracture mechanics).
- Sensitivity analysis of the numerical model has revealed that the initiation of slip at the concrete/steel interface is independent of the tensile strength of the slip interface, $f_{st,slip}$. However, once slip is initiated the propagation of the slip is dependent on the tensile strength of this interface.
- The bond-slip behavior utilized for the numerical model, is adequate for the formulation of the relationship. The relationship is cubic and attains a constant level of bond for a given slip, dt^0. The numerical model is very sensitive to changes in the value assigned to dt^0.
- The correlation between the results from the numerical model and the experimental results is very good for all three damage mechanisms analysed. Additionally the input parameters for the fracture mechanical behavior of the three interfaces utilized for the three mechanisms have values assigned that are taken directly from independent testing or appears to be in the correct order of magnitude. This emphasizes that the numerical model reproduces the physical processes, ie the damage formation correctly and that the model is based on a physical correct basis.

Acknowledgements

The first author gratefully acknowledge the full financial support of the Ph.D. study “Application of Fibre Reinforced in Civil Infrastructure” by the Danish Agency for Science, Technology and Innovation, COWI A/S, DTU, Bekaert NV, Grace, and the Danish Road Directorate.

References

[Aldea et al., 1999] Aldea, A.-M., Shah, S.P. and Karr, A. (1999), Effect of Cracking on Water and Chloride Permeability of Concrete, *Journal of Materials in Civil Engineering* **11** (3), 181-187.

[Carol et al., 1997] Carol, I., Prat, P.C. and López, C.M. (1997), Normal/shear cracking model: Application to discrete crack analysis, *Journal of Engineering Mechanics* **123**, 765-773.

[Dörr, 1980] Dörr, K. (1980), *Ein Beitrag zur Berechnung con Stahlbetonscheiber unter besonderer Berücksichtung des Verbundverhaltens*, PhD thesis. University of Darmstadt. Darmstadt, Germany.

[Edvardsen, 1999] Edvardsen, C. (1999), Water Permeability and Autogenous Healing of Cracks in Concrete, *ACI Materials Journal* **96** (4), 448-454.

[Francois and Arliguie, 1998] Francois, R. And Arliguie, G. (1998), Influence of service cracking on reinforcement steel corrosion, *Journal of Materials in Civil Engineering* **10** (1), 14-20.

[Hillerborg et al., 1976] Hillerborg, A., Modéer, M. and Petersson, P.-E. (1976), Analysis of crack formation and crack growth in concrete by means of fracture mechanics and finite elements, *Cement and Concrete Research* **6** (6), 773-782.

[Kazemi et al., 2007] Kazemi, M.T., Fazileh, F. and Ebrahiminiezhad, M.A. (2007), Cohesive Crack Model and Fracture Energy of Steel-Fiber-Reinforced-Concrete Notched Cylindrical Specimens, *Journals of Materials in Civil Engineering* **19** (10), 884-890.

[Kennedy, 1956] Kennedy, T.B. (1956), Tensile Crack Exposure Tests of Stressed Reinforced Concrete Beams, *ACI Journal* **56** (6), 1049-1063.

[Lourenco and Rots, 1997] Lourenco, P.B. and Rots, J.G. (1997), Multisurface interface model for analysis of masonry structures, *Journal of Engineering Mechanics* **123**, 660-668.

[Löfgren et al., 2005] Löfgren, I., Olesen, J.F. and Flansbjer, M. (2005), *Application of WST-method for fracture testing of fibre-reinforced concrete*, NT Technical Report, Norway.

[Michel et al.,2012] Michel, A., Solgaard, A.O.S., Pease, B.J., Geiker, M., Stang, H. and Olesen, J.F. (2012), Corrosion along the reinforcement – experimental analyses, submitted for *Materials and Structures* February 2012.

[Mohammed et al., 2001] Mohammed, T., Otsuki, N., Hisada, M. and Shibata, T. (2001), Effect of crack width and bar type on corrosion of steel in concrete, *Journal of Materials in Civil Engineering* **13** (3), 194-201.

[Nielsen et al., 2010] Nielsen, L.O., Mougaard, J.F., Jacobsen, J.S. and Poulsen, P.N. (2010), A mixed mode for fracture in concrete, *Proceedings of FraMCoS 2010*.

[Olsen, 2010] Olsen, T. (2010), *Modelling of the Shear Capcity of Reinforced Concrete Beams*, Master's thesis, Department of Civil Engineering,Technical University of Denmark, Lyngby, Denmark.

[Pease et al., 2006] Pease, B.J., Geiker, M., Stang, H. and Weiss, J. (2006), Photogrammetric assessment of flexure induced cracking of reinforced concrete beams under service loads, *Proceedings of the second international RILEM symposium – advances in concrete through science and engineering*.

[Pease et al., 2011] Pease, B.J., Geiker, M., Stang, H. and Weiss, J. (2011), The design of an instrumented rebar for assessment of corrosion in cracked concrete, *Materials and Structures* **44** (7), 1259-1271.

[Rendell et al., 2002] Rendell, F, Jauberthie, R. and Grantham, M. (2002), *Deteriorated Concrete Inspection – Inspection and physiochemical analysis*, Thomas Telford, London.

[Schießl and Raupach, 1997] Schießl, P. and Raupach, M. (1997), Laboratory studies and calculations on the influence of crack width on chloride-induced corrosion of steel in concrete, *ACI Materials Journal* **94** (1), 56-62.

[Skoček and Stang, 2010] Skoček, J., and Stang, H. (2010), Application of optical deformation analysis system on wedge splitting test and its inverse analysis, *Materials and Structures* **43**, 63-72.

[Solgaard et al., 2012] Solgaard, A.O.S., Michel, H. and Stang, H. (2012), Debonding at the Concrete/steel Interface in Reinforced Concrete Beams – Experimental Investigations: Part I, *Submitted for publication in Materials and Structures* February 2012.

[Tammo and Thelandersson, 2009a] Tammo, K. and Thelandersson, S. (2009a), Nonlinear analysis of crack widths in reinforced concrete, *Magazine of Concrete Research* **61** (1), 23-34.

[Tammo and Thelandersson, 2009b] Tammo, K. and Thelandersson, S. (2009b), Crack widths near reinforcement bars for beams in bending, *Journal of the FIB* **10** (1), 27-34.

[Wang et al., 1997] Wang, K., Jansen, D.C., Shah, S.P. and Karr, A.F. (1997), Permeability Study of Cracked Concrete, *Cement and Concrete Research* **27** (3), 381-393.

[Win et al., 2004] Win, P.P., Watanabe, M. and Machida, A. (2004), Penetration Profile of Chloride Ion in Cracked Reinforced Concrete, *Cement and Concrete Research* **34**, 1073-1079.

Paper VIII

” Experimental investigation of the relation between damage at the concrete-steel interface and initiation of reinforcement corrosion in plain and fibre reinforced concrete”

A. Michel, A.O.S. Solgaard, B.J. Pease, M.R. Geiker, H. Stang & J.F. Olesen

Published in: *Corrosion Science.*

Volume 77, December 2013

ISSN 0010-938X

ELSEVIER

CORROSION SCIENCE

The Journal on Environmental Degradation of Materials and its Control

Editor-in-Chief: G. T. BURSTEIN, University of Cambridge, U.K.

An Official Journal of the Institute of Corrosion

CONTENTS

Contents continued on outside back cover

http://www.elsevier.com/locate/corsci

Corrosion Science 77 (2013) 308–321

Contents lists available at ScienceDirect

Corrosion Science

journal homepage: www.elsevier.com/locate/corsci

Experimental investigation of the relation between damage at the concrete-steel interface and initiation of reinforcement corrosion in plain and fibre reinforced concrete

A. Michel [a,c,*], A.O.S. Solgaard [a,b], B.J. Pease [a], M.R. Geiker [a,c], H. Stang [a], J.F. Olesen [a]

[a] Department of Civil Engineering, Technical University of Denmark (DTU), Kgs. Lyngby, Denmark
[b] COWI A/S Denmark, Kgs. Lyngby, Denmark
[c] Department of Structural Engineering, Norwegian University of Science and Technology (NTNU), Trondheim, Norway

ARTICLE INFO

Article history:
Received 7 January 2013
Accepted 22 August 2013
Available online 2 September 2013

Keywords:
A. Steel reinforced concrete
C. Atmospheric corrosion

ABSTRACT

Cracks in covering concrete are known to hasten initiation of steel corrosion in reinforced concrete structures. To minimise the impact of cracks on the deterioration of reinforced concrete structures, current approaches in (inter)national design codes often limit the concrete surface crack width. Recent investigations however, indicate that the concrete-reinforcement interfacial condition is a more fundamental criterion related to reinforcement corrosion. This work investigates the relation between macroscopic damage at the concrete-steel interface and corrosion initiation of reinforcement embedded in plain and fibre reinforced concrete. Comparisons of experimental and numerical results indicate a strong correlation between corrosion initiation and interfacial condition.

1. Introduction

Concrete reinforced with steel bars is nowadays the most used manmade construction material in the world. Embedding steel in concrete has several advantages and helps to overcome shortcomings of both materials. Concrete has a high compressive strength, but a low tensile strength and is therefore reinforced for structural purposes, while the steel is protected by the concrete from potentially harmful environmental exposure. Usually, the reinforcement in uncracked concrete is protected due to the high alkalinity (pH around 13) [1] and the concrete cover as a physical barrier itself against the ingress of corrosion initiating substances, such as water, chloride ions, carbon dioxide and oxygen. In the case of uncracked and uncontaminated concrete, the quality and thickness of the concrete cover are the most influential factors for reinforcement corrosion. In practice however, cracks can be found in nearly all reinforced concrete structures originating from hygral or thermal shrinkage and/or mechanical loading.

Within the past decades, numerous investigations on the impact cracks have on the ingress of corrosion initiating substances and reinforcement corrosion have generally concluded that cracks facilitate rapid ingress [2–9] and subsequently reduce the time to corrosion initiation. Both laboratory studies [10–15] and in situ observations [16–20] have noted an expedited corrosion initiation in cracked concrete compared to pristine concrete. Commonly used approaches, see e.g. [10,11,13–17,19,20], attempt to relate corrosion initiation and propagation to the concrete surface crack width. Thus, controlling concrete surface crack widths has become the norm to attempt to minimise the impact of cracks on corrosion-induced deterioration in structural design codes and recommendations [21–27]. Various probabilistic, empirical, and quasi-analytical cracking models are utilised in these structural design codes to predict crack widths based upon numerous geometric and stress (or strain) parameters. However, predicted and observed crack widths can vary significantly [28]. Further, a number of studies (both from laboratory and in situ observations) indicate that the concrete surface crack width alone cannot accurately assess the impact of cracks on reinforcement corrosion as other factors, such as concrete cover thickness [13,17], concrete composition (in particular water-to-cement ratio [11,13,29–31] and addition of supplementary cementitious materials [10,32,33]), stress level in the reinforcement [34], and crack orientation [35] alter the influence of the crack width on reinforcement corrosion.

One possible explanation for the lacking relationship between concrete surface crack width and reinforcement corrosion behaviour is that the surface crack width alone does not reliably describe the condition of the concrete-reinforcement interface [36,37]. The condition of the concrete-reinforcement interface appears to be a more fundamental criterion than the concrete surface crack width influencing the corrosion protection ordinarily provided by

* Corresponding author at: Department of Civil Engineering, Technical University of Denmark (DTU), Kgs. Lyngby, Denmark. Tel.: +45 4525 1656; fax: +45 4588 3282.
E-mail address: almic@byg.dtu.dk (A. Michel).
URL: http://www.dtu.dk (A. Michel).

0010-938X/$ - see front matter © 2013 Elsevier Ltd. All rights reserved.
http://dx.doi.org/10.1016/j.corsci.2013.08.019

concrete. Several references report accelerated corrosion initiation and relatively excessive cross-sectional reductions (compared to reinforcement with good cohesion with concrete) take place at sites of various interfacial defects, including entrapped or cast-in voids [38–41], casting joints [42], spalled concrete [20], and interfacial slip and separation caused by mechanical loading [43]. Results of experimental studies indicate that such interfacial defects at the concrete-reinforcement interface reduce the critical chloride threshold for corrosion initiation, see e.g. [38,41]. This, coupled with the increased ingress of corrosion-initiating substances associated with concrete cracks described above, clearly illustrates the potential deleterious impact of concrete cracks on reinforced concrete structures.

The main focus of this study was to test the hypothesis that controlling the concrete-reinforcement interfacial condition can be used as a single indicator for the impact of cracks on the risk of corrosion initiation along the reinforcement. The relation between interfacial damage and risk of corrosion initiation along the reinforcement was investigated for plain (PC) and steel fibre reinforced concrete (SFRC) beams subjected to flexural loading. A numerical model, developed and calibrated using specimens with similar geometries and identical materials, provided estimates on the extent of interfacial damage for the applied loads and measured surface crack widths. The impact of concrete cover thickness, concrete composition, stress level in the reinforcement and crack orientation on the mechanical response of the beam, i.e. cracking and interfacial damage was directly accounted for in the numerical model. Location- and time-dependent corrosion measurements along the reinforcement were performed using recently developed "instrumented rebars", which have a largely similar mechanical behaviour as conventional reinforcement [43]. For each beam, the open circuit corrosion potential (OCP) was measured at 17 locations and the macrocell current at 8 locations along the instrumented rebar. Comparisons of the cracking behaviour in [43] indicated the formation of interfacial damage due to flexural loading, i.e. slip and separation between the concrete and steel, is very similar for the conventional and instrumented rebar. Therefore, the instrumented rebar is a useful tool to investigate a potential link between mechanically-induced concrete-reinforcement interfacial damage and the corrosion response of the reinforcement. However, it should be mentioned that a practical application of instrumented rebars may be difficult due to the intensive monitoring equipment required for continuous OCP and macrocell current measurements. Nevertheless, previous results [36,43] and results of the present study indicate that instrumented rebars are suitable for laboratory investigations to study the effect of load-induced damage on reinforcement corrosion and to strengthen the hypothesis that load-induced interfacial damage can be used as an indicator for the risk of reinforcement corrosion.

2. Experimental investigations

To investigate the impact of cracks and the associated interfacial damage between concrete and reinforcement on the initiation of corrosion, reinforced concrete specimens were prepared, cracked, and tested in a corrosive environment. Experimental studies included mechanical and electrochemical testing as well as destructive visual investigation of plain (PC) and steel fibre reinforced (SFRC) specimens. During mechanical testing, photogrammetric investigations were performed to monitor load-induced cracking, slip, and separation between concrete and reinforcement. In addition, fracture mechanical properties of the different concrete compositions were determined using inverse analysis of experimental results obtained from three point bending tests (3PBT) as described in [44]. The 3PBTs were conducted in accordance with [45,46]. Electrochemical testing included time- and location-dependent OCP and macrocell current measurements with so-called instrumented rebars, which were embedded in each of the tested specimens along with a conventional rebar. The test matrix for the various experimental investigations is given in Table 1, including information on the naming convention and numbers of tested specimens. For each concrete composition, three specimens (MSF) were tested to determine fracture mechanical properties by inverse analysis of 3PBT results. Results of individual specimens of one concrete composition were then averaged. Four specimens (MSA) were tested for each concrete composition, i.e. two different concrete cover thicknesses (20 and 60 mm), to investigate load-induced cracking and associated interfacial damage by means of photogrammetry and subsequent digital image correlation. However, for simplicity, only results of specimens with a concrete cover thickness of 60 mm are presented in this study. Finally, one specimen (ESE) was tested for each concrete composition to study the influence of cracking and interfacial damage on the initiation of reinforcement corrosion using instrumented rebars, which allow for continuous OCP and macrocell current measurements. After termination of electrochemical testing, the electrochemical test specimens (ESE) were used for destructive visual investigations.

2.1. Materials and specimen preparation

Beams of plain (PC) and steel fibre reinforced concrete (SFRC) with a water-to-cement ratio of 0.43 were cast. Aalborg Rapid® Portland cement (type 52.5N cement [47]) was used and the mix designs for the different concrete compositions are given in Table 2. DRAMIX 65/35 fibres (hooked ended and made from cold drawn black steel) were used for the SFRC mixes with a length of 35 mm and diameter of 0.55 mm. As reinforcement, two rebars with 12 mm diameter, i.e. one conventional rebar and one instrumented rebar (described in Section 2.2), were embedded in each of the $290 \times 310 \times 650$ mm^3 (height × width × length) prisms. The steel fibre reinforced beams were cast in oversize to avoid fibre orientation caused by the sides of the moulds. After casting, the beams were stored for 24 h in laboratory conditions under a plastic sheet (i.e. 20 ± 2 °C) and then demolded. Upon demoulding, the beams were stored in lime rich water for additional 28 days at 20 ± 2 °C until testing. Prior to cracking and testing, the SFRC beams were cut using a water-cooled concrete saw. Unreinforced MSF beams, i.e. specimens used for the determination of fracture mechanical properties, were cut to $150 \times 150 \times 650$ mm^3 in accordance with the size recommended in [45]. Specimens used for photogrammetric investigations (MSA) were cut to $150 \times 120 \times 650$ mm^3, where part of the concrete covering the reinforcement was removed to allow for monitoring of load-induced cracking and interfacial damage. However, a minute concrete cover remained (approximately 3–5 mm) to, among others, avoid damaging the concrete-reinforcement interface during the cutting process. Finally, a stochastic black and white speckle pattern was applied to the remaining concrete cover, which was used later for photogrammetric investigations. The final dimensions of the ESE beams, i.e. specimens used for electrochemical testing, were $190 \times 150 \times 650$ mm^3 with 60 mm

Table 1
Test matrix for experimental investigations.

Experimental investigation	Concrete composition		
	PC	SFRC	
	Fibre content (vol.%)		
	0.0	0.5	1.0
Fracture mechanical properties	MSF 1-3	MSF 4-6	MSF 7-9
Photogrammetric investigations	MSA 1-4	MSA 5-8	MSA 9-12
Electrochemical testing	ESE 1	ESE 2	ESE 3

Table 2
Mix designs of investigated concrete compositions.

Constituent	PC (kg/m^3)	SFRC 0.5 vol.% (kg/m^3)	SFRC 1.0 vol.% (kg/m^3)
Cement	375	375	375
Water	156	156	156
Sand (0–4 mm)	760	755	750
Gravel (4–8 mm)	56	56	56
Stones (8–16 mm)	1025	1018	1011
Fibres	–	39	78

concrete cover thickness. A sketch of the cutting procedure for the different specimens is shown in Fig. 1, where the dark grey area represents the final specimen geometry. Detailed information on initial and final specimen dimensions can be found in Table 3.

2.2. Instrumented rebar

A sketch of the design of the instrumented rebar is illustrated in Fig. 2. The applicability of the instrumented rebar to monitor time- and location-dependent OCP in concrete, while having a similar mechanical behaviour as a conventional rebar, was tested and presented in [36,43].

The instrumented rebar consisted of three individual sections of standard 12 mm diameter deformed rebar cut to lengths, which were connected via screw threads. The mid-section of the instrumented rebar was hollowed providing a 6 mm diameter void along the centre. Hollowing of the instrumented rebar resulted in a 6.25% reduction in bending stiffness (i.e., EI), a 25% reduction in cross-sectional area, and an axial stiffness (i.e., EA) equivalent to a standard rebar with a 10.39 mm nominal diameter. Seventeen holes, with 4.5 mm diameter, were drilled through the outer surface with a 10 mm spacing. In each hole, a 4 mm diameter steel pin was placed. A lead wire was soldered to each of the steel pins and afterwards encased in glue-coated heat-shrink tube to ensure electrical disconnection between the individual steel pins and the rebar. Finally, the hollowed section was filled with epoxy to protect the wires, electrical connections, and steel pins. The two solid rebar sections were connected to the hollowed mid-section using threaded connections. In contrast, to the configuration presented in [36,43] the sensors were installed flush in this study as results in [36,43] indicated that protruding sensors reduce the load-induced separation between reinforcement and concrete to some extent.

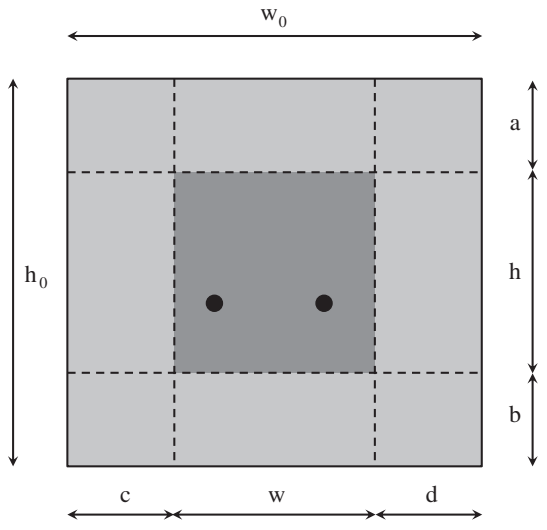

Fig. 1. Cutting of MSF, MSA, and ESE specimens. Please note: sketch is not to scale.

Table 3
Initial, final, and cutting dimensions for tested specimens.

Parameter (mm)	Specimen		
	MSF	MSA	ESE
a	40	40	0
b	100	100	100
c	80	80	80
d	80	110	80
h	150	150	150
h_0	290	290	290
w	150	120	150
w_0	310	310	310

2.3. Photogrammetric investigations

To monitor load-induced cracking and the associated interfacial damage of the MSA specimens (see Table 1), photogrammetric equipment was used. The set-up of the photogrammetric equipment is illustrated in Fig. 3 consisting of two charged-coupled device (CCD) cameras placed on a rig parallel to the specimen. The two CCD cameras were positioned at a mutual distance from the specimen and the angle between the cameras was constant. An area of approximately 350 × 150 mm^2 (width × height) was thereby monitored by both cameras, which was positioned around the centre of the specimen. Images with the CCD cameras were recorded every two seconds until testing was terminated. Captured images were subsequently processed with a commercially available software package [48], which utilised the stochastic speckle pattern to identify unique regions, called facets, on the specimen surface at each measurement time. The software tracks the movements of the facets and utilises standard digital image correlation (DIC) techniques to compute, among others, deformations and strain fields (see Fig. 4) at the specimen surface. DIC also allows for identification of cracks as zones with localised strain. Additional information on the hardware used and the DIC technique is available in [49,50].

All specimens were tested in a load-controlled set-up. Experimental results covered applied load as well as strain and deformation fields at the specimen surface. Interfacial damage, i.e. slip and separation between reinforcement and concrete were determined from DIC results measuring the relative displacement between points adjacent to the reinforcement. In addition, slip and separation between concrete and reinforcement were determined for various distances from the centre of the primary bending crack.

2.4. Electrochemical testing

2.4.1. Loading and environmental exposure

Fig. 5 illustrates the customised steel cracking frames, which were used to hold open cracks and interfacial damage. As the steel cracking frames were not designed to induce cracks (because of insufficient stiffness of steel channel and threaded rods), a standard loading machine was used to pre-crack the beams. During pre-cracking, load was applied to estimated cracking loads predicted by the numerical cracking model described in Section 3. The pre-cracked beams were then loaded in the customised steel cracking frames to preset load levels given in Table 4 and the crack mouth opening displacement (CMOD) at the tensile surface and applied load were measured. Load was measured and recorded using customised ring load cells, which were tested and calibrated before using a standard loading machine. Load was applied by tightening the bolts until the defined target load was reached. After

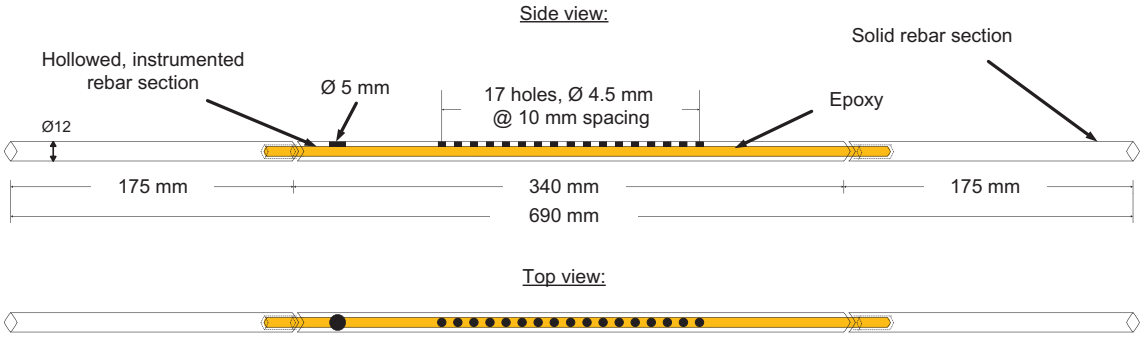

Fig. 2. Design of instrumented rebar for time- and location-dependent OCP measurements (Note: ribs are not shown in sketch), after [43].

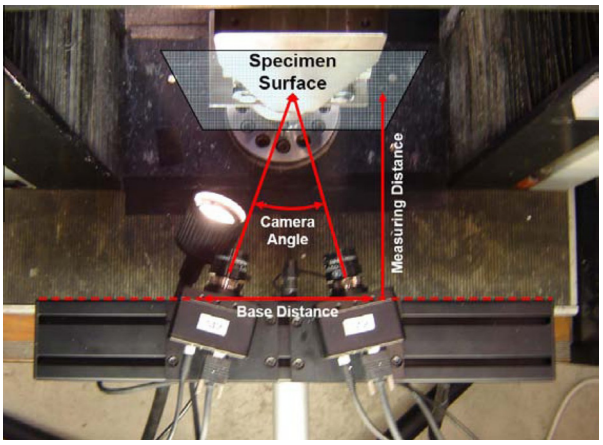

Fig. 3. Set-up of photogrammetric equipment, from [43].

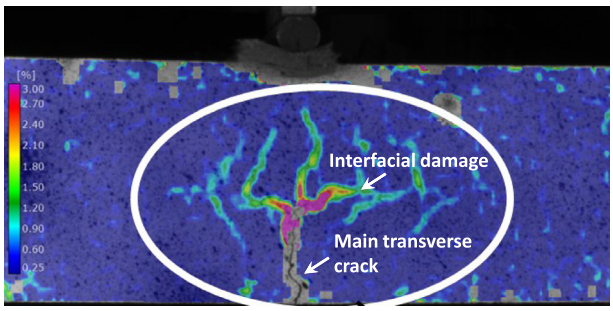

Fig. 4. Results of DIC measurements, indicating main transverse crack and associated damage due to mechanical loading. Please note: colour scale indicates strain calculated by DIC.

application of the load, the sides of each beam were sealed using silicone caulk to prevent leaking of the test solution throughout the exposure. Afterwards, a plastic ponding dike was placed on the tension surface, i.e. over the main bending crack, and the area outside the ponding dike sealed with silicone caulk. The reservoir was filled with a 3% sodium chloride (NaCl) solution by weight and refilled as necessary during testing. The sodium chloride concentration was chosen to reflect chloride concentrations, which may be found under in situ conditions. Possible impacts of sodium chloride concentration variations were not part of the present study.

2.4.2. OCP and macrocell current measurements

Open circuit corrosion potentials (OCP) of all sensors along the instrumented rebar were measured against a standard calomel electrode (SCE), which was placed in the ponding reservoir. The reference electrodes were maintained on a weekly basis. Maintenance included refilling with saturated potassium chloride solution, potassium chloride crystals, and calibration against a silver/silver chloride reference electrode in a pH buffered solution. Due to the frequent maintenance and constant temperature of the exposure solution, the readings of the reference electrode were regarded stable.

In addition to the potential measurements, macrocell current measurements were taken for half of the sensors along the instrumented rebar. The electrical connection between the counter electrode and working electrode (individual sensors along the instrumented rebar) may be established over a resistor, and the macrocell current is measured as the proportional potential over the resistor, or as done in the present study, over a zero-impedance-ammeter, i.e. without introducing resistance to the system. A ruthenium/iridium mixed metal oxide activated titanium mesh (MMO) was used as a counter electrode, which was also placed

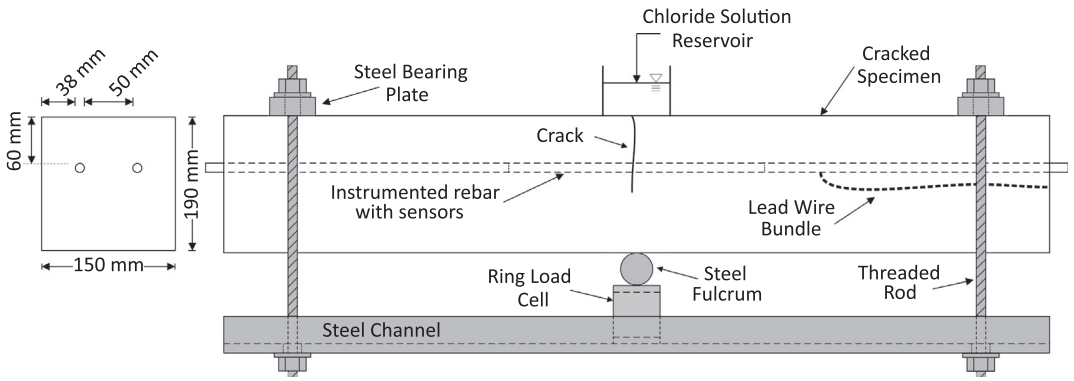

Fig. 5. Steel cracking frames for loading of beams with specimen illustrating the instrumented rebar and ponding reservoir, after [43].

Table 4
Applied loads, measured CMODs, and estimated extent of slip and separation for all materials tested.

Specimen	Load[a] (kN)	CMOD[b] (mm)	Extent of slip[c,d] (mm)	Extent of separation[c,d] (mm)
PC	31.2	0.069	±325	~ ± 40
SFRC 0.5 vol.%	45.7	0.139	±325	~ ± 70
SFRC 1.0 vol.%	35.6	0.068	±325	~ ± 35

[a] Measured with customised ring load cells.
[b] Measured average CMOD at concrete tensile face.
[c] Estimated by finite element model (see Section 3).
[d] Distance from main bending crack.

in the ponding reservoir. The measured current flow between the individual sensors and MMO was transferred to a voltage output before connection to the corresponding data logger terminals. The transformation was performed by two electrically separated ammeters, which were driven by two rechargeable 9 V block batteries. The batteries were automatically recharged to keep the supply voltage at a constant level. In this way, the ammeters were operated with a stable supply voltage that was insulated from any perturbation sources. The ammeters provided an exact linear relation between voltage output and current input with a transformation factor of 1 V/mA. The ammeters were nulled, based on the applied supply voltage and zero current before the electrical connection between working and counter electrode was established. When the individual sensors were connected to the MMO, a mixed corrosion potential was obtained and the current flow through the ammeters was enabled without introducing resistance. While for the passive state of sensors current flows of approximately zero μA were measured, considerably higher current flows were measured for active sensors, see e.g. Fig. 11(b). Since the exposure area of the individual sensors of the instrumented rebar was well defined (0.126 cm^2), the measured current flows allowed for an estimate of the corrosion current density. The increase in current flow with initiation of active corrosion was sharp and well defined, so that the onset of corrosion could be clearly identified. However, it should be emphasised that only the macrocell current between the dissimilar was measured and consequently the micro- and macrocell corrosion activity on the preferential corroding metal surface is not reflected. Nevertheless, the technique is frequently used in the area of reinforcement corrosion due to its simplicity and clear indication of corrosion initiation by a sharp increase in macrocell current with depassivation, see e.g. [51–53]. Furthermore, it can be assumed that the measured macrocell current flows contributed the major part of the corrosion activity of the individual sensors in the present experimental set up as the anodic area was considerably smaller than the cathodic area (approximately 3 cm^2), see e.g. [51,52].

OCP and current flow measurements were taken automatically every 2 h by a LabVIEW controlled system using cluster measurements to minimise the number of data logging channels [54]. For each measurement time, a switch card hosting up to eight electrodes (sensors) was connected to a SCE and the OCP recorded until the system automatically switched to the next card and established a new connection. After connecting to each of the individual cards, a delay period of 2 min was set in the program at which the OCP was measured and recorded for each sensor along the instrumented rebar.

In addition, to the electrochemical OCP and macrocell current measurements, destructive visual investigations were conducted after terminating the electrochemical testing. The concrete covering the instrumented and standard rebar was removed cutting 25 mm deep notches above and below the rebars and crack opening the beam using chisel and hammer. Visual inspections included the extent and amount of corrosion as well as penetration of chloride ions (spraying silver nitrate on the concrete as an indicator) in the concrete and along the instrumented and standard rebar.

3. Modelling of load-induced cracking and interfacial damage

3.1. Model description

To estimate the extent of load-induced interfacial damage along the reinforcement for the tested flexural beams, a finite element method (FEM) model was used. The model was based on a two dimensional, plain strain formulation that allows for simulation of cracking and interfacial damage, i.e. slip and separation between reinforcement and concrete, in reinforced concrete subjected to flexural loading. The basic concept of the modelling approach is given in Fig. 6. To simulate the different damage phenomena in concrete and along the reinforcement associated with flexural loading (i.e. cracking, slip, and separation) a number of zero thickness interface domains are incorporated in the model. The various interface domains are established in serial and parallel connection to represent a realistic mechanical response of the beam during loading and the subsequent formation of associated damage. In the FEM model, slip denotes the local displacement between the reinforcement and the surrounding concrete parallel to the reinforcement, while separation corresponds to the deformation between the reinforcement and the surrounding concrete perpendicular to the reinforcement.

Formation and propagation of load-induced damage in the crack, concrete, and separation interface (see Fig. 6) was modelled by a fictitious cracking approach [55] where the tension softening behaviour is based on a cohesive discrete cracking model with multi-linear softening relations, which may be given as follows:

$$\sigma = \begin{cases} \sigma_e(\varepsilon) = E_{conc}\varepsilon & \text{Pre} - \text{cracked state} \\ \sigma_w(w) = g(w) f_{t,conc} & \text{Cracked state} \end{cases} \quad (1)$$

where σ_e is the elastic stress, E_{conc} the Young's modulus of concrete, ε the elastic strain, σ_w the normal bridging stress as a function of the crack width w, g the dimensionless cohesive relationship and $f_{t,conc}$ the concrete tensile strength. Formulation of the multi-linear softening relations used to describe the dimensionless cohesive relationship, g, was adopted from [44] and may be given as follows:

$$g(w) = b_i - a_i w \text{ for } w_{i-1} < w < w_i \text{ and } i = 1, \ldots, n \quad (2)$$

where a_i describes the slopes of the cohesive branches, b_i the intercepts between the cohesive branches and w_i may be defined as follows:

$$w_i = \frac{b_i - b_{i+1}}{a_i + a_{i+1}} \text{ for } i = 1, \ldots, n-1 \text{ and } w_n = w_{crit} = \frac{b_n}{a_n} \quad (3)$$

where w_{crit} is the critical crack width. Further, it is assumed that no stresses are transferred across the crack once $w > w_{crit}$. For the crack and concrete interface, n was set to 3, while $n = 1$ (i.e. linear tension softening behaviour) was chosen for the separation interface.

To describe the slip between concrete and reinforcement a modified cubic-relationship between the shear stress and slip, proposed in [56], was used, which may be given as follows:

$$t_t = \begin{cases} f_{t,slip}\left(1.4\left(\frac{\Delta u_t}{\Delta u_t^0}\right)^3 - 4.5\left(\frac{\Delta u_t}{\Delta u_t^0}\right)^2 + 5\left(\frac{\Delta u_t}{\Delta u_t^0}\right)\right) & \text{for } 0 \leqslant \Delta u_t < \Delta u_t^0 \\ 1.9 f_{t,slip} & \text{for } \Delta u_t \geqslant \Delta u_t^0 \end{cases} \quad (4)$$

where t_t is the shear stress, $f_{t,slip}$ the strength of the slip interface, u_t the slip, and u_t^0 the value at which the curve reaches a plateau. For the different concrete compositions, the strength of the slip interface, $f_{t,slip}$, and u_t^0 were modified during the FEM simulations to fit the experimental observations.

Although, mainly physical meaningful parameters are used in the FEM model to describe the different damage phenomena in the concrete domain and along the concrete-reinforcement interface due to flexural loading, it should be noted that the formation of slip and separation at the concrete-reinforcement interface was modelled as independent processes. The authors are aware that the combination of these damage processes may be described by mixed-mode fracture behaviour. However, despite many efforts, see e.g. [57–59], there still appears to be a lack of proper mixed-mode behaviour formulations, which can be implemented in models for FEM simulations.

3.2. Numerical model, input parameters, and mesh analysis

For the solution of the problem the commercial FEM software package TNO DIANA was used. The model consisted of 1184 quadrangular elements with 2353 nodes representing half of the beam due to symmetry of loading and boundary conditions of the three point bending test (see Fig. 5). Nonlinear solution of the system of equations was obtained using a standard Newton–Raphson method with a displacement controlled convergence criterion.

To investigate the impact of varying mesh sizes on the solution of the problem, a range of interface discretisations were studied. Number of elements along the crack, separation, and slip interface were varied between 10 and 100 elements. Results of the mesh analysis are given in Fig. 7. For all interfaces, no considerable effect on the solution of the problem (less than 1% difference between the different mesh sizes) was found once more than 20 elements were used to discretize the interfaces. Based upon the results presented in Fig. 7, the crack, slip, and separation interfaces were discretized with 60 elements each.

An overview of the required input parameters for the developed FEM model to simulate load-induced damage in PC and SFRC beams is given in Table 5. Input parameters cover elastic and fracture mechanical properties of steel and concrete as well as cracking, slip, and separation interface. The reduced cross section of the instrumented rebar (hollowed part) is directly accounted for in the FEM model. To fit the experimental results (see Section 4.1.2), the tensile strength of the slip interface, $f_{t,slip}$, and the value, u_t^0, (see Eq. (4)) were varied during the numerical simulations.

4. Results

Experimental and numerical results for plain and steel fibre reinforced concrete are presented in the following. Results of mechanical testing include fracture mechanical properties, photogrammetric investigations on load-induced cracking, slip and separation at the concrete-reinforcement interface, and comparisons between experimental (i.e. photogrammetric investigations) and numerical results for the various concrete compositions. All experimental and numerical results are presented for crack mouth opening displacement (CMOD) at the concrete tensile surface, separation, and slip at the concrete-reinforcement interface against applied load. Electrochemical results cover information on time- and location-dependent open circuit corrosion potential (OCP) and macrocell current measurements for the various concrete compositions. Finally, visual observations of the extent of corrosion along the instrumented and standard rebar and chloride ion ingress are given.

4.1. Mechanical testing

4.1.1. Fracture mechanical properties

As mentioned previously, inverse analysis of experimental results of 3PBTs was used to determine fracture mechanical properties of the different concrete compositions tested in this study (see Table 2). Selected experimental results and results of the corresponding inverse analysis are given in Fig. 8.

A very good agreement between experimental and numerical results, obtained by inverse analysis of load-CMOD curves, is found for all specimens tested. Furthermore, the impact of fibres on the mechanical response is clearly observed, i.e. an increasing ductile material behaviour with increasing fibre content. Fracture energy, G_f, and tensile strength, $f_{t,conc}$, of the various concrete compositions determined by means of inverse analysis are given in Table 6. The multi-linear cohesive relations used in the FEM model to describe the tension softening behaviour (see Eq. (2)) of the different concrete compositions are presented in Fig. 9.

4.1.2. Experimental and numerical results of load-induced damage

Experimental and numerical results illustrating load-induced damage, i.e. cracking, slip and separation between concrete and reinforcement, are given in Fig. 10 as a function of the applied load. For simplicity, comparisons between experimental and numerical results are only given for one specimen, i.e. MSA 11 (1.0 vol.% SFRC) with 60 mm concrete cover thickness. However, similar results were obtained for all concrete compositions tested in this study, i.e. PC and SFRC specimens with 20/60 mm concrete cover

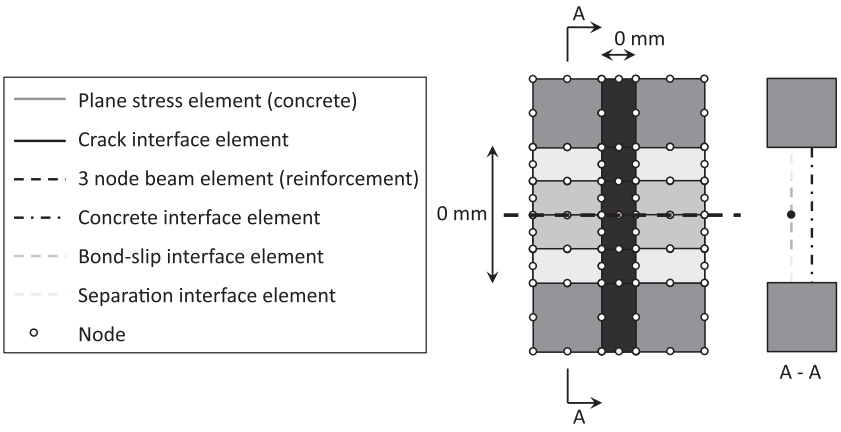

Fig. 6. Concept of the serial-parallel model simulating cracking and interfacial damage. Please note: illustration is not to scale.

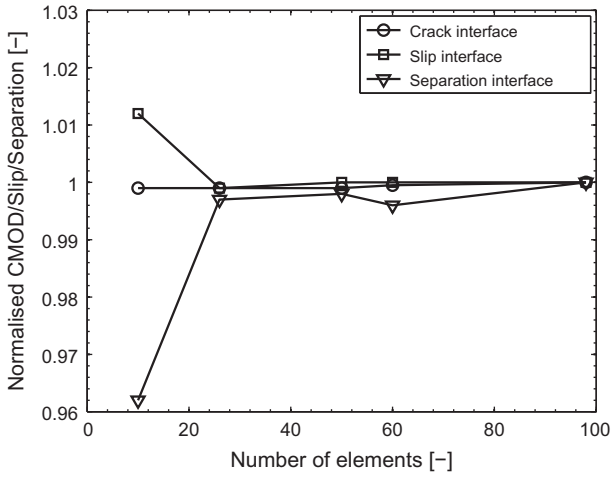

Fig. 7. Normalised results of mesh analysis.

thickness, respectively. It should be noted that although multiple cracking occurred in most specimens during mechanical loading, results are presented for the primary bending crack, which was defined as the first crack being formed. For all specimens the primary bending crack was located at or near the centre of the specimen.

Fig. 10(a) illustrates experimental and numerical results of the crack mouth opening displacement (CMOD) at the concrete tensile surface against the applied load. It is seen from the presented results that the numerical model can accurately capture both, crack initiation and increase in crack width. It should be further noticed that the fracture mechanical properties describing the tension softening behaviour of the material (see Eq. (2)) were determined independently from 3PBTs, i.e. no fitting of fracture mechanical parameters was performed to reproduce the experimental data. A comparison between numerical and experimental results concerning slip and separation between concrete and reinforcement (at 10 mm distance from the main bending crack) is given in Fig. 10(b). It is seen from the presented results that the developed FEM model can properly reproduce both damage phenomena. The numerical model is further capable of simulating the initiation as well as propagation of slip and separation at the concrete-reinforcement interface due to increasing load. The observed scatter in the experimental data is most likely attributed to the limited resolution of the photogrammetric equipment used in this study.

4.2. Electrochemical testing

4.2.1. Plain reinforced concrete

Typical OCP and macrocell current density measurements for plain reinforced concrete are given in Fig. 11 for 24 days of exposure. Results are presented for selected sensors of the instrumented rebar and indentified by their distance from the main bending crack. It can be seen from the results that OCPs are decreasing for sensors located closer to the crack throughout the exposure time, which indicates a change in the favoured thermodynamical corrosion state from passive to active. The change in thermodynamical state of sensors located in the vicinity of the crack was confirmed by corresponding macrocell current density measurements. In contrast to sensors located closer to the main bending crack, the OCP for the sensor located at a distance of 70 mm from the crack initially decreases slightly to a potential of approximately −0.7 V_{SCE} and then gradually increases to approximately −0.2 V_{SCE} (see Fig. 11(a)). The behaviour of the sensor might be explained by an initial lack of oxygen (due to previous storage under water) as well as variations in the moisture content and concrete resistivity. Also, considerable smaller current densities were observed for sensors located furthest from the crack (see Fig. 11(b)), which facilitate the assumption of the passive state of the sensor.

Contour plots illustrating results of all sensor locations along the instrumented rebar for plain reinforced concrete are shown in Fig. 12. Results are given as a function of the exposure time (in days) and location from the crack (in mm) as well as OCP (in V_{SCE}) and macrocell current density (in μA/cm^2), which are indicated by a colour scale.

Initially, corrosion potentials around −0.2 to 0 V_{SCE} were measured for all sensors along the instrumented rebar. As mentioned earlier, considerable lower OCPs were measured for sensors located in a distance between 40 and 80 mm from the crack, which may be attributed to a lack of oxygen. Similar OCPs of passive reinforcement in an oxygen deprived environment can be found in the literature, see e.g. [60]. As time progressed, a considerable decrease in OCP was seen for all sensors located between −40 and 30 mm from the crack indicating initiation of corrosion. No decrease in OCP was measured during the exposure time for sensors located between −80 and −40 mm from the crack. Concurrent macrocell current density measurements for sensors located 10–80 mm from the crack correlate well with the decrease in OCP. Macrocell current densities up to approximately 150 μA/cm^2 were measured for actively corroding sensors. For sensors located in the region between 30 and 80 mm considerable smaller current densities were measured, which confirms the assumption that the initial low potential was not attributed to active corrosion.

In addition to the electrochemical measurements, simulated results of the slip and separation between the reinforcement and

Table 5
FEM model input parameters to simulate load-induced damage.

Parameter	Symbol	Value	Unit
Young's modulus concrete	E_{conc}	28000	(MPa)
Poisson ratio concrete	μ_{conc}	0.2	(−)
Tensile strength concrete	$f_{t,conc}$	See Table 6	(MPa)
Young's modulus steel	E_{steel}	210000	(MPa)
Poisson ratio steel	μ_{steel}	0.3	(−)
Yield strength steel	$f_{y,steel}$	550	(MPa)
Tensile strength slip interface	$f_{t,slip}$	Fitted	(MPa)
Constant slip value	u_t^0	Fitted	(mm)
Tensile strength separation interface	$f_{t,sep}$	0.03	(MPa)

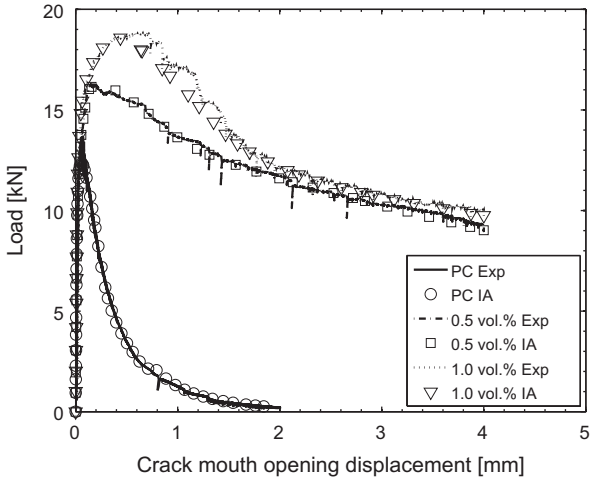

Fig. 8. Selected experimental (Exp) and inverse analysis (IA) load-CMOD curves for concrete compositions tested in this study.

Table 6
Fracture energy (G_f) and tensile strength ($f_{t,conc}$) determined from inverse analysis of 3PBTs.

Concrete Composition	$f_{t,conc}$		G_f	
	Mean (MPa)	St. Dev. (MPa)	Mean (J/m^2)	St. Dev. (J/m^2)
PC	1.8	0.1	569	55
SFRC 0.5 vol.%	1.7	0.1	4700	700
SFRC 1.0 vol.%	1.7	0.6	9000	2800

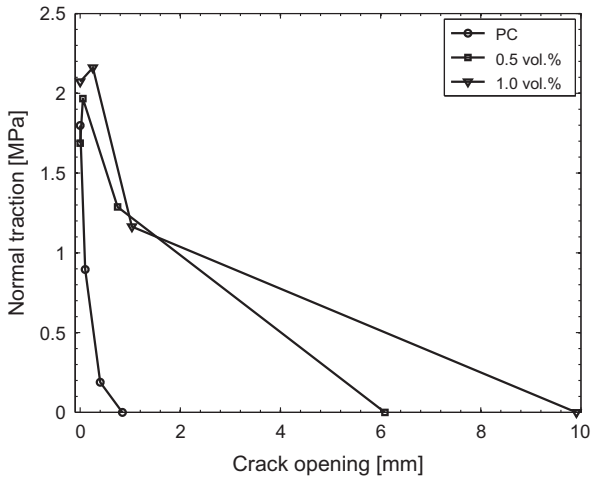

Fig. 9. Cohesive relations (mean of three test specimens for each concrete composition) for PC and SFRC (0.5 vol.% and 1.0 vol.%) to describe tension softening behaviour (see Eq. (1)).

concrete are illustrated in Fig. 12(c). As can be seen from the figure, 7 to approximately 12 μm slip are estimated along the reinforcement between −80 and 80 mm from the crack. Separation between the reinforcement and concrete is estimated to extend approximately from −40 to 40 mm from the crack. Comparing electrochemical and mechanical results, a very good correlation between the simulated extent of separation and measured extent of active corrosion can be found (see Fig. 12).

4.2.2. Steel fibre reinforced concrete

Selected OCP and macrocell current density measurements for specimens ESE 2 and 3 are given in Figs. 13 and 14, respectively. Results are presented for sensors located 10, 40, and 70 mm from the main bending crack for ESE 2 (0.5 vol.% SFRC). In contrast to the OCP measurements for ESE 1, considerable potential drops were observed for sensors located 10 and 40 mm from the crack. For the sensor located closest to the crack (10 mm), a first drop in OCP was seen after approximately 1.5 days of exposure, which was accompanied by an increase in macrocell current density. The OCP drop was however, smaller than usually described in literature (approximately −0.2 V_{SCE}) indicating a change in state of corrosion, see e.g. [54]. After approximately 3 days of exposure, the sensor located 40 mm from the crack showed a drop in OCP and at the same time an increase in current density was recorded. A gradual decease in OCP can be seen for the sensor located furthest from the crack (70 mm) and a sudden increase in macrocell current density after approximately 3.5 days of exposure indicating active corrosion.

Fig. 14 shows OCP and current density measurements for sensors located 10, 20, and 70 mm from the main bending crack for the ESE 3 specimen (1.0 vol.% SFRC). Similar to the results presented for plain reinforced concrete (ESE 1), a rather gradual decrease than a sudden drop in OCP can be observed for the sensors

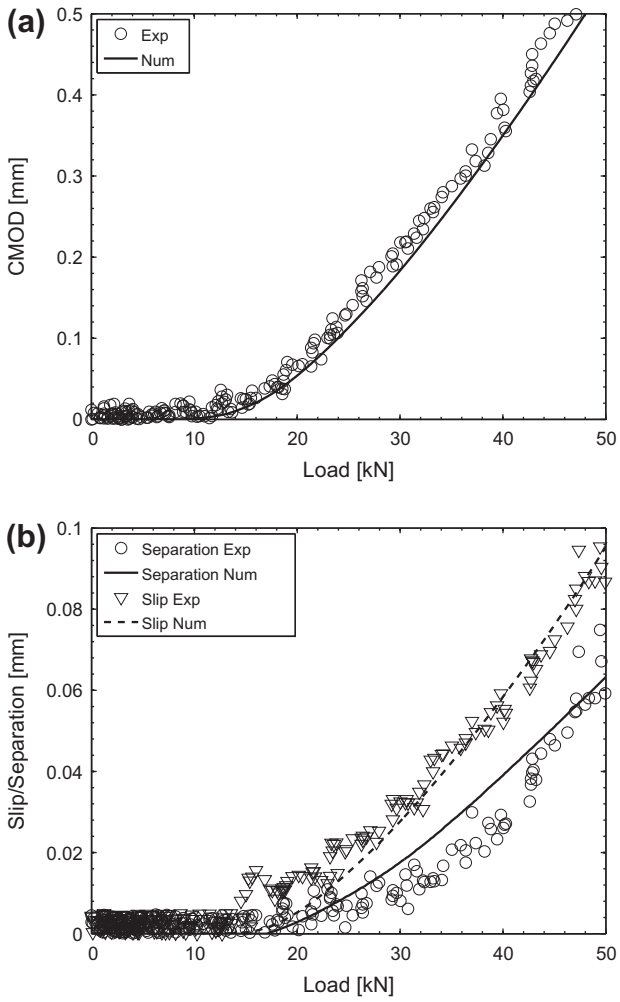

Fig. 10. Experimental and numerical results illustrating (a) CMOD and (b) slip and separation between concrete and reinforcement (at 10 mm distance from main bending crack) as a function of load for MSA 11 (1.0 vol.% SFRC).

located closest to the crack. However, concurrent macrocell current density measurements showed a considerable increase for these sensors indicating active corrosion. Throughout the complete exposure no decrease in OCP or increase in current density was measured for the sensor located 70 mm from the crack, which indicates a passive state of the sensor.

Contour plots showing results for all sensors along the instrumented rebar are given in Figs. 15 and 16 for specimens ESE 2 and 3 (i.e. 0.5 vol.% and 1.0 vol.% SFRC), respectively. Results presented include OCP measurements in a region between −80 mm and 80 mm and macrocell current density measurements between 10 mm and 80 mm from the main bending crack. Initially, values between approximately −0.2 to 0 V_{SCE} were measured for the sensors along the instrumented rebar for ESE 2 (see Fig. 15). With progressing exposure time all sensors located between −70 mm and 70 mm from the bending crack showed a considerable decrease in OCP, which was accompanied with an increase in macrocell current density indicating active corrosion in that region. Furthermore, it can be seen that with increasing distance from the crack, initiation of corrosion was delayed as indicated by the macrocell current density measurements in Fig. 15(b). For the various sensors along the instrumented rebar, macrocell current densities up to approximately 150 μA/cm^2 were recorded during the exposure time. Comparisons between the extent of simulated interfacial damage, in particular the separation between concrete

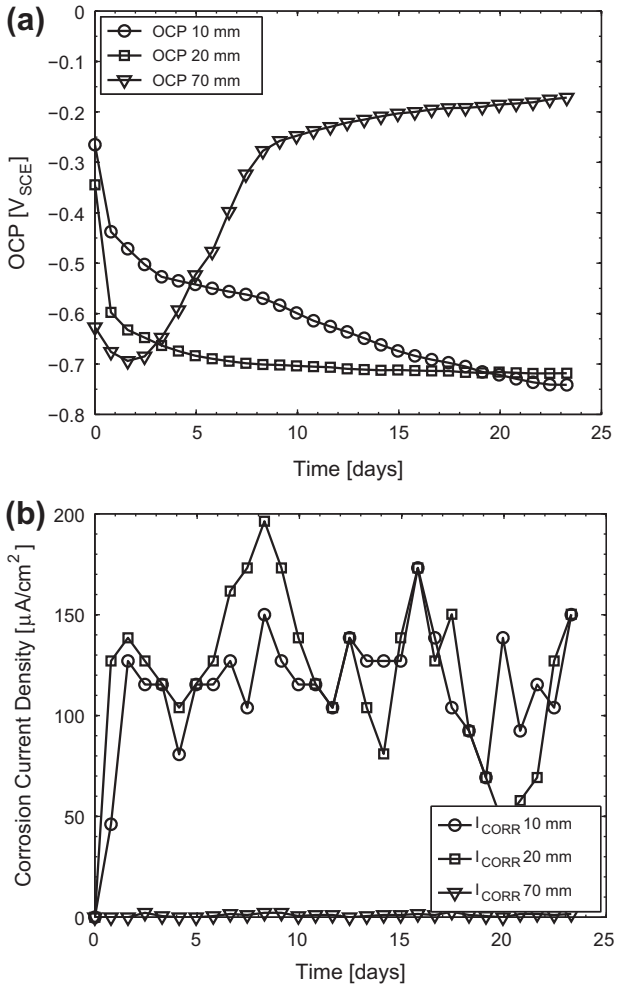

Fig. 11. (a) corrosion potential (OCP) and (b) corrosion current density (ICORR) measurements of selected sensors along the instrumented rebar for ESE 1 (PC). Sensors are identified by their distance to the main bending crack.

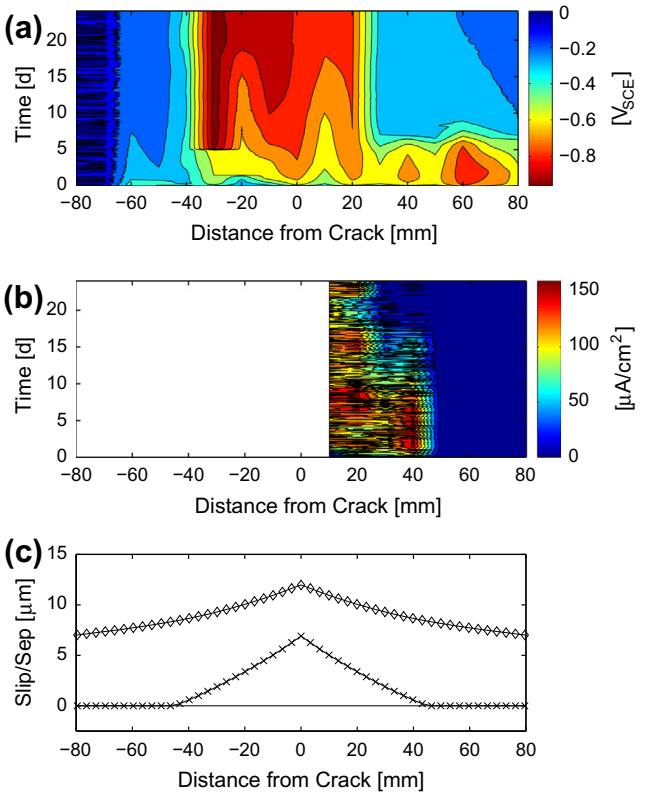

Fig. 12. (a) location- and time-dependent OCP and (b) corrosion current density (only for half of the sensors) measurements for ESE 1 (PC). (c) Simulated extent of slip (diamond symbols) and separation (cross symbols) between concrete and reinforcement.

and reinforcement, correlate very well with the extent of measured active corrosion. Both, electrochemically measured active corrosion and simulated separation are seen in a region between −70 mm and 70 mm from the main transverse crack (see Fig. 15).

Similar initial OCPs, as for ESE 1 and ESE 2 (i.e. PC and 0.5 vol.% SFRC), were measured for ESE 3 (i.e. 1.0 vol.% SFRC) with values ranging from −0.2 to 0 V_{SCE}. With increasing exposure time, decreasing OCPs were observed for sensors located −30 mm to 30 mm from the main bending crack indicating initiation of corrosion (see Fig. 16(a)). Concurrent macrocell current density measurements taken for sensors in this region also showed an increased current density confirming the assumption of active corrosion. For actively corroding sensors along the instrumented rebar, macrocell current densities up to approximately 150 µA/cm^2 were recorded during the exposure time. Sensors located outside this region (in the region between −80 mm and −30 mm and 30–80 mm), showed neither an increase in macrocell current density nor a decrease in OCP throughout the exposure period indicating no change in corrosion state, i.e. the sensors remained in the passive state. Comparisons of the electrochemical measurements (OCP and macrocell current density) and mechanical results showed again a good correlation between the simulated extent of separation (−35 mm to 35 mm from crack) and measured risk of corrosion (−30 mm to 30 mm).

4.3. Visual observations

Exemplary results of destructive visual observations are presented in Figs. 17 and 18, respectively. Fig. 17 illustrates the extent of chloride ingress (indicated by the broken line), the crack path (indicated by the solid line) and signs of rust stains (indicated by circled areas) observed in ESE 2 (0.5 vol.% SFRC). Silver nitrate was used to highlight the chloride ingress at the concrete surface.

The extent of chloride ingress is clearly visible along the main bending crack path and in the vicinity of the reinforcement in Fig. 17. The ingress extended around 85 mm from the crack in both directions along the reinforcement. No considerable ingress in the bulk material was observed indicating the interfacial damage along the reinforcement, in particular the separation between reinforcement and concrete, acted as a rapid pathway for the chloride ingress as proposed by e.g. [36]. Similar observations, i.e. extent of chloride ingress along the reinforcement and crack path, were made for the conventional reinforcement. Measured extents of chloride ingress for ESE 1 and ESE 3 (i.e. PC and 1.0 vol.% SFRC) were substantially less as the crack mouth opening displacement at the concrete tensile surface and extent of separation between concrete and reinforcement was considerably lower (see Table 4). In all specimens rust stains were found throughout the area of chloride ingress indicating active corrosion of the reinforcement (instrumented as well as conventional reinforcement). No visual signs of active corrosion were seen outside the area where chloride ions were indicated by silver nitrate.

In addition to the chloride ingress, the extent of corrosion for all instrumented and conventional rebars was investigated with a stereomicroscope. A typical image obtained for a sensor of an instrumented rebar (10 mm distance from crack) previously

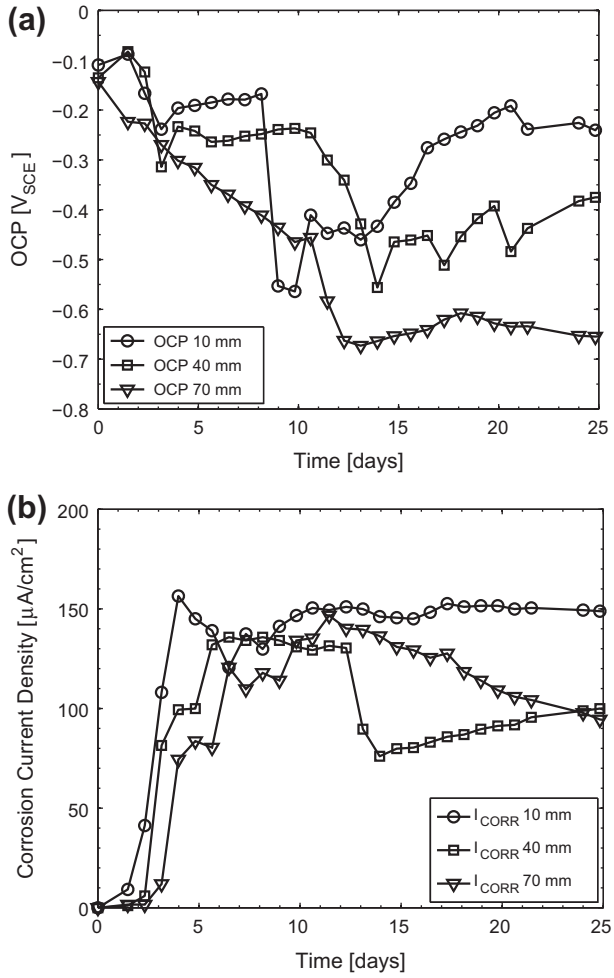

Fig. 13. (a) corrosion potential (OCP) and (b) corrosion current density (ICORR) measurements of selected sensors along the instrumented rebar for ESE 2 (0.5 vol.% SFRC). Sensors are identified by their distance to the main transverse crack.

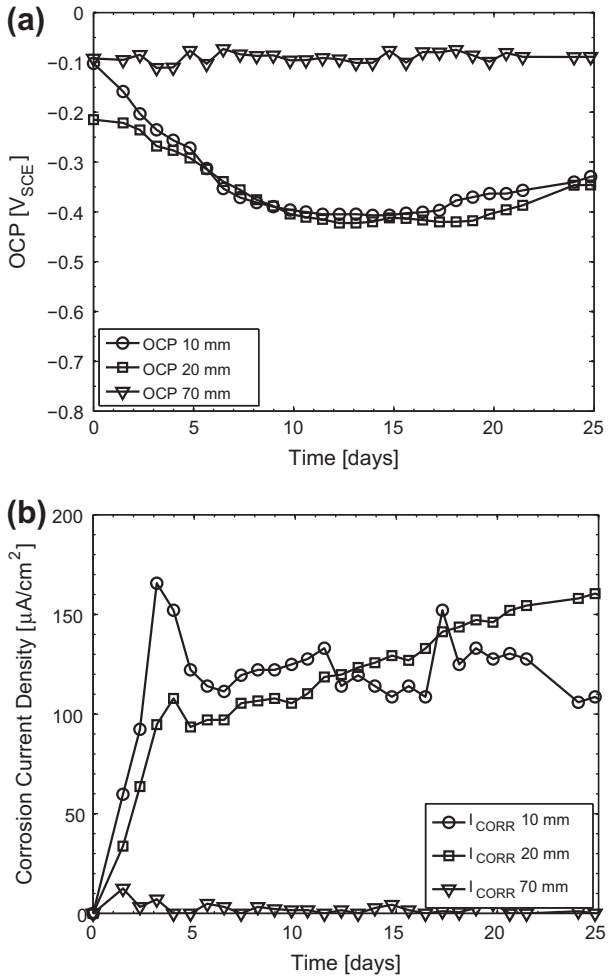

Fig. 14. (a) corrosion potential (OCP) and (b) corrosion current density (ICORR) measurements of selected sensors along the instrumented rebar for ESE 3 (1.0 vol.% SFRC). Sensors are identified by their distance to the main transverse crack.

embedded in ESE 3 (1.0 vol.% SFRC) is given in Fig. 18. The location of the sensor is highlighted by a broken line in the figure. Clear signs of corrosion can be seen at the surface of the sensor as well as the surface of the rebar confirming the open circuit corrosion potentials and macrocell current density measurements. Similar results were obtained for all sensors indicating active corrosion throughout the electrochemical measurements. Furthermore, similar extents of corrosion were seen along the conventional and instrumented rebar for all materials tested, i.e. PC, 0.5 and 1.0 vol.% SFRC, as indicated by the electrochemical measurements.

5. Discussion of results

As outlined in the introduction, it is current state-of-the-art in many standards, recommendations, and scientific research projects to relate the concrete surface crack width to (initiation of) reinforcement corrosion. At the same time a number of publications can be found in the literature that indicate lacking relations between the surface crack width and (initiation of) reinforcement corrosion. In the present study it was hypothesised that (load-induced) interfacial damage, in particular the separation between concrete and reinforcement, is a more fundamental indicator for the susceptibility of reinforcement to early corrosion initiation. To investigate this hypothesis, mechanical and electrochemical measurement techniques in conjunction with a novel physics based mechanical model were applied. In the following sections the results obtained in the present study by the experimental and numerical techniques outlined previously are discussed.

It should be noted that the present study focused solely on concrete-reinforcement interfacial damage in form of separation and slip between reinforcement and concrete and the impact of fracture mechanical properties of plain and fibre reinforced concrete. Factors such as surface roughness and treatment of the reinforcement, which may affect the concrete-reinforcement interfacial damage, were not investigated. Furthermore, it should be kept in mind that the applied technique to monitor load-induced damage, i.e. cracking, slip, and separation, was limited to observations on the macroscopic level. Application of high resolution cameras for DIC measurements as well as other techniques, such as e.g. scanning electron microscopy and acoustic emission, have been shown by others, see e.g. [63–65], to be more suitable for observations of load-induced damage at the microscopic level. However, previous research indicated that concrete with isolated microcracks has a similar resistance to ingress as uncracked concrete [66] and as the developed mechanical model (see Section 3) and the proposed hypothesis are currently limited to the macroscopic level, it is the authors' opinion that the applied experimental and numerical methods were adequate for the present study.

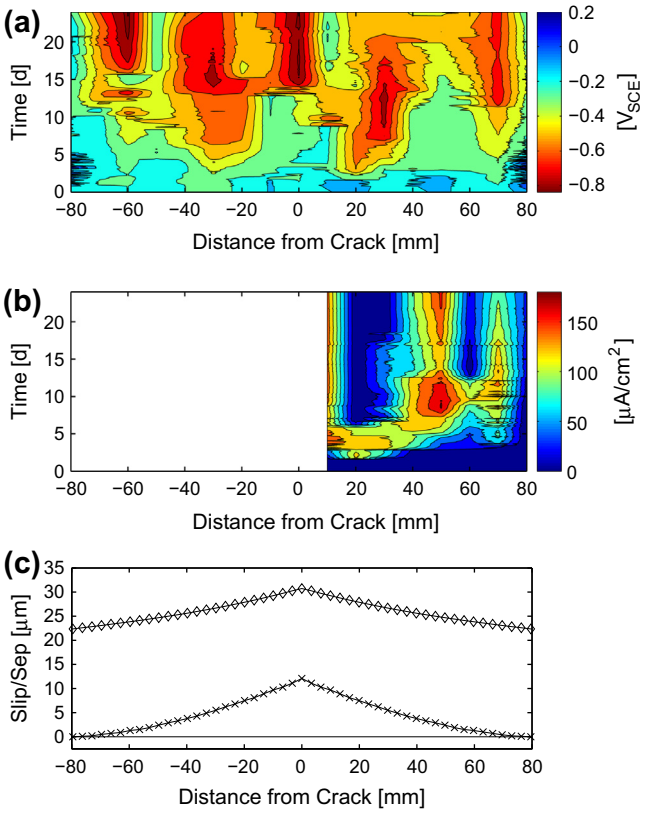

Fig. 15. (a) location- and time-dependent OCP and (b) corrosion current density (only for half of the sensors) measurements for ESE 2 (0.5 vol.% SFRC). (c) simulated extent of slip (diamond symbols) and separation (cross symbols) between concrete and reinforcement.

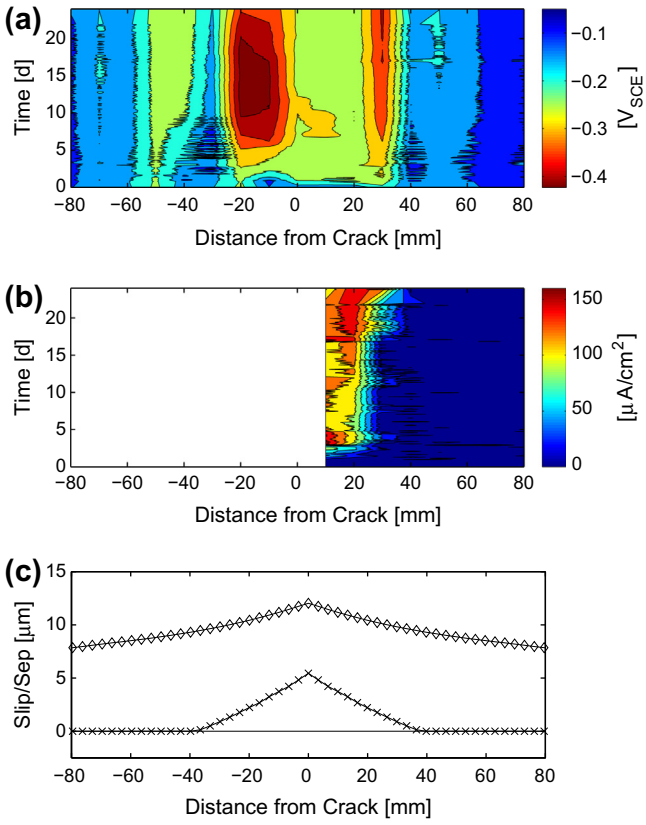

Fig. 16. (a) location- and time-dependent OCP and (b) corrosion current density (only for half of the sensors) measurements for ESE 3 (1.0 vol.% SFRC). (c) simulated extent of slip (diamond symbols) and separation (cross symbols) between concrete and reinforcement.

5.1. Fracture mechanical properties and load-induced damage

Fracture mechanical properties of the cracking interface in the FEM model (see Fig. 6) describing the initiation and propagation of a load-induced bending crack were determined by inverse analysis of independent experimental investigations (see Section 4.1.1). Results of the inverse analysis, i.e. tensile strength and fracture energy, were presented in Table 6 for the different concrete compositions tested in this study. From the results it can be seen that the addition of fibres has no considerable influence on the tensile strength of the concrete. However, with increasing amounts of fibres, the ductility of the concrete, described by the fracture energy, is considerably increased. Similar observations were made by e.g. [61,62].

For all load-induced damage phenomena, i.e. cracking, slip, and separation, very good agreements between experimental and numerical results were found for the different concrete compositions tested in this study (see Fig. 10). Formation of the main bending crack was observed for loads between 15 and 18 kN for the different concrete composition, which was in good agreement with results of the numerical simulations. Initiation of separation between concrete and reinforcement was observed for higher loads for all concrete compositions. The numerical model was also able to simulate this phenomenon indicating the load-induced damage is reproduced in a physically correct manner. Furthermore, the influence of additional fibres on various damage phenomena, e.g. decreased CMOD, slip, and separation with increasing fibre content, was accurately reproduced by the developed FEM model.

To fit the experimental data, two parameters were varied in the FEM model, i.e. the tensile strength of the slip interface, $f_{t,slip}$, and

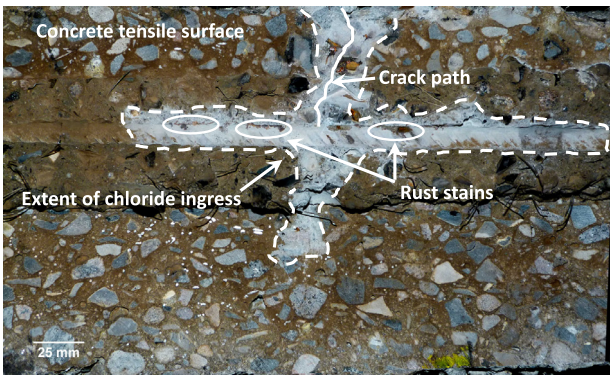

Fig. 17. Extent of chloride ingress (broken line), crack path (solid line) and rust stains (circled areas) in ESE 2 (0.5 vol.% SFRC) specimen after termination of experiment.

u_t^0. Values used for the tensile strength of the slip interface for the different concrete compositions were in the same order of magnitude (1.1–2.6 MPa). However, no correlation between the fibre content and the fitted tensile strength of the slip interface was observed. The strength of the separation interface, $f_{t,sep}$, was set to 0.03 MPa for all investigated concrete compositions, which was considerably lower than the tensile strength of the slip and crack interface (see Fig. 6), respectively. The separation interface accounts for the chemical adhesion between concrete and steel for which, to the authors' knowledge, mechanical properties have not been described in the literature. Furthermore, results of a

Fig. 18. Sensor (indicated by broken line) of instrumented rebar located next to main bending crack with signs of corrosion at the sensor and the instrumented rebar for ESE 3 (1.0 vol.% SFRC) beam.

parametric study on the impact of $f_{t,sep}$ showed no considerable impact on the investigated damage phenomena (cracking, slip, and separation). Numerical results indicated that the separation is controlled by the mechanical properties of the concrete interface connecting the upper and lower part of the concrete domain (see Fig. 6), which accounts for the formation of internal cracks caused by local stress transfer from the reinforcement to the concrete via the ribs.

5.2. Open circuit corrosion potential and macrocell current density measurements

Comparisons of contour plots presented in Section 4.2, showed similar open circuit corrosion potentials (OCPs) for all concrete compositions tested at the beginning of exposure. Initially, OCPs of approximately −0.2 to 0 V_{SCE} were measured indicating a passive corrosion state of the reinforcement. Similar OCP values for passive reinforcement are reported in the literature, see e.g. [43,54]. With progressing time, an either gradual decrease or sudden drop in OCP was seen for certain sensors along the instrumented rebar indicating active corrosion was thermodynamically favoured. For the ESE 1 and ESE 3 specimens (i.e. PC and 1.0 vol.% SFRC) a gradual decrease in potential was observed immediately after ponding, while for ESE 2 (i.e. 0.5 vol.% SFRC) a sudden drop in OCP was seen. OCPs for ESE 1 and ESE 2 decreased to values of approximately −0.8 V_{SCE} and −0.4 V_{SCE} for ESE 3, which is in good agreement with values that have been reported in the literature for active corrosion, see e.g. [17,67]. Signs of active corrosion were observed for OCP drops ranging from approximately 0.1 to 0.4 V_{SCE} for the different concrete compositions. Active corrosion was confirmed by concurrent macrocell current density measurements.

However, time to corrosion initiation and extent of corrosion varied for the tested PC and SFRC beams. Macrocell current density measurements obtained for ESE 2 and ESE 3 (i.e. SFRC specimens) showed a delay in active corrosion compared to ESE 1. Signs of active corrosion were recorded after approximately 1 day of exposure for ESE 3 and 1.5 days of exposure for ESE 2, respectively. Similar macrocell current densities (up to approximately 150 μA/cm^2) were measured for all concrete compositions, which is in good agreement with values that have been reported in literature for comparable anode-to-cathode ratios, see e.g. [51,52]. No considerable influence of the fibre content on the macrocell current density was observed in this study, which was confirmed by visual observations indicating similar depths of corrosion for the conventional and instrumented rebars embedded in the test specimens.

5.3. Correlation between interfacial damage, crack width, and risk of corrosion

The presented results facilitate the hypothesis that the concrete-reinforcement interfacial condition can be used as a reliable indicator to quantify the impact of load-induced cracks on the risk of corrosion initiation along the reinforcement. Very good agreements between the simulated interfacial damage, in particular the separation between reinforcement and concrete, and extent of active corrosion along the instrumented rebar (indicated by the electrochemical measurements) were obtained for all concrete compositions tested. For ESE 1 (i.e. PC), active corrosion was measured for sensors located at a distance of −40 mm to 35 mm from the main bending crack compared to around −40 mm to 40 mm simulated by the FEM model (see Fig. 12). Extents of separation were simulated and active corrosion measured in a region between −70 mm to 70 mm and −30 mm to 30 mm from the main transverse crack for ESE 2 and ESE 3 (i.e. 0.5 vol.% SFRC and 1.0 vol.% SFRC), respectively (see Figs. 15 and 16).

Similar to the interfacial damage, a good correlation between the crack width at the concrete surface and extent of corrosion along the reinforcement was found for the specimens tested in this study. For a crack width of approximately 0.07 mm at the concrete surface (see Table 4), similar extents of corrosion were found for ESE 1 (around 40 mm) and ESE 3 (around 35 mm), respectively. However, for larger crack widths at the concrete surface, the correlation between crack width and extent of corrosion may not hold true, especially with regards to the use of SFRC as experimental and numerical results of the mechanical testing indicate that the addition of steel fibres alters the extent of interfacial damage compared to PC.

5.4. Visual observations

Electrochemical measurements (OCP and macrocell current density) and numerical simulations of separation between reinforcement and concrete are in good agreement with visual observations (chloride ingress and extent of corrosion along the instrumented and conventional reinforcement) for all concrete compositions tested.

The highest lateral chloride ingress along the reinforcement was observed for ESE 2 (around 80 mm in both directions from the main bending crack) with a measured surface crack width of 0.139 mm. Less lateral ingress of chloride ions was observed for ESE 1 (around 45 mm in both directions) and ESE 3 (around 40 mm in both directions) with measured surface crack widths of 0.068 mm and 0.069 mm, respectively. Visual signs of corrosion for the conventional and instrumented rebar were obtained for all specimens in the region where chloride ions were indicated by the application of silver nitrate. Within the same region, electrochemical measurements, i.e. OCP and macrocell current density measurements, of sensors along the embedded instrumented rebars indicated active corrosion for all tested concrete compositions. Furthermore, similar extents of separation between the reinforcement and concrete were simulated by means of a finite element model for all materials. Slightly higher extents of chloride ingress measured by visual observations may be attributed to

additional transport phenomena, such as convection and/or diffusion of chloride ions, throughout the time of exposure.

6. Conclusions

In this study plain concrete (PC) and steel fibre reinforced concrete (SFRC) flexural beams were cracked and exposed to a 3% sodium chloride solution. Instrumented rebars, embedded in the beams, provided location- and time-dependent open circuit corrosion potential (OCP) and macrocell current density measurements. From the presented electrochemical measurements (OCP and macrocell current density measurements), mechanical simulations (predictions of the extent of slip and separation between concrete and reinforcement) and destructive visual observations (extent of chloride ingress and corrosion along the conventional and instrumented reinforcement) it may be concluded that:

(1) The concrete-reinforcement interfacial condition can be used as a reliable indicator to quantify the impact of load-induced cracks on the risk of corrosion initiation along the reinforcement. In particular, the simulated extent of separation along the reinforcement is in very good agreement with all experimental observations, i.e. mechanical, electrochemical, and visual.
(2) The presented FEM model can simulate various damage phenomena (cracking, slip, and separation) associated with three point bending tests, which was demonstrated comparing experimental results obtained from photogrammetric investigations and numerical results for three different concrete compositions. Input parameters describing the fracture mechanical behaviour of the crack, slip, and separation interface were either obtained from independent tests or varied to fit experimental data, where fitted parameters appear to be in the correct order of magnitude.
(3) Since the applied FEM model directly accounts for the impact of various parameters (e.g. concrete cover thickness, concrete composition, stress level in the reinforcement and crack orientation) on the mechanical response of the beam (extent and magnitude of slip and separation between reinforcement and concrete), it is the authors' opinion that the predicted interfacial damage may be used as a parameter to quantify the risk of corrosion initiation in subsequent service life analyses.

Acknowledgements

The first author gratefully acknowledges the financial support of Femern Bælt A/S, Sund & Bælt Holding A/S and The Danish Agency for Science, Technology and Innovation as well as COIN (COncrete INnovation centre, www.coinweb.no) and its partners for facilitating the research behind this paper. Financial supports of the Ph.D. study "Application of Fibre Reinforced Concrete in Civil Infrastructure" by the Danish Agency for Science, Technology and Innovation, COWI A/S, DTU, Bekaert NV, Grace, and the Danish Road Directorate are also acknowledged as well as financial contributions from the Danish Expert Centre for Infrastructure.

References

[1] L. Bertolini, B. Elsener, P. Pedeferri, R. Polder, Corrosion of Steel in Concrete Prevention, Diagnosis, Repair, Wiley-VCH Verlag GmbH & Co. KgaA, Weinheim, 2004.
[2] S. Jacobsen, J. Marchand, L. Boisvert, Effect of cracking and healing on chloride transport in OPC concrete, Cem. Concr. Res. 26 (6) (1996) 869–881.
[3] C.M. Aldea, S. Shah, A. Karr, Permeability of cracked concrete, Mater. Struct. 32 (219) (1999) 370–376.
[4] C. Edvardsen, Water permeability and autogenous healing of cracks in concrete, ACI Mater. J. 96 (4) (1999) 448–454.
[5] N. Gowripalan, V. Sirivivatnanon, C. Lim, Chloride diffusivity of concrete cracked in flexure, Cem. Concr. Res. 30 (5) (2000) 725–730.
[6] O. Rodriguez, R. Hooton, Influence of cracks on chloride ingress into concrete, ACI Mater. J. 100 (2) (2003) 120–126.
[7] P. Win, M. Watanabe, A. Machida, Penetration profile of chloride ions in cracked reinforced concrete, Cem. Concr. Res. 34 (7) (2004) 1073–1079.
[8] W.D. Lindquist, D. Darwin, J. Browning, G.G. Miller, Effect of cracking on chloride content in concrete bridge decks, ACI Mater. J. 103 (6) (2006) 467–473.
[9] B. Pease, J. Couch, M. Geiker, H. Stang, J. Weiss, Assessing the portion of the crack length contributing to water sorption using X-ray absorption measurements on concrete wedge splitting specimens, In: ConcreteLife'09: Second International RILEM Workshop on Concrete Durability and Service Life Planning, Haifa, Israel, 2009.
[10] O. Gautefall, O. Vennesland, Effects of cracks on the corrosion of embedded steel in silica-concrete compared to ordinary concrete, Nordic Concr. Res. 2 (1983) 17–28.
[11] N. Berke, M. Dallaire, M. Hicks, R. Hoopes, Corrosion of steel in cracked concrete, Corros. Eng. 49 (11) (1993) 934–943.
[12] A. Arya, F. Ofori-Darko, Influence of crack frequency on reinforcement corrosion in concrete, Cem. Concr. Res. 26 (3) (1996) 345–353.
[13] P. Schießl, M. Raupach, Laboratory studies and calculations on the influence of crack width on chloride induced corrosion of steel in concrete, ACI Mater. J. 94 (1) (1997) 56–62.
[14] R. Francois, G. Arliguie, Effect of microcracking and cracking on the development of corrosion in reinforced concrete members, Mag. Concr. Res. 51 (2) (1999) 143–150.
[15] T. Mohammed, N. Otsuki, M. Hisada, T. Shibata, Effect of crack width and bar type on corrosion of steel in concrete, J. Mater. Civ. Eng. 13 (3) (2001) 194–201.
[16] G. Rehm, H.L. Moll, Versuche zum Studium des Einflußes der Rissbreite auf die Rostbildung an der Bewehrung von Stahlbetonbauteilen, Deutscher Ausschuss für Stahlbeton 169 (1964).
[17] P. Schießl, Zur Frage der zulässigen Rissbreite und der erforderlichen Betondeckung im Stahlbetonbau unter besonderer Berücksichtigung der Karbonatisierung des Betons, Deutscher Ausschuss für Stahlbeton 255 (1976).
[18] P. Fidjestol, N. Nilson, Field test of reinforcement corrosion in concrete, ACI Special Publication 65 (1980) 205–217.
[19] K. Katawaki, Corrosion of steel in the concrete exposed to seawater spray zone, In: Symposium proceedings on cracking of concrete structures, 1977, pp. 133–136.
[20] E.F. O'Neil, Study of reinforced concrete beams exposed to marine environment, ACI Special Publication 65 (1980) 113–132.
[21] ACI Committee 224, ACI 224R–01: Control of cracking in concrete structures, 2001, pp. 22.
[22] Eurocode 2, Design of concrete structures, Part 1, General rules and rules for buildings, BS EN 1992–1-1, 2004.
[23] AIJ, Recommendations for Practice of Crack Control in Reinforced Concrete Buildings (Design and Construction), 2006, (in Japanese).
[24] New Zealand Standard, Concrete Structure, Part1-The Design of Concrete Structures, NZS3101: Part 1, 1995.
[25] German Committee on Reinforced Concrete (DAfStb), Guideline waterproof concrete, constructions, 2003.
[26] AASHTO, LRFD Bridge Design Specifications, SI Units, 4th ed., 2007.
[27] DIN 1045-1, Reinforced concrete and prestressed concrete structures, Part 1: Design and construction, DIN 1045-1, 2008.
[28] P. Schießl, E. Wölfel, Konstruktionsregeln zur Beschränkung der Rissbreite – Grundlage zur Neufassung DIN 1045, Abschnitt 17.6 (Entwurf 1985), Beton- und Stahlbetonbau 81 (1) (1986) 8–15.
[29] S. Miyazato, Y. Hiraishi, Transport properties and steel corrosion in ductile fiber reinforced cement composites, In: Proceedings of the 11th international conference on Fracture, Turin, Italy, 2005.
[30] M. Otieno, M. Alexander, H.-D. Beushausen, Corrosion in cracked and uncracked concrete – influence of crack width, concrete quality and crack reopening, Mag. Concr. Res. 62 (6) (2010) 393–404.
[31] M. Makita, Y. Mori, K. Katawaki, Marine corrosion behavior of reinforced concrete exposed at tokyo bay, ACI Special Publication 65 (1980) 271–290.
[32] T. Marcotte, C. Hansson, The influence of silica fume on the corrosion resistance of steel in high performance concrete exposed to simulated sea water, J. Mater. Sci. 28 (2003) 4765–4776.
[33] A. Scott, M. Alexander, The influence of binder type, cracking and cover on corrosion rates of steel in chloride contaminated concrete, Mag. Concr. Res. 59 (7) (2007) 495–505.
[34] S. Yoon, K. Wang, J. Weiss, S. Shah, Interaction between loading, corrosion, and serviceability of reinforced concrete, ACI Mater. J. 97 (6) (2000) 637–644.
[35] A. Poursaee A, C.M. Hansson, The influence of longitudinal cracks on the corrosion protection afforded reinforcing steel in high performance concrete, Cem. Concr. Res. 38 (8-9) (2008) 1098–1105.
[36] B.J. Pease, Influence of concrete cracking on ingress and reinforcement corrosion. Ph.D thesis, Technical University of Denmark. Kgs. Lyngby, Denmark, 2010.
[37] K. Tammo, S. Thelandersson, Nonlinear analysis of crack widths in reinforced concrete, Mag. Concr. Res. 61 (1) (2009) 23–34.

[38] N. Buenfeld, G. Glass, B. Reddy, F. Viles, Process for the protection of reinforcement in reinforced concrete, United States Patent #6685822, Alexandria, VA, USA, 2004.
[39] T. Mohammed, N. Otsuki, H. Hamada, T. Yamaji, Chloride-induced corrosion of steel bars in concrete with presence of gap at steel-concrete interface, ACI Mater. J. 99 (2) (2002) 149–156.
[40] P. Nygaard, Effect of steel-concrete interface defects on the chloride threshold for reinforcement corrosion, Master thesis, Technical University of Denmark, Kgs. Lyngby, Denmark, 2003.
[41] P. Nygaard, M.R. Geiker, A method for measuring the chloride threshold level required to initiate reinforcement corrosion in concrete, Mater. Struct. 38 (278) (2005) 489–494.
[42] S. Nagataki, N. Otsuki, A. Moriwake, S. Miyazato, Influence of permeation of oxygen and chloride ions through joints on macro-cell corrosion, ACI Special Publication 170-68 (1997) 1333–1355.
[43] B.J. Pease, M. Geiker, H. Stang, J. Weiss, The design of an instrumented rebar for assessment of corrosion in cracked concrete, Mater. Struct. 44 (7) (2011) 1259–1271.
[44] J. Skoček, H. Stang, Application of optical deformation analysis system on wedge splitting test and its inverse analysis, Mater. Struct. 43 (1) (2010) 63–72.
[45] Recommendation of RILEM TC 162-TDF, Test and design methods for steel fibre reinforced concrete: bending test, Mater. Struct. 35 (253) (2002) 579–582.
[46] DS/EN 14651-A1, Test method for metallic fibre concrete – measuring the flexural tensile strength (limit or proportionality (LOP), residual), Technical Report, Danish Standard Association, 2007.
[47] DS/EN 197-1, Cement – part 1: composition, specification and conformity criteria for common cements, 2001.
[48] GOM. Aramis user manual – Software, Aramis v6.1 and higher. GOM Optical Measuring Techniques, 2009.
[49] B. Pease, M. Geiker, H. Stang, J. Weiss, Photogrammetric assessment of flexure induced cracking of reinforced concrete beams under service loads, In: Proceedings 2nd International RILEM Symposium Advances in Concrete through Science and Engineering, Québec, Canada, 2006.
[50] E. Pereira, G. Fischer, J. Barros, Image-based detection and analysis of crack propagation in cementitious composites, In: Proceedings of International Conference on Advances in Construction Materials through Science and Engineering, Hong Kong, China, 2011.
[51] C. Andrade, I.R. Maribona, S. Feliu, J.A. Gonzalez, S. Feliu, The effect of macrocells between active and passive areas of steel reinforcements, Corros. Sci. 33 (2) (1992) 237–242.
[52] C. Andrade, P. Garcés, I. Martínez, Galvanic currents and corrosion rates of reinforcements measured in cells simulating different pitting areas caused by chloride attack in sodium hydroxide, Corros. Sci. 50 (2008) 2959–2964.
[53] S.P. Holmes, G.D. Wilcox, P.J. Robins, G.K. Glass, A.C. Roberts, Responsive behaviour of galvanic anodes in concrete and the basis for its utilisation, Corros. Sci. 50 (2011) 3450–3454.
[54] A. Küter, Management of reinforcement corrosion: a thermodynamical approach, PhD thesis, Technical University of Denmark, Kgs. Lyngby, Denmark, 2009.
[55] A. Hillerborg, M. Modéer, P.-E. Petersson, Analysis of crack formation and crack growth in concrete by means of fracture mechanics and finite elements, Cem. Concr. Res. 6 (6) (1976) 773–782.
[56] K. Dörr, Ein Beitrag zur Berechnung von Stahlbetonscheiben unter besonderer Berücksichtigung des Verbundverhaltens, PhD thesis, University of Darmstadt, Darmstadt, Germany, 1980.
[57] I. Carol, P.C. Prat, C.M. López, Normal/shear cracking model: Application to discrete crack analysis, J. Eng. Mech. 123 (8) (1997) 765–773.
[58] P.B. Lourenco, J.G. Rots, Multisurface interface model for analysis of masonry structures, J. Eng. Mech. 123 (7) (1997) 660–668.
[59] L.O. Nielsen, J.F. Mougaard, J.S. Jacobsen, P.N. Poulsen, A mixed mode for fracture in concrete, In: Proceedings of 7th International Conference on Fracture Mechanics of Concrete and Concrete Structures (FraMCoS7), Jeju, Korea, 2010.
[60] H. Arup, The mechanisms of protection of steel by concrete, in: A.P. Crane (Ed.), Corrosion of reinforcement in concrete construction, Horwood, Chichester, England, 1983.
[61] M.T. Kazemi, F. Fazileh, M.A. Ebrahiminiezhad, Cohesive crack model and fracture energy of steel-fiber-reinforced-concrete notched cylindrical specimens, J. Mat. Civ. Eng. 19 (10) (2007) 884–890.
[62] I. Löfgren, J.F. Olesen, M. Flansbjer, Application of WST-method for fracture testing of fibre-reinforced concrete, NT Technical Report, Norway, 2005.
[63] X.-S. Wang, B.-S. Wu, Q.-Y. Wang, Online SEM investigation of microcrack characteristics of concretes at various temperatures, Cem. Concr. Res. 35 (2005) 1385–1390.
[64] J. Rupil, S. Roux, F. Hild, L. Vincent, Fatigue microcrack detection with digital image correlation, J. Strain Anal. Eng. Des. 46 (6) (2011) 492–509.
[65] F. Finck, M. Yamanouchi, H.-W. Reinhardt, C.U. Grosse, Evaluation of mode I failure of concrete in a splitting test using acoustic emission technique, Inter. J. Fract. 124 (2003) 139–152.
[66] B. Pease, A. Michel, M. Geiker, H. Stang, Modelling moisture ingress through simplified concrete crack geometries, In: Proceedings of International Congress on Durability of Concrete (ICDC 2012), Trondheim, Norway, 2012.
[67] B. Elsener, C. Andrade, J. Gulikers, R. Polder, M. Raupach, Half-cell potential measurements – potential mapping on reinforced concrete structures, Mater. Struct. 36 (261) (2003) 461–471.

Paper IX

” Modeling Formation of Cracks in Concrete Cover due to Reinforcement Corrosion”

A. Michel, A.O.S. Solgaard, M.R. Geiker, H. Stang & J.F. Olesen

Published in: *Proceedings of FraMCos 7 (7th International Conference on Fracture Mechanics of Concrete and Concrete Structures), May 23-28, 2010, Jeju, Korea.*

Modeling Formation of Cracks in Concrete Cover due to Reinforcement Corrosion

A. Michel, M. R. Geiker, H. Stang & J. F. Olesen
Department of Civil Engineering, Technical University of Denmark

A. O. S. Solgaard
COWI A/S & Department of Civil Engineering, Technical University of Denmark

ABSTRACT: An electrochemical and mechanical modeling approach to simulate formation of corrosion induced cracks in reinforced concrete structures is presented. The electrochemical model allows simulation of the propagation of macro cell corrosion in a homogeneous defect-free concrete-steel system. To simulate cracking a finite element based crack propagation model is proposed. To demonstrate the potential use of the combined modeling approach a numerical example is provided where the influence of various exposure conditions on the corrosion current density and subsequent formation of cracks is illustrated.

1 INTRODUCTION

One of the major deterioration problems of reinforced concrete structures is corrosion of steel causing considerable damages and costs due to maintenance and repair needs. In Europe more than € 250 billion are spent annually for maintenance and repair of concrete structures due to deterioration (Li (2004)), in which corrosion of reinforcing steel is estimated to be related to 90% of the degradation problems (Rendell et al. (2002)). Corrosion can cause formation of cracks in the concrete cover as well as cross sectional reduction of reinforcement area affecting strength and serviceability of reinforced concrete structures. Prediction of the corrosion process as well as the subsequent formation and propagation of cracks could be used for prediction of residual service life and support maintenance planning of reinforced concrete structures.

A variety of models dealing with corrosion induced concrete cover cracking can be found in the literature. The available models can be broadly divided into empirical, e.g. Alonso et al. (1998), analytical, e.g. Bazant (1979) and Chernin et al. (2009), and numerical models, e.g. Molina et al (1993). Some of the models include various phenomena associated with corrosion induced cover cracking, such as diffusion of corrosion products, e.g. Liu & Weyers (1998) and debonding, e.g. Noghabai (1999). Most of the models show reasonable agreement with experimental results obtained from accelerated corrosion tests, e.g. Andrade et al. (1993) and Val et al. (2009). However, the use of the models to predict corrosion induced cover cracking is limited since a constant corrosion rate is assumed, which is unlikely for concrete structures subjected to realistic exposure conditions.

In the present paper the theoretical framework for a combined modeling approach is presented, which allows prediction of the corrosion rate of steel in concrete and the resulting formation of cracks in the concrete cover. The formation of $Fe_2O_3 \cdot H_2O$ as uniformly distributed corrosion products is assumed (see e.g. Marcotte & Hansson (2007), Küter (2009)). In contrast to previously presented models, the proposed electrochemical and mechanical modeling approach does not assume a constant corrosion rate of the reinforcement. An electrochemical corrosion model is used to predict the corrosion rate of the reinforcement accounting for the impact of varying exposure conditions. Focus is placed on the propagation stage of macro cell corrosion with prescribed anodic and cathodic reinforcement regions. Application of Faraday´s law allows to link the FEM based corrosion model with a crack propagation model by determining the rate of formation of corrosion products from predicted corrosion current densities. To model the corrosion induced cracks in the concrete cover, a FEM based crack model is proposed. The developed model focuses on the propagation of cracks in the concrete cover. Cracking of the concrete is described by a cohesive discrete cracking approach with a multi-linear softening cohesive relation. The expansive nature of the corrosion products is modeled using a thermal analogy. The assumptions made in the present study allow a conservative prediction of the corrosion rate of reinforcement and

the subsequent corrosion induced concrete cover cracking.

Finally, a numerical example is given illustrating the potential use of the proposed modeling approach taking into account the impact of various exposure conditions on the corrosion rate of steel and the corrosion induced cover cracking.

2 MODELLING APPROACH

2.1 *Two-phase FEM based corrosion model*

To model the corrosion process of reinforcement in concrete structures a physio-chemical, FEM based corrosion model has been established. In the model electrochemical corrosion processes are combined with transport mechanisms to allow simulation of the propagation of macro cell corrosion in a homogeneous defect-free concrete-steel system. The system modeled is illustrated in Figure 1. Since the proposed corrosion model is dealing with the propagation stage of reinforcement corrosion the anodic and cathodic areas of the reinforcement are prescribed.

For the description of the electrochemical processes in the concrete pore solution acting as electrolyte two physical laws can be used (see e.g. Warkus et al. (2006)). The first one is Laplace's equation, which describes the potential distribution in the concrete pore solution assuming electrical charge conservation and isotropic conductivity

$$\nabla^2 \phi = 0 \tag{1}$$

where ∇ = nabla operator and ϕ = potential. The second is Ohm´s law describing the rate of dissolution of iron on the steel surface in concrete if the potential distribution and the resistivity of the electrolyte are known (Isgor & Razaqpur (2006))

$$i = -\frac{1}{\rho_T}\frac{\partial \phi}{\partial n} \tag{2}$$

where i = current density, ρ_T = concrete resistivity and n = direction normal to the rebar surface.

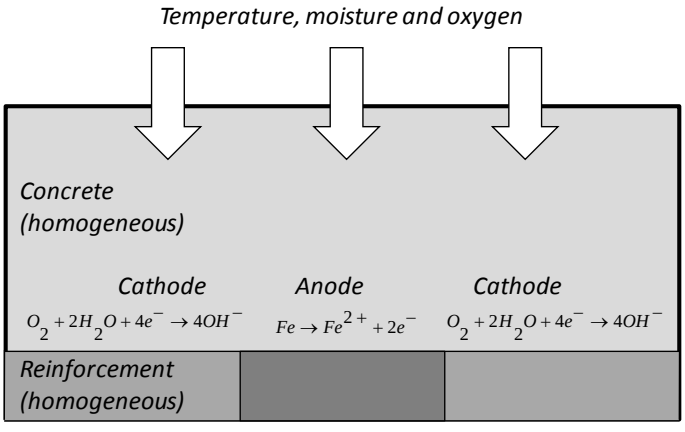

Figure 1: Two-phase FEM based corrosion model.

In order to solve Laplace´s equation (Eq. 1) appropriate boundary conditions are needed in the form of so-called polarization or potential-current curves quantifying the relation between current and potential at the steel surface. For the anodic and cathodic regions of the steel surface the boundary conditions can be defined as

$$\phi = \phi_A \quad \text{and} \quad \phi = \phi_C \tag{3}$$

where ϕ_A = anodic potential and ϕ_C = cathodic potential. Assuming that the steel surface polarizes due to activation and concentration polarization, the boundary conditions for the anodic and cathodic regions of the steel can be expressed as follows

$$i_A = i_{0,A}{}^{\alpha_A}$$

$$\text{with} \quad \alpha_A = \exp\left(\ln 10 \frac{\phi_A - E_{0,A}}{b_A}\right) \tag{4}$$

where i_A = anodic current density, $i_{0,A}$ = anodic exchange current density, $E_{0,A}$ = anodic equilibrium potential and b_A = anodic Tafel constant and

$$i_C = i_{0,C}\frac{1-\alpha_C}{1+\frac{i_{0,C}}{i_{Lim}}\alpha_C}$$

$$\text{with} \quad \alpha_C = \exp\left(-\ln 10 \frac{\phi_C - E_{0,C}}{b_C}\right) \tag{5}$$

where i_C = cathodic current density, $i_{0,C}$ = cathodic exchange current density, $E_{0,C}$ = cathodic equilibrium potential, b_C = cathodic Tafel constant and i_{Lim} = limiting current density. More information on the theory of polarization phenomena of metals in an electrolyte can be found e.g. in Stern & Geary (1957) and Bardal (2004).

Potential distribution in the concrete pore solution and hence the corrosion rate of the reinforcement (see Eq. 2) are strongly influenced by exposure conditions as well as material properties of the reinforced concrete structure. To account for the impact of environmental conditions and material properties on the polarization behavior of the steel surface a set of partial differential equations (PDE's) is solved. In particular the distribution of temperature, moisture, oxygen and resistivity in the concrete domain and along the concrete-steel interface are of interest.

Distribution of a potential, such as temperature, moisture and oxygen gradients, as well as the corrosion process itself in concrete and along the concrete-steel interface can be described by a quasi-harmonic equation of the form (Isgor & Razaqpur (2006))

$$\alpha \frac{\partial X}{\partial t} + \nabla\left(D_X \nabla X\right) + Q = 0 \tag{6}$$

where α = coefficient representing material properties, X = potential, t = time, D_X = corresponding transport functions for potential X and Q = sink term for negative values and a source term for positive values.

The time dependent moisture distribution in the concrete domain is determined by solving Equation (6) with a moisture dependent transport coefficient as corresponding transport function for the moisture potential. A number of empirical and analytical expressions for the moisture dependent transport coefficient can be found in the literature e.g. in Künzel (1994), Bazant (1994) and Pel (1995). In the present study an exponential function for the moisture dependent transport coefficient proposed by Wittmann (1992) is selected to describe the moisture transport in concrete

$$D_{RH} = a + b\exp\left(RHc\right) \tag{7}$$

where D_{RH} = moisture transport function, a,b,c = non-physical fitting parameters and RH = relative humidity. It should be noted that effects of hysteresis (see e.g. Scheffler (2009)) are not taken into account in the present modeling approach. However, to demonstrate the potential use of the proposed combined modeling approach to predict the corrosion rate as well as propagation of cracks in the cover of reinforced concrete structures such a simplification seems to be appropriate.

The limiting current density term, i_{Lim}, introduced in Equation (5) describing the polarization of cathodic reinforcement sites indicates that oxygen availability plays an important role in the polarization behavior. A function for i_{Lim} can be obtained combining Faraday´s law with Fick's law and may be written as follows

$$i_{Lim} = \frac{zFD_{O2,T}c_B}{d} \tag{8}$$

where z = number of electrons transferred, F = Faraday's constant, $D_{O2,T}$ = oxygen transport function, c_B = oxygen concentration at the concrete surface and d = concrete cover thickness. To describe the oxygen transport in concrete an empirical expression proposed by Papadakis et al. (1991) is chosen

$$D_{O2} = 1.92 \cdot 10^{-6} \varepsilon_p \left(1 - RH\right)^{2.2} \tag{9}$$

where D_{O2} = oxygen transport function at reference temperature and ε_P = concrete porosity. The influence of the temperature on the oxygen transport is modeled with an Arrhenius equation

$$D_{O2,T} = D_{O2} \exp\left(\frac{\Delta U_{O2}}{RT}\right) \tag{10}$$

where ΔU_{O2} = activation energy for oxygen diffusion, R = universal gas constant and T = absolute temperature. Values for the activation energy of oxygen diffusion can be found e.g. in Page & Lambert (1987) and Isgor et al. (2009).

Furthermore, the concrete resistivity, which is affected by numerous factors, such as the moisture content, concrete microstructure, ion concentration, temperature and possible fiber content, plays an important role in determining the polarization of the steel surface in concrete. Values for concrete resistivity for various exposure conditions and different concrete moisture contents can be found in the literature, e.g. in Polder (2001). For simplicity it is assumed that the resistivity only depends on the moisture content and temperature in the present model. Experimental studies investigating the relation between moisture content and resistivity for different concrete and mortar types have been carried out and can be found e.g. in Hötte (2003).

To describe the moisture dependence of the concrete resistivity a power law is used in the present model

$$\rho = c\sqrt{\frac{\frac{1}{MC} - a}{b}} \tag{11}$$

where ρ = concrete resistivity at reference temperature, a,b,c = non-physical fitting parameters and MC = moisture content. Experimental data presented by Hötte (2003) and fitted data (Eq. 11), for a CEM 1 concrete is given in Figure 2. The influence of temperature on the resistivity is modeled with an Arrhenius equation

$$\rho_T = \rho \exp\left(\frac{\Delta U_{RH}}{RT}\right) \tag{12}$$

where ρ_T = concrete resistivity and ΔU_{RH} = activation energy for moisture transport. Values for the activation energy of moisture transport can be found e.g. in Chrisp et al. (2001).

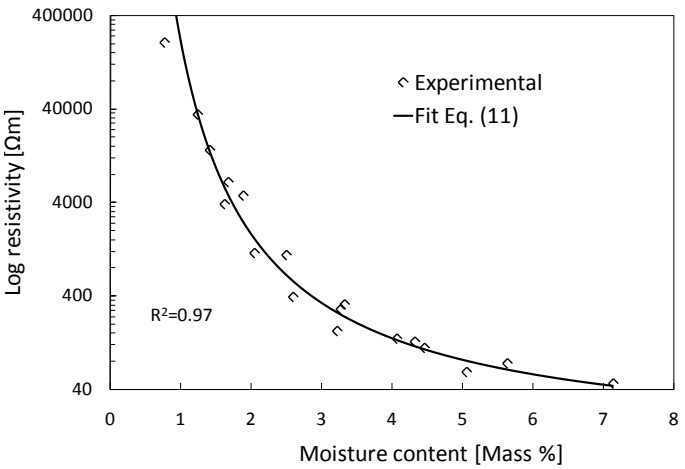

Figure 2: Experimental (Hötte (2003)) and fitted data for concrete resistivity as a function of moisture content.

2.2 *FEM based crack propagation model*

After the corrosion current density along the concrete steel interface is predicted by the corrosion model, deformations and crack propagation in the concrete cover due to the formation of expansive corrosion products can be determined using the proposed FEM based crack propagation model. The present fracture mechanics model assumes uniform corrosion along the reinforcement leading to a 2D problem in a plain strain formulation. The crack propagation in the concrete cover of reinforced concrete structures is modeled assuming that no corrosion products diffuse into concrete pores, voids or cracks.

In the proposed model two different fracture types are considered accounting for the crack propagation in the concrete cover due to corrosion. The underlying assumption of the proposed model for cracking in the concrete cover is Mode-I crack propagation. It is assumed that the crack propagates in the concrete cover when the tensile stresses due to expansion of the corrosion products exceed the tensile strength of the concrete. Debonding effects between concrete and reinforcement are described by Mixed-mode crack propagation. Both phenomena, cracking in the concrete cover and debonding, are described by a discrete cracking approach in the present model. Tension softening is described based on a cohesive discrete cracking model in which multi-linear softening relations are adopted from Skoček & Stang (2009). The fracture energy of the Mode-1 crack opening behavior during the Mixed-mode crack propagation (debonding effects) is reduced by a factor of 10 compared to pure Mode-I crack propagation to account for a reduced bonding between concrete and corrosion products. A constant shear modulus of 10GPa after cracking is assumed for the Mixed-mode crack propagation.

Zero-thickness cohesive interface elements are implemented perpendicular (simulating Mode-I crack propagation in the concrete cover) and circumferential (simulating Mixed-mode crack propagation) to the reinforcement allowing crack propagation only in the implemented interface elements. However, comparing with experimental results of crack patterns due to expansion of corrosion products (see e.g. Andrade et al. (1993), Alonso et al. (1998) and Val et al. (2009)) the definition of a prescribed crack path seems to be appropriate.

Linear elastic material properties are defined for the semi-infinite concrete body, corrosion layer and reinforcement section (see Fig. 3). Elastic material properties for the corrosion products can be found in the literature (see e.g. Molina et al. (1993), Suda et al. (1993) and Caré et al. (2008)). For the present model material properties proposed by Ouglova et al. (2006) are used. A Young´s modulus of 2.1 GPa and a Poisson ratio of 0.2 are defined for the corrosion layer.

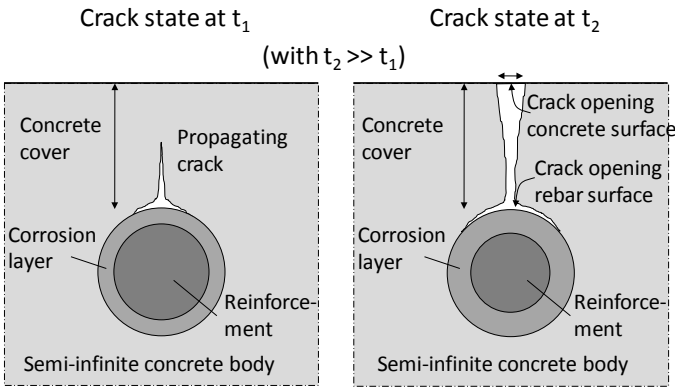

Figure 3: Crack propagation in proposed FEM model.

Since corrosion of reinforcement is not a typical load scenario in commercial FEM codes a special way of load application is used to model the propagation of cracks in the concrete cover. Initially, the cross sectional area of the reinforcement, reduced due to corrosion, is determined, and afterwards the expansion of the corroded reinforcement section is modeled. Crack propagation as well as load application in the FEM model and basic geometrical considerations are illustrated in Figure 3 and Figure 4, respectively. For the determination of the corroded reinforcement section Faraday´s law is used, which describes the relation between thickness reduction per time unit and corrosion current density, predicted by the FEM based corrosion model

$$X(t) = \frac{M}{zF\rho}\int_0^t i_{corr}(t)dt \tag{13}$$

where $X(t)$ = thickness reduction, $i_{corr}(t)$ = corrosion current density, M = mol mass of the metal, z = number of electrons in the reaction equation for the anodic reaction and ρ = density of the metal. For the present model 100% current efficiency is assumed meaning that all corrosion current is used for dissolution of iron.

Initially, the reinforcement with a radius R_O is embedded in the concrete.

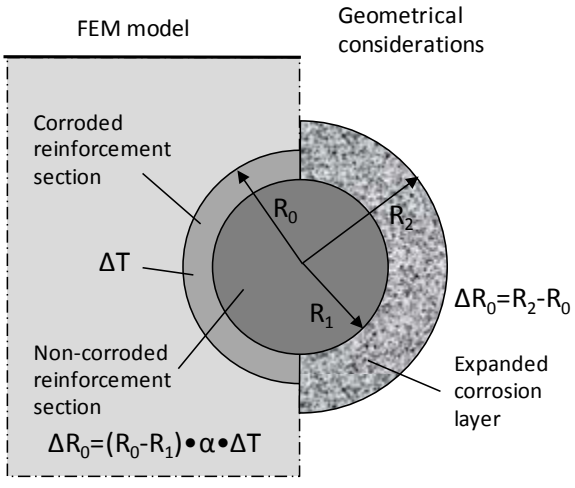

Figure 4: Load application in FEM model (left) and basic geometrical considerations (right) of crack propagation model.

Assuming uniform corrosion the cross sectional reduction of the reinforcement can be calculated

$$R_1 = R_0 - X \tag{14}$$

where R_1 = remaining radius of non-corroded reinforcement, R_0 = initial radius of reinforcement and X = thickness reduction according to Equation (13).
The linear expansion coefficient η can be written as follows

$$\eta = \frac{\Delta R_0}{X} \tag{15}$$

where ΔR_0 = increase of the initial radius of the reinforcement due to the expansion of corrosion products.

A thermal analogy is used to model the expansive nature of the corrosion products applying a thermal load to the corroded reinforcement section (see Fig. 4). Assuming a constant coefficient of thermal expansion, the applied temperature increment has to represent the formed corrosion product. Furthermore, the resulting thermal expansion has to be equal to the linear expansion coefficient in Equation 15. As mentioned before, the formation of uniformly distributed $Fe_2O_3 \cdot H_2O$ as corrosion product is assumed with a volume expansion coefficient of 6.3. Assuming isotropic material properties of the corrosion products, the linear expansion coefficient is one third of the volume expansion coefficient. Hence, the linear expansion coefficient applied to the corroded reinforcement section in proposed crack propagation model is 2.1 assuming the formation of $Fe_2O_3 \cdot H_2O$ as corrosion product.

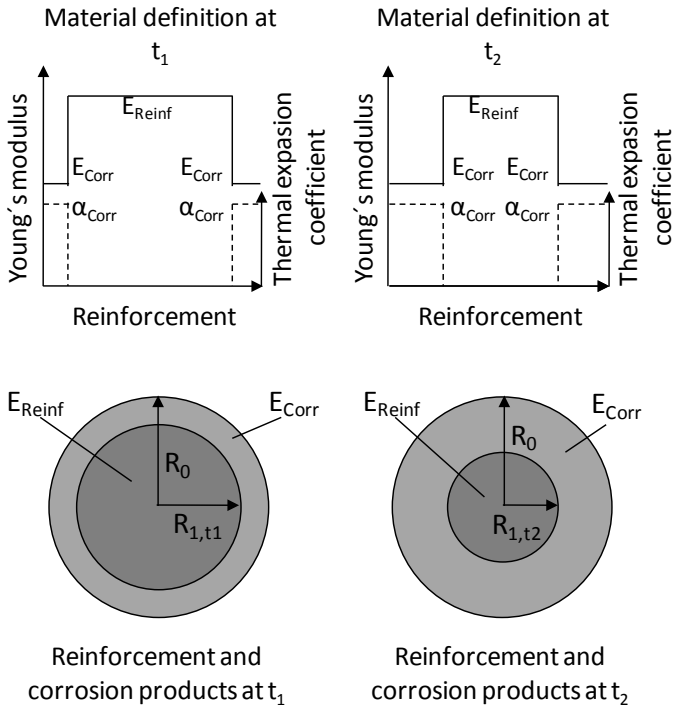

Figure 5: Time dependent material definitions for reinforcement and corrosion layer in crack propagation model.

Since the corroded reinforcement section increases over time (see Eq. 13 and 14) the area which is subjected to the thermal load needs to be revaluated to obtain the correct stress state in the model. For each time step of the analysis the corresponding material properties have to be assigned to the correct domains in the finite element model. This is because the stress distribution and hence the crack propagation in the surrounding concrete depends on the interaction between the remaining reinforcement section, the corrosion layer and the elastic part of the semi-infinite concrete body. The time dependent material definitions and load application proposed for the present crack propagation model are given in Figure 5.

3 NUMERICAL EXAMPLE

To demonstrate the potential use of the proposed combined modeling approach a numerical example is given.

Initially, the corrosion model is used to predict the corrosion current density for various exposure conditions (varying moisture contents, temperature and oxygen). The model geometry for the numerical example is given in Figure 6. The polarization behavior of the reinforcement described by Equations (4) and (5) for the anodic and cathodic sites, respectively are illustrated in Figure 7. To reduce computational time the symmetrical properties of the system are utilized and only half of the geometry is modeled. The input parameters used in the analysis are given in Table 1. For the numerical solution of the time dependent corrosion problem, involving solution of Equations (1), (2) and (6), the commercial FEM software COMSOL Multiphysics is used. 5725 triangular elements are used to describe the concrete and steel domain, with a finer mesh in the anodic reinforcement region. Lagrange quadratic elements are used as element type and the time steps are chosen by the solver.

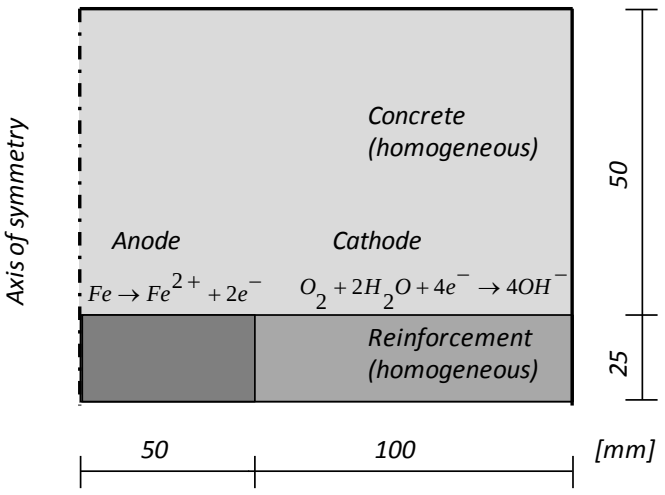

Figure 6: Corrosion model geometry for numerical example (not to scale).

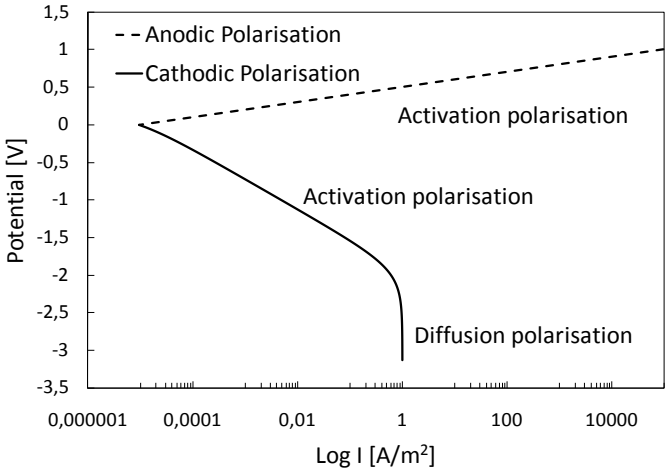

Figure 7: Corrosion model boundary conditions for numerical example.

Table 1: Input parameters (corrosion and crack propagation model) for numerical example.

Parameter	Value	Dimension
Anodic exchange current density at equilibrium	1.88 E-04	A/m^2
Anodic equilibrium potential	-0.78	V
Anodic Tafel constant	0.06	V/dec
Cathodic exchange current density at equilibrium	6.25 E-06	A/m^2
Cathodic equilibrium potential	0.16	V
Cathodic Tafel constant	0.16	V/dec
Concrete resistivity	Eq. (11)	ohm m
Initial bulk humidity	0.9	-
Moisture transport	Eq. (6) and (7)	m/s^2
Limiting current density	Eq. (8)	A/m^2
Oxygen transport	Eq. (6) and (9)	m/s^2
Temperature	Eq. (6)	K
Concrete cover	50	mm
Reinforcement diameter	25	mm
Corroded reinforcement section	Eq. (13)	mm
Young´s modulus reinforcement	210	GPa
Poisson ratio reinforcement	0.3	-
Young´s modulus concrete	30	GPa
Poisson ratio concrete	0.2	-
Tensile strength concrete	4	MPa
Young´s modulus corrosion products	2.1	GPa
Poisson ratio corrosion products	0.2	-
Thermal expansion coefficient corrosion products	2.1	-/K
Temperature increment	1	K

The FEM based crack propagation model is used to demonstrate the influence of varying corrosion rates, predicted by the corrosion model, on the propagation of corrosion induced cracks in the concrete cover of reinforced concrete structures. The model geometry chosen for the numerical example is illustrated in Figure 8. A model size of 225mm proved to be sufficient to represent the semi-infinite concrete body, which was checked before actual simulations were carried out with the crack propagation model. The implemented cohesive relations for the interface elements perpendicular and circumferential to the reinforcement are given in Figure 9. Input parameters used in the example are given in Table 1. To simulate the crack propagation due to the expansive nature of corrosion products the commercial FEM software DIANA is used. 902 quadrangular elements (2864 DOF´s) are used to describe the interface, concrete, reinforcement and corrosion layer domain in the model. Nonlinear solution is obtained using a standard Newton-Raphson method with a displacement controlled convergence criterion.

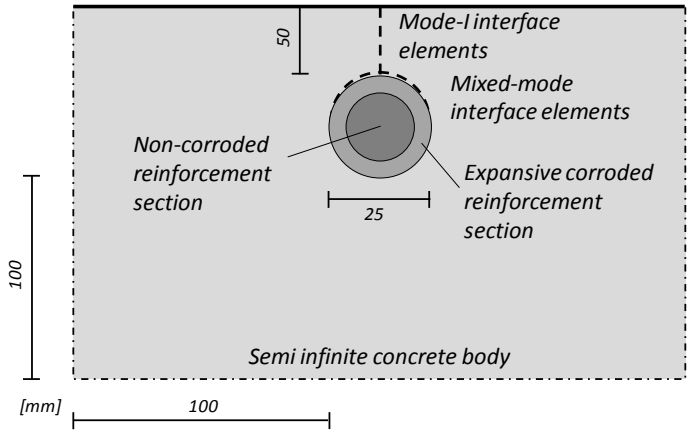

Figure 8: Crack propagation model geometry for numerical example (not to scale).

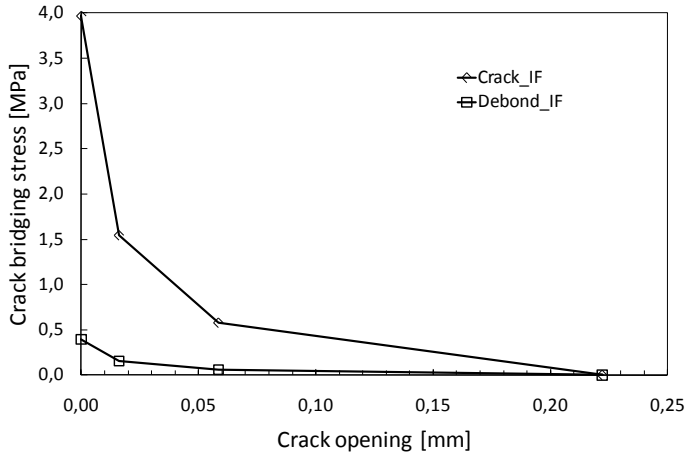

Figure 9: Cohesive relation for Mode-I and Mixed-mode interface elements in numerical example after Skoček & Stang (2009).

4 RESULTS

Results of the numerical example are presented in Figures 10-12. Initially, the FEM based corrosion model was used to predict corrosion current densities for varying exposure conditions. Afterwards, the proposed crack model was used to relate the predicted corrosion current densities and model the propagation of cracks in the surrounding concrete due to formation of expansive corrosion products.

4.1 *Corrosion model*

To demonstrate the potential use of the corrosion model, corrosion current densities were predicted

with the model for three different exposure scenarios. For the presented numerical example the effects of varying relative humidity, temperature and oxygen content on the corrosion current density were studied. More details on the three exposure scenarios are given in Table 2. Results of the numerical simulation are given in Figure 10. It is evident from the results that the corrosion current density depends on the investigated exposure scenarios. The most pronounced effect can be observed for exposure scenario 1, following the changing moisture content in the concrete due to the applied boundary conditions and moisture transport function. The impact of exposure scenarios 2 and 3 appears to be less distinct for the investigated geometry and boundary conditions.

Table 2: Parameters describing different exposure scenarios.

Scenario	Relative humidity [-]	Temperature [K]	Oxygen [mol/m^3]
1	0.72 - 0.91	295	1
2	0.8	275 - 295	1
3	0.8	295	0.2 - 1

4.2 *Crack propagation model*

Crack openings for different locations in the surrounding concrete as a function of the corrosion layer thickness are given in Figure 11. As expected, the crack opens first at the rebar surface due to the expansion of the corrosion layer and is propagating towards the concrete surface. As soon as the crack reaches the concrete surface a linear relation between thickness of corrosion layer and crack opening can be observed. Figure 12 illustrates the crack opening at the concrete surface as a function of time for the predicted corrosion current densities. It is evident from the results that crack opening as well as propagation depend on the corrosion current density predicted by the corrosion model. For the presented numerical example it can be seen, that the crack opening as well as the crack propagation are delayed for the corrosion current densities determined for the exposure scenarios 2 and 3 compared to exposure scenario 1.

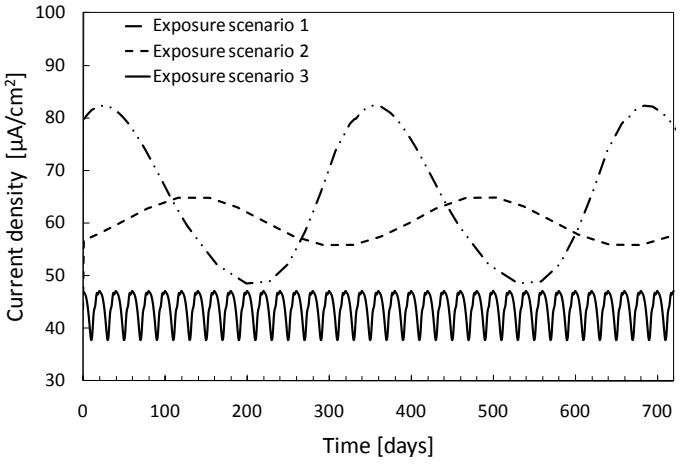

Figure 10: Corrosion current densities for exposure scenarios.

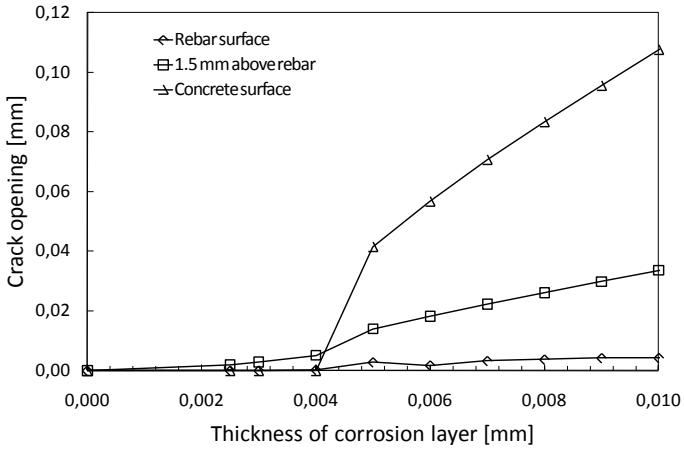

Figure 11: Crack opening depending on corrosion layer thickness for model geometry and cohesive relation.

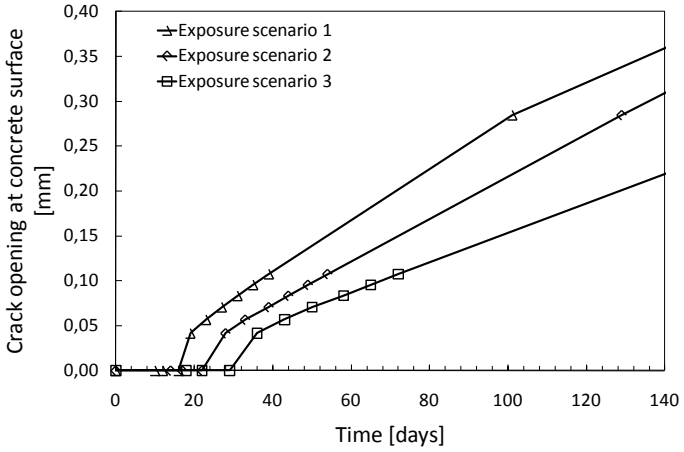

Figure 12: Crack opening at concrete surface for predicted corrosion current densities.

5 SUMMARY AND CONCLUSIONS

A combined electrochemical and mechanical modeling approach to simulate the formation of cracks in reinforced concrete structures due to corrosion was presented. A two-phase finite element based corrosion model was used to determine the corrosion current density of steel in concrete taking into account the impact of varying exposure conditions. A crack propagation model was used to simulate the formation of cracks in the concrete cover due to the expansive nature of formed corrosion products. The proposed crack propagation model does not take into account the diffusion of corrosion products into concrete pores, voids or cracks, resulting in an overestimation of the crack propagation. Furthermore, the presented modeling approach does not take the influence of corrosion induced cracks on the transport properties of the concrete into account.

To demonstrate the potential use of the proposed combined modeling approach a numerical example was presented. In the example the influence of various parameters of the corrosion model on the crack propagation were investigated. The presented results illustrate the major impact of the corrosion current

density on the crack propagation. Furthermore, the need for a realistic prediction of the corrosion rate as well as selection of the corrosion products formed to simulate formation of corrosion induced concrete cover cracking is evident from the presented results.

For a better understanding of the corrosion process in concrete structures as well as subsequent formation of cracks, future investigations should also focus on the impact of concrete material parameters, model geometry as well as mechanical properties of the corrosion products formed (see e. g. Solgaard et al. (2009)).

6 ACKNOWLEDGMENTS

The first author gratefully acknowledges the financial support of Femern Bælt A/S, Sund & Belt Holding A/S and The Danish Agency for Science, Technology and Innovation.

REFERENCES

Alonso, C., Andrade, C., Rodriguez, J., & Diez, J. M. 1998. Factors controlling cracking of concrete affected by reinforcement corrosion. *Materials and Structures* 31: 435-441.

Andrade, C., Alonso, C., & Molina, F. J. 1993. Cover cracking as a function of bar corrosion: Part 1 - Experimental test. *Materials and Structures* 26: 453-464.

Bardal, E. 2004. Corrosion and Protection. *Engineering Materials and Processes*. London, UK: Springer, 1st edition.

Bazant, Z. P. 1979. Physical model for steel corrosion in concrete sea structures - Application. *Journal of the Structural Division* 105: 1155–1166.

Bazant, Z., Xi, Y., Molina, L. & Jennings, H. M. 1994. Moisture Diffusion in Cementitious Materials - Moisture Capacity and Diffusivity. *Advanced Cement Based Materials* 1: 258-266.

Caré, S., Nguyen, Q. T., L´Hostis, V. & Berthaud, B. 2008. Mechanical properties of the rust layer induced by impressed current method in reinforced mortar. *Cement and Concrete Research* 38: 1079-1091.

Chernin, L., Val, V. D. & Volokh K. Y. 2009. Analytical modelling of concrete cover cracking by corrosion of reinforcement. *Materials and Structures published online*.

Chrisp, T. M., Starrs, G., McCarter, W. J., Rouchotas, E. & Blewett, J. 2001. Temperature - conductivity relationships for concrete: An activation energy approach. *Journal of Material Science Letters* 20: 1085-1087.

Hötte, C. 2003. Bestimmung des Feuchtezustandes von Mauerwerk mit Hilfe von Multiring-Elektroden - Untersuchungen zum Ankoppelungsmörtel und an Probewänden. *Diplomarbeit* Technische Hochschule Aachen, Institut für Bauforschung.

Isgor, B. O. & Razaqpur, G. A. 2006. Modelling steel corrosion in concrete structures. *Materials and Structures* 39: 291–302.

Isgor, O. B., Pour-Ghaz, M. & Ghods, P. 2009. The effect of temperature on the corrosion of steel in concrete. Part 2: Model verification and parametric study. *Corrosion Science* 51: 426-433.

Künzel, H. M. 1994. Verfahren zur ein- und zweidimensionalen Berechnung des gekoppelten Wärme- und Feuchtetransports in Bauteilen mit einfachen Kennwerten. *PhD Thesis* Universität Stuttgart.

Küter, A. 2009. Management of reinforcement corrosion - A thermodynamical approach. *PhD Thesis* Department of Civil Engineering, Technical University of Denmark.

Li, V. 2004. A New Research Framework for Sustainable Infrastructures. *Seminar* Department of Civil Engineering, Technical University of Denmark.

Liu, Y. & Weyers, R. E. 1998. Modeling the time-to-corrosion cracking in chloride contaminated reinforced concrete structures. *ACI Materials Journal* 95: 675-681.

Marcotte, T. D. & Hansson, C. M. 2007. Corrosion products that form on steel within cement paste. *Materials and Structures* 40: 325-340.

Molina, F. J., Alonso, C., & Andrade, C. 1993. Cover cracking as a function of rebar corrosion: part 2 - numerical model. *Materials and Structures* 26: 532–548.

Noghabai, K. 1999. FE-Modelling of cover splitting due to corrosion by use of inner softening band. *Materials and Structures* 32: 486-491.

Ouglova, A. Berthaud, Y. Francois, M. & Foct, F. 2006. Mechanical properties of an iron oxide formed by corrosion in reinforced concrete structures. *Corrosion Science* 48: 3988-4000.

Page, C. L. & Lambert, P. 1987. Kinetics of oxygen diffusion in hardened cement pastes. *Journal of Material Science* 22: 942-946.

Papadakis, V. G., Vayenas, C. G. & Fardis, M. N. 1991. Physical and Chemical Characteristics Affecting the Durability of Concrete. *ACI Materials Journal* 8: 186-196.

Pel, L. 1995. Moisture transport in building materials. *PhD Thesis* Eindhoven University of Technology.

Polder, R. B. 2001. Test methods for onsite measurement of resistivity of concrete - a RILEM TC-154 technical recommendation. *Construction and building materials* 15: 125-131.

Rendell, F., Jauberthie, R. & Grantham, M. 2002. Deteriorated Concrete - Inspection and physicochemical analysis. London, UK: Thomas Telford, 1st edition.

Scheffler, G. A. 2009. Validation of hygrothermal material modelling under consideration of the hysteresis of moisture storage. *PhD Thesis* Technische Universität Dresden.

Skoček, J. & Stang, H. 2009. Upscaling of fracture properties - discrete modeling. *Submitted to Cement and Concrete Research*.

Solgaard, A. O. S., Michel, A., Stang, H., Geiker, M. R., Edwardsen, C. & Küter, A. 2009. Numerical modeling of cracking of concrete due to corrosion of reinforcement - Impact of cover thickness and concrete toughness. *FraMCos-7 - 7th International Conference on Fracture Mechanics of Concrete and Concrete Structures; Conference proceedings. Jeju, Korea, 23-28 May 2010.*

Stern, M. & Geary, A. L. 1957. Electrochemical polarization I. A theoretical analysis of the shape of polarization curves. *Journal of the Electrochemical Society* 104: 56–63.

Suda, K., Misra, S. & Motohashi, K. 1993. Corrosion products of reinforcing bars embedded in concrete. *Corrosion Science* 35: 1543-1549.

Val, D. V., Chernin, L. & Stewart, M. G. 2009. Experimental and numerical investigation of corrosion-induced cover cracking in reinforced concrete structures. *Journal of Structural Engineering* 135: 376-385.

Warkus, J., Raupach, M. & Gulikers, J. 2006. Numerical modeling of corrosion - Theoretical backgrounds -. *Materials and Corrosion* 57: 614-617.

Wittmann, F. H. 1992. Feuchtigkeitstransport und Dauerhaftigkeit von Beton. *Wissenschaftlich Technische Arbeitsgemeinschaft für Bauwerkserhaltung und Denkmalpflege*.

Paper X

” Monitoring reinforcement corrosion and corrosion-induced cracking using non-destructive x-ray attenuation measurements”

A. Michel, B.J. Pease, M.R. Geiker, H. Stang & J.F. Olesen

Published in: *Cement and Concrete Research.*

Cement and Concrete Research 41 (2011) 1085–1094

Contents lists available at ScienceDirect

Cement and Concrete Research

journal homepage: http://ees.elsevier.com/CEMCON/default.asp

Monitoring reinforcement corrosion and corrosion-induced cracking using non-destructive x-ray attenuation measurements

Alexander Michel [a], Brad J. Pease [a,*], Mette R. Geiker [a,b], Henrik Stang [a], John Forbes Olesen [a]

[a] Technical University of Denmark (DTU), Department of Civil Engineering, Brovej—Building 118, DK-2800 Kgs. Lyngby, Denmark
[b] Norwegian University of Science and Technology (NTNU), Department of Structural Engineering, Trondheim, Norway

ARTICLE INFO

Article history:
Received 3 December 2010
Accepted 17 June 2011

Keywords:
B. Crack detection
B. EDX
C. Corrosion
D. Reinforcement
Non-destructive testing (NDT)

ABSTRACT

To test the applicability of the x-ray attenuation method to monitor corrosion products as well as the formation and propagation of cracks in cementitious materials, reinforced mortar samples were tested under accelerated corrosion conditions. Experimental results demonstrate x-ray attenuation measurements can track time-dependent development of corrosion products and the subsequent initiation and propagation of corrosion-induced cracks. Also, x-ray attenuation measurements allowed determination of the actual concentration of the corrosion products averaged through the specimen thickness. The total mass loss of steel, obtained by the x-ray attenuation method, was found to be in very good agreement with the mass loss obtained by gravimetric method as well as Faraday's law. Results of the presented experimental approach provide pertinent information for the further development and verification of numerical tools simulating corrosion-induced damage in reinforced concrete.

1. Introduction

Corrosion of reinforcement in reinforced concrete structures is a major deterioration problem causing considerable costs due to durability design, maintenance, and repair needs. Therefore, the development of models to predict the (residual) service life of reinforced concrete structures subjected to corrosion has gained momentum in the past decades. Service life models attempt to describe the initiation and propagation phases of reinforcement corrosion (e.g., Refs. [1–3]) and numerous mechanical models have been developed to describe the subsequent consequences of reinforcement corrosion (i.e., corrosion-induced concrete cracking or spalling) (e.g., Refs. [4–6]). The proposed models can be broadly divided into empirical [4], analytical, [5,7–11], and numerical [6,12–16] models. An initial model to simulate corrosion-induced concrete cracking in Ref. [5] considered only expansion of reinforcement, inducing an internal pressure on the surrounding concrete. This model significantly underestimated the time-to-crack initiation. The initial model was extended and the concept of the "porous" or "diffusion" zone was introduced (e.g., Ref. [8]) to adjust the model to fit experimental data. Later, additional parameters were included in the various models to describe different phenomena related to corrosion-induced concrete cracking, e.g., debonding [12] and creep/shrinkage [14].

The commonly called "diffusion" or "porous" zone is a vital parameter in the proposed corrosion-induced concrete cracking models. The zone describes a region of concrete around the reinforcement which can accommodate expansive corrosion products, delaying stress development in the concrete. This region has a major influence on the predicted time-to-crack initiation and the crack propagation behavior [8,10,15]. These commonly used terms ("diffusion" or "porous" zone) are however potentially misleading and/or confusing. The entire concrete surrounding is porous, not just a certain region in close proximity to the reinforcement. Also, development of solid corrosion products is likely not governed by diffusion alone. Diffusion (i.e., transport of matter due to concentration gradients) may describe the movement of ions present in the concrete pore solution (e.g., Cl^-, Ca^+, K^+) or formed during the corrosion process (e.g., Fe^{2+}, Fe^{3+}) through the concrete pore system. However, solid corrosion products (e.g., Fe_2O_3, Fe_3O_4), which actually induce the internal pressures, precipitate. Therefore, the "diffusion" or "porous" zone is referred to as the corrosion accommodating region (CAR) throughout this paper and is suggested as an alternative term to more accurately describe this region.

Inconsistent values are cited for the CAR, ranging from 0.002 to approximately 0.12 mm in thickness [7]. In some cases, the size of the CAR is "determined" by adjusting the value to provide model outputs in line with experimental results [8,9,15,16]. Other experimental methods (e.g., image correlation [10], acoustic emission [17], ultrasound and thermography [18], etc.) are capable of detecting corrosion-induced damages; however, to date these techniques are not capable of providing simultaneous real-time measurements on the amount and/or location(s) of corrosion products. Experimental

* Corresponding author.
E-mail address: bjp@byg.dtu.dk (B.J. Pease).

0008-8846/$ – see front matter © 2011 Elsevier Ltd. All rights reserved.
doi:10.1016/j.cemconres.2011.06.006

methods to physically measure the thickness of the CAR include cutting, sawing and impregnating samples [10]. These destructive methods are potentially invasive, causing possible movement or washing away of corrosion products and hindering reliable measurements.

2. Research significance

Model predictions of corrosion-induced concrete cracking behavior are heavily dependent upon the size of the corrosion accommodating region (CAR). However, a reliable method to measure the size of the CAR has been lacking. This paper focuses on the application of a non-destructive test method, x-ray attenuation measurements, to monitor the time-dependent development of corrosion products and subsequent corrosion-induced cracking. X-ray attenuation measurements are commonly used to monitor moisture movements in concrete and other porous materials (e.g., Refs. [19–23]). Advantages of the x-ray attenuation technique include the non-invasive nature of the method and the ability to directly measure time-dependent changes in concentration of water (i.e., moisture content). This study investigates the ability of the technique to monitor changes in concentration of corrosion products during reinforcement corrosion and to detect cracking of the surrounding concrete.

3. Experimental approach

To test the applicability of the x-ray attenuation method to monitor the development of corrosion products and cracking behavior in cementitious materials, reinforced mortar samples were tested under accelerated corrosion conditions. All materials and testing methods are described below.

3.1. Materials and specimen preparation

Aalborg Rapid® portland cement (Type 52.5N cement [24]) was used. The mix contained 375 kg/m^3 cement, 1125 kg/m^3 fine aggregates (0–4 mm Class E sand in accordance with Ref. [25]), and had a water-to-cement ratio of 0.50. No chlorides were added to the mix, as corrosion was induced by applying electrical current as described in Section 3.2.1. As reinforcement, a smooth steel rod with 8 mm diameter was embedded in the center of the $4\times6\times15$ cm^3 prism. Fig. 1(a) illustrates the cross-section of the mortar specimen.

After casting, the specimen was stored for 24 hours under a plastic sheet in laboratory conditions (i.e., 20 ± 2°C) and was then demolded. Upon demolding, the specimen was stored under water for additional 24 hours at 20 ± 2°C. The 15 cm long prisms were cut in 2 cm lengths using a water-cooled concrete saw. A lead wire was soldered to the reinforcement to allow for accelerated corrosion. All specimen surfaces, except the top and bottom surfaces (see Fig. 1(a) for orientation), were then sealed with paraffin wax. The top and bottom were left unsealed to allow access of oxygen from the top and moisture/current from the bottom. A second, reference specimen (see Fig. 1(a)) was created using the identical procedure (i.e., materials, specimen dimension, curing, cutting, etc.); however, the reference specimen was un-reinforced and completely sealed with paraffin wax to maintain constant moisture conditions.

3.2. Testing procedures

The experimental set up, given in Fig. 1(a), consisted of the reinforced mortar specimen partially submerged in a tap water bath, a sealed reference sample, and a steel shield. The gap between the reference specimen and the reinforced mortar specimen was covered with a steel shield to prevent a free path for x-ray photons to pass through, which may damage the x-ray equipment. Details concerning the accelerated corrosion and x-ray measurement techniques are discussed in the following sections.

3.2.1. Accelerated corrosion

To impress an electrical current through the counter electrode (ruthenium/iridium mixed metal oxide activated titanium mesh) a DC regulator was used. Electrical connection between the working (reinforcement) and counter electrodes was realized by placing the mortar specimen in tap water (no chlorides were added to the solution). The current density applied during the accelerated test was 250 μA/cm^2. It should be noted that such current densities certainly exceed natural conditions. However, as the focus of this work was to test the applicability of x-ray attenuation technique to detect and monitor corrosion products, the applied current density was considered adequate.

3.2.2. X-ray measurement technique

A GNI x-ray facility located at the Technical University of Denmark [26] was used for x-ray attenuation measurements. Fig. 2 shows the x-ray source (a polychromatic x-ray source), a 252×256 pixel x-ray camera, and a programmable three-axis motion frame for moving the source and camera, which are housed in a shielded, environmentally controlled chamber. The x-ray source excitation settings used were a voltage of 80 keV and a current of 75 μA. The x-ray source was automatically ramped up to these settings over a 200 second "warm-up" period and the x-ray source was allowed to stabilize for 600 seconds prior to recording images.

A single measurement consisted of 20 x-ray camera images recorded with an integration time of 1 second. The intensities measured by individual pixels from the 20 images were summed. So-called dark current images (i.e., x-ray camera images recorded

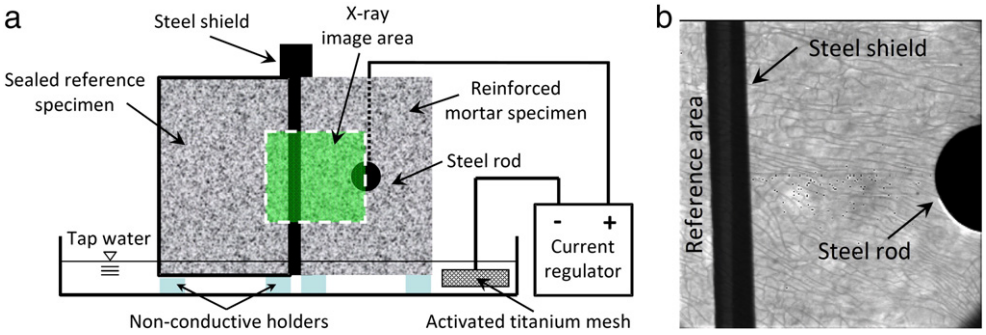

Fig. 1. (a) Experimental set up for accelerated corrosion applying an impressed current with x-ray measurement area indicated, and (b) a typical x-ray image of transmitted intensity showing the steel rod, steel shield, measurement specimen, and the reference area.

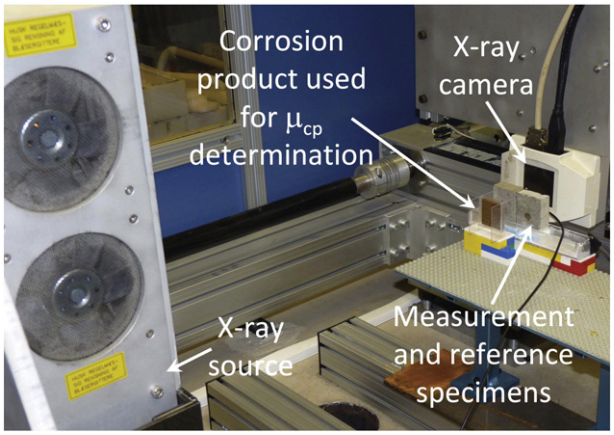

Fig. 2. X-ray attenuation measurement system with experimental setup consisting of the x-ray source and camera along with the specimens. A container filled with corrosion products (Fe_2O_3) was placed in front of the reference specimen to determine linear attenuation coefficient of corrosion products, μ_{cp} (discussed in Section 3.2.4).

while x-ray source is turned off), recorded prior to all x-ray measurements, were subtracted from the measured intensities. Fig. 1 shows the location and size of the measured area along with a typical image captured by the x-ray camera. The area of the reference specimen captured in the x-ray images was used to normalize all images. Before any current was applied to the reinforcement, the specimen was measured three times (i.e., a total of 60 images) in its initial state. After commencing the accelerated corrosion testing, x-ray measurements were recorded every hour, on the hour, for the first 25 hours, followed by measurements every 2 hours until termination of the test at 147 hours. Testing was terminated due to extensive corrosion-induced damage to the mortar. Additional information on the x-ray measurement procedure (i.e., dark current measurements, use of reference samples, etc.) is available in the literature [23,27–29].

As illustrated in Fig. 3, x-ray photons produced by the source interact with the specimen and corrosion products prior to reaching the x-ray camera. The following sections describe the theoretical background of the x-ray attenuation technique and its potential applicability to monitor corrosion of steel reinforcement embedded in cementitious materials.

3.2.3. Theoretical background of x-ray measurement technique

Fig. 3(a) shows the fundamental layout of an x-ray attenuation measurement. The x-ray source produces a polychromatic beam of x-ray photons (i.e., photons with varying energy levels) with a given incident intensity, I_0, which passes through a test specimen with a thickness, t. As the x-ray photons pass through the specimen a portion of the incident intensity, I_0 is attenuated (i.e., absorbed and scattered) and the transmitted intensity, I is recorded by the 64,512 individual pixels in the x-ray camera. The attenuation behavior of a monochromatic x-ray photon (i.e., photons with a single energy level) is described by the Beer–Lambert law (Eq. 1) [20,30]:

$$I = I_0 \cdot e^{-\mu \cdot t} \tag{1}$$

where, μ is the linear attenuation coefficient. The linear attenuation coefficient has units of cm^{-1}, while intensity and transmitted intensity are unitless quantities of "counts" or "hits" of individual x-ray photons. As mentioned, the Beer–Lambert law describes attenuation of monochromatic x-ray photons; however, a polychromatic x-ray source was utilized here. Polychromatic x-ray photon beams undergo beam hardening [31] during interactions with the specimens as all elements and compounds preferentially attenuate lower energy x-ray photons [33], resulting in an increase in the average energy (or "hardening") of the x-ray photon beam. To account for this discrepancy, the linear attenuation coefficient, μ in Eq. (1) must be replaced by the effective attenuation coefficient, μ_{ef} [22,23] as shown in Eq. (2).

$$I = I_0 \cdot e^{-\mu_{ef} \cdot t} \tag{2}$$

The effective attenuation coefficient, μ_{ef}, which accounts for beam hardening effects, must be directly measured and varies with the thickness of the material (and likely with varying x-ray sources due to changes in x-ray photon spectra).

Commonly, x-ray experiments to track conditional changes in a material (i.e., moisture conditions or, in this case, content of corrosion products) are described as the composite system illustrated in Fig. 3 (b) [19,20,22,23,27–29]. The composite system consists of a non-corroded, saturated reinforced mortar specimen with thickness, t_m in series with corrosion products with thickness, t_{cp}. Based on Eq. (2), the transmitted intensity of the polychromatic x-ray source before reinforcement corrosion, I_{non} is described by Eq. (3):

$$I_{non} = I_0 \cdot e^{-\mu_{ef,m} \cdot t_m} \tag{3}$$

where $\mu_{ef,m}$ is the effective attenuation coefficient of mortar. The transmitted intensity of polychromatic x-ray beam before reinforcement corrosion, I_{non} continues and interacts with the corrosion products. The corrosion products further reduce the transmitted intensity as described by Eq. (4):

$$I_{corr} = I_{non} \cdot e^{-\mu_{ef,cp} \cdot t_{cp}} = I_0 \cdot e^{-\mu_{ef,m} \cdot t_m - \mu_{ef,cp} \cdot t_{cp}} \tag{4}$$

where I_{corr} is the transmitted intensity after corrosion, and $\mu_{ef,cp}$ is the effective attenuation coefficient of the corrosion product.

The change in concentration of corrosion products in the specimen, Δc_{cp} (g/cm^3) is calculated as change in corrosion products within the specimen volume or, assuming a constant cross-section, a change in corrosion products within the specimen thickness according to Eq. (5):

$$\Delta c_{cp} = \frac{\rho_{cp} \cdot \Delta V_{cp}}{V} = \frac{\rho_{cp} \cdot \Delta t_{cp}}{t} \tag{5}$$

where ρ_{cp} is the density of the corrosion products (g/cm^3), ΔV_{cp} is the change in volume of corrosion products within the specimen's volume, V, and Δt_{cp} is the change in thickness of corrosion products within the specimen's thickness, t.

Combining Eqs. (4) and (5) yields Eq. (6), which relates the transmitted intensity after corrosion, I_{corr} to the change in concentration of corrosion products, Δc_{cp}:

$$I_{corr} = I_{non} \cdot e^{-\left(\mu_{ef,cp} \cdot \Delta c_{cp} \cdot t\right)/\rho_{cp}} \tag{6}$$

and solving for change in concentration of corrosion products, Δc_{cp} (g/cm^3) yields Eq. (7):

$$\Delta c_{cp} = -\frac{\rho_{cp}}{\mu_{ef,cp} \cdot t} \cdot ln\left(\frac{I_{corr}}{I_{non}}\right). \tag{7}$$

The transmitted intensity prior to corrosion, I_{non} is a specimen's initial non-corroded condition, while I_{corr} was measured at various times after application of a constant current. Therefore, by measuring I_{corr} over time and using Eq. (7) the concentration of corrosion products can be directly measured as a function of time and two dimensional space (i.e., x-ray camera provides location-dependent information), if $\mu_{ef,cp}$ and ρ_{cp} are known. The following section describes methods to determine $\mu_{ef,cp}$, while values for ρ_{cp} are available in the literature [32].

3.2.4. Attenuation coefficients of potential corrosion products

Linear attenuation coefficient of corrosion products, μ_{cp} can be determined via calculations using tabulated data on the linear

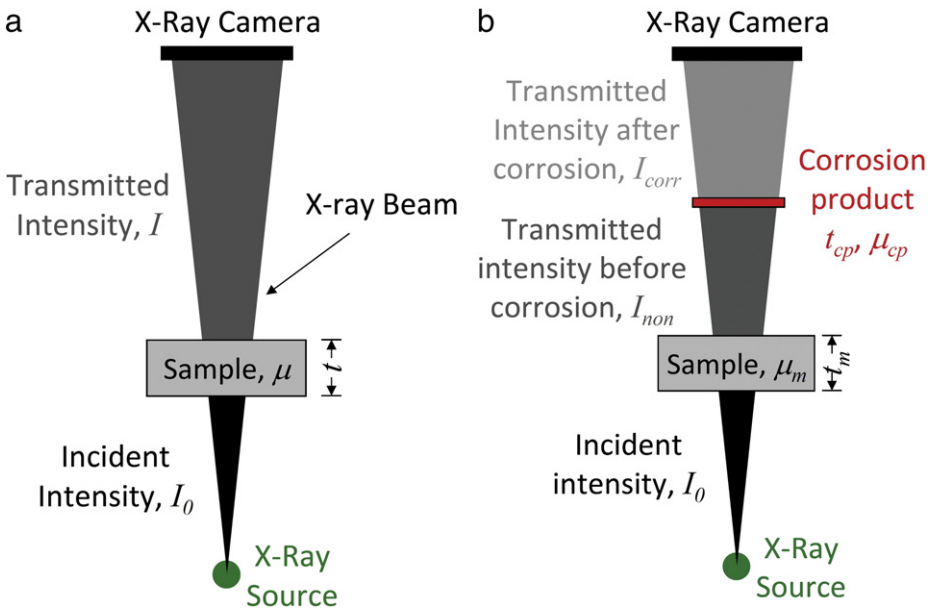

Fig. 3. Fundamental explanation of use of x-ray attenuation measurements: (a) Schematic description of Beer–Lambert law (Eq. 1) and (b) effect of change in concentration of corrosion products on x-ray attenuation measurements as described by a composite of the initial specimen and a thickness of corrosion products representing reinforcement corrosion.

attenuation coefficients of elements presented in Ref. [33]. For direct measurements of the effective attenuation coefficient, red rust (i.e., Fe_2O_3) was collected, pulverized using a mortar and pestle, and placed and compacted in acrylic containers in varying thicknesses (0, 1, 3, and 5 mm). As shown in Fig. 2, the acrylic containers were placed in front of the reference sample and the transmitted intensities were measured at varying x-ray source voltage settings (70, 80, 90, 100, and 110 keV) with the containers empty and then filled with corrosion products. The effective attenuation coefficient of the corrosion products, $\mu_{ef,cp}$ can then be calculated in accordance with Eq. (4). The same procedure is used to determine the effective attenuation coefficient of water in other investigations [20,23]. All measurements were taken with an x-ray source current setting of 75 μA. Also, the linear attenuation coefficients of compounds can be calculated as described in Ref. [33] and previously applied in Ref. [23,27] based on compound density and stoichiometry. Linear attenuation coefficients of several potential corrosion products (Fe_2O_3, Fe_3O_4, $Fe(OH)_2$, $Fe(OH)_3$, and $FeCl_2^+$) [34] and water (H_2O) were calculated.

4. Experimental results

4.1. Attenuation coefficients of corrosion products and measurement resolution

Fig. 4 shows the calculated linear attenuation coefficients for water and various thermodynamically feasible reinforcement corrosion products, determined as described in Section 3.2.4. The measured effective attenuation coefficients for Fe_2O_3 correlate well with calculated values of the linear attenuation coefficient. The linear attenuation coefficients of the various corrosion products are, in most cases, over an order of magnitude higher than that of water. Therefore, according to Eq. (1), corrosion products (which are also more dense than water, see Table 1) are more effective at attenuating x-rays than water. Of the various corrosion products considered, Fe_3O_4 has the highest linear attenuation coefficients followed by Fe_2O_3, $Fe(OH)_3$, $Fe(OH)_2$, and $FeCl_2^+$. EDS and XRD measurements performed on the mortar adjacent to the steel bar confirmed the presence of either Fe_2O_3 or Fe_3O_4.

According to Eq. (8) [22], the change in concentration corresponding to the attenuation of a single x-ray photon (concentration resolution, $R_{\Delta c}$) of the x-ray attenuation measurement is controlled by the effective attenuation coefficient (for polychromatic x-ray sources) and density of a substance, x moving within a porous material:

$$R_{\Delta c} = -\frac{\rho_x}{\mu_{ef,x} \cdot t} \cdot ln\left(\frac{I_{non}-1}{I_{non}}\right) \tag{8}$$

where ρ_x is the density of a substance x, $\mu_{ef,x}$ is the effective attenuation coefficient of a substance x, and I_{non} is the transmitted intensity from the initial, non-corroded specimen. Table 1 provides the density, linear attenuation coefficients (and measured effective attenuation coefficient of Fe_2O_3) at 80 keV, and the concentration resolution for water and the various corrosion products considered. Linear attenuation coefficients were used to calculate concentration resolutions due to the good correlation between the linear and effective attenuation coefficients of Fe_2O_3; however, effective attenuation coefficients should be measured and utilized when other corrosion products are anticipated. For Fe_2O_3, both linear and effective

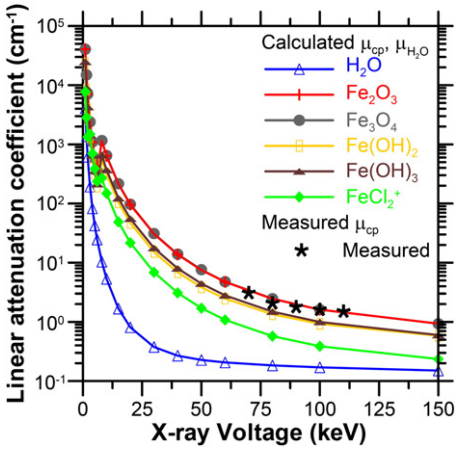

Fig. 4. X-ray attenuation spectra for water (H_2O) and various thermodynamically feasible corrosion products. The black stars indicate measured values of the effective attenuation coefficient for corrosion products.

Table 1
Density (ρ), linear attenuation coefficients (μ, at 80 keV), and concentration resolution ($R_{\Delta c}$) for various substances.

Substance	ρ [g/cm^3]	μ [cm^{-1}]	$R_{\Delta c}$ [mg/cm^3]
Water	1.00	0.184	0.599
Fe_2O_3	5.24	2.447 (2.142)[b]	0.235 (0.269)
Fe_3O_4	5.17	2.466	0.230
$Fe(OH)_2$	3.40	1.484	0.252
$Fe(OH)_3$	3.40	1.343	0.278
$FeCl_2^+$	1.39[a]	0.574	0.266

[a] Density given for tetrahydrate, which is green in color [32].
[b] Values in parentheses are measured effective attenuation coefficient (μ_{ef}, at 80 keV) and corresponding resolution.

attenuation coefficients (at 80 keV) and the resulting concentration resolutions are presented. For I_{non}, the average transmitted intensity from the specimen in its original, non-corroded condition was used. For the x-ray energy used (μ_x and I_{non} vary with x-ray energy), $R_{\Delta c}$ of water was 0.599 mg/cm^3, while $R_{\Delta c}$ enhanced to between 0.230 mg/cm^3 and 0.278 mg/cm^3 for the various corrosion products. Based on Eq. (8) and Table 1, concentration resolution is inherently improved (over that of water) when monitoring reinforcement corrosion products.

4.2. Image analysis of x-ray attenuation measurements

Fig. 5 in the electronic version of this paper (5-EV, see link in Appendix A.) is compiled videos consisting of calculated x-ray images of change in concentration of corrosion products (i.e., Eq. 7) between 3 and 147 hours of accelerated corrosion testing. Each image is identified by a sequence number and the time passed after initiation of accelerated corrosion testing in the bottom left corner in both videos. In Fig. 5(a)-EV the first several frames of the video highlight specimen details including the rebar, mortar and a size scale. Throughout the video duration in Fig. 5(a)-EV additional details and phenomena are pointed out and labeled as they appear, including corrosion products (light gray to white in color), initiation and propagation of cracks (dark gray to black in color), the probable filling of an entrapped pore with corrosion products, and excessive corrosion-induced deformations of the mortar. The video in Fig. 5 (b)-EV consists of the same images; however, with an increased frame rate and without pauses. The higher frame rate more clearly shows the excessive corrosion-induced deformations of the mortar. Deformation of a part of the specimen induces measurement distortions as the pixel dependent initial transmitted intensity, I_{non} no longer accurately coincides with the transmitted intensity after corrosion, I_{corr}. As seen most clearly after 127 hours (image 75) in both videos, excessive deformations (and resulting measurement distortion) give the appearance of corrosion products being deposited relatively far from the rebar surface.

Fig. 5 in the printed version of this paper (5-PV), is calculated x-ray images (i.e., Eq. 7) after (a) 14 and (b) 147 hours of accelerated corrosion testing. The image highlights the location of corrosion products (light gray to white in color) and cracks (dark gray to black in color). Fig. 5(a)-PV clearly shows that an initial crack has formed along with the location and amount of corrosion products required to induce the crack. Fig. 5(b)-PV shows that substantially more corrosion products have formed after 147 hours at the interface of the concrete and steel, both increasing the size of the initial crack and inducing a second crack. Additionally, as discussed above, excessive movement of the mortar and the resulting measurement distortion are most clearly visible in the top-right corner of Fig. 5(b)-PV.

Contour plots in Figs. 6 and 7 provide location-dependent information on calculated concentrations of corrosion products (Eq. 7) at various times during the accelerated corrosion testing. Fig. 6, which shows the entire x-ray image area of the measured specimen, has contours to highlight both the cracks and the concentration of corrosion products, after (a) 14 hours, (b) 71 hours, and (c) 119 hours of accelerated corrosion. The assumed type of corrosion product was Fe_2O_3, with a measured average (averaged from the varying thicknesses of corrosion product measured) effective attenuation coefficient of 2.142 cm^{-1} at 80 keV, 5.24 g/cm^3 density, and the specimen thickness was 2.0 cm. The contour plots illustrate the concentration of corrosion products in g/cm^3, which is a summation of the amount of corrosion products through the thickness of the specimen. Cracks result in negative contour values as the number of transmitted x-ray photons

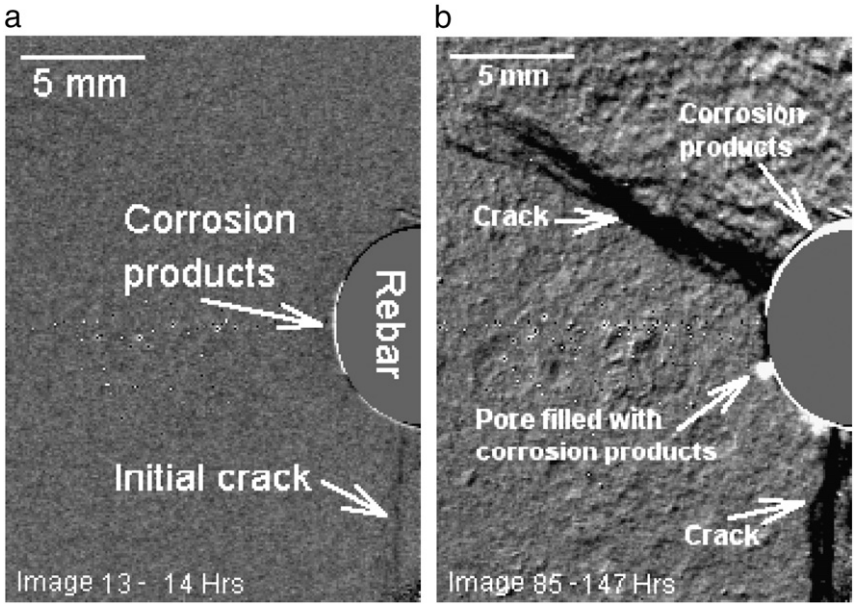

Fig. 5. (Printed version) Calculated image (i.e., Eq. 7) after (a) 14 and (b) 147 hours of accelerated corrosion testing. (Electronic version—video links in Appendix A.) Videos compiled from calculated images between 3 and 147 hours of accelerated corrosion testing (a) with various events highlighted and (b) with a higher frame rate to better illustrate corrosion-induced deformations of surrounding mortar.

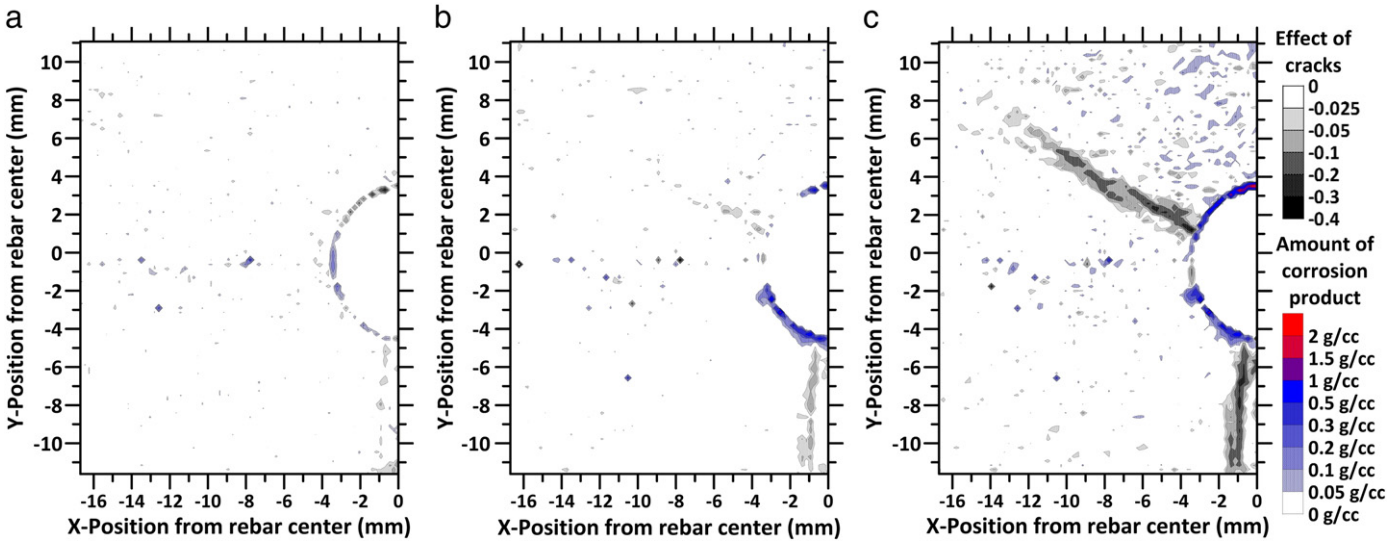

Fig. 6. Contour plots highlighting the effect of cracks on x-ray attenuation measurements and concentration of corrosion products after (a) 14 hours, (b) 71 hours, and (c) 119 hours (note: the effect of cracks is a unitless factor described by the natural log portion of Eq. 7).

increases. Fig. 7 shows a zoomed portion of the original image and excludes contours describing cracks. All contour plots are shown with units of g/cc (i.e., gram per cubic centimeter, g/cm^3).

Further detailed descriptions of Figs. 5 (for both the electronic and print versions) and 6 are included in the following sections.

4.3. Corrosion-induced cracking and deformation behavior

The development of corrosion products, described in the following section, resulted in the formation of two cracks within the measured region and a third crack, which was observed outside of the area recorded by x-ray. Fig. 5(a)-EV indicates that the first crack begins to form below the steel after 13 hours (image 12) of accelerated corrosion testing. The effect of the first crack can begin to be seen in the contour plot shown in Fig. 6(a). Figs. 5-EV and 6(a),(b),(c) indicate the width of the initial crack continuously increased during testing.

After 57 hours (image 40) a second crack developed in the upper half of the mortar. The second crack initiated at or near the surface of the steel and propagated outward toward the mortar's surface. The second crack appears to be widest at the concrete–steel interface, with decreasing width as it extends away from the steel. Quantification of the crack width is not possible with the x-ray attenuation measurement, as the effect of cracks is averaged through the 2.0 cm thick specimen measured. During propagation of the second crack, particularly from 97 hours (image 60) to the end of the test, excessive deformation of the mortar occurred. The deformation is clearly seen in Fig. 5(b)-EV in the upper and side portion of the mortar. The mortar deformation causes distortions in calculated corrosion product concentration images (i.e., Eq. 7), which is seen most clearly in the top portion of the mortar. Values for I_{non} are specific to a particular pixel/location, and as the deformations occur the measured I_{corr} values no longer match to the original corresponding I_{non}. The influence of this distortion is clearly shown in Figs. 6(c) and 7(c), through the apparent formation of corrosion products far from the steel. These apparent formations are attributed to distortions and not the actual formation of corrosion products. The deformation of the side portion of the mortar appears to have caused separation between the mortar and the steel, as indicated in image 75 (127 hours). As this occurs, the corrosion products appear to either relocate or disappear. Most likely the corrosion products remain in place, but the effect of the crack controls the x-ray attenuation measurement results in such a damaged specimen. This, along with measurement distortions induced by excessive deformations, is a limitation of the presented approach. Also, the x-ray attenuation data are an average through the specimen thickness. Thus, if both corrosion products and a crack form at the same location, the two behaviors are averaged through the specimen thickness, potentially resulting in errant quantifications of the amount of corrosion products or qualification of the cracking behavior. However, before cracking occurs, calculated concentrations of corrosion products remain accurate.

The first and secondary crack can be seen in their final states (147 hours, image 85) in Fig. 5(b)-PV. Excessive deformation and resulting distortion of the calculated image (Eq. 7) are also apparent in Fig. 5(b)-PV.

The contour plots in Fig. 6(a),(b),(c) illustrate the effect of the cracks. In Fig. 6(a) (14 hours, image 13) the initial crack has recently formed and a line of negative contours is seen directly below the rebar. Fig. 6(b) (71 hours, image 47) indicates the initial crack has likely increased in size and connectedness, and a second crack has initiated from the steel surface. Fig. 6(c) shows both cracks have further increased in size and the impact of calculated image distortion is clearly seen in the upper portion of the mortar.

4.4. Development and location of corrosion products

Fig. 5(a)-EV shows corrosion products were clearly detected at the concrete–steel interface after 9 hours (image 8) of accelerated corrosion testing. Initially, the corrosion products formed on the side-facing surface of the steel; however, with additional time corrosion products start to form on the bottom-facing surface. After 16 hours (image 15) corrosion products begin to protrude into an entrapped void near the steel surface. Corrosion products penetrate deeper into the mortar as accelerated corrosion testing continued, and after 33 hours (image 28) corrosion products are seen on the top-facing surface of the steel. After 89 hours (image 56) additional corrosion products appear to enter the entrapped pore; however, after the second crack propagates nearly all corrosion products appear to form near the top-facing surface of the steel. This observation is quantified and verified by Figs. 7 and 8, as discussed in the following paragraph. After 127 hours (image 75), excessive deformation of the mortar above the steel occurs as corrosion products no longer appear to protrude into the mortar, but rather push the mortar out of the way.

The zoomed contour plots in Fig. 7(a), (b), and (c) quantify and summarize the information presented in Fig. 5(a)-EV. Fig. 7(a)

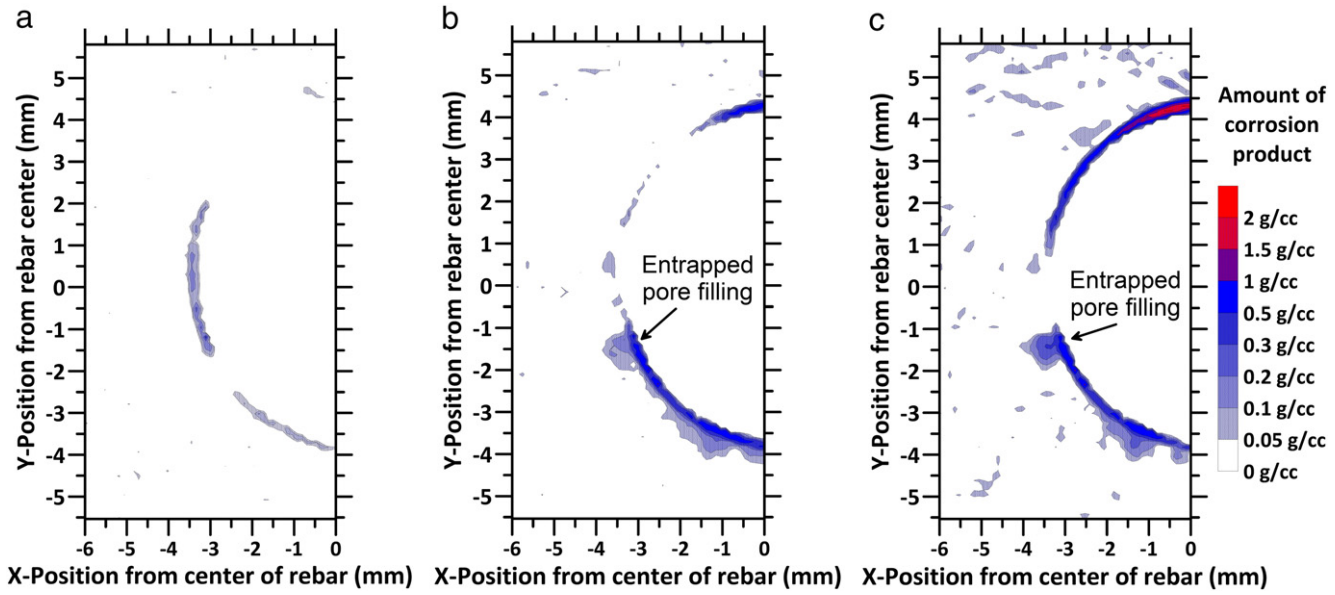

Fig. 7. Zoomed contour plots highlighting only concentration of corrosion products after (a) 14 hours, (b) 71 hours and (c) 119 hours.

indicates that concentration of corrosion product ranged up to a maximum between 0.1 and 0.2 g/cm^3 after 14 hours. The concentration of corrosion products and area where corrosion products exist increased after 71 hours (Fig. 7(b)) and the filling of the entrapped pore is clearly shown. Between 71 and 119 hours, Fig. 7(b) and (c), respectively, a great deal of additional corrosion products formed near the top-facing side of the rebar. Fig. 8 shows a contour plot of the additional corrosion products formed between 71 and 119 hours. Fig. 8 confirms that up to 1.5 g/cm^3 of corrosion product formed near the top-facing surface of the rebar, while during the same time a maximum increase of only 0.2 g/cm^3 occurred near the lower portion of the rebar.

Through further image analysis, polar transformation of results shown in Fig. 7(c) are presented in Fig. 9. Polar transformation allows plotting of the circular surface of the rebar as a flat surface, from which corrosion products protrude. The concentration of corrosion products was averaged over the radius up to 1.0 mm from the rebar surface as presented in Fig. 10. Fig. 10 illustrates concentrations of corrosion products both increase and penetrate deeper into the mortar specimen with increased time. The polar transformation also facilitates estimation of size of the CAR. In this case (where a very high corrosion-inducing current was applied), as shown by the solid circular symbol plot (13 hours) the CAR was between 0.09 and 0.18 mm. The accelerated nature of this initial test may have not provided sufficient time for realistic penetration of corrosion products into the surrounding mortar. With the presented experimental setup a single pixel of the x-ray camera corresponds to a 0.89×0.89 mm^2 area of the specimen. Previously reported values for the CAR vary between 0.002 to 0.12 mm, indicating improved spatial resolution of the x-ray images may be required.

Fig. 11(a) and (b) show an SEM image of the mortar near the concrete–steel interface and an EDS mapping of iron, calcium, and silicon in the same region, respectively. Fig. 11(b) indicates iron (i.e., corrosion products) indeed penetrated into the microstructure of the cement paste, with particular areas of increased iron content.

The concentration of corrosion products at the end of testing (147 hours, image 85) was integrated to estimate a total mass loss of the rebar due to corrosion during the test. Values for mass loss were also estimated by Faraday's law and measured through gravimetric means (i.e. weighing). Table 2 shows the various means to measure and estimated mass loss resulted in very good agreements. A 9% difference was found between weight and x-ray measurement methods. A higher discrepancy in mass loss (43%) between Faraday's law estimation and x-ray method may be explained by the assumption in Faraday's law of 100% current efficiency (meaning that all current applied is used in the electrochemical reaction to dissolve the iron). It should also be mentioned that only one half of the rebar was monitored during this testing (see Fig. 1(b)). To obtain the total mass loss from x-ray attenuation measurements, symmetry (i.e., in terms of concentration of corrosion products) was assumed.

5. Discussion of results

X-ray attenuation measurements of corrosion products are more effective (i.e., improved inherent concentration resolution) than the more common monitoring of water movements in cementitious

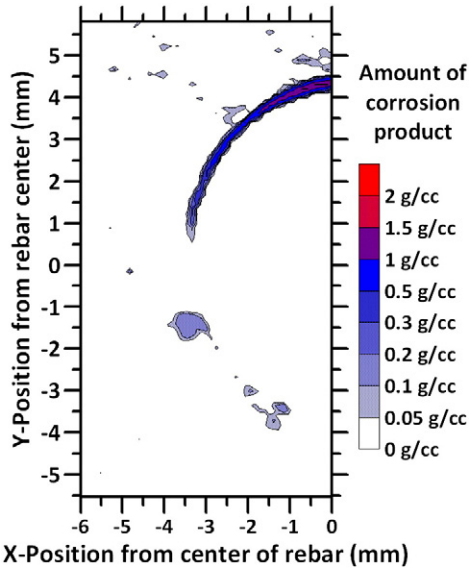

Fig. 8. Additional concentration of corrosion products between 71 hours and 119 hours of accelerated corrosion testing (i.e., Fig. 6(c) minus Fig. 6(b)).

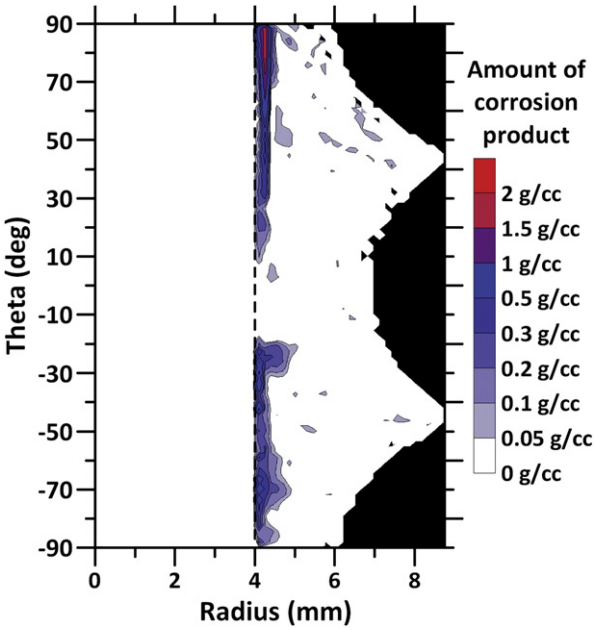

Fig. 9. Polar transformation contour plots of corrosion product concentrations after 119 hours (i.e., Fig. 6(c)).

materials. The x-ray attenuation measurement is non-destructive and does not influence the accelerated corrosion testing method. Further, the current applied to induce corrosion (i.e., accelerated corrosion method) does not appear to interact with the x-ray photons transmitted through the measurement specimen.

Corrosion-induced cracks were seen to form at or near the concrete–steel interface and propagate outward to the specimen surface (in agreement with previous model behaviors [6,13]). Further, comparisons of the development of corrosion products and the corrosion-induced cracking of the mortar specimen provided the following insights. The development of additional corrosion products appears to be linked to the degree of damage (i.e., cracking) at the interface of the steel and surrounding mortar. Prior to extensive cracking (i.e., before 71 hours, image 47) the corrosion products appear to penetrate into the pores of the mortar. However, after more extensive cracking the corrosion products appear to form between the steel and mortar, simply moving the mortar rather than penetrating into it. Additionally, as shown in Fig. 8, corrosion products appear to favor forming at the damaged interface, as nearly all additional corrosion products were seen to form in this region after 71 hours.

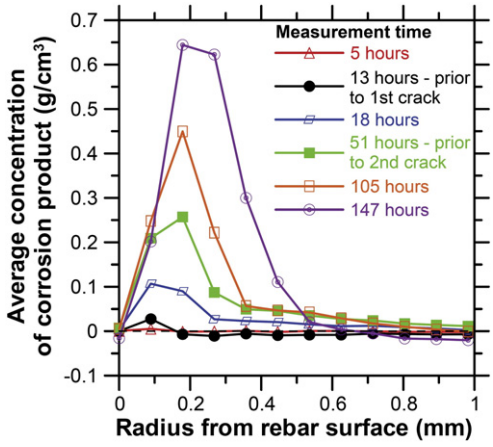

Fig. 10. Average concentration of corrosion products as a function of radius from the rebar surface at varying times (5, 13, 18, 51, 105, and 147 hours).

It is evident from the results that the x-ray attenuation method is suitable to track the time-dependent development of the corrosion products and subsequent initiation and propagation of cracks due to the expansive nature of the corrosion products. While a relatively high current was applied to induce corrosion to test the applicability of the measurement technique, results clearly indicate that corrosion products and corrosion-induced cracking under natural corrosion conditions would similarly be detected (assuming location of specimen, x-ray source, and camera is constant as discussed below). Furthermore, the experimental method allows for the determination of the actual concentration of the corrosion products averaged through the specimen thickness. Measurement distortions due to excessive deformations of the mortar occurred; however, future measurements would likely stop well before similar distortions occur. The most important information from the technique (i.e., amount and location(s) of corrosion products necessary to induce cracking) is collected well before excessive distortions are observed. Polar transformation of the x-ray images provides the average amount of corrosion products as a function of the radius (i.e., distance from rebar surface) and time prior to initiation of cracking in the reinforced mortar sample. In other words, the x-ray attenuation method can directly measure the size of the CAR as both the corrosion and the corrosion-induced cracking behaviors are monitored. Further parametric studies are needed; however the presented technique should provide unique insight on the corrosion process (including amount and location of corrosion products and time-to-cracking) under laboratory conditions, improving understanding and modeling of reinforcement corrosion and subsequent corrosion-induced concrete cracking.

The presented method could be applied for in-situ measurement of the extent of reinforcement corrosion and resulting damage; however, many practical issues would need to be considered. As seen in Fig. 5(b) and discussed previously, movement of the specimen caused measurement distortions. Therefore, positions of the x-ray source, camera, and measured area must be constant at differing measurement times. With possible measurement intervals in the range of a year or more, identical positioning may be difficult. Furthermore, effects of other various transient behaviors in concrete (e.g., moisture movements, possible leaching, etc.) on the x-ray attenuation measurements would need to be isolated or corrected. A similar, yet limited radiography technique (i.e., γ-ray imaging) has been applied for in-situ determinations of rebar location and can even estimate cross-section reductions of reinforcement due to corrosion [35]. γ-Ray imaging, identically to medical/dental radiography, detects the denser steel (analogous to bone, teeth) within the less dense concrete (analogous to human soft tissues) in a single measurement. However, radiography does not provide the necessary information to calculate concentration changes (see Eq. 7) and appears (based on results presented in Ref. [35]) unable to assess the location of corrosion products and any corrosion-induced cracking of the surrounding concrete.

6. Summary and conclusions

The applicability of x-ray attenuation measurements to monitor the development of corrosion products as well as initiation and propagation of cracks in cementitious materials was presented. Results obtained from x-ray attenuation measurements and subsequent image analyses of reinforced mortar samples tested under accelerated corrosion conditions indicate that:

1. The x-ray attenuation measurements do not affect accelerated corrosion testing and the current applied to induce corrosion does not appear to interact with x-ray photons.

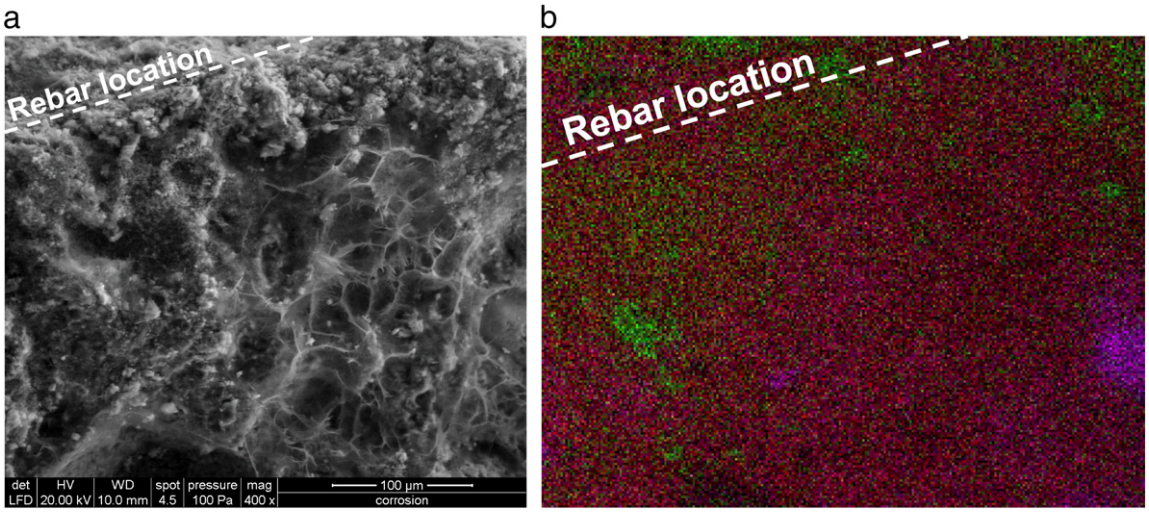

Fig. 11. (a) SEM image of mortar surrounding steel rebar with rebar location noted, (b) EDS mapping of Fe (green), Ca (red), and Si (purple) in the same area.

2. X-ray attenuation measurement allow non-destructive monitoring of corrosion products and it has been found that:
   - Similar to previous observations, corrosion products were seen to form at or near the steel surface for the corrosion conditions investigated.
   - Corrosion products initially penetrate into the mortar.
   - After excessive deformation due to corrosion-induced cracking the corrosion products appear to form between the steel and mortar, simply moving the mortar rather than penetrating into it.
3. The concentration of corrosion products can be determined as a function of time and space with the x-ray attenuation measurements.
   - The total mass loss of steel obtained by the x-ray attenuation method correlates well with determination of the mass loss by gravimetric means as well as Faraday's law.
4. Initiation and propagation of corrosion-induced cracking can be monitored.
   - Results of the x-ray attenuation measurements allow monitoring of crack initiation at or near the steel surface as well as propagation of the crack outward toward the mortar's surface.

Further detailed study is warranted into applying this method to measure the impact cracks have on moisture ingress and the subsequent reinforcement corrosion in a single test specimen (i.e., full service life). X-ray measurements provide a direct measure of the moisture ingress and corrosion behaviors, including both the location and amount of moisture and corrosion products.

Acknowledgements

The first author gratefully acknowledges the financial support of Taumoses Legat as well as Femern Bælt A/S, Sund & Bælt Holding A/S and The Danish Agency for Science, Technology and Innovation. Financial contributions from the Danish Expert Centre for Infrastructure Constructions are also greatly appreciated. Furthermore, the authors acknowledge the assistance of Adéla Peterová.

Table 2
Comparison of mass loss obtained by different measurement techniques. Deviation from x-ray determination shown.

Test method	Mass loss	Deviation
	[g]	[%]
Faraday's law	0.19	43
X-ray attenuation	0.11	–
Weighing	0.12	9

Appendix A. Supplementary data

Supplementary data to this article can be found online at doi:10.1016/j.ydbio.2011.06.020.

References

[1] J. Gulikers, M. Raupach, Numerical models for the propagation period of reinforcement corrosion—comparison of a case study calculated by different researchers, Materials and Corrosion 57 (8) (2006) 618–627.
[2] O.B. Isgor, A.G. Razaqpur, Modelling steel corrosion in concrete structures, Materials and Structures 39 (287) (2006) 259–270.
[3] A. Michel, M. Geiker, H. Stang, J. Olesen, Numerical modelling of reinforcement corrosion in concrete structures, Proceedings of the 8th fib PhD Symposium, Kgs. Lyngby, Denmark, 2010.
[4] C. Alonso, C. Andrade, J. Rodriguez, J.M. Diez, Factors controlling cracking of concrete affected by reinforcement corrosion, Materials and Structures 31 (211) (1998) 435–441.
[5] Z. Bažant, Physical model for steel corrosion in concrete sea structures—application, Journal of the Structural Division 105 (1979) 1155–1166.
[6] F.J. Molina, C. Alonso, C. Andrade, Cover cracking as a function of rebar corrosion: part 2—numerical model, Materials and Structures 26 (9) (1993) 532–548.
[7] L. Chernin, D.V. Val, K.Y. Volokh, Analytical modelling of concrete cover cracking caused by corrosion of reinforcement, Materials and Structures 43 (4) (2010) 543–556.
[8] Y. Liu, R. Weyers, Modeling the time-to-corrosion cracking in chloride contaminated reinforced concrete, ACI Materials Journal 95 (6) (1998) 675–681.
[9] T. El Maaddawy, K. Soudki, A model for prediction of time from corrosion initiation to corrosion cracking, Cement and Concrete Composites 29 (3) (2007) 168–175.
[10] S. Caré, Q. Nguyen, V. L'Hostis, Y. Berthaud, Mechanical properties of the rust layer induced by impressed current method in reinforced mortar, Cement and Concrete Research 38 (8–9) (2008) 1079–1091.
[11] C.-Q. Li, Y. Yang, R.E. Melchers, Prediction of reinforcement corrosion in concrete and its effects on concrete cracking and strength reduction, ACI Materials Journal 105 (1) (2008) 3–10.
[12] K. Noghabai, FE-modelling of cover splitting due to corrosion by use of inner softening band, Materials and Structures 32 (221) (1999) 486.
[13] S.F.U. Ahmed, M. Maalej, H. Mihashi, Cover cracking of reinforced concrete beam due to corrosion of steel, ACI Materials Journal 104 (2) (2007) 153–161.
[14] E. Bohner, H. Müller, S. Bröhl, Investigations on the mechanism of concrete cover cracking due to reinforcement corrosion, FraMCos-7—7th International Conference on Fracture Mechanics of Concrete and Concrete Structures, Jeju, Korea, 2010.
[15] D.V. Val, L. Chernin, M.G. Stewart, Experimental and numerical investigation of corrosion-induced cover cracking in reinforced concrete structures, Journal of Structural Engineering 135 (2009) 376–385.
[16] I. Petre-Lazar, Aging assessment of concrete structures submitted to steel corrosion, Ph.D. thesis, Laval University, Quebec, Canada, (in French) (2000).

[17] Y. Kawasaki, Y. Tomoda, M. Ohtsu, AE monitoring of corrosion process in cyclic wet–dry test, Construction and Building Materials 24 (12) (2010) 2353–2357 special Issue on Fracture, Acoustic Emission and NDE in Concrete (KIFA-5).
[18] D. Aggelis, E. Kordatos, D. Soulioti, T. Matikas, Combined use of thermography and ultrasound for the characterization of subsurface cracks in concrete, Construction and Building Materials 24 (10) (2010) 1888–1897.
[19] P.H. Baker, D. Bailly, M. Campbell, G.H. Galbraith, R.C. McLean, N. Poffa, C.H. Sanders, The application of x-ray absorption to building moisture transport studies, Measurement 40 (9–10) (2007) 951–959.
[20] K. Hansen, S. Jensen, L. Gerward, K. Singh, Dual-energy x-ray absorptiometry for the simultaneous determination of density and moisture content in porous structural materials, Proceedings of the 5th Symposium on Building Physics in the Nordic Countries, Vol. 1, Gothenburg, Sweden, 1999, pp. 281–288.
[21] J. Hu, P. Stroeven, X-ray absorption study of drying cement paste and mortar, Cement and Concrete Research 33 (3) (2003) 397–403.
[22] S. Roels, J. Carmeliet, Analysis of moisture flow in porous materials using microfocus x-ray radiography, International Journal of Heat and Mass Transfer 49 (25) (2006) 4762–4772.
[23] G. Sant, J. Weiss, Using x-ray absorption to assess moisture movement in cement-based materials, Journal of ASTM International 6 (9) (2009) 1–15.
[24] DS/EN 197-1 Cement—part 1: composition, specification and conformity criteria for common cements, 2001 29 pp.
[25] DS-2426, Concrete—materials—rules for application EN 206-1 in Denmark, Tech. rep, Danish Standards Association, 2004.
[26] www.gni.dk GNI X-ray System, Technical University of Denmark, 2010.
[27] B. Pease, Influence of concrete cracking on ingress and reinforcement corrosion, Ph.D. thesis, Technical University of Denmark, Kgs. Lyngby, Denmark (December 2010).
[28] B. Pease, J. Couch, M. Geiker, H. Stang, J. Weiss, Assessing the portion of the crack length contributing to water sorption using x-ray absorption measurements on concrete wedge splitting specimens, ConcreteLife'09: Second International RILEM Workshop on Concrete Durability and Service Life Planning, Haifa, Israel, 2009.
[29] M. Pour-Ghaz, F. Rajabipour, J. Couch, J. Weiss, Numerical and experimental assessment of unsaturated fluid transport in saw-cut (notched) concrete elements, ACI SP 266—Modeling as a Solution to Concrete Problems, American Concrete Institute, 2009, pp. 73–83.
[30] G. Knoll, Radiation Detection and Measurement, J. Wiley, 1989.
[31] R.A. Brooks, G.D. Chiro, Beam hardening in x-ray reconstructive tomography, Physics in Medicine and Biology 21 (3) (1976) 390–398.
[32] P. Patnaik, Handbook of Inorganic Chemicals, McGraw-Hill, 2003.
[33] J. Hubbell, S. Seltzer, Tables of x-ray mass attenuation coefficients and mass energy-absorption coefficients, Tech. Rep. NISTIR 5632, National Institute of Standards and Technology, Maryland, USA, 2004.
[34] A. Küter, Management of reinforcement corrosion: A thermodynamical approach, Ph.D. thesis, Technical University of Denmark, Kgs. Lyngby, Denmark (April 2009).
[35] M.A. Mariscotti, F. Jalinoos, T. Frigerio, M. Ruffolo, P. Thieberger, Gamma-ray imaging for void and corrosion assessment—safety and utility of the technology make it appropriate for field application, Concrete International 31 (11) (2009) 48–53.

Paper XI

” Experimental Determination of the Penetration Depth of Corrosion Products and Time to Corrosion-Induced Cracking in Reinforced Cement Based Materials”

A. Michel, B.J. Pease, A. Peterová & M.R. Geiker

Published in: *Proceedings of ICDC (International Congress on Durability of Concrete), June 17-21, 2012, Trondheim, Norway*

and

Article in press*: Cement and Concrete Composites.*

2012 ICDC
INTERNATIONAL CONGRESS on DURABILITY of CONCRETE

EXPERIMENTAL DETERMINATION OF THE PENETRATION DEPTH OF CORROSION PRODUCTS AND TIME TO CORROSION-INDUCED CRACKING IN REINFORCED CEMENT BASED MATERIALS

Alexander Michel[1], Brad J. Pease[1], Adéla Peterová[2], Mette R. Geiker[1,3]

[1] Technical University of Denmark, Kgs. Lyngby, Denmark
[2] Institute of Chemical Technology Prague, Prague, Czech Republic
[3] Norwegian University of Science and Technology, Trondheim, Norway

ABSTRACT

This paper introduces a non-destructive test method to monitor the development of corrosion products as well as the corrosion-induced formation and propagation of cracks in cementitious materials. A parametric experimental investigation (utilizing x-ray attenuation measurement technique) was conducted to describe the impact of water-to-cement ratio and corrosion current density (i.e., corrosion rate) on the reinforcement corrosion process. Focus was placed, in particular on the determination of the corrosion accommodating region (CAR) and time to corrosion-induced cracking. Experimental results showed that x-ray attenuation measurements allow determination of the actual concentrations of corrosion products averaged through the specimen thickness. The total mass loss of steel measured by x-ray attenuation was found to be in very good agreement with the calculated mass loss obtained by Faraday's law. Furthermore, experimental results demonstrated that the depth of penetration of corrosion products as well as time to corrosion-induced cracking is varying for the different water-to-cement ratios and applied corrosion current densities.

Key-words: Corrosion, crack detection, non-destructive testing (NDT), reinforcement.

INTRODUCTION

The development of numerical tools to describe and predict initiation, e.g. [1, 2], and propagation, e.g. [3, 4], of reinforcement corrosion as well as subsequent corrosion-induced damages has gained momentum in the past decades. In particular, finite element method (FEM) [8-10], analytical [6, 7] as well as empirical approaches [5] to predict the deterioration in reinforced concrete structures subjected to corrosion have been developed in vast amounts.

Although, good agreements with experimental data are presented for most of the developed approaches, two crucial factors have to be pointed out. First, the corrosion rates applied during experimental tests used for validation of the proposed models, e.g. [11, 12], exceed corrosion rates reported for actual structures by several orders of magnitude [13]. Second, more recent

approaches introduced a factor, i.e. the "porous" or "diffusion" zone (these terms are omitted in this paper and replaced with the more accurate term, corrosion accommodation region (CAR)), which might be used to fit experimental data without direct observation or verification of the actual size. Recently, an experimental technique has been presented that allows for a direct determination of the CAR as well as the observation of formation and propagation of corrosion-induced cracks in a non-destructive manner [14]. During this initial study to investigate the applicability of the experimental technique, a corrosion current density of 250 $\mu A/cm^2$ was applied, which exceeds natural corrosion rates by several orders of magnitude. It is the authors' opinion that the movement of corrosion products in cementitious materials depends among others on the corrosion current density. Hence, for a realistic determination of the CAR realistic corrosion current densities need to be applied.

This paper focuses on the application of x-ray attenuation measurement to monitor the time-dependent development of corrosion products and corrosion-induced cracks. Results of an experimental study are presented, on the influence of corrosion current density and water-to-cement ratio (w/c) on the CAR as well as formation and propagation of corrosion-induced cracks in reinforced cementitious materials. Corrosion current densities used in the experimental study range from 10 $\mu A/cm^2$ to 100 $\mu A/cm^2$, in which 10 $\mu A/cm^2$ has been reported as a realistic corrosion current density for actual structures subjected to corrosion [13]. The results presented, particularly data on the concentration and location of corrosion products within the investigated material, may be used to improve current approaches to model corrosion-induced cracking.

EXPERIMENTAL APPROACH

Materials and specimen preparation

Aalborg Rapid® Portland cement (CEM I 52.5 N) was used for the preparation of all mixtures containing 50 Vol% fine aggregates (0-4 mm Class E sand). Specimens with varying w/c (0.3, 0.4 and 0.5) were prepared for accelerated corrosion testing. Plasticizer (Sika Viscocrete-2300HE) was added to the specimens with 0.3 (0.5 % by weight of cement) and 0.4 (0.3 % by weight of cement) w/c to maintain a similar workability as for specimens with a w/c of 0.5. No chlorides were added to the mix, as corrosion was induced by applying electrical current as described in the following section. As reinforcement a smooth steel rod with a diameter of 10 mm was embedded in the centre of the $10 \times 10 \times 50$ cm^3 prisms. After casting the prisms were stored in the molds under a plastic sheet in laboratory conditions (i.e. 20 ± 2 °C) and then demolded. Upon demolding, the prisms were stored for additional 6 days under water at 20 ± 2 °C. Finally, the 50 cm long prisms were cut in 2.3 cm lengths using a water-cooled concrete saw and a lead wire was attached to the reinforcement to allow for accelerated corrosion testing.

Accelerated corrosion

Nine specimens (3 different w/c and 3 different corrosion current densities) were connected to DC regulators to allow for accelerated corrosion testing at the same time. The experimental set up used is illustrated in Fig. 1 and an overview of the experimental program is given in Table 1. To impress an electrical current through the counter electrode (ruthenium/iridium mixed metal oxide activated titanium mesh) a commercial DC regulator was used. Electrical connection between the working (reinforcement) and counter electrodes was realized by placing the mortar specimen in tap water (no chlorides were added to the solution). Specimens of identical current

densities were connected in series (see Fig. 1) to ensure the same corrosion current density was applied to all specimens of a test series.

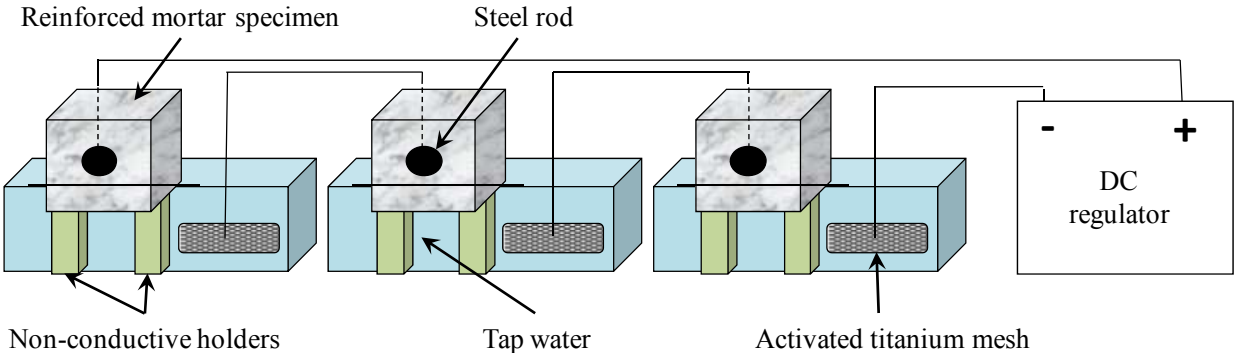

Figure 1 – Experimental set up for accelerated corrosion testing.

Table 1 – Overview of investigated parameters.

Test Series	I			II			III		
Corrosion current density [μA/cm^2]	100			50			10		
w/c	0.5	0.4	0.3	0.5	0.4	0.3	0.5	0.4	0.3

X-ray attenuation measurement technique

A GNI x-ray facility located at the Technical University of Denmark [15] was used to monitor the time-dependent development of corrosion products and subsequent formation and propagation of cracks in reinforced cementitious specimens. Fig. 2 illustrates the facility, consisting of a polychromatic x-ray source, a 252×256 pixel x-ray camera, and a programmable three-axis motion frame for moving the source and camera, which are housed in a shielded, environmentally controlled chamber. The x-ray source excitation settings used were a voltage of 80 keV and a current of 75μA. The x-ray source was automatically ramped up to these settings over a 120 second "warm-up" period and the x-ray source was allowed to stabilize for 60 seconds prior to recording images. A single measurement consisted of 60 x-ray camera images recorded with an integration time of 1 second each (i.e., 60 second integration time). The intensities measured by individual pixels from the 60 images were summed. So-called dark current images (i.e., x-ray camera images recorded while x-ray source is turned off), recorded prior to all x-ray measurements, were subtracted from the measured intensities.

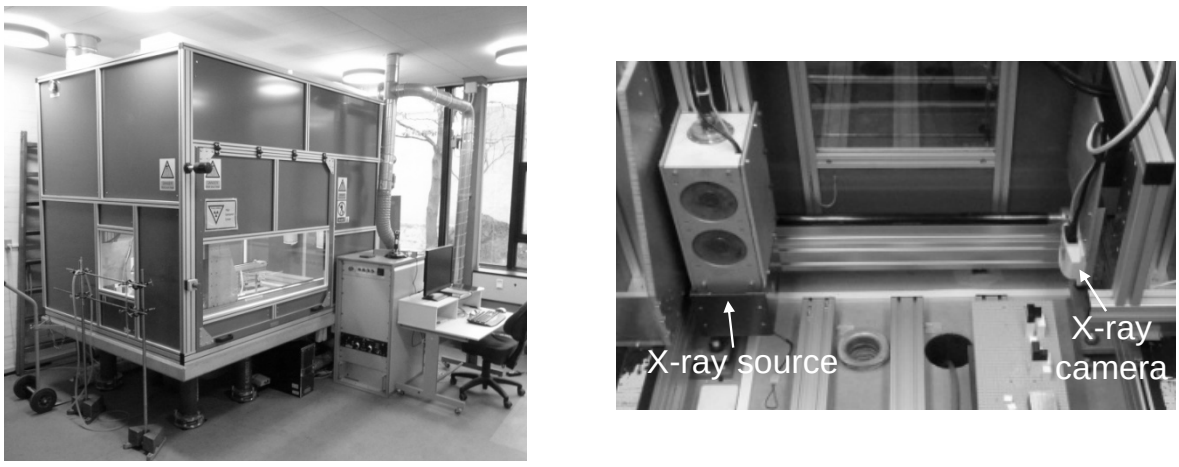

a) b)

Figure 2 – a) X-ray measurement system consisting of b) the x-ray source and the x-ray camera.

Before any corrosion current was applied to the reinforcement, each specimen was measured three times (i.e., a total of 180 images) in its initial state. After commencing the accelerated corrosion testing, x-ray measurements were recorded every 4 hours for test series I, every 12 hours for test series II, and every 24 hours for test series III until termination of the test. Testing was terminated when specimens showed extensive corrosion-induced damage. Additional information on the x-ray measurement procedure (i.e., dark current measurements, use of reference samples, etc.) is available in the literature [16-18].

Theoretical background of x-ray attenuation measurement technique

Fig. 3a) shows the fundamental layout of an x-ray attenuation measurement, in which the x-ray source produces a polychromatic beam of x-ray photons (i.e., photons with varying energy levels). As the x-ray photons pass through the specimen a portion of the incident intensity is attenuated (i.e., absorbed and scattered) and the transmitted intensity is recorded by the x-ray camera. The attenuation behaviour of a polychromatic x-ray photon, accounting for the effects of beam hardening, is described by the Beer–Lambert law (Eq. 1) [19]:

$$I_{non} = I_0 e^{-\mu_{eff,m} t} \quad \text{Eq. 1}$$

where I_{non} is the transmitted intensity of x-ray photons, I_0 the incident intensity, $\mu_{eff,m}$ the effective attenuation coefficient of mortar and t the thickness of the specimen. More information on the effect of beam hardening on x-ray attenuation measurements and derivation of Eq. 1 can be found in e.g. [14].

The composite system illustrated in Fig. 3b) is typically used to describe conditional changes, i.e. change in concentration of moisture content or here corrosion products, by x-ray attenuation measurements [20, 21]. The composite system consists of a non-corroded, specimen in series with corrosion products. The transmitted intensity of the polychromatic x-ray source before reinforcement corrosion, described by Eq. 1, continues and interacts with the corrosion products. The corrosion products further reduce the transmitted intensity as described by Eq. 2:

$$I_{corr} = I_{non} e^{-\mu_{eff,cp} t_{cp}} = I_0 e^{-\mu_{eff,m} t - \mu_{eff,cp} t_{cp}} \quad \text{Eq. 2}$$

where I_{corr} is the transmitted intensity after corrosion, $\mu_{eff,cp}$ the effective attenuation coefficient of the corrosion product and t_{cp} the thickness of corrosion products. Furthermore, the change in concentration of corrosion products in the specimen (within the specimen volume or, assuming a constant cross-section within the specimen thickness) can be calculated as follows:

$$\Delta c_{cp} = \frac{\rho_{cp} \Delta V_{cp}}{V} = \frac{\rho_{cp} \Delta t_{cp}}{t} \quad \text{Eq. 3}$$

where ρ_{cp} is the density of the corrosion products, ΔV_{cp} is the change in volume of corrosion products, V the specimen's volume and Δt_{cp} the change in thickness of corrosion products. Combining Eq. (2) and (3) yields Eq. (4), which relates the transmitted intensity after corrosion, to the change in concentration of corrosion products:

$$I_{corr} = I_{non} e^{(-\mu_{eff,cp} \Delta c_{cp} t)/\rho_{cp}} \quad \text{Eq. 4}$$

Solving for change in concentration of corrosion products yields Eq. (5):

$$\Delta c_{cp} = -\frac{\rho_{cp}}{\mu_{eff,cp}} ln\left(\frac{I_{corr}}{I_{non}}\right) \quad \text{Eq. 5}$$

Eq. 5 can be used to directly measure the concentration of corrosion products as a function of space and time, when I_{non} (transmitted intensity prior to corrosion) is measured initially and I_{corr} (transmitted intensity after corrosion) measured at various times after commencing the accelerated corrosion test.

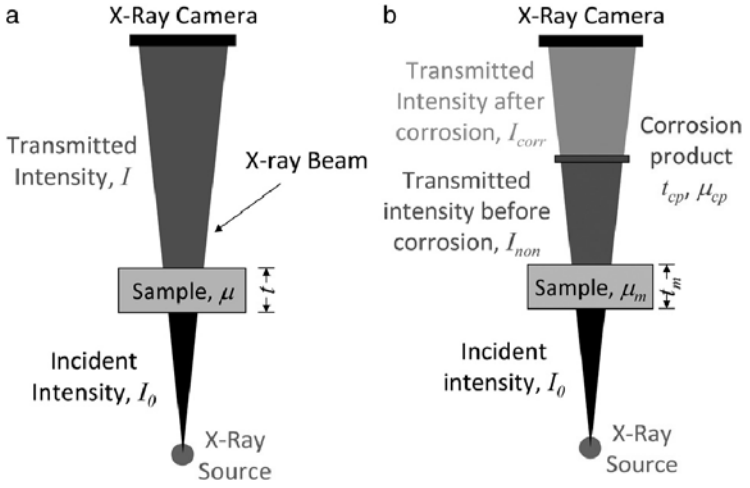

Figure 3 – Fundamental explanation of use of x-ray attenuation measurements: a) schematic description of Beer-Lambert law (Eq. 1) and b) effect of change in concentration of corrosion product [16] (where t is the thickness and μ the attenuation coefficient).

EXPERIMENTAL RESULTS AND DISCUSSION

Image analysis of x-ray attenuation measurement

As an example, calculated x-ray images of change in concentration of corrosion products (see Eq. 5) are illustrated in Figure 4 for different times of accelerated corrosion. The images include details on the rebar (black), corrosion products (white), cracks (dark gray to black), and the wire used to induce corrosion. The wire, extending from the right of the rebar and continuing out of the measured area, is a source of 'noise' in the data. In Fig. 4a) the wire appears dark grey to black; however later in Figs. 4b) and c) the wire appears white. The white colour, which is indicative of corrosion products, is likely due to a small movement of the wire from its original location. When extracting the data presented below from calculated x-ray images, the wire-affected region was ignored.

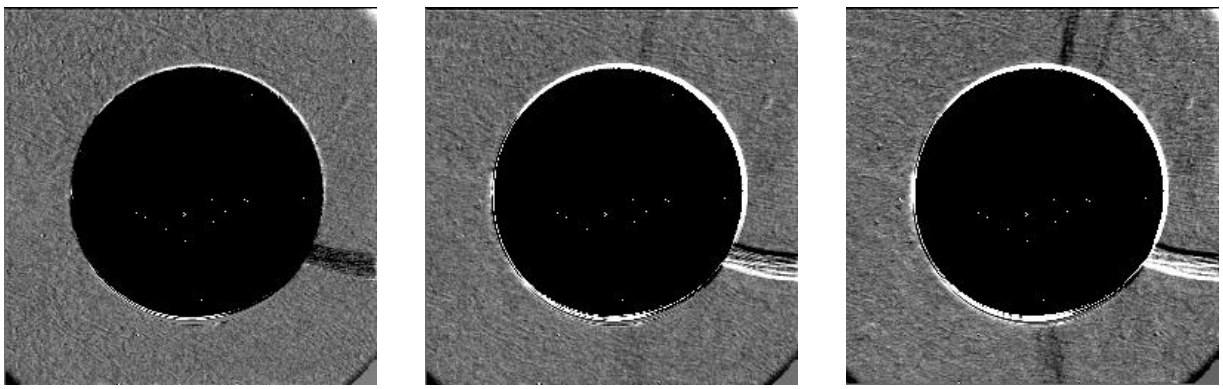

a) b) c)

Figure 4 – Calculated x-ray images after a) 3.5 days, b) 6 days and c) 9 days, illustrating corrosion products (light gray to white) and crack (dark gray to black). Specimen with w/c 0.5 subjected to 100 μA/cm^2 corrosion current density.

Development of corrosion products and corrosion-induced cracking

Contour plots derived from calculated x-ray images presented in Fig. 4 can be used to provide location-dependent information on calculated concentrations of corrosion products (see Eq. 5) at various times during the accelerated corrosion testing. For all contour plots provided in the following, the assumed type of corrosion products was Fe_2O_3, which has been confirmed by scanning electron microscope (SEM) and x-ray diffraction (XRD) measurements during an initial study [14]. The concentration of corrosion products is given in g/cm^3, which is a summation of the amount of corrosion products through the thickness of the specimen. Cracks result in negative contour values as the number of transmitted x-ray photons increases.

Fig. 5 presents contour plots for test series I, i.e. specimens with w/c 0.5, 0.4 and 0.3, respectively, subjected to 100 µA/cm^2 of corrosion current density. Corrosion-induced cracking was detected after 4 days (w/c 0.5), 5.8 days (w/c 0.4) and 9.5 days (w/c 0.3) of accelerated corrosion and is illustrated by a line of negative contours in the figures (please note that the results illustrated in Fig. 5a), b) and c) are for later measurement times for better visibility of cracks in the contour plots). Similar contour plots are given for specimens of test series II and III subjected to 50 µA/cm^2 and 10 µA/cm^2 corrosion current density in Fig. 6 and 7, respectively. Corrosion-induced cracking was detected after 11.5 days (w/c 0.5), 12 days (w/c 0.4) and 79 days (w/c 0.3) for specimens of test series II subjected to 50 µA/cm^2 corrosion current density. No corrosion-induced cracks were detected after 93 days of accelerated corrosion testing for specimens of test series III subjected to 10 µA/cm^2 corrosion current density (see Fig. 5a-c). More information, in particular, on the amount and location of corrosion products for the various specimens tested under accelerated corrosion is given in the following.

Through further image analysis, i.e. polar transformation, the circular surface of the rebar can be plotted as a flat surface from which corrosion products protrude, which facilitates estimation of the corrosion accommodating region (CAR). Exemplary, polar transformation of results for test series I, i.e. 100 µA/cm^2 and w/c 0.5, 0.4 and 0.3, respectively, are given in Fig. 8. Furthermore, the amount of corrosion products was averaged over the radius up to 1.0 mm from the rebar surface for all test series. Results of the average concentration of corrosion products as a function of the radius from the rebar surface are given in Fig. 9, 10 and 11 for all specimens tested. Solid lines in the graphs indicate the average profile of corrosion products when formation of a crack was detected by the x-ray attenuation technique, while broken lines illustrate average corrosion product profiles at selected measurement times.

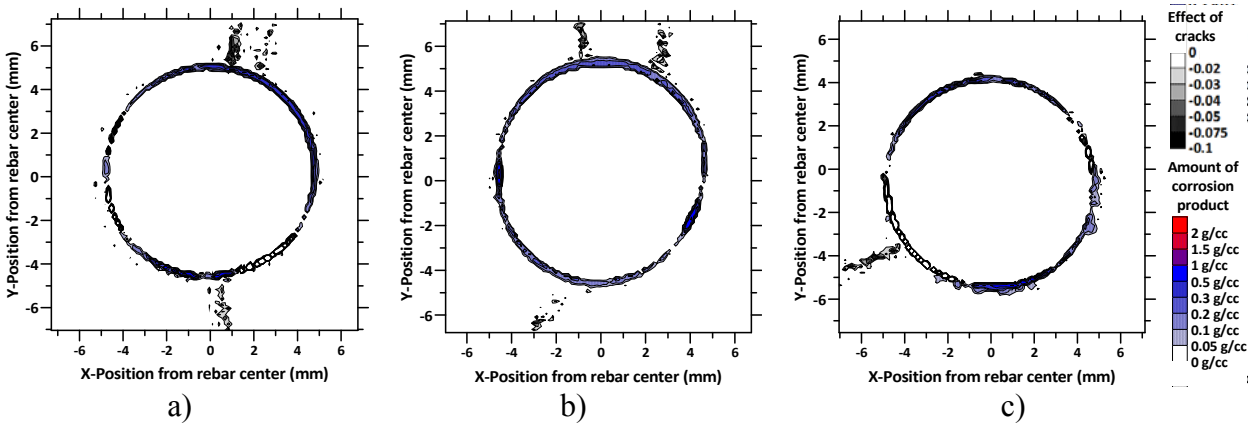

Figure 5 - Contour plots highlighting the effect of cracks on x-ray attenuation measurements and concentration of corrosion products after a) 7.8 days (w/c 0.5), b) 9.5 days (w/c 0.4), and c) 74 days (w/c 0.3) of accelerated corrosion (current applied 100 µA/cm^2). (Note: the effect of cracks is a unitless factor described by the natural log portion of Eq. 5).

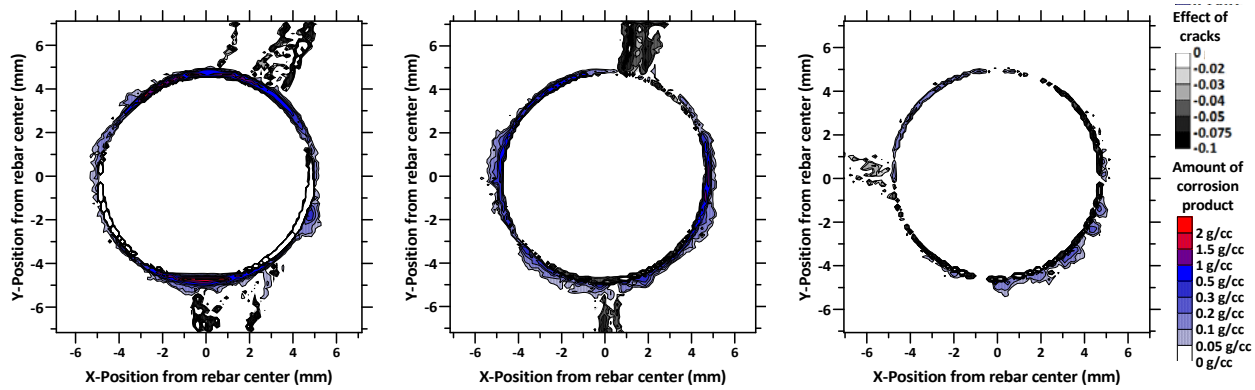

a) b) c)

Figure 6 - Contour plots highlighting the effect of cracks on x-ray attenuation measurements and concentration of corrosion products after a) 74 days (w/c 0.5), b) 73 days (w/c 0.4), and c) 89 days (w/c 0.3) of accelerated corrosion (current applied 50 μA/cm^2). (Note: the effect of cracks is a unitless factor described by the natural log portion of Eq. 5).

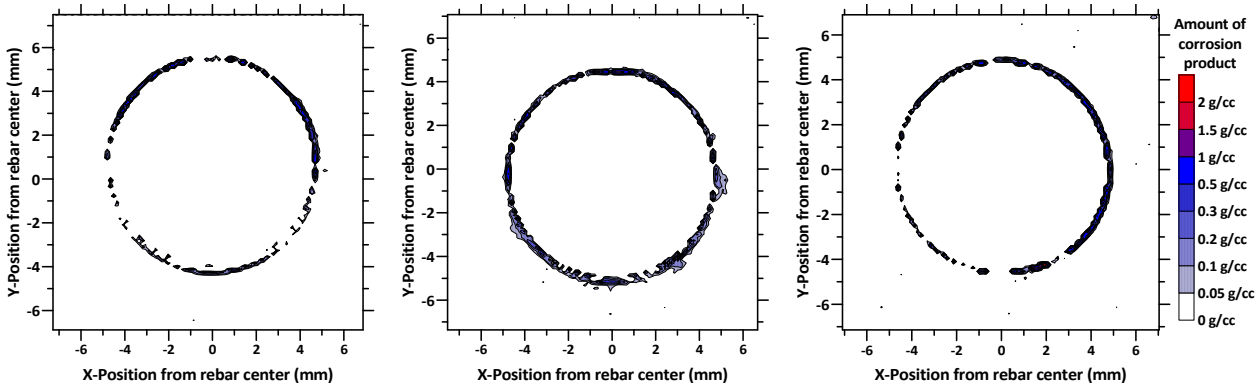

a) b) c)

Figure 7 - Contour plots the concentration of corrosion products after a) 93 days (w/c 0.5), b) 93 days (w/c 0.4), and c) 93 days (w/c 0.3) of accelerated corrosion (current applied 10 μA/cm^2), no cracks visible yet.

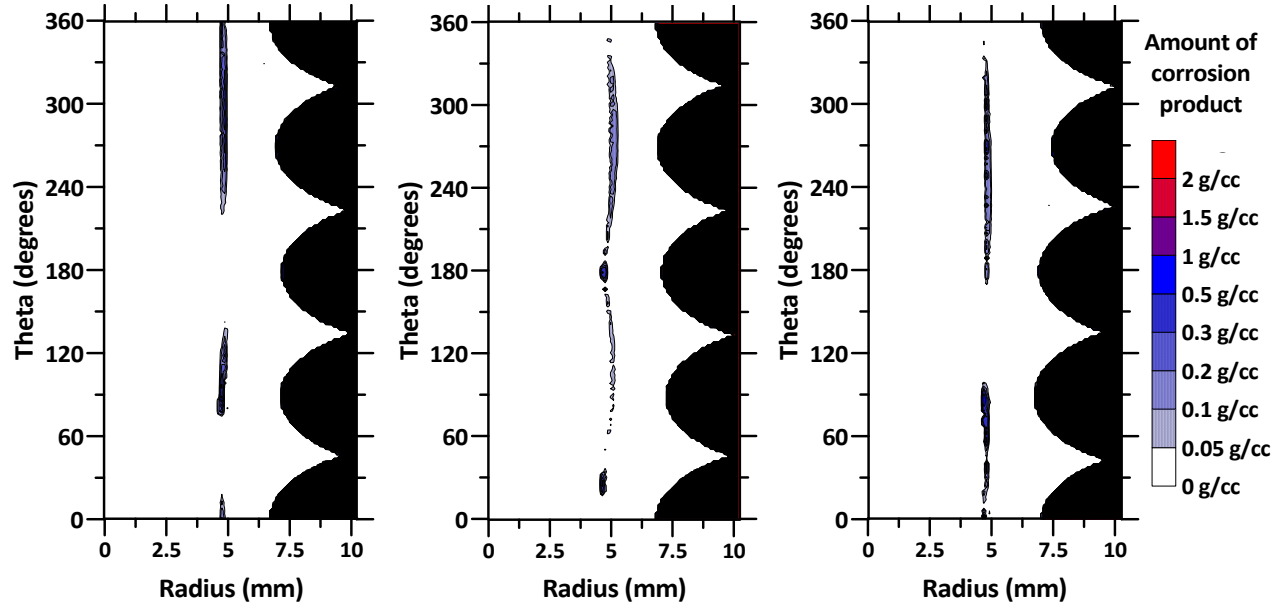

a) b) c)

Figure 8 – Polar transformation contour plots after a) 4 days (w/c 0.5), b) 5.8 days (w/c 0.4), and c) 9.5 days (w/c 0.3) of accelerated corrosion (current applied 100 μA/cm^2).

Penetration depth of corrosion products

In general, it can be seen from all graphs presented (Fig. 9 - 11) that the amount of corrosion products is increasing and further penetrating into the concrete as time progresses, independent of w/c and applied corrosion current density. However, the penetration depth of corrosion products is varying for the various w/c and applied corrosion current densities. Results presented in Fig. 9 - 11 indicate that with decreasing corrosion current density the depth of penetration of corrosion products is increased. Comparing for example the average corrosion product profiles at the time of crack initiation (corresponding to similar total amounts of corrosion products) in Fig. 9a) and Fig. 10a), it can be seen that the depth of penetration is increased from around 0.225 mm to around 0.4 mm from the rebar surface. Furthermore, the results indicate that the depth of penetration is reduced as the w/c is reduced for the same corrosion current density. Comparing the average corrosion product profiles in Fig. 10a), b) and c) as well as Fig. 11a) and c) for similar measurement times, the effect appears most pronounced for test series II and III compared to test series I. For test series II, the penetration depth of corrosion products is reduced from around 0.45 mm (w/c 0.5) to 0.35 mm (w/c 0.4) and finally 0.11 mm (w/c 0.3) for x-ray measurements taken around 10 - 12 days. Similar observations can be made for specimens of test series III, where the penetration depth is reduced from around 0.225 mm (w/c 0.5) to 0.17 mm (w/c 0.3) after 93 days of accelerated corrosion testing. The increased depth of penetration in test series III Fig. 11b) is most likely due to the filling of interfacial defects, such as air voids (see Fig. 7b)).

Comparing the results presented in Fig. 9 for test series I, it can be seen that the penetration depth is similar for all w/c (around 0.225 mm at crack initiation). However, profiles of the average corrosion products concentration are varying for the various specimens tested. For specimens with a w/c of 0.5 and 0.4 the maximum concentration of corrosion products can be found inside the concrete, while for specimens with a w/c of 0.3 the highest concentration of corrosion products is located at the concrete-steel interface. This indicates that for lower w/c less corrosion products can penetrate the concrete and rather accumulate at the concrete-steel interface. Similar trends can be seen for all test series tested, i.e. for the different corrosion current densities applied.

In addition to the average corrosion product profiles, the amount of corrosion products was integrated to estimate the total amount of corrosion products. Results for each x-ray measurement taken are presented in Fig. 12 for a) w/c 0.5 and 100 $\mu A/cm^2$, b) w/c 0.4 and 50 $\mu A/cm^2$ and c) w/c 0.3 and 10 $\mu A/cm^2$. Values for the total amount of corrosion products are also estimated by Faraday's law. A good agreement between the results obtained from the x-ray attenuation technique and Faraday's law can be found for all w/c and corrosion current densities tested. No gravimetric measurements were performed. However, results presented in an initial study [14] show a very good correlation with gravimetric measurements, too.

Values for the size of the CAR obtained at time to crack initiation from the present study, range from around 0.175 mm to 0.45 mm from the rebar surface. The obtained values are within the upper range of sizes (0.002 mm to 0.12 mm) reported in literature previously [7, 22], but exceed most values reported by several orders of magnitude. Differences obtained in values for the size of the CAR, compared to the present study might be caused by the application of very high corrosion current densities, as results of the present study indicate that the size of CAR is dependent on both, the w/c and applied corrosion current density. Furthermore, previously used experimental methods to physically measure the thickness of the CAR include cutting, sawing and impregnating samples [22]. These destructive methods are potentially invasive, causing possible movement or washing away of corrosion products and hindering reliable measurements.

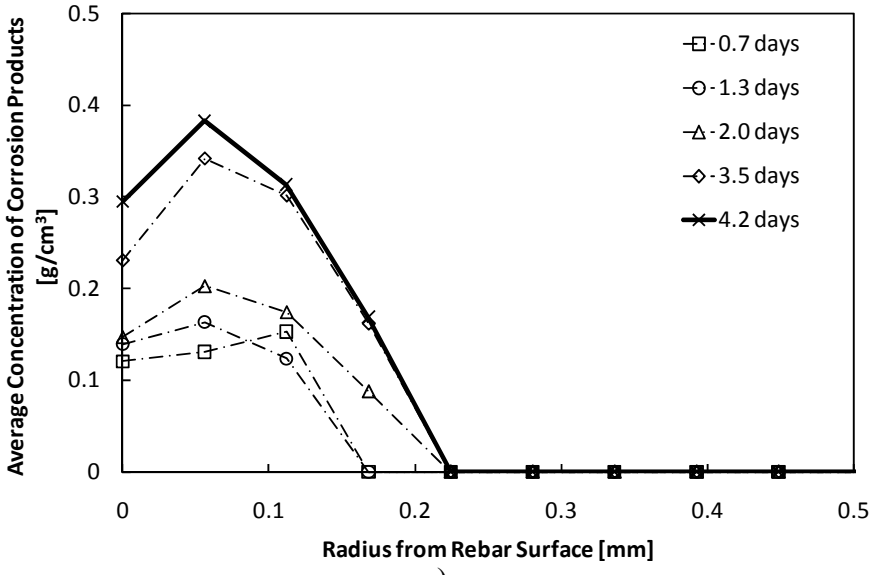

a)

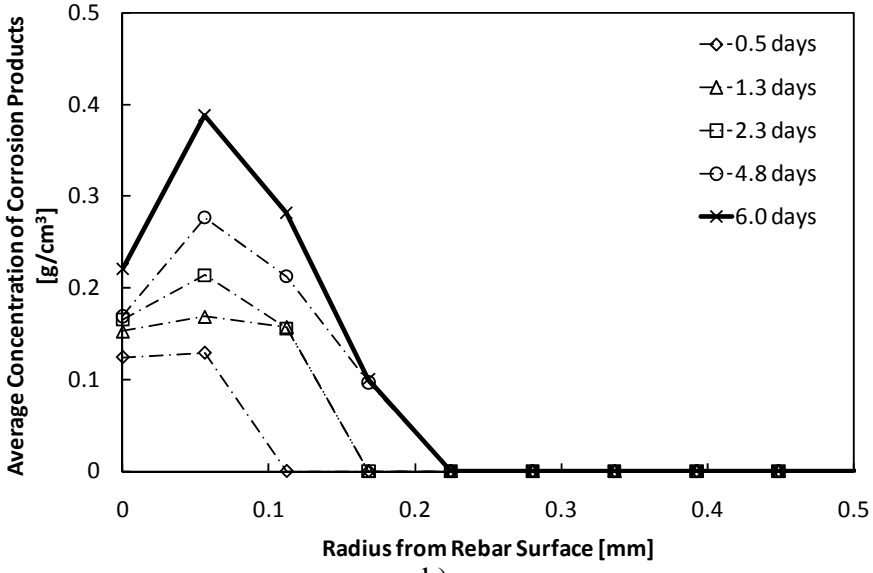

b)

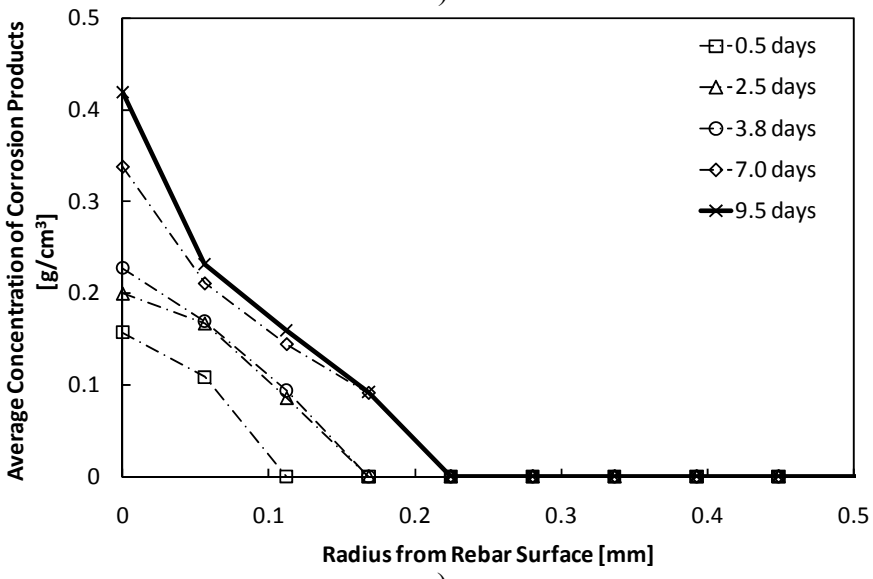

c)

Figure 9 – Average concentration of corrosion products as a function of radius from the rebar surface at varying times for a) 0.5 w/c, b) 0.4 w/c and c) 0.3 w/c and 100 μA/cm^2 corrosion current density. The solid line indicates the time when a crack was first observed (4.2, 6 and 9.5 days).

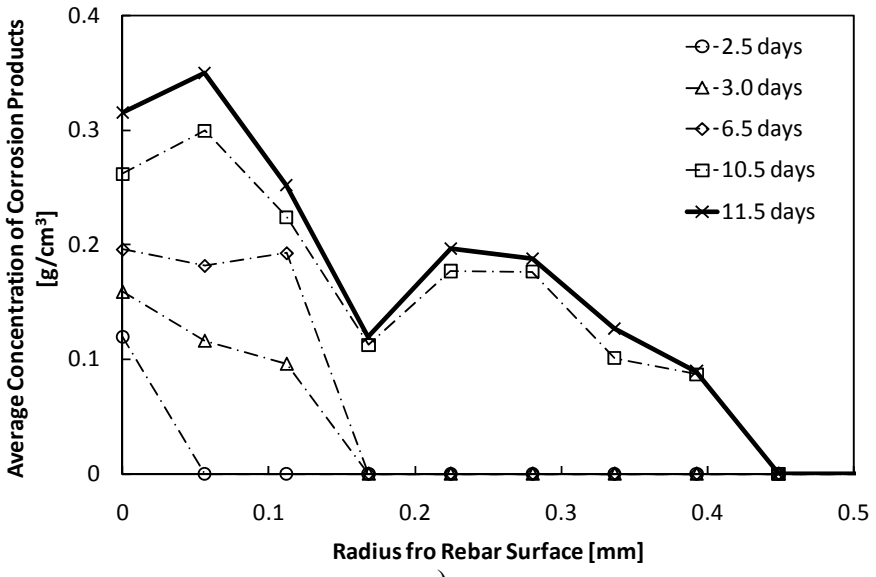

a)

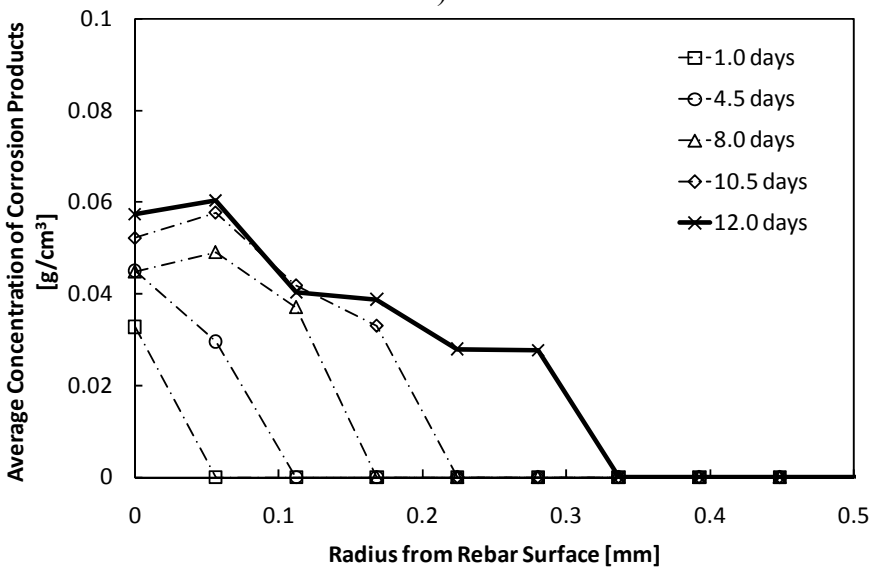

b)

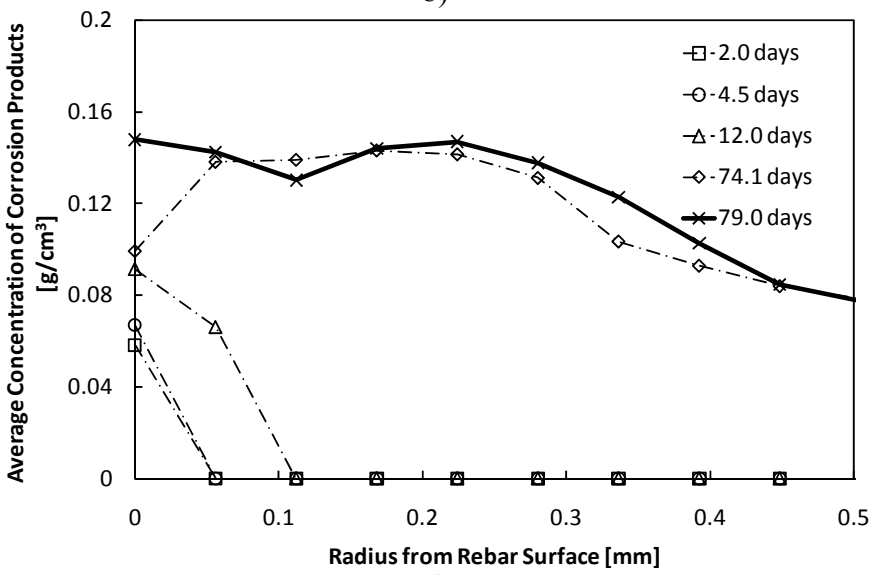

c)

Figure 10 – Average concentration of corrosion products as a function of radius from the rebar surface at varying times for a) 0.5 w/c, b) 0.4 w/c and c) 0.3 w/c and 50 μA/cm^2 corrosion current density. The solid line indicates the time when a crack was first observed (11.5, 12 and 79 days).

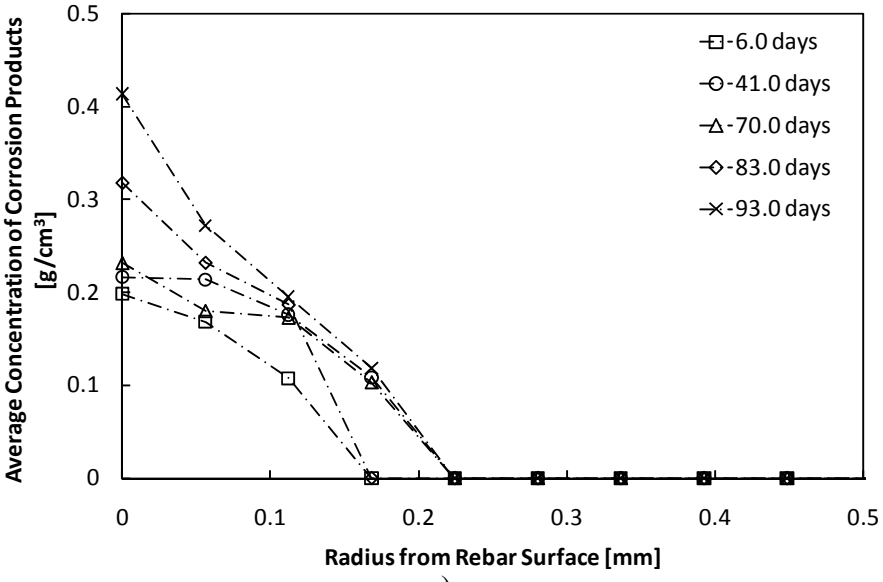

a)

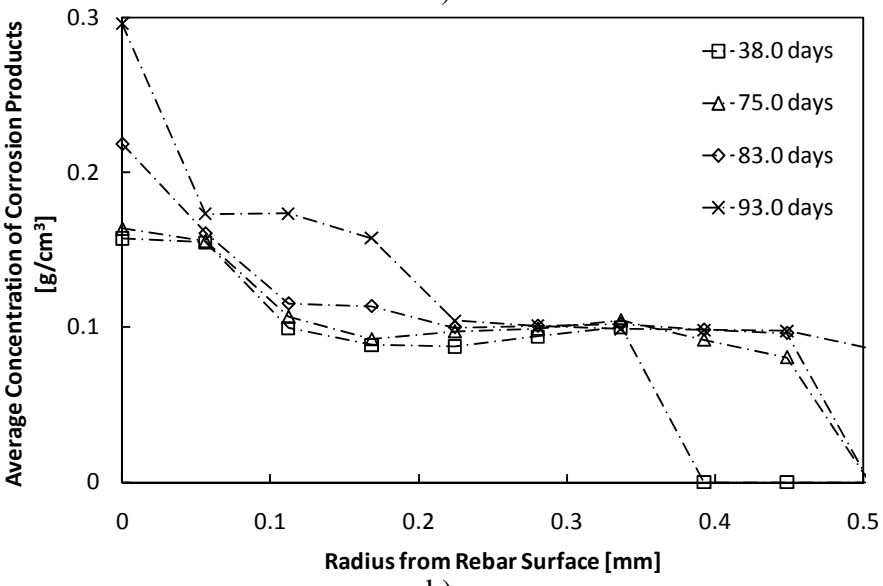

b)

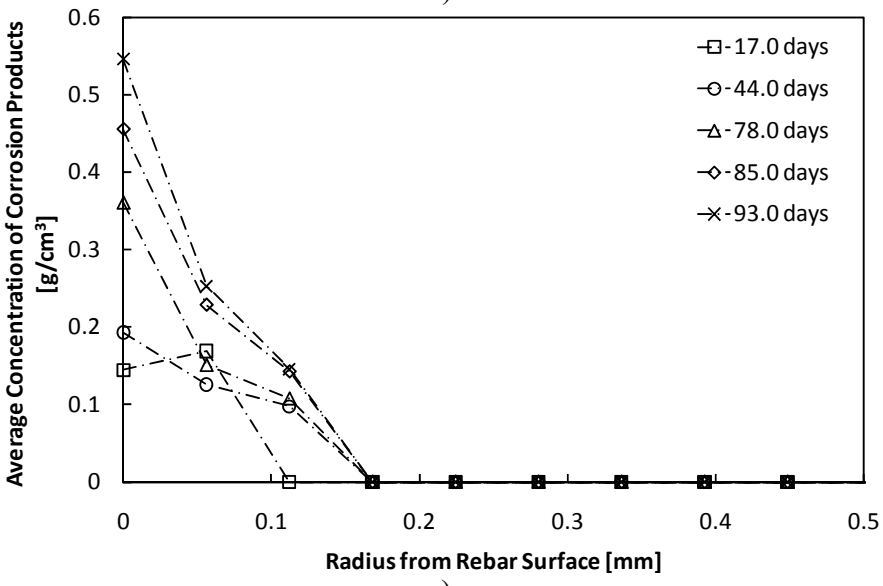

c)

Figure 11 – Average concentration of corrosion products as a function of radius from the rebar surface at varying times for a) 0.5 w/c, b) 0.4 w/c and c) 0.3 w/c and 10 μA/cm^2 corrosion current density.

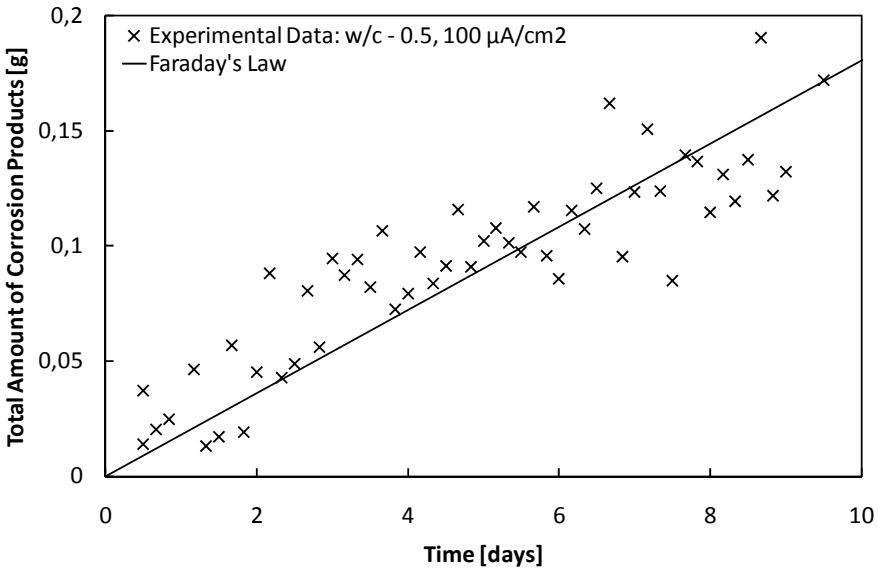

a)

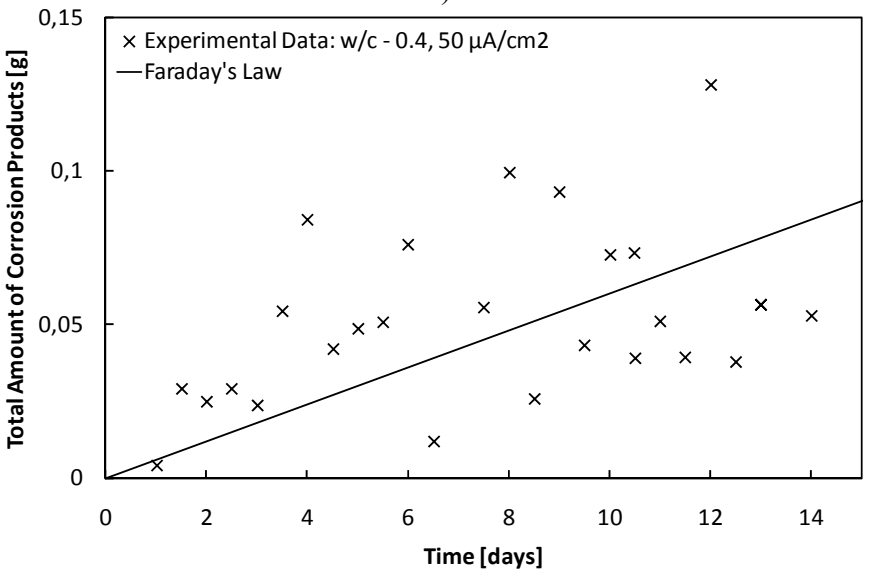

b)

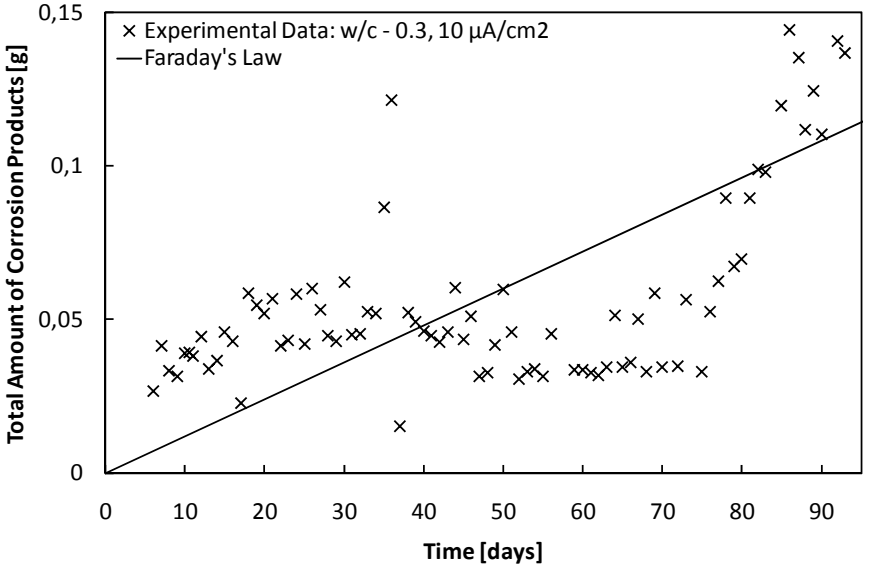

c)

Figure 12 – Comparison between the total amount of corrosion obtained from Faraday's law and x-ray attenuation technique for a) 100 µA/cm^2 and 0.5 w/c, b) 50 µA/cm^2 and 0.4 w/c and c) 10 µA/cm^2 and 0.3 w/c.

PERSPECTIVES

Results presented for the individual test series are summarized and presented in Fig. 13 and 14. Variations of the size of the CAR are presented in Fig. 13 for similar total amounts of corrosion (around 0.07 g, i.e. the total amount of corrosion as the first crack was detected in specimens of test series I). The summarized results in Fig. 13 support the assumption that the CAR is a function of the w/c and corrosion current density. Results indicate that the size of the CAR is increased as the w/c is increased and/or the corrosion current density decreased.

An overview of the time to corrosion-induced cracking is given in Fig. 14, where the previously given results are summarized for all test series. No corrosion-induced cracks were detected after 93 days of accelerated corrosion testing for specimens of test series III subjected to 10 $\mu A/cm^2$ corrosion current density. The results presented in Fig. 14 indicate that the time to crack formation is dependent of both the w/c and corrosion current density. It can be seen that the time to crack formation is increased as either the w/c and/or the corrosion current density is decreased. However, it has to be pointed out that exact determination of the time to corrosion-induced cracking is difficult with the present experimental technique as the impact of the cracks on the x-ray attenuation is averaged through the thickness of the specimen. For a more accurate determination of the time to corrosion-induced cracking, the x-ray attenuation technique may be combined with acoustic emission or photogrammetric measurements.

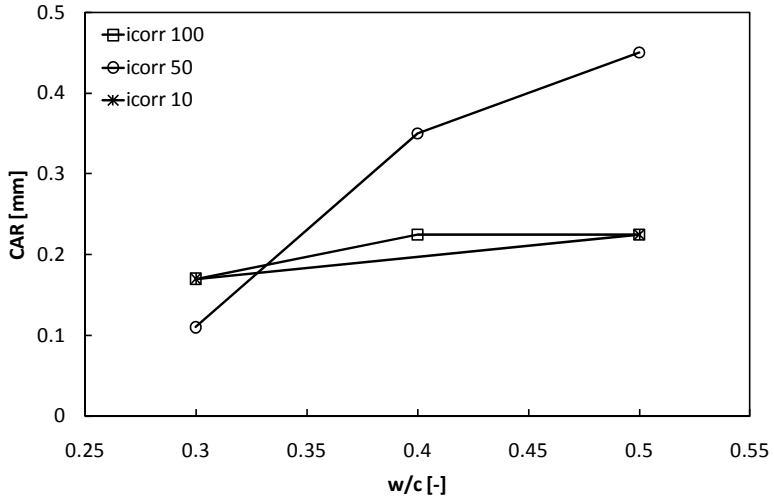

Figure 13 – Size of the CAR as a function of w/c and corrosion current density for a total amount of corrosion of around 0.072 g.

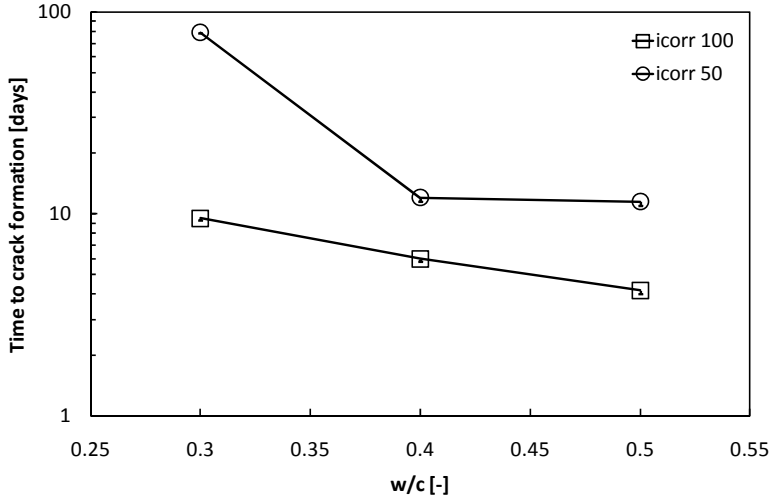

Figure 14 – Time to corrosion-induced crack formation as a function of w/c and corrosion current density for test series I and II. No cracks were detected for specimens of test series III.

SUMMARY AND CONCLUSION

An experimental method, i.e. the x-ray attenuation technique, was used that allows for a direct and non-destructive determination of the corrosion accommodating region (CAR), which is an important input parameter in numerical simulations of corrosion-induced concrete cracking. Within the present study, specimens with different water-to-cement (w/c) were subjected to various corrosion current densities and the size of the CAR was determined. From the results presented it can be concluded that:

- The concentration of corrosion products can be determined as a function of time and space with the x-ray attenuation measurements. The total mass loss of steel obtained by the x-ray attenuation method correlates well with determination of the mass loss by Faraday's law.
- The depth of penetration of corrosion products is varying for the different w/c and applied corrosion current densities.
    - Results presented show that with decreasing corrosion current density the depth of penetration of corrosion products is increased and
    - That the depth of penetration is reduced as the w/c is reduced for the same corrosion current density.
    - Differences obtained for the size of the CAR compared to previously reported values might be due to the application of very high corrosion current densities and invasive experimental methods to physically measure the size of the CAR.
- The time of corrosion-induced crack formation is dependent on the w/c and corrosion current density.
    - Results presented show that the time to crack initiation is prolonged as the w/c is reduced and/or the corrosion current density decreased.
    - Values for the size of the CAR obtained from the present study range from around 0.11 mm to 0.45 mm at crack initiation depending on w/c and applied corrosion current density. No cracks were detected after 93 days of accelerated corrosion for specimens subjected to 10 $\mu A/cm^2$.
    - Although, results of the x-ray attenuation measurements allow monitoring of crack initiation as well as propagation,
        - Determination of the time to crack initiation is difficult, due the fact that the effect of cracks on the x-ray measurements is averaged through the thickness of the specimen.
        - A combination of x-ray attenuation measurements with photogrammetric or acoustic emission measurements might allow for a more precise determination of the initiation of corrosion-induced cracks.

ACKNOWLEDGEMENTS

Financial contributions from the Danish Expert Centre for Infrastructure Constructions and the project ‘Sustainable Rehabilitation of Civil and Building Structures’ funded by Nordic Innovation Centre, project no. 08190 SR are greatly appreciated. The first author gratefully acknowledges the financial support of Femern Bælt A/S, Sund & Bælt Holding A/S, and The Danish Agency for Science, Technology and Innovation.

REFERENCES

[1] Atkins, C. P., et al., "Modelling corrosion initiation of steel in concrete," Proceedings of the Institution of Civil Engineers, Construction Materials **160** CM2, 81–85, 2007.

[2] Val, D. V., et al., "Probabilistic evaluation of initiation time of chloride-induced corrosion," Reliability Engineering and System Safety **93**, 364–372, 2008.

[3] Gulikers, J., et al., "Numerical models for the propagation period of reinforcement corrosion," Materials and Corrosion **57**, 618-627, 2006.

[4] Michel, A., et al., "Numerical modelling of reinforcement corrosion in concrete structures," Proceedings of the 8th fib PhD Symposium, Kgs. Lyngby, Denmark, 2010.

[5] Alonso, C., et al., "Factors controlling cracking of concrete affected by reinforcement corrosion," Materials and Structures **31**, 435-441, 1998.

[6] Bažant, Z., "Physical model for steel corrosion in concrete sea structures - application," Journal of the Structural Division **105**, 1155–1166, 1979.

[7] Chernin, L., et al., "Analytical modelling of concrete cover cracking caused by corrosion of reinforcement," Materials and Structures **43**, 543-556, 2010.

[8] Molina, F.J., et al., "Cover cracking as a function of rebar corrosion: part 2 - numerical model," Materials and Structures **26**, 532-548, 1993.

[9] Liu, Y., et al., "Modeling the time-to-corrosion cracking in chloride contaminated reinforced concrete," ACI Materials Journal **95**, 675-681, 1998.

[10] Maaddawy, T. El, et al., "A model for prediction of time from corrosion initiation to corrosion cracking," Cement and Concrete Composites **29**, 168-175, 2007.

[11] Andrade, C., et al., "Cover cracking as a function of bar corrosion: Part 1 - Experimental test," Materials and Structures **26**, 453-464, 1993.

[12] Vu, K., et al., "Corrosion-Induced Cracking: Experimental Data and Predictive Models," ACI Structural Journal **102**, 719-726, 2005.

[13] Tuutti, K., "Corrosion of Steel in Concrete," Swedish Cement and Concrete Research Institute at the Institute of Technology, Stockholm, 4-82, 1982.

[14] Michel, A., et al., "Monitoring reinforcement corrosion and corrosion-induced cracking using non-destructive x-ray attenuation measurements," Cement and Concrete Research **41**, 1085-1094, 2011.

[15] www.gni.dk, GNI X-ray System, Technical University of Denmark, 2010.

[16] Pease, B. "Influence of concrete cracking on ingress and reinforcement corrosion," Ph.D. thesis, Technical University of Denmark, Kgs. Lyngby, Denmark, 2010.

[17] Pease, B., et al., "Assessing the portion of the crack length contributing to water sorption using x-ray absorption measurements on concrete wedge splitting specimens," ConcreteLife'09: Second International RILEM Workshop on Concrete Durability and Service Life Planning, Haifa, Israel, 2009.

[18] Pour-Ghaz, M., et al., "Numerical and experimental assessment of unsaturated fluid transport in saw-cut (notched) concrete elements," ACI SP 266 - Modeling as a Solution to Concrete Problems, American Concrete Institute, 73–83, 2009.

[19] Knoll, G. "Radiation Detection and Measurement," J. Wiley, 1989.

[20] Baker, P. H., et al., "The application of x-ray absorption to building moisture transport studies," Measurement **40**, 951-959, 2007.

[21] Hansen, K. K., et al., "Dual-energy x-ray absorptiometry for the simultaneous determination of density and moisture content in porous structural materials," Proceedings of the 5th Symposium on Building Physics in the Nordic Countries, Vol. 1, Gothenburg, Sweden, 281-288, 1999.

[22] Caré, S., "Mechanical properties of the rust layer induced by impressed current method in reinforced mortar," Cement and Concrete Research **38**, 1079–1091, 2008.

Paper XII

” Estimation of elastic modulus of reinforcement corrosion products using inverse analysis of photogrammetric measurements for input in corrosion-induced cracking model”

B.J. Pease, A. Michel, A.E.A. Thybo & H. Stang

Published in: *Proceedings of IABAMAS 2012 (6th International Conference on Bridge Maintenance, Safety and Management), July 8-12, 2012, Villa Erba, Italy.*

Estimation of elastic modulus of reinforcement corrosion products using inverse analysis of digital image correlation measurements for input in corrosion-induced cracking model

B.J. Pease, A. Michel, A.E.A. Thybo & H. Stang
Technical University of Denmark, Department of Civil Engineering, Kgs. Lyngby, Denmark

ABSTRACT: A combined experimental and numerical approach for estimating the elastic modulus of reinforcement corrosion products is presented. Deformations between steel and mortar were measured using digital image correlation during accelerated corrosion testing at 100 μA/cm^2 (~1.16 mm/year). Measured deformations were compared to a numerical corrosion model that considers electrochemical, transport, and mechanical processes, including penetration of corrosion products into a 'corrosion-accommodating region,' provided by the mortar's capillary porosity, directly surrounding the steel. Comparing model and experimental results provides an order-of-magnitude approximation of corrosion product stiffness of 2.0 GPa.

1 INTRODUCTION

Deterioration models, developed to better understand corrosion-induced cracking processes in reinforced concrete, have highlighted a key parameter in the cracking process – namely, the elastic properties of reinforcement corrosion products (Molina et al. 1993, Solgaard et al., submitted). Citing a lack of experimental observations, Molina et al. (1993) assumed water comprised the majority of corrosion products and therefore used water's elastic properties (2 GPa elastic modulus, 0.5 Poisson's ratio) to characterize the mechanical properties of corrosion products. Direct measurement of elastic properties of corrosion products is complicated by the materials' stratified lamina nature. However, recently works attempted to quantify properties of reinforcement corrosion products.

In (Ouglova et al., 2006) samples of corrosion products (γ-FeO(OH)) were manufactured in a synthetic pore solution simulating a carbonated concrete with pH 9, dried, compacted to varying volume fractions, and elastic properties were assessed using ultrasonic pulse velocity. Results indicate that the elastic modulus depends on the compaction of corrosion products, with values ranging from <1 GPa to approximately 3.6 GPa with γ-FeO(OH) volume fractions of approximately 0.4 to 0.65, respectively (Ouglova et al., 2006). Therefore, the properties of reinforcement corrosion products formed in-situ (in reinforced concrete) are likely affected by the degree of confinement provided by surrounding concrete.

Elastic properties of corrosion products formed in-situ (via 100 μA/cm^2 direct current) were estimated by comparing model predicted corrosion-induced deformation between the steel and surrounding matrix to corresponding deformations measured by microscopic image correlation from a small area (1.3 mm^2) of the steel-concrete interface (Caré et al., 2008). Estimates of elastic modulus of corrosion products ranged from approximately 0.04 to 0.25 GPa with corresponding modeled corrosion thicknesses varying from 10 to 60 μm. The model proposed in (Caré et al., 2008) assumed corrosion products form uniformly and exclusively at the concrete/steel interface, inducing deformations between the steel and concrete. However, results from x-ray attenuation investigations of the reinforcement corrosion process (Michel et al., 2011, submitted, Pease et al., submitted) indicate 1) corrosion products penetrate into the surrounding cementitious material (mortar in this case) in a 'corrosion accommodating region' (*CAR*), and 2) formation of corrosion products is non-uniform (Fig. 1). By not considering the *CAR* and possibly other factors, such as stress re-

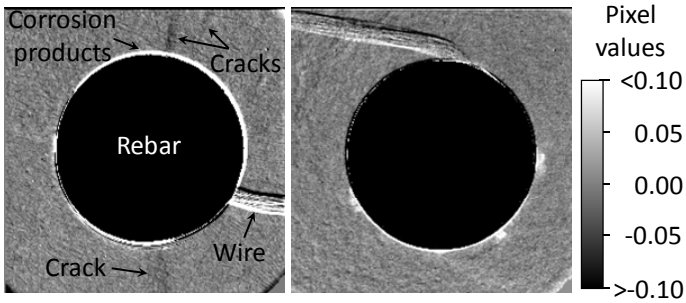

Figure 1. Calculated images from x-ray investigations, (a) highlights rebar, corrosion products, cracks, and wire (used to pass current), and (b) shows corrosion products penetrating in surrounding matrix without cracks observed.

laxation due to concrete creep, etc., elastic modulus estimates in (Caré et al., 2008) are likely underestimated.

The aim of the investigation presented in this paper was, similarly to the approach in (Caré et al., 2008), to compare model predicted and measured corrosion-induced deformations between corroding steel rebar and the surrounding matrix (mortar here) to estimate elastic properties of corrosion products. The model however includes the impact of the *CAR* and creep of the surrounding matrix, and measurements from image correlation consider the entire steel-mortar interface.

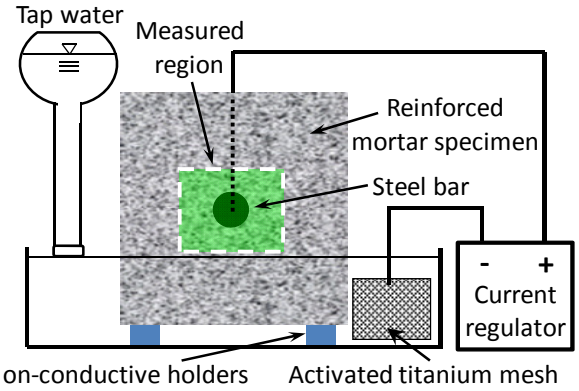

Figure 2. Experimental setup for accelerated corrosion by impressed current, 'measured region' indicating area captured in digital images.

2 EXPERIMENTAL APPROACH

2.1 *Mixture proportions and specimen preparation*

Experiments were conducted on reinforced mortar specimen with 0.50 w/c using Aalborg Rapid® portland cement (Type 52.5N cement (DS/EN 197-1, 2001)). The mixture contained 375 kg/m^3 cement and 50% by volume fine aggregates (0–4 mm Class E sand in accordance with (DS-2426, 2004)). No chlorides were added to the mix, as corrosion was induced by applying electrical current as described below. A smooth 10 mm steel dowel rod was embedded in the centre of 10×10×50 cm^3 prism as illustrated in Figure 2. The mortar was mixed using a standard mortar mixer and mixing procedures (ASTM Standard C305 2011), placed in a form and consolidated by rodding and vibrating.

After casting, the mortar prism was stored in moulds for 24 hours under a plastic sheet at 20±2°C, and then demoulded. Upon demoulding, the specimen was stored under water for 6 additional days at 20 ±2°C. The 50 cm long prism was cut perpendicular to the embedded steel bar in 2.3 cm lengths using a water-cooled concrete saw, resulting in 10×10×2.3 cm^3 samples. A lead wire was soldered to the reinforcement on one side of the specimen to allow for accelerated corrosion, while the opposite side had a stochastic black and white speckle pattern applied using spray paint for digital image correlation (DIC) described below. A DC regulator was used to impress electrical current through a ruthenium/iridium mixed metal oxide activated titanium mesh counter electrode. Tap water (no chlorides added) provided an electrical connection between the working (steel bar) and counter electrode by partially submerging specimen in acrylic pond. The water level was maintained at approximately 1 cm below the steel bar for the entire test duration by a water-filled inverted volumetric flask (Fig. 2). A current density of 100 μA/cm^2, or corrosion rate of approximately 1.16 mm/year according to Faraday's law (assuming formation of Fe^{2+}), was applied and testing continued until cracking was detected by DIC.

2.2 *Digital image correlation (DIC) technique*

During accelerated corrosion testing, digital images were repeatedly captured at 10 minute intervals using a Nikon D3X 24.5 megapixel (6048×4032 pixel) camera body with a 60 mm focal length macro lens (AF-S Micro Nikkor 60mm f/2.8G ED). Prior to initiation of accelerated corrosion testing, 3 images were captured of the specimen surface, with a fourth image including a scale. The lens was placed 60 mm from the specimen surface, resulting in images with dimensions of approximately 31×41 mm^2, with each pixel representing 7.8×7.8 μm^2 of physical space. An LED ring flash was affixed directly to the lens to evenly light the specimen's surface. The f-stop was set manually at f/29 to maximize depth of field and exposure time was set such that the exposure value (EV) was zero (as to not over- or underexpose images).

Captured images were input into a commercially-available software package (GOM, 2009), which utilizes the stochastic speckle pattern to identify unique regions, called facets, on the specimen surface at each measurement time. Facet size was set to 15×15 pixels (116×116 μm^2). The software tracks the movements of the facets and utilizes standard DIC techniques to compute deformations of the specimen surface. Additional information on the hardware used and the DIC technique is available in Pereira et al. (2011) and Pease et al. (2006), respectively.

A trial test, to assess DIC measurement accuracy, was conducted by placing two mortar prisms side-by-side with flat faces touching each other. Prisms were fixed to a micrometer setup with 1 μm gradations with one prism stationary and the second moving with controlled distances. Two 2.5 mm extensiometers were used to provide comparative displacement measurements between the fixed and moving mortar prisms. The moving prism was translated by the micrometer setup to varying locations. At each location 3 digital images and 20 extensiometer measurements were recorded.

3 EXPERIMENTAL RESULTS

Figure 3 compares deformations measured, from the trial test setup, by DIC and extensiometers. The photo insert shows the two mortar prisms with rubber bands used to fix the extensiometers, and ten red line segments that indicate DIC measurement locations. DIC measurements were averaged from 10 locations and, as shown in Figure 3, correlate well with extensiometer measurements. The circular symbols (Fig. 3) show the absolute difference in measurements at given extensiometer measured deformations. A maximum difference of 0.29 microns (μm) was found. Agreement between the measurement techniques remained consistent regardless of deformations, up to 26.2 μm.

Figure 4 provides DIC measured corrosion-induced deformations between the steel and mortar at the various 'clock' positions indicated in the photo insert. Please note the 2, 6, 7, 9, and 11 o'clock position measurements are excluded in Figure 4, however minimum and maximum measured deformations are provided (i.e., excluded measurements fall within the extents of the plotted data). Corrosion-induced deformations are clearly non-uniform at the various measurement locations around the steel circumference. Deformations at the 3 o'clock position slowly increases to approximately 3 μm after 5 days, when the deformation rate increases. A maximum deformation of 15 μm was measured when the test was terminated at 9.2 days (testing stopped due to formation of cracks shown in Fig. 5 and discussed below). Increases in slope are observed at approximately the same time at other locations, including 2, 4, and 5 o'clock positions. However, the deformation magnitudes vary at these locations. Further, negative deformations are measured between the 6-12 o'clock positions to a minimum of approximately -9.5 μm. Minimum and maximum deformations occurred at the 12 and 3 o'clock positions, respectively. This, coupled with results from x-ray investigations discussed in the introduction (Fig. 1), clearly indicates corrosion products formed in a locally varying and non-uniform manner during accelerated corrosion testing.

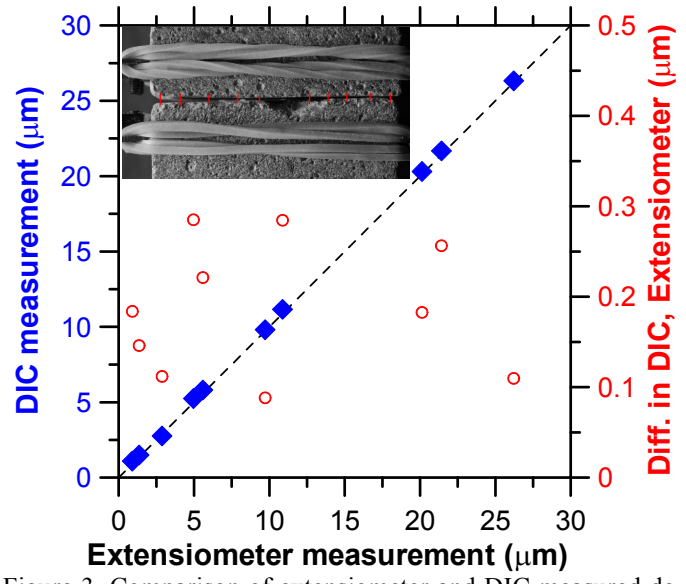

Figure 3. Comparison of extensiometer and DIC measured deformations in trial test setup, diamonds indicate measurements comparison, open circles shows measurement differences. Image shows trial setup with location of DIC measurements indicated, rubber bands used to hold extensiometers.

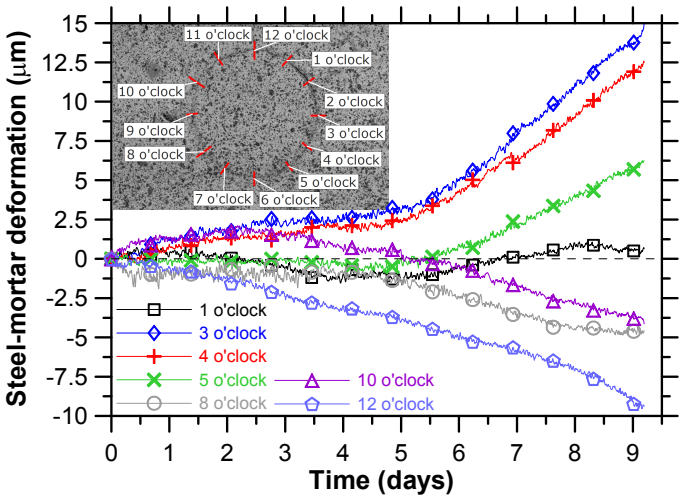

Figure 4. Deformations measured using DIC between steel and mortar at varying locations identified in the inset image.

Figure 5 shows the width of microcracks that were observed by the DIC measurements. Microcrack locations are provided in the photo insert and the numbering coincides with the order of observation. The 'dummy' crack provides measured deformations from a crack-free location, which yields an average 'width' of -0.004 ± 0.55 μm over the test duration. Crack 1 and 2 form nearly simultaneously after approximately 1.5 days, and increase to a maximum width of approximately 2 μm between 3 and 4 days. Crack 1 recovers slightly to a width of approximately 1 μm before increasing in width at 5.25 days, whereas Crack 2 continually reduces in crack

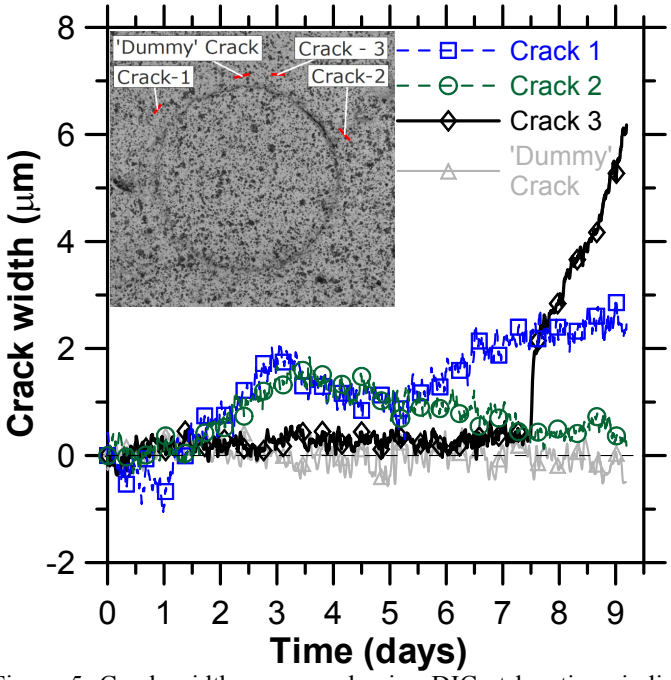

Figure 5. Crack widths measured using DIC at locations indicated in the inset image, 'dummy' crack indicates deformations measured from a location without a crack.

width. Crack 1 and 2 remained minimal in length near the steel surface, and did not propagate into the mortar. Crack 3 formed at 7.5 days and crack width rapidly increased to approximately 6 μm at 9.2 days. Testing was stopped due to the formation of Crack 3, which began to propagate from the steel towards the specimen surface (i.e., damage began to localize). Crack 1 and 2 appeared to be local, isolated microcracks, potentially providing connections between previously isolated pores.

4 CORROSION-INDUCED CRACKING MODELLING APPROACH

A combined electrochemical, transport, and mechanical modelling approach, developed in Michel et al. (2010), provides the basis for simulations of the formation of corrosion-induced deformation and cracking presented here. The original model (Michel et al., 2010, Solgaard et al., submitted) is based on the finite element method (FEM), and assumes:

- Uniform corrosion along the length and around the circumference of the steel, leading to a 2D plain strain formulation,
- Corrosion products form exclusively in the steel-cementitious matrix interface,
- The modelled system consists of four distinct regions, the cementitious matrix, the steel, a corrosion layer, and a predefined crack path.

The mechanical model considers cracking of the cementitious matrix along the predefined crack path and delamination at the steel-matrix interface, the former being modelled according to mode-I fracture and the latter being modelled according to mixed-mode (combined mode I and II) fracture. To account for expansion of the corrosion products, the model uses a thermal analogy by applying an equivalent thermal load to the corrosion layer (Molina et al., 1993). All model dimensions were equivalent to specimen dimensions discussed above and illustrated in Figure 2.

Additional details on the original model can be found in the literature (Michel et al., 2010, Solgaard et al., submitted), while detailed descriptions of modifications made to the original model to 1) consider penetration of corrosion products into the cementitious matrix and 2) creep of the cementitious matrix follow.

4.1 *Implementing penetration of corrosion products*

Faraday's law is used to determine the time-dependent steel radius reduction, *X(t)* [mm] due to a constant corrosion current density i_{corr} [A/mm^2]:

$$X(t) = \frac{M \cdot i_{corr}}{z \cdot F \cdot \rho} \Delta t \tag{1}$$

where M = molar mass of Fe [g/mol], z = anodic reaction valence [-], F = Faraday's constant [96,485 A·s/mol], ρ = density of the metal [g/mm^3], and Δt = duration of current application [s]. Using Equation 1, the expanded volume of corrosion products, V_{cp} [mm^3] is determined by:

$$V_{cp} = \eta_{vol} \cdot V_{sc} = \eta_{vol} \cdot \pi \cdot l_A \cdot \left(r^2 - \left(r - X(t)\right)^2\right) \tag{2}$$

where η_{vol} = unitless volumetric expansion coefficient of corrosion products and V_{sc} = volume of consumed steel [mm^3], which dependent on the radius reduction of steel, *X(t)*, the original steel radius, r [mm] and the length of the anode, l_A [mm]. Previous work using an identical experimental setup found that Fe_2O_3 was the likely corrosion product formed (Michel et al., 2011), which has a theoretical η_{vol}-value of 2.1.

As discussed in the introduction section (Fig. 1), corrosion products penetrate into the *CAR* of the cementitious matrix. Figure 6 provides a schematic of the idealized filling process of the *CAR*, which is assumed to consist of the cementitious matrix's capillary porosity, ϕ as approximated by Power's law (Powers & Brownyard, 1947):

$$\phi = \frac{w/c - 0.36 \cdot \alpha}{w/c + 0.32} \tag{3}$$

where the degree of hydration, α, for 0.50 w/c Aalborg Rapid® portland cement paste under similar curing conditions (7 days at 20° C) was measured as 0.65 (Forsberg & Rasmussen 2011). The size of the *CAR* controls the considered volume of cementitious matrix, V_{cm}, as:

$$V_{cm} = \pi \cdot l_A \cdot \left(r + CAR\right)^2 - r^2 \tag{4}$$

and by introducing porosity, ϕ the volume of the *CAR*, V_{CAR} [mm^3] is computed as:

$$V_{CAR} = \phi \cdot V_{cm} \tag{5}$$

As illustrated in Figure 6, the *CAR* size is assumed to increase with additional time (and volume of corrosion products) due to the formation of microcracks connecting additional capillary pores further from the steel surface. Equation 6 describes the increase in the initial *CAR* size prior to microcracking, CAR_0 [mm] to the maximum *CAR*, CAR_{MAX} [mm] as:

$$CAR = CAR_0 + \left(CAR_{MAX} - CAR_0\right) \cdot \kappa \tag{6}$$

where κ describes the change in connectivity of capillary pores inside the *CAR* and varies between 0 and 1, according to Equation 7:

$$\kappa = \begin{cases} 0 & \text{if} \quad t \le 1.5 \text{ days} \\ t/t_c & \text{if} \quad 1.5 \text{ days} < t \le t_c \\ 1 & \text{if} \quad t > t_c \end{cases} \tag{7}$$

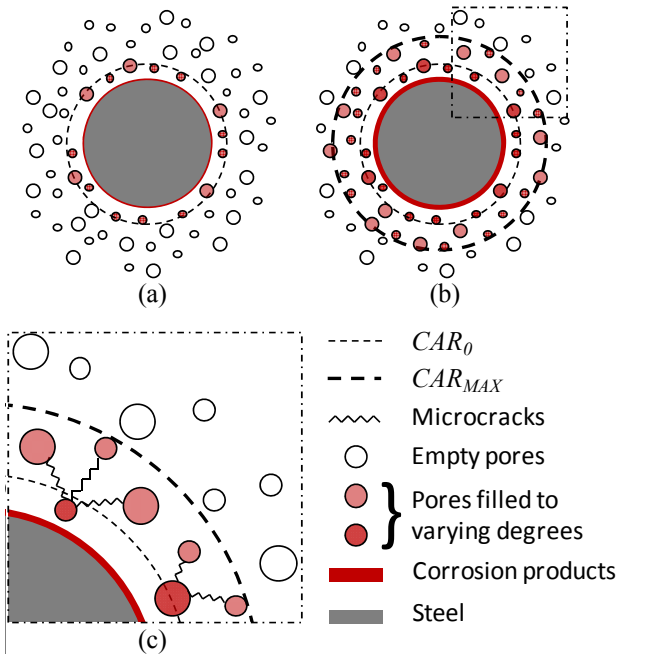

Figure 6. Conceptual schematic of idealized filling process of capillary porosity with corrosion products: (a) shows the initial *CAR*, CAR_0, (b) the subsequent increase in *CAR* size to a maximum, CAR_{MAX} and filling of additional pores due to (c) formation of microcracks between pores allowing movement of corrosion products.

where t is the time in days and t_c indicates the time when the *CAR* reaches a maximum, CAR_{MAX}. As shown in Figure 7, values for κ increase after 1.5 days, based on Figure 5 that indicates the first microcracks form at approximately 1.5 days. The final pores are considered to connect to the *CAR* after 5 days (i.e., t_c = 5 days), which corresponds to the increased rate of deformations between the steel and mortar as shown in Figure 4. Values for CAR_0 and CAR_{MAX} were set at 0.14 and 0.28 mm, respectively, based upon x-ray studies on a companion specimen (i.e., 0.50 w/c, 100 µm/cm^2 corrosion rate, identical curing, etc.) that showed corrosion products gradually penetrated into the mortar to approximately 0.17 mm after 0.7 days of accelerated corrosion and 0.28 mm at the time of cracking (Michel et al., submitted, Pease et al., submitted). Mortar used for experiments contained 50% by volume fine aggregate; however, due to edge effects and the relatively small size of the *CAR*, effects of the aggregate on V_{CAR} are assumed negligible.

As the model uses a 2D plain strain formulation, a linear expansion coefficient, η_{lin} is required to describe the expansion of the corrosion layer, ΔR as:

$$\eta_{lin} = \frac{\Delta R}{X(t)} = \alpha_{fict} \cdot \Delta T \tag{8}$$

where the second term describes the thermal analogue used to account for the expansion of corrosion products with α_{fict} = fictitious thermal expansion coefficient [K^{-1}] and ΔT = equivalent temperature increment [K]. Isotropic expansion of corrosion products is assumed (i.e., $\eta_{lin} = \eta_{vol}/3 = 0.70$). Introducing an adjusted equivalent temperature increment, ΔT_{CAR} in Equation 8 provides one method to account for the *CAR* as shown in Equation 9:

$$\Delta T_{CAR} = \lambda_{CAR} \cdot \Delta T \tag{9}$$

where λ_{CAR} describes the partial penetration of corrosion products into V_{CAR} as:

$$\lambda_{CAR} = \begin{cases} \left(\frac{V_{cp}}{V_{CAR}}\right)^n & \text{if } V_{cp} < V_{CAR} \\ 1 & \text{if } V_{cp} \geq V_{CAR} \end{cases} \tag{10}$$

where n describes the shape of the λ_{CAR} curve as shown in Figure 7. A value for n of 1.3 was found to provide the best fit to experimental data. Equations 9 and 10 reduce the expansion of the corrosion layer until V_{cp} (Eq. 2) exceeds V_{CAR} (Eq. 5), and the corrosion accommodating pore volume is considered full. The portion of corrosion products that penetrate the cementitious matrix are considered by the model to not induce stress. Relationships describing the increase in *CAR* size (Eq. 6) and the partial penetration of corrosion products (Eq. 10) are first order approximation and should be investigated further.

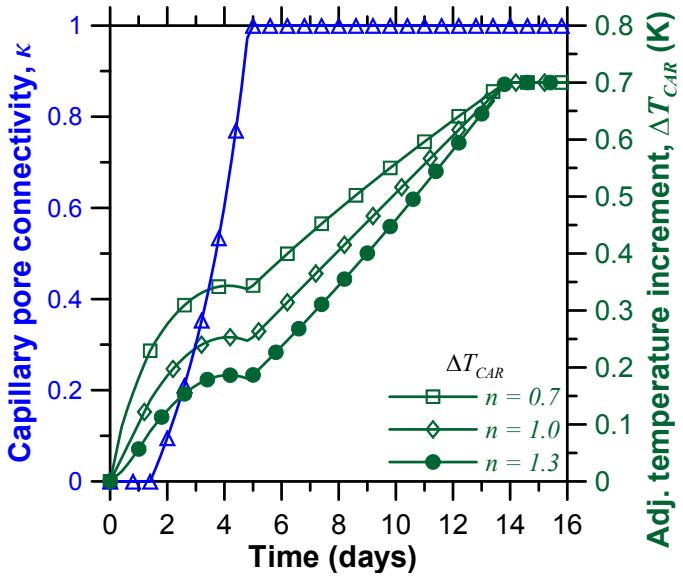

Figure 7. Time-dependent values for κ (Eq. 6) and adjusted temperature increment, ΔT_{CAR} (Eq. 9) that consider partial penetration of corrosion products into the cementitious matrix for various n-values (Eq. 10).

4.2 *Implementation of Creep*

Creep, which is affected by various parameters such as the ambient environmental conditions and duration of loading, relaxes a portion of the corrosion-induced stresses in the cementitious matrix. Stress relaxation is considered by an effective elastic modulus of the cementitious matrix at each time step as described in (e.g., Eurocode 2, 2003):

$$E_{c,eff} = \frac{E_c}{1 + \varphi(t, t_0)} \tag{10}$$

where $E_{c,eff}$ and E_c are the effective and secant elastic modulus [MPa], respectively, $\varphi(t,t_0)$ is the creep coefficient, which is a function of t and t_0, the age of cementitious matrix and time at loading [days].

5 COMPARISON OF MODEL, EXPERIMENTAL RESULTS

Figure 9 illustrates modeled corrosion-induced deformation between the steel and cementitious matrix at various locations around the steel surface. Locations are described by polar angle coordinates, where 0° marks the locations where the predefined crack path intersects the steel-matrix interface. After crack formation, modeled deformations adjacent to the crack (i.e., near 0°) increased in comparison to other locations due to local delamination of the elements. Increased local deformations near the crack are most clearly seen after 7.0 and 9.2 days in Figure 9. Nevertheless, the model, which assumes a uniform deposition of corrosion products in the corrosion layer, predicts uniform deformations between the steel and cementitious matrix. However, experimental observations indicate non-uniform deformations. A comparison of modeled and measured deformations is provided in Figure 9 at 3.0 days. The model predicted deformation between the steel and cementitious matrix was 1.8 µm, while DIC measurements vary from -2.5 µm at 0° (12 o'clock in Fig. 4) to +2.4 µm at 90° (3 o'clock). Figure 9 indicates non-uniformity of the accelerated corrosion process should be considered in future models.

While the current model assumes a uniform deposition of corrosion products and therefore cannot accurately model all corrosion-induced deformations, Figure 10 illustrates the model can accurately describe certain locations and appears to capture important processes of the corrosion-induced deformation process. Figure 10 compares averaged (between ±180°, Fig. 9) modeled time-dependent deformations between the steel and cementitious matrix for varying elastic modulus of corrosion products, E_{cp} to the average of DIC measurements taken from the 3 and 4 o'clock positions. Regardless of E_{cp}-values, modeled corrosion-induced deformations begin at approximately 1 day and increase more rapidly with

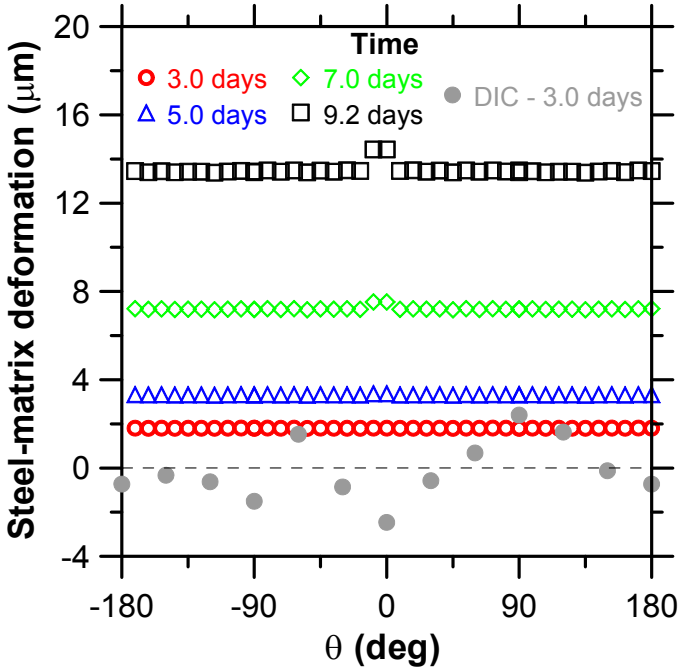

Figure 9. Modeled corrosion-induced deformations between steel and cementitious matrix for E_{cp} = 2.0 GPa at varying locations of the steel surface expressed as polar coordinates. For DIC measurements – clockwise from 12 to 6 o'clock corresponds to 0 to +180°, counterclockwise from 12 to 6 o'clock corresponds to 0 to -180°.

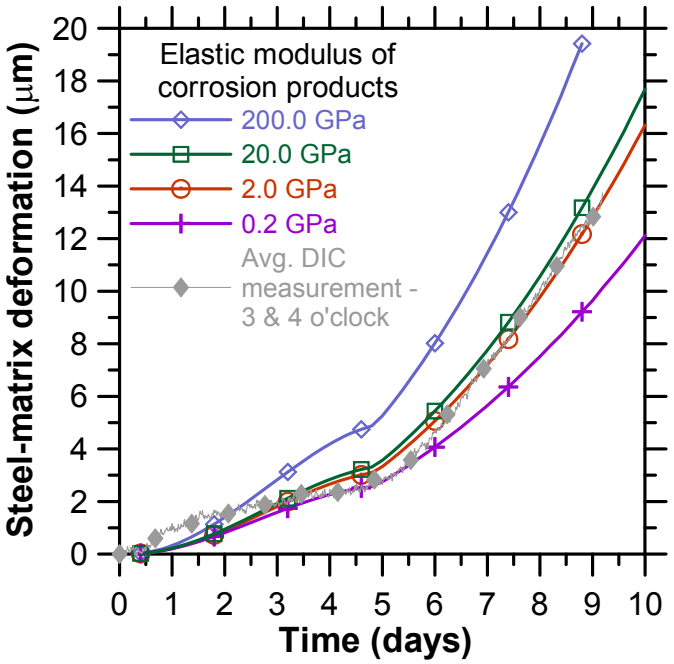

Figure 10. Averaged modeled corrosion-induced deformations between steel and cementitious matrix for varying E_{cp} with comparison to averaged DIC measured deformation from 3 and 4 o'clock positions (Fig. 4).

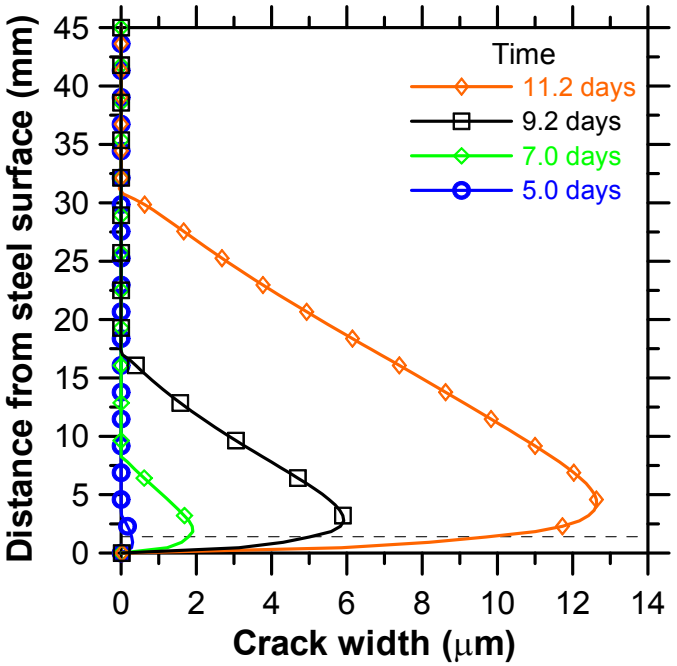

Figure 11. Modeled corrosion-induced crack width profiles for E_{cp} = 2.0 GPa at varying times, with broken line at 1.4 mm from the steel surface indicates location of crack widths plotted in Figure 12.

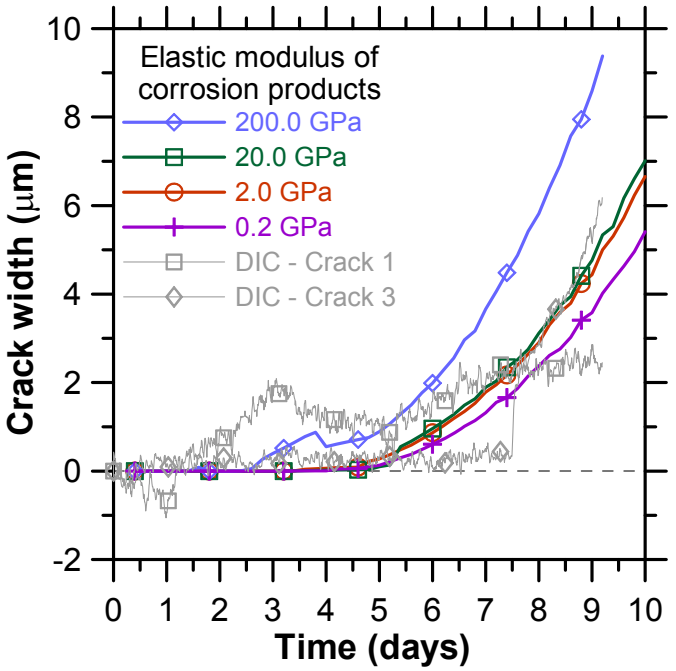

Figure 12. Modeled corrosion-induced crack widths 1.4 mm from steel surface for varying E_{cp} with comparison to maximum extent of DIC measured crack widths (i.e., Crack 1 and 3 from Fig. 5).

increased E_{cp}. Modeled deformations initially increase slower than experimental measurements which increase from approximately 0 μm at 0.5 days to 2.0 μm at 3 days. The differing behaviors at these earlier times may be caused by the modeled expansion of the *CAR* size (Eq. 6) and/or the portion of corrosion products deposited in the corrosion layer (Eq. 10) and indicates further investigations are required to ascertain and more accurately describe the controlling mechanisms. Similar to experimental data, modeled deformations increased more rapidly after approximately 5 days. An order-of-magnitude investigation of E_{cp}-values indicates 2.0 GPa provides the best fit to experimental results (Fig. 10), while a value of 0.2 GPa (similar in scale to estimates of E_{cp} in Caré et al. (2008)) significantly underestimates corrosion-induced deformations after 6 days of accelerated corrosion. Figure 10 shows increasing E_{cp} from 2.0 to 20.0 GPa causes only minor changes in the resulting deformations, compared to deformation changes caused by E_{cp} changes from 0.2 to 2.0 GPa and 20.0 to 200.0 GPa.

Figure 11 illustrates model predicted corrosion-induced crack width profiles along the predefined crack path after various times. A numerically significant crack width (> 0.001 μm) was first observed for E_{cp} of 2.0 GPa after 3 days at approximately 0.5 mm from the steel surface. As Figure 11 shows, cracks initiate and maximum crack width remain near the steel surface (while the crack does not reach the surface of the cementitious matrix (Solgaard et al., submitted)) and additional time is required to propagate the crack tip to the specimen surface.

Figure 12 compares modeled crack width with the maximum extent of measured crack widths. The model predicted crack widths were taken 1.4 mm from the steel surface, as indicated by the broken line in Figure 11, to correspond to the approximate locations of DIC crack width measurements shown in Figure 5. As described in the previous section a single crack is modeled and therefore microcracking behavior (e.g., crack 1 in Fig. 12) is neither considered nor accurately estimated by the model. However, the rapid crack growth measured for crack 3 corresponds well to model predicted crack widths for E_{cp} of 2.0 and 20.0 GPa. The width of crack 3 increased from 2.9 μm at 8 days to 6.2 μm at 9.2 days when the test was terminated, while the modeled crack width measured at 2.9 μm after 8 days and 5.0 μm after 9.2 days for E_{cp} of 2.0 GPa. Similar to the modeled deformations between steel and cementitious matrix (Fig. 10), varying E_{cp}-values from 0.2 to 2.0 GPa and 20.0 to 200.0 GPa had a major impact on model predicted crack width behavior, compared to a relatively minor impact of E_{cp}-values from 2.0 to 20.0 GPa.

6 SUMMARY AND CONCLUSIONS

This paper, which presents a comparison of corrosion-induced deformations measured by digital image correlation (DIC) and modeled by a corrosion-induced cracking model, has concluded:

- DIC measured deformations, from a 31×41 mm^2 surface area using a 24.5 megapixel (6048×4032 pixels) images, correlate well with extenisometer measured deformations. A maximum difference in measurement techniques of 0.29 μm was observed for deformations from 0 to 26.2 μm.
- DIC measured deformations between steel and mortar indicated corrosion-induced deformations are non-uniform around the steel surface with deformation ranging from approximately -9.5 to +15 μm after 9.2 days of accelerated corrosion at a current density of 100 μA/cm^2 (or corrosion rate of approximately 1.16 mm/year). Corrosion-induced cracking, detected by DIC measurements, consisted initially of multiple microcracks that formed after approximately 1.5 days of accelerated corrosion. After 7.5 days a larger, controlling crack formed, rapidly increased in width, and propagated towards the surface of the cementitious matrix. The microcracks remained short in length, did not propagate toward the specimen surface, and potentially provided connections between previously isolated capillary pores space in the cementitious matrix.
- Based on experimental results, a corrosion-induced cracking model was modified to account for the partial penetration of corrosion products into the cementitious matrix surrounding the corroding steel. Corrosion products were considered to form simultaneously in a corrosion layer at the interface of the steel and the cementitious matrix

and in a corrosion-accommodating region *(CAR)* of the cementitious matrix. The *CAR* is considered to consist of the capillary pores space and to increase in size due to microcracks connecting additional pore space further from the steel surface.

– Comparisons of modeled and experimental data indicated a common assumption of uniform deposition of corrosion products around the steel surface is inaccurate. Additionally, values for the elastic modulus of corrosion products between 2.0 and 20.0 GPa provided most accurate fits to experimental results; however, further experiments and improvements to the model (e.g., consideration of non-uniform corrosion process) are needed.

ACKNOWLEDGEMENTS

Financial contributions from the Danish Expert Centre for Infrastructure Constructions and COWIFonden are greatly appreciated. The second author gratefully acknowledges the financial support of Femern Bælt A/S, Sund & Bælt Holding A/S, and The Danish Agency for Science, Technology and Innovation.

REFERENCES

ASTM Standard C305 2011. Standard Practice for Mechanical Mixing of Hydraulic Cement Pastes and Mortars of Plastic Consistency. *ASTM Int. DOI: 10.1520/C0305-11*.

Caré, S., Nguyen, Q., L'Hostis, V. & Berthaud, Y. 2008. Mechanical properties of the rust layer induced by impressed current method in reinforced mortar. *Cement and Concrete Research* 38(8-9): 1079-1091.

DS/EN 197-1 2001. Cement—Part 1: Composition, specification and conformity criteria for common cements. *Danish Standards Association*, 29 pp.

DS-2426 2004. Concrete—Materials—Rules for application EN 206-1 in Denmark. *Danish Standards Association.*

Eurocode 2 2003. Design of Concrete Structures. *European Committee for Standardization (CEN).*

Forsberg, A., Rasmussen, A. 2011. Transportengenskaber for beton med superabsorberende polymerer. *Bachelor Thesis (in Danish), Technical University of Denmark*, 82 pp.

GOM, 2009. Aramis user manual – Software, Aramis v6.1 and higher. *GOM Optical Measuring Techniques.*

Michel, A., Geiker, M., Stang, H., Olesen, J. & Solgaard, A. 2010. Modeling Formation of Cracks in Concrete Cover due to Reinforcement Corrosion. *Proc. 7th Int. Conf. on Fracture Mechanics of Concrete and Concrete Structures (FraMCoS-7), Jeju, Korea,* 944-951.

Michel, A., Pease, B., Geiker, M., Stang, H. & Olesen, J. 2011. Monitoring reinforcement corrosion and corrosion-induced cracking using non-destructive x-ray attenuation measurements. *Cement and Concrete Research* 41(11): 1085-1094.

Michel, A., Pease, B., Peterová, A. & Geiker, M. Submitted. Experimental determination of the penetration depth of corrosion products and time to corrosion-induced cracking in reinforced cement based materials. *Int. Cong. on Durability of Concrete (ICDC 2012), Trondheim, Norway, 17-21 July 2012.*

Molina, F., Alonso, C. & Andrade, C. 1993. Cover cracking as a function of rebar corrosion: Part 2 - Numerical model. *Materials and Structures* 26(9): 532-548.

Ouglova, A., Berthaud, Y., François, M. & Foct, F. 2006. Mechanical properties of an iron oxide formed by corrosion in reinforced concrete structures. *Corrosion Science* 48(12): 3988-4000.

Pease, B., Geiker, M., Stang, H. & Weiss, J. 2006. Photogrammetric assessment of flexure induced cracking of reinforced concrete beams under service loads. *Proc. 2nd Int. RILEM Symposium Advances in Concrete through Science and Engineering, Québec, Canada, September 11-13.*

Pease, B., Michel, A. & Stang, H. Submitted. Quantifying movements of corrosion products in reinforced concrete using x-ray attenuation measurements. *2nd Int. Conf. on Microstructure Related Durability of Cementitious Composites (MicroDurability), Amsterdam, The Netherlands, 11-13 April 2012.*

Pereira, E., Fischer, G. & Barros, J. 2011. Image-based detection and analysis of crack propagation in cementitious composites. *Proc. Int. Conf. on Advances in Construction Materials through Science and Engineering, Hong Kong, China, 5-7 September.*

Powers, T. & Brownyard, T. 1947. Studies of the Physical Properties of Hardened Portland Cement Paste. *J. American Concrete Institute* 43(9): 933-992.

Solgaard, A., Michel A. & Stang H. Submitted. Concrete cover cracking in relation to uniform reinforcement corrosion and SLD. *Materials and Structures*.

Paper XIII

” Concrete cover cracking due to uniform reinforcement corrosion”

A.O.S. Solgaard, A. Michel, M. Geiker & H. Stang

Published in: *Materials and Structures.*

Concrete cover cracking due to uniform reinforcement corrosion

Anders Ole Stubbe Solgaard, Alexander Michel, Mette Geiker & Henrik Stang

Materials and Structures

ISSN 1359-5997
Volume 46
Number 11

Mater Struct (2013) 46:1781-1799
DOI 10.1617/s11527-013-0016-6

Springer

Materials and Structures (2013) 46:1781–1799
DOI 10.1617/s11527-013-0016-6

ORIGINAL ARTICLE

Concrete cover cracking due to uniform reinforcement corrosion

Anders Ole Stubbe Solgaard · Alexander Michel · Mette Geiker · Henrik Stang

Received: 26 July 2012 / Accepted: 17 January 2013 / Published online: 21 February 2013

Abstract Service life design (SLD) is an important tool for civil engineers to ensure that the structural integrity and functionality of the structure is not compromised within a given time frame, i.e. the service life. In SLD of reinforced concrete structures, reinforcement corrosion is of major concern and reinforcement de-passivation is a frequently used limit state. The present paper investigates an alternative limit state: corrosion-induced cover cracking. Results from numerical simulations of concrete cover cracking due to reinforcement corrosion are presented. The potential additional service life is calculated using literature data on corrosion rate and Faraday's law. The parameters varied comprise reinforcement diameter, concrete cover thickness and concrete material properties, viz. concrete tensile strength and ductility (plain concrete and fibre reinforced concrete). Results obtained from the numerical simulations reveal that, depending on the serviceability limit state applied, the service life of a reinforced concrete structure can be increased significantly by allowing minor damage of the cover.

Keywords Service life design · Cracking of concrete cover · Numerical simulations · Fibre reinforced concrete

A. O. S. Solgaard (✉)
COWI A/S Denmark, Kongens Lyngby, Denmark
e-mail: adso@cowi.dk
URL: www.byg.dtu.dk

A. O. S. Solgaard · A. Michel · M. Geiker · H. Stang
Department of Civil Engineering, Technical University of Denmark, Kongens Lyngby, Denmark

M. Geiker
Department of Structural Engineering, Norwegian University of Science and Technology (NTNU), Trondheim, Norway

1 Introduction

Over the last decades service life design (SLD) has become an important tool within civil engineering for design of durable reinforced concrete structures. The concept of SLD is used to assure that, within a given time frame during which the structure is routinely maintained, i.e. the service life, little or no repair is required to maintain the purpose and integrity of the structure. A typically used requirement for reinforced concrete structures at risk of reinforcement corrosion, is that no corrosion of embedded reinforcement takes place within the service life of the structure [10, 11]. To fulfil such a requirement, existing guidelines for SLD e.g. [10, 11] establish that the end of service life has been reached when the passive layer of embedded reinforcement has been broken down. In other words de-passivation of the reinforcing steel is typically used as a serviceability limit state. In e.g. [11] other limit states associated with reinforcement corrosion are also considered, however, associated models for analyses

are not described as opposed to models associated with the de-passivation limit state. One of the concepts founding the basis of SLD for reinforced concrete structures is Tuutti's model of reinforcement corrosion [29], establishing that reinforcement corrosion is divided into two phases, viz. the initiation phase and the propagation phase. The propagation phase was further characterized in terms of various types of cracking damage in [11], including 'formation of cracks' and 'spalling of the concrete cover'.

During the initiation phase substances like Cl^- and CO_2 may ingress through the concrete cover leading to de-passivation of the reinforcing steel (at the end of initiation phase). During the propagation phase the actual corrosion of the reinforcement takes place. The formation of solid corrosion products will lead to a build-up of pressure in the concrete/steel interface as the corrosion products take up more volume than the steel consumed.

The italicized labels in Fig. 1 characterize the structural consequences in the concrete surrounding the reinforcement due to reinforcement corrosion; "*Damage*" refers to the formation and propagation of cracks inside the concrete cover, "*Cracking*" refers to the formation and opening of cracks reaching the concrete cover surface, and "*Spalling*" refers to the phenomenon of cover concrete being pushed off due to the corrosion process and the expansive nature of the corrosion products. The above definitions are used in this study; the definitions used in the literature vary. The crack initiation at the concrete/steel interface and the formation of damage prior to cracking reaching the concrete surface has been experimentally observed by Michel et al. [20].

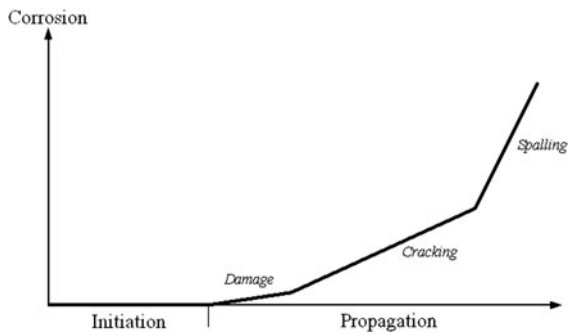

Fig. 1 Model for corrosion initiation and propagation and the terminology used in the current study for characterizing the propagation phase. After Tuutti [29] and *fib* Model Code for Service Life Design [11]

The transition from the damage phase to the cracking phase, cf. Fig. 1, is defined as the time when the crack, which propagates through the concrete cover from the reinforcement towards the concrete cover surface, reaches the cover surface. However, since the exact time is difficult to determine when inspecting existing structures as well as in numerical simulations of concrete cover cracking, in the present paper a value of the crack width at the concrete surface, W, of $W = 50$ μm is used to define the end of the damage phase, viz. $W_{\mathrm{lim,c}} = 50$ μm. A crack of approx. $W = 50$ μm is the smallest crack possible to observe with the naked eye, a so-called hairline crack, and the value is also used in existing guidelines for SLD, e.g. [10] as the definition of crack initiation.

Another characteristic state of the corroding reinforced concrete structure can be defined as the time for which W attains a certain value. This state could be defined as the end of the cracking phase (not necessarily corresponding to the start of the concrete spalling phase). Both the end of the damage phase and the end of the cracking phase could be used as limit states. The end of the cracking phase has previously been suggested as a durability limit state e.g. by Andrade et al. [2] and the corresponding crack width limit should be dependent on exposure conditions, concrete type etc.

A vast amount of literature concerning concrete cover cracking caused by reinforcement corrosion already exists, covering, among others, experimental observations [26, 1, 2], analytical models [3, 7, 16] and FEM-based models for cracking [7, 14, 28]. Several modelling approaches have been proposed based on experimental results, e.g. a model for the prediction of time of the initiation of corrosion-induced cracking by Liu and Weyers [16], and models for the prediction of crack width as a function of the volume of corrosion products [21, 30]. Previous models described in the literature introduce a so-called *porous zone* or *corrosion accommodating region* around the reinforcement capable of accommodating corrosion products [16, 30]. Thus, according to this assumption, not all the corrosion products formed during the corrosion process contribute to the build-up of pressure in the concrete/steel interface. The properties of this corrosion accommodating region viz. thickness, porosity, etc. are of importance for the relationship between formation and propagation of cracks and the associated number of corrosion

products. Consequently, since the properties of this corrosion accommodating region are unknown, it is possible to vary them in order to fit a proposed model to experimental data. Though numerous models concerning cracking of concrete cover due to reinforcement corrosion already exists, the models have not been operationalized for SLD.

The objective of the present paper is to present a fracture mechanics based numerical model for the simulation of damage and cracking of cover concrete in reinforced concrete structures due to uniform reinforcement corrosion. Moreover, it is the objective of the paper to illustrate the applicability of such analyses for SLD of reinforced concrete structures using operational limit states related to the corrosion propagation phase. Finally, the ability of such models to address design issues such as the possible use of fibre reinforced concrete (FRC) to increase durability is demonstrated.

The numerical model is a fracture mechanics based finite element (FE) model, with fracture mechanical properties based on the so-called effective cohesive relationship of concrete. The damage and cracking phases of the concrete cover are analysed by the use of the model for different combinations of concrete cover thickness and reinforcement diameter. The influence of the extent of the corrosion is the analysis itself. As previously explained, the end of the damage phase is defined as the time for which $W = W_{\mathrm{lim,d}} = 50$ μm, whereas the end of the cracking phase is defined as the time for which $W = W_{\mathrm{lim,c}} = 0.2$ mm, which is in line with the durability limit states suggested in [2]. The limit state for the damage phase has been set to $W_{\mathrm{lim,d}} = 50$ μm. This value is considered as an operational zero-value for such numerical simulations, as the exact transition from the un-cracked state to the cracked state is difficult to determine more accurately (convergence of the model). The model does not consider spalling of cover concrete since this phase is beyond the durability limit state of concrete, which is the main focus area of the present paper. It should be further noticed that the limit states proposed cannot be seen as stand-alone limit states, since the extent of corrosion required to form such cracks may reduce the mechanical properties, i.e. load-bearing capacity of the structure, significantly. Therefore a proper assessment of the load-bearing capacity of corroded, reinforced concrete structures has to be carried out in conjunction with these limit states.

Results from the numerical mechanical modelling in terms of the relation between damage and/or cracking of concrete cover and extent of uniform reinforcement corrosion causing formation of solid products at the steel–concrete interface can be related to time, by the use of Faraday's law. Hence, results presented in this paper can, as will be shown, be directly linked to SLD making the use of limit states associated with reinforcement corrosion operational. It is emphasized, that this is only applicable for uniform reinforcement corrosion and for the formation of solid corrosion products which may not be the case for chloride-induced corrosion.

2 Model description

The numerical model for the simulation of damage and cracking in concrete cover related to uniform corrosion of reinforcement embedded in homogenous defect-free concrete is presented in the following. The model simulates the expansion of corrosion products and the associated damage and cracking in the concrete cover for a semi-infinite concrete body assuming 2D plane strain and discrete crack formation.

Cracking of concrete covers due to reinforcement corrosion might be divided into two distinct phases, viz. the damage phase and the cracking phase, as illustrated in Figs. 2, 3, showing in Fig. 2 the relationship between concrete surface crack width, W, and the change in un-constrained rebar radius, ΔR, (due to corrosion). In Fig. 3 the change in ΔR is associated to different cracking configurations with $\Delta R_{\mathrm{crit,c}}$ denoting the radius change associated with the transition from the damage state to the cracking state.

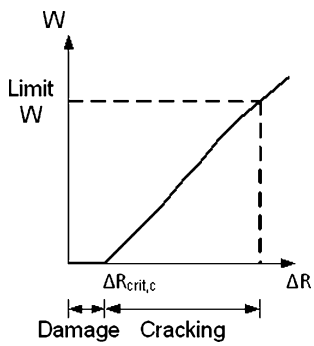

Fig. 2 Schematic of damage and cracking of concrete cover during the propagation phase. Inspired by [30]

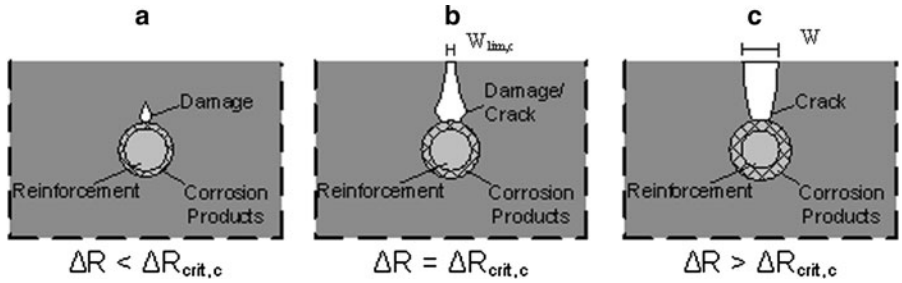

Fig. 3 Damage and cracking in a semi-infinite concrete body. **a** $\Delta R < \Delta R_{crit,c}$ $W = 0$, **b** limit of damage phase, $\Delta R = \Delta R_{crit,c}$ $W = W_{lim,c}$ and **c** Cracking $\Delta R > \Delta R_{crit,c}$ $W > W_{lim,c}$. The illustrations are not in scale

The damage is initiated at the concrete/steel interface. However, the damage has not reached the cover concrete surface, for $\Delta R < \Delta R_{crit,c}$, as illustrated in Fig. 3a. The thickness of corrosion products increases as the corrosion process continues and eventually $\Delta R = \Delta R_{crit,c}$, as illustrated in Fig. 3b. For $\Delta R = \Delta R_{crit,c}$ the end of the damage phase has been reached, i.e. the damage has reached the concrete surface. Once the damage has reached the concrete surface, the cracking phase has been initiated, and the crack continues to open for $\Delta R > \Delta R_{crit,c}$, cf. Fig. 3c. Secondary radial cracks may be formed during the corrosion process. However, such cracks are not taken into consideration in the present model.

Furthermore the model described in the following does not account for a corrosion accommodating region around the reinforcement. Hence, all corrosion products formed contribute to the build-up of pressure at the concrete/steel interface. Recent investigations [20]; Pease et al. [24] show that movement of corrosion products into the surrounding concrete can be significant, especially in the early stages of the corrosion process, while corrosion products tend to concentrate on or close to the rebar at later stages. Thus it is expected that the model presented furnishes a conservative estimate of the relationship between damage/cracking and the associated amount of corrosion products. Further details and descriptions of the model are given in the following.

2.1 Modelling corrosion of reinforcement

Reinforcement embedded in sound, "un-contaminated" concrete is thermodynamically passive due to the high alkalinity of concrete (~pH 13) [4]. However substances like Cl^- and CO_2 may ingress through the concrete cover leading to de-passivation of the reinforcement. Various types of corrosion products can be formed, dependent on primarily the oxygen and chloride availability. It is in this paper assumed that solid products are formed homogeneously around the reinforcement. Since the solid phase corrosion products take up more volume than the consumed steel, a pressure is built up on the concrete/steel interface due to the confinement by the surrounding concrete. The volume and linear expansion coefficients of some of the most common corrosion products potentially forming on embedded reinforcement are given in Table 1.

It is assumed that the corrosion products are homogeneous and isotropic and that the primary corrosion product is hydrated hematite ($Fe_2O_3 \cdot H_2O$). Within the present model, this expansion is modelled by the use of a fictitious thermal load, an approach also utilized by e.g. Molina et al. [21]. Modelling of the transformation from steel to corrosion products and the associated expansion of corrosion products is outlined in Fig. 4.

Step 0 Reinforcement with initial radius, R_0, is modelled.

Step 1 A prescribed corrosion depth, X, is applied to the model, cf. Fig. 4. The virgin steel bar is transformed into a two-phase domain, viz. steel and corrosion products with different material properties: The inner domain consists of steel, with Young's modulus and Poisson's ratio of steel, E_{st} and γ_{st} respectively, whereas the outer domain consists of corrosion products

Table 1 Expansion coefficients of selected common corrosion products

Identification	Chemical composition	η_{vol} [−]	η_{lin} [−]
Magnetite	1/3 Fe_3O_4	2.08	0.69
Hematite	1/2 Fe_2O_3	2.12	0.71
Goethite	α-FeOOH	2.91	0.97
Lepidocrocite	$Fe_2O_3 \cdot H_2O$	6.40	2.13

From [6]

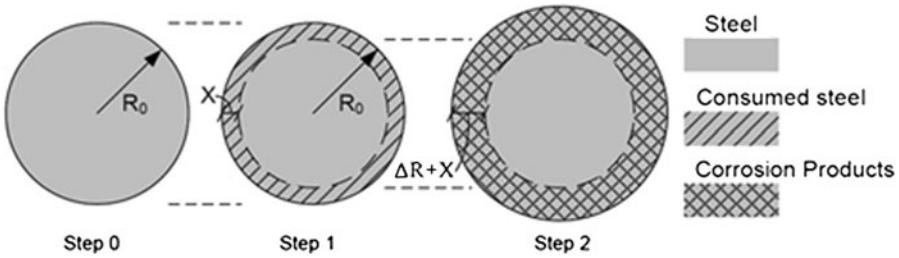

Fig. 4 Schematic illustration of modelling the expansion of corrosion products

with the properties of the corrosion product investigated, E_{cor} and γ_{cor} respectively. Further a fictitious thermal expansion coefficient is assigned to the outer domain.

Step 2 A fictitious thermal load, T_{cor}, adjusted to the fictitious expansion coefficient and together corresponding to the linear expansion coefficient of the corrosion products, is applied to the outer domain. The thermal load leads to an increase in volume of the outer domain, viz. the corrosion products, cf. Fig. 4.

The free expansion of the corrosion products shown in Fig. 4 is hindered due to the confinement of the surrounding concrete. The pressure sustained by the confining concrete is illustrated in Fig. 5.

The fictitious thermal, linear load applied to the outer domain appears from Eq. (1)

$$T_{cor} \cdot \alpha_{cor} = \eta_{lin} \tag{1}$$

where α_{cor} is the fictitious thermal expansion coefficient of the corrosion products.

The volume of the unconstrained corrosion products formed appears in Eq. (2):

$$V_{cor} = (1 + \eta_{vol}) \cdot V_S \tag{2}$$

where V_{cor} is the volume of corrosion products and V_S is the volume of steel consumed. The approximation used in Eq. (3) can be used for the connection between the unconstrained increase of the radius of the reinforcement, ΔR, and the corrosion depth, X:

$$\Delta R = \eta_{lin} \cdot X \tag{3}$$

Thus the thickness of the corrosion products is given by $X + X \cdot \eta_{lin}$ as shown in Fig. 4.

2.2 Fracture mechanical model

The mechanical model for the damage and cracking of concrete cover is based on non-linear fracture mechanical theory and models damage and cracking in a 2D semi-infinite concrete body, assuming plane strain. The expansion of corrosion products described above results in damage and crack formation in the concrete cover, cf. Fig. 3, and a debonding of the concrete/steel interface. The model is illustrated in Fig. 6.

Zero-thickness interface elements are placed vertically through the concrete cover above the centre line of the reinforcement and on the circumference of the

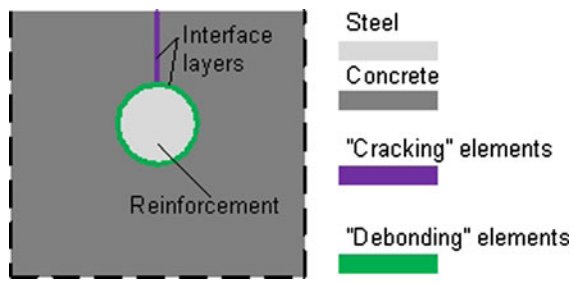

Fig. 6 Schematic of fracture mechanical model for simulation of damage and cracking

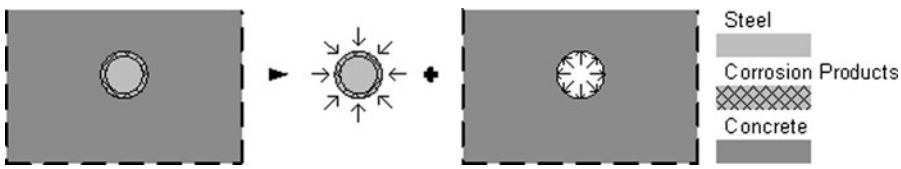

Fig. 5 Illustration of internal pressure due to the expansion of corrosion products. Inspired by Liu and Weyers [16]

reinforcement, cf. Fig. 6. The interface elements through the concrete cover model Mode I fracture, whereas the interface elements on the circumference of the reinforcement account for the debonding in the concrete/steel interface, which is governed by sliding and separation. Debonding is modelled by the use of Mode I elements with a reduced strength for the separation whereas the sliding is modelled by applying constant shear stiffness after cracking. The remaining part of the concrete body has been modelled assuming linear elastic properties.

The mechanical properties of the interface elements are described from Eq. (4):

$$\sigma = \begin{cases} \sigma_e \varepsilon = E_c \cdot \varepsilon & \text{Pre-cracked state} \\ \sigma_w w = -a_1 \cdot w \cdot f_t & \text{Cracked state} \end{cases} \quad (4)$$

where σ_e is the elastic stress, ε is the elastic strain, $\sigma_w(w)$ is the bridging stress as a function of the crack opening w, a_1 is the slope of the softening branch and f_t refers to either $f_{t,D}$ or $f_{t,C}$ for the debonding and cracking elements respectively. The principles of the cohesive law governing the mechanical properties of cracked concrete, cf. Eq. (4) are described in Fig. 7.

The cohesive laws for the cracking elements, and the debonding elements, are sketched in Fig. 7 where w_{crit} refers to the critical crack opening of the concrete, for which no stress is transferred across the crack. As seen from Eq. (4) the mechanical response of the cracked concrete elements is simplified by the use of a decreasing linear function. For the modelling approach described later in this paper, it is assumed that the strength of the debonding elements, $f_{t,D}$, is 1/10 of the strength of the cracking elements, $f_{t,C}$. The value of $f_{t,D}$ is based on the assumption that the adhesion between the reinforcement and the confining concrete is significantly reduced due to the corrosion process. The fracture energy, G_f, is the energy dissipated per unit area in Mode I in the crack represented by Eq. (5):

$$G_f = \int_0^{W_{crit}} \sigma(w) dw \quad (5)$$

As the fracture energy given from Eq. (5) is not a sufficient measure for the toughness of concrete, [13], the toughness of concrete is often described in terms of the characteristic length, l_{ch}, [27]. The characteristic length was introduced by Hillerborg et al. [13], and is defined by Eq. (6):

$$l_{ch} = \frac{E_c \cdot G_f}{f_t^2} \quad (6)$$

The FE-based cracking model was established and solved by the use of the commercial software TNO DIANA. The problem was solved for plane strain. Damage and cracking were investigated by monitoring the horizontal displacement of nodes in the vertical interface, cf. Fig. 6. The vertical interface consists of 100 elements, regardless of concrete cover thickness. The semi-infinite concrete body as well as the reinforcement domain has been modelled from quadrangular elements, utilizing a total of 2,150–2,772 nodes and 978–1,280 elements depending on the geometry analysed, viz. concrete cover thickness, C, and reinforcement diameter, D.

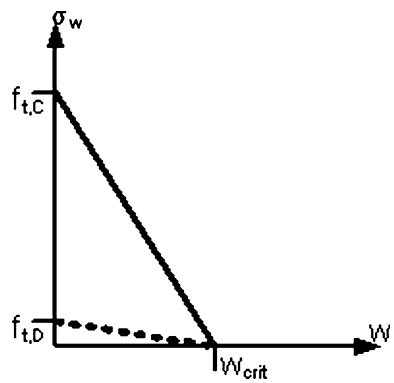

Fig. 7 Schematic of mono-linear softening curve of concrete

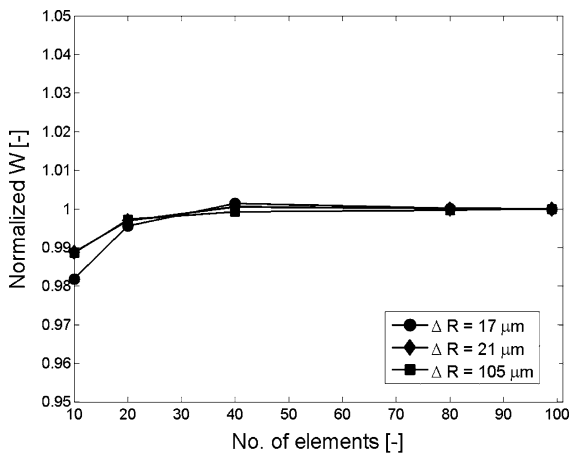

Fig. 8 Normalized results from analyses of mesh convergence

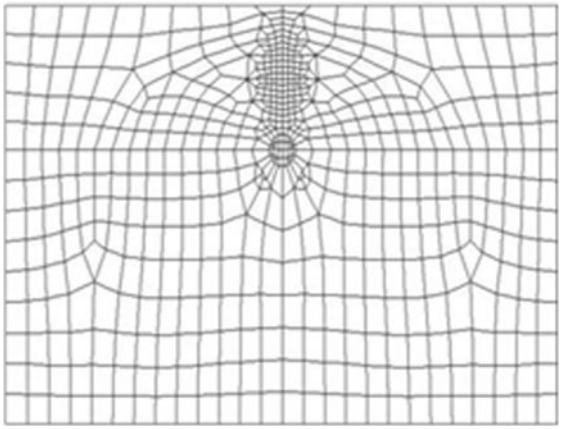

Fig. 9 Mesh for numerical simulations

The number of elements in the interface has proven sufficient. Selected results studying the convergence of the solution as a function of the interface discretisation for FRC2, cf. Table 3, $C = 60$ mm and $D = 20$ mm are depicted in Fig. 8.

The convergence analysis was carried out for 10, 20, 40, 80 and 100 elements in the interface. Results given in Fig. 8 have been normalized with respect to the results for 100 elements. It is seen that maximum deviation is approx. 2 % when increasing the number of elements in the vertical interface from 10 elements to 100 elements and changing the number of elements in the interface from 40 to 100 only affects the results with less than 2 ‰. Hence it is concluded, that the number of elements in the vertical interface is sufficient and it is actually possible to reduce the number of elements to optimize computational time without compromising the accuracy of the simulations significantly.

The mesh used for the numerical simulations is shown in Fig. 9. It is seen that the mesh is significantly denser at the vertical interface in order to increase the accuracy of the numerical simulations. The measures of the semi-infinite concrete body are 100 mm on each side of the reinforcement, except from cover side, which has revealed to be sufficient.

The debonding at the concrete/steel interface is modelled with the assumption that the strength of the "debonding" elements, $f_{t,D}$, is one tenth of the cracking strength $f_{t,C}$. Sensitivity analyses of the numerical model not presented here have established that the influence of $f_{t,D}$ on the damage and cracking is negligible. Thus, the results presented in this paper are not dependent on $f_{t,D}$.

2.3 Limitations for numerical simulations

The numerical model presented above has been used for the assessment of damage and cracking connected with uniform reinforcement corrosion in a semi-infinite concrete body. The authors are aware that uniform corrosion of embedded reinforcement is not to be expected in chloride exposed concrete structures. The term uniform refers to corrosion where the anodic and cathodic reactions take place close to each other and alternate as seen for example in carbonated concrete. Although, the numerical simulations are time-dependent, the model does not account for time-dependent properties of the concrete matrix e.g. creep. Additionally, the model is built on the assumption that the corrosion products do not precipitate into either the concrete matrix or the crack. Hence all corrosion products formed contribute to the build-up of pressure at the concrete/steel interface which reduces the time-to-cracking compared to the case where corrosion products can penetrate into the concrete matrix and/or the crack. Further it is assumed that the corrosion products are hydrated hematite corresponding to a linear expansion coefficient of 2.1 when the steel is corroding.

Due to constraints in the FE-modelling, the minimum corrosion depth modelled is 2.5 μm.

The mechanical model is only capable of simulating damage and cracking in a pre-defined path, cf. Fig. 6. However, the location of the pre-defined crack path, viz. vertically above the reinforcement through the concrete cover, is in accordance with experimental observations, e.g. [5, 21]. Since the present framework for SLD of reinforced concrete structures is based on the formation of cracks in the concrete cover, secondary cracks which are formed subsequently to the crack through the concrete cover and not propagating to the concrete cover surface are not considered in the model.

Overall it is assumed that the numerical model presents a conservative estimate of the connection between extent of uniform corrosion of reinforcement and crack initiation, propagation and crack opening displacement at concrete surface. With this combined effect of the simplifications, of which some are on the safe side and some may be on the unsafe side, it is still possible to simulate the crack formation cf. Sect. 2.4 and this is the basis of the work provided in this paper.

2.4 Verification of numerical model

The numerical model presented above was verified against experimental data obtained by Vu et al. [30]. The experimental observations were carried out in an accelerated corrosion set-up applying a constant current, leading to a constant current density to the steel reinforcement, $i_{cor} = 100$ μA/cm^2. The applied current density is related to the amount of steel consumed by the use of Faraday's law, assuming no other causes for corrosion, uniform corrosion and 100 % current efficiency:

$$X(t) = \frac{M_{Fe} \cdot i_{cor} \cdot \Delta t}{\rho_s \cdot n \cdot F} \quad (7)$$

where M_{Fe} is the molar mass of iron, i_{cor} is the corrosion current density, Δt is time, ρ_s is the density of steel, n is the valence of the corrosion product and F is Faraday's constant. As i_{cor} is the corrosion current normalized with the surface area it will be seen from Eq. (5) that assuming constant corrosion current, i.e. identical conditions for various reinforcement diameters, requires different time scales to form the same corrosion depth, X. Further information about the experimental investigations is given in [30].

Experimental results in terms of concrete surface crack width as a function of time as well as the corresponding numerical simulation are shown in Fig. 10.

The verification of the numerical model shown in Fig. 10 is carried out for $E_c = 42.25$ MPa, $f_t = 3.94$ MPa, $D = 16$ mm and $\eta_{vol} = 2.94$ obtained from [30]. Young's modulus of corrosion products has been set to $E_{cor} = 2.1$ GPa, which is in accordance with experimental observations obtained by Ouglova et al. [22].

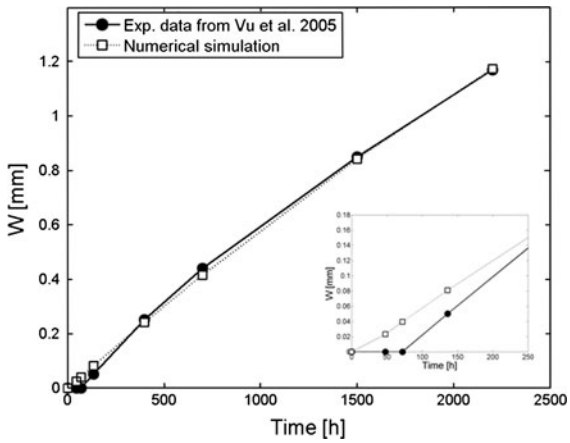

Fig. 10 Verification of numerical model with data from [30] showing concrete surface crack against time in accelerated tests and the corresponding numerical simulation

It is seen from Fig. 10 that the numerical model is capable of simulating the experimental data well for crack widths larger than 0.2 mm. However, the time-to cracking is underestimated when using the model compared to the experimental data, i.e. the numerical model presents a conservative approach to corrosion-induced cracking. This is caused by the limitations of the numerical model, i.e. all solid corrosion products formed contribute to the build-up of pressure at the concrete/steel interface as discussed previously.

3 Parameter study

A parametric study is described in the following, studying the influence of various factors, covering geometrical as well as material aspects. Four key parameters have been varied:

- Reinforcement diameter.
- Concrete cover thickness.
- Tensile strength of concrete.
- Fracture energy of concrete.

Simulations are carried out for various extents of corrosion, i.e. corrosion depths, X.

The geometrical parameters, viz. reinforcement diameter and concrete cover thickness, and the material parameters, viz. tensile strength and fracture energy of concrete, are described in separate subsections in the following.

Table 2 Range of geometrical parameters

Parameter	Identification	Min. value	Max. value	Unit
Concrete cover thickness	C	10	80	mm
Reinforcement diameter	D	5	20	mm
Corrosion depth	X	2.5	50	μm

Table 3 Concrete material properties investigated in numerical simulations

Identification	Concrete properties				Concrete/steel interface properties			
	$f_{t,C}$ (MPa)	w_{crit} (mm)	G_f (J/m^2)	l_{ch} (mm)	$f_{t,D}$ (MPa)	w_{crit} (mm)	G_f (J/m^2)	l_{ch} (mm)
PC1	2	0.2	200	1,500	0.2	0.2	20	15,000
PC2	4	0.2	400	780	0.4	0.2	40	7,800
PC3	6	0.2	600	520	0.6	0.2	60	5,200
FRC1	2	7.5	7,500	58,000	0.2	7.5	750	58×10^4
FRC2	4	7.5	15,000	29,000	0.4	7.5	1,500	29×10^4
FRC3	6	7.5	22,500	19,000	0.6	7.5	2,250	19×10^4

3.1 Geometrical parameters

The range of concrete cover thicknesses and reinforcement diameters used for the numerical simulations are given in Table 2.

The ranges of concrete cover thicknesses and reinforcement diameters given in Table 2 are within limits used for reinforced concrete structures in the civil infrastructure, depending on exposure conditions and structural purpose. The limits of corrosion depths given in Table 2 are negligible compared to the initial diameter of the reinforcement and thus it is assumed not sufficient to compromise the load-bearing capacity of a reinforced structure.

3.2 Concrete material properties

Two parameters, viz. tensile strength and fracture energy of concrete have been varied in order to quantify the influence of material properties on the damage and cracking of concrete covers due to uniform reinforcement corrosion. The fracture mechanical properties of the model, cf. Fig. 6 are given in Table 3.

The six combinations of concrete material properties given in Table 3 are divided into plain concrete (PC1–PC3) and fibre reinforced concrete (FRC1–FRC3). The cohesive relationship of plain concrete does not vary significantly and the critical crack width opening, w_{crit}, of plain concrete is within the range 0.1–0.4 mm dependent on e.g. *w/c* ratio and aggregate size [23]. However, the addition of even relatively small numbers of steel fibres changes the mechanical properties significantly [15, 18]. Values given in Table 3 for the mechanical properties of FRC correspond to the addition of app. 0.5–1.0 vol% of steel fibres and are comparable in terms of critical crack width, w_{crit}, with experimental data [17]. Thus, though data given in Table 3 is not obtained from specific experimental investigations, the parameters reflect typical properties of PC and FRC respectively.

3.3 Constants

Properties of the elastic domains, i.e. the virgin reinforcement steel, the corrosion products and the confining concrete without the interface layers are constant for all numerical simulations. The properties are given in Table 4.

Values for the properties of steel and concrete are typical values for those materials. The mechanical properties of corrosion products depend on the type of

Table 4 Constants for elastic domains

Constant	Identification	Value	Unit
Young's modulus of steel	E_s	210	GPa
Young's modulus of concrete	E_c	31	GPa
Young's modulus of corrosion products	E_{cor}	2.1	GPa
Poisson's ratio of steel	γ_s	0.3	–
Poisson's ratio of concrete	γ_c	0.2	–
Poisson's ratio of corrosion products	γ_{cor}	0.2	–
Linear expansion coefficient of corrosion products	η_{lin}	2.1	–

corrosion product, the conditions under which they are formed, e.g. availability of oxygen, confinement etc. Due to the obvious difficulties in measuring properties of confined corrosion products, the amount of available literature is sparse. The difficulties in assessing the properties of such corrosion products are further described in e.g. [8, 9] describing the development and the time-dependency of the formation of corrosion products in embedded steel. The mechanical properties of corrosion products, viz. Poisson's ratio and Young's modulus, given in Table 4 are obtained by Ouglova et al. [22], and Pease et al. [25] have shown that these values are representative for solid corrosion products formed on embedded reinforcement and further that their influence on the deformations in the corroding reinforcement/concrete interface is relatively weak. The linear expansion of corrosion products corresponds to that of hydrated hematite, $Fe_2O_3 \cdot H_2O$, [6].

4 Results and discussion

The numerical studies of reinforcement corrosion and associated damage and cracking of concrete cover are described in the following. Results are presented in terms of W, concrete surface crack width, and corresponding ΔR, viz. the increase in the radius of the embedded reinforcement caused by the expansion of the corrosion products, see Eq. (3). The section is divided into separate subsections treating damage and cracking of concrete cover respectively. The two limit states already described, viz. the end of the damage phase and crack width limit in the cracking phase, corresponding to $W = W_{\mathrm{lim,c}}$ and $W = W_{\mathrm{lim,d}}$ respectively are illustrated in Fig. 11, showing W as a function of ΔR for $C = 60$ mm, $D = 5$ mm and concrete quality PC2.

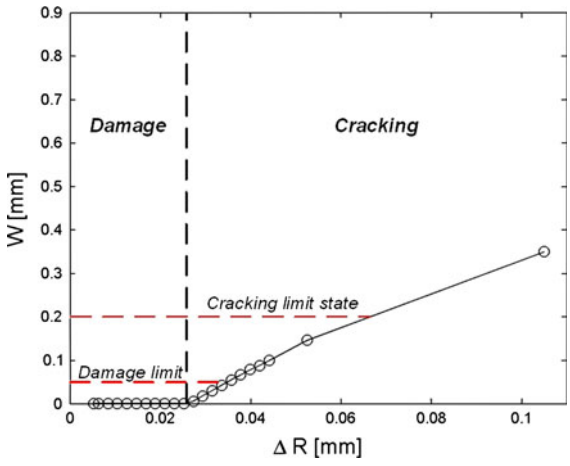

Fig. 11 Calculated crack width at surface, W, for $C = 60$ mm and $D = 5$ mm and PC2, as function of increase in radius of reinforcement ΔR. The limit stages for damage and cracking are illustrated in the figure

It is shown in Fig. 11 that a non-negligible ΔR_{crit}, is required before the damage phase is exceeded, which is also illustrated in Fig. 3. Subsequently, in the cracking phase, W at the concrete surface is almost a linear function of the increase in corrosion products. Similar results have been obtained for other values and combinations of C, D and concrete quality. This linear trend in the $\Delta R - W$ relationship during the cracking phase has been experimentally observed by e.g. Vu et al. [30] and described by Andrade et al. [2].

4.1 Formation of damage and cracking in concrete cover

The damage and cracking of the concrete cover have been simulated for all geometries and combinations of concrete material properties given in Table 3. Damage and cracking in the concrete cover for $C = 60$ mm, $D = 5$ mm, and concrete quality PC2 for various values of the increase of the reinforcement radius are shown in Figs. 12, 13.

Similar plots have been obtained for other combinations of D, C and concrete quality.

Initially a closed crack, i.e. damage, is formed within the concrete cover, cf. Fig. 12. Damage is

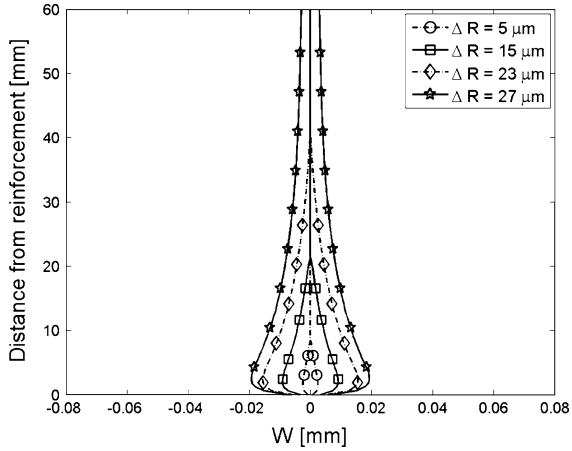

Fig. 12 Damage in cover, for $D = 5$ mm, $C = 60$ mm and PC2

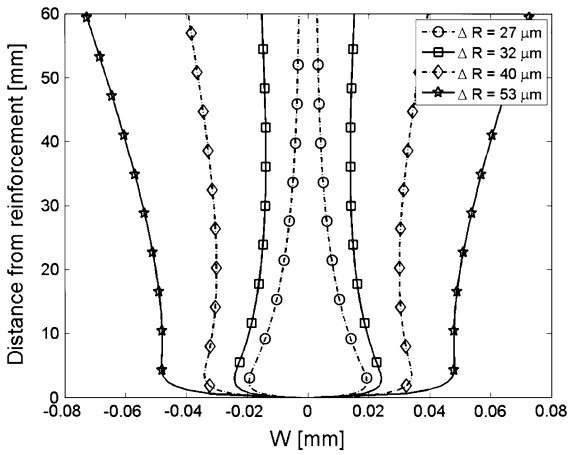

Fig. 13 Cracking in cover, for $D = 5$ mm, $C = 60$ mm and PC2

formed for small values—but not negligible—of ΔR, cf. Figs. 11, 12. The damage front is propagating, as the expansion of the corrosion products increases and eventually it reaches the concrete surface, cf. Fig. 12, and the cracking phase has been reached. Once the cracking phase is reached, the crack opening at the concrete surface is increased rapidly as a function of ΔR, cf. Fig. 13. The formation of a closed crack, which propagates from the surface of the reinforcement towards the concrete cover surface, has been experimentally observed by the application of X-ray equipment on corroding reinforcement embedded in concrete, e.g. Michel et al. [20].

4.2 The damage limit state

Damage and the associated ΔR have been investigated for various combinations of f_t, C, D and w_{crit}. The ranges of the parameter variation are given in Tables 2 and 3. The increase in the reinforcement radius required to reach the damage limit state, viz. ΔR_{crit}, depends on the concrete material properties and the geometry of the reinforced concrete body, i.e. reinforcement diameter and concrete cover thickness. In general, the simulations reveal that the limit of the damage phase, i.e. $W = W_{lim,c}$, has been reached for $\Delta R_{crit} = 13$–46 μm for PC and $\Delta R_{crit} = 13$–57 μm for FRC for $10 \leq C \leq 60$ mm and $5 \leq D \leq 20$ mm. The influence of the various parameters is seen from Figs. 14, 15, 16, 17, 18, 19, 20 and 21.

4.2.1 *The influence of concrete tensile strength*

The critical increase in reinforcement radius, ΔR_{crit}, as a function of the tensile strength, f_t, is shown in Figs. 14, 15 for plain concrete (PC1–PC3) for $D = 5$ mm and $D = 20$ mm respectively.

The same relationship, but for fibre reinforced concrete (FRC1–FRC3), is given in Figs. 16, 17 for $D = 5$ mm and $D = 20$ mm respectively.

Figs. 14, 15, 16 and 17 illustrate that there is a linear correlation between ΔR_{crit}, and f_t for $C = 30$–60 mm when $D = 5$ mm and $C = 40$–80 mm when $D = 20$ mm. For smaller covers the simulations do not reveal the same relationship. However, this is probably due to the limitations of the numerical model since the minimum corrosion depth in the numerical model is 2.5 μm, corresponding to $\Delta R \approx 5$ μm which is presumably greater than the critical increase of the reinforcement radius caused by the corrosion process ΔR_{crit} for these smaller covers. Results for such small covers are not presented.

The linear correlation in the $f_t - \Delta R_{crit}$ relationship is valid for PC as well as FRC, cf. Figs. 14, 15, 16 and 17. However, comparing the figures concerning PC (Figs. 14, 15) with the figures concerning FRC (Figs. 16, 17) it can be seen that the regression line for FRC lies higher compared to that of PC. This indicates that the propagation of the damage front is restrained when the fracture energy of the concrete matrix is increased.

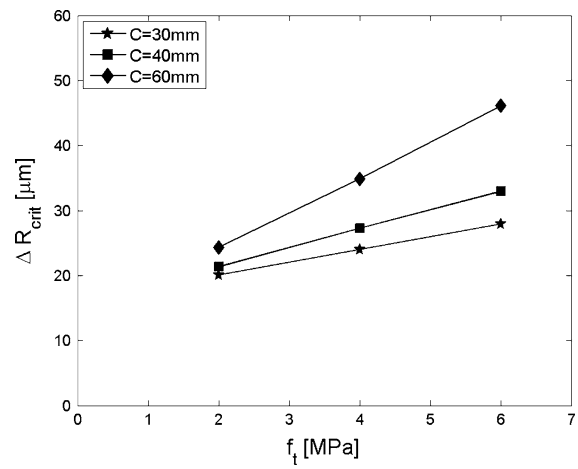

Fig. 14 ΔR_{crit} versus f_t for $D = 5$ mm, PC1–PC3

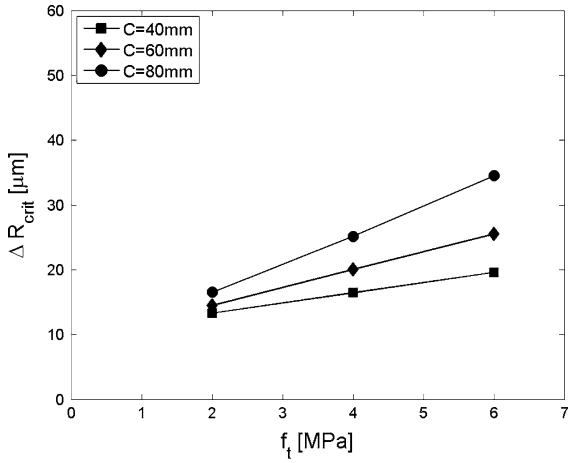

Fig. 15 ΔR_{crit} versus f_t for $D = 20$ mm, PC1–PC3

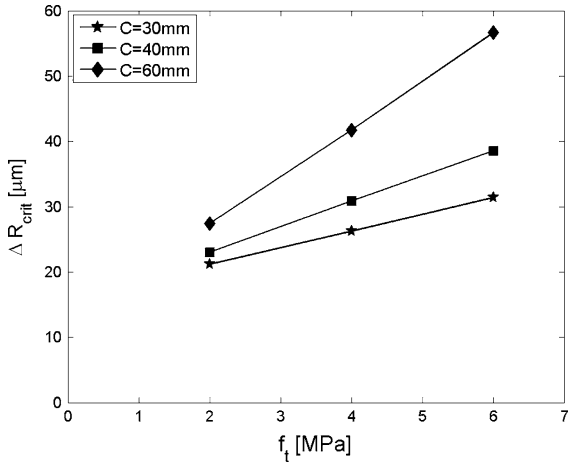

Fig. 16 ΔR_{crit} versus f_t for $D = 5$ mm, FRC1–FRC3

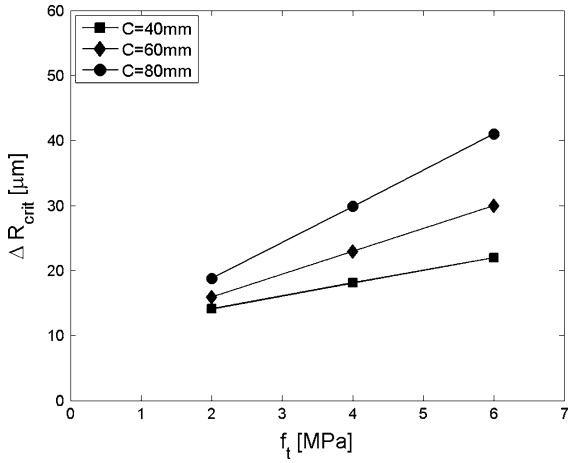

Fig. 17 ΔR_{crit} versus f_t for $D = 20$ mm, FRC1–FRC3

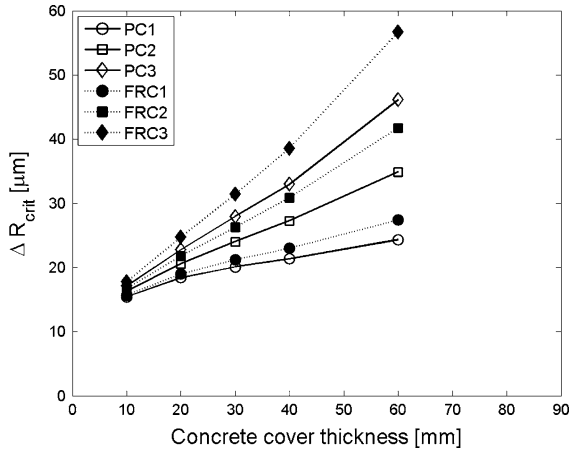

Fig. 18 ΔR_{crit} versus C for various f_t and w_{crit}, $D = 5$ mm

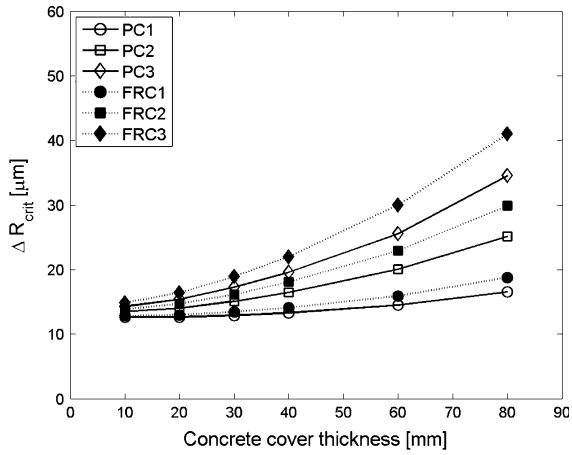

Fig. 19 ΔR_{crit} versus C for various f_t and w_{crit}, $D = 20$ mm

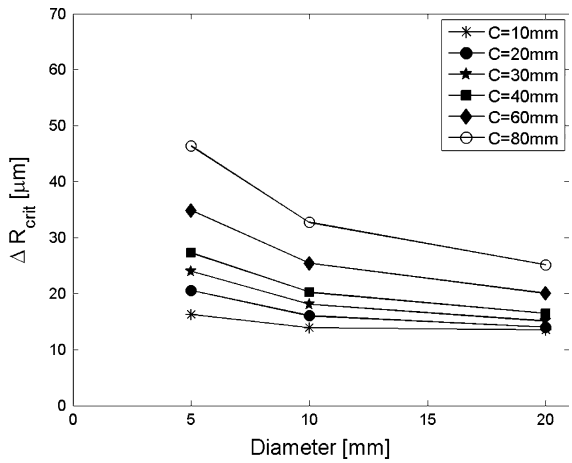

Fig. 20 ΔR_{crit} versus D for various C, PC2

4.2.2 The influence of fracture energy

The influence of the fracture energy of the concrete matrix on the relationship between ΔR_{crit} and damage is seen from Figs. 18, 19 for $D = 5$ mm and $D = 20$ mm respectively for different concrete cover thicknesses.

As can be seen from Figs. 18, 19 the influence of increasing the fracture energy of the concrete matrix becomes more pronounced when the tensile strength is increased. As an example, the increase in ΔR_{crit} for $C = 60$ mm and $f_t = 2$ MPa is 17 and 9 % for $D = 5$ mm and $D = 20$ mm respectively, whereas the increase for the same cover and diameters but with an increased tensile strength, $f_t = 6$ MPa, is 23 and 17 % respectively. The increase in ΔR_{crit} between PC and FRC is an increasing function of the concrete cover thickness, cf. Figs. 18, 19. Hence, the geometrical influence of the concrete cover thickness is important. For small covers, the increase in ΔR_{crit} by shifting from PC to FRC is negligible, whereas the gain is quite significant for larger concrete cover thicknesses. The explanation of this phenomenon is as follows; for the smallest cover thicknesses, the cohesive stress associated with the end of the damage phase is almost constant (and equal to the tensile strength) due to the small crack openings for both PC and FRC. The result is little difference in resistance and ΔR_{crit} between the PC and FRC cases. For the largest concrete covers the cohesive stress at the end of the damage state is far from constant along the crack due to the larger crack openings while the stress is closer to constant in the FRC case because of the more flat softening curve—thus giving rise to a significant difference in resistance and ΔR_{crit}.

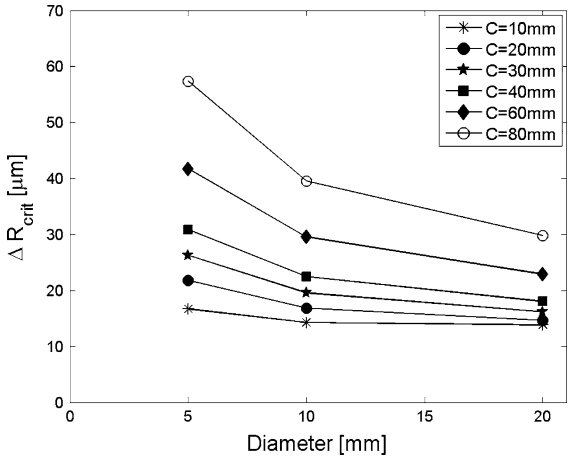

Fig. 21 ΔR_{crit} versus D for various C, FRC2

4.2.3 The influence of reinforcement diameter

The critical increase of the reinforcement radius required to reach the damage limit state varies with the diameter of the reinforcement. The critical increase of the radius of the embedded reinforcement at the damage limit state as a function of the reinforcement diameter is shown for various thicknesses of concrete cover for PC2 and FRC2 in Figs. 20, 21 respectively.

The influence of the reinforcement diameter on the critical increase of the reinforcement radius to reach the end of the damage phase is very limited for small covers, viz. almost the same corrosion depth initiates the crack at the concrete surface, cf. Figs. 20, 21. However, increasing the concrete cover thickness results in a more pronounced dependence between ΔR_{crit} and the reinforcement diameter. For all covers, the relationship between ΔR_{crit} and reinforcement diameter descends asymptotically, indicating that beyond a certain value of reinforcement diameter there is little variation in the ΔR_{crit} versus D relationship.

4.3 The cracking limit state

Cracking of the concrete cover is investigated for the same parameters as the damage phase, viz. cover thickness, reinforcement diameter and concrete material properties, cf. Tables 2 and 3. The cracking limit state is illustrated in Fig. 11. The cracking phase and the associated crack formation in the concrete cover are illustrated in Fig. 13 whereas Figs. 22, 23, 24 and 25 depict the opening at the concrete cover surface. Figure 13 illustrates the crack formation in the concrete cover when the damage front has reached the concrete cover surface. It can be seen that once the damage limit is reached, the crack mainly opens at the concrete surface when the radius of the reinforcement is increased.

The increase in reinforcement radius required to reach $W = W_{lim,c}$ as a function of concrete cover thickness and reinforcement diameter is shown in Figs. 22, 23, 24 and 25 respectively. Results from the numerical simulations reveal that the cracking limit state is reached for $\Delta R = 38$–74 μm for PC and $\Delta R = 42$–105 μm for FRC for $10 \leq C \leq 60$ mm and $5 \leq D \leq 20$ mm.

4.3.1 The influence of fracture energy

The influence of the fracture energy, G_f, to reach the cracking limit state, is analyzed in the following and illustrated as a function of the concrete cover thickness for all concrete qualities investigated and $D = 5$ mm and $D = 20$ mm in Figs. 22, 23.

For PC the required ΔR to exceed the cracking limit state shows only a negligible variation as a function of the cover thickness for constant reinforcement diameter, cf. the hollow symbols in Figs. 22, 23. Comparing PC and FRC with the same tensile strength it is seen that the addition of fibres results in a substantial increase in ΔR for $D = 5$ mm, cf. Fig. 22. Moreover, this effect gets more pronounced for increasing tensile strength of the concrete matrix. For $D = 20$ mm, the increase in ΔR is not as clear as for $D = 5$ mm, when comparing PC and FRC, cf. Fig. 23.

4.3.2 The influence of reinforcement diameter and cover thickness

The influences of geometry, viz. reinforcement diameter and concrete cover thickness are shown in Figs. 24, 25. The figures illustrate the relationship between ΔR for $W = W_{\mathrm{lim,c}}$ and the diameter of reinforcement for $C = 10$–80 mm, for PC2 and FRC2, respectively.

For all cover thicknesses, regardless of concrete fracture energy the relationship descends asymptotically. However, it will also be seen for PC, i.e. Fig. 24, that ΔR for $D = 5$ mm increases up to $C = 30$ mm, after which ΔR is a decreasing function of the concrete

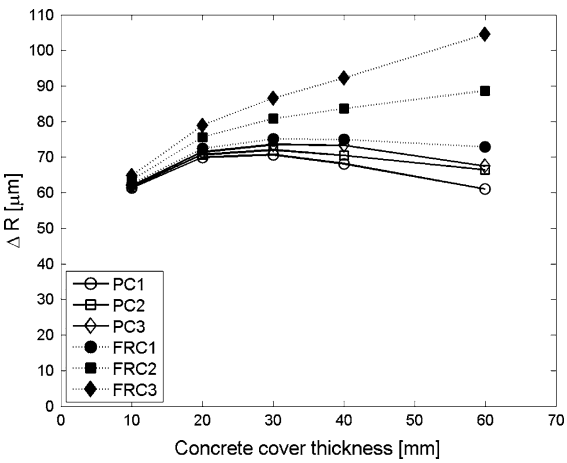

Fig. 22 ΔR (for $W = W_{\mathrm{lim,c}}$) versus C, $D = 5$ mm

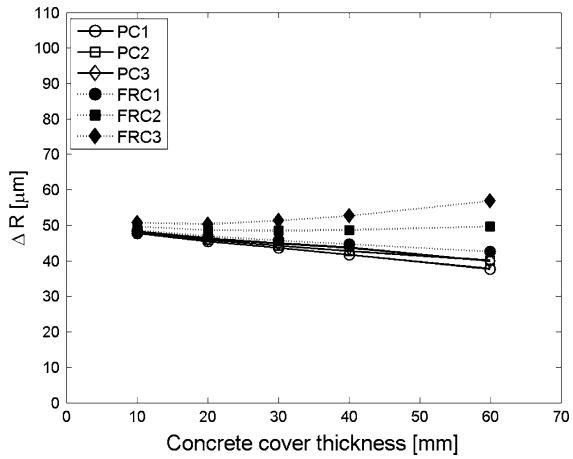

Fig. 23 ΔR (for $W = W_{\mathrm{lim,c}}$) versus C, $D = 20$ mm

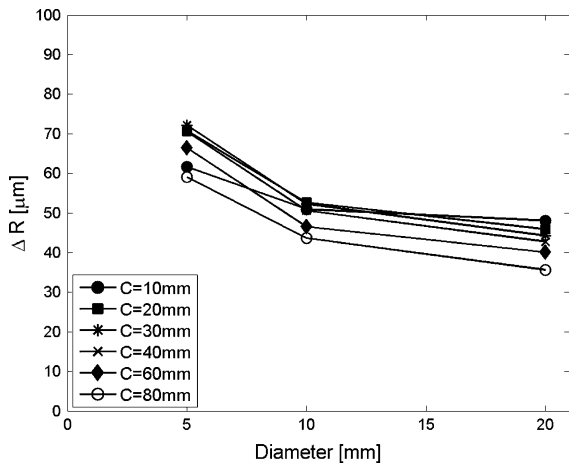

Fig. 24 ΔR (for $W = W_{\mathrm{lim,c}}$) versus D for various C, PC2

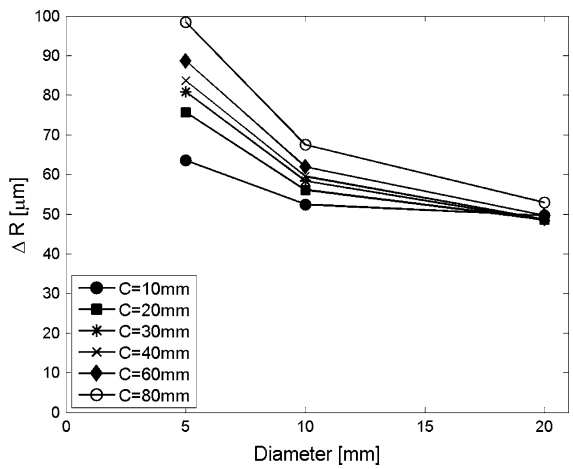

Fig. 25 ΔR (for $W = W_{\mathrm{lim,c}}$) versus D for various C, FRC2

cover thickness. The same tendency is seen for $D = 10$ mm. The same phenomenon is not seen for FRC, since a larger cover always results in an increased ΔR, cf. Fig. 25.

The increased cover thickness, which was seen as beneficial with regard to the damage limit, cf. previous section and Figs. 20, 21, is a drawback with regard to the cracking limit state, cf. Figs. 24, 25. For PC, the possibility of redistributing stresses is overshadowed by the geometrical aspect of the increased cover thickness, i.e. an increased rotation of the cover concrete around the rotation point (the center of the reinforcement), because the crack opening due to rotation is proportional to the concrete cover thickness. For FRC, the beneficial effect of an increased concrete cover thickness is not cancelled out by the increased rotation connected with the increasing concrete cover thickness due to the favorable stress distribution over the length of the crack even for large crack openings.

Comparing the required ΔR for $W = W_{\mathrm{lim,c}}$ ($W = 0.2$ mm) for the same tensile strength, but different fracture energy, viz. $w_{\mathrm{crit}} = 0.2$ mm and $w_{\mathrm{crit}} = 7.5$ mm cf. Figs. 24, 25 respectively it can be seen that ΔR is increased significantly when the fracture energy is increased and that this effect, as discussed before, is larger for larger concrete covers.

Assuming that service life of reinforced concrete structures can be defined as being exceeded when a given W is reached, cf. considerations given above, service life can be increased significantly by increasing the fracture energy of the concrete matrix, assuming the same exposure conditions, transport properties of the concrete matrix, etc. for PC and FRC.

4.4 General discussion

Results obtained for the simulation of damage and cracking in concrete covers due to uniform reinforcement corrosion, presented in the previous sections are discussed in the following, and comparisons with data from the literature are given, in the relevant passages.

Results from the numerical simulations have been presented in terms of W and corresponding ΔR. The reason for this is twofold: (1) The pressure built up at the concrete/steel interface is directly connected to the expansion of the corrosion products. Relative changes in volume of the most (non-chloride containing) corrosion products formed on embedded steel varies significantly, within a range of 2–6.3 cf. Herholdt et al. [12] and Table 1. Thus the corrosion depth is not a direct measure for the increase of the radius of the reinforcement and the corresponding build-up of pressure and therefore it is the authors' opinion that it is a misleading to present crack formation with the associated corrosion depth. (2) The simulations are carried out for only one type of corrosion products. In this case there is a unique relationship between X and ΔR. However, since most results in the literature concerning cracking in concrete covers are presented in terms of W and the assumed corresponding corrosion depth, comparisons of simulated data and experimental data from the literature will be based upon the corrosion depth, X.

Experimental results reported in the literature concerning the cracking phase are given in terms of assumed corrosion depth, X_{crit}, and related W at concrete surface, e.g. $X_{\mathrm{crit}} = 15$–18 μm for $W \approx 50$ μm [2], $X_{\mathrm{crit}} = 10$–65 μm for $W \approx 50$ μm [30] and $X_{\mathrm{crit}} = 15$–30 μm for $W \approx 50$ μm [1] for varying tensile strength of concrete, f_t, concrete cover thickness, C, and reinforcement diameter, D. Values of X_{crit} given above have not been measured but are calculated based on Faraday's law, Eq. (7), assuming 100 % current efficiency, which may be incorrect and thus used as an explanation for the scatter of the results. However, the results given in the literature corresponds well with results from the numerical simulations presented here.

The model has been compared with accelerated experimental results presented in [30], cf. Fig. 10. The numerical model reproduces the experimental results very accurately. Though there is a limit in the prediction of the end of the damage phase, viz. $W = 50$ μm, it is the authors' opinion that there is a good correlation between numerical and experimental results. The difference in the prediction of the end of the damage phase may be reduced if a corrosion accommodating region [20] around the reinforcement is taken into account. However, more knowledge gained from experimental observations about the properties of this corrosion accommodating region is required before it can be implemented in the model, cf. explanation given later in this section.

The formation of damage and the associated cross section reduction of the reinforcement are in themselves not sufficient to affect the overall integrity of the structure as the corrosion depth is within the range of a few microns to create damage. Hence, in the light

of that it may be possible to extend the service life by including the damage phase in the service life. Note that this only refers to uniform reinforcement corrosion and not other types of corrosion like e.g. pitting corrosion, which might have fatal consequences to the overall integrity and functionality of a reinforced concrete structure, even for relatively limited corrosion attacks.

The existence of the corrosion accommodating region is recognized by the authors. However, since the properties of this corrosion accommodating region, e.g. porosity and thickness have not been thoroughly described on the basis of experimental observations, it was omitted for the numerical simulations. Furthermore, it is assumed that the corrosion products do not precipitate into the crack formed.

Finally, it is noted that the model does not take the formation of secondary cracks into account. Thus the expansive nature of the corrosion products contributes only to the formation of the crack vertically through the concrete cover which may result in an underestimation of the corrosion products required to open up the crack to a pre-defined W.

Taking those three limitations of the model into account, the numerical model presents a conservative estimate of the duration of the damage phase and the ΔR–W relationship for the cracking phase. Thus the results presented here forms a conservative approach.

4.5 Interpretation of data in an SLD perspective

The results in terms of the increase of the reinforcement radius required to reach the damage or cracking limit state are related to time in order to set them into a service life perspective. According to e.g. Bertolini et al. [4], corrosion rates can be divided into six categories. The corrosion rate is governed by, among other things, the oxygen availability, concrete resistivity and extent of carbonation. The categories are given in Table 5.

Assuming uniform corrosion and constant current rate, the $X(t)$ can be calculated based on Faraday's law, cf. Eq. (7).

As previously mentioned, the damage phase is reached for $\Delta R = 13$–46 μm and $\Delta R = 13$–57 μm for PC and FRC, respectively ($10 \leq C \leq 60$ mm and $5 \leq D \leq 20$ mm). Results for the time required to form this thickness of corrosion products are given in Table 6, along with corresponding C and D.

From Table 6 it appears that it is possible to increase the service life of a reinforced concrete structure by at least a year in most situations by accepting the damage phase as part of the service life. For low corrosion rates, the gain in service life, on the assumptions previously given is significant: up to 29 years, cf. Table 6.

The time required to reach the cracking limit state, is calculated in the same way as above, assuming uniform corrosion, constant corrosion rate and no movement of corrosion products into the crack or the bulk concrete. The required increase of the radius of the embedded reinforcement to reach the cracking

Table 5 Categorization of corrosion current densities

Corrosion rate category	Corrosion current density (mA/m^2)
Negligible	<0.2
Low	0.2–0.4
Moderate	0.4–0.9
Intermediate	0.9–4.3
High	4.3–8.5
Very high	>8.5

Modified from [4]

Table 6 Time to reach damage limit, based on Faraday's law

	ΔR limits (μm)	C (mm)	D (mm)	Required time [years]				
				Low $i_{cor} = 0.2$ (mA/m^2)	Moderate $i_{cor} = 0.4$ (mA/m^2)	Intermediate $i_{cor} = 0.9$ (mA/m^2)	High $i_{cor} = 4.3$ (mA/m^2)	Very high $i_{cor} = 8.5$ (mA/m^2)
PC	13	10	20	6.5	2.6	1.3	0.3	0.1
	46	60	5	23	9.2	4.6	0.9	0.5
FRC	13	10	20	6.5	2.6	1.3	0.3	0.1
	57	60	5	29	11	5.7	1.1	0.6

Table 7 Time to reach cracking limit state, based on Faraday's law

	ΔR limits (μm)	C (mm)	D (mm)	Required time [years]				
				Low $i_{cor} = 0.2$ (mA/m^2)	Moderate $i_{cor} = 0.4$ (mA/m^2)	Intermediate $i_{cor} = 0.9$ (mA/m^2)	High $i_{cor} = 4.3$ (mA/m^2)	Very high $i_{cor} = 8.5$ (mA/m^2)
PC	38	60	20	19	7.6	3.8	0.8	0.4
	74	30	5	37	15	7.4	1.5	0.7
FRC	42	60	20	21	8.4	4.2	0.8	0.4
	105	60	5	53	21	11	2.1	1.1

limit state is, as already explained, $\Delta R = 38$–74 μm for PC and for FRC $\Delta R = 42$–105 μm for $10 \leq C \leq 60$ mm and $5 \leq D \leq 20$ mm. Results are given in Table 7.

The results given in Table 7 indicate that the service life of a reinforced concrete structure can, under certain conditions, be increased significantly allowing cracks up to $W = 0.2$ mm in the cover concrete, assuming that the cracks do not influence the corrosion rate. Furthermore, it is worth noticing that the gain in time is significant comparing FRC with PC, viz. approximately 50 %, comparing maximum values of ΔR of PC and FRC respectively in Table 7.

5 Conclusions

Cracking of concrete cover due to uniform reinforcement corrosion has been investigated by the use of an FE model based on the fictitious crack model. Simulations have been carried out for various combinations of concrete cover thickness, reinforcement diameter, and concrete material properties to identify governing parameters for damage and subsequent cracking of the concrete cover. Based on the investigation, it is concluded:

- Results from the numerical model compare well with experimental observations from the literature. However, the time-to cracking is underestimated by the numerical model.
- The tensile strength of the concrete is the most important parameter with regard to the damage limit state.
- Increasing the concrete cover thickness always increases the ΔR associated with reaching the damage limit state.
- Increasing the concrete cover thickness only increases the ΔR associated with the cracking limit state, if the fracture energy is high—with a low fracture energy increasing the cover thickness can lead to a reduced ΔR due to geometrical effects associated with the crack opening profile.
- Increasing the fracture energy has little effect on the ΔR associated with the damage limit state due to the small crack openings associated with this state.
- Increasing the fracture energy extends the ΔR associated with the cracking limit state.

The paper presents simplified analyses of the results from the mechanical model and sets them into SLD perspectives. Based on these calculations, significant service life may be gained allowing the formation of small cracks in the concrete cover. Estimates given in the paper show up to 37 years of additional service life if cracks up to $W = 0.2$ mm are allowed in the concrete cover for PC. This gain in service life can be increased by an additional 50 % if the cover consists of FRC compared to PC.

6 Future work

Based on the results, discussions and conclusions presented it is suggested to couple the numerical mechanical model with a model for the formation of corrosion cells on embedded reinforcement as shown by e.g. Michel et al. [19]. Establishing a link between fracture mechanical models and electrochemical models would be the next step towards operational SLD models including the propagation phase. However, before the model could be used within such an SLD framework it should be verified with more experimental data.

A link between the changed transport properties of the concrete due to the formation of cracks and the corrosion rate of embedded reinforcement should be established in future work, in order to establish a more realistic link between reinforcement corrosion and the width of corrosion-induced cracks.

Given that the corrosion accommodating region around the reinforcement plays a significant role in the time-to cracking it is of importance to clarify experimentally the properties of the corrosion accommodating region. Hence, it is suggested that experimental observations concerning, among other things, the influence of *w*/*c* ratio, concrete composition, reinforcement diameter and corrosion rate on the properties of the corrosion accommodating region should be carried out. The experimental observations should be carried out as non-destructive measurements, e.g. X-ray measurements and accompanying inverse analysis of results as done by Michel et al. [20].

Moreover, the mechanical properties of corrosion products under confinement should be analyzed experimentally to verify the value used for the present work.

Finally, models for the impact of cross sectional reduction on the structural performance should be developed to cover chloride-induced corrosion where inhomogeneous corrosion and formation of different types of corrosion products is likely to occur.

Acknowledgments The first author gratefully acknowledges the full financial support of the PhD project "Application of FRC in Civil Infrastructure" by the Danish Agency for Science, Technology and Innovation, COWI A/S, DTU, Bekaert NV, Grace and the Danish Road Directorate. The second author acknowledges the financial support from Femern Bælt A/S, Sund & Bælt Holding A/S, and the Danish Agency for Science, Technology and Innovation.

References

1. Alonso C, Andrade C, Rodriguez J, Diez JM (1998) Factors controlling cracking of concrete affected by reinforcement corrosion. Mater Struct 31:435–441
2. Andrade C, Alonso C, Molina FJ (1993) Cover cracking as a function of bar corrosion: part 1-experimental test. Mater Struct 26:453–464
3. Bazant ZP (1979) Physical model for steel corrosion in concrete sea structures—application. J Struct Div ASCE 105:1155–1166
4. Bertolini L, Elsener B, Pedeferri P, Polder R (2004) Corrosion of steel in concrete, prevention, diagnosis, repair. Wiley, Weinheim
5. Cabrera JG (1996) Deterioration of concrete due to reinforcement steel corrosion. Cement Concrete Comp 18:47–59
6. Caré S, Nguyen QT, L'Hostis V, Berthaud Y (2008) Mechanical properties of the rust layer induced by impressed current method in reinforced mortar. Cement Concrete Res 38:1079–1091
7. Chernin L, Val DV, Volokh KY (2010) Analytical modelling of concrete cover cracking caused by corrosion of reinforcement. Mater Struct 43:543–556
8. Chitty W-J, Dillmann P, L'Hostis V, Lombard C (2005) Long-term corrosion resistance of metallic reinforcements in concrete—a study of corrosion mechanisms based on archaeological artefacts. Corros Sci 47:1555–1581
9. Demoulin A, Trigance C, Neff D, Foy E, Dillmann P, L'Hostis V (2010) The evolution of the corrosion of iron in hydraulic binders analysed from 46- and 260-year-old buildings. Corros Sci 52:3168–3179
10. DuraCrete (2000) Probabilistic performance based durability design of concrete structures. The European Union-Brite EuRam III
11. *fib* (2006) fib Bulletin 34, Model code for service life design. Tech. Rep. fib Bulletin 34, International Federation for Structural Concrete (fib)
12. Herholdt A, Justesen CFP, Nepper-Christensen P (1985) Beton Bogen. Aalborg Portland A/S, Aalborg
13. Hillerborg A, Modéer M, Petersson P-E (1976) Analysis of crack formation and crack growth in concrete by means of fracture mechanics and finite elements. Cement Concrete Res 6:773–782
14. Isgor BO, Razaqpur GA (2006) Modelling steel corrosion in concrete structures. Mater Struct 39:291–302
15. Kazemi MT, Fazileh F, Ebrahiminiezhad MA (2007) Cohesive crack model and fracture energy of steel-fiber-reinforced-concrete notched cylindrical specimens. J Mater Civil Eng 19:884–890
16. Liu Y, Weyers RE (1998) Modeling the time-to-corrosion cracking in chloride contaminated reinforced concrete structures. ACI Mater J 95:675–681
17. Löfgren I, Olesen JF, Flansbjer M (2005) Application of WST-method for fracture testing of fibre-reinforced concrete. NT Technical Report, Norway
18. Löfgren I, Stang H, Olesen JF (2008) The WST method, a fracture mechanics test method for FRC. Mater Struct 47:197–211
19. Michel A, Solgaard AOS, Geiker MR, Stang H, Olesen JF (2010) Modeling formation of cracks in concrete cover due to reinforcement corrosion. In: Proceedings for FraMCos-7—7th International Conference on Fracture Mechanics of Concrete and Concrete Structures, Jeju
20. Michel A, Pease BJ, Geiker MR, Stang H, Olesen JF (2011) Monitoring reinforcement corrosion and corrosion-induced cracking using non-destructive X-ray attenuation measurements. Cement Concrete Res 41:1085–1094
21. Molina FJ, Alonso C, Andrade C (1993) Cover cracking as a function of rebar corrosion: part 2—numerical model. Mater Struct 26:532–548
22. Ouglova A, Berthaud Y, François M, Foct F (2006) Mechanical properties of an iron oxide formed by corrosion in reinforced concrete structures. Corros Sci 48:3988–4000
23. Pease BJ, Skoček J, Geiker MR, Stang H, Weiss J (2007) The wedge splitting test: influence of aggregate size and

water-to-cement ratio. In: Proceedings of the RILEM Transport Mechanisms Workshop, Ghent
24. Pease BJ, Michel A, Stang H (2012) Quantifying movements of corrosion products in reinforced concrete using X-Ray attenuation measurements. In: Proceedings for 2nd International Conference on Microdurability, Amsterdam
25. Pease BJ, Michel A, Thybo AEA, Stang H (2012) Estimation of elastic modulus of reinforcement corrosion products using inverse analysis of digital image correlation measurements for input in corrosion-induced cracking model. In: Proceedings of 6th International Conference on Bridge maintenance, safety and management (IABMAS), Lake Como
26. Rasheeduzzafar Al-Saadoun SS, Al-Gahtani AS (1992) Corrosion cracking in relation to bar diameter, cover and concrete quality. J Mater Civil Eng 4:327–342
27. Rosselló C, Elices M, Guinea GV (2005) Fracture of model concrete: 2. Fracture energy and characteristic length. Cement Concrete Res 36:1345–1353
28. Suda K, Misra S, Motohashi K (1993) Corrosion products of reinforcing bars embedded in concrete. Corros Sci 35: 1543–1548
29. Tuutti K (1982) Corrosion of steel in concrete. Report 4–82. Swedish Cement and Concrete Research Institute, Stockholm, Sweden
30. Vu K, Stewart MG, Mullard J (2005) Corrosion-induced cracking: experimental data and predictive models. ACI Struct J 102:719–726

Rising awareness for the need of sustainable design of reinforced concrete structures demands among others tools for both qualitative and quantitative service life prediction.

This Ph.D. thesis proposes a framework for service life prediction of reinforced concrete structures in corrosive environments. Combined simulations of ingress of aggressive substances, electrochemical, and mechanical processes, are used to predict the time-to initiation and propagation of reinforcement corrosion as well as corrosion-induced concrete damages.

DTU Civil Engineering
Department of Civil Engineering
Technical University of Denmark

Brovej, Building 118
2800 Kgs. Lyngby
Telephone 45 25 17 00

www.byg.dtu.dk

ISBN: 9788778773494
ISSN: 1601-2917